TECHNISCHE UNIVERSITÄT WIEN
Vienna University of Technology

IAP

Dissertation

Complex oxide surfaces studied at the atomic scale with AFM/STM and DFT

ausgeführt zum Zwecke der Erlangung des akademischen Grades eines Doktors der technischen Wissenschaften unter der Leitung von

Doc. Mgr. Martin Setvín, PhD

und

Univ.-Prof. Dipl. Ing. Dr. techn. Dr. h.c. Ulrike Diebold

Institut für Angewandte Physik (E134)

eingereicht an der Technischen Universität Wien,
Fakultät für Physik

durch

MSc Igor Sokolović

01652652

Wien, September 2021

Die approbierte gedruckte Originalversion dieser Dissertation ist an der TU Wien Bibliothek verfügbar.
The approved original version of this doctoral thesis is available in print at TU Wien Bibliothek.
TU Bibliothek Your knowledge hub WIEN

I am grateful to my Mentors for making this Thesis happen:

Martin Setvin
for teaching and guiding me through the world of AFM/STM,

Michael Schmid
for always having advice, usually for the most difficult parts,

Michele Reticcioli and Cesare Franchini
for teaching and guiding me through the world of DFT,

and

Ulrike Diebold
for introducing me to Surface Science and making me forever in love with the field.

Ich danke dem Institut für Angewandte Physik und der Technischen Universität Wien für die Bereitstellung eines hervorragenden Forschungsumfelds, und dem Fonds zur Förderung der wissenschaftlichen Forschung für die finanzielle Unterstützung durch die Doktorandenschule “Solids4Fun” (W 1243) und das “SuPer”-Projekt (P32148-N36).

Захвалан сам мојој љубави Маји на свој подршци кроз ове године.
Захвалан сам Давиду, Драгани, Верици и Милану што су увек веровали у мене.
Ову тезу од срца посвећујем вама.

Die approbierte gedruckte Originalversion dieser Dissertation ist an der TU Wien Bibliothek verfügbar.
The approved original version of this doctoral thesis is available in print at TU Wien Bibliothek.
TU Bibliothek Your knowledge hub WIEN

Abstract

The largest portion of solid-state matter on Earth naturally appears in the form of oxides, which constitute the majority of its crust. Most elements in the periodic table are found throughout nature in an oxide form, and the extraction of pure elements usually proceeds through reduction from their corresponding oxide. Although much more complex than pure elemental solids, their widespread availability and stability in atmospheric conditions is responsible for a vast research interest in their bulk, powder, and surface properties. Many oxides were already shown to exhibit a plethora of intriguing physical phenomena at a wide range of thermodynamic and electromagnetic conditions. In the upcoming years, the technical application of oxides in well-controlled processes, such as hetero/homogeneous catalysis and electronics at the nanometer or sub-nanometer scale, are projected to increase in both magnitude and scope.

Each material interacts with its environment through its exposed facets – the surfaces, where the solids are available for various applications. Surface Science employs a variety of experimental and theoretical techniques to investigate processes occurring at the different facets of solids. In recent years, the study of surfaces has achieved atomic precision, allowing observations of fundamental phenomena occurring at the atomic level. In this Thesis, a Surface Science approach is employed to studying several oxide surfaces in well-controlled conditions such as the ultrahigh vacuum (UHV) and low temperatures. Revealing fundamental properties and mechanisms under these conditions constitutes a strong foundation for understanding and predicting the behavior of surfaces in less controlled environments. In the research that led to this Thesis, surfaces of several complex oxide surfaces were investigated, with the largest focus on two model oxides: rutile TiO_2 and the $SrTiO_3$.

Chapter 1 introduces the Surface Physics techniques used in this Thesis. The main emphasis is put on the experimental non-contact Atomic Force Microscopy (nc-AFM) and Scanning Tunneling Microscopy (STM) techniques that readily image surfaces with a resolution down to a single atom, and the theoretical Density Functional Theory (DFT) approach that realistically models quantum mechanical properties of surface atoms and their interactions. These techniques were commonly applied together, to provide complementary information regarding a given physical system.

Chapter 2 focuses on the interaction of a model transition-metal binary oxide surface, the $TiO_2(110)$ surface, with small gas molecules, with a resolution of a single atom or a single electronic orbital. The polaronic ground state of the reduced $TiO_2(110)$ is introduced, which is shown using AFM/STM and DFT to change in the presence of adsorbed molecules. The polaronic ground state is slightly altered by the presence of weakly adsorbed CO, while it completely vanishes in the presence of strongly adsorbed O_2, which uses the polaronic electrons to form strong chemical bonds to the underlying surface. These results illuminate and resolve many long-standing questions about the fundamental processes occurring at this technologically-relevant surface.

Chapter 3 focuses on the bulk-terminated model perovskite oxide surface, $SrTiO_3(001)$. The surface was created by cleaving single crystal samples *in situ*, i.e., in UHV. Such bulk-terminated surfaces are shown to be the closest to pristine at the atomic level, and they were obtained through a strain-assisted ferroelectric transition during cleaving. A novel cleaving procedure is introduced and systematically studied, and the cleaved surfaces are shown to exhibit several intriguing phenomena as a consequence of their bulk-termination. The TiO_2 termination of $SrTiO_3(001)$ undergoes an insulator-to-metal transition during cleaving, while the SrO termination remains semiconducting. The two terminations are laterally alternating at the surface, and switch at polariziation domain walls. Depending on the amount of external doping (with niobium), cleaved surfaces exhibit different morphologies, with the size of two different surface terminations ranging from nanometer to micromater/millimeter scale. The broken symmetry of the cleaved surfaces is shown to be responsible for charge separation under UV illumination, a phenomenon otherwise forbidden by the cubic symmetry of the system. These results demonstrate a way to create and utilize $SrTiO_3(001)$ surfaces with intriguing and promising properties, and the pave way to their applications in many different fields previously unrelated to these surfaces.

Chapter 4 demonstrates an advancement in the comparison between theoretically and experimentally obtained results on surfaces at the atomic level through simulations of the AFM contrast using DFT. It is shown that realistic AFM images can be simulated despite a series of approximations, and that chemical sensitivity can be pertained – a central advantage of the AFM technique.

Die approbierte gedruckte Originalversion dieser Dissertation ist an der TU Wien Bibliothek verfügbar.
The approved original version of this doctoral thesis is available in print at TU Wien Bibliothek.
TU Bibliothek Your knowledge hub WIEN

Kurzfassung

Der größte Teil der festen Materie auf der Erde kommt natürlich in Form von Oxiden vor, die auch den größten Teil der Erdkruste ausmachen. Die meisten Elemente des Periodensystems kommen in der Natur in oxidischer Form vor, und die Gewinnung reiner Elemente erfolgt in der Regel durch chemische Reduktion des entsprechenden Oxids. Obwohl diese Materialien sehr viel komplexer sind als reine elementare Feststoffe, ist ihre weit verbreitete Verfügbarkeit und ihre Stabilität unter atmosphärischen Bedingungen der Grund für das große Forschungsinteresse an ihren Materialeigenschaften. Bei vielen Oxiden wurde bereits gezeigt, dass sie eine Fülle von faszinierenden physikalischen Phänomenen aufweisen. Es ist anzunehmen, dass in den kommenden Jahren die technische Anwendung von Oxiden in wohlkontrollierten Prozessen wie der hetero-/homogenen Katalyse und der Elektronik auf der Nanometer- oder Subnanometerskala in Umfang noch zunehmen werden.

Jedes Material interagiert mit seiner Umgebung über seine exponierten Facetten - die Oberflächen, an denen Feststoffe für verschiedene Anwendungen zur Verfügung stehen. Die Oberflächenwissenschaften setzen eine Vielzahl von experimentellen und theoretischen Techniken ein, um Prozesse zu untersuchen, die an verschiedenen Facetten unterschiedlicher Festkörper ablaufen. In den letzten Jahren wurde die Untersuchung von Oberflächen mit atomarer Präzision möglich, was die Beobachtung grundlegender Phänomene auf atomarer Ebene erlaubt. In dieser Arbeit wird ein oberflächenwissenschaftlicher Ansatz zur Untersuchung verschiedener Oxidoberflächen unter gut kontrollierten Bedingungen, meist Ultrahochvakuum (UHV) und niedrigen Temperaturen, verwendet. Die eingehende Untersuchung von Eigenschaften und Mechanismen unter diesen Bedingungen bildet die Basis für das Verständnis und die Vorhersage des Verhaltens von Oberflächen unter weniger kontrollierten Umgebungen. Im Rahmen der Forschungsarbeiten, die zu dieser Dissertation geführt haben, wurden die Oberflächen mehrerer komplexer Oxide untersucht, wobei der Schwerpunkt auf zwei Modelloxiden lag: Rutil TiO_2 und Perowskit $SrTiO_3$.

In Kapitel 1 werden die in dieser Arbeit verwendeten Techniken der Oberflächenphysik vorgestellt. Der Schwerpunkt liegt dabei auf den experimentellen Techniken non-contact Atomic Force Microscopy (nc-AFM) und Scanning Tunneling Microscopy (STM), die es ermöglichen, Oberflächen mit einer Auflösung von einem einzigen Atom abzubilden, sowie auf dem theoretischen Ansatz der Dichtefunktionaltheorie (DFT), der die quantenmechanischen Eigenschaften von Oberflächenatomen und ihre Wechselwirkungen mit anderen Atomen realistisch modelliert. Die vorgestellten Techniken wurden in der Regel gemeinsam angewendet, um ergänzende Informationen über ein bestimmt physikalische Systeme zu erhalten.

Kapitel 2 befasst sich mit der Wechselwirkung einer Modelloberfläche eines binären Übergangsmetalloxids, der $TiO_2(110)$-Oberfläche, mit kleinen Gasmolekülen mit einer Auflösung von einem einzigen Atom oder einem einzigen elektronischen Orbital. Der polaronische Grundzustand des reduzierten $TiO_2(110)$ wird vorgestellt, der sich mit Hilfe von AFM/STM und DFT in Gegenwart einzelner Moleküle verändert. Der polaronische Grundzustand wird durch die Anwesenheit von schwach adsorbiertem CO geringfügig verändert, während er in Anwesenheit von stark adsorbiertem O_2, welches die polaronischen Elektronen zur Bildung starker chemischer Bindungen mit der darunter liegenden Oberfläche nutzt, vollständig verschwindet. Diese Ergebnisse beleuchten und klären die seit langem untersuchten fundamentalen Prozesse, die an dieser technologisch relevanten Oberfläche ablaufen.

Kapitel 3 konzentriert sich auf die Modelloberfläche eines Perowskit-Oxids mit Bulk-Terminierung, auf das $SrTiO_3(001)$. Die Oberfläche wurde durch die Spaltung von Einkristallproben $in-situ$ (also unter UHV Bedingungen) dargestellt. Es wird gezeigt, dass solche Oberflächen mit Bulk-Terminierung auf atomarer Ebene der idealen Oberfläche am nächsten kommen, und dass sie durch einen durch elastische Spannung unterstützten ferroelektrischen Übergang während der Spaltung erzeugt wurden. Ein neuartige Spaltverfahren wird beschrieben und systematisch untersucht, und es zeigt sich, dass die gespaltenen Oberflächen als Folge ihrer Bulk-Terminierung mehrere faszinierende Phänomene aufweisen. Die TiO_2-terminierte Oberflächen von $SrTiO_3(001)$ erfährt während der Spaltung einen Isolator-Metall-Übergang, während die SrO-Terminierung halbleitend bleibt. Die beiden Terminieriung wechseln sich der Oberfläche ab und schalten an den Domänenwänden der Polarisierung um. Je nach Beigabe einer externen Dotierung (Niobium) weisen die gespaltenen Oberflächen unterschiedliche Morphologien auf, wobei die Größe der beiden unterschiedlichen Oberflächenabschlüsse von der Nanometer- bis zur Mikrometer-/Millimeterskala reicht. Die gebrochene Symmetrie der gespaltenen Oberflächen ist nachweislich für die Ladungstrennung unter UV-Beleuchtung verantwortlich, ein Phänomen, das ansonsten durch die kubische Symmetrie des Systems verhindert wird. Diese Ergebnisse zeigen einen Weg auf, $SrTiO_3(001)$-Oberflächen mit faszinierenden und vielversprechenden Eigenschaften zu erzeugen und zu nutzen, und ebnen den Weg für ihre Anwendung in neuen Bereichen.

Die approbierte gedruckte Originalversion dieser Dissertation ist an der TU Wien Bibliothek verfügbar.
The approved original version of this doctoral thesis is available in print at TU Wien Bibliothek.
TU Bibliothek Your knowledge hub WIEN

Kapitel 4 beschreibt eine Fortentwicklung beim Vergleich zwischen theoretisch und experimentell gewonnenen Ergebnissen über Oberflächen auf atomarer Ebene durch Simulationen des AFM-Kontrasts mit DFT. Es wird gezeigt, dass trotz einer Reihe von Näherungen realistische AFM-Bilder simuliert werden können, und dass diese Aufschlusss über die chemische Zusammensetzung geben – ein zentraler Vorteil der AFM-Technik.

Die approbierte gedruckte Originalversion dieser Dissertation ist an der TU Wien Bibliothek verfügbar.
The approved original version of this doctoral thesis is available in print at TU Wien Bibliothek.
TU WIEN Bibliothek Your knowledge hub

Contents

1 Methods **1**
- 1.1 Density-functional theory – DFT . . . 1
  - 1.1.1 Principle . . . 1
  - 1.1.2 Realization . . . 4
- 1.2 Low-energy electron diffraction – LEED . . . 7
- 1.3 X-ray photoelectron spectroscopy – XPS . . . 10
- 1.4 Scanning tunneling microscopy – STM . . . 14
  - 1.4.1 Principle and realization . . . 14
  - 1.4.2 Contrast formation . . . 16
  - 1.4.3 Scanning tunneling spectroscopy . . . 19
- 1.5 Noncontact atomic force microscopy – nc-AFM (AFM) . . . 21
  - 1.5.1 Principle . . . 21
  - 1.5.2 Sensors . . . 24
  - 1.5.3 Forces . . . 27
  - 1.5.4 Contrast formation . . . 30
  - 1.5.5 Force-distance curves . . . 30
  - 1.5.6 Tip termination . . . 33
  - 1.5.7 Kelvin parabolas . . . 34

2 Interaction of the rutile TiO_2(110) surface with adsorbates **37**
- 2.1 Introduction . . . 37
- 2.2 Clean rutile TiO_2(110)-(1×1) surface . . . 38
- 2.3 Polaronic ground state of the rutile TiO_2(110)-(1×1) surface . . . 41
- 2.4 Adsorption of CO on clean, reduced rutile TiO_2(110) . . . 47
- 2.5 Adsorption of O_2 on clean, reduced rutile TiO_2(110) . . . 53
  - 2.5.1 Experimentally observed adsorption configurations . . . 54
  - 2.5.2 DFT calculations and the O_2 charge state . . . 57
  - 2.5.3 AFM contrast and the $F_{ts}(z)$ curves . . . 61
  - 2.5.4 Charge injection/removal from the O_2 . . . 64
  - 2.5.5 Annealing . . . 66
  - 2.5.6 UV-induced reactions . . . 68
  - 2.5.7 Conclusions . . . 74
- 2.6 Summary and Outlook . . . 76

3 Bulk-truncated $SrTiO_3$(001) surface **77**
- 3.1 Introduction $SrTiO_3$ . . . 77
  - 3.1.1 Introduction to the $SrTiO_3$(001) surface . . . 78
  - 3.1.2 Standard $SrTiO_3$(001) surface preparation . . . 79
- 3.2 Utilizing strain-induced ferroelectricity to cleave atomically flat surfaces . . . 82
  - 3.2.1 $SrTiO_3$ as an incipient ferroelectric . . . 82
  - 3.2.2 Cleaving procedure . . . 83
  - 3.2.3 Atomically resolved terminations . . . 85
  - 3.2.4 Morphology of a cleaved surface . . . 89
  - 3.2.5 Surface polarity . . . 90

Die approbierte gedruckte Originalversion dieser Dissertation ist an der TU Wien Bibliothek verfügbar.
The approved original version of this doctoral thesis is available in print at TU Wien Bibliothek.
TU WIEN Bibliothek Your knowledge hub

3.2.6 Conclusions . . . 93
3.3 The search for a pristine, unreconstructed $SrTiO_3(001)$ surface . . . 95
3.3.1 Thermal stability of the bulk-terminated $SrTiO_3(001)$ surface . . . 95
3.3.2 Atomically resolved study of etched $SrTiO_3(001)$ surfaces . . . 102
3.3.3 Conclusions . . . 110
3.4 Empirical insights into the novel perovskite cleaving procedure . . . 112
3.4.1 Cleaving device . . . 112
3.4.2 Quantum phase transition during cleaving . . . 116
3.4.3 Optical photographs . . . 117
3.4.4 SEM measurements . . . 119
3.4.5 Relation to other works on cleaved $SrTiO_3(001)$ surfaces . . . 121
3.4.6 Application of the cleaving device to another perovskite oxide . . . 123
3.4.7 Conclusions . . . 124
3.5 Influence of variable Nb doping levels on the properties of cleaved $SrTiO_3(001)$ . . . 126
3.6 UV irradiation of the two terminations . . . 132
3.7 Controlled charge removal from the SrO termination . . . 140
3.8 Peculiar dissipation . . . 144
3.8.1 CO adsorption on the cleaved SrO termination . . . 144
3.8.2 Crashed tip on a contaminated surface . . . 147
3.9 Summary and Outlook . . . 149

4 AFM contrast simulations **151**
4.1 Transforming simulated force-distance curves to AFM images – DAC simulator . . . 152
4.2 Case study on NaI(001) . . . 156
4.2.1 Electrostatic model . . . 157
4.2.2 Probe Particle model . . . 158
4.2.3 DAC simulator . . . 160
4.2.4 Conclusions . . . 162
4.3 Summary and Outlook . . . 163

5 Summary and Outlook **164**

Die approbierte gedruckte Originalversion dieser Dissertation ist an der TU Wien Bibliothek verfügbar.
The approved original version of this doctoral thesis is available in print at TU Wien Bibliothek.
TU Bibliothek Your knowledge hub WIEN

Die approbierte gedruckte Originalversion dieser Dissertation ist an der TU Wien Bibliothek verfügbar.
The approved original version of this doctoral thesis is available in print at TU Wien Bibliothek.
TU Bibliothek Your knowledge hub WIEN

Chapter 1

Methods

1.1 Density-functional theory – DFT

Density-functional theory, abbreviated as DFT, is a powerful theoretical tool for the quantum-mechanical modeling of complex solid state materials. It was originally proposed and derived by Hohenberg, Kohn and Sham [1, 2], for which Kohn received the Nobel prize in Chemistry in 1998 [3]. In DFT, the quantum-mechanical properties of a solid are calculated from first principles. This means that DFT modeling provides calculated values for the unit cell size, atomic relaxations, electronic properties, band structure, optical properties of a solid etc., using only the quantum representation of the constituent atoms and their relative mutual positions. In other words, the structure of a solid in DFT is not derived from empirical experimental observations, but from the fundamental quantum mechanical properties of the constituent atoms in a particular geometry. DFT can therefore provide unprecedented insight and predict structural models and physical properties of solids. This advantage is commonly employed to provide complementary interpretation of the obtained experimental results, as well as predict structural models and physical properties of solids that were not previously investigated experimentally.

1.1.1 Principle

In quantum mechanics, a solid can be completely characterized with a single many-body wavefunction Ψ that depends on the position of each of the N electrons and M ions in the solid:

$$\Psi = \Psi\left(\overrightarrow{r_1}, \overrightarrow{r_2}, ..., \overrightarrow{r_N}; \overrightarrow{R_1}, \overrightarrow{R_2}, ..., \overrightarrow{R_M}\right) \tag{1.1}$$

where $\overrightarrow{r_i}$ is the position of an electron, and $\overrightarrow{R_I}$ is the position of an ion. When a solid is at equilibrium, *i.e.*, in the absence of external stimuli, the exact many-body wavefunction can be obtained by solving the time-independent, non-relativistic Schrödinger equation:

$$\begin{aligned} \hat{H}\Psi = \left(\hat{T} + V\left(\overrightarrow{r}\right)\right)\Psi = \Bigg[-\sum_i \frac{\hbar^2}{2m_\mathrm{e}}\nabla_i^2 - \sum_I \frac{\hbar^2}{2m_I}\nabla_I^2 + \\ + \frac{1}{2}\sum_{i\neq j}\frac{e^2}{4\pi\epsilon_0}\frac{1}{|\overrightarrow{r_i} - \overrightarrow{r_i}|} + \frac{1}{2}\sum_{I\neq J}\frac{e^2}{4\pi\epsilon_0}\frac{Z_I Z_j}{\left|\overrightarrow{R_I} - \overrightarrow{R_J}\right|} - \frac{1}{2}\sum_{i,I}\frac{e^2}{4\pi\epsilon_0}\frac{Z_I}{\left|\overrightarrow{r_I} - \overrightarrow{R_I}\right|}\Bigg]\Psi\left(\overrightarrow{r_1}, ..., \overrightarrow{r_N}; \overrightarrow{R_1}, ..., \overrightarrow{R_M}\right) = \\ = E_\mathrm{tot}\Psi\left(\overrightarrow{r_1}, ..., \overrightarrow{r_N}; \overrightarrow{R_1}, ..., \overrightarrow{R_M}\right) \end{aligned} \tag{1.2}$$

where m_e and m_I are the masses, $\overrightarrow{r_i}$ and $\overrightarrow{R_I}$, are the positions, and e and Z_I are the charges of electrons and ions in a solid, respectively. Dielectric susceptibility of vacuum is denoted as ϵ_0, and $\hbar$ is the reduced Plank's constant [4]. The kinetic energy operator (denoted as $\hat{T}$), acts on each electron and each ion independently, and is given explicitly by the two first terms in the bracket in eq. 1.2. The interaction of charged particles (denoted as $V\left(\overrightarrow{r}\right)$) is modeled by the Coulomb interaction between pairs of electrons, pairs of ions, and electrons and ions, which are expressed as the third, fourth, and fifth term in the bracket in eq. 1.2. The total energy of the

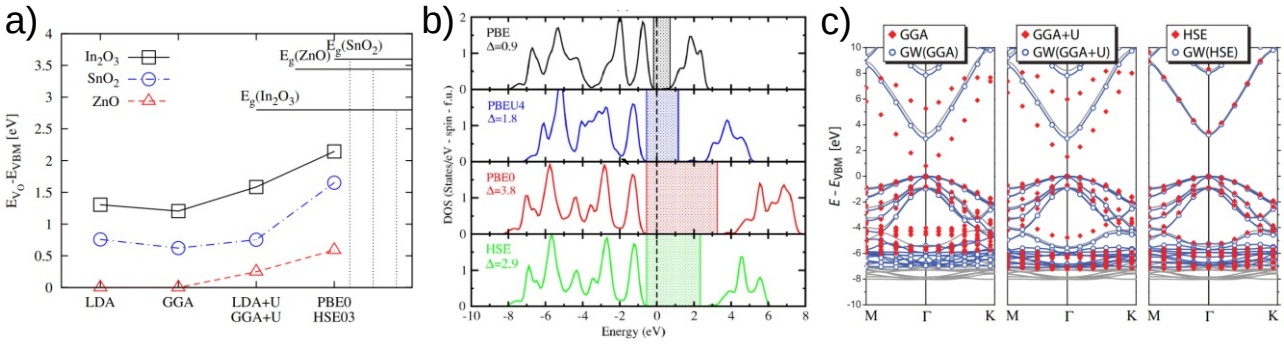

Figure 1: **Comparison of different exchange-correlation functionals used in DFT calculations.**
a) The energy of the in-gap electronic state associated with the oxygen vacancy in three different oxides. The energies are defined with respect to the valence band maximum, and calculated with six different functionals. Reprinted top panel of Figure 2 [5] from [Péter Ágoston, Karsten Albe, Risto M. Nieminen, and Martti J. Puska, *Physical Review Letters*, 103, 245501 (2009)] with permission of Author(s) and APS. Copyright (2009) American Physical Society. b) The density of states in MnO calculated with four different functionals. Each functional gives qualitatively similar results, but the value of the band gap differs drastically.
Reprinted top-left panel of Figure 3 [6] from [Cesare Franchini, Reimund Podloucky, Joachim Paier, Martijn Marsman, and Georg Kresse, *Physical Review B*, 75, 195128 (2007)] with permission of Author(s) and APS. Copyright (2007) American Physical Society.
c) Band structure of ZnO calculated with three different DFT functionals and compared to the GW functionals. Reprinted Figure 3 [7] from [Linda Y. Lim, Stephan Lany, Young Jun Chang, Eli Rotenberg, Alex Zunger, and Michael F. Toney, *Physical Review B*, 86, 235113 (2012)] with permission of Author(s) and APS. Copyright (2012) American Physical Society.

system E_{tot} is the eigenvalue of the many-body Schrödinger equation, and its lowest eigenvalue describes the ground state of the solid, from which many physical properties of the solid could be calculated.

The many-body Schrödinger equation has to be solved self-consistently, which poses a great numerical challenge. The wavefunction has to evaluated on a reasonably dense grid, which could be defined with a spacing of 0.1 Åin three dimensions. For a typical unit cell, this would correspond to $N_G \approx$40000 grid points. If only two Be atoms are considered $M = 2$ in such a unit cell, with two electrons each $N = 4$, the wavefunction of the solid would have to evaluated in $N_G^{N+M} \approx 10^{10}$ points. Moreover, if two O atoms are considered, the evaluation would have to be performed in $N_G^{16+2} \approx 10^{22}$ points. This "exponential wall" of drastically increasing computational cost with a slight increase in the solid complexity, renders the exact solution of the many-body Schrödinger equation hardly reachable in practice.

There are several approximations that can be utilized to reduce the complexity of the many-body Schrödinger equation. The frozen nuclei approximation considers atomic cores as frozen, in which case the kinetic energy of ions is equal to zero (application of the second term in the bracket in eq. 1.2), while the ion-ion potential interaction (fourth term in the bracket in eq. 1.2) is a constant that can be removed from the total energy to redefine the energy of the system as $E = E_{tot} - \frac{1}{2}\sum_{I \neq J} \frac{e^2}{4\pi\epsilon_0} \frac{Z_I Z_j}{|\overrightarrow{R_I} - \overrightarrow{R_J}|}$. Then, the coordinates of the atomic nuclei can be considered as external parameters, and the wavefunction of the system expressed through electron coordinates only $\Psi(\overrightarrow{r_1}, ..., \overrightarrow{r_N})$. The complexity of the many-body Schrödinger equation can be significantly reduced by transforming it to a set of single-electron Schrödinger equations. Only one term in the many-body Schrödinger equation deals with the mutual Coulomb interaction of electrons (third term in the bracket in eq. 1.2), so the wavefunction $\Psi(\overrightarrow{r_1}, ..., \overrightarrow{r_N})$ can be expressed as a function of the single-electron wavefunctions $\phi_i(\overrightarrow{r_i})$. In the single-electron approximation, the interaction between an electron and each ion in the solid can be expressed as a sum of individual pair-wise Coulomb interactions $V_n(\overrightarrow{r}) = -\sum_I \frac{e}{4\pi\epsilon_0} \frac{Z_I}{|\overrightarrow{r} - \overrightarrow{R_I}|}$, in which case the fifth term in the bracket in eq. 1.2 becomes $+\sum_i V_n(\overrightarrow{r_i})$. To obey the Pauli's principle of exclusion, the electron wavefunction of the system can be expressed as a Slater determinant of the single-electron wavefunctions. The interaction of a single electron with the other electrons in the system (third term in the bracket in eq. 1.2) can be approximated through the classical mean-field theory in which a single electron experiences the potential originating form the

Die approbierte gedruckte Originalversion dieser Dissertation ist an der TU Wien Bibliothek verfügbar.
The approved original version of this doctoral thesis is available in print at TU Wien Bibliothek.
TU Bibliothek Your knowledge hub WIEN

averaged density of other electrons, *i.e.*, the Hartree potential $V_{\mathrm{H}}(\overrightarrow{r}) = \frac{e^2}{4\pi\epsilon_0}\int d\overrightarrow{r'}\frac{n(\overrightarrow{r'})}{\left|\overrightarrow{r}-\overrightarrow{r'}\right|}$ [8]. These approximations transform the many-body Schrödinger equation to a set of single-electron Schrödinger equations. The only remaining non-local interaction (third term in eq. 1.2) that addresses the overlap of the wavefunction of individual electrons, can be approximated through the Fock exchange potential $V_{\mathrm{X}}(\overrightarrow{r},\overrightarrow{r'}) = -\frac{e^2}{4\pi\epsilon_0}\sum_j \frac{\phi_j^*(\overrightarrow{r'})\phi_j(\overrightarrow{r'})}{\left|\overrightarrow{r}-\overrightarrow{r'}\right|}$ [9], with the assumption of orthogonality of the single-electron wavefunctions $\int d\overrightarrow{r}\phi_i^*(\overrightarrow{r})\phi_j(\overrightarrow{r}) = \delta_{ij}$. With these approximations, the solid can be modeled through a set of Hartree-Fock equations [10]:

$$\left[-\frac{\hbar^2}{2m_{\mathrm{e}}}\nabla^2 + V_n(\overrightarrow{r}) + V_{\mathrm{H}}(\overrightarrow{r})\right]\phi_i(\overrightarrow{r}) + \int d\overrightarrow{r'}V_{\mathrm{X}}(\overrightarrow{r},\overrightarrow{r'})\phi_i(\overrightarrow{r'}) = \varepsilon_i\phi_i(\overrightarrow{r}) \tag{1.3}$$

where ϵ_i is an energy eigenvalue of a single electron, and the energy of the system is a sum of the individual eigenvalues $E = \sum_i^N \varepsilon_i$.

Hartree-Fock equations (eq. 1.3) can be transformed to a set of local equations by approximating the Fock exchange potential with a local exchange potential $V_x(\overrightarrow{r})$, which, if chosen properly, describes the quantum-mechanical interaction of two electrons well. An additional potential that will account for electron correlation $V_c(\overrightarrow{r})$ can be added to the Hartree-Fock equations. The correlation potential $V_c(\overrightarrow{r})$ accounts for the probability of having an electron at a position $\overrightarrow{r}$ if the coordinates of the other electrons are known. With these two additions, Hartree-Fock equations transform into Kohn-Sham equations [2]:

$$\left[-\frac{\hbar^2}{2m_{\mathrm{e}}}\nabla^2 + V_n(\overrightarrow{r}) + V_{\mathrm{H}}(\overrightarrow{r}) + V_x(\overrightarrow{r}) + V_c(\overrightarrow{r})\right]\phi_i(\overrightarrow{r}) = \varepsilon_i\phi_i(\overrightarrow{r}) \tag{1.4}$$

that constitute a set of N three-dimensional equations. The choice of the local Fock exchange potential $V_x(\overrightarrow{r})$ and the correlation potential $V_c(\overrightarrow{r})$ is a key to obtaining a good approximation of the $3N$-dimensional many-body Schrödinger equation with the N 3-dimensional Kohn-Sham equations. These two potentials are usually combined together to form an exchange-correlation potential. If a perfectly appropriate exchange-correlation potential is known, the solution to Kohn-Sham equations yields an exact solution for the ground state of the system.

The DFT approximation is built upon the Kohn-Sham equations (eq. 1.4), supplemented with the Hohenberg-Kohn theorem. The Hohenberg-Kohn theorem states that the ground state of the solid is uniquely determined by the electron density [1]. This dependence is indirect and proceeds through steps: First, the electron density uniquely determines the Coulomb potential of the nuclei $V_n(\overrightarrow{r}) = V_n(n(\overrightarrow{r}))$; second, the many-body wavefunction is uniquely determined by the external potential of the nuclei $\Psi(\overrightarrow{r_1},...,\overrightarrow{r_N}) = \Psi(V_n(n(\overrightarrow{r})))$; third, the energy of the ground state depends on the many-body wavefunction of the solid. The three relations can be combined as:

$$E = E(\Psi(\overrightarrow{r_1},...,\overrightarrow{r_N})) = E(\Psi(V_n(n(\overrightarrow{r})))) = F[n(\overrightarrow{r})] \tag{1.5}$$

to express the energy of the ground state as a functional of the electron density. The Hohenberg-Kohn theorem is not valid for excited systems, where the total energy can be expressed only as the functional of the many-body wavefunction $E = E(\Psi(\overrightarrow{r_1},...,\overrightarrow{r_N}))$. When the Hohenberg-Kohn theorem (eq. 1.5) is applied to the Kohn-Sham equations (eq. 1.4), the energy of the ground state can be determined as:

$$E = \int d\overrightarrow{r}\,n(\overrightarrow{r})\,V_n(\overrightarrow{r}) - \sum_i \int d\overrightarrow{r}\,\phi_i^*(\overrightarrow{r})\,\frac{\hbar^2}{2m_{\mathrm{e}}}\nabla^2\phi_i(\overrightarrow{r}) + \frac{1}{2}\left(\frac{e^2}{4\pi\epsilon_0}\right)^2\int\int d\overrightarrow{r}\,d\overrightarrow{r'}\,\frac{n(\overrightarrow{r})\,n\left(\overrightarrow{r'}\right)}{\left|\overrightarrow{r}-\overrightarrow{r'}\right|} + E_{xc}[n]\,. \tag{1.6}$$

The equation above is the basis of the DFT. The first three terms account for the kinetic and the Coulomb energy of independent electrons, while the final term is the exchange and correlation energy $E_{xc}[n]$ that accounts for everything that is missing or omitted in the appropriate transformation from the many-body Schrödinger equation to the single-electron Schrödinger equations. The modeling of a solid using DFT is commonly refereed to as $ab-initio$ modeling because it employs only the fundamental properties of matter (as seen in eq. 1.4), and avoids the fitting from the experimentally observed data.

The exchange-correlation functional of the electron density $E_{xc}[n]$ plays a substantial role in DFT calculations. The proper approximation of $E_{xc}[n]$ is necessary to ensure physically reasonable results. There are

Die approbierte gedruckte Originalversion dieser Dissertation ist an der TU Wien Bibliothek verfügbar.
The approved original version of this doctoral thesis is available in print at TU Wien Bibliothek.
TU Bibliothek Your knowledge hub WIEN

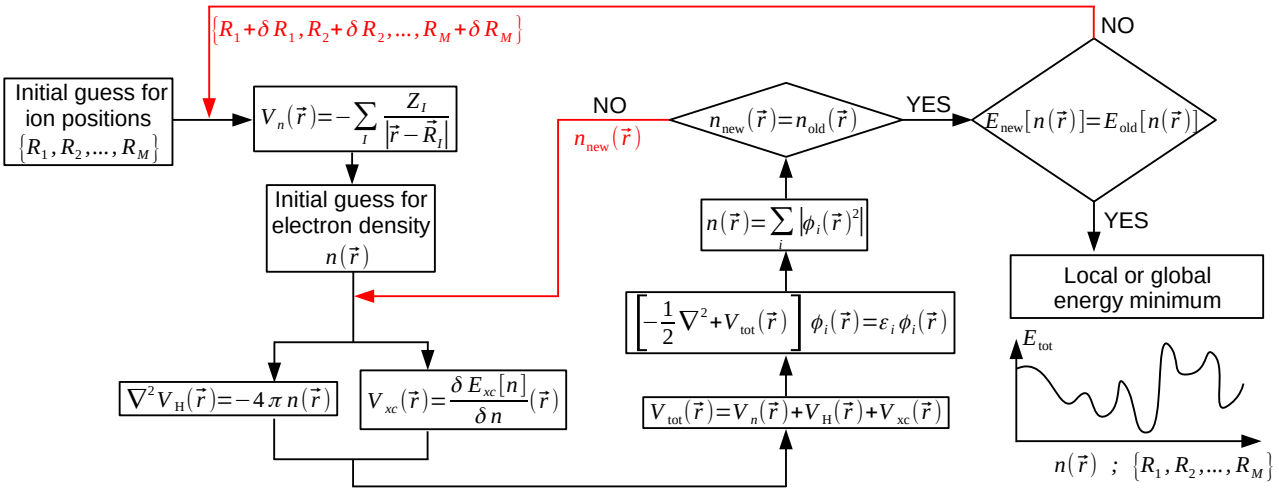

Figure 2: **Illustration of a DFT calculation scheme.** Labels are consistent with the derivation of Hartree-Fock equations in the text, while the red lines indicate the return to the beginning of the calculation scheme until the total energy converges to an either local or global minimum. The graph at the bottom right illustrates the energy landscape of the system with several local and one global minima.

several widely employed functionals that vary by complexity, and as a consequence by the computational cost. One way to assess the exchange-correlation functional is to approximate electrons in a solid as a piece-wise homogeneous electron gas within infinitesimally small volumes, *i.e.*, to consider the electrons as behaving as an electron gas locally [11]. This approximation is referred to as the local density approximation [12], abbreviated as LDA, and it was proven to be well applicable in metals where the electrons resemble the free electron gas the most. An improvement of the LDA method is to consider the gradients of the electron density between the infinitesimally small volumes. This approach is referred to as the global-gradient approximation [13], abbreviated as GGA. The GGA parametrization developed by Perdew, Burke, and Ernzerhof (PBE) is commonly employed [14, 15], and is well applicable to semiconductors and insulators as well. The PBE functional can be supplemented with the terms that more specifically account for electron correlation. One approach is adding an on-site, orbital-specific interaction by introducing the Hubbard U (PBE+U), an integral ingredient of the tight-binding model [16]. Hubbard U [17] accounts for the electron-electron repulsive interaction within a single electronic shell of an atom. Functionals that partially incorporate a part of the explicit exchange-correlation interaction ($V_X(\vec{r}, \vec{r'})$) in the Hartree-Fock equations (eq. 1.3) are referred to as the hybrid functionals (HSE), and their computational cost is larger than the LDA, PBE, and PBE+U functionals. Several functionals, and their effect on the calculated physical quantities obtained from DFT calculations, and GW calculations [18] that estimate the many-body Schrödinger equation using Green's functions and screened Coulomb potential, are exemplified in Fig. 1. While the results obtained with different functionals are qualitatively similar, their quantitative precision differs. In practice, functionals are chosen such that they yield results with satisfying precision, while maintaining reasonable computational cost.

1.1.2 Realization

The Kohn-Sham equations in DFT are solved numerically, through the use of a self-consistent calculations. Figure 2 illustrates the calculation scheme in DFT. Calculations are provided with the initial guess for the atomic/ionic positions of the solid, and the initial guess for the electron density. Than, the ionic cores are frozen, and the calculation enters the loop for calculating and optimizing the electron density using the set of Kohn-Sham equations (eq. 1.4). Each calculated electron density is returned to the beginning of the loop (red line in Fig. 2), until the returned and newly calculated electron density become the same, *i.e.*, until the electron density converges. This yields a value for the total energy of the system for a particular set of frozen ionic coordinates. The process is repeated for an altered set of ionic coordinates (red line in Fig. 2), and a new total energy of the system is obtained. The ionic positions ($R_I + \delta R_I$) can be altered in several different ways (Verlet algorithm, variable metric algorithm, conjugate gradient algorithm etc.) before starting a new calculation loop.

Die approbierte gedruckte Originalversion dieser Dissertation ist an der TU Wien Bibliothek verfügbar.
The approved original version of this doctoral thesis is available in print at TU Wien Bibliothek.
TU WIEN Bibliothek Your knowledge hub

The entire process of electronic and ionic relaxations is repeated until the total energy of the system converges, *i.e.*, until the calculations yield the minimum of the total energy. This energy minimum is not necessarily the ground state of the system (the global minimum in the illustrated energy landscape in Fig. 2), and the calculations are usually repeated with significantly different initial guesses for the ionic positions and electronic densities in order to avoid the possibility of repeatedly converging to a local energy minimum. Once a global energy minimum is located with a satisfying certainty, the ionic positions and single-electron wavefunctions that produce this energy eigenvalue define the ground state of the modeled solid.

Reaching the converged ground state of a solid requires many iterations of the scheme illustrated in Fig. 2. This makes DFT calculations computationally demanding, and nowadays they are commonly performed on a modern supercomputer. Several steps of the DFT calculations allow for parallelizations, which are well implemented in most modern supercomputers through OpenMP [19] and MPI [20] standards. Most of the calculations that led to this Thesis were performed on the Vienna Scientific Cluster 3 supercomputer system (VSC-3) which consists of 2020 computing nodes with two 8-core processors each [21].

The numerical implementations for performing DFT calculations are also very extensive, which is why they are usually performed in specifically designed environments suited for DFT calculations. All DFT results performed in the research that led to this Thesis were obtained using the Vienna *ab initio* simulation package, abbreviated as VASP [22, 23, 24]. One specific characteristic of VASP is that, unlike WIEN2k for example [25, 26, 27], it does not include all electrons of an atom into the explicit calculations. Instead, the core electrons are approximated with a projector-augmented wave pseudopotential [28] that efficiently mimic the electrostatic field originating from these electrons, which usually do play a critical role in the binding of solids. This type of approximation increases the speed of performing DFT calculations, while still preserving reasonable accuracy. The rest of the electrons, *i.e.*, the valence electrons of each atom, are explicitly modeled in a plane wave basis set.

Using a well-developed simulation environment for performing DFT calculations reduces the amount of necessary input information, because DFT results are obtained from first principles. In practice, VASP requires the initial guess for the atomic positions, and their chemical fingerprints. This is provided by inputing a single unit cell of the solid, which is then internally transformed to an infinite three-dimensional grid of the periodic unit cells, where the electrons are subjected to the Bloch theorem [29]. A user must choose the number of Bloch vectors considered in the calculations by supplying VASP with their explicit positions in the Brillouin zone, *i.e.*fsi, by providing VASP with the directions of the k-points in which the energy will be evaluated. Performing calculations in many k-points significantly increases the computational cost, and a trade-off is often chosen between the accuracy and the computation cost. The convergence of the energy with the number of k-points, however, must be ensured. Modeling a solid surface, *i.e.*, a solid-vacuum interface, requires input in the form of a single unit cell of the desired solid and its surface face that is supplemented by a large-enough volume of vacuum; when such a unit cell is periodically replicated in three-dimensions, it consists of infinitely many parallel slabs of the infinitely spreading material in two directions, separated by a thick vacuum layer in the third direction. Naturally, the volume filled with atoms within a unit cell needs to be at least several layers thick in order to emulate the presence of both the surface and the bulk material. VASP additionally requires the choice of PAW pseudopotentials for the atoms within the unit cell: depending on the desired accuracy, a larger number of electrons can be explicitly accounted for by choosing different pseudopotentials that increase the number of valence electron shells. Finally, VASP needs to be supplied with a set of different flags that define the algorithms, precisions, and the physical quantities that a user desires from a calculation.

Once a ground state of a solid is obtained through DFT calculations, many physical properties of the solid and its reactions toward external stimuli can be calculated. The solid can be perturbed by applying pressure, adding lattice vibrations, creating defects, adsorbing atoms or molecules, etc., which yields a total energy of the ground state of the perturbed solid. This energy can be compared with the energy of the isolated system to reveal the preferable system configurations, or adsorption/formation/cohesion energies. The electronic structure can also be investigated in detail from the converged DFT calculation. For example, the density of states (DOS) can be calculated, *i.e.*, the distribution of electronic states at different energies with respect to the Fermi energy of a solid, as seen in the example of MnO in Fig. 1b. The distribution of electronic states associated with individual atoms, *i.e.*, the atom-projected DOS (PDOS), can also be disentangled from the total DOS. This can be seen in the example in Fig. 1a, where the energy of the electronic states associated with an oxygen vacancy in three different oxides is plotted. The band dispersion relation can also be obtained by calculating the energy of the system at different points in the Brillouin zone as shown in the example of ZnO in Fig. 1c.

Beside the electronic structure of the surface, a major portion of DFT calculations in surface physics is directed towards the prediction or explanation of the surface geometries, adsorbate behavior on surfaces, sur-

Die approbierte gedruckte Originalversion dieser Dissertation ist an der TU Wien Bibliothek verfügbar.
The approved original version of this doctoral thesis is available in print at TU Wien Bibliothek.
TU WIEN Bibliothek Your knowledge hub

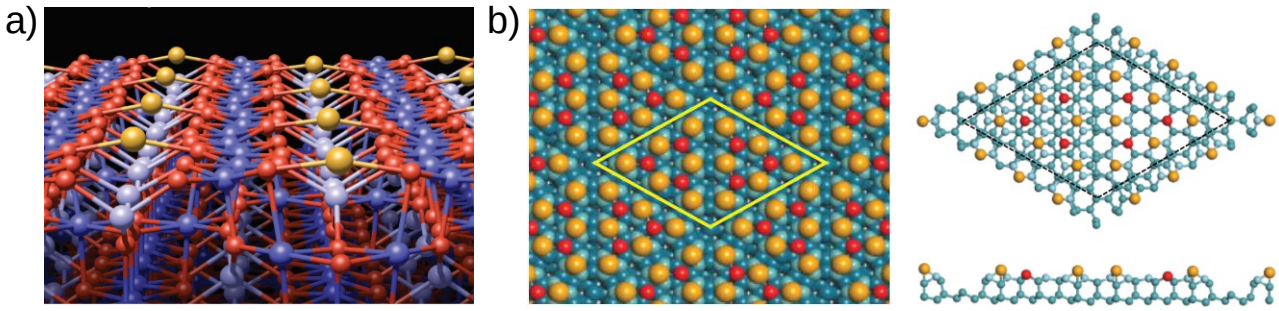

Figure 3: **DFT optimizations of the surface geometry.**
a) Converged DFT geometry of the $(\sqrt{2} \times \sqrt{2})$R45° reconstruction on the $Fe_3O_4(001)$ surface with subsurface cation vacancies, and individual Au atoms adsorbed.
Reprinted Figure 1(e) [30] from [R. Bliem, E. McDermott, P. Ferstl, M. Setvín, O. Gamba, J. Pavelec,M. A. Schneider, M. Schmid, U. Diebold, P. Blaha, L. Hammer, and G. S. Parkinson, *Science*, 346, 1215 (2014)] with permission from AAAS.
b) Converged DFT geometry of the famous Si(111)(7×7) reconstruction viewed from the top. The right panel shows a single, large unit cell and the left panel shows the corresponding surface after the periodic boundary conditions were imposed on the single unit cell.
Reprinted Figure 1 and bottom-right panel of Figure 2 [31] from [Manuel Smeu, Hong Guo, Wei Ji, and Robert A. Wolkow, *Physical Review B*, 85, 195315 (2012)] with permission of Author(s) and APS. Copyright (2012) American Physical Society.

face reconstructions, and other structural properties. For example, DFT calculations provided an excellent description of a subsurface cation vacancy on the $(\sqrt{2} \times \sqrt{2})$R45° reconstructed magnetite (001) surface, and Fig. 3a shows the DFT optimized model of Au single atoms adsorbed to this surface. The DFT structurally optimized result of the famous Si(111)(7×7) reconstruction can be seen in Fig. 3b. The left panel shows the process of periodical repetition of a single unit cell to create a solid surface, while the right panel focuses on the details within the structural unit. This large unit cell has four types of inequivalent Si atoms, marked by different colors in both panels in Fig. 3b. This particular reconstructions will be observed with other methods throughout this Chapter.

Die approbierte gedruckte Originalversion dieser Dissertation ist an der TU Wien Bibliothek verfügbar.
The approved original version of this doctoral thesis is available in print at TU Wien Bibliothek.
TU Bibliothek Your knowledge hub WIEN

1.2 Low-energy electron diffraction – LEED

Low-energy electron diffraction, abbreviated as LEED, is the first and the oldest surface physics technique. It inadvertently emerged from the experiments of Davisson and Germer [32, 33] during their efforts on proving the De Broglie's theory of the wave-like nature of electrons and other particles [34]. In these experiments, electrons with kinetic energies in the range of $E_{\mathrm{K}} \in [40, 68]\,\mathrm{eV}$ were directed perpendicular to the (111) face of single crystalline nickel, and the intensity of "reflected" electrons was observed to highly depend on the detection angle. The outgoing electrons were in fact diffracted on the crystal lattice of Ni(111), and the highest intensity of outgoing electrons was observed at the angles where the constructive superposition of electrons was achieved according to the Bragg's law, previously derived for the diffraction of x-rays on the crystal lattice [35]:

$$n\lambda = d \sin\theta \tag{1.7}$$

where n is the diffraction order, d is the lattice spacing of the Ni(111) face, θ is the angle of the observer with respect to the surface normal. The wavelength of the incoming light λ or the incoming electrons λ_e in a non-relativistic, low-kinetic-energy approximation can be expressed as:

$$\lambda_e = h\left(m_{0\mathrm{e}} E_{\mathrm{K}}\right)^{-\frac{1}{2}} \tag{1.8}$$

where h is the Plank's constant [4] and $m_{0\mathrm{e}}$ is the rest mass of the electron [36]. The electron wavelength can also be conveniently expressed $\lambda_e[\text{Å}] \approx \sqrt{\frac{150}{E_{\mathrm{K}}[\mathrm{eV}]}}$. Low-energy electrons that are directed towards the crystal samples in LEED, have their wavelength λ_e in the range of the interatomic distances at crystal surfaces: incoming electrons with the kinetic energy of E_{K}=15 eV have the wavelength of $\lambda_e = 3.162\,\text{Å}$, while the electrons with the kinetic energy of E_{K}=150 eV have the wavelength of $\lambda_e = 1\,\text{Å}$. Electrons in this range of wavelengths have the smallest inelastic mean free path [37], which implies that only electrons that are diffracted in the near-surface region will exit the surface after elastic scattering, making LEED a highly surface-sensitive technique. Typical electron energies used in LEED vary between 40 eV and 500 eV, depending on the surface under investigation.

An ordered crystal surface consists of periodical arrangement of scattering centers for the impinging electrons. The incoming electrons are scattered in the ionic and electronic field of the crystal surface. They are diffracted along well-defined directions, dependent of the incoming electron energy, the lattice spacing between the ionic scatterers, and the corresponding electron density at the surface. In the approximation of only a single scattering event for each incoming electron, *i.e.*, the kinematic approximation, and the consideration of elastic scattering alone, the outgoing electrons have the same intensity of the momentum in inverse space $\sqrt{\left|\overrightarrow{k_f}\right|^2}$ as the incoming electrons $\sqrt{\left|\overrightarrow{k_i}\right|^2}$. The intensity $I(\overrightarrow{K}, \overrightarrow{k_i})$ of the diffracted electrons at a given angle in the reciprocal space depends on the momentum of the incoming electrons $\overrightarrow{k_i}$ and their relation to the momentum of the outgoing electrons $\overrightarrow{K} = \overrightarrow{k_f} - \overrightarrow{k_i}$. It is proportional to the periodic properties of the surface through [38]:

$$I(\overrightarrow{K}, \overrightarrow{k_i}) = \left|G\left(\overrightarrow{K}\right)\right|^2 \left|F\left(\overrightarrow{K}\right)\right|^2 \tag{1.9}$$

where $G\left(\overrightarrow{K}\right)$ is the lattice factor, and $F\left(\overrightarrow{K}\right)$ is the dynamical form (structure) factor. The lattice factor $G\left(\overrightarrow{K}\right)$ is a Fourier transform of the unit-cell periodicities at the surface, while the form factor $F\left(\overrightarrow{K}\right)$ is the Fourier transform of the motif within each unit cell. The convolution of these two functions in real space defines the atomic positions in an infinite surface lattice, and it is represented with a product in the inverse space according to the convolution theorem [39]. In other words, the diffraction spots in LEED directly reveal the two-dimensional Fourier transform of the surface structure.

When the surface structure is purely two-dimensional, the Fourier component of the distribution of scattering centers in the third dimension is constant - each point of the two-dimensional Fourier transform of the surface structure is penetrated by a line of constant intensity. These lines in inverse space are called lattice rods. The diffraction of impinging electrons occurs at the two-dimensional surface, but the outgoing electrons are scattered in three dimensions. The angle of constructive diffraction of the incoming electrons occurs at the angles at which the Ewald sphere [40], defined by the radius of $\sqrt{\left|\overrightarrow{k_i}\right|^2}$, is intercepted by the surface lattice rods in reciprocal space, as illustrated in the right panel in Fig. 4. When the energy of the incoming electrons (and

Die approbierte gedruckte Originalversion dieser Dissertation ist an der TU Wien Bibliothek verfügbar.
The approved original version of this doctoral thesis is available in print at TU Wien Bibliothek.
TU Bibliothek Your knowledge hub WIEN

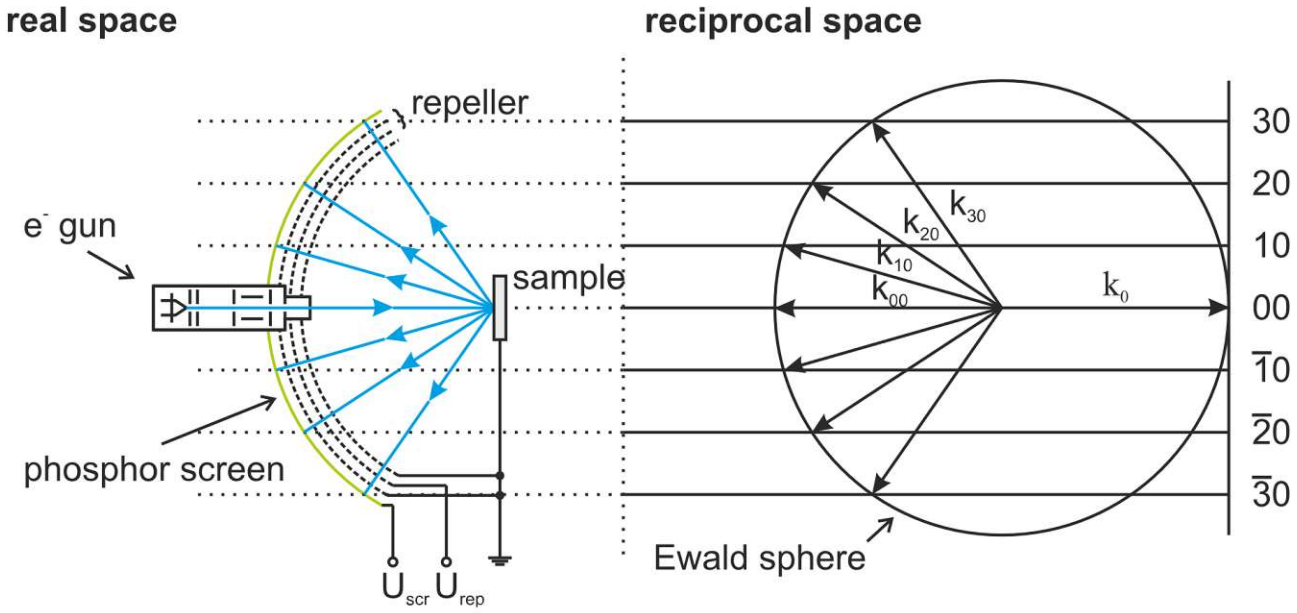

Figure 4: **Illustration of a LEED measurement setup.**
The left panel illustrates the experimental realization of electron irradiation of the sample and the detection of diffracted electrons. The right panel illustrates the intersection of the surface lattice rods with the Ewald sphere at a fixed electron energy.
Reprinted Figure [41] from SPA-LEED control software – WinSPA documentation with permission of the Author.

the energy of outgoing electrons in kinematic approximation) is increased/decreased, the radius of the Ewald sphere is increased/decreased. As the radius of the Ewald sphere increases, it intercepts more lattice rods. This is readily observed in LEED experiments at different energies: at low electron energies, there are only a few well-separated diffraction spots, while at high electron energies there are many LEED spots located much closer to each other.

A typical experimental LEED measurement setup is shown in Fig. 4. Thermal electrons are isotropically emitted from a heated filament, but only a portion of them pases through the Wehnelt cylinder closest to the filament. The width of the emitted beam of electrons can therefore be adjusted by adjusting the repelling potential of the Wehnelt cylinder. The kinetic energy of this narrow beam of electrons is determined by the potential of the electron-emitting cathode, that is set to a negative potential with respect to the ground. The crystal surface at a ground potential, is usually set to be perpendicular to the narrow beam of the electrons, such that the momentum of the impinging electrons in the inverse space $\overrightarrow{k_i}$ is well-defined and eq. 1.7 is directly applicable. The outgoing, diffracted electrons $\overrightarrow{k_f}$ have the same energy as the impinging electrons, but are diffracted along different angles, recorded by a LEED screen. Outgoing electrons can be also inelastically scattered on the surface thus lowering their energy, but they are filtered out with hemispherical retarding voltage grids between the sample and the detection screen. The detection is usually performed using a phosphor fluorescent screen, which locally converts the energy of the impinging electrons to light. For this fluorescence to occur, the outgoing electrons that passed the retarding grid must be accelerated by a screen voltage of few keV.

Figure 5 shows some examples of LEED measurements. An appearance of the superstructure due to the adsorption of N atoms is illustrated in Fig. 5a. The clean Rh(100) surface, with a square surface symmetry, exhibits the LEED pattern at low electron energies that shows only the main diffraction spots (0,1), (0,-1), (1,0), (-1,0), (1,1), (1,-1),(-1,1), and (-1,-1), but not all spots are visible in the image due to the experimental limitations. When N is dosed to the surface in a full monolayer (ML), nitrogen atoms assume adsorption positions in every other hollow site along the four-fold symmetry axes of the Rh(100) surface [42]. In other words, they form a $c(2\times2)$ superstructure which is clearly visible in the LEED pattern: beside the main diffraction points from the Rh(100) substrate, additional (1/2,1/2), (1/2,-1/2), (-1/2,1/2), and (-1/2,-1/2) appear. Figure 5b

Die approbierte gedruckte Originalversion dieser Dissertation ist an der TU Wien Bibliothek verfügbar.
The approved original version of this doctoral thesis is available in print at TU Wien Bibliothek.
TU Bibliothek Your knowledge hub WIEN

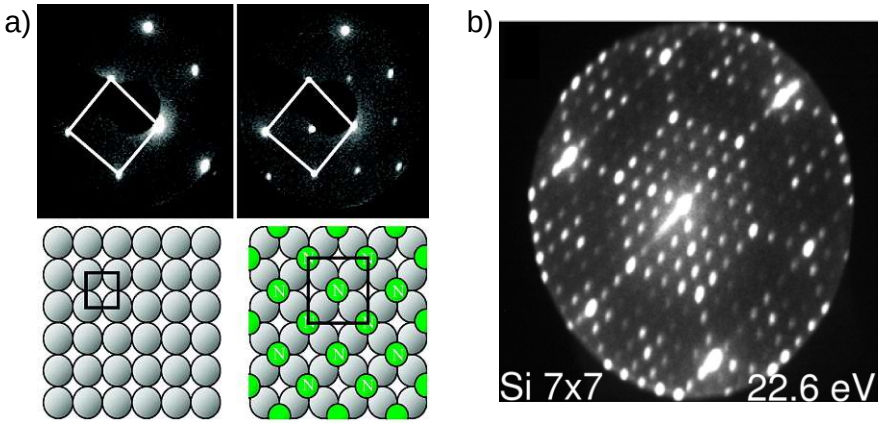

Figure 5: **LEED patterns of pristine and reconstructed surfaces.**
a) LEED patterns (top) and ball models viewed from the top (bottom) before (left) and after (right) N adsorption to clean Rh(001) surface. LEED reveals that the N atoms adsorb in a $c(2\times2)$ superstructure.
Reprinted Figure 1 [42] with permission from [Maarten M. M. Jansen, Ben E. Nieuwenhuys, Daniel Curulla Ferré, and J. W. (Hans) Niemantsverdriet, *The Journal of Physical Chemistry C*, 113, 12277 (2009)]. Copyright (2009) American Chemical Society.
b) LEED pattern of the famous Si(111)(7×7) reconstruction, for which a structural model is shown in Fig. 3b.
Reprinted Figure 1(b) [44] with permission from [B. Qi, S. Ólafsson, M. Göthelid, H.P. Gislason, and B. Agnarsson, *Thin Solid Films*, 531, 61 (2013)]. Copyright (2013) Elsevier.

shows the LEED pattern of the famous (7×7) reconstruction of the Si(111) surface. Silicon crystallizes in a fcc crystal structure, which determines the hexagonal symmetry of its (111) faces, thus the main LEED spots of this surface have a six-fold symmetry. When a clean Si(111) surface is heated above 700 °C in vacuum, it rearranges the (7×7) reconstruction to minimize the surface energy [43]. Three additional LEED spots appear between the neighboring main diffraction spots of the unreconstructed surface, and many others between the second-order diffraction spots, but all preserve the six-fold symmetry.

Both examples above illustrate that LEED is a powerful technique that gives quick insight into the long-range order at the surface. In the research that led to this Thesis, only qualitative LEED was performed, where the kinetic approximation of diffraction is valid enough. LEED can also be used quantitatively, by monitoring the change of the intensity of LEED spots with a change of incoming electron energy, *i.e.*, recording $I(E_K)$ curves. The experimental variation of intensity is then compared to the calculated variation of intensity, obtained by applying the dynamical scattering theory (multiple single-electron scattering events) to the proposed structural model.

The diffracted electrons detected by a phosphor screen in LEED originate from the region of the sample that is exposed to the impinging low-energy electron. This area is usually large, in the order of 1 mm^2, and amounts to the majority of the sample surface. Even perfect crystal surfaces are usually not uniform across the entire sample: rotational domains of surfaces with symmetries lower than four-fold symmetry, domains with different electronic and structural properties, differently reconstructed domains etc. are routinely present across the surface area as large as the size of the incident electron beam. In that case, LEED patterns will exhibit spots corresponding to each domain that is irradiated by electrons. However, there is a minimum limit to the detection of periodic structures within domains. The distribution of large, uniform domains can be represented by a wide Gaussian function, and very small domains can be represented with a very narrow Gaussian function in real space. Since LEED shows direct insight into the Fourier transform of the real-space structure, large domains will be detected as very sharp and narrow LEED spots, while LEED spots originating from the small domains will be convoluted by a wide Gaussian. This means that as the domains on the surface shrink, their LEED spots will smear out. There is a limit of the domain size that can no longer be recognized as a spot in LEED, and it is referred to as the transfer width of the instrument. Domains smaller than the transfer width, which is in the range of 10 nm, will be detected only as the background contribution to a LEED pattern.

Die approbierte gedruckte Originalversion dieser Dissertation ist an der TU Wien Bibliothek verfügbar.
The approved original version of this doctoral thesis is available in print at TU Wien Bibliothek.
TU Bibliothek Your knowledge hub WIEN

1.3 X-ray photoelectron spectroscopy – XPS

X-ray photoelectron spectroscopy, abbreviated as XPS, is a powerful technique for studying the chemical composition of a surface. The working principle of XPS lies is the fact that when the high-energy photons in the X-ray domain of the electromagnetic spectrum are shining on the sample surface, electrons from core-levels of the surface atoms are photoemitted. Photoemitted electrons leave the surface and enter the vacuum if they gain sufficient energy, *i.e.*, if their kinetic energies E_{Kin} after interaction with a X-ray photon are larger than the sum of their binding energy E_{Bin} and the work function of the material ϕ_{sample}. All photoelectrons emitted from a given core-level of a surface element will have the same kinetic energy, with only slight smearing due to the slight polychrome nature of the incoming X-rays, intrinsic width of the X-ray photons, local variation of the of the atomic/ionic potential, different chemical environments, electron correlations etc. Detection of the photoemitted electrons' energy is performed using an electron analyzer, which measures the kinetic energy of the incoming electrons with respect to the Fermi level of the analyzer. The measured kinetic energy can be transformed into the electrons' binding energy according to eq. 1.10, as will be discussed later. The chemical identification of the surface atoms is performed by plotting a spectra of the intensity of the incoming electrons with different binding energy, and comparing the result with the standardized data for the binding energies of elements in a large number of different solids.

Figure 6 shows the principle of operation for a typical XPS experiment. X-rays are produced by a laboratory X-ray source like the one sketched in Fig. 6a for experiments performed in-house. Heated filament emits electrons, which are then accelerated towards an anode in a large potential difference between the anode and the filament, in the order of $\mathrm{E_{Kin,e}} \approx 10\,\mathrm{keV}$. High-energy electrons hit and ionize the film of an elemental material covering the surface of the anode, referred to as the anode material. The ionized element of the anode subsequently returns to the ground state by electron recombination from the high-energy orbital to the empty core-level, and releases an X-ray photon during the process. Typical anode materials are elemental magnesium and aluminum. They can readily loose an electron from a $1s$ orbital when bombarded with high-energy electrons, since the binding energy for an electron in $1s$ orbital is $\mathrm{E_{Bin}}$=1303.4 eV for Mg [45] and $\mathrm{E_{Bin}}$=1558.2 eV for Al [46], while the incoming electron energy is $\mathrm{E_{Kin,e}} \approx 10\,\mathrm{keV}$. Core-holes are then neutralized by electron recombination that is most probable to occur from the $2p_{3/2}$ orbital with $\mathrm{E_{Bin}}$=49.8 eV for Mg [47] and $\mathrm{E_{Bin}}$=71.6 eV for Al [48]. This transition $2p_{3/2} \rightarrow 1s$ is often radiative for Mg and Al, and these two anode materials produce Mg Kα_1 and Al Kα_1 (Siegbahn notation [49]) or Mg K-L$_3$ and Al K-L$_3$ (IUPAC notation [50]) characteristic X-rays at $h\nu$=1253.6 eV and $h\nu$=1486.6 eV, respectively. Radiative $2p_{1/2} \rightarrow 1s$ transitions can also occur to produce Mg Kα_2 and Al Kα_2 (Mg K-L$_2$ and Al K-L$_2$), but for the Mg and Al elements these two transitions are very close in energy and are commonly jointly referred to as the Mg Kα and Al Kα lines. Other characteristic lines such are Kα', Kα_3 and Kα_4 are present in the polychrome X-ray source but with much lower intensity. The characteristic X-ray lines are superimposed on the large background photon signal originating from the suddenly decelerated electrons upon collision with the anode material, *i.e.*, Bremsstrahlung radiation. This radiation is filtered at the exit slit of the X-ray source either by a Cu(110) crystal monochromator, or a thin aluminum window. The emitted X-rays are not focused in laboratory conditions, and the X-ray source should be as close to the sample as possible for the highest yield. The angle of the incident X-rays with respect to the surface normal of the sample determines the penetration depth of the incoming photons, because it depends only on the normal component of the total momentum $k_\perp$. When the X-rays impinge on the sample along the sample normal, the penetration depth of the high-energy photons is many layers into the surface, while when the X-rays reach the sample under a very small, grazing angle, the $k_\perp$ is only a portion of the total wavevector $\overrightarrow{k}$. XPS is a highly surface-sensitive technique due to the limited (several nanometers) electron mean free path within a solid: even if the X-ray photon ionizes an atom deep within the surface, the emitted electron will scatter inelastically with other electrons before reaching the vacuum above the surface, and the detected photoemitted electrons thus have to originate in the vicinity of the surface.

A single photo-emission event is illustrated in Fig. 6b, for a case when a single X-ray photon of energy $h\nu$ an ejects electron from the inner K shell of a surface atom. The electron that is ejected from a K shell of the atom can leave the sample and enter the vacuum above the surface only if its energy gain is larger than the work function of the sample, *i.e.*, only if $h\nu - E_{\mathrm{Bin,K}} > \phi_{\mathrm{sample}}$, with a kinetic energy of $E_{\mathrm{Kin}} = h\nu - E_{\mathrm{Bin,K}} - \phi_{\mathrm{sample}}$. Otherwise, the ejected electron will not enter free states in vacuum but rather jump to an excited state that has a non-zero matrix element for transitions from the K shell. The remaining core-hole in the K shell has to be neutralized by electron recombination from a higher-energy orbital. Non-radiative recombination is likely to occur, but two recombination processes illustrated in Fig. 6b are also possible: radiative recombination and an Auger process. In case of a radiative recombination, an electron from a L shell will fill the hole in the K shell,

Die approbierte gedruckte Originalversion dieser Dissertation ist an der TU Wien Bibliothek verfügbar.
The approved original version of this doctoral thesis is available in print at TU Wien Bibliothek.
TU Bibliothek Your knowledge hub WIEN

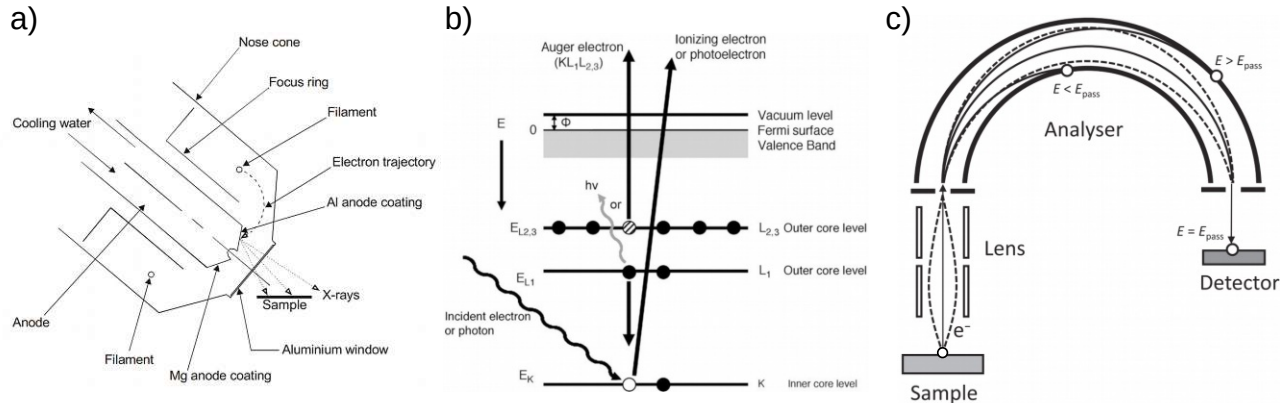

Figure 6: **A schematic of an XPS measurement.**
a) A sketch of the schematics of the Scienta Omicron DAR 400 X-ray source. Created X-rays exit the X-ray source and impinge on the sample.
Reprinted image with permission from [51] Scienta Omicron
b) An illustration of the core-levels of a surface atom. Incoming X-ray photons can ionize the surface atoms by photoemission or Auger processes.
Reprinted Figure 16.42 [52] with permission from [D. R. Baer and S. Thevuthasan, *Handbook of Deposition Technologies for Films and Coatings*, Chapter 16 - Characterization of Thin Films and Coatings, 749 (2010)]. Copyright (2010) Elsevier.
c) A sketch of the detection scheme in XPS. The electrons emitted from the sample enter the slit of the hemispherical analyzer, where they are separated by kinetic energies. Counting the detected electrons at given kinetic energies results in a XP spectra.
Reprinted Figure 5 [53] with permission from [Alexander G.Shard, *Characterization of Nanoparticles*, Chapter 4.3.1 - X-ray photoelectron spectroscopy, 349 (2020)]. Copyright (2020) Elsevier.

followed by an emission of a characteristic photon - this is the same process that is responsible for generating X-rays in an X-ray source.

For most light elements in the periodic table, a recombination through an Auger process is more likely than radiative recombination, due to the Fermi's golden rule. In an Auger process, an electron from a L shell fills the hole in the K shell, and the excess energy $E_{\mathrm{Bin,K}} - E_{\mathrm{Bin,L_1}}$ is transfered to another electron in the L_2 or L_3 shell. When this excess energy, lowered by the binding energy of an electron in L_2 shell for example, is larger than the work function of the sample, *i.e.*, when $E_{\mathrm{Bin,K}} - (E_{\mathrm{Bin,L_1}} + E_{\mathrm{Bin,L_2}}) > \phi_{\mathrm{sample}}$, the electron leaves the sample and enters the vacuum above the surface. These electrons are referred to as Auger electrons, and their kinetic energy is independent of the energy of the incident X-ray that initially ionized a surface atom $E_{\mathrm{Auger}} = E_{\mathrm{Bin,K}} - (E_{\mathrm{Bin,L_1}} + E_{\mathrm{Bin,L_2}}) - \phi_{\mathrm{sample}}$. The momentum direction of the photoemitted and Auger electrons is not isotropic, but depends on the emission angle function with respect to the angle of the incoming X-rays. The emission angle function is proportional to the third Legendre's polynomial that describes the orbital wavefunctions within the atom by spherical harmonics, and must be taken into account when performing quantitative XPS measurements. For qualitative XPS, only the high electron count per second is necessary, which can be achieved when the angle between the X-ray source and the analyzer fits the "magic angle" of $\arctan\sqrt{2} \approx 54,7°$. In order to collect as many photoemitted electrons as possible the sample is located in the vicinity of the entry slit of the electron-energy analyzer. Electrons that pass the entry slit of the electron-energy analyzer are first focused using electrostatic focusing Einzel-lenses, after which they enter a hemispherical chamber with an uniform electric field applied perpendicular to the electron trajectory, illustrated in Fig. 6c. Due to the presence of the electric field, and according to Maxwell's equations, electrons will experience radial acceleration and assume a trajectory with radius r. This radius is defined by the strength of the electric field E and depends on the kinetic energy of the electron as $r = 2E_{\mathrm{Kin}}/qE$, where q is the elemental charge. Therefore, hemispherical analyzer detects kinetic energies of the incoming electrons. In general, an x-ray photoelectron spectrum (XP spectrum) can be produced by changing the strength of the applied electric field E in a given range, and measuring the amount of electrons that reach the electron detector at each value of the applied field,

Die approbierte gedruckte Originalversion dieser Dissertation ist an der TU Wien Bibliothek verfügbar.
The approved original version of this doctoral thesis is available in print at TU Wien Bibliothek.
TU Bibliothek Your knowledge hub WIEN

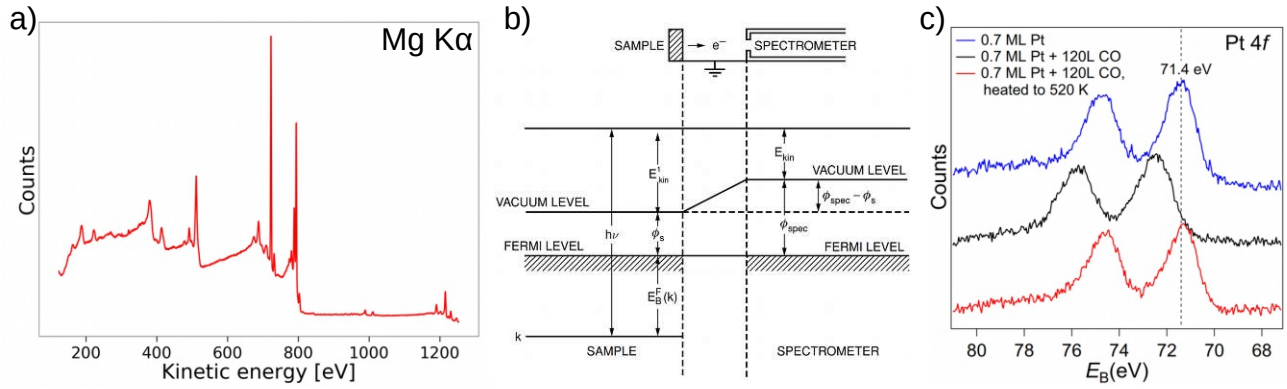

Figure 7: **Examples of XPS measurements and conversion between kinetic and binding energies.**
a) A typical measured XP spectrum of a clean rutile $TiO_2(110)$ surface obtained with Mg Kα X-rays, plotted against the measured kinetic energies of the photoemitted electrons.
b) Alignment of the energy levels in the sample and the XPS analyzer, that illustrates how the electron kinetic energies are measured with respect to the Fermi level of the sample.
Reprinted Figure 10.6 [54] with permission from [Terry L. Alford, Leonard C. Feldman, and James W. Mayer, *Fundamentals of Nanoscale Film Analysis*, Chapter 10 - X-ray Photoelectron Spectroscopy, 149 (2007)]. Copyright (2007) Springer Nature.
c) The detailed XP spectrum in the range of the binding energies of the Pt 4f doublet state, obtained with Mg Kα X-rays on the $Fe_3O_4(110)$ surface after deposition of atomic platinum to the surface, and subsequent dosing of molecular CO.
Reprinted left panel in Figure 5 [55] with permission from [Roland Bliem, Jessi E. S. van der Hoeven, Jan Hulva, Jiří Pavelec, Oscar Gamba, Petra E. de Jongh, Michael Schmid, Peter Blaha, Ulrike Diebold, and Gareth S. Parkinson, *Proceedings of the National Academy of Sciences*, 113, 8921 (2016)].

i.e., at each kinetic energy of the incoming electrons. In laboratory setups however, the radius r of the electron trajectory within the analyzer is usually set to a constant value – this implies that only electrons with one energy, defined as the pass energy, can reach the electron detector. In this setup, the energy of the collected electrons can be varied in a broad range (from 0 eV to 2 keV for example) by subjecting them to a retarding potential prior to their entry into the hemispherical trajectory. Counting the number of detected electrons against the value of the retarding potential at which they were detected then creates an XP spectrum, an example of which is shown in Fig. 7a.

Once an electron is emitted into the vacuum and passes through the electron analyzer towards the electron detector, measured kinetic energy does not correspond to the kinetic energy of the electron in vacuum in the vicinity of the sample. Instead, the radius of the trajectory through the hemispherical analyzer is determined by the kinetic energy of the electron with respect to the vacuum level of the analyzer, as illustrated in Fig. 7b. Fermi levels of the sample $E_{\mathrm{F,s}}$ and the analyzer $E_{\mathrm{F,a}}$ are aligned when both are properly grounded to the same ground, and differ only when there is an applied potential difference U between them, such is the retarding potential of the hemispherical analyzer. The measured kinetic energy of the electrons in the hemispherical analyzer $E_{\mathrm{Kin,a}}$ are obtained with respect to the vacuum level of the analyzer $E_{\mathrm{V,a}}$, which is further related to the Fermi level of the analyzer through the work function of the analyzer ϕ_{a}. When the work function of the analyzer is known (calibrated on the valence edge of Au), measured kinetic energies can be transformed to binding energies E_{Bin} of the photoemitted electrons from the sample as:

$$E_{\mathrm{Bin}} = h\nu - E_{\mathrm{Kin,a}} - (eU + \phi_{\mathrm{a}}) \tag{1.10}$$

which are a fingerprint of different chemical elements on the surface. The essence of the qualitative XPS technique is the comparison of the peaks in the binding energies, with the standardized values for the binding energies of electrons that is known for most elements in the periodic table [56]. This makes XPS a powerful technique for identification of surface elements and possible contaminants.

Fig. 7c demonstrates one of the additional applications of XPS measurements. It shows a small region of the XPS of the $Fe_3O_4(110)$ surface that was covered 0.7 ML of platinum, and the kinetic energies have been

Die approbierte gedruckte Originalversion dieser Dissertation ist an der TU Wien Bibliothek verfügbar.
The approved original version of this doctoral thesis is available in print at TU Wien Bibliothek.
TU Bibliothek WIEN Your knowledge hub

transformed to the binding energy according to 1.10. The spectrum focuses on the binding energies of the valence $4f$ levels of Pt atoms on the surface. After the deposition of CO to the Pt covered surface, the Pt $4f$ doublet shifts to higher binding energies. This indicates that the Pt atoms play a role during the CO adsorption: the increase in the binding energy of the electrons in the Pt $4f$ orbital indicates that these electrons became more tightly bound. Commonly, this occurs due to the electron donation from the Pt atom to the CO in this example, which reduces the electronegative screening of the positive Pt core. The remaining electrons within Pt $4f$ orbitals experience stronger attraction to the Pt core, and their photoemission requires slightly higher energy. In this experiment, annealing this surface to 520 K will desorb the CO and the Pt $4f$ levels will return to their original state. Therefore, beside chemical identification, XPS can be thoroughly utilized for observing the surface chemical reaction by measuring the shifts in the binding energies of the surface atoms.

There are more advanced applications of the XPS technique, such is the imaging the spatial distribution of the chemical composition on the surface through the analyzer [57], quantification of the XPS intensity and the cross-sections for the photoemission to obtain the concentrations of the elements on the surface [58], determining the geometric properties of the surface structure by X-ray photoelectron diffraction [59] etc. In the research that led to this Thesis, XPS was performed only qualitatively.

Die approbierte gedruckte Originalversion dieser Dissertation ist an der TU Wien Bibliothek verfügbar.
The approved original version of this doctoral thesis is available in print at TU Wien Bibliothek.
TU Bibliothek Your knowledge hub WIEN

1.4 Scanning tunneling microscopy – STM

Scanning tunneling microscopy, abbreviated as STM, is one of the most beautiful surface science techniques. It can readily provide real-space images of single crystal surfaces with the spatial resolution of a single atom, or a single electronic orbital. The technique was experimentally developed in the beginning of the 1980's by Gerd Binnig and Heinrich Rohrer [60, 61] for which they received the Nobel prize in Physics in 1986 [62]. Nowadays, it is widely employed in many surface physics laboratories throughout the world, and it is used to study the geometrical and electronic arrangements on bare surfaces, and their interaction with adsorbates.

1.4.1 Principle and realization

At the heart of the STM technique lies the quantum-mechanical electron tunneling through a dielectric barrier between two materials that are not in contact. The probability of electron tunneling between two metals depends on the shape and the size of the potential barrier between them. Fig. 8 sketches several one-dimensional potential barriers for electron tunneling. Electrons that transfer from one side to the other side of the barrier even if their energy is lower than the height of the potential barrier $E_\mathrm{e} < U_0$, are considered to be tunneled between the two materials. In other words, the wavefunction of an electron is non-zero on both sides of the barrier, as well as within the barrier. The simplest case for studying quantum-mechanical tunneling is the rectangular potential barrier sketched in Fig. 8a. Solving the time-independent Schrödinger's equation for electrons on either side and within the barrier, while preserving the wavefunction continuity at the borders of the three regions, results in the probability of electron tunneling. For electrons residing on one side of the barrier, the tunneling probability depends on the square of the modulus of the electron wavefunction $\psi(\overrightarrow{r})$ on the other side of the potential barrier. In Wentzel–Kramers–Brillouin (WKB) approximation [63], the transmission T through a rectangular barrier is:

$$T = |\psi(\overrightarrow{r})|^2 \approx e^{-2d\sqrt{\frac{2m_\mathrm{e}(U_0-E)}{\hbar^2}}} = e^{-2d\sqrt{\frac{2m_\mathrm{e}(\phi-E)}{\hbar^2}}} \tag{1.11}$$

where d is the width of the one-dimensional potential barrier, *i.e.*, separation distance between the two metals. The simple rectangular barrier is representative when the electrons are tunneled between two metals with equal work functions, which determine the height of the potential barrier $U_0 = \phi = \phi_1 = \phi_2$.

A more realistic tunneling barrier is sketched in Fig. 8b, where tunneling occurs between two different metals that are characterized by different work functions $\phi_1 \neq \phi_2$, and the height of the potential barrier $U(x)$ varies with the position x. Additionally, the metal on the right side is biased on a positive potential V, which lowers the energy of all electron levels. Therefore, the Fermi levels are no longer aligned, and there is a potential energy difference eV between them. The work function of the biased metal was shifted downwards by eV as well, so the difference between the vacuum levels of the two metals is $\phi_1 - \phi_2 - \mathrm{e}V$. Therefore, the potential barrier for tunneling from the Fermi level of the metal on the left to the vicinity of the Fermi level of the metal on the right is defined by a slope of eV on the bottom, and $\phi_1 - \phi_2 - \mathrm{e}V$ on the top. In other words, it is a trapezoidal potential barrier that is characterized by transmission T in WKB approximation:

$$T = |\psi(\overrightarrow{r})|^2 \approx e^{-\frac{4}{3}\frac{d}{\Delta\phi+eV}\sqrt{\frac{2m_\mathrm{e}}{\hbar^2}}\left[(\phi_2-eV-E)^{\frac{3}{2}}-(\phi_1-E)^{\frac{3}{2}}\right]} \tag{1.12}$$

which is valid when the applied bias voltage is smaller than the work function of the biased metal, as illustrated in Fig. 8b.

The trapezoidal potential barrier represents the idealized tunneling barrier at $T = 0\,\mathrm{K}$, when the Fermi-Dirac distribution of both metals is a step-function. A realistic potential barrier for tunneling is more complex due to the presence of image charges for example, and Fig. 8c sketches an arbitrarily shaped potential barrier. In general, the transmission through the regularly shaped potential barriers can be analytically derived. When the potential barrier is of arbitrary shape $U(x)$ as in Fig. 8c, it is easier to calculate the total transmission numerically by dividing the potential barrier into N infinitesimally small, regularly shaped barriers of Δx width. The total transmission T is then the product of the individual transmissions through each barrier $T_i(x)$, and can be expressed in WKB approximation as:

$$T \approx \prod_{i=1}^{N} T_i(x) \approxeq \prod_{i=1}^{N} e^{-2\sqrt{\frac{2m_\mathrm{e}}{\hbar^2}}\Delta x\sqrt{U(x_i)-E}} = e^{-2\sqrt{\frac{2m_\mathrm{e}}{\hbar^2}}\sum_{i=1}^{N}\sqrt{U(x_i)-E}\Delta x} = e^{-2\sqrt{\frac{2m_\mathrm{e}}{\hbar^2}}\int_0^d\sqrt{U(x')-E}dx'} \tag{1.13}$$

and solved numerically.

Die approbierte gedruckte Originalversion dieser Dissertation ist an der TU Wien Bibliothek verfügbar.
The approved original version of this doctoral thesis is available in print at TU Wien Bibliothek.
TU Bibliothek Your knowledge hub WIEN

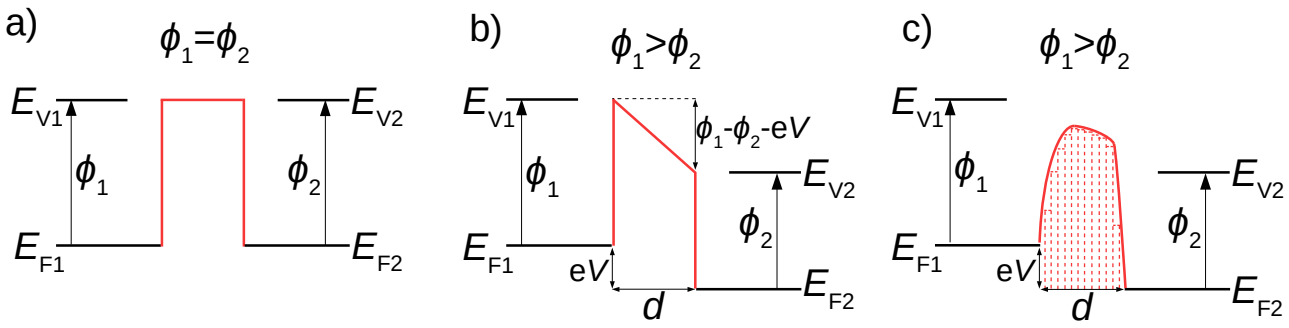

Figure 8: **Sketch of one-dimensional potential barriers for the quantum tunneling.** a) Tunneling between two identical metals through a rectangular potential barrier. b) Tunneling between two different metals through a trapezoidal potential barrier. c) Tunneling between two different metals through an arbitrarily shaped potential barrier that can be decomposed as a series of rectangular barriers.

In all of the discussed possibilities for the shape of the potential barrier, it is clear that the transmission, and the electron tunneling rate, strongly depend on the mutual separation of the two metals. The distance between two metals d contributes to the decay of the tunneling probability much more than other relevant quantities, such are the work-function differences and the applied biases. This makes the realization of the STM technique possible: two metals can approach extremely close to each other, and the tunneling current will be detected only at distances in the order of 1–5 typical ionic radii. In other words, when two metals are approaching each other, detecting the tunneling current implies that they are very close to each other, but still not in contact.

A schematic of a typical STM measurement setup is illustrated in Fig. 9. All STM measurement are performed inside a vibration isolated measurement head illustrated in Fig. 9a. It consists of the sharp metal rod, *i.e.*, the *tip*, the surface under investigation , *i.e.*, the *sample*, the piezoelectric tube used for lateral and vertical motion, the stick-slip-motion motor, and all necessary electrical contacts. The electronic elements are only contacted inside the measurement head, while their connections lead to instruments outside of the chamber, with the exception of the tunneling-current amplifier that is often situated close to the source of current to increase the detection limit and reduce the noise. In a typical setup, either the tip or the sample remain fixed in position, while the other element can move. The sketch in Fig. 9a illustrates the scenario in which the sample is fixed, and the tip can move laterally and vertically because it is situated on top of the piezoelectric tube; when the tip is fixed then the sample is connected to a piezoelectric tube. The two elements are gradually approached to each other until the tunneling current is detected, after which the approach stops to prevent the destructive collision of the two elements.

The distance between the tip and the sample can be regulated very precisely using a piezoelectric tube, illustrated in Fig. 9b. It operates by utilizing piezoelectric properties of certain materials – they change their volume depending on the strength and the direction of the applied voltage. By applying different voltages at the sides of the piezoelectric tube, the tube will bend laterally. If the same voltage is applied simultaneously at all sides of the piezoelectric tube, the tube will shrink or contract depending on the polarity of the applied voltage. Usually, they are constructed from lead zirconate titanate, because its piezoelectric properties are very well characterized, and lateral expansion/contraction can occur at reasonable voltage values. This ensures very precise motion of the tip with respect to the sample, and can be altered by values lower than 0.1 pm in each direction. This implies that the values of the tunneling current between the tip and the sample can be precisely regulated by slight changes in the vertical distance between the two. It is important to note that the absolute distance between the tip and the sample is not clear in STM, and also questionable from the physical perspective, since the interaction of materials mutually separated by 1–5 ionic radii blurs conventional notions of distance.

STM provides spatial images of the electronic structure of the sample by moving the tip position in a well-defined grid of equally spaced points over the selected surface area. This can be performed in constant-height mode $z = const.$, after the tip was brought sufficiently close to the surface such that the tunneling current I_t is detected. The tip is then moved laterally and the magnitude of the tunneling current is recorded at each point, which creates a two-dimensional map of the electronic structure over the given surface area $I_t(x, y)|_{z=const.}$. The other mode of operation is referred to as the constant-current mode $I_t = const.$. In this case, the vertical

Die approbierte gedruckte Originalversion dieser Dissertation ist an der TU Wien Bibliothek verfügbar.
The approved original version of this doctoral thesis is available in print at TU Wien Bibliothek.
TU Bibliothek WIEN Your knowledge hub

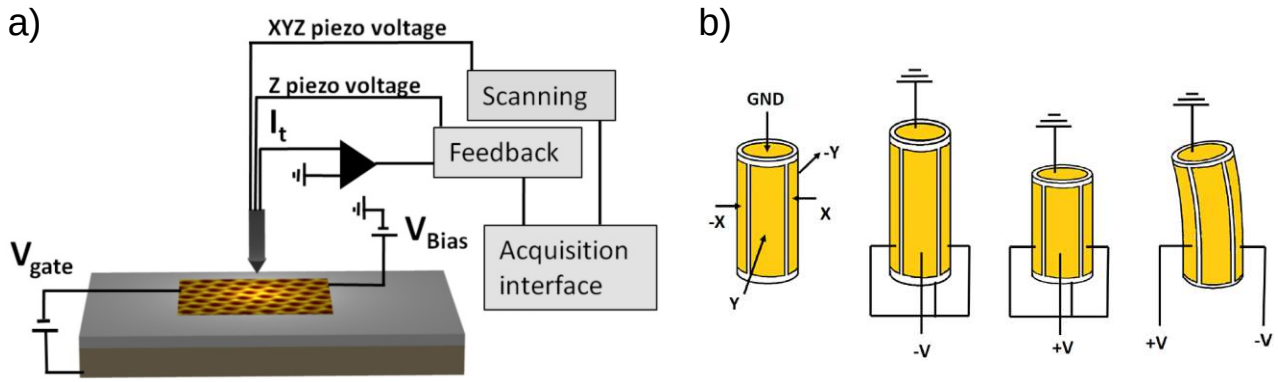

Figure 9: **Sketch of the STM working principle.**
a) Illustration of the STM measurement setup.
Reprinted Figure 5 [65] with permission from [Adina Luican-Mayer and Eva Y. Andrei, *Physics of Graphene*, Chapter - Probing Dirac Fermions in Graphene by Scanning Tunneling Microscopy and Spectroscopy, 29 (2013)]. Copyright (2013) Springer Nature.
b) Illustration of the piezoelectric tube with five electrical contacts for high voltage. The tube controllably bends or extends/contracts depending on the magnitude and the polarity of the applied voltage.
Reprinted Figure 2.7 [66] from Somesh Chandra Ganguli, *arXiv preprint arXiv:1609.03487* (2016) with permission of the Author.

distance between the tip and the sample varies depending on the magnitude of the tunneling current at each point. This creates a two-dimensional map of the vertical extent of the surface electronic states into the vacuum $z(x,y)|_{I_t=const.}$. Namely, when a single value is chosen as the desired magnitude of the tunneling current I_r, the tip will move closer to the surface if $I_t < I_r$, or further away from the surface if $I_t > I_r$. In the constant-current mode of STM operation, illustrated in Fig. 10a, a feedback loop controls the distance between the tip and the sample. The feedback loop is calculating the difference between the measured and the reference tunneling current $I_t - I_r$, and outputs the voltage V_f that corresponds to the difference of the two in amplitude $V_f(I_t - I_r)$, with polarity that depends whether $I_t > I_r$ or $I_t < I_r$. This voltage is then superimposed through the PID controller [64] to the reference voltage of the piezoelectric tube's vertical direction, and the tip is vertically approached to or retracted from the surface when necessary.

The detected current in STM originates from electrons that are tunneling between the surface and the most protruding atom of the tip. Since the electron transmission through vacuum barrier depends exponentially on the separation of the tip and the sample, the exact shape of the STM tip apex is not critical. Fig. 10b illustrates a realistic tip apex; it consists of many separate tip apices, but the tunneling will occur only from the most protruding one. In the sketched example, the tunneling contribution of the second tip apex is negligible since it is two atomic layers further away from the surface than the dominant tip; it contributes to roughly 1–10% of the tunneling current. Although the presence of the additional tip apices is not crucial when studying atomically flat surfaces, it becomes bothersome if the surface has terraces, large clusters, or point defects, which can create ghost images of the features recorded by the dominant tip apex. A singe, atomically sharp tip apex is therefore always desirable while performing STM.

1.4.2 Contrast formation

The tunneling current will always appear between two metallic materials in experiments, and the lack of the *a priori* knowledge of the shape of the potential barrier does not prevent STM measurements. Fig. 11 illustrates the electron tunneling between energy levels of two materials that are sufficiently close to each other. The tunneling of electrons can only occur from the occupied electronic states of one material to the unoccupied states of the other. Tunneling between occupied states is forbidden by the Pauli's exclusion principle. In the absence of the external biasing, the Fermi levels of two metals are aligned and the tunneling will occur only due to the possible Fermi-Dirac's smearing at $T > 0$. When one metal is biased by an infinitesimally small amount of positive bias, as illustrated in Fig. 11a, a single unoccupied state above its Fermi level will have the same energy as the electrons at the Fermi level of the other metal. The tunneling then occurs from a single occupied

Die approbierte gedruckte Originalversion dieser Dissertation ist an der TU Wien Bibliothek verfügbar.
The approved original version of this doctoral thesis is available in print at TU Wien Bibliothek.
TU Bibliothek Your knowledge hub WIEN

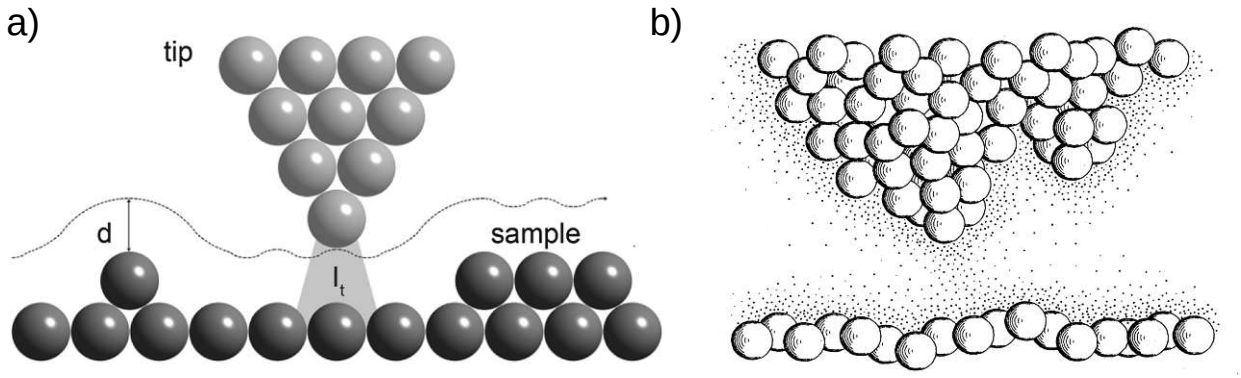

Figure 10: **Ball models of a tip and a surface during STM scanning.**
a) STM measurement in the constant-current mode. The tip follows the contour of equal local density of states above the surface.
Reprinted Figure 1 [67] with permission of Royal Society of Chemistry, from [Matthew S. J. Marshall and Martin R. Castell, *Chemical Society Reviews*, 43, 2226 (2014)]; permission conveyed through Copyright Clearance Center, Inc.
b) Illustration of an irregular tip with several protrusions. In most cases, the tunneling occurs only between the most-protruding atom of the entire macroscopic tip and the sample, which especially holds true for atomically flat surfaces with no terraces or protruding defects.
Reprinted bottom panel of Figure 2 [62] from [Gerd Binnig and Heinrich Rohrer, *Reviews of Modern Physics*, 59, 615 (1987)] with permission of APS. Copyright (1987) American Physical Society.

state below the Fermi level of one metal, to a single unoccupied state above the Fermi level of the other metal, and the tunneling current depends on the transmission, *i.e.*, the overlap of the electron wavefunctions of these two states.

In typical experiments, the sample is biased by 0–3 V in either polarity. In Fig. 11b the metal on the right side represents the sample that was biased by positive voltage, while the metal on the left side represents the grounded tip. Elastic electron tunneling occurs from all occupied electronic states of the tip within the energy range $E \in [E_{\mathrm{F1}} - eV, E_{\mathrm{F1}}]$, to all unoccupied electronic states of the sample within the energy range $E \in [E_{\mathrm{F2}}, E_{\mathrm{F2}} + eV]$. The tunneling current thus depends on the overlap of all the electron wavefunctions of the tip with all the electron wavefunctions of the sample at the same energy. In a commonly used approximation developed by Tersoff and Hamann soon after the realization of the first STM machine [68], the tunneling current between these states can be calculated within the first-order perturbation theory as [69]:

$$I_t = \frac{2\pi e}{\hbar} \sum_{\mu\nu} f(E_\mu) \left[1 - f(E_\nu + eV)\right] |M_{\mu\nu}|^2 \, \delta\left(E_\mu - E_\nu\right) \tag{1.14}$$

where $f(E_\mu)$ is the value of the Fermi-Dirac distribution of occupied electronic states in the tip at energy (E_μ), $1 - f(E_\nu + eV)$ is the value of the Fermi-Dirac distribution of unoccupied electronic states in the sample at energy (E_ν), $\delta\left(E_\mu - E_\nu\right)$ is Kronecker's delta function ensuring elastic tunneling between the states of the tip and the sample with the same energy $E_\mu = E\nu$. $M_{\mu\nu}$ is the Bardeen's transition matrix [70], whose elements correspond to the overlaps of the wavefunctions of the tip $\psi_\mu(\overrightarrow{r})$ and the sample $\psi_\nu(\overrightarrow{r})$ in the absence of an applied bias, and it is calculated within the volume between the tip and the surface as:

$$M_{\mu\nu} = -\frac{\hbar^2}{2m_e} \int d\overrightarrow{S} \left(\psi^*_\mu(\overrightarrow{r}) \nabla \psi_\nu(\overrightarrow{r}) - \psi^*_\nu(\overrightarrow{r}) \nabla \psi_\mu(\overrightarrow{r})\right) \tag{1.15}$$

Therefore, Tersoff-Hamann model explicitly accounts for the density of states at the tip and the surface, namely for the overlap of wavefunctions of the tip and the sample at their discrete energy eigenvalues. The three-dimensional reality of tunneling between the tip and the sample can be simplified by modeling the final atom at the tip apex with spherical s-wave orbitals that extend into vacuum furthest away from the tip. The constant-current STM images then follow the contours of constant local density of states over the surface. The spatial resolution for the interatomic distances on the surface scanned with a tip modeled by an s-wave orbital is worse

Die approbierte gedruckte Originalversion dieser Dissertation ist an der TU Wien Bibliothek verfügbar.
The approved original version of this doctoral thesis is available in print at TU Wien Bibliothek.
TU Bibliothek Your knowledge hub WIEN

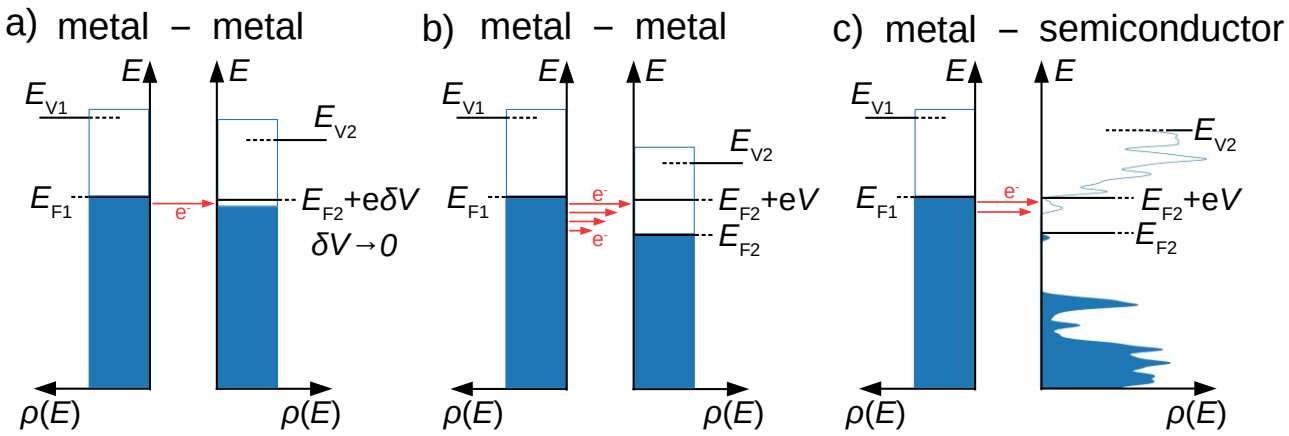

Figure 11: **Sketch of the tunneling between electronic states of the sample and the STM tip.** a) Tunneling between one occupied state in the metallic tip to one unoccupied state of the metallic sample positively biased by infinitesimally small voltage δV. b) Tunneling between a series of occupied states in the metallic tip to a series of unoccupied states of the positively biased, metallic sample. c) Tunneling between a series of occupied states in the metallic tip to a series of unoccupied states of the positively biased, semiconducting sample.

than imaging the surface by a tip represented with an d_{z^2} orbital. This plays a role in studying metal surfaces where interatomic distances are small, and a d-band metal tip such is W, Ir, or Pt should be used [71]. On the other hand, the shape of the tip's valence orbital is not as important when studying surfaces of oxides or reconstructed surfaces where interatomic distances are much larger.

The main prerequisite necessary for employing STM is the sample conductivity, *i.e.*, the band gap of the sample must not be too large. Otherwise, the electronic states in the valence and conducting band will not be available with the application of reasonable values of bias voltages. STM is therefore restricted to investigation of metal and semiconductor surfaces, and their interaction with various non-insulating adsorbates, while insulating surfaces cannot be investigated with STM. Naturally, the STM tip must be reasonably conductive as well. Tips are usually prepared in such a way that they are fully conducting, additionally ensuring the absence of a band gap and the constant distribution of electronic states with energy in the valence band of the tip. Electron tunneling between a metallic tip and a positively biased, semiconducting sample is illustrated in Fig. 11c. In this example, the sample is an n-type semiconductor with the Fermi level close to the conduction band. Biasing the sample by more than +1 V will align the Fermi level of the metallic tip with the bottom of the conduction band of the sample, and empty-states STM can be performed. When the samples are positively biased (as in the examples so far) the electrons are tunneled from the tip to the unoccupied states of the sample. This is commonly referred to as the empty-states STM because constant-current STM images will display the distribution of the sample's unoccupied states across the surface, and an example can be seen in Fig. 12b.

The application of negative bias on the sample will shift all its energy levels upwards, and electrons will tunnel from the sample into the tip. This is commonly referred to as the filled-states STM because constant-current STM images will display the distribution of the sample's occupied states across the surface, and an example can be seen in Fig. 12c. The tunneling current in Tersoff-Hamann approach still follows eq. 1.14 in filled-states STM, but μ and ν indexes have to be interchanged, and the Bardeen's matrix transposed $M_{\nu\mu} = M^T_{\mu\nu}$. The n-type semiconductor in Fig. 11c posseses an occupied electronic state within the band gap. The negative biasing of the sample will align the Fermi level of the sample with the empty conduction states at the tip. With the proper choice of negative bias voltage on the sample, (≈-1 V in this example), the Fermi level of the tip will be lower in energy than the in-gap state of the sample, but still higher than the top of its the valence band. Then, the tunneling occurs only from the in-gap state towards the tip, and a detailed map of the in-gap state over the surface can be achieved. If the negative bias is greater than -3 V in this example, the top of the valence band of the sample will become higher in energy than the Fermi level of the tip, and the tunneling will occur towards the tip from both, the in-gap state and the valance states of the sample.

Die approbierte gedruckte Originalversion dieser Dissertation ist an der TU Wien Bibliothek verfügbar.
The approved original version of this doctoral thesis is available in print at TU Wien Bibliothek.
TU Bibliothek Your knowledge hub WIEN

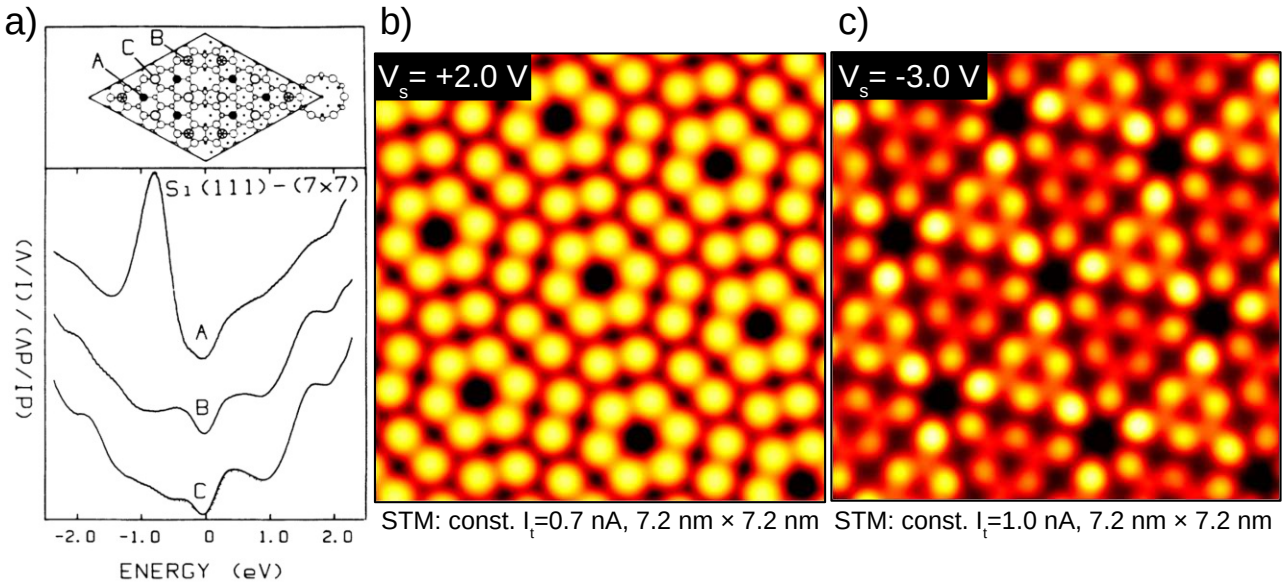

Figure 12: **STM images and electronic structure of the Si(111)(7×7) reconstruction.**
a) STS measurements revealing the local density of states over several points in the (7×7) unit cell. Rest atom (A) exhibits higher occupancy in the valence band compared to adatoms (B and C).
Reprinted Figure 1 [72] from [R. Wolkow and Ph. Avouris, *Physical Review Letters*, 60, 1049 (1988)] with permission of Author(s) and APS. Copyright (1988) American Physical Society.
b) Empty-states STM image of the (7×7) reconstruction, showing all atoms as equivalent.
Reprinted Figure 2(a) [73] with permission from [Lewys Jones, Shuqiu Wang, Xiao Hu, Shams ur Rahman, and Martin R. Castell, *Advanced Structural and Chemical Imaging*, 4, 1 (2018)] under the Creative Commons CC BY license.
c) Filled-states STM image of the same region as in (b), differentiating between faulted and unfaulted halves of the (7×7) unit cell.
Reprinted Figure 2(b) [73] from [Lewys Jones, Shuqiu Wang, Xiao Hu, Shams ur Rahman, and Martin R. Castell, *Advanced Structural and Chemical Imaging*, 4, 1 (2018)] under the Creative Commons CC BY license.

1.4.3 Scanning tunneling spectroscopy

STM can be used to reveal the density of states on the surface, through a method called scanning tunneling spectroscopy, abbreviated as STS. The STS technique exploits the fact that the tunneling current depends on the number of occupied or unoccupied electronic states that fall into the energy window between the tip and the biased sample (or vice versa):

$$I_t \propto \int_{E_{\mathrm{F1}}-eV}^{E_{\mathrm{F1}}} dE T(E)\rho_1(E)\rho_2(E+eV) \tag{1.16}$$

where $\rho_1(E)$ and $\rho_2(E+eV)$ are the density of states at tip and sample, respectively, and $T(E)$ is the transmission at energy E. Increasing the biasing voltage by infinitesimally small amount reveals the newly encompassed electronic states that fall in the additional infinitesimally small energy window. The change in the measured tunneling current with the change of biasing voltage therefore reveals the density of states of both the tip and the sample in this small energy window.

While performing STS, it is the best practice to prepare a metal tip, so that the density of states at the tip is constant in energy $\rho_1(E) = \rho_1$. When the distance between the tip and the surface is kept constant, and if the transmission is assumed to be independent of the energy, the sample's density of states in the small $e\delta V$ energy window can be expressed as:

$$\rho_2(eV + e\delta V) - \rho_2(eV) \propto \frac{dI_t}{dV} \tag{1.17}$$

Die approbierte gedruckte Originalversion dieser Dissertation ist an der TU Wien Bibliothek verfügbar.
The approved original version of this doctoral thesis is available in print at TU Wien Bibliothek.
TU Bibliothek WIEN Your knowledge hub

or sometimes as the derivative of the logarithms of I_t and V, when the transmission cannot be approximated as a constant. In order to reduce the noise of the obtained values, the differentiation in 1.17 is usually not performed numerically, but with a lock-in amplifier instead.

An example of a STS spectrum is shown in Fig. 12a, taken over the (7×7) reconstruction of the P-doped Si(111) surface. Like STM, STS is a highly local technique that captures the electronic states only above the surface atoms above which the atomically sharp tip is positioned. In the example in Fig. 12a, the STS was measured over three characteristic points in the (7×7) reconstruction (marked in the inset), measuring the local density of states at these points. Each spectrum is characterized by a 0.2 eV band gap, and the density of electronic states is different at each of the points: positions marked as B (corner adatom) and C (center adatom) have significant density of electronic states 0.4 eV below the Fermi level, but the position A (rest atom) is characterized by a much higher electronic occupancy at 0.8 eV below the Fermi level than the other two positions. The higher population in the valence band of the rest atom (A) is a consequence of the charge donation from the two adatoms (B and C) [72]. STS is therefore a powerful tool that can distinguish between different local density of states with the resolution of a single atom.

Fig. 12b and Fig. 12c show an example of the Si(111)(7×7) reconstruction imaged with empty- and filled-states constant-current STM. The two images were obtained over exactly the same region, yet the information is much richer when both are present: the empty-states STM shows the equivalent dangling bonds of 12 atoms per unit cell, while the filled-states STM shows the same atoms with clearly higher contrast over the rest atoms. Additionally, the filled-states STM clearly resolves two separate triangular patterns, corresponding to the faulted and unfaulted halves of the Si(111)(7×7) reconstruction, while both are imaged equivalently in empty-states STM.

Die approbierte gedruckte Originalversion dieser Dissertation ist an der TU Wien Bibliothek verfügbar.
The approved original version of this doctoral thesis is available in print at TU Wien Bibliothek.
TU Bibliothek Your knowledge hub WIEN

1.5 Noncontact atomic force microscopy – nc-AFM (AFM)

Noncontact atomic force microscopy, abbreviated as nc-AFM, is the latest development in the family of atomic force microscopy techniques. It is the youngest technique among the surface physics techniques discussed so far, with unprecedented insight into the real-space atomic structure of the crystal surfaces. The experimental setup for atomic force microscopy is very similar as the setup for performing STM measurements, with the difference that an atomically sharp STM tip is mounted on an oscillating cantilever sensor, which differs from one family of atomic force microscopes to another. Atomic force microscopy is ideal for studying a wide variety of materials because, unlike STM, it does not require conductive samples for signal detection. Although not limited to studies of conductors and semiconductors, the atomic force microscopy has to overcome the limitation of very small forces between the tip and the sample, and the early measurements were not nearly able to reflect the atomic structure as well as the STM. Unsurprisingly, the first atomic force microscope was invented by Binning, the inventor of STM, and the first experiments were realized soon after the realization of the first STM [74]. They were performed in the so-called contact mode [75], where the tip apex is mechanically dragged over a small surface area, and the vertical deflection of the cantilever reflects the surface morphology. Force detection is also possible in the so-called tapping mode [76] (or intermittent contact mode), where the cantilever with an atomically sharp tip is oscillated and comes to contact only at the extreme, turn-over point of the oscillation. Both the contact and the tapping AFM modes are not suitable for atomic resolution, and nowadays they are mostly used to record large scale morphology of a sample surface in gaseous or liquid environments [77]. The nc-AFM on the other hand, readily offers the possibility of atomic resolution in UHV [78]. There, the oscillating sensor is equipped with a STM tip glued to the end of the oscillating prong, and once it comes to the vicinity of the sample, the atoms at the tip apex electrostatically, chemically, and quantum-mechanically interact with the atoms of the surface. Just like STM, the nc-AFM technique is highly local, and the two are usually performed simultaneously.

1.5.1 Principle

The nc-AFM (AFM hereafter) technique builds on the fact that a harmonic oscillator that is oscillating at its resonant frequency will change the resonant frequency when placed in an external, inhomogeneous force field that originates from the tip-sample interaction. An equation of motion for a harmonic oscillator with effective mass m_{eff}, a spring constant k that is damped by a damping coefficient Γ, that oscillates in only one dimension along the trajectory $z(t)$, can be expressed as:

$$m_{\text{eff}}\frac{d^2z}{dt^2} + \Gamma\frac{dz}{dt} + kz = 0 \tag{1.18}$$

This equation has three solutions that depend on the strength of the damping coefficient Γ: an underdamped solution when $\Gamma < \sqrt{4m_{\text{eff}}k}$, critically damped when $\Gamma = \sqrt{4m_{\text{eff}}k}$, and overdamped when $\Gamma > \sqrt{4m_{\text{eff}}k}$. When the oscillations are performed with a high-quality oscillator in UHV, in the absence of external forces, the damping coefficient is small and the oscillations are underdamped. Then, the periodic oscillations are exponentially decaying over time:

$$z(t) = Ae^{-\frac{\Gamma}{2m_{\text{eff}}}t}\cos(\omega_0 t + \phi) \quad ; \quad \Gamma << \sqrt{4m_{\text{eff}}k} \tag{1.19}$$

where $\omega_0 = \sqrt{\frac{k}{m_{\text{eff}}}}$ is the resonance frequency, *i.e.*, the natural frequency of the unperturbed oscillator, and ϕ is the phase. In other words, when the oscillator gains energy from any type of sudden and short disturbance, it will oscillate at its natural resonance frequency ω_0 with the highest amplitude until the excess energy is dissipated and $z(t) = 0$ when $t \to \infty$. Since the oscillator in UHV is damped only by its intrinsic properties, it is instructive to introduce a factor Q that will relate the mass, the natural frequency and the self-damping through:

$$Q = \frac{m_{\text{eff}}\omega_0}{\Gamma} \tag{1.20}$$

The Q factor measures how many oscillations will occur for a damped oscillator before the energy of oscillations decays by $\frac{1}{e}$. Thus, the factor Q is called the quality factor.

In nc-AFM, the oscillator is constantly driven so that is permanently oscillating, *i.e.*, the energy dissipated in each oscillation cycle is replenished by an external driving force. In this case, the equation of motion is

Die approbierte gedruckte Originalversion dieser Dissertation ist an der TU Wien Bibliothek verfügbar.
The approved original version of this doctoral thesis is available in print at TU Wien Bibliothek.
TU Bibliothek Your knowledge hub WIEN

supplemented by a periodic driving force $F_d(t)$ with the driving frequency ω_d:

$$m_{\text{eff}}\frac{d^2z}{dt^2}+\Gamma\frac{dz}{dt}+kz=F_d(t)=F_d\cos(\omega_d t) \tag{1.21}$$

The solution to this inhomogeneous equation of motion is a superposition of the homogeneous solution $z(t)_{\text{h}}$ of the underdamped oscillator 1.19, and the particular solution $z(t)_{\text{p}}$ that is dependent on the properties of the driving force:

$$\begin{aligned} z(t)=z(t)_{\text{h}}+z(t)_{\text{p}} =& A_{\text{h}}e^{-\frac{\Gamma}{2m_{\text{eff}}}t}\cos(\omega_0 t)+ \\ &+\frac{F_d}{\sqrt{m_{\text{eff}}^2\left(\omega_0^2-\omega_d^2\right)^2+\left(\Gamma\omega_d\right)^2}}\cos\left(\omega_d t-\arctan\left(\frac{\Gamma\omega_d}{m_{\text{eff}}\left(\omega_0^2-\omega_d^2\right)}\right)\right) \end{aligned} \tag{1.22}$$

The homogeneous solution is a transient solution because it depends on the initial parameters of the underdamped oscillator without driving, and decays exponentially over time $z(t)_{\text{h}}=0$ when $t\to\infty$. On the other hand, the particular solution is a steady-state solution because it describes the oscillation of the driven underdamped oscillator after the transient solution has been completely damped. The steady-state oscillations proceed with the frequency of the driving force ω_d, and the oscillation amplitude dependent on the difference between the driving ω_d and the natural frequency ω_0 . When the frequency of the driving force is equal to the natural frequency of the oscillator, then:

$$z(t)=\frac{F_d}{\Gamma\omega_0}\cos\left(\omega_0 t-\frac{\pi}{2}\right)=\frac{F_d}{\Gamma\omega_0}\sin(\omega_0 t)=\frac{Q}{k}F_d\sin(\omega_0 t) \quad ; \quad \omega_d=\omega_0 \tag{1.23}$$

and the oscillator is at resonance. The resonance is characterized by high oscillation amplitudes that are shifted by 90 ° with respect to the driving force.

In nc-AFM, the tip of the mechanical oscillator that is oscillating at resonance frequency (equation 1.23) approaches the sample surface until the forces between the tip and the sample $F_{\text{ts}}(t)$ start to appear. In a static approximation, the tip-sample force is dependent only on the mutual separation of the two. Namely, the tip-sample force depends only on the position of the oscillator $F_{\text{ts}}(z(t))$ with respect to the sample, and the equation of motion can be expressed as:

$$m_{\text{eff}}\frac{d^2z}{dt^2}+\Gamma\frac{dz}{dt}+kz=F_d\cos(\omega' t)+F_{\text{ts}}(z(t)) \tag{1.24}$$

The presence of the additional force $F_{\text{ts}}(z(t))\neq 0$ will force the oscillator to alter its resonance frequency ω', and the position $z(t)$ will depend on the new, altered resonance frequency. When the general form of $z(t)=A\sin(\omega' t)$ ($\phi=\pi/2$ at resonance) is inserted into equation 1.24, and the equation of motion is additionally multiplied by $z(t)$, and integrated over one period of oscillations $t\in[0,T]$, then:

$$2A^2m\pi\left(\omega_0-\omega'\right)=-2A^2m\pi\Delta\omega=\int_0^T dtF_{\text{ts}}(z(t))A\sin\omega' t \quad ; \quad \omega'\approx\omega_0 \quad ; \quad \Delta\omega=\omega'-\omega_0 \tag{1.25}$$

under assumption that the change in oscillation frequency $\Delta\omega$ is small. The temporal integral on the right side of equation 1.25 is the temporal average of the tip-sample interaction:

$$\langle F_{\text{ts}}(z)z(t)\rangle\equiv\frac{1}{T}\int_0^T dtF_{\text{ts}}(z(t))A\sin\omega' t \tag{1.26}$$

and the frequency shift can be expressed through the averaged tip-sample interaction during one oscillation cycle [79]:

$$\Delta f=-\frac{f_0}{A^2k}\langle F_{\text{ts}}(z)z(t)\rangle \tag{1.27}$$

Therefore, an idly oscillating driven and damped oscillator will change its resonant frequency once it approaches the sample surface sufficiently close that tip-sample forces $F_{\text{ts}}(z(t))$ start to appear. In this sense, nc-AFM is equivalent to STM: in STM the proximity of the tip and the sample is detected via the tunneling current, while in nc-AFM it is detected via the change in the resonance frequency of the oscillator.

Die approbierte gedruckte Originalversion dieser Dissertation ist an der TU Wien Bibliothek verfügbar.
The approved original version of this doctoral thesis is available in print at TU Wien Bibliothek.
TU Bibliothek Your knowledge hub WIEN

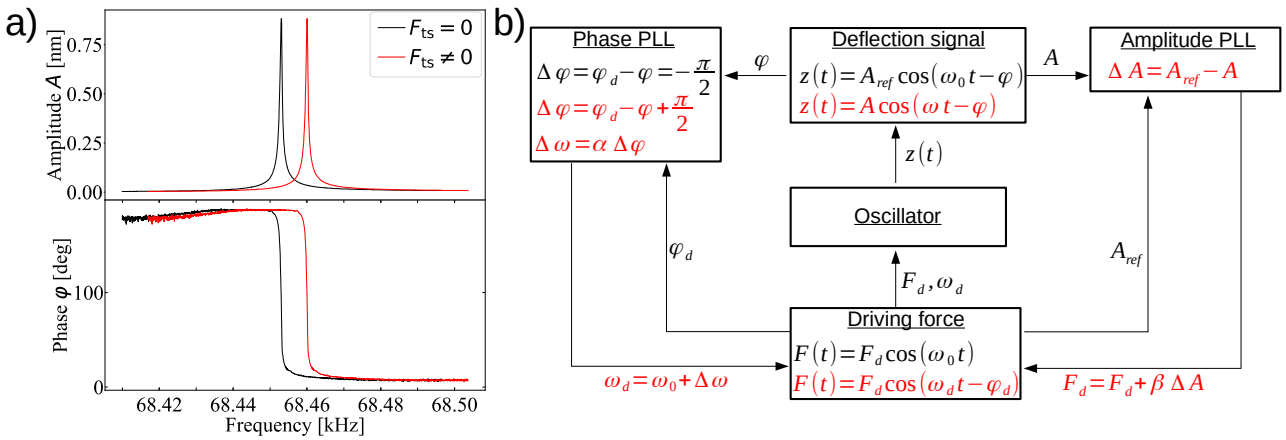

Figure 13: **The working principle of the detection of tip-sample forces in nc-AFM.** a) Detected amplitude $A(f_d)$ (top panel) and phase of the oscillations $\varphi(f_d)$ (bottom panel) with the change in the driving frequency f_d, measured in the vicinity of the natural resonance frequency of this oscillator $f_0 = 68.4535\,\text{kHz}$. b) Block diagram illustrating the resonant driving of the oscillator and the preservation of the constant oscillation amplitude by using two separate PLLs. In both (a) and (b), black lines indicate the behavior of the oscillator in the absence of the external force $F_{\text{ts}} = 0$, while the behavior of the oscillator in the presence of the external force $F_{\text{ts}} \neq 0$ is illustrated with red lines.

Figure 13 illustrates the working principle of the tip-sample force detection in nc-AFM. The amplitude and the phase dependence of an undisturbed oscillator $F_{ts}(z(t)) = 0$ are shown in black in Fig. 13a. When the oscillator is driven at its natural $f_d = f_0$ frequency (f_0=68.4535 kHz in this example) by a certain amplitude of the driving force F_d, oscillations proceed with a recognizably high amplitude A, and the two oscillations have a phase difference $\Delta\varphi = \varphi_d - \varphi_0$ of exactly $\frac{\pi}{2}$ with respect to the driving force, as in eq. 1.23. On the other hand, when the oscillator is driven by a different frequency $f_d \neq f_0$, the amplitude of oscillations is negligible compared to the amplitude at the resonance, and the phase difference between the oscillating and the driving signal is $\Delta\varphi \neq \frac{\pi}{2}$. The shift of the resonance frequency of the oscillator due to the tip-sample interaction $F_{ts}(z(t)) \neq 0$ is illustrated in Fig. 13a in red lines. The amplitude and the phase dependence of the disturbed oscillator would show that there is a new, altered driving frequency f_d' for which the oscillator enters resonance.

The appearance of tip-sample forces can be detected as both, a sudden decay of the oscillating amplitude $A \to 0$, or as a change of the phase shift between the driving and the oscillating signals $\Delta\varphi \neq \frac{\pi}{2}$. This enables two different modes of operation in nc-AFM: amplitude-modulated (AM nc-AFM) and frequency-modulated (FM nc-AFM). In AM nc-AFM, the oscillator is always driven with the same driving frequency $f_d \approx f_0$, that is very close to the natural frequency of the oscillator. Then, the tip-sample interaction results in either a decrease or an increase of the oscillation amplitude, depending whether the tip-sample interaction drives the natural frequency of the oscillator closer of further away from the driving frequency, *i.e.*, whether the tip-sample interaction is attractive or repulsive. The change in the detected amplitude of oscillations is indicative of the strength of the interaction, but the relation between the two is non-linear in the vicinity of f_0, as can be seen in Fig. 13a. Although the experimental requirements for the AM nc-AFM are more modest, the availability of the sensors with high Q factors enable the FM nc-AFM measurement modes, which provides superior characterization of the tip-sample forces.

In FM nc-AFM, the amplitude of oscillations is always kept constant at the desired reference value $A = A_{\text{ref}}$, and the oscillator is always driven at its resonance frequency $f_d = f' \neq f_0$ that differs from the natural frequency in the presence of tip-sample forces $F_{ts}(z(t)) \neq 0$. According to eq. 1.22, the phase difference between the driving force and the oscillations will be equal to $\Delta\varphi = \varphi_d - \varphi = \pi$ and $\Delta\varphi = 0$ when the oscillator is driven by frequencies lower $f_d < f_0$ and higher $f_d > f_0$ than the natural frequency, respectively. This provides a method for locating the actual resonance frequency of the oscillator in the presence of tip-sample forces: If the phase difference is $\Delta\varphi \in \left[\pi, \frac{\pi}{2}\right)$ then the driving frequency needs to be increased, while if the phase difference is $\Delta\varphi \in (\pi, 0]$ then the driving frequency needs to be decreased. A PID feedback loop is employed until the phase difference becomes $\Delta\varphi = \frac{\pi}{2}$ and the oscillator is driven at the new resonance frequency $f_d = f'$. The difference between the altered resonance frequency and the natural frequency of the oscillator, *i.e.*, the frequency shift

Die approbierte gedruckte Originalversion dieser Dissertation ist an der TU Wien Bibliothek verfügbar.
The approved original version of this doctoral thesis is available in print at TU Wien Bibliothek.
TU Bibliothek Your knowledge hub WIEN

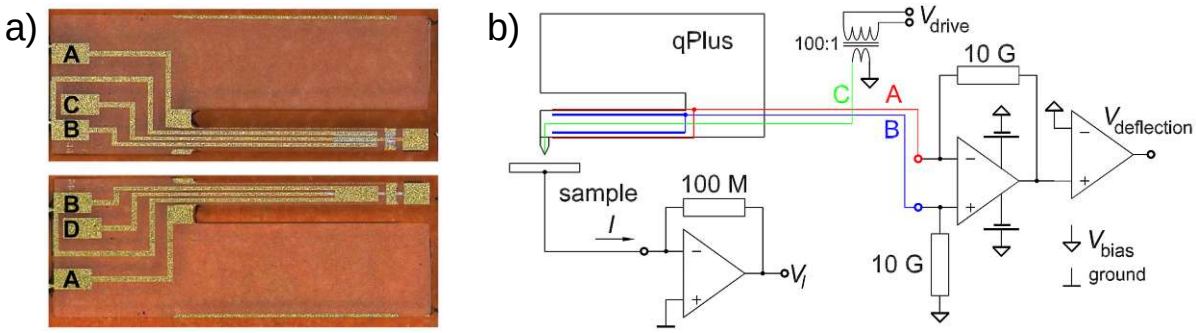

Figure 14: **The qPlus sensor and the differential preamplifier design.**
a) Photographs of both sides of the fourth generation of qPlus sensors. The points A, B, C, and D correspond to the four electrical contacts on the sensor used for transmitting the Q+, Q-, tunneling current and excitation signals, respectively.
Reprinted Figure 12 [80] with permission from [Franz J. Giessibl, *Review of Scientific Instruments*, 90, 011101 (2019)]. Copyright (2019) AIP Publishing.
b) Schematics of the electrical wiring of the contacts on the fourth generation of qPlus sensors. The voltage between the oscillating prong and the quartz base, Q+ and Q-, is connected to the differential preamplifier that gives the deflection signal as the output.
Reprinted Figure 15 [80] with permission from [Franz J. Giessibl, *Review of Scientific Instruments*, 90, 011101 (2019)]. Copyright (2019) AIP Publishing.

$\Delta f = f' - f_0$ is measured. The frequency shift is indicative of the strength of the tip-sample forces according to eq. 1.27. FM nc-AFM also discriminates positive and negative frequency shifts, which are indicative whether the tip-sample interaction is repulsive or attractive.

The experimental realization of the FM nc-AFM is illustrated in Fig. 13b. The deflection signal from the oscillator reveals its position over time $z(t)$, which is determined by its amplitude, frequency, and phase $z(t) = Acos(\omega t - \varphi)$. The amplitude is kept constant at the desired reference value through a phase-locked loop (PLL) control system that detects the difference between the actual amplitude of the oscillation A and the desired reference amplitude A_{ref}. This difference is then superimposed (factor β in Fig. 13b) to the previous amplitude of the driving force F_d through a PID regulator. The system is always kept at a resonance through another PLL control system that measures the phase shift between the driving and the oscillating signal $\Delta\varphi$. This difference is superimposed (factor α in Fig. 13b) to the previous frequency of the driving force f_d. Both α and $\frac{k}{Q}$ parameters are determined from the calibration of the unperturbed oscillator around its natural frequency as in Fig. 13a. The quality factor Q is experimentally determined as the ratio between the resonance frequency f_0 (at a given driving force amplitude F_d) and the full-half-width of the resonance curve δf as:

$$Q = \frac{\omega_0}{\delta\omega} = \frac{f_0}{\delta f} \tag{1.28}$$

The Q factor implies that the higher quality oscillators will have a narrow resonance curve.

1.5.2 Sensors

The tip-sample forces encountered in experiments are very small, in the order of several hundred pN. The detection of such small forces poses requirements on the properties of the oscillator. The sensor and the sample must be in close vicinity to each other, usually closer than 5 nm, but still separated enough so that they are not in contact. At these distances, snap-to-contact is likely to occur when the potential energy of the oscillator is smaller than the potential energy of its interaction with the sample. For this reason, the oscillator must be very stiff, *i.e.*, have a large spring constant k to ensure that the energy of the oscillator by far exceeds the energy of the interaction with the sample. On the other hand, a large stiffness k imposes a challenge for the amplitude of the driving force according to equation 1.23. The stiffness of the cantilever needs to be compensated with a large Q factor in order to keep the requirements for the driving amplitude reasonable. Moreover, the mechanical properties of the oscillator must enable it to detect perturbations caused by $F_{\text{ts}} \neq 0$. According to eq. 1.27, the

Die approbierte gedruckte Originalversion dieser Dissertation ist an der TU Wien Bibliothek verfügbar.
The approved original version of this doctoral thesis is available in print at TU Wien Bibliothek.
TU Bibliothek Your knowledge hub WIEN

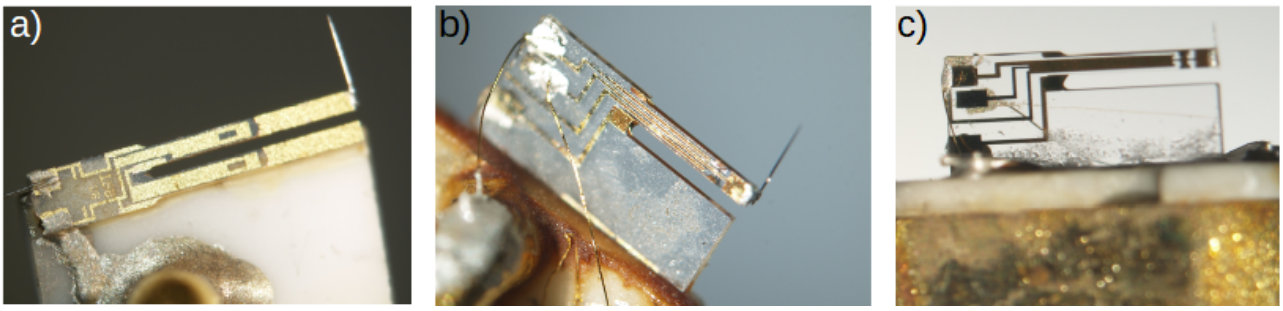

Figure 15: **Photographs of different Giessibl qPlus sensors and mountings.** a) Second generation qPlus sensor mounted for an Omicron STM/AFM measurement head. b) Third generation qPlus sensor mounted for an Omicron STM/AFM measurement head. c) Third generation qPlus sensor mounted for an Sigma STM/AFM measurement head.

amplitude of oscillations A needs to be small, and the natural frequency f_0 needs to be high, in order to reduce the effects of the stiff cantilever, and make the experimental frequency shifts detectable.

Altogether, the nc-AFM oscillator must be stiff, must have a high natural frequency with high quality factor, and must oscillate with small amplitudes in order to detect the frequency shifts occurring due to the small tip-sample forces. There are several solutions that meet these requirements, among which the qPlus sensor designed by Giessibl stands out as the simplest and most reliable. A photograph of the fourth-generation qPlus sensor [80] and the detection scheme for the deflection signal are shown in Fig. 14. The fourth generation of qPlus sensors are entirely constructed from quartz due to its piezoelectric properties. Electrodes and contacts are created by controllably evaporating a gold film onto the respective positions on the sensor. A thin, oscillating prong is covered with four contacts, marked with A, B, C, and D in Fig. 14a. As the sensor oscillates, opposite charges appear on the opposite sides of the oscillating beam due to the deformation of the piezoelectric material. These charges are collected through contacts A and B, which produce a current signal that is proportional to the cantilever deflection $z(t)$. The number of oscillating charges is modest, thus the current corresponding to the deflection signal has to be amplified. Figure 14b illustrates the differential preamplifier that is placed close to the oscillating sensor in UHV, and operates at either room temperature or cryogenic temperatures [81]. After the signal amplification, the amplitude and the phase of the oscillations is discriminated, and two PLLs described as in Fig. 13b can be employed. The fourth generation of qPlus sensors have additional C and D electrodes (Figure 14a) running along the oscillating prong. Electrode C enables STM measurements, because it conducts the tunneling current I_t between a sample and a conducting tip that can be attached (glued) at the end of the oscillating prong. Electrode D does not span to the end of the oscillating prong as the electrode C, and it is used to electrically excite the cantilever through the piezoelectric effect, *i.e.*, to electrically apply the driving force $F_d cos(\omega_d t)$ [80]. The cantilever oscillation can also be excited mechanically, by shaking the entire sensor at its resonance frequency. This is performed by superimposing the usual voltage on the z-electrode of the piezoelectric tube, responsible for the precise scanning across the surface, with an alternating voltage that corresponds to $F_d cos(\omega_0 t)$. When the sensor is mechanically excited, there is no need for an electrode D on the sensors (Figure 14a), and the third generation qPlus sensors [82] or older can be used.

Figure 15 shows optical photographs of the sensor types and mountings used in the research that led to this Thesis. The first [84] and the second [85] generation of the qPlus sensors were piezoelectric tuning forks that were obtained from regular wrist watches. The second generation of the qPlus sensor, mounted on a Omicron sensor holder, is shown in Fig. 15a. They are manufactured such that their natural frequency is $f_0 = 32.768\,\mathrm{kHz}$ (exactly 2^{15} oscillations per second), and are used together with 15 frequency dividers in wrist watches to provide precise 1 second time intervals. In wrist watches, the tuning fork oscillates freely with two prongs oscillating in anti-phase. For the application in nc-AFM measurements, one prong of the tuning fork has to be fixed to the support at the sensor holder beneath, with the other prong oscillating in vertical direction towards to, and away from the sample. Figures 15b and 15c show the third-generation qPlus sensors mounted on an Omicron and Sigma sensor holders, respectively. They are identical to the sensor in Fig. 14a, but they lack the fourth contact (D) used for electrical excitation. The third generation of qPlus sensors can be manufactured with different mechanical properties, depending mainly on the size of the oscillating prong. The sensors used in this Thesis were characterized by the cantilever stiffness k=1800–4500 N/m, cantilever length L=1000–2400 μm, and

Die approbierte gedruckte Originalversion dieser Dissertation ist an der TU Wien Bibliothek verfügbar.
The approved original version of this doctoral thesis is available in print at TU Wien Bibliothek.
TU Bibliothek Your knowledge hub WIEN

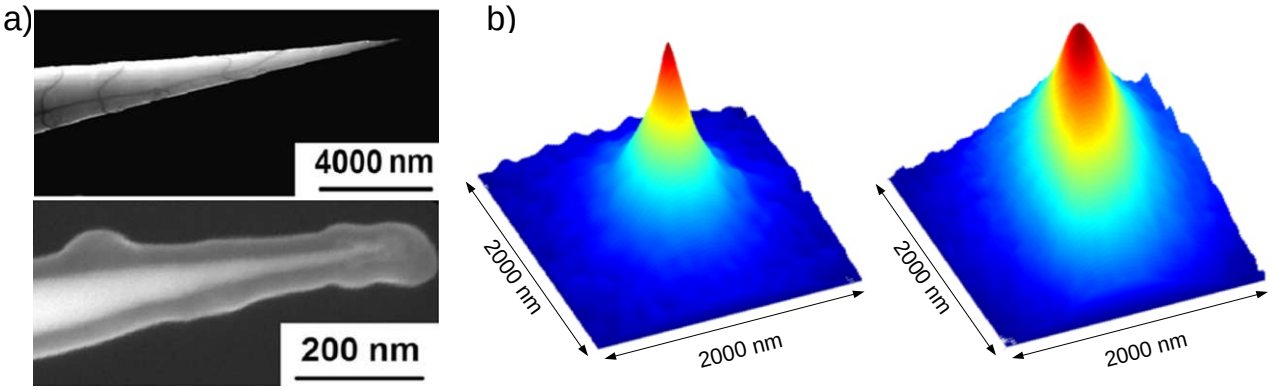

Figure 16: **Shape of the sharp tips used in AFM.** a) The apex of an electrochemically etched W tip imaged by SEM with small (top) and large (bottom) magnification. Large magnification SEM image reveals that the tip apex is covered in an oxide layer.
Reprinted Figure 1(a) and Figure 1(b) [83] with permission from [M. Setvín, J. Javorskỳ, D. Turčinková, and I. Matolínová, P. Sobotík, P. Kocán, and I. Ošt'ádal, *Ultramicroscopy*, 113, 152 (2012)]. Copyright (2012) Elsevier.
b) Microscopic shape of the tip apex, obtained from the AFM investigations of electron polarons in Ti-doped hematite films. Both tips are atomically sharp, but their microscopic shapes differ. Measurements performed by Jesús Ruben Lopez Redondo as a part of a paper in preparation.

the resonance frequency f_0=24–80 kHz.

All AFM sensors in Fig. 15 are equipped with a conductive tip glued to the end of the oscillating prong, that serves as the probe of the atomic forces in AFM or the tunneling current in STM. The tips are usually constructed from W, and their sharpness is achieved by electrochemical etching. An example of a tungsten tip is shown in Fig. 16a. The tip etching procedure operates under same principles for both, the STM and the AFM tips, with the difference that the AFM tips are usually much thiner and shorter, in order to avoid over-encumberment of the oscillating prong and altering the mechanical properties of the sensor. Electrochemical etching is performed by immersing a desired portion of a tungsten wire, that defines the length of the tip, into a 2% molar solution of NaOH, in which a circular electrode is placed at a negative potential [86]. The tungsten wire is subjected to a positive electric potential, which attracts the OH^- ions from NaOH solution to etch the tungsten wire in a circular manner at the contact point of the tungsten wire with the surface of the solution. When the etching of a single tip is nearing completion, the piece of the tungsten wire that was immersed into the NaOH solution will develop a very sharp cone at the point of the immersion into the liquid, and will subsequently detach from the rest of the wire to land at the bottom of the dish containing the NaOH solution. This procedure creates very sharp tips, seen in the top panel of Fig. 16a, which are subsequently glued to the top of the oscillating prong of an AFM sensor. Tips that are prepared *ex-situ* by this procedure are usually covered with a thick layer of oxide material, seen in the SEM image of the tip apex in the bottom panel of Fig. 16a. Upon introduction to UHV, the tips are additionally sharpened, and the oxide material is removed from the tip apex by performing field emission in the vicinity of a rod at a high positive potential of 1 kV, in 1×10^{-6} mbar Ar partial pressure. Argon ions are accelerated in the vicinity of the sharp tip and perform the "self-sputtering" on the tip apex, according to a procedure described in [83].

A microscopic shape of two different tip apices can be seen in Fig. 16b. Both shapes in Fig. 16b were discerned from real AFM measurements over thin film of hematite $Fe_2O_3(1\bar{1}02)$ surface that was doped with 0.03 at% of Ti. On these insulating films, charge trapping can occur under certain conditions. In experiments that led to Fig. 16b, electrons were injected into an insulating hematite surface which subsequently trapped the excess electrons as electron polarons. The presence of electron polarons was discerned by performing maps of the local contact potential in the vicinity of the electron injection point on the surface. Since the localization of electron polarons around the injection point is aided by the electric field of the tip (and can be manipulated accordingly), their spatial distribution depicts the strength of the electric field from the tip. At the same time, the electric field between the tip and the flat sample depends on the shape of the tip apex. Therefore, the trapped electron polarons on hematite can be used to image the shape of an AFM tip. Although both tips have an atomically

Die approbierte gedruckte Originalversion dieser Dissertation ist an der TU Wien Bibliothek verfügbar.
The approved original version of this doctoral thesis is available in print at TU Wien Bibliothek.
TU Bibliothek Your knowledge hub WIEN

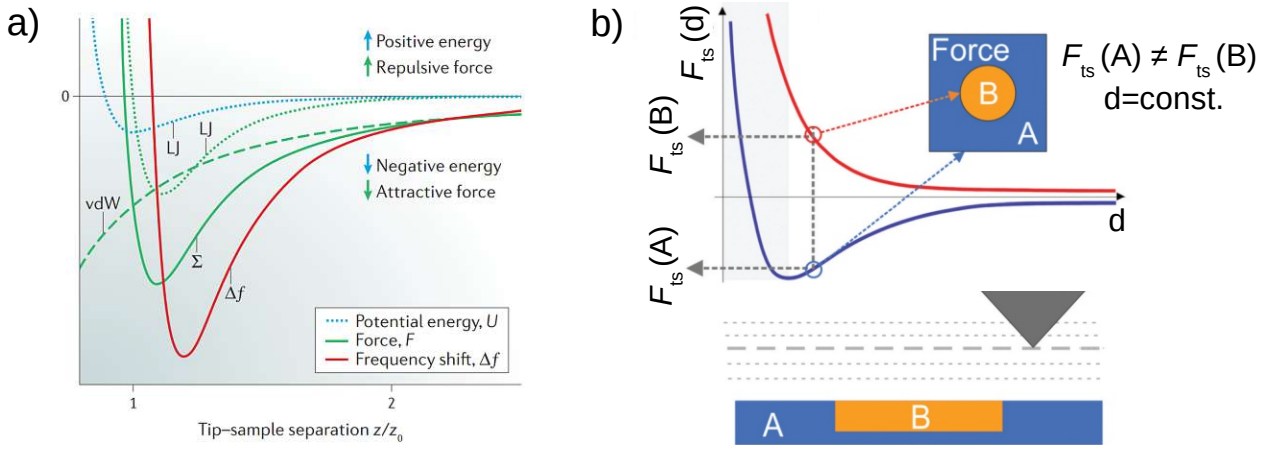

Figure 17: **Illustration of the tip-sample forces F_{ts}.**
a) An example of a distance-dependent strength of the tip-sample potential U_{ts}, and the corresponding total force F_{ts} (denoted as Σ) and the frequency shift Δf_{ts} . The graph shows separate force contributions from the chemical forces F_{chem}, modeled from the Lennard-Jones potential (denoted as LJ), and the van der Waals forces F_{vdW} (denoted as vdW). The electrostatic force is missing since it was compensated by applying an electric field in this example.
Reprinted Figure 1(b) [87] with permission from [Niko Pavliček and Leo Gross, *Nature Reviews Chemistry*, 1, 1 (2017)]. Copyright (2017) Springer Nature.
b) Working principle of the contrast formation in AFM. Different species on the surface exhibit different tip-sample forces, and thus different frequency shifts.
Reprinted bottom-left part of Figure 3 [88] with permission of Royal Society of Chemistry, from [Lisa Almonte and Jaime Colchero, *Nanoscale*, 9, 2903 (2017)]; permission conveyed through Copyright Clearance Center, Inc.

sharp apex, Fig. 16b illustrates that their macroscopic shape drastically differs, which can play an important role in some experiments.

1.5.3 Forces

In AFM, an atomically sharp tip apex, that is oscillating together with the AFM sensor, is approached to the vicinity of a sample surface. When the separation of the sample and the tip apex d is small enough, in the range of 200–5000 pm, tip-sample forces appear. Unlike STM, where only the tunneling probabilities between the tip and the sample at a given energy are relevant, in AFM there are several distinct contributions to the total force acting between the tip and the sample F_{ts}. In general, when F_{ts} is a conservative force and the tip and the sample are not in contact, the total force acting on the tip can be divided into long-range electrostatic F_{es} and van der Waals forces F_{vdW}, and short-range chemical forces F_{chem}. The total force, and its individual contributions, depend on the oscillating separation between the tip and the sample $d(t)$. At a constant separation between the tip and the sample $d(t) = d$, the total force acting on the tip can be expressed as:

$$F_{\mathrm{ts}}(d) = F_{\mathrm{es}}(d) + F_{\mathrm{vdW}}(d) + F_{\mathrm{chem}}(d) = -\frac{\partial}{\partial d}\left[U_{\mathrm{es}}(d) + U_{\mathrm{vdW}}(d) + U_{\mathrm{chem}}(d)\right] \tag{1.29}$$

The individual contribution of each force is significant, and practice shows that each of them is responsible for the force contrast over different sites on the surface. Figure 17a illustrates the deconvolution of the total force between a tip and a sample, in the absence of the electrostatic force. The constituent forces can be qualitatively described by expressing them through simple analytical solutions.

The long-range electrostatic force between the tip and the sample originates from the electric field that is a consequence of the mismatch between the work functions of the two $\Delta\phi = \phi_{\mathrm{sample}} - \phi_{\mathrm{tip}}$. This difference is commonly referred to as the local contact potential difference (LCPD) $V_{\mathrm{LCPD}} = \Delta\phi/e$ [91]. Either the tip or the sample are usually set to a given bias voltage V_{B}, and the total voltage between the tip and the sample is then $V_{\mathrm{tot}} = V_{\mathrm{B}} - V_{\mathrm{LCPD}}$. The electrostatic force due to this voltage difference can be derived by considering the tip-sample junction as a capacitor with one infinitely large plate and a atomically sharp cone as the other

Die approbierte gedruckte Originalversion dieser Dissertation ist an der TU Wien Bibliothek verfügbar.
The approved original version of this doctoral thesis is available in print at TU Wien Bibliothek.
TU Bibliothek Your knowledge hub WIEN

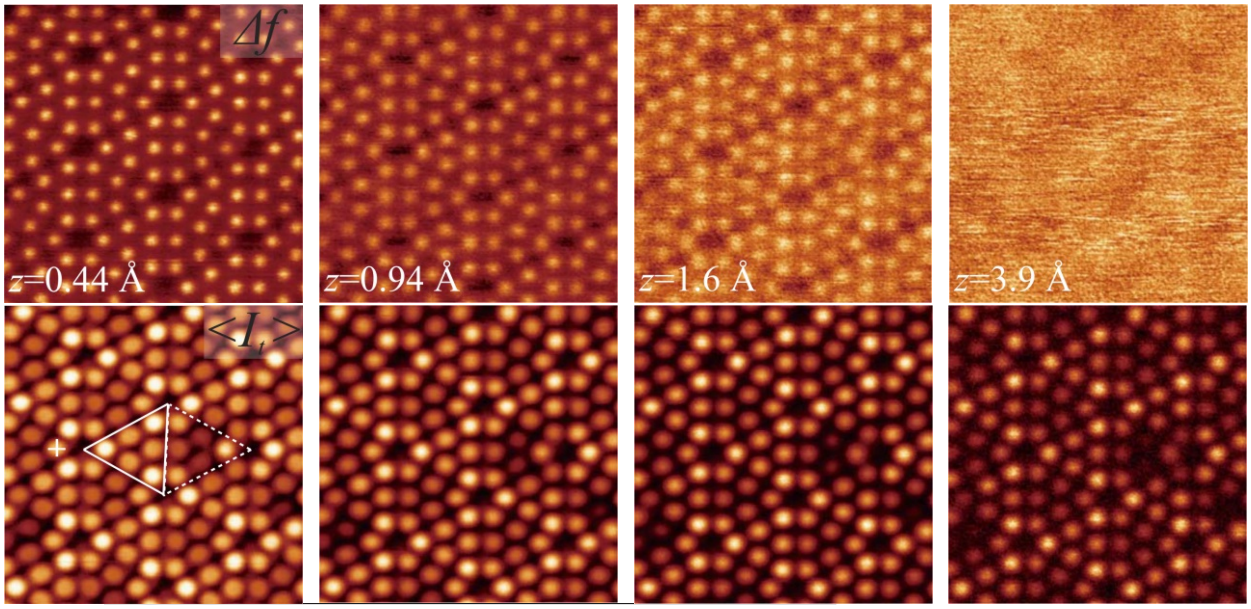

Figure 18: **Simultaneous AFM and STM measurements over the Si(111)(7×7) reconstruction.** Constant-height AFM images (top row) and simultaneous filled-states constant-height STM images (bottom row) of the Si(111)(7×7) reconstruction (model shown in Fig. 3) at different distances from the surface. AFM images were performed using a cantilever with natural frequency $f_0 \approx$150 kHz, oscillation amplitude A=20 nm, and sample bias V_S=-200 meV.
Reprinted Figure 2 [89] from [Yoshiaki Sugimoto, Yuuki Nakajima, Daisuke Sawada, Ken-ichi Morita, Masayuki Abe, and Seizo Morita, *Physical Review B*, 81, 245322 (2010)] with permission of Author(s) and APS. Copyright (2010) American Physical Society.

electrode. In this capacitor, the voltage difference is kept constant at V_{tot}, and only the capacitance of the junction $C(d)$ is changed during oscillations. The potential energy stored in a capacitor is $U_{\text{c}} = \frac{1}{2}CV_{\text{tot}}^2$, but the total potential energy of the junction U_{es} takes into account the $U_{\text{L}} = -CV_{\text{tot}}^2$ loss of energy for keeping the potential difference constant $V_{\text{tot}} = const.$ by transferring charge between electrodes. From the total energy of this capacitor U_{es}, the electrostatic force F_{es} can be expressed as:

$$F_{\text{es}}(d, V_{\text{tot}}) = -\nabla\left(U_{\text{C}} + U_{\text{L}}\right) = -\nabla\left(-\frac{1}{2}C(d)V_{\text{tot}}^2\right) = \frac{1}{2}V_{\text{tot}}^2\frac{\partial C(d)}{\partial d} = \frac{1}{2}\left(V_{\text{B}} - V_{\text{LCPD}}\right)^2\frac{\partial C(d)}{\partial d} \tag{1.30}$$

The electrostatic force is always attractive since the $\frac{\partial C(d)}{\partial d}$ term is always negative [92]. The F_{es} is long-ranged, since the $\frac{\partial C(d)}{\partial d}$ term is roughly proportional to d^{-2}. According to eq. 1.30, the contribution of this force can be nullified when the biasing potential is selected to be exactly equal to the LCPD between the tip and the sample $V_{\text{B}} = V_{\text{LCPD}}$, as was performed in the example in Fig. 17a.

The van der Waals force F_{vdW} between the tip and the sample is another long-ranged force that is also always attractive. It can be modeled as the long-range interaction between a cone with the radius R that represents the tip apex, and an infinite plane that represents the sample surface. Then, the van der Waals interaction can be expressed as [93]:

$$F_{\text{vdW}} = -\frac{2HR^3}{3d^2\left(d+2R\right)^2} \approxeq -\frac{HR}{6d^2} \quad ; \quad d << R \tag{1.31}$$

where H is the Hamaker constant, and the final approximation is valid when the tip-sample separation is smaller than the tip apex radius. The equation above is widely employed in qualitative analysis, but many different models for the van der Waals force in AFM have been developed [94, 95]. Naturally, the van der Waals force cannot be nullified under any conditions, but it can be minimized by both, reducing the size of the tip apex to a single atom, and by preparing the sample surface such that it is characterized by large, atomically flat terraces

Die approbierte gedruckte Originalversion dieser Dissertation ist an der TU Wien Bibliothek verfügbar.
The approved original version of this doctoral thesis is available in print at TU Wien Bibliothek.
TU WIEN Bibliothek Your knowledge hub

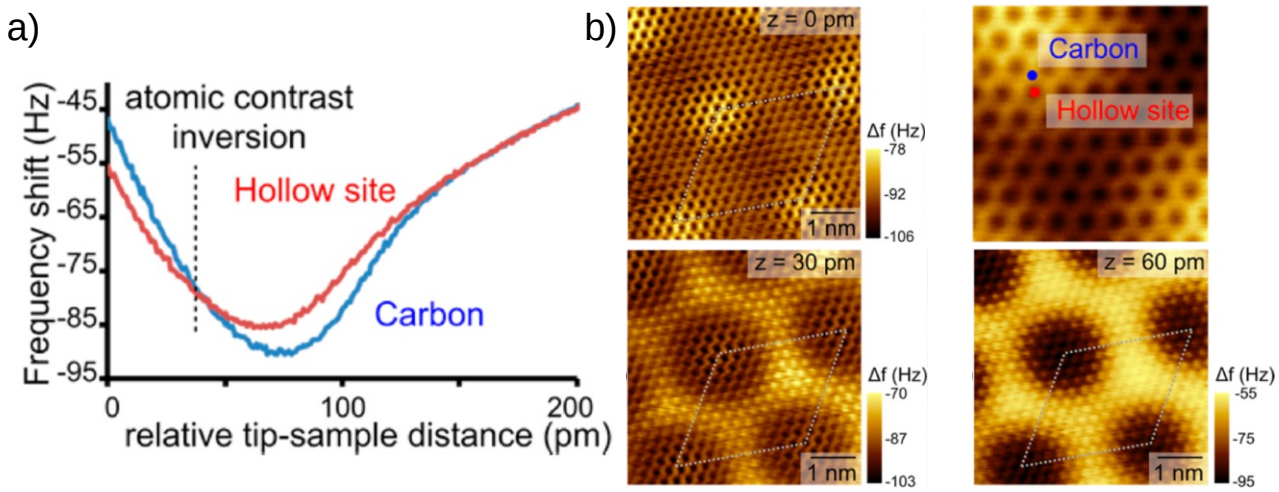

Figure 19: **Distance-dependent AFM contrast on epitaxially grown graphene on an Ir(111) surface.** a) Frequency shift vs. distance $\Delta f(z)$ curves taken over the carbon atom and the hollow site on the graphene layer. The distinct AFM contrast between these two points responsible for the atomic resolution is quantified in their different $\Delta f(z)$ curves.
Reprinted Figure 1(c) [90] with permission from [Mark P. Boneschanscher, Joost van der Lit, Zhixiang Sun, Ingmar Swart, Peter Liljeroth, and Daniël Vanmaekelbergh, *ACS Nano*, 6, 10216 (2012)]. Copyright (2012) American Chemical Society.
b) Top panel shows a constant-height AFM image at close distance to the surface, together with the atomically resolved small-scale image showing the two distinct sites in the graphene lattice. Bottom panel shows constant-height images at intermediate and large distances from the surface.
Reprinted Figure 1(a,c) [90] with permission from [Mark P. Boneschanscher, Joost van der Lit, Zhixiang Sun, Ingmar Swart, Peter Liljeroth, and Daniël Vanmaekelbergh, *ACS Nano*, 6, 10216 (2012)]. Copyright (2012) American Chemical Society.

without large protrusions. The attraction due to the F_{vdW} is measurable at distances larger than 1 nm, and it is usually detectable as far as 5 nm from the surface.

The chemical force acting between the tip and the sample F_{chem} is short-ranged, and can be either attractive or repulsive, depending on the mutual separation of the two. In a simple case, the chemical interaction of the two atoms can be expressed through the Morse potential, that turned out to be a reliable approximation to the chemical force in AFM [96]. The Morse potential $U_{\mathrm{M}}(E_{\mathrm{bond}}, d, \kappa)$ depends on the equilibrium distance d_0, the energy of the chemical bond E_{bond}, the actual distance between the atoms d, as well as the decay length κ of the interaction [97]. Accordingly, the chemical force F_{chem} can be expressed as:

$$F_{\mathrm{chem}} = -\nabla U_{\mathrm{M}}(E_{\mathrm{bond}}, d, \kappa) = 2E_{\mathrm{bond}}\kappa \left[e^{-\kappa(d-d_0)} - e^{-2\kappa(d-d_0)}\right] \tag{1.32}$$

and the inverse exponential dependence on the distance is responsible for its the short-ranged nature. The chemical force is alternatively also described as originating from the Lennard-Jones potential between the atoms/molecules on the tip and the sample (as in the Fig. 17a). The Lennard-Jones potential $U_{\mathrm{LJ}}(E_{\mathrm{bond}}, d, \sigma)$ depends on the energy of the chemical bond E_{bond}, the actual distance between the atoms d, and the van der Waals radius of the particles σ [98]. Accordingly, the chemical force F_{chem} can be expressed as:

$$F_{\mathrm{chem}} = -\nabla U_{\mathrm{LJ}}(E_{\mathrm{bond}}, d, \sigma) = -\nabla 4E_{\mathrm{bond}} \left[\left(\frac{\sigma}{d}\right)^{12} - \left(\frac{\sigma}{d}\right)^{6}\right] = 4E_{\mathrm{bond}} \left[\frac{12}{d}\left(\frac{\sigma}{d}\right)^{12} - \frac{6}{d}\left(\frac{\sigma}{d}\right)^{6}\right] \tag{1.33}$$

The Morse and the Lennard-Jones potential are in many ways equivalent, and match exactly in the vicinity of the equilibrium separation between the tip and the sample [99]. In both cases, there are two individual components in F_{chem} that describe the longer-ranged attraction of two atoms/molecules towards their equilibrium separation (second terms in equations 1.32 and 1.33), and the shorter-ranged repulsion between the two atoms/molecules that appears when their separation is smaller than the equilibrium distance (first term in equations 1.32 and

Die approbierte gedruckte Originalversion dieser Dissertation ist an der TU Wien Bibliothek verfügbar.
The approved original version of this doctoral thesis is available in print at TU Wien Bibliothek.
TU Bibliothek WIEN Your knowledge hub

1.33). In other words, as the separation of the tip and the sample is decreased, the chemical force will act attractively towards the tip if there is a preference for chemical bonding between the atoms/molecules on the sample and the tip, and finally start repelling the tip due to the Pauli repulsion when the wavefunctions of the electrons in the inner shells of the atoms/molecules on the tip and the sample start to overlap. In the example in Fig. 17a, the tip is chemically attracted by the sample in the vicinity of their equilibrium separation, while smaller separations lead to strong Pauli repulsion of the tip.

The exact deconvolution of the total force into its constituents, and the quantification of their origin, is challenging both experimentally and theoretically. There are many studies tackling this issue, which is additionally complicated by the different balance between the constituent forces in each individual case study. Nevertheless, AFM is standing out as one of the most promising techniques for quantifying the fundamental interactions between atoms and molecules [100, 101].

1.5.4 Contrast formation

AFM studies mostly focus on surfaces of multi-component samples, or on complex adsorbates on well-defined substrates. Different chemical species on the surface, and their different physical properties such are charge, coordination, and geometric alignment, will act on the tip with a distinctly different directionality and magnitude of the total force. This constitutes the working principle of the contrast formation in AFM, and is illustrated in Fig. 17b. In this example, the tip is moved over a surface at a constant tip-sample separation $d = const.$, *i.e.*, in a constant-height mode. When the tip is positioned over the region B in this example, it will experience repulsive forces, while it will experience attractive forces when it is positioned over the region A.

AFM measurements are preferably performed in the constant-height mode $d = const.$, because the results are more straightforward to interpret: Surface species that are imaged with the strongest Δf signal are usually the geometrically most protruding species. Additionally, when there are at least two species with opposite chemical contrast (as in the illustration in Fig. 17b), the contrast obtained in constant-height AFM provides information about the chemical/physical properties of each species, instead of introducing ambiguities about their geometric alignment. Another great advantage of the constant-height AFM mode is that applying sample bias, and simultaneously collecting the tunneling current during the scanning, will additionally yield a simultaneous constant-height STM image. Figure 18 shows an example of the simultaneous AFM/STM measurements over the famous Si(111)(7×7) reconstruction, at different tip-sample distances. At short distances (leftmost two panels of Fig. 18) both AFM and simultaneous STM show atomic resolution. At larger distances however (rightmost two panels of Fig. 18) the main contribution to the AFM signal becomes the van der Waals interaction [89] and the individual atoms are hardly distinguishable; STM on the other hand, still provides atomic resolution due to the longer-ranged overlap of the wavefunctions of the tip and the sample. Distances marked in panels in Fig. 18 are defined with respect to an arbitrary point, and do not represent the absolute distances between the tip and the sample. A commonly encountered contrast inversion above the surface species when the tip-sample distance is reduced is not observed in AFM images in Fig. 18, because each image was obtained at tip-sample distances larger than the distance at which the saddle-point of the tip-sample forces is located [89].

AFM can be also operated in constant-frequency-shift mode $\Delta f = const.$, analogous to the constant-current mode $I_\mathrm{t} = const.$ in STM. Unlike the exponential increase of the tunneling current in STM, in AFM the total tip-sample force is not monotonous as the tip-sample separation is reduced. Instead, the tip-sample force is commonly attractive at far distances and in the vicinity of the saddle point at an equilibrium distance from the surface, but becomes repulsive when the tip-sample distance is further reduced. This poses a challenge for the feedback loop that needs to ensure a constant-frequency shift, because the change of the tip-sample separation with the change in the detected frequency shift must be performed in two opposite ways at the two sides of the saddle point. Constant-frequency-shift mode $\Delta f = const.$ is therefore used with very weak set-points for the tip-sample interaction, *i.e.*, at large distances from the surface. This mode of operation is often employed to investigate the large-scale morphology of a surface, because it ensures that the tip does not crash on a step-up between two terraces. Additionally, when AFM is performed at elevated temperatures where thermal drift is significant, constant-frequency-shift AFM helps in preventing the tip from crashing towards, or drifting away from the surface.

1.5.5 Force-distance curves

The tip-sample interaction can be quantified with AFM by performing the so-called z-spectroscopy, *i.e.*, by positioning the AFM tip above a certain point of interest and measuring the frequency shift as the tip is

Die approbierte gedruckte Originalversion dieser Dissertation ist an der TU Wien Bibliothek verfügbar.
The approved original version of this doctoral thesis is available in print at TU Wien Bibliothek.
TU Bibliothek Your knowledge hub WIEN

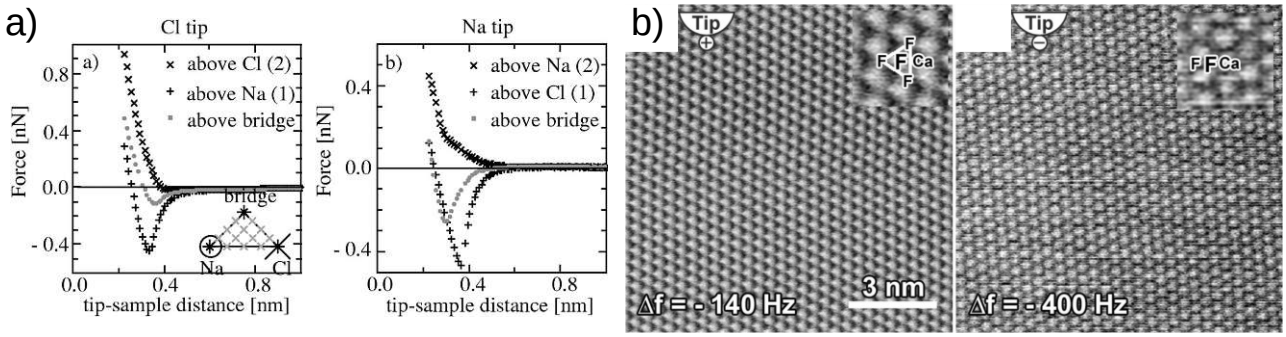

Figure 20: **AFM contrast formation on ionic surfaces imaged with anion and cation tips.**
a) Force-distance curves $F_{\mathrm{ts}}(z)$ above Na and Cl atoms of the NaCl(001) ionic surface obtained with an anion Cl^-- and cation Na^+-terminated tips.
Reprinted Figure 4 [102] from [M. A. Lantz, R. Hoffmann, A. S. Foster, A. Baratoff, H. J. Hug, H. R. Hidber, and H.-J. Güntherodt, *Physical Review B*, 74, 245426 (2006)] with permission of Author(s) and APS. Copyright (2012) American Physical Society.
b) Constant-frequency-shift AFM images of the $CaF_2(111)$ surface obtained with a cation (left panel) Ca^{2+}- and anion (right panel) F^--terminated tip. Bright color indicates repulsion, while dark color indicates attraction in the two images.
Reprinted Figure 2 [103] with permission of IOP Publishing, Ltd., from [Shintaro Fujii and Masamichi Fujihira, *Nanotechnology*, 8, 084011 (2007)]; permission conveyed through Copyright Clearance Center, Inc.

gradually approached towards the sample. This procedure results in a frequency shift vs. distance curve $\Delta f(z)$, as the red-colored curve in Fig. 17a. Figure 19 shows an example of frequency shift vs. distance curves and constant-height AFM measurements on epitaxially grown graphene on an Ir (111) substrate [90]. The two frequency shift vs. distance curves $\Delta f(z)$ in Fig. 19a were obtained over inequivalent sites on graphene, explicitly shown in the top right panel in Fig. 19b. They are similar at large distances from the surface due to long-range van der Waals and electrostatic interaction, but differ in the vicinity of the saddle point and at closer distances to the surface. These differences are responsible for the observed frequency shift contrasts and the atomic resolution. Figure 19b illustrates the commonly observed contrast inversion in constant-height AFM images. At a large relative tip-sample distance (z=60 pm in this example), carbon atoms act attractively towards the AFM tip through the long-range forces as well as the short-ranged chemical forces, while at a small relative tip-sample distance (z=0 pm in this example) carbon atoms start to repel the tip due to a combination of electrostatic and Pauli repulsion. At an intermediate relative tip-sample distance (z=30 pm in this example) the contrast inversion occurs, and carbon atoms change their interaction with the AFM tip from attraction to repulsion. The distance at which the contrast inversion occurs, and whether it will occur at all, depends on the physical and chemical properties of the tip and the sample.

In order to quantify the fundamental interactions between the atoms at the tip apex and the surface, frequency shift vs. distance curves $\Delta f(z)$ need to be transformed to force-distance $F_{\mathrm{ts}}(d)$ curves in post-processing. According to eq. 1.27, the frequency shift at a given tip-sample distance can mathematically be obtained by differentiating a known force-distance curve. Equation 1.27 can be analytically solved when the tip-sample force is modeled with a general inverse power-law of the tip-sample distance d as $F_{\mathrm{ts}}(d) = -Cd^{-n}$, where C is the tip-sample force constant. Then, two different regimes of tip-sample interactions can be realized, depending on the amplitude A of the cantilever oscillations. When the amplitude of oscillations A is small compared to the tip-sample separation $d - A$ at the closest point of the approach during one oscillation cycle, the frequency shift can be related to the tip-sample forces F_{ts} through a small amplitude approximation as [104]:

$$\Delta f(d, k, f_0) \approxeq \frac{f_0}{2k} \frac{\partial^2 V_{\mathrm{ts}}(z = d - A)}{\partial z^2} \quad ; \quad A \ll d - A \tag{1.34}$$

where V_{ts} is the tip-sample interaction potential, d is the mean separation between the tip and the sample, z is the coordinate of vertical oscillations $z \in [d - A, d + A]$, f_0 is the natural frequency, and k is the stiffness of the cantilever. In the opposite case, when the amplitude of the oscillations A is large compared to the tip-sample separation $d - A$ at the closest point of the approach during one oscillation cycle, the frequency shift can be

Die approbierte gedruckte Originalversion dieser Dissertation ist an der TU Wien Bibliothek verfügbar.
The approved original version of this doctoral thesis is available in print at TU Wien Bibliothek.
TU Bibliothek WIEN Your knowledge hub

related to the tip-sample forces F_{ts} through a large amplitude approximation as [104]:

$$\Delta f(d,k,A,f_0,n) \approxeq -\frac{1}{\pi\sqrt{2}}\frac{f_0}{kA^{\frac{3}{2}}}\frac{C}{(d-A)^{n-\frac{1}{2}}}\int_{-\infty}^{+\infty} dy \frac{1}{(1+y^2)^n} \quad ; \quad A \gg d-A \tag{1.35}$$

where C is the force constant, n is the power in the inverse power law for the force vs. distance, the last integral term accounts for the loss of tip-sample interaction throughout the most of the oscillation cycle when the tip is too far away from the sample, and the rest of the terms are equivalent to those in eq. 1.34.

Both equations 1.34 and 1.35 illustrate that the amplitude of oscillations A determines the measured frequency shift, and change in A will yield different frequency shift in a completely equivalent tip-sample interaction potential. The small amplitude mode of measurements yields higher frequency shifts than the large amplitude mode, and thus increases the signal-to-noise ratio. Intuitively, the stronger frequency shifts in AFM operated with small amplitudes can be understood as originating from the increased tip-sample interaction when the majority of the tip's oscillation cycle is performed within the region of the strong tip-sample interaction potential. When AFM is performed with large amplitudes however, the tip is located away from the region of strong tip-sample interaction potential throughout the majority of the tip's oscillation cycle, and the measured frequency shifts are smaller. Both modes of operation are used during typical AFM measurements. Large amplitude AFM is preferred when performing large-scale constant-frequency-shift measurements over several terraces on the sample surface, because measurements with only weak tip-sample interaction are safer to perform on a large scale. Small amplitude AFM is usually performed when obtaining atomic resolution in constant-height mode, because strong tip-sample interaction yields better spatial resolution of single atoms on the sample surface.

Although the transformation between the tip-sample force-distance curve $F_{\mathrm{ts}}(z \in [d-A, d+A])$ and the frequency shift vs. distance curve $\Delta f(d)$ is straightforward according to equations 1.34 and 1.35, the inverse transformation from $\Delta f(z)$ to $F_{\mathrm{ts}}(z)$ is not trivial. It requires an integration of the frequency shift over the range of the oscillations, and it is usually performed on the frequency shift vs. distance curves that are obtained with a small amplitude of oscillations. This transformation from $\Delta f(d)$ to $F_{\mathrm{ts}}(d)$ can be performed at the point of the closest approach of the tip to the sample $z = d - A$ with the so-called Sader's inversion formula [105]. In the limiting cases, Sader's inversion formula can be expressed for the small-oscillation-amplitude approximation as [105]:

$$F_{\mathrm{ts}}(d-A) = \frac{2k}{f_0}\int_{d-A}^{\infty} dz \Delta f(z) \quad ; \quad A \ll d-A \tag{1.36}$$

and the large-oscillation-amplitude approximation as [105]:

$$F_{\mathrm{ts}}(d-A) = -\frac{\sqrt{2}kA^{\frac{3}{2}}}{f_0}\int_{d-A}^{\infty} dz \frac{1}{\sqrt{z-(d-A)}}\frac{d(\Delta f)}{dz} \quad ; \quad A \gg d-A. \tag{1.37}$$

In both limiting cases, the transformation from $\Delta f(z)$ curves to $F_{\mathrm{ts}}(d)$ curves is dependent on the properties of the cantilever, such is the stiffness k or the natural frequency f_0. Therefore, the tip-sample interaction is usually reported through force-distance curves $F_{\mathrm{ts}}(z)$, which are universal across different experimentally used cantilevers.

The general Sader's inversion formula, and its two limiting cases expressed in equations 1.36 and 1.37, are well-posed when the interatomic force can be expressed as a linear combination of exponential functions [106]. All tip-sample force components described in equations 1.30–1.33 belong to Laplace space, and the Sader's inversion formula is valid for them. In experimentally obtained frequency shift vs. distance curves, the tip-sample force is susceptible to the most rapid changes in the vicinity of the inflection point, and the amplitude of oscillations needs to be selected such that is larger than one half of the inflection point distance from the sample $A > z_{\mathrm{inf}}/2$ [106, 107].

Force-distance curves $F_{\mathrm{ts}}(z)$ are the best quantitative indicator of the tip-sample interaction. Figure 20a shows force distance curves obtained over Na cations and Cl anions on an ionic NaCl(001) surface, with an AFM tip terminated by either Na^+ or Cl^- atom. Comparing the force-distance curves obtained with different tips reveals that a Na-terminated tip will experience repulsion over the surface Na atoms and attraction over the surface Cl atoms, while a Cl-terminated tip will experience opposite forces over the surface atoms. Therefore, the frequency shift contrast in AFM images shows attraction over one ion sublattice, and the repulsion over

Die approbierte gedruckte Originalversion dieser Dissertation ist an der TU Wien Bibliothek verfügbar.
The approved original version of this doctoral thesis is available in print at TU Wien Bibliothek.
TU Bibliothek Your knowledge hub WIEN

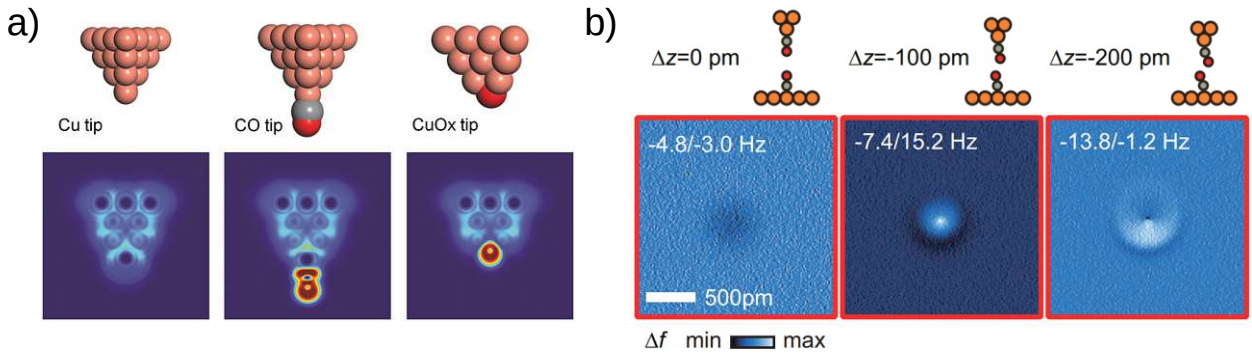

Figure 21: **Different AFM tip terminations.**
a) Illustration of a copper tip terminated with a copper atom, oxygen atom, and a CO molecule. The bottom row illustrates the calculated electron localization at the tip apex.
Reprinted Figure 9 [108] with permission of Royal Society of Chemistry, from [Harry Mönig, *Chemical Communications*, 54, 9874 (2018)]; permission conveyed through Copyright Clearance Center, Inc. This Figure is a slight modification of Figure S7 [109] for which a permission was also obtained from [Harry Mönig, Saeed Amirjalayer, Alexander Timmer, Zhixin Hu, Lacheng Liu, Oscar Díaz Arado, Marvin Cnudde, Cristian Alejandro Strassert, Wei Ji, Michael Rohlfing and Harald Fuchs, *Nature Nanotechnology*, 13, 371 (2018)]. Copyright (2018) Springer Nature.
b) Constant-height AFM images of a CO molecule imaged with a CO terminated tip, *i.e.*, the COFI method. The CO at the tip bends around the CO molecule at the surface as the tip-sample distance is reduced.
Reprinted Figure 5 [110] from [Alexander Gustafsson, Norio Okabayashi, Angelo Peronio, Franz J. Giessibl, and Magnus Paulsson, *Physical Review B*, 96, 085415 (2017)] with permission of Author(s) and APS. Copyright (2017) American Physical Society.

the other ion sublattice, depending on the tip termination. Figure 20b illustrates this tip-dependent contrast inversion over the ionic $CaF_2(111)$ surface. The cation-terminated tip (left panel) will image the F sublattice as attractive (bright spots) and Ca sublattice as repulsive (dark spots), while the anion-terminated tip (right panel) will image the two sublattices with an opposite contrast.

1.5.6 Tip termination

The tip termination in plays a crucial role in contrast formation in AFM (exemplified in Fig. 20). For comparison, in STM the only requirement for the tip termination is metallicity, which ensures the constant density of states at the tip. Additionally, the tip apex has to be sharper in AFM compared to STM, because the tip-sample forces do not decay as fast as the tunneling current: Small secondary tips (as the one in Fig. 10b) significantley contribute to the overall frequency shift through long-range van der Waals and electrostatic interactions. These factors make the tip preparation in AFM a discipline on its own, and there are many different methods for an AFM tip preparation at the atomic scale.

Some common tip apices are illustrated in Fig. 21. A typical preparation procedure for an AFM tip apex begins by coating a very sharp metallic tip with a layer of copper, or another noble metal. Subsequently, the very apex is decorated by a single atom of choice. Figure 21a illustrates three tip terminations of a copper-coated AFM tip, and the spatial distribution of their corresponding valence electron orbitals: the bare copper, oxygen-terminated, and CO-terminated apex. All of these tip terminations are atomically sharp, and they can be readily prepared on a Cu(110) surface. A bare Cu tip can be prepared in the same way as an STM tip, while the O- and CO-terminated tips are prepared by dosing O and CO to a Cu(110) surface, respectively, and transferring them from the surface to the tip by bias pulses or controlled mechanical contact [109]. The sharpness of the tip apex can be inferred from a small frequency shift after tip preparation, due to the reduced influence of the van der Waals forces of atoms behind the tip apex. A very popular tip decoration is a single CO molecule. The presence of a single CO molecule on a tip apex can be inferred through the so-called COFI method [113, 114], illustrated in Figure 21b. Once a single CO molecule is transfered to a tip apex, imaging another CO molecule still present on the surface will show a perfectly round feature at larger distances, which becomes recognizably distorted due to the repulsion of the two CO molecules at the surface and the tip at

Die approbierte gedruckte Originalversion dieser Dissertation ist an der TU Wien Bibliothek verfügbar.
The approved original version of this doctoral thesis is available in print at TU Wien Bibliothek.
TU Bibliothek Your knowledge hub WIEN

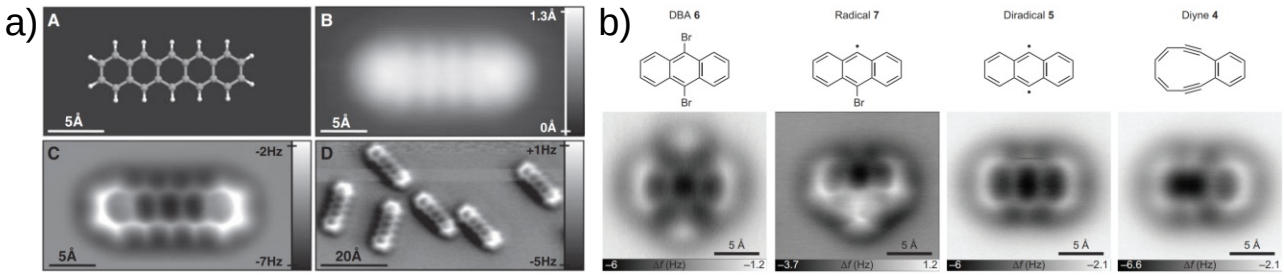

Figure 22: **Organic molecules resolved with a CO-terminated AFM tip.**
a) Pentacene adsorption on 2 ML NaCl/Cu(111): ball-and-stick model in top-left panel, constant-current STM image in top-right panel, two constant-height AFM images in the two bottom panels. STM and AFM images acquired with a CO-terminated tip.
Reprinted Figure 1 [111] from [Leo Gross, Fabian Mohn, Nikolaj Moll, Peter Liljeroth, and Gerhard Meyer, *Science*, 325, 1110 (2009)] with permission from AAAS.
b)The adsorption of 9,10-dibromoanthracene on a 2 ML NaCl/Cu(111), and its subsequent manipulation (debromination) imaged with atomically resolved constant-height AFM with a CO-terminated tip.
Reprinted Figure 2 [112] with permission from [Bruno Schuler, Shadi Fatayer, Fabian Mohn, Nikolaj Moll, Niko Pavliček, Gerhard Meyer, Diego Peña, and Leo Gross, *Nature Chemistry*, 8, 220 (2016)]. Copyright (2016) Springer Nature.

smaller distances, shown in constant-height AFM images in Figure 21b. The repulsion between the two CO molecules results in lateral bending of both, since a CO molecule is usually adsorbed perpendicularly to either the tip or the sample. The lateral freedom of movement for a CO at the tip apex is commonly referred to as the tip bending.

Decoration of the tip with a CO molecule is common in AFM studies, because these tips are well defined and well characterized, and because they provide unprecedented resolution of complex organic molecules. Figure 22 shows two examples of the capabilities of the CO-terminated AFM tip apex. The first example of the pentacene molecule adsorbed on Cu(111) [111], shown in Fig. 22a, illustrates that organic molecules can be resolved so well with a CO-terminated tip that the AFM images resemble the models in chemical textbooks. The excellent resolution capabilities with a CO-terminated AFM tips even enables performing and following chemical reactions on adsorbed molecules, shown in Fig. 22b. In this example, 9,10-dibromoanthracene molecules were adsorbed to an insulating bilayer of NaCl grown over the metallic Cu(111) surface. Afterwards, Br atoms were controllably removed from these molecules, and the reactants were observed with submolecular resolution using CO-terminated tips to reveal the Bergman cyclization reaction pathway [112].

1.5.7 Kelvin parabolas

The strength of the electrostatic tip-sample forces can also be quantified with AFM by performing the so-called bias spectroscopy, *i.e.*, by positioning a tip over a point on the surface at a constant height and varying the applied bias potential, while measuring the frequency shift at each bias value. This procedure results in the Kelvin parabola that has a shape of a negative parabola with a maximum at a negative (sometimes 0 Hz) frequency shift. According to eq. 1.30, the electrostatic force between the tip and the sample will become 0 N when the applied value of bias is equal to the local contact potential difference of the tip and the sample. Therefore, the maximum of the Kelvin parabola indicates the relative difference of work functions of the tip and the sample. When the tip is coated in a material with a known work function, which can be calibrated on a Cu(110) surface for example, Kelvin parabolas reveal the work function of the investigated sample.

A change in the work function of a sample under external stimuli indicates that a charging/discharging event occurred, *i.e.*, that the Fermi level of a sample has changed. Figure 23a shows the shift in the maximum of the Kelvin parabolas performed before and after illumination of a diamond sample with a nitrogen vacancy. The nitrogen vacancy that acts as a p-dopant, is photo-excited by visible light and consequently transfers electrons to the conduction band. This is observed as a shift of the Kelvin parabola towards the lower bias value, indicating an upwards shift of the Fermi level of the sample [115]. AFM is a highly local technique, which allows highly spatially resolved LCPD measurements, illustrated in Fig. 23b. O_2 molecules adsorb as either

Die approbierte gedruckte Originalversion dieser Dissertation ist an der TU Wien Bibliothek verfügbar.
The approved original version of this doctoral thesis is available in print at TU Wien Bibliothek.
TU Bibliothek Your knowledge hub WIEN

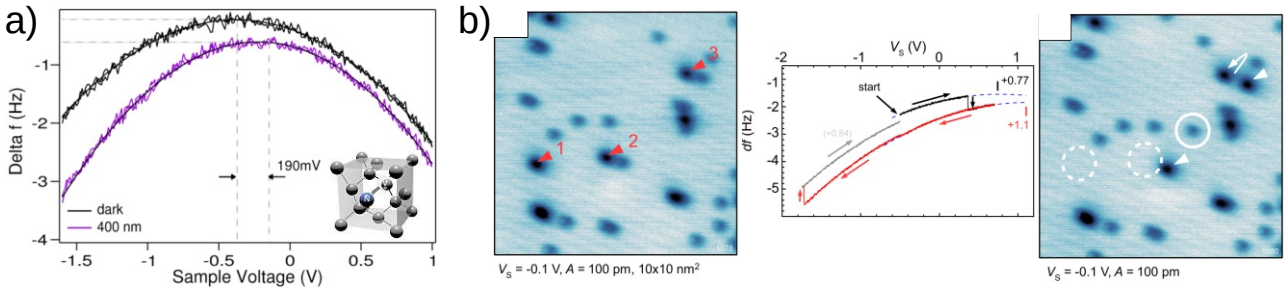

Figure 23: **Kelvin parabolas indicating ionization and charging events.**
a) Kelvin parabolas over the N-vacancy center in diamond with (black line) and without illumination (purple line). The LCPD values of the two parabolas differ, implying a photoionization process occurring under 400 nm light illumination.
Reprinted Figure 1 [115] with permission from [Rémy Pawlak, Thilo Glatzel, Vincent Pichot, Loïc Schmidlin, Shigeki Kawai, Sweetlana Fremy, Denis Spitzer, and Ernst Meyer, *The Journal of Physical Chemistry C*, 113, 12277 (2009)]. Copyright (2009) American Chemical Society.
b) Constant-height AFM image of O_2 species on the anatase TiO_2(101) surface (left panel). Kelvin parabolas before and after charging (center panel) of the O_2 molecules show a shift in the LCPD. After each marked O_2 molecule was subjected to the same treatment, the resulting surface was imaged with constant-height AFM (right panel).
Reprinted left panel in Figure 4(a,c,d) [116] with permission from [Martin Setvín, Jan Hulva, Gareth S. Parkinson, Michael Schmid, and Ulrike Diebold, *Proceedings of the National Academy of Sciences*, 114, E2556 (2017)].

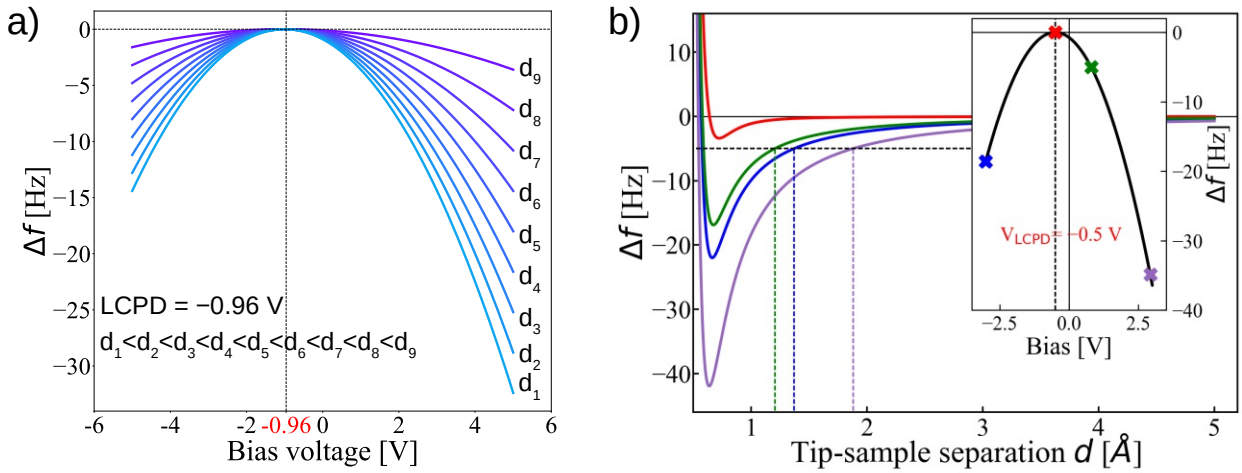

Figure 24: **The strength of the electrostatic tip-sample interaction.** a) Illustration of different Kelvin parabolas at several tip-sample distances from the surface. The electrostatic interaction is stronger at small, and weaker at large tip-sample distances. b) Illustration of total tip-sample forces at varying strengths of the electrostatic interaction. Differently colored curves correspond to force-distance curves taken with different bias voltages, marked by the respectively colored "x" on the Kelvin parabola in the inset. The black horizontal dashed line indicates the set-point of the constant-frequency shift AFM mode ($\Delta f = const. = -5\,\mathrm{Hz}$), and the colored vertical dashed lines indicate the corresponding tip-sample distance where the frequency shift is equal to the set-point.

single charged on neutral molecules on anatase TiO_2(101) surface, and the local Kelvin parabolas indicate their charge state: charged molecules have the maximum of the Kelvin parabola at higher bias values compared to neutral molecules [116]. In the example in Fig. 23b, marked molecules in the left panel are the charged O_2 molecules that have been discharged by a bias ramp to roughly $-1.6\,\mathrm{V}$. This transformed them into neutral

Die approbierte gedruckte Originalversion dieser Dissertation ist an der TU Wien Bibliothek verfügbar.
The approved original version of this doctoral thesis is available in print at TU Wien Bibliothek.
TU Bibliothek Your knowledge hub WIEN

molecules with an increased mobility, and constant-height AFM after the process (rightmost panel of Fig. 23b) confirms that they are no longer present at their original positions.

Kelvin parabolas offer great insight into the Fermi and vacuum levels of the samples. Moreover, performing a Kelvin parabola during AFM measurements is useful for evaluating the strength of the electrostatic tip-sample interactions, and adjusting the measurement parameters accordingly. Figure 23a illustrates Kelvin parabolas obtained at different tip-sample distances. The electrostatic tip-sample interactions are stronger at small tip-sample distances, which is characterized by a Kelvin parabola with a smaller curvature in the vicinity of the maximum. The sample bias value is often chosen such that it matches the LCPD so that the electrostatic tip-sample forces are minimized during measurements. The strength of the electrostatic interaction also influences the constant-frequency shift AFM measurements, as illustrated in Fig. 23b. A given frequency shift set-point in constant-frequency shift AFM $\Delta f = const.$ will correspond to different tip-sample distances at different bias values. When the bias value differs greatly from the LCPD, the overall tip-sample interaction is stronger due to the increased electrostatic forces, and the chosen $\Delta f = const.$ set-point will keep the tip at a larger distance from a sample (purple and blue lines in Fig. 23b). On the other hand, if the bias value is close the LCPD, the overall tip-sample interaction is smaller, and the given $\Delta f = const.$ set-point will keep the tip at a smaller distance from a sample (green line in Fig. 23b), or even crash the tip towards the sample when the electrostatic interaction is so small that the given $\Delta f = const.$ cannot be achieved even at the bottom of the tip-sample attraction well (red line in Fig. 23b). Therefore, the electrostatic forces should be taken into consideration while performing measurements in either the constant-height or the constant-frequency-shift AFM mode.

Die approbierte gedruckte Originalversion dieser Dissertation ist an der TU Wien Bibliothek verfügbar.
The approved original version of this doctoral thesis is available in print at TU Wien Bibliothek.
TU WIEN Bibliothek Your knowledge hub

Chapter 2

Interaction of the rutile $TiO_2(110)$ surface with adsorbates

2.1 Introduction

Titanium dioxide, TiO_2, is a member of the binary, transition-metal oxide class of materials, and is the most abundantly used in daily applications compared to the others. It is mostly used in the form of a white powder, which makes it is an indispensable component of many white pigments and dyes [117]. Additionally, TiO_2 is non-toxic [118] (unless inhaled in large quantities [119]), so it can commonly be found in different dietary products that are artificially colored white, in which case the TiO_2 ingredient is labeled as E171. Titanium dioxide is mainly produced from the ilmenite ore ($FeTiO_3$), from which it is separated either by the sulfate or chloride process. The largest ilmenite mines are located in Norway and Canada, and its presence was also confirmed on the Lunar surface [120].

Among many polymorphs of TiO_2, three are the most stable: rutile and anatase TiO_2 with tetragonal bulk symmetry, and brookite with orthorhombic bulk symmetry. The rutile TiO_2 is the energetically most stable structure [121], and is thus the most common naturally occurring TiO_2 in the single-crystal form. A photograph of a rutile TiO_2 single crystal can be seen in Fig. 25a. Both rutile or anatase TiO_2 structures can be prepared in powdered form, and their micro- and nano-particles can be precisely tailored into different shapes and sizes [122, 123].

Rutile TiO_2 bulk structure is characterized by the tetragonal P42/mnm symmetry, with the unit-cell vectors of $a = c = 4.5936$ Å and $b = 2.9586$ Å at 298 K [127]. The tetrahedral unit cell of rutile TiO_2 can be seen in Fig. 25b. A Ti atom in the center of each unit cell is coordinated to 6 O atoms, arranged in the characteristic oxygen octahedron. The bulk TiO_2 structure can be constructed by infinitely repeating the oxygen octahedron (seen in Fig. 25b), with the additional stacking rule that each added oxygen octahedron in all directions needs to be rotated by 90° over the [110] axis. Bulk rutile TiO_2 is a bulk semiconductor, with a 3.06 eV direct band gap [128]. The band gap energy is sufficiently large to adsorb UV irradiation, and powdered rutile TiO_2 is commonly used as a cosmetic sunscreen [129]. Reduced rutile TiO_2 can be conducting under application of sufficient voltage, and it exhibits a polaronic conductance; conductivity is a consequence of polaron hopping along the direction of the applied voltage [130]. Below 20 K rutile TiO_2 becomes insulating, since the mobility of polarons is drastically decreased [131]. Rutile TiO_2 is typically n-type doped, due to the intrinsic electron donating defects such are bulk oxygen vacancies (donating 2 electrons) and titanium interstitials (donating 4 electrons) [132]. Bulk rutile TiO_2 has found possible advanced applications as a memsistor [133, 134], anode material for Li incorporation in Li-ion batteries [135], or within solar cells [136], while rutile TiO_2 powders shows promise for water purification processes [137].

The most energetically stable surface of the single crystalline rutile TiO_2 is the (110) face, with the lowest Gibbs free energy compared to the rest [138]. A Wulff construction of the single crystal rutile TiO_2 can be seen in Fig. 25c, clearly showing the [110] as the preferred surface orientation. The rutile TiO_2 is considered a representative of the transition metal oxides family, and its most stable (110) face has therefore been extensively studied. In fact, rutile $TiO_2(110)$ surface is considered a model system for studying the phenomena on oxide surfaces. This surface is extensively described in the following Section.

Die approbierte gedruckte Originalversion dieser Dissertation ist an der TU Wien Bibliothek verfügbar.
The approved original version of this doctoral thesis is available in print at TU Wien Bibliothek.
TU Bibliothek Your knowledge hub WIEN

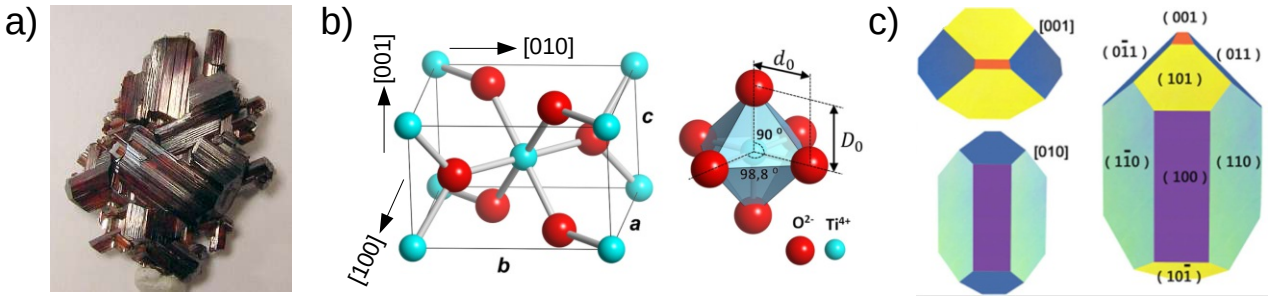

Figure 25: **Bulk rutile TiO_2.**
a) A photograph of a natural rutile TiO_2 crystal.
Image [124] taken with permission from Rob Lavinsky, iRocks.com under the CC-BY-SA-3.0 license.
b) Model of the rutile TiO_2 bulk unit cell (left), and the oxygen octahedron with a Ti atom in the center (right). Reprinted Figure 1 [125] from [G. C. Vásquez, S. Zh. Karazhanov, D. Maestre, A. Cremades, J. Piqueras, and S. E. Foss, *Physical Review B*, 94, 235209 (2016)] with permission of Author(s) and APS. Copyright (2016) American Physical Society.
c) Wulff construction of the surfaces on the single crystal TiO_2.
Reprinted Figure 4(a) [126] with permission from [Fengzhou Jiang, Lei Yang, Dali Zhou, Gang He, Jiabei Zhou, Fanhou Wang, and Zhi-Gang Chen, *Applied Surface Science*, 436, 989 (2018)]. Copyright (2018) Elsevier.

2.2 Clean rutile TiO_2(110)-(1×1) surface

Rutile TiO_2(110) surface is considered one of the most well-known and well-understood transition metal oxide surfaces up do date [139]. Figure 26 shows the ball-and stick structural models of a rutile TiO_2(110) surface slab. When a (110) surface is created, each oxygen octahedron with the main axis oriented along the [$\bar{1}$10] exposes one oxygen atom to the surface (along the [110] direction), while those octahedra with the main axis oriented along the [110] direction loose the protruding oxygen atom along the [110] direction. This creates a surface with every other row of terminal oxygen atoms missing, as illustrated in Fig. 26a. The rows of two-fold coordinated protruding oxygen atoms are commonly referred to as the rows of bridging oxygen atoms O_{br}, because each O_{br} is located in a bridging site between two lattice Ti_{6c} atoms below. Between the O_{br} rows, there are two rows of terminal O_{3c} and one row of terminal Ti_{5c} exposed at the surface. The TiO_2(110) surface is characterized by a rectangular unit cell that spans 6.48 Å and 2.95 Å along the [$\bar{1}$10] and [001] directions, respectively, and Fig. 26b shows the (110) surface viewed from the top with three neighboring unit cells marked by a dashed line.

The most common defects on the rutile TiO_2(110) surface are missing oxygen atoms in the O_{br} rows, commonly referred to as the oxygen vacancies V_O. A presence of a single V_O, viewed from the top, is illustrated in Fig. 26c. The oxygen vacancies are a common active site responsible for many on-surface reactions, the most important of which is dissociation of water molecules [140]. Each missing oxygen atom from the O_{br} rows reduces the stoichiometry, and the remaining surface is therefore doped with two excess electrons per each V_O, due to the absence of previously formally negatively charged oxygen atom O_{br}^{2-}. The rutile TiO_2(110) surfaces are semiconducting, similar to the bulk crystals, with a characteristic band gap of ≈3.2 eV [141]. Therefore, rutile TiO_2(110) surfaces can be photo-active only for the ultraviolet light with the $\lambda < 390$ nm, after which this surface becomes an efficient photocatalyst [142]. The Fermi level of the rutile TiO_2(110) surface can be externally manipulated by different dopants [143], or by the intrinsic V_O defects that are responsible for the n-type doping and lifting of the Fermi level closer to the conduction band.

Clean TiO_2(110) surfaces used in the research that led to this Thesis were commonly prepared in vacuum, by ion sputtering and high temperature annealing. Examples of such surfaces are shown in Fig. 27. The flat surface morphology with reasonably large terraces (visible in large-area scans in Fig. 27) were obtained by annealing to temperatures in the 700–800 °C range; annealing the surface to lower temperatures resulted in a surface covered with 10–20 nm large TiO_2(110) islands. Surface cleanliness was achieved by focused bombardment with 1 μA of Ar^+ ions accelerated to 1–2 keV kinetic energies. A typical preparation cycle consisted of first degassing the surface at 700 °C for 2–3 h, and subsequently repeating the cycles of 1 keV Ar^+ sputtering for 10 min followed by annealing at 750 °C for 15 min. This type of surface preparation preferentially removes oxygen from the lattice, and subsequently creates oxygen vacancies. Beside the point V_O defects, the surface prepared this way

Die approbierte gedruckte Originalversion dieser Dissertation ist an der TU Wien Bibliothek verfügbar.
The approved original version of this doctoral thesis is available in print at TU Wien Bibliothek.
TU Bibliothek Your knowledge hub WIEN

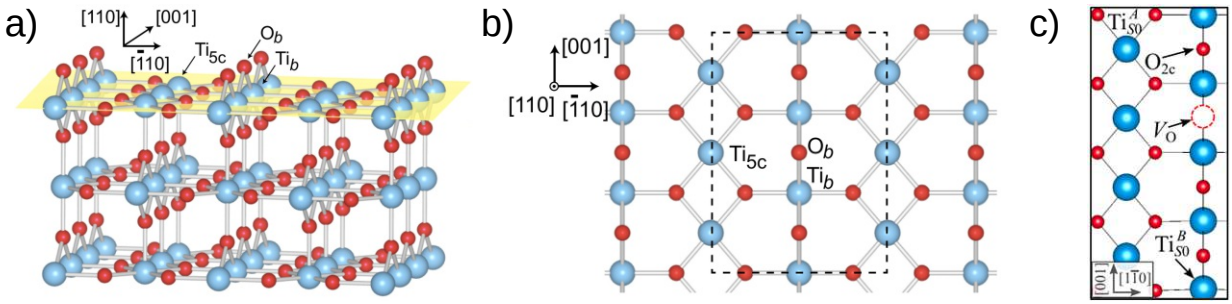

Figure 26: **Ball-and stick models of the rutile TiO_2(110) surface.**
a) A stoichiometric rutile TiO_2(110) surface with rows of terminal Ti_{5c} atoms and bridging oxygen O_{2c} atoms viewed from the side. Titanium atoms are displayed as blue, and oxygen atoms as red.
Reprinted Figure 1(a) [147] with permission from [P. G. Moses, A. Janotti, C. Franchini, G. Kresse, and C. G. Van de Walle, *Journal of Applied Physics*, 119, 181503 (2016)]. Copyright (2016) AIP Publishing.
b) The same surface viewed from the top.
Reprinted Figure 1(b) [147] with permission from [P. G. Moses, A. Janotti, C. Franchini, G. Kresse, and C. G. Van de Walle, *Journal of Applied Physics*, 119, 181503 (2016)]. Copyright (2016) AIP Publishing.
c) Rutile TiO_2(110) surface with a characteristic bridging oxygen vacancy defect V_O, viewed from the top.
Reprinted Figure 1(b) [148] from [Michele Reticcioli, Martin Setvín, Michael Schmid, Ulrike Diebold, and Cesare Franchini, *Physical Review B*, 98, 045306 (2018)] with permission of Author(s) and APS. Copyright (2018) American Physical Society.

are unreconstructed, *i.e.*, (1×1) terminated. However, after the critical oxygen vacancy concentration on the surface is reached, the surface assumes a (1×2) reconstruction [144]. The process of creating oxygen vacancies is not straightforward however: after the sputtering preferentially removes oxygen from the surface, subsequent annealing leads to mixing of the material in the crystal, and a portion of O atoms on the surface are replenished from the bulk [145]. When this cleaning procedure in UHV is performed extensively, the entire single crystal TiO_2 becomes reduced with by oxygen vacancies throughout the bulk. This effect can be easily observed because the entire single crystal rutile TiO_2 changes its color from originally white (band gap larger than the visible light) to dark black (reduced band gap due to intrinsic n-type doping) [145]. The reduction of the single crystal stoichiometry to $TiO_x (x < 2)$ also leads to an excess of Ti atoms, which assume an interstitial site within the bulk, commonly referred to as the titanium interstitials Ti_{int}. Each Ti_{int} donates three or four electrons to the crystal, enhancing the intrinsic n-type doping [132]. A bulk-reduced black rutile TiO_2 crystal can be re-oxidized by baking at 800 °C in a mixture of O_2 and Ar at 1 bar pressure, which restores the original white color to the crystal [146].

The semiconducting nature of the rutile TiO_2(110) surface enables performing STM measurements, as the ones shown in Fig. 27a. These empty-states STM images were performed with bias values far below the value of the band gap, which is possible due to the proximity of Fermi level to the conduction band in this n-type semiconductor. The small-area STM image (right panel of Fig. 27a) shows alterating bright and dark rows of atoms running along the [001] direction, and the dark rows are occasionally interrupted by a single bright feature. According to the model of the rutile TiO_2(110) surface (shown in Fig. 26), the geometrically protruding O_{br} rows are expected to be shown as "bright", *i.e.*, with higher apparent height in STM. However, this is not the case, and the counter-intuitive STM contrast on the rutile TiO_2(110) surface is dominated by the electronic structure of the surface rather than its geometry [149]. The Ti 3*d* states constitute the bottom of the conduction band in rutile TiO_2(110) surface, and tunneling from the STM tip into the empty states will occur into the Ti 3*d* states at lower positive bias values, where the STM imaging is stable without disruption of the tip due to the high electric fields [150]. Therefore, the typical STM contrast in the right panel of Fig. 27a shows: protruding O_{br} rows as dark, geometrically lower Ti_{5c} rows as bright, and single V_Os as bright spots on the dark O_{br} rows. The coverage of the V_Os in the right panel of Fig. 27a is roughly 0.15 ML, implying a 15% reduction state of the surface.

A large-area, $\Delta f = const.$ AFM image in the left panel of Fig. 27b shows a morphology of a clean rutile TiO_2(110)-(1×1) surface, with irregular terrace steps and pits within terraces: Although clean and unreconstructed, this particular surface was not annealed to high-enough temperatures to ensure large, undisrupted

Die approbierte gedruckte Originalversion dieser Dissertation ist an der TU Wien Bibliothek verfügbar.
The approved original version of this doctoral thesis is available in print at TU Wien Bibliothek.
TU Bibliothek Your knowledge hub WIEN

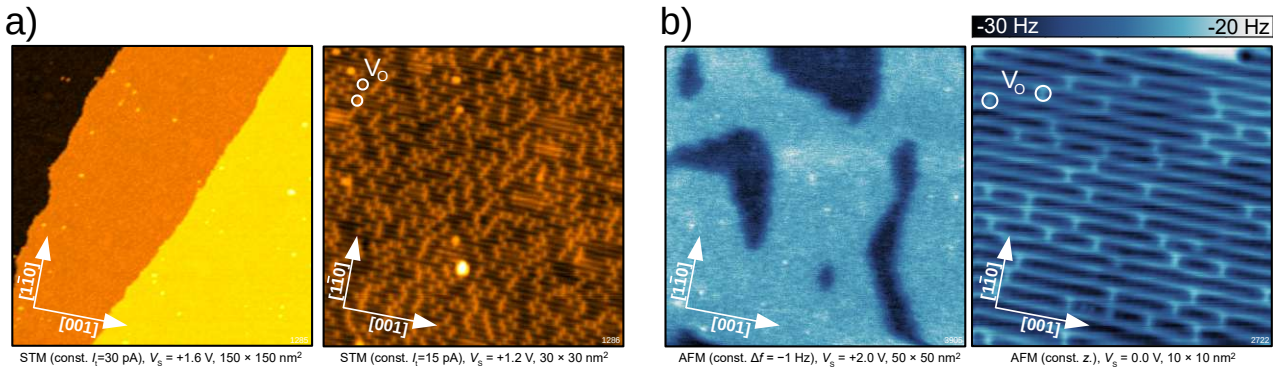

Figure 27: **Clean reduced rutile TiO_2(110)-(1×1) surface with oxygen vacancies.** a) Constant-current STM images, showing the large-area morphology (left panel) and the details of the atomic arrangement (right panel). Bright rows correspond to the rows of Ti_{5c} atoms, dark rows correspond to rows of O_{br} atoms, small bright spots correspond to single bridging-oxygen vacancies, and large bright spots correspond to isolated contaminants. b) Constant-frequency-shift AFM image (left panel), showing the large-area morphology, and the constant-height AFM image (right panel), focusing on the details of the atomic arrangement. Bright rows (weaker Δf signal) correspond to geometrically lower rows of Ti_{5c} atoms, dark rows (stronger, attractive Δf signal) correspond to geometrically protruding rows of O_{br} atoms, and bright features (weaker Δf signal) on the O_{br} rows correspond to missing O_{br} atoms – oxygen vacancies V_Os.

terraces. The small-area, constant-height AFM image in the right panel of Fig. 27b reveals the true geometry of the surface, contrary to the counter-intuitive contrast in STM. Here, higher attractive forces act on the tip from the geometrically protruding rows of O_{br} atoms and they are imaged as dark. The weaker attractive forces between the tip and the surface (bright) are recorded above the geometrically lower rows of Ti_{5c} atoms and the missing O atoms on the O_{br} rows, due to the absence of short-range chemical forces. This particular surface in the right panel of Fig. 27b is covered with roughly 6.8% of oxygen vacancies.

Die approbierte gedruckte Originalversion dieser Dissertation ist an der TU Wien Bibliothek verfügbar.
The approved original version of this doctoral thesis is available in print at TU Wien Bibliothek.
TU Bibliothek Your knowledge hub WIEN

2.3 Polaronic ground state of the rutile TiO_2(110)-(1×1) surface

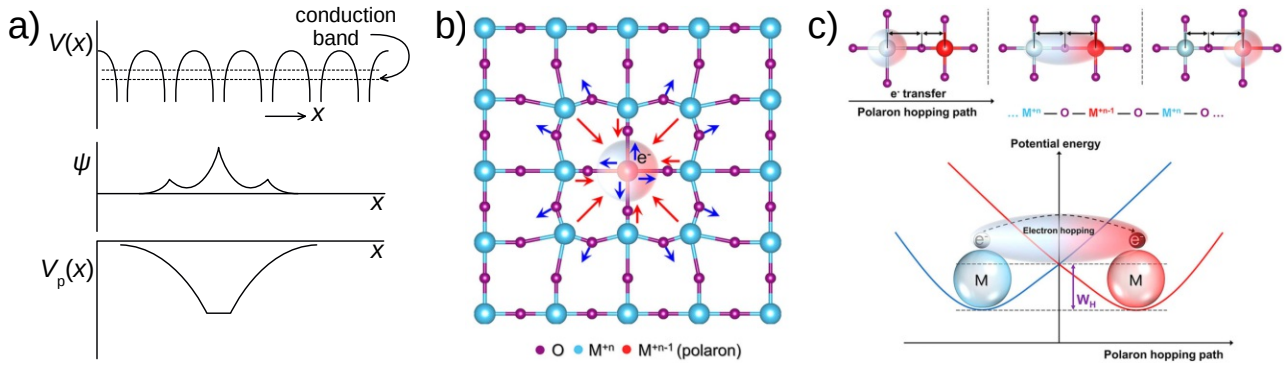

Figure 28: **Small electron polarons in transition metal oxides.**
a) Electron potential energy in a the perfect, undistorted solid (top), and the wavefunction (middle) and the electron potential (bottom) in the vicinity of the electron-trapping ion in a solid.
Image strongly inspired by Figure 4 in [I. G. Austin and N. F. Mott, *Advances in Physics*, 18, 41 (1969)] [151].
b) Illustration of the ionic distortion around a polaron-hosting metal ion in a MO_2 (M=metal) transition metal oxide.
Reprinted Figure 1(b) [152] with permission from [Yuriy Natanzon, Amram Azulay, and Yaron Amouyal, *Israel Journal of Chemistry*, 60, 768 (2020)]. Copyright (2020) John Wiley and Sons.
c) Illustration of the polaron hopping process (top) and the electron potential energy on the two neighboring electron-trapping ions in a solid (bottom).
Reprinted Figure 1(c) and Figure 1(d) [152] with permission from [Yuriy Natanzon, Amram Azulay, and Yaron Amouyal, *Israel Journal of Chemistry*, 60, 768 (2020)]. Copyright (2020) John Wiley and Sons.

The electronic structure of a stoichiometric and clean TiO_2(110)-(1×1) surface is characterized by a 3.2 eV band gap with O 2*p* and Ti 3*d* states populating the top of the valence band and the bottom of the conduction band, respectively. The reduced TiO_2(110)-(1×1) surface on the other hand, implies the presence of two excess electrons per single V_O, and the exact distribution and electronic states associated with these electrons had long been discussed [153]. The XPS of a reduced TiO_2(110) surface commonly display a shoulder on the lower-binding-energy edge of the Ti 2*p* signal [154], associated with electron-enriched Ti^{3+} atoms. Other techniques, such are electron paramagnetic resonance or electron-energy loss spectroscopy, also indicate the presence of the Ti^{3+} atoms in the near-surface region [155]. These electron-hosting Ti atoms are commonly assumed to be a consequence of the electron-donating titanium interstitials, but the Ti atoms hosting the excess electrons donated by V_Os would also show the same Ti^{3+} signature [156]. It was shown in a series of recent studies [157, 148, 158] that the electrons donated by each V_O are trapped in the form of small electronic polarons at the Ti atoms in regular sites in the surface and subsurface region of a reduced surface. The electron trapping is an intrinsic property of the rutile TiO_2, and the electrons donated by each Ti_{int} are also trapped in the form of electronic polarons. Titanium interstitials are prevalently distributed in the bulk and in the deep sub-surface layers of the crystal, especially in the reduced TiO_2(110) surfaces where the formally positively charged V_Os electrostatically repel the positively charged Ti_{int} atoms. TiO_2(110) surface preparation in UHV preferentially creates V_Os, making it unlikely for Ti_{int} atoms to reside close to the surfaces prepared under reducing conditions [146]. Therefore, surface-sensitive techniques are less likely to detect Ti^{3+} atoms related to the interstitials, and the near-surface Ti_{6c} atoms that host electrons from a nearby V_O are a more likely origin of the Ti^{3+} spectral fingerprint.

The localization of an electron around a displaced ion proceeds through the coupling of an electron with an optical phonon(s) in a solid [159]. A quasiparticle created through this electron-phonon coupling is commonly referred to as the electron polaron. The potential energy of an electron polaron can be expressed as [151]:

$$V_p(r) = -\frac{e^2}{4\pi r}\left(\frac{1}{\epsilon_\infty} - \frac{1}{\epsilon_0}\right) \tag{2.1}$$

Die approbierte gedruckte Originalversion dieser Dissertation ist an der TU Wien Bibliothek verfügbar.
The approved original version of this doctoral thesis is available in print at TU Wien Bibliothek.
TU Bibliothek Your knowledge hub WIEN

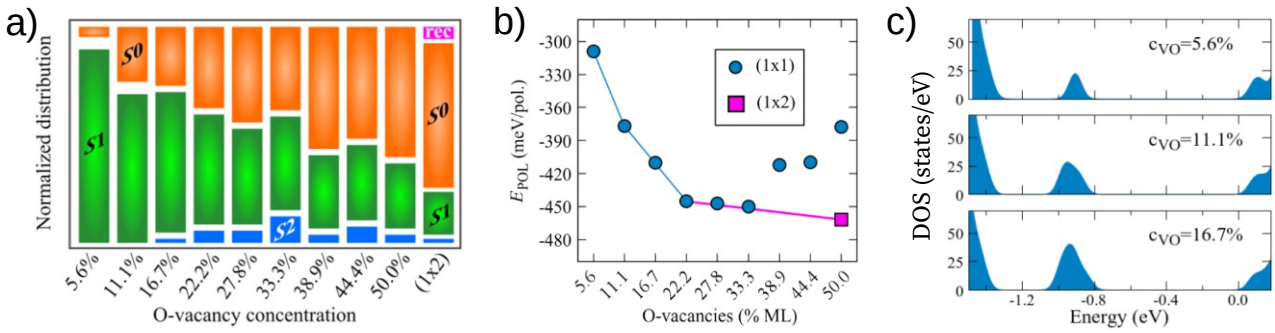

Figure 29: **Calculated properties of polarons on rutile TiO_2(110) surface reduced by V_Os alone.**
a) Distribution of polaron types as a function of the reduction state.
Reprinted Figure 3(b) [148] from [Michele Reticcioli, Martin Setvín, Michael Schmid, Ulrike Diebold, and Cesare Franchini, *Physical Review B*, 98, 045306 (2018)] with permission of Author(s) and APS. Copyright (2018) American Physical Society.
b) Polaron energy as a function of the reduction state.
Reprinted Figure 5(a) [157] with permission from [Michele Reticcioli, Martin Setvín, Xianfeng Hao, Peter Flauger, Georg Kresse, Michael Schmid, Ulrike Diebold, and Cesare Franchini, *Physical Review X*, 7, 031053 (2017)]. under the Creative Commons Attribution 4.0 International license.
c) Polaronic in-gap state in the calculated density of states.
Reprinted Figure S9 [157] with permission from [Michele Reticcioli, Martin Setvín, Xianfeng Hao, Peter Flauger, Georg Kresse, Michael Schmid, Ulrike Diebold, and Cesare Franchini, *Physical Review X*, 7, 031053 (2017)]. under the Creative Commons Attribution 4.0 International license.

i.e., as an electron potential energy gain by displacing an ion in a flexible solid (described by a high-frequency dielectric constant ϵ_∞) compared to an electron energy in static, stiff sold (described by static dielectric constant ϵ_0). The potential energy above can be considered constant up to a characteristic polaron radius r_p, $V_p(r) = -\frac{e^2}{4\pi r_p}\left(\frac{1}{\epsilon_\infty} - \frac{1}{\epsilon_0}\right)$ and decaying as r^{-1} outside of this radius. Figure 28a illustrates the electron potential in a perfect periodic solid (top panel), the $V_p(r)$ potential (bottom panel), and the electron wavefunction at the polaronic site (middle panel). Electron polarons can be classified in three representative categories according to the size of the characteristic polaron radius r_p: small or Holstein polarons [160] when r_p is smaller than the interatomic distance in a solid, large or Fröhlich polarons [161] when r_p is much larger than the interatomic distance in a solid, and an intermediate case where a small polaron extends over several neighboring ions in a solid (this case is illustrated in Figure 28a).

In a rutile TiO_2 solid, Ti $3d$ electrons are donated to the O $2p$ states during covalent bonding. This makes O $2p$ states fully occupied, and the excess electrons from a V_O can experience self-trapping only by filling the Ti $3d$ states. The TiO_2 solid is likely to host small electron polarons, or Holstein polarons, by localization in narrow Ti $3d$ t_{2g} states that have no overlap with the neighboring O $2p$ states [151]. Moreover, the formation of small polarons in transition metal oxides is further supported by strong electron-phonon coupling [162]. While Fröhlich polarons can be described through a perturbation Hamiltonian of a single electron coupling to a spectra of phonons, Holstein polarons can be described using the Hubbard-Holstein Hamiltonian [163]:

$$H = -t\sum_{i,\delta,\sigma} c^\dagger_{i\sigma}c_{i+\delta\sigma} + U\sum_i n_{i\uparrow}n_{i\downarrow} + \omega_0\sum_i b^\dagger_i b_i + g\sum_{i\sigma} n_{i\sigma}\left(b^\dagger_i - b_i\right) \tag{2.2}$$

where summation over i and $i+\delta$ is performed over all atoms and their nearest neighbors, summation over σ accounts for different spin states, t is the polaron hopping rate between nearest neighbors, U is the Hubbard's on-site electron-electron repulsion, ω_0 is the phonon frequency, and g is the electron-phonon coupling strength. The equation above is presented in the second quantization, where $c^\dagger_{i\sigma}$ and $c_{i\sigma}$ are the fermionic electron creation and annihilation operators at a site i, $n_{i\sigma}$ is the fermionic number operator $n_{i\sigma} = c^\dagger_{i\sigma}c_{i\sigma}$, and $b^\dagger_i$ and b_i are bosonic phonon creation and annihilation operators at a site i. The Hubbard-Holstein Hamiltonian above is a mixture of the Hubbard Hamiltonian, that does not account for the electron-phonon coupling, and the Holstein Hamiltonian that does not account for the on-site electron-electron repulsion.

Die approbierte gedruckte Originalversion dieser Dissertation ist an der TU Wien Bibliothek verfügbar.
The approved original version of this doctoral thesis is available in print at TU Wien Bibliothek.
TU Bibliothek Your knowledge hub WIEN

Figure 28b illustrates (the illustration is over-exaggerated) a small electron polaron in a transition metal oxide MO_2: a formally positive ion that donated its electrons to the electronegative O atoms in the lattice, can host an excess electron by first polarizing the medium in the vicinity. There is an important distinction between self-trapped electrons in the form of a polaron, and the electrons trapped in a defect state. Electrons that are localized on a defect cannot move through the lattice, unless the defects are uniformly distributed around the solid such that they must be considered as an additional, periodic trapping center rather than a point impurity. On the other hand, an electron polaron can hop between neighboring metal ions, as illustrated in Fig. 28c. The polaron hopping proceeds through the transfer of local polarization, similarly as in the initial electron-trapping process [164]. It requires a certain activation energy (that follows the Arrhenius law), and is characterized with the hopping probability expressed through the first term in eq. 2.2. The electrical conductivity in the semiconducting rutile TiO_2 bulk crystal proceeds exactly through the polaron hopping process [165]: if a voltage is applied to the sides of the bulk crystal, the measured electron current propagates through small polaron hopping. In rutile TiO_2, the activation energy for polarons was estimated as 24 meV [166] or 75–88 meV [167], and even the intrinsically reduced rutile TiO_2 becomes insulating below 15 K when the polaron hopping freezes. The formation of polarons in TiO_2 and other transition metal oxides is enhanced near the surface due to the increased lattice flexibility in the surface and subsurface region [168, 169].

The theoretical modeling of polaronic effects can be performed within the modified DFT framework that includes the electron-electron repulsion described through Hubbard parameter U and electron exchange interaction described through exchange parameter J. This approach is commonly referred to as the DFT+U framework. The Dudarev rotationally invariant approach [170] was used in the research that led to this Thesis, in which the Hamiltonian in eq. 1.4 is supplemented with an additional energy term that depends only on the difference of the Hubbard and exchange parameter $E_{\mathrm{U}}(U') = E_{\mathrm{U}}(U - J)$. The proper choice of $U' = U - J$ is therefore required to describe the polaron energy E_{U}. For bulk rutile TiO_2, it was determined through the use of constrained random phase approximation (RPA) that the optimum values for the effective on-site repulsion parameter is U'=3.9 eV, with U=4 eV and J=0.1 eV [171]. It is noteworthy that the DFT frameworks that do not include this effective on-site repulsion (U'), as the GGA framework for example, are not successful in localizing excess electrons and prefer the delocalized solutions: the GGA calculations commonly converge to an unphysical metallic solution with the excess electrons distributed evenly across all Ti atoms within the lattice. The DFT+U on the other hand, localizes the electrons on regular Ti sites which prevents the unphysical insulator-to-metal transition in TiO_2.

The ground state of the rutile TiO_2(110) surface with oxygen vacancies as the only defects, was extensively investigated in [157, 148, 158], and some results are summarized in Fig. 29. When a TiO_2(110) surface hosts a small or moderate number of oxygen vacancies, up to 0.33 ML, the excess electrons are predominately hosted on subsurface Ti atoms. Most of them are localized in the first subsurface layer, when they are referred to as the S_1 polarons, as reported in Fig. 29a. At these reduction states, a portion of the polarons are located on Ti atoms in the second subsurface layer, when they are referred to as the S_2 polarons. A significant portion of polarons is also located at the Ti_{5c} atoms in the surface layer, the so-called surface polarons S_0, and their proportion increases with the increase in the V_O concentration. These results can be rationalized by the Coulomb repulsion between the polarons: when the number of excess electrons increases, they can no longer all remain localized in the subsurface layer S_1, but also localize with slightly higher energy in the surface S_0 and sub-subsurface S_2 layers to reduce the electrostatic repulsion. At higher reduction states of the TiO_2(110) surface, namely when the V_O concentration exceeds 0.5 ML, the spatial dispersion of polarons in several surface layers is no longer an efficient method in reducing the electrostatic repulsion between them, but the surface instead reconstructs to a (1×2) superstructure to reduce the surface energy [157]. Rutile TiO_2(110) surfaces used in the research that led to this Thesis were always kept at a small to moderate level of reduction, with the concentration of V_Os in the 0.05–0.2 ML range. At these conditions, the ground state is characterized by mostly the subsurface S_1 polarons.

The polaron formation energy E_{pol} at different concentration of excess electrons (2 times the concentration of V_Os) is reported in Fig. 29b. It is calculated as the energy gain (reduction of the total energy) of localizing an excess electron on a Ti atom, compared to a metallic surface with delocalized electrons. Therefore, the calculated E_{pol} is averaged over all polarons present in the slab (S_0, S_1, and S_2 polarons), in order to characterize the proclivity of the rutile TiO_2 towards localizing electrons. At small concentration of V_Os, the polaron formation energy is ≈-350 meV, which is sufficiently advantageous to drive the reduced rutile TiO_2(110) surface to this polaronic ground state. At higher V_O concentrations the E_{pol} saturates at ≈-450 meV, after which the transition to the (1×2) reconstruction is triggered.

Electron polarons in rutile TiO_2 are characterized by a pronounced in-gap state in the density of states

Die approbierte gedruckte Originalversion dieser Dissertation ist an der TU Wien Bibliothek verfügbar.
The approved original version of this doctoral thesis is available in print at TU Wien Bibliothek.
TU Bibliothek Your knowledge hub WIEN

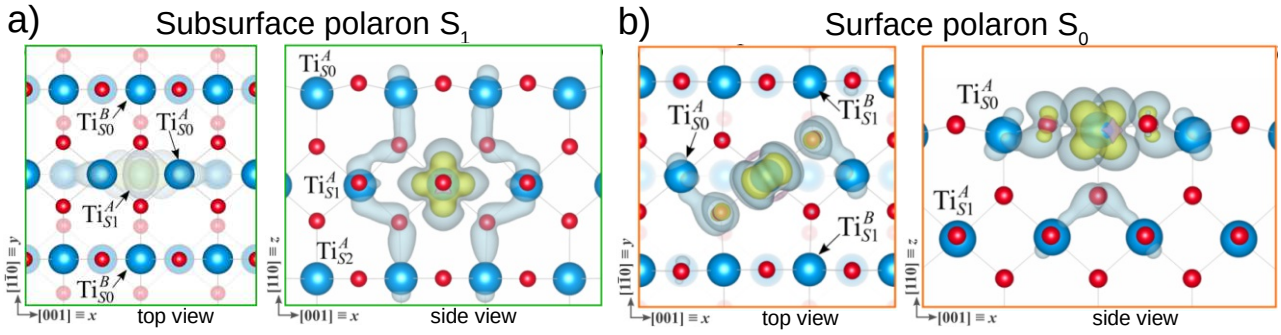

Figure 30: **Calculated shape of the charge distribution of a single polaron in the vicinity of a V_O on rutile TiO_2(110) surface.**
a) Charge distribution of a single surface polaron (S_0) localized on a 3*d* orbital of a single surface Ti_{5c} atom in top and side view.
Reprinted Figure 6(c,d) [148] from [Michele Reticcioli, Martin Setvín, Michael Schmid, Ulrike Diebold, and Cesare Franchini, *Physical Review B*, 98, 045306 (2018)] with permission of Author(s) and APS. Copyright (2018) American Physical Society.
b) Charge distribution of a single subsurface polaron (S_1) localized on a 3*d* orbital of a single subsurface Ti_{6c} atom in top and side view.
Reprinted Figure 6(a,b) [148] from [Michele Reticcioli, Martin Setvín, Michael Schmid, Ulrike Diebold, and Cesare Franchini, *Physical Review B*, 98, 045306 (2018)] with permission of Author(s) and APS. Copyright (2018) American Physical Society.

[172, 173], as reported in Fig. 29c. This in-gap state is formed by filling the unoccupied Ti 3*d* that previously constituted the bottom of the conduction band. In other words, these states are shifted below the Fermi level upon the formation of an electron polaron. An opposite would hold true for a speculated hole polaron in TiO_2: a previously occupied O 2*p* valence state would become unoccupied and would form an in-gap state above the Fermi level (p-type doping). The presence of hole polarons has not been experimentally reported so far, and the theory predicts their de-localization in rutile TiO_2 in contrast to the localized electron polarons, while in the *p*-doped anatase TiO_2 hole polarons are predicted to be localized in contrast to the delocalized electron polarons [174, 175]. According to the result in Fig. 29c, the increase of excess electrons in TiO_2 (increase of the V_O concentration) results in the gradual filling and energetic spread of this in-gap state, but the resulting DOS still shows that the insulator-to-metal transition is avoided by localization of polarons; same holds true for even higher V_O concentrations than the ones shown in Fig. 29c.

The spatial distribution of the most commonly present S_1 and S_0 polarons in the ground state of the rutile TiO_2(110) surface is shown in Fig. 30. The calculated polaron shapes Fig. 30 display the charge state of a single electron. Each of these electrons is accompanied by a distortion in the position to the polaron-hosting Ti atom and the surrounding polarized solid, but these distortions are almost negligibly small compared to the span of the electronic cloud to be easily visualized in Fig. 30; x, y, and z directions are defined as the [001], $1\bar{1}0$, and [110], respectively. Both S_1 and S_0 (and S_2 as well) polaron types occupy the Ti 3*d* states, which are split into five levels due to the octahedral crystal field splitting. The polarons therefore have the *d*-like geometries, but they are not localized on a single electronic orbital and occupy a superposition of several *d*-orbitals instead. Subsurface S_1 polarons were calculated to have $0.57\,e^-$ and $0.14\,e^-$ on the d_{z^2} and $d_{x^2-y^2}$ orbitals, respectively, while the surface S_0 polaron was calculated to have $0.22\,e^-$ and $0.48\,e^-$ on the d_{xz} and d_{yz} orbitals, respectively [148]. The remaining $0.28\,e^-$ and $0.3\,e^-$ for the S_1 and S_0 polarons, respectively, are nonlocal and spread over the neighboring atoms, as visible in Fig. 30.

The modeled characteristics of electron polarons on the TiO_2(110) surface (Figs. 29 and 30) were confirmed experimentally in [157], as shown in Fig. 31. There, the surface was investigated with STM and AFM, at liquid nitrogen temperature of $T = 77.8\,K$ where polaron hopping is still active and the rutile TiO_2(110) surface can conduct current under the applied bias voltage. Figure. 31a shows constant-height STM (left and right panel) and AFM (center panel) images of the clean surface area of a reduced rutile TiO_2(110) surface with (locally) 16.7% of V_Os. The AFM image was obtained with an O-terminated tip, which experiences electrostatic and

Die approbierte gedruckte Originalversion dieser Dissertation ist an der TU Wien Bibliothek verfügbar.
The approved original version of this doctoral thesis is available in print at TU Wien Bibliothek.
TU Bibliothek Your knowledge hub WIEN

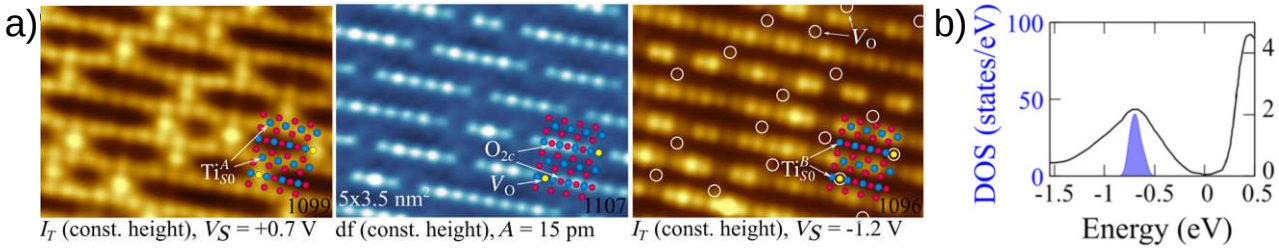

Figure 31: **Experimental observation of polarons on a clean TiO_2(110)-(1×1) surface with oxygen vacancies.**
a) Constant-height empty-state STM, AFM, and filled-state STM images (left to right) of the same surface area.
Reprinted Figure 1(g,f,h) [157] with permission from [Michele Reticcioli, Martin Setvín, Xianfeng Hao, Peter Flauger, Georg Kresse, Michael Schmid, Ulrike Diebold, and Cesare Franchini, *Physical Review X*, 7, 031053 (2017)]. under the Creative Commons Attribution 4.0 International license.
b) Measured (black curve) and calculated (blue curve) DOS of the electronic state within the TiO_2(110)-(1×1) band gap. Fermi level is located at 0 eV, and the in-gap feature associated with polarons is located at ≈-0.7 eV.
Reprinted Figure 1(d) [157] with permission from [Michele Reticcioli, Martin Setvín, Xianfeng Hao, Peter Flauger, Georg Kresse, Michael Schmid, Ulrike Diebold, and Cesare Franchini, *Physical Review X*, 7, 031053 (2017)]. under the Creative Commons Attribution 4.0 International license.

Pauli repulsion with the geometrically protruding O_{br} atoms pm the surface, and only the long-range van der Waals attraction. The constant-height AFM image was also obtained at close distance to the surface, which is why the individual O atoms are well-resolved as single white spheres. The V_Os are recorded as missing O atoms, while the terminal Ti_{5c} atoms are contributing to the overall detected force only through weak long-range forces due to their geometrically lower-lying position with comparison to the O_{br} rows. Upon careful inspection, it is noticeable that the O_{br} atoms in the vicinity of a V_O display a certain modulation in intensity. Since all O_{br} atoms on the surface are chemically identical, the AFM contrast is sensitive to the geometric protrusion of individual atoms. This implies that O_{br} atoms in the vicinity of a V_O display a modulation in the height: The next-nearest-neighboring O_{br} atoms to the V_O are most geometrically protruding (the brightest in AFM) compared to other O_{br} atoms. This result is in accordance with the DFT+U calculations of the the ground state of this surface, which predicts a lattice distortion around the V_O that is related to a nearby polarization field responsible for electron trapping. This type of geometric surface relaxation is seen in more details in Figs. 41 and 42 below.

The constant-height STM images in Fig. 31a focus on the electronic properties of the clean, reduced surface. The well-resolved rows of individual atoms in empty-states STM (left panel of Fig. 31a) correspond to terminal Ti_{5c} atoms due to the overlap of unoccupied Ti 3d states with the wavefunctions of the tip, while the individual bright spots correspond to V_Os. This is a typical empty-states STM contrast already discussed in Fig. 27a. On the other hand, the filled-states STM (right panel of Fig. 31a) reveals additional insights into the surface properties. The -1.2 V applied bias voltage to the sample is insufficient for reaching the O 2p-derived valence band of the reduced rutile TiO_2(110), which is why the O_{br} are still imaged as dark in STM (no current). Since filled states of O are located closer to the valence edge than the occupied states of Ti, one would expect that there is a complete absence of the tunneling current at negative bias values this low. However, empty-states STM clearly shows bright rows of atoms that geometrically correspond to the rows of Ti_{5c} atoms. This tunneling towards the STM tip at this bias value of -1.2 eV is possible because the tunneling is performed from the the polaronic in-gap state, that lies ≈0.7 eV below the Fermi level. This image therefore clearly shows the spatial distribution of polarons at the surface. This result is in excellent accord with calculated properties of S_1 polarons at the surface, which are predicted to be the predominant polaron type at this level of reduction. The S_1 polaron, depicted in Fig. 30a, extends from the polaron-hosting Ti_{6c} atoms towards terminal Ti_{5c} atoms through the nonlocal electronic cloud. The brightest signal in filled-states STM occurs above the two next-nearest-neighboring Ti_{5c} atoms with respect to the V_O. Since the excess electrons repel each other, the calculated distribution of S_1 polarons associated with a single V_O predicts that the energetically most favorable polaron formation sites are the two Ti_{6c} atoms in the two neighboring rows of Ti_{6c}, which are separated by the O_{br} row with an V_O. The polaronic in-gap state can also be quantified using STS, as reported in Fig. 31b. The

Die approbierte gedruckte Originalversion dieser Dissertation ist an der TU Wien Bibliothek verfügbar.
The approved original version of this doctoral thesis is available in print at TU Wien Bibliothek.
TU Bibliothek Your knowledge hub WIEN

calculated DOS was shifted upwards by ≈0.25 eV to coincide with the experimentally measured position of the in-gap peak in STS, since DFT+U calculations generally lack the precision of the band gap size and therefore the relative energy positions of all in-gap features as well. Beside the justified energy discrepancy, the measured STS and calculated DOS are in excellent accord, which provides additional experimental confirmation of the polaronic nature of excess electrons in reduced rutile TiO_2(110).

Since the clean, reduced TiO_2(110) surface had been well-characterized, the influence of the external stimuli on the ground state of this surface can be precisely examined. The following sections focus on the influence of adsorbates on the polarons at TiO_2(110).

Die approbierte gedruckte Originalversion dieser Dissertation ist an der TU Wien Bibliothek verfügbar.
The approved original version of this doctoral thesis is available in print at TU Wien Bibliothek.
TU WIEN Bibliothek Your knowledge hub

2.4 Adsorption of CO on clean, reduced rutile $TiO_2(110)$

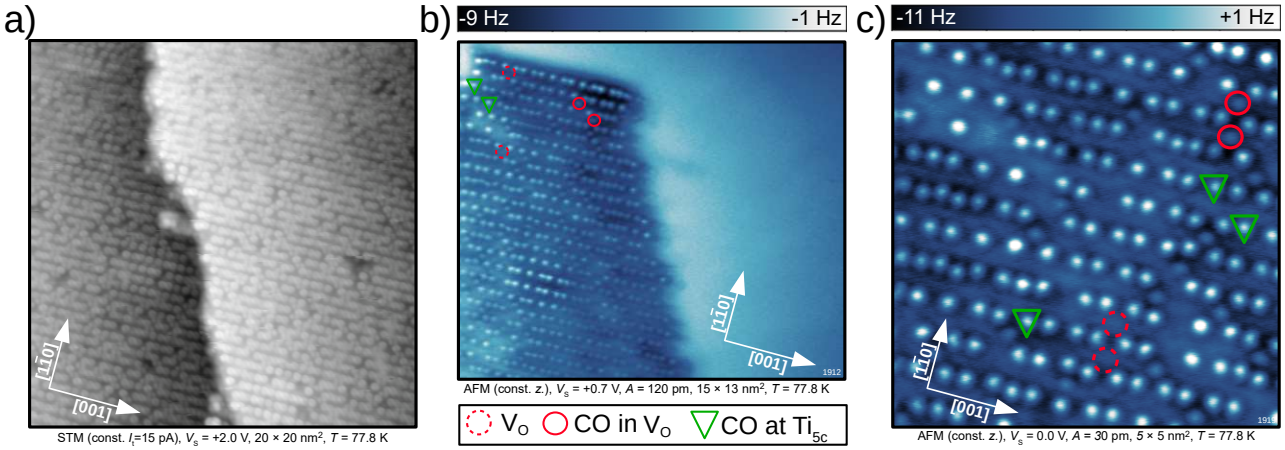

Figure 32: **Adsorption of 1 L of CO on the reduced rutile $TiO_2(110)$ surface at 100 K.** a) Constant-current STM image of the CO-covered surface. Each observable spherical protrusion corresponds to one CO molecule. b) Large-area constant-height AFM image of the CO-covered surface. The majority of the CO molecules are adsorbed on the Ti_{5c} rows (triangles), and some in the oxygen vacancies (full circles). The AFM image also captures a terrace step downwards, where only the CO molecules adsorbed on the upper terrace are resolved. c) Small-area constant-height AFM image of the CO-covered surface. Individual CO molecules are clearly imaged with a CO-terminated tip. Empty oxygen vacancies are not visible due to the protruding CO atoms on the Ti_{5c} rows, but their presence can be inferred as described in the text.

The adsorption of CO molecules on rutile $TiO_2(110)$ surface is interesting from several points of view: investigating the adsorption sites on the model photocatalyst rutile $TiO_2(110)$ surface [176], investigating the efficiency of relevant catalytic reactions such as CO oxidation [143], or probing the surface electronic structure [178]. For example, nanoscopic clusters on the reduced $TiO_2(110)$ surface were shown to be an efficient catalyst for the oxidation of the poisonous CO into CO_2 [179, 180]. The increased interest in this topic has produced a significant body of literature, which surprisingly did not reach a common consensus on even the CO adsorption sites. In the study presented in this Section, this issue is approached experimentally by studying the CO adsorption using nc-AFM at cryogenic temperatures, and theoretically by performing DFT+U calculations, which explicitly take into account the polaronic ground state of the surface. This Section is based on a recent publication titled "Interplay between Adsorbates and Polarons: CO on rutile $TiO_2(110)$" [181].

Figure 32 shows STM and AFM images of a clean, reduced rutile $TiO_2(110)$ surface with ≈9% of V_Os exposed to 1 L of CO at the sample temperature of 100 K. At T =100 K CO molecules have a high sticking coefficient on this surface, roughly equal to 1, and exposure to 1 L of CO will result in a surface almost completely covered by CO molecules. This can be seen in the empty-states STM image in Fig. 32a. Bright, isolated spheres correspond to individual CO molecules, which adsorb in neighboring sites that run along the [001] direction. The STM image also shows a sporadic presence of bright, isolated spheres in between the bright rows, and the concentration of these features roughly correspond to the concentration of V_Os prior to CO exposure. Therefore, it is safe to assume that the rows of CO molecules along the [001] direction are adsorbed to the underlying Ti_{5c} atoms, and that the isolated features between these rows are the CO molecules adsorbed inside the V_Os.

Additional insight into the CO adsorption configurations is revealed by the constant-height AFM images in Figs. 32b and 32c. In both images, CO atoms on the surface act repulsively towards the tip. The AFM tip termination is a single CO molecule that was relatively easily transfered from the CO-covered surface to the Cu-terminated tip during the previous STM scan. It is noticeable that the STM image in Fig. 32a is a bit "fuzzy", due to the tip-induced manipulation of the adsorbates on the surface, making it very likely that a CO molecule can jump towards the metallic tip to functionalize the tip with a single CO molecule. This eases the identification of the configuration of the CO adsorbate on the surface: as expected, the carbon atom is bound towards the surface atoms, and the O atom is sticking out of the surface. The same CO adsorption is assumed on a metallic tip, and the observed contrast is due to the O-O atom repulsion between the tip and the adsorbate.

Die approbierte gedruckte Originalversion dieser Dissertation ist an der TU Wien Bibliothek verfügbar.
The approved original version of this doctoral thesis is available in print at TU Wien Bibliothek.
TU Bibliothek Your knowledge hub WIEN

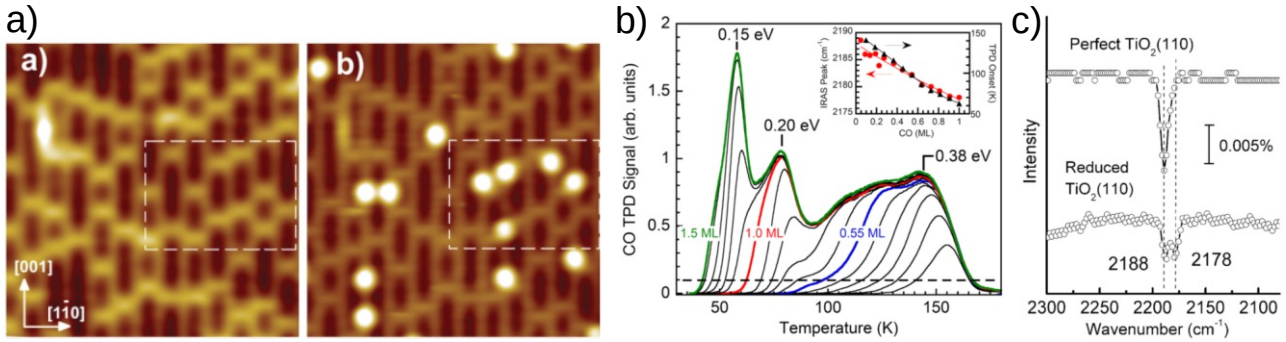

Figure 33: **Experimental research results in literature on CO adsorption on reduced rutile TiO_2(110) surfaces.**
a) STM images ($8\times8\,nm^2$) of the same region before (left panel) and after (right panel) the adsorption of 0.1 L of CO dosed at 80 K.
Reprinted Figure 1(a,b) [176] with permission from [Yan Zhao, Zhuo Wang, Xuefeng Cui, Tian Huang, Bing Wang, Yi Luo, Jinlong Yang, and Jianguo Hou, *Journal of the American Chemical Society*, 131, 7958 (2009)]. Copyright (2009) American Chemical Society.
b) Temperature-programmed desorption (TPD) spectrum of various CO coverages dosed at 35 K, showing two separate first-order desorption peaks.
Reprinted Figure 2 [177] with permission from [Nikolay G. Petrik and Greg A. Kimmel, *The Journal of Physical Chemistry Letters*, 3, 3425 (2012)]. Copyright (2012) American Chemical Society.
c) Reflection-absorption IR spectroscopy (RAIRS) spectrum of 1 L of CO adsorbed at 110 K, showing two distinct stretching frequencies of the CO adsorbed to a reduced TiO_2(110) surface in contrast to the stoichiometric surface.
Reprinted Figure 1 and Figure 1 [178] with permission from [Mingchun Xu, Heshmat Noei, Karin Fink, Martin Muhler, Yuemin Wang, and Christof Wöll, *Angewandte Chemie International Edition*, 51, 4731 (2012)]. Copyright (2012) John Wiley and Sons.

Since there is no chemical attraction between the two CO molecules oriented towards each other by their O atoms, the clear, repulsive AFM imaging of the CO adsorption needs not be taken at very close distances to the surface.

The AFM images in Fig. 32 also show that individual CO molecules are adsorbed on the rows running along the [001] direction, with the sporadic presence of CO molecules between these rows. The contrast observed in constant-height AFM is sensitive to the geometric alignment of the adsorbates, as illustrated in Fig. 32b: the CO molecules on a terrace are excellently resolved, while there is no signal from the CO molecules adsorbed on the terrace below. Naturally, AFM is very sensitive to much smaller height differences, as can be seen within one terrace on Fig. 32b and Fig. 32c, which allows for clear identification of distinct adsorption sites, in accord with the previous assumption. The CO molecules along [001] rows are adsorbed to Ti_{5c} atoms underneath (marked with a green triangle), while the sporadic CO molecules in between these rows are adsorbed within V_Os (marked with a full red circle), with their C atom oriented towards the surface and their O atom protruding from the surface. These adsorption configurations result in a surface at which CO molecules adsorbed at different sites have roughly equal geometric protrusion from the surface. Indeed, all CO atoms in AFM images are imaged with comparable values of the frequency shift.

The CO adsorption configurations can be clearly resolved in Fig. 32c, with relevant sites marked by symbols described in the legend in Fig. 32b. Most CO molecules adsorb to the Ti_{5c} rows at this high coverage, while some V_Os are filled by a CO molecule. It is evident that the CO molecules within V_Os are less protruding than the CO molecules on the Ti_{5c} rows due to the slightly lower repulsion forces measured above them. Despite the high coverage of CO molecules, not all V_Os are filled by a molecule, and some empty V_Os are marked by a dashed red circle. The CO molecules adsorbed on the Ti_{5c} rows are geometrically protruding higher than the O_{br} rows by at least 2 Å, making the O_{br} rows undetectable in constant-height AFM. The presence of empty V_Os must therefore be indirectly inferred. It can be observed in Fig. 32c that when a CO molecule fills a V_O (full red circle), the neighboring Ti_{5c} sites tend to remain unoccupied. Instead, CO molecules commonly adsorb to each

Die approbierte gedruckte Originalversion dieser Dissertation ist an der TU Wien Bibliothek verfügbar.
The approved original version of this doctoral thesis is available in print at TU Wien Bibliothek.
TU Bibliothek Your knowledge hub WIEN

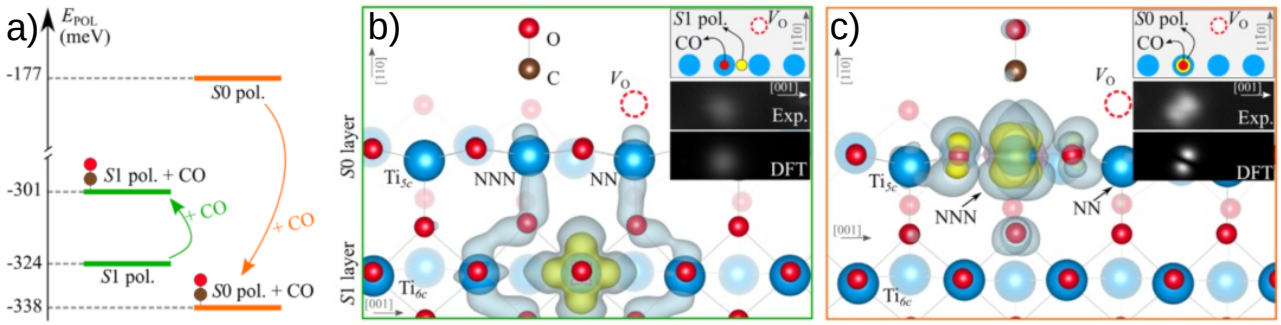

Figure 34: **DFT-predicted interaction of CO molecules and polarons on a reduced TiO_2(110) surface.** a) Calculated polaron formation energy in the absence and the presence of an adsorbed CO at a Ti_{5c} site. b) Calculated spatial charge density of the intrinsic S_0 polaron after adsorption of a CO at a Ti_{5c} site. c) Calculated spatial charge density of the intrinsic S_1 polaron after adsorption of a CO at a Ti_{5c} site. Calculations in (a)–(c) performed by Michele Reticcioli and Cesare Franchini.

next-neighboring Ti_{5c} site with respect to the filled V_O. This phenomenon indicates that the CO adsorption at the nearest-neighboring Ti_{5c} site to the CO-filled V_O is energetically unfavorable when compared to the next-neighboring Ti_{5c} site to the CO-filled V_O. Extending this observation to the CO adsorption preference with respect to an empty V_O enables the determination of an empty V_O's position from the CO adsorption in its vicinity. The position of empty V_Os marked in Fig. 32c (dashed red circles) was inferred from the presence of a CO molecule at each next-nearest-neighboring, and an absence of CO molecules at each nearest-neighboring Ti_{5c} sites. This assignment is further confirmed by literature and theoretical calculations presented below.

Figure. 33 shows some relevant results from the research of CO adsorption to this surface in literature. Empty-states STM images in Fig. 33a reveal the favorable CO adsorption sites at small CO coverages, directly observed by comparing the same surface region before and after CO dosage. The majority of CO molecules are adsorbed at the next-nearest-neighboring Ti_{5c} sites with respect to the empty V_Os [176], confirming the inference of the empty V_O positions in Fig. 32c. Additionally, the results reveal that this adsorption preference is preserved even in the vicinity of CO-filled V_Os. Some CO molecules in Fig. 33a are still adsorbed at unrelated Ti_{5c} sites, but this deviation can be rationalized by the possible presence of Ar species in the subsurface region (implemented within the TiO_2(110) during UHV sputter/anneal cleaning cycles) that alter these adsorption sites. The results from integral surface science techniques found in literature can be seen in Figs. 33b and 33c. Temperature-programmed desorption (TPD) results in Fig. 33b show that there are two distinct CO adsorption configurations on a reduced rutile TiO_2(110) at sub-monolayer coverages, and that their adsorption energies differ by ≈200 meV [177]. Similarly, the reflection-absorption IR spectroscopy (RAIRS) results in Fig. 33b show that there are two distinct CO adsorption configurations on a reduced rutile TiO_2(110) surface (compared to only one adsorption site on the stoichiometric surface) that differ by their internal molecular stretching frequencies. Both of these integral results are in accord with the findings in Fig. 32 that the CO can adsorb at both, the Ti_{5c} sites and in the V_Os. The experiments and theory below shows that the distinction between these two sites is not straightforward however, and that an additional adsorption configuration exists.

From a theoretical perspective, the adsorption of a CO molecule to a polaronic ground state of a reduced rutile TiO_2(110) is a good way to test the interaction of polarons with a simple adsorbate. The DFT+U calculations (U_{eff}=3.9 eV) predict that the dipole moment of the CO molecule, adsorbed with the formally positive C atom towards the surface, influences the polaron distribution, as shown in Fig. 34. In fact, the presence of a CO molecule alters the ground state of a TiO_2(110) surface slab with V_O(s), by promoting subsurface polarons towards the surface to form a complex of a surface polaron S_0 and the adsorbed CO molecule CO+S_0, as shown by the calculated polaron energy in the absence/presence of CO adsorbates in Fig. 34a. While S_0 polarons were calculated to be unfavorable at low reduction rates of the surface (Fig. 29b), their coupling to the adsorbed CO decreases their polaronic energy. On the other hand, the polaronic energy of S_1 polarons increases upon formation of a S_1+CO complex. Both polaron+CO complexes are illustrated through the charge distribution plots in Figs. 34b and 34c. The S_1 polaron is calculated to retain the same characteristic spatial distribution as in the absence of CO with a d_{z^2} and $d_{x^2-y^2}$-like orbital character at the hosting Ti_{6c} site, and $\approx \frac{1}{3}$ of the charge distributed on the surrounding atoms. Only very little (0.1%) polaronic charge is transferred to the adsorbed

Die approbierte gedruckte Originalversion dieser Dissertation ist an der TU Wien Bibliothek verfügbar.
The approved original version of this doctoral thesis is available in print at TU Wien Bibliothek.
TU Bibliothek Your knowledge hub WIEN

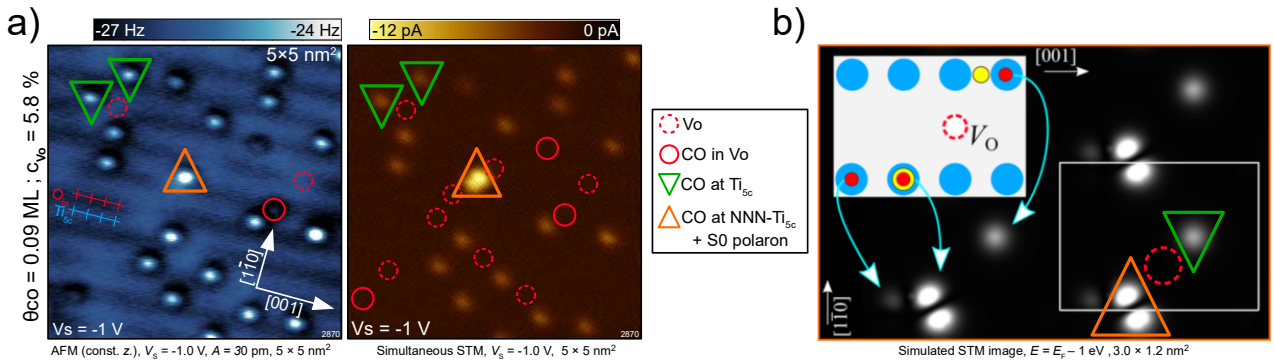

Figure 35: **Low coverage of CO molecules adsorbed to a rutile TiO_2(110) surface with a low coverage of V_Os.** a) Constant-height AFM (left panel) and simultaneous STM (right panel) images of the 0.09 ML of CO adsorbed at a surface with 0.06 ML of V_Os. Four distinct sites are marked in the images, described in the legend. b) Simulated constant-height STM image (1 eV below the Fermi level) of a small coverage of CO molecules adsorbed to a surface with a low reduction state. The distinct sites are marked in the same way as in (a). STM simulations performed by Michele Reticcioli and Cesare Franchini.

CO molecule. On the other hand, a polaron in the S_0 layer strongly interacts with the CO molecule. The S_0 polaron acquires a stronger d_{yz} (54%) character as compared to the case with no adsorbates (43%), and a non-negligible portion of the polaronic charge (1%) is transferred to the $2\pi^*$ antibonding orbital [182] of the adsorbed CO molecule.

The predicted interaction of polarons with the adsorbed CO molecules can be observed experimentally, as shown in constant-height AFM image in Fig. 35a. In these experiments, a low dose of CO molecules was dosed to a rutile TiO_2(110) surface with a low reduction state, similar to the one used in calculations in Fig. 34a. The adsorption of CO in experiment shown in Fig. 35a was performed at 100 K, while the imaging was performed at 10.8 K, where the rutile TiO_2(110) surface is still conducting. The tip-sample distance, the oscillation amplitude, and the strength of the electrostatic forces (bias) were chosen such that the constant-height AFM image in Fig. 35a shows both the CO-populated and empty V_Os, together with other CO molecules adsorbed to Ti_{5c} rows. At this reduction level and CO coverage, the CO molecules avoid adsorption at nearest-neighboring Ti_{5c} (NN-Ti_{5c}) sites to the V_O. However, it can be observed that not all CO molecules are adsorbed in the preferable next-nearest-neighboring Ti_{5c} (NNN-Ti_{5c}) sites. In fact, most are adsorbed to Ti_{5c} sites uncorrelated to the position of a V_O. This discrepancy with the literature result shown in Fig. 33a can be rationalized by the lower surface reduction state in Fig. 35a – dosing CO to a surface with a higher reduction rate yields the reported adsorption preference (Fig. 36b). Alternatively, it could be rationalized by the fact that the surface region shown in Fig. 35a was not subjected to scanning in empty-states STM beforehand, which could be responsible for driving the CO to its lowest-energy adsorption site: empty-states STM used in imaging in Fig. 33a can lead to lateral diffusion of CO, as demonstrated by the "fuzzy" imaging in Fig. 32a.

The simultaneous constant-height filled-states STM imaging in Fig. 35a reveals the coupling between polarons and CO molecules. The sample bias value was selected such that the top of the valence band is not reached, and only the in-gap states are imaged. Since most CO molecules are adsorbed to a Ti_{5c} site unrelated to the V_O (green triangles), they are seen as a weak singular spots in STM. One CO molecule, adsorbed at the NNN-Ti_{5c} site with respect to a V_O, is coupled to a S_0 polaron. It is imaged as a double-lobed feature, even though the simultaneous AFM clearly shows the presence of a single CO molecule at this position. The double-lobed feature is in fact the antibonding $2\pi^*$ orbital of the adsorbed CO molecule, that is populated by the polaronic charge and is therefore visible in filled-states STM imaging. This identification of a single, weakly-populated molecular orbital of the adsorbed CO molecules in filled-states STM is confirmed by the simulated STM contrast (using Tersoff-Hamann approach) shown in Fig. 35c. Here, two CO molecules were adsorbed in a single a unit cell of the rutile TiO_2(110) surface and forced to interact with one S_0 and one S_1 polaron, marked in the same way as in the AFM/STM images.

The calculated CO adsorption energy at different sites is shown in Fig. 36a for two reduction states of the surface. Qualitatively, the CO adsorption to both reduction states is predicted to be the same. The adsorption within the V_O and at the NNN-Ti_{5c} sites are calculated to be energetically most favorable. When the CO

Die approbierte gedruckte Originalversion dieser Dissertation ist an der TU Wien Bibliothek verfügbar.
The approved original version of this doctoral thesis is available in print at TU Wien Bibliothek.
TU Bibliothek Your knowledge hub WIEN

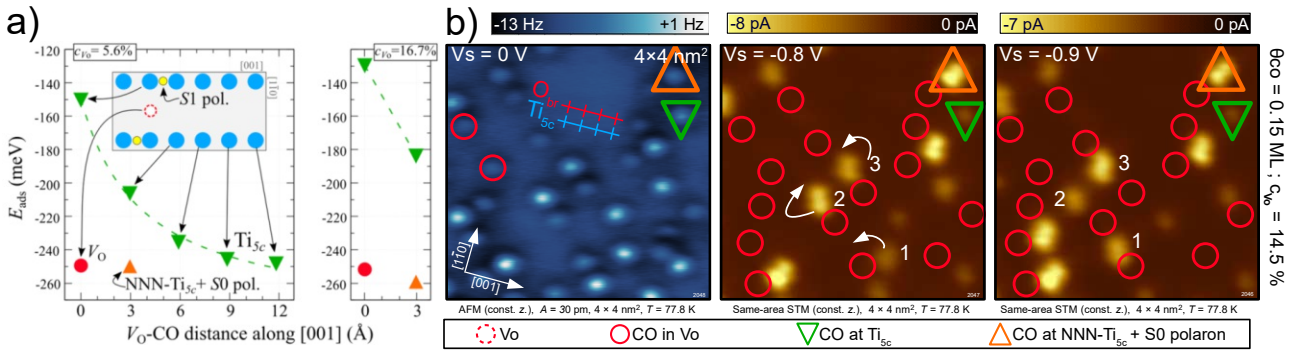

Figure 36: **Low coverage of CO molecules adsorbed to a rutile TiO_2(110) surface with a high coverage of V_Os.** a) Calculated site-dependent CO adsorption energy with respect to the distance from the V_O site at a surface with a low- (left panel) and high-reduction (right panel) state. Calculations performed by Michele Reticcioli and Cesare Franchini. b) Constant-height AFM (left panel) and same-area STM (middle and right panel) images of 0.15 ML of CO adsorbed at a surface with 0.15 ML of V_Os. Four distinct sites are marked in the images, described in the legend.

molecules at NNN-Ti_{5c} sites are coupled to S_0 polarons, their adsorption energy is almost degenerate with the adsorption energy within V_Os. The calculated adsorption energy with respect to the position of a V_O also shows that the adsorption at NN-Ti_{5c} is highly unfavorable, while the adsorption energy decreases with the increase of the distance from the V_O. At large distances from a V_O, the adsorption to a Ti_{5c} row becomes almost as favorable as the adsorption at the lowest-energy sites, explaining the common adsorption at Ti_{5c} sites unrelated to the V_Os on the surface with a low reduction state in Fig. 35a. However, the availability of these sites drastically decreases with the increase in the reduction state, due to the uniform distribution of V_Os across the surface, and adsorption at V_O and NNN-Ti5c+S_0 stands out as favorable.

The adsorption of the same, low dose of CO molecules as in Fig. 35a to a surface with 15% of V_Os is shown in Fig. 36b. The AFM imaging conditions in the left panel of Fig. 36b did not allow detection of empty V_Os, and the low CO coverage prevents the inference of their position as in Figs. 32b and 32c. The distinction between the CO molecules adsorbed at Ti_{5c} rows and O_{br} rows (within a V_O) was performed through the aid of constant-height STM imaging (middle and right panel of Fig. 36b): molecules adsorbed within V_Os do not have a signature in-gap state, while those adsorbed to Ti_{5c} rows have a characteristic signature after interaction with either S_0 or S_1 polarons. The experiment confirms that CO molecules adsorbed at the stronger-reduced TiO_2(110) surface preferentially adsorb in either V_Os or NNN-Ti_{5c} sites. Moreover, filled-states STM reveals that all CO molecules at NNN-Ti_{5c} sites have partially-filled $2\pi^*$ orbitals due to their coupling with a S_0 polaron. The theory predicts only a single (and symmetry equivalent) orientation of the CO+S_0 polaron complex that is determined by the polaron geometry. However, the $2\pi^*$ orbitals seem to be freely oriented across the surface in Fig. 36b, possibly due to the polaron-polaron repulsion on a highly-reduced surface, which leads to the energy minimization of neighboring polarons by reorientation.

Comparing two successive constant-height STM images in Fig. 36b reveals that the CO molecules are mobile at the surface during scanning at 78 K. This mobility is most probably due to the application of -0.8 V sample bias, which leads to lateral manipulation of the surface species. These STM images were procured with a maximum tunneling current of < 8 pA, which is much smaller than values typically used in literature, illustrating once more the advantages of AFM imaging without bias. The scanning-induced lateral CO motion in Fig. 36b shows that the motion of CO molecules is not followed by the motion of the underlying polarons. The CO molecule marked as "1", that was previously coupled to a S_1 polaron, moved towards the NNN-Ti_{5c} adsorption site, where it became coupled to a S_0 polaron. On the contrary, the CO molecule marked as "2" decoupled from a S_0 polaron and transfered to a neighboring site with weak coupling with the S_1 polaron. The CO molecules marked as "3" transfered between two NNN-Ti_{5c} sites (related to different V_Os) and coupled to a different S_0 polaron. These experiments illustrate the importance of accounting for polarons as the intrinsic properties of the rutile TiO_2(110) surface, as they are not destroyed by weak physisorption of CO molecules.

After dosing a full monolayer of CO, a highly reduced rutile TiO_2(110) surface was imaged with constant-height AFM and simultaneous STM in Fig. 37a. The CO molecules follow the adsorption rules deduced so far, although some molecules seem to be adsorbed in the NN-Ti_{5c} sites. This could be the consequence of the applied

Die approbierte gedruckte Originalversion dieser Dissertation ist an der TU Wien Bibliothek verfügbar.
The approved original version of this doctoral thesis is available in print at TU Wien Bibliothek.
TU Bibliothek Your knowledge hub WIEN

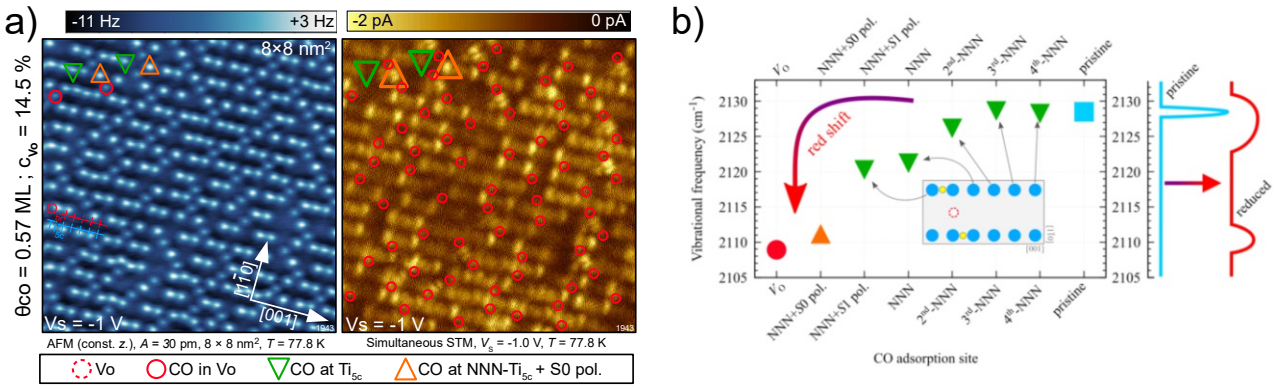

Figure 37: **High coverage of CO molecules adsorbed to a rutile $TiO_2(110)$ surface with a high coverage of V_Os.** a) Constant-height AFM (left panel) and simultaneous STM (right panel) images of 0.57 ML of CO adsorbed at a surface with 0.15 ML of V_Os. Four distinct sites are marked in the images, described in the legend. b) Calculated vibrational frequencies of CO molecules adsorbed at a pristine and a reduced surface. Calculations performed by Michele Reticcioli and Cesare Franchini.

bias voltage during scanning, as already demonstrated in Fig. 36b. CO molecules adsorbed at Ti_{5c} sites where no polarons are available usually display a very weak signal in STM that can be attributed to non-local tails of the surrounding polaronic charge. Interestingly, the CO molecules adsorbed between two V_Os have a particularly strong STM signal with a pronounced orientation along the line connecting the two V_Os, possibly due to the electrostatic attraction between the formally positive V_Os and the electronegative lobes of the partially filled $2\pi^*$ molecular orbital of the CO molecule coupled with a S_0 polaron. The high CO coverage is usually necessary for performing integral measurements in literature, as in Fig. 33c. The DFT+U calculations on the polaron+CO complexes also show two distinct stretching frequencies. Both, the CO molecule + S_0 polaron at the NNN-Ti_{5c} site and the CO molecule in the V_O, are calculated to have similar vibrational frequencies, significantly smaller that the CO molecules bound to an unrelated Ti_{5c} site with only the weak coupling to the S_1 polaron. The observed splitting in the vibrational frequencies of the adsorbed CO to the reduced rutile $TiO_2(110)$ surface is therefore due to the different adsorption sites, and due to the CO interaction with the S_0 polarons.

In conclusion, this study has explicitly shown that the interaction of polarons with adsorbates needs to be taken into account when investigating the adsorption (especially the physisorption) of gases on the reduced surface of transition metal oxides that are promising polaronic materials. It is noteworthy that the polarons created by electrons donated from Ti_{int}s were calculated to interact with the adsorbed COs in a completely equivalent manner. This is unsurprising since the Ti_{int}s are predicted to be efficient electron donors even at high lateral distance [183, 184], and therefore do not alter the adsorption process except for the promotion of polaron formation.

Die approbierte gedruckte Originalversion dieser Dissertation ist an der TU Wien Bibliothek verfügbar.
The approved original version of this doctoral thesis is available in print at TU Wien Bibliothek.
TU Bibliothek Your knowledge hub WIEN

2.5 Adsorption of O_2 on clean, reduced rutile $TiO_2(110)$

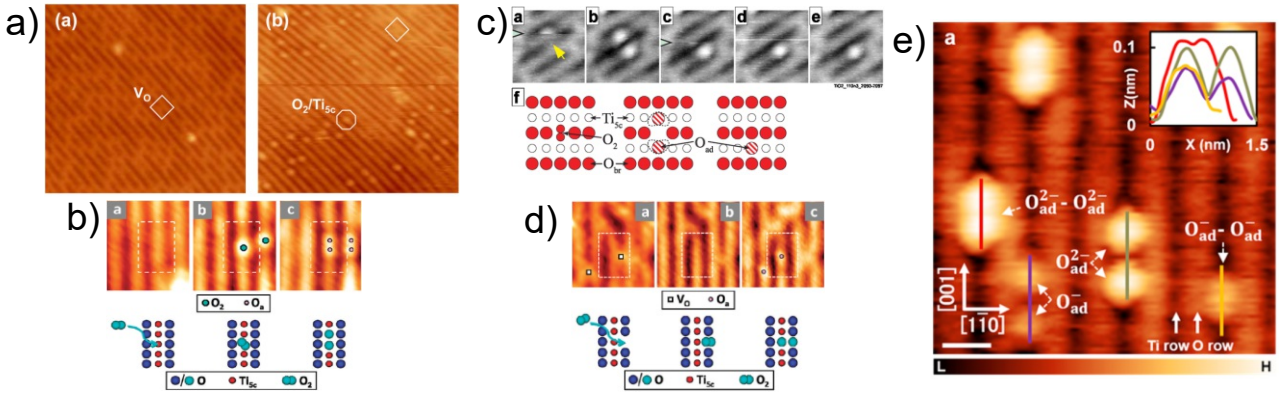

Figure 38: **Literature overview on O_2 adsorption on reduced rutile $TiO_2(110)$ surfaces.**
a) Empty-states STM images (V_S=+0.8 V, I_t=5 pA) of the same region before (left panel) and after (right panel) dosing ≈0.11 ML of O_2 at 100 K. The reduction of the number of empty V_Os and the appearance of circular species on Ti_{5c} rows is noticeable.
Reprinted Figure 7(a,b) [185] with permission from [Michael A. Henderson, Mingmin Shen, Zhi-Tao Wang, and Igor Lyubinetsky, *The Journal of Physical Chemistry C*, 117, 5774 (2013)]. Copyright (2013) American Chemical Society.
b) Empty-states STM images (V_S=+0.6 V, I_t=1 pA) during O_2 dosing at 50 K. Two circular features appear (middle panel) which further split during STM scanning into two features each (right panel).
Reprinted Figure 3 [186] with permission from [Zhi-Tao Wang, Yingge Du, Zdenek Dohnálek, and Igor Lyubinetsky, *The Journal of Physical Chemistry Letters*, 1, 3524 (2010)]. Copyright (2010) American Chemical Society.
c) Empty-states STM images (V_S=+1.8 V, I_t=3 pA) of a clean, reduced surface with 0.045 L of O_2 dosed at 100 K. Images focus on the elusive feature adsorbed within a single V_O, that is noticeably unstable during STM scanning. The bottom row is an illustration of the STM-induced dissociation/association of the O_2 molecule within a V_O.
Reprinted Figure 2 [187] from [Philipp Scheiber, Alexander Riss, Michael Schmid, Peter Varga, and Ulrike Diebold, *Physical Review Letters*, 105, 216101 (2010)] with permission of Author(s) and APS. Copyright (2010) American Physical Society.
d) Empty-states STM images (V_S=+0.8 V, I_t=3 pA) during O_2 dosing at 50 K. An empty V_O (left panel) is filled by an adsorbate (middle panel) which dissociates into two circular features (right panel) after STM scanning.
Reprinted Figure 2 [186] with permission from [Zhi-Tao Wang, Yingge Du, Zdenek Dohnálek, and Igor Lyubinetsky, *The Journal of Physical Chemistry Letters*, 1, 3524 (2010)]. Copyright (2010) American Chemical Society.
e) Noncontact AFM image (V_S=0.0 V) of a clean, stoichiometric surface after O_2 dosing at 300 K. This is the first AFM image of this adsorption problem, and, unlike STM, it shows many different species with distinct contrasts.
Reprinted Figure 1(a) [188] with permission from [Yuuki Adachi, Huan Fei Wen, Quanzhen Zhang, Masato Miyazaki, Yasuhiro Sugawara, Hongqian Sang, Jan Brndiar, Lev Kantorovich, Ivan Štich, and Yan Jun Li, *ACS Nano*, 13, 6917 (2019)]. Copyright (2019) American Chemical Society.

The interaction of O_2 with metal oxide surfaces plays a key role in many applications including gas sensing [189], heterogeneous catalysis [190], water purification [142], the oxygen evolution [191] and oxygen reduction reactions [192], or memristive switching [193]. Adsorption of molecular oxygen on rutile $TiO_2(110)$, a prototypical metal oxide surface, attracted a lot of attention over the past decades [194, 195, 196, 197, 198, 199, 200, 201]. Despite extensive work on this fundamental problem, even basic O_2 adsorption configurations remained unclear, which has lead to puzzling observations regarding the thermal and photochemistry of this important molecule. This Section is based on a recent publication titled "Resolving the adsorption of molecular O_2 on the rutile $TiO_2(110)$ surface by noncontact atomic force microscopy" [202].

Die approbierte gedruckte Originalversion dieser Dissertation ist an der TU Wien Bibliothek verfügbar.
The approved original version of this doctoral thesis is available in print at TU Wien Bibliothek.
TU Bibliothek Your knowledge hub WIEN

Figure 38 illustrates some challenges and successes of previous studies of O_2 adsorption during the last two decades: the direct insight into the adsorption configurations was sought after using empty-states STM imaging in Figs. 38a–38d, while Fig. 38e shows one of the most recent reports on this adsorption problem using nc-AFM. The appearance of adsorbates on the Ti_{5c} rows after dosing O_2 to a reduced sample at low temperatures is shown in Figs. 38a and 38b. While Fig. 38a reports that the newly adsorbed species (visible as isolated bright spheres) are stable and withstand consecutive imaging, Fig. 38b reports that these adsorbates instead split into two adsorbates after prolonged STM scanning with the application of a positive bias to the sample. Similar results were obtained for the O_2 molecules adsorbed within an V_O, as illustrated in Figs. 38c–38d. Scanning a reduced surface after exposure to O_2 at low temperatures reveals that there are some species within the O_{br} rows that are particularly unstable during STM imaging. Careful selection of the biasing values and the values of the tunneling current even allows for the appearance and reappearance of isolated features on the Ti_{5c} rows on either side from the unstable point in the O_{br} rows, as seen in Fig. 38c. If these scanning conditions are not carefully met, the O_2 within a V_O simply dissociates to heal the oxygen vacancy with one O atom and leave the other O atom on the Ti_{5c} row nearby, as seen in Fig. 38d. Since the STM scanning clearly induces unwanted dissociation events on the adsorbed O_2 species, a recent study addressed this issue by scanning the stoichiometric surface exposed to O_2 at room temperature without the application of biasing voltage, which is possible only through the use of nc-AFM. A resulting constant-frequency shift AFM image can be seen in Fig. 38e, which shows many different features on the surface, each with a distinct contrast. This result is directly opposite to many previous STM studies that show only one type of contrast over the adsorbates on the Ti_{5c} rows, and an unstable contrast over one adsorbate within the V_O. The original publication proposed that different charge states of the adsorbates [188] (marked in the image) are responsible for several distinct contrasts, mainly because the imaging was performed with a chemically active Pt/Ir AFM tip. However, similar results have been reported in previous STM studies, where the richness of the different adsorbates was re-interpreted to arise from different hydroxyl-complexes that appear after dosing O_2 to a surface pre-covered by some H_2O molecules [203, 204, 205].

The study presented in this Section aimed to resolve these long-standing issues by utilizing the non-destructive AFM imaging with a superior resolution in a well-controlled experimental environment.

2.5.1 Experimentally observed adsorption configurations

The vast body of literature on the adsorption of O_2 on the rutile $TiO_2(110)$ surface contains many different results, some of which unfortunately conflicting, but several conclusions provide an excellent basis for this research. Oxygen molecules prefer dissociative adsorption when dosed on a $TiO_2(110)$ surface with oxygen vacancies V_Os at room temperature [206, 207, 208, 183, 209, 210, 188, 211]. On the other hand, the results of low-temperature O_2 dosing (<150 K) are ambiguous: Scanning probe techniques mostly report dissociative adsorption [212, 211, 213, 214], while area-averaging techniques show a strong preference for molecular adsorption [214, 215, 216, 217, 218, 219, 220, 221, 222, 223, 224, 225, 226, 227]. The adsorption of molecular O_2 inside a V_O was the first adsorption hypothesis confirmed experimentally [187, 228, 186, 229, 185], but later it was deduced that O_2 molecules can also chemisorb to the rows of five-fold coordinated Ti atoms Ti_{5c} [186, 229, 185]. The exact O_2 adsorption configurations however, and the temperature range in which they are present, still remain unclear. The standard analysis technique, STM, can easily dissociate the adsorbed molecules and requires very delicate conditions to avoid manipulation of the molecular O_2 [187, 228, 229, 186, 185].

The constant-height AFM images in Figs. 39a and 39b show a reduced rutile (110) surface with adsorbed oxygen. The image contrast is predominantly formed by repulsion between the O-functionalized AFM tip apex and surface O atoms. The geometrically protruding rows of surface bridging oxygen atoms are clearly resolved, occasionally interrupted by oxygen vacancies. This imaging contrast provides direct access to the oxygen anion sublattice of the surface, and complements the cation sublattice contrast typically obtained in STM imaging [149].

Figure 39a shows a surface with an initial concentration of oxygen vacancies of $c_{V_O} \approx 0.05$ ML, subsequently exposed to 0.1 L of O_2 at a sample temperature of 10 K (measured at 4.8 K). Some oxygen vacancies remain unoccupied (marked with a white circle in Fig. 39a), while others are populated with an O_2 molecule (marked by a purple circle). These molecules are adsorbed with their bond axis in the $[1\bar{1}0]$ direction, perpendicular to the direction of the O_{br} rows. The appearance of these molecules in the AFM images indicates that they lie flat, incorporated in an O_{br} row. There are two molecularly bound O_2 species on the Ti_{5c} rows (O_2/Ti_{5c}), both flat according to the equal frequency shift over the constituent atoms inside each molecule. The molecule with its bond axis aligned parallel to the [001] direction of O_{br} rows (marked with a green circle in the AFM

Die approbierte gedruckte Originalversion dieser Dissertation ist an der TU Wien Bibliothek verfügbar.
The approved original version of this doctoral thesis is available in print at TU Wien Bibliothek.
TU WIEN Bibliothek Your knowledge hub

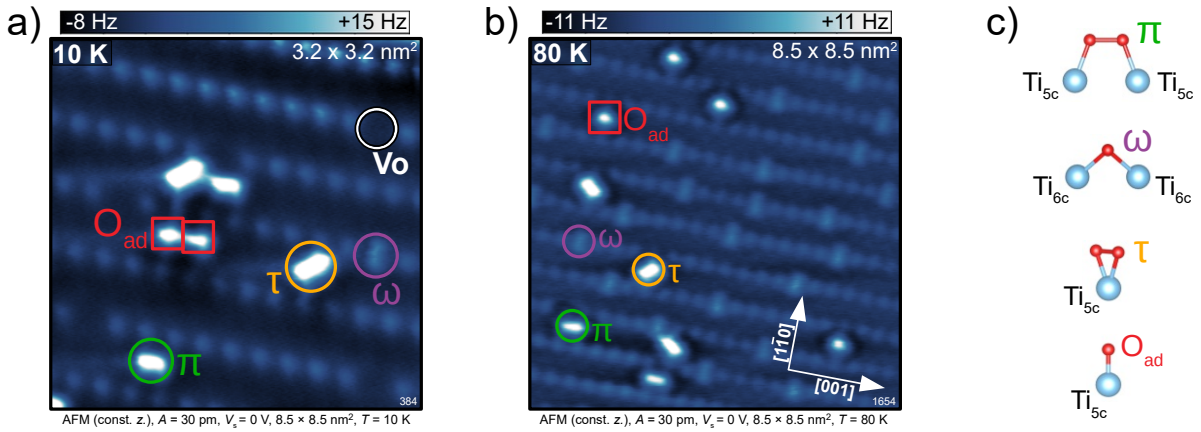

Figure 39: **Adsorption of molecular O_2 to a clean, reduced rutile TiO_2(110) surface.** a) Constant-height AFM image of 0.1 L of O_2 adsorbed at a surface reduced by c_{Vo} ≈0.05 ML of oxygen vacancies at 10 K. An oxygen vacancy is marked by a white, outlined circle, while the four characteristic adsorption configurations are marked with corresponding shapes and colors. b) Constant-height AFM image of 0.5 L of O_2 adsorbed at a surface reduced by c_{Vo} ≈0.08 ML of oxygen vacancies at 100 K. Labeling is consistent with the panel in (a) c) Legend for the different adsorption configurations labeled in (a) and (b), with a ball-and-stick model of each adsorption geometry; blue atoms represent Ti while red atoms represent O.

images) is bound to two underlying, neighboring Ti_{5c} atoms. The molecule with the bond axis rotated by 45° towards the O_{br} rows (marked with an orange circle in the AFM images) is bound to only one Ti_{5c} atom directly underneath. For simplicity, the following nomenclature is adopted for the molecules throughout the text: ω for the molecules inside the **o**xygen vacancy, π for the molecules **p**aralell to the O_{br} rows and τ for the molecules **t**urned towards the O_{br} rows. The τ and π molecules are not only differently rotated but also sit in different adsorption sites, shifted half a unit cell along [001].

The last species present in Fig. 39a are oxygen adatoms (marked with a red square in the AFM images), originating from the dissociation of molecular oxygen. Oxygen does not spontaneously dissociate at this temperature. In Fig. 39a, oxygen adatoms were created by tip-induced dissociation in order to have all species present in a single image. Here, a voltage pulse of +1.3 V was applied to dissociate a single π molecule. The adatoms commonly appear as isolated spheres located directly above one Ti_{5c} atom (red square in Fig. 39b). Their unusual, asymmetric contrast in Fig.39a is a consequence of their mutual proximity and tip bending [230, 231].

Figure 39b show the surface after dosing 0.5 L of oxygen at $T = 80$ K. At these conditions, all oxygen vacancies are filled by ω molecules, and additional π and τ molecules adsorb on the Ti_{5c} rows. All observed adsorbates are illustrated and labeled according to the adopted nomenclature in Fig.39c, and their geometries will be discussed in more detail in the following sections.

The comparison of the results presented in Fig. 39 and the literature results presented in Fig. 38 clearly indicates that the key requirement to unambiguously observe the molecularly adsorbed oxygen species is measuring with AFM at zero sample bias, *i.e.*, with no charge injection into the molecules. Under these conditions, the ω molecule is clearly imaged as a two-atom feature within an O_{br} row, while the π and τ molecules are observed as two clearly distinct species. This allows clear identification of the geometries of O_2/V_O and O_2/Ti_{5c}, whose existence was previously inferred from the disappearance of the oxygen vacancies, or the appearance of faint features on the Ti_{5c} rows after O_2 exposure, respectively, by using very delicate conditions in STM [187, 228, 186, 229, 185]. With the unambiguous insight into the adsorption configurations, some theoretically proposed adsorption configurations can be excluded, as π, τ, and ω molecules are the only molecular species observed throughout experiments. There is no indication of other proposed species, such as the tetraoxygen [232, 233].

A noticeable difference between the adsorption configurations observed with AFM (Fig. 39) and adsorption configurations observed with STM in literature (Fig. 38) is the absence of a rotated O_2/Ti_{5c} species, *i.e.*, the τ molecules. For this reason, the surface shown in Fig.39b was studied using STM in order to determine whether the presence of τ molecules can be inferred from STM alone. Figure 40a is a large-area image showing

Die approbierte gedruckte Originalversion dieser Dissertation ist an der TU Wien Bibliothek verfügbar.
The approved original version of this doctoral thesis is available in print at TU Wien Bibliothek.
TU WIEN Bibliothek Your knowledge hub

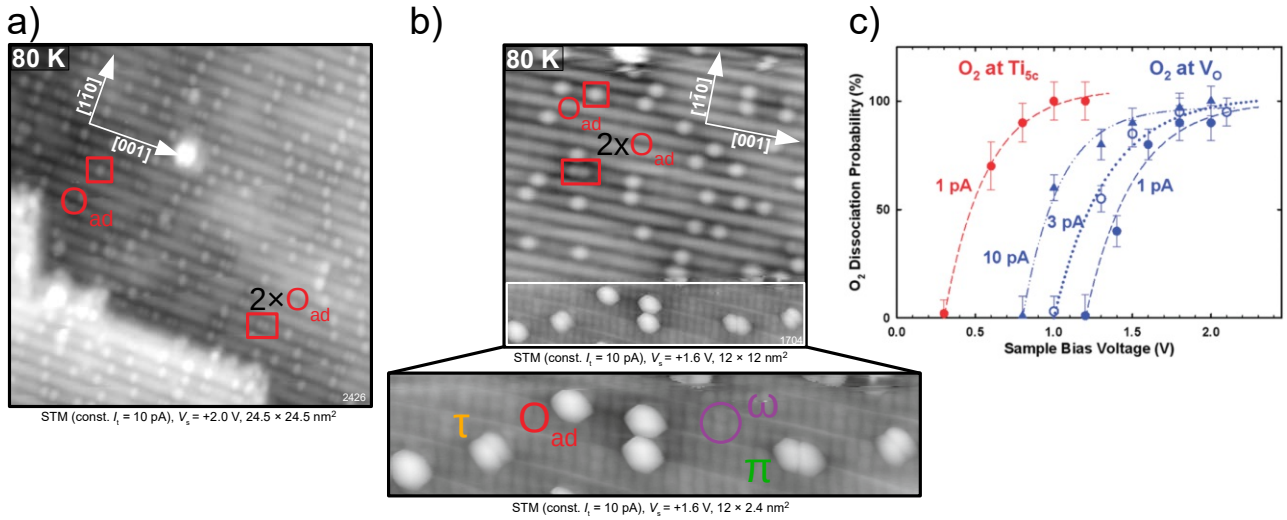

Figure 40: **STM-induced dissociation of adsorbed O_2 molecules.**
a) Empty-states STM image (V_S=+2.0 V, I_t=10 pA) of the surface with ≈0.2 ML of O_2 dosed at 100 K. No molecular species are visible since all are dissociated with these scanning conditions, and only isolated O_{ad} and pairs of O_{ad}s remain on the surface.
b) Empty-states STM images (V_S=+1.6 V, I_t=10 pA) of the surface with ≈0.2 ML of O_2 dosed at 100 K. The upper part of the image shows a typical empty-states STM contrast (just as in (a)), while the bottom part of the image, enlarged in the inset, shows a highly untypical STM contrast taken at a very close distance to the surface. This peculiar contrast manages to capture all different molecular species without dissociation, but the imaging conditions are unstable and the contrast is therefore short-lived.
c) Reported probabilities of dissociation for different O_2 species during STM-scanning, dependent on the STM scanning parameters; π and τ molecules are represented together with a red line (regular STM is unable to distinguish between them), and ω molecules are represented with a blue line.
Reprinted Figure 4 [186] with permission from [Zhi-Tao Wang, Yingge Du, Zdenek Dohnálek, and Igor Lyubinetsky, *The Journal of Physical Chemistry Letters*, 1, 3524 (2010)]. Copyright (2010) American Chemical Society.

the typical empty-states STM contrast on this surface: Ti_{5c} rows are imaged as protrusions and O_{br} rows as depressions. The dark O_{br} rows are featureless and show no presence of ω molecules or oxygen vacancies. Similarly, the bright Ti_{5c} rows show neither π nor τ molecules. Instead, the Ti_{5c} rows are covered with either single O_{ad} originating from the tip-induced dissociation of ω molecules, or paired O_{ad} features originating from the tip-induced dissociation of π or τ molecules. With a clear access to only the dissociation products via STM scanning, it is almost impossible to discern the presence of two different O_2/Ti_{5c} molecules which both dissociate in the same manner. Scanning with delicate conditions (as in Fig. 38b) does not yield a well-enough resolution to provide contrast differences between π or τ molecules prior to their inevitable dissociation. Therefore, the observation of a novel τ species once the surface is studied with non-destructive AFM is not surprising.

Figure 40b shows a smaller-area STM image with two distinct contrasts in the image and one tip-change event. The top part of Fig. 40b shows a typical STM contrast with atomic resolution on O_{ad}, same as in Fig. 40a. It is noteworthy that this type of clear imaging can be considered excellent. The bottom part of Fig. 40b is enlarged in the inset and shows an extremely rare STM contrast in which the O_{br} rows are atomically resolved and bright, while the Ti_{5c} rows are imaged as thin lines. Additionally, all the adsorbates are visible and recognized with atomic resolution in this STM contrast, marked in the inset of Fig. 40b. This type of contrast is attributed to a barely conducting tip, which had to be approached very close to the surface. At such proximity, the STM imaging contrast is affected by the tip-surface interactions, and the STM images carry similar information as the AFM images. This tip-decoration additionally does not dissociate the adsorbates, which is highly peculiar according to the reported stability of the adsorbates that is highly dependent on the STM imaging conditions, shown in Fig. 40c. This type of tip decoration is not stable when imaging this surface

Die approbierte gedruckte Originalversion dieser Dissertation ist an der TU Wien Bibliothek verfügbar.
The approved original version of this doctoral thesis is available in print at TU Wien Bibliothek.
TU Bibliothek Your knowledge hub WIEN

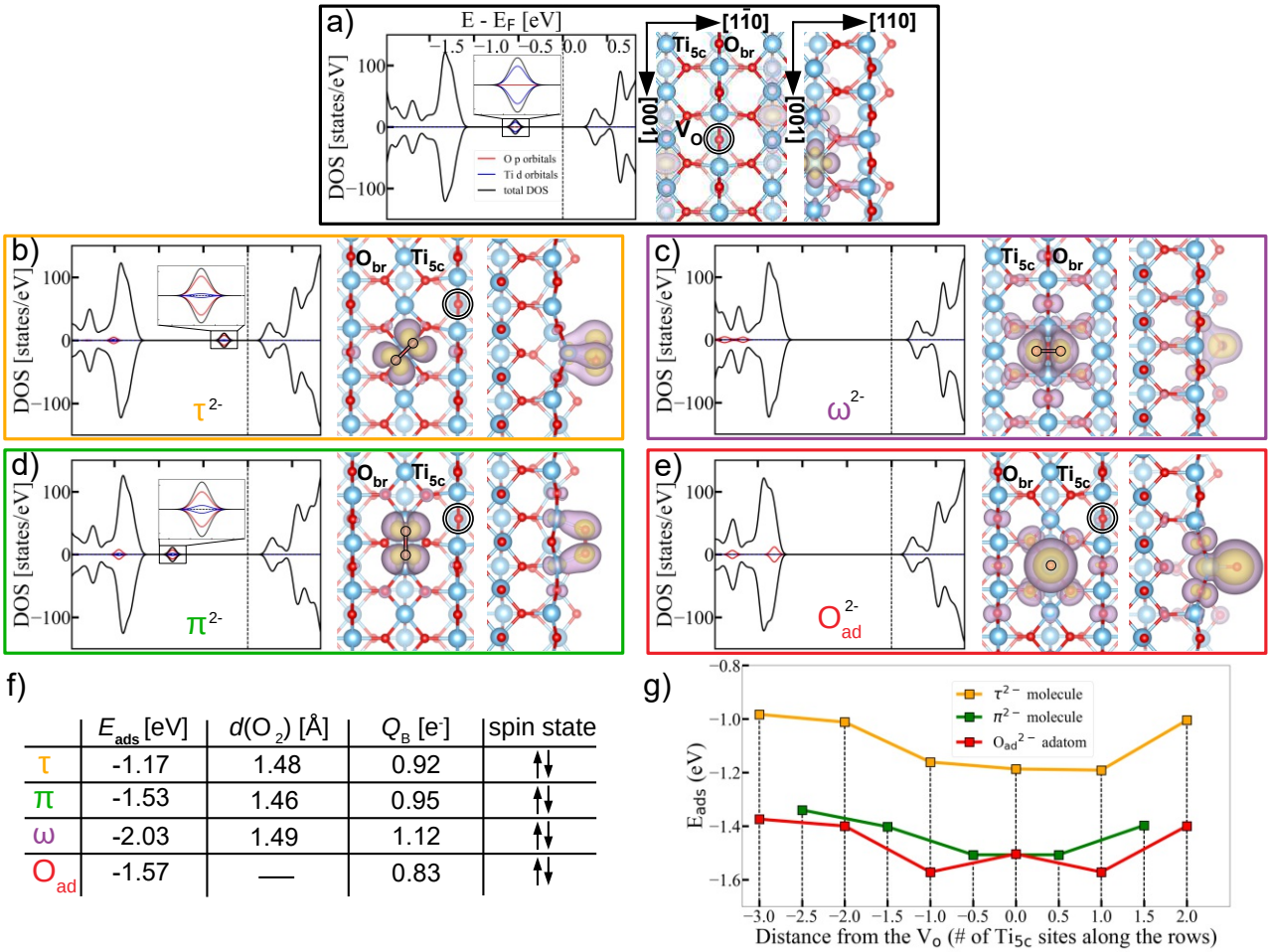

	E_{ads} [eV]	$d(O_2)$ [Å]	Q_B [e⁻]	spin state
τ	-1.17	1.48	0.92	↑↓
π	-1.53	1.46	0.95	↑↓
ω	-2.03	1.49	1.12	↑↓
O_{ad}	-1.57	—	0.83	↑↓

Figure 41: **DFT calculations of the preferred O_2 adsorption configurations.** a) Density of states and ball-and-stick models of the ground state of the rutile $TiO_2(110)$ surface with $c_{V_O} \approx 0.048$ ML of oxygen vacancies. The in-gap state is emphasized in the inset, and decomposed into contributions from O $2p$ orbitals and polaronic Ti $3d$ orbitals. The ball-and-stick model additionally shows the partial charge density of the two polarons associated with a single V_O. b-e) Density of states and ball-and-stick models of the τ, ω, π, and O_{ad} adsorption configurations, respectively. The optimized adsorption configurations are all doubly negatively charged. Both, the DOSes and the ball-and-stick models follow the same scales, orientations, and labels as in panel (a), and also focus on the origin and the spatial distribution of the highest-energy occupied states on the adsorbed O_2 molecules. f) Table summarizing the calculated properties of the adsorbates: adsorption energy E_{ads}, bond length $d(O_2)$, Bader charge Q_B, and spin state of the adsorbed molecules. g) Adsorption energy at different position of the favorable adsorbates with respect to an empty V_O.

and the tip-change occurs quickly (Fig. 40b is imaged bottom-up). Moreover, this type of peculiar close-distance contrast was observed only once during this research, and could not be controllably re-obtained.

2.5.2 DFT calculations and the O_2 charge state

The vast interest in this particular adsorption problem resulted in a large theoretical effort during the last two decades. Throughout literature, ω molecules were predicted to be the preferred molecular adsorption configuration [234, 235, 236, 237, 238, 239, 240], while DFT calculations mostly predict π molecules as the second most favorable molecular adsorption configuration [235, 240, 236, 238, 237]. Even though τ molecules were never observed experimentally, DFT calculations predicted their existence [234, 235, 240, 241, 236, 242, 243, 238, 239, 237] with various adsorption energies, albeit always smaller than the adsorption energy of ω molecules.

Die approbierte gedruckte Originalversion dieser Dissertation ist an der TU Wien Bibliothek verfügbar.
The approved original version of this doctoral thesis is available in print at TU Wien Bibliothek.
TU Bibliothek Your knowledge hub WIEN

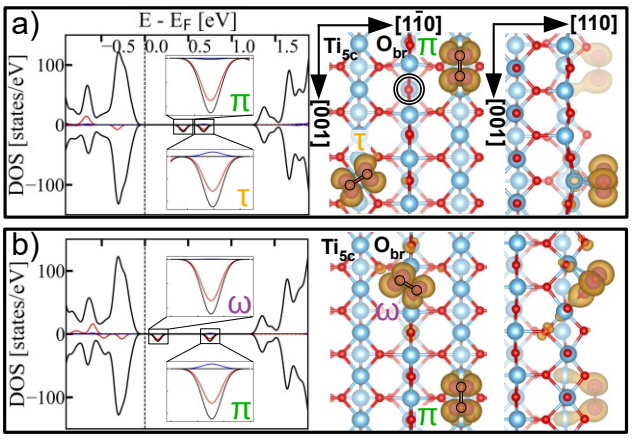

c)

	E_{ads} [eV]	d(O_2) [Å]	Q_B [e$^-$]	spin state
π & τ	-0.69 per O_2	1.38	0.58	↑
		1.39	0.48	↑
ω & π	-0.74 per O_2	1.39	0.66	↑
		1.38	0.57	↑

d)

E_{ads}	no added e$^-$	1 added e$^-$	2 added e$^-$
τ	+3.36	+0.98	-1.01
π	+3.17	-0.75	-1.49
O_{ad}	+1.72	+0.07	-1.58

Figure 42: **DFT calculations of the unfavorable superoxo O_2 adsorption configurations.** a–b) The density of states and the ball-and-stick models of the π molecule co-adsorbed with τ and ω molecules, respectively, to a rutile $TiO_2(110)$ surface with c_{V_O} ≈0.048 ML of oxygen vacancies. Co-adsorbed molecules take one polaronic electron each. The inset in the DOSes focuses on the contributions to the unoccupied in-gap state, and the partial charge densities plot the spatial distribution of this unoccupied electronic orbital. c) Table summarizing the calculated properties of the O_2 molecules adsorbed in the superoxo charge state: the adsorption energy E_{ads}, bond length $d(O_2)$, Bader charge Q_B, and the spin state. d) Table summarizing the adsorption energy of the oxygen species at the Ti_{5c} rows on a stoichiometric $TiO_2(110)$ surface without and with the addition of external electrons.

The charge state of the adsorbed O_2 molecules has been discussed for a long time with major disagreement between experiment and theory. While theory mostly finds the adsorbed molecules to be doubly negative, *i.e.*, in the peroxo state [234, 235, 241, 236, 242, 243, 237], experimental data were often interpreted as singly charged negative, *i.e.*, superoxo molecules [220, 221, 222, 223, 229, 224, 225, 226]. Electron donation from the surface, resulting in an O_2 anion, is required for the chemisorption [243]. The surface excess electrons mostly originate from the intrinsic bridging oxygen vacancy defect V_O, but can also be provided either by coadsorbates (for example OH) or titanium interstitials Ti_{int} [243]. Naturally, on stoichiometric $TiO_2(110)$ surfaces without defects there is no electron donation, and the molecular O_2 only physisorbs [244, 245].

The development of modern augmentation to the DFT calculations, as the implementation of hybrid functionals or the addition of Hubbard's U to describe the on-site Coulomb interaction potential between electrons of a single atom, yields predictions with improved accuracy as compared to calculations performed 10 or 20 years ago. Moreover, the best description of the ground state of the reduced $TiO_2(110)$ surface was achieved only recently through the introduction of electron polarons (previous two Sections). Revisiting the DFT optimization of O_2 adsorption on this surface was therefore called for, since it additionally reveals the influence of polarons on the simple adsorbates and vice versa.

Simulating the adsorption of O_2 molecules was performed using the DFT+U approach, with an effective U value of 3.9 eV. Calculations were performed by adsorbing a single O_2 or O on a reduced 6×2 surface slab with one V_O. This corresponds to a V_O concentration of 1/12 ML (=8.3%), similar to the experimental conditions. Fig. 41a shows the ground state of the reduced slab as a starting point of each adsorption scenario. The oxygen vacancy is a donor, which provides two excess electrons to the slab. These electrons form small polarons due to their coupling with lattice distortions, and they preferentially localize on the next-nearest subsurface Ti_{6c} atoms. They form the characteristic Ti^{3+} in-gap states in the calculated DOS, shown in the left panel of Fig. 41a and enlarged in the inset. The inset focuses on the individual contributions to the in-gap state from the Ti and O atoms at the surface. In the ground state, the in-gap state is populated by the polarons residing in the Ti 3d states. The spatial distribution of electrons responsible for the in-gap states (right panel of Fig. 41a) confirms their localization on polaron-hosting subsurface Ti_{6c} atoms. Calculated adsorption energies E_{ads}, oxygen bond lengths $d(O_2)$, Bader charges Q_B, and spin states of the adsorbates are summarized in the table in Fig. 41f. The adsorption energies of adsorbed molecules were calculated according to:

$$E_{ads}^{O_2} = E_{TiO_2+O_2} - (E_{TiO_2} + E_{O_2}) \quad ,$$

Die approbierte gedruckte Originalversion dieser Dissertation ist an der TU Wien Bibliothek verfügbar.
The approved original version of this doctoral thesis is available in print at TU Wien Bibliothek.
TU Bibliothek Your knowledge hub WIEN

where E_{TiO_2} is the total energy of the minimum-energy, polaron-hosting ground state of the clean slab reduced by one V_O, $E_{TiO_2+O_2}$ is the total energy of the surface slab with the adsorbed molecular oxygen and E_{O_2} represents the energy of the O_2 molecule in the gas phase. Similarly, the adsorption energies of oxygen adatoms were calculated as:

$$E^{O}_{ads} = E_{TiO_2+O} - (E_{TiO_2} + E_{O_2/2}) \quad ,$$

where E_{TiO_2+O} is the total energy of the surface slab with the adsorbed oxygen adatom and $E_{O_2/2}$ is one half of O_2 molecule energy in the gas phase.

Figures 41b–41e show the slab after adsorbing the oxygen species in geometries corresponding to the AFM measurements, with the DOS plots and structure images organized as in Fig. 41a. Common to the presence of all adsorbed species is the depletion of the polaron state. As a consequence, there is a dramatic change of the in-gap state of the clean, reduced slab; the in-gap state even shifts into the valence band in Figures 41c and 41e.

The τ molecule (Fig. 41b) is calculated to have the weakest adsorption energy, followed by the π molecule (Fig. 41d). Both molecules preserve an in-gap state in the total DOS. The origin of the in-gap state, enlarged in the insets, clearly illustrates a charge transfer from the polaron-hosting Ti_{6c} sites to the $2\pi^*$ orbitals of the adsorbed molecules. The spatial distribution of these two in-gap electrons is illustrated in the right side of the panels. They are shared between the constituent atoms of the O_2 molecule and preserve their opposite spins, yielding a zero net magnetization on the molecule. Therefore both, π and τ molecules accept two available polaronic electrons from the slab, making them peroxo molecules O_2^{2-}. Bader charges [246] of the covalently bound adsorbates are usually significantly lower than nominal oxidation states [247, 248, 249], since they do not account for the electrons used in the covalent bond formation to the underlying Ti atom(s). A Bader charge of the molecules (sum of Bader charges of the constituent atoms) of $Q_B \approx 1$ implies that roughly one electronic charge is used for creating two chemical bonds to the underlying Ti atom(s) to which these molecules are directly bound. The calculated bond lengths of 1.46 Å and 1.48 Å for the π and τ molecule, respectively, are larger than gas-phase O_2 (DFT value 1.28 Å) and additionally support their peroxo assignment [250].

The calculated molecular species with the highest adsorption energy is the ω molecule (Fig. 41c). This adsorption configuration is characterized by the disappearance of the in-gap state and the corresponding states are shifted deep into the valence band. The spatial charge-distribution plot in Fig. 41c shows the sum of all p-type contributions from the molecular states of the ω molecule. The complete disappearance of the in-gap state and the appearance of symmetric features in the projected DOS on this molecule indicate that the two excess electrons of opposite spin, present in the reduced slab, transfer to the ω molecule, again making it a peroxo O_2^{2-} species. A calculated bond length of 1.48 Å, no net magnetization, and a Bader charge larger than 1 confirm this charge transfer and the peroxo character. Simulating adsorption of an isolated oxygen adatom on top of a Ti_{5c} atom (Fig. 41e) also shows the disappearance of the in-gap state. The p-type states associated with the adatom are shifted to the valence band and indicate the transfer of all the excess electrons to the adatom, making it a doubly negative ionosorbed O_{ad}^{2-} atom.

The dependence of the adsorption energy E_{ads} of adsorbed oxygen in different configurations as a function of the distance along [001] from the empty oxygen vacancy in the surface slab (the same 8.3% reduced slab used throughout the research) is shown in Fig. 41g. It shows an attractive interaction between the adsorbate and the V_O (as expected for species with opposite charge), with a saturating trend further away from the V_O. The variation is less than 10% of the highest adsorption energy (the lowest value of E_{ads}) for each species. This distance dependence is not too pronounced, as confirmed experimentally in the AFM images in Fig. 39, where the adsorbed molecules show no obvious correlation with the position of oxygen vacancies. The existence of isolated O_{ad} is solely due to the vacancy-mediated dissociation channel, which leaves an O_{ad} on Ti_{5c} and one O_{br} to heal the vacancy. Thus, for oxygen adatoms created by dissociation in oxygen vacancies, the position is necessarily related to the position of the V_O where it originates from. Dissociation puts these O_{ad} directly adjacent to the V_O [187] since the diffusion to the energetically more favorable nearest-neighbor position with regard to the oxygen vacancy is hindered at low temperatures [206].

The π molecule shows a symmetric energy-distance curve in Fig. 41g with the degenerate position of the minimum, since this molecule is bound to two underlying lattice Ti_{5c} atoms. The adsorption energy vs. position of the τ molecule is not symmetric due to the directional character of this molecule: the molecule prefers to orient one of its constituent O atoms towards the empty V_O due to electrostatic attraction of the negative O atom and the positive V_O. Therefore, it prefers adsorption on one Ti_{5c} away from the vacancy to being adsorbed directly next to a vacancy. All adsorbed species in Figures 41b–41e were placed in their minimum-energy positions with respect to the empty V_O, and represent the ground state of the combined surface+adsorbate system.

In Fig. 42 the adsorption configurations of superoxo species was investigated. The superoxo species were successfully formed by co-adsorbing two molecules in configurations corresponding to a peroxo charge state to

Die approbierte gedruckte Originalversion dieser Dissertation ist an der TU Wien Bibliothek verfügbar.
The approved original version of this doctoral thesis is available in print at TU Wien Bibliothek.
TU Bibliothek Your knowledge hub WIEN

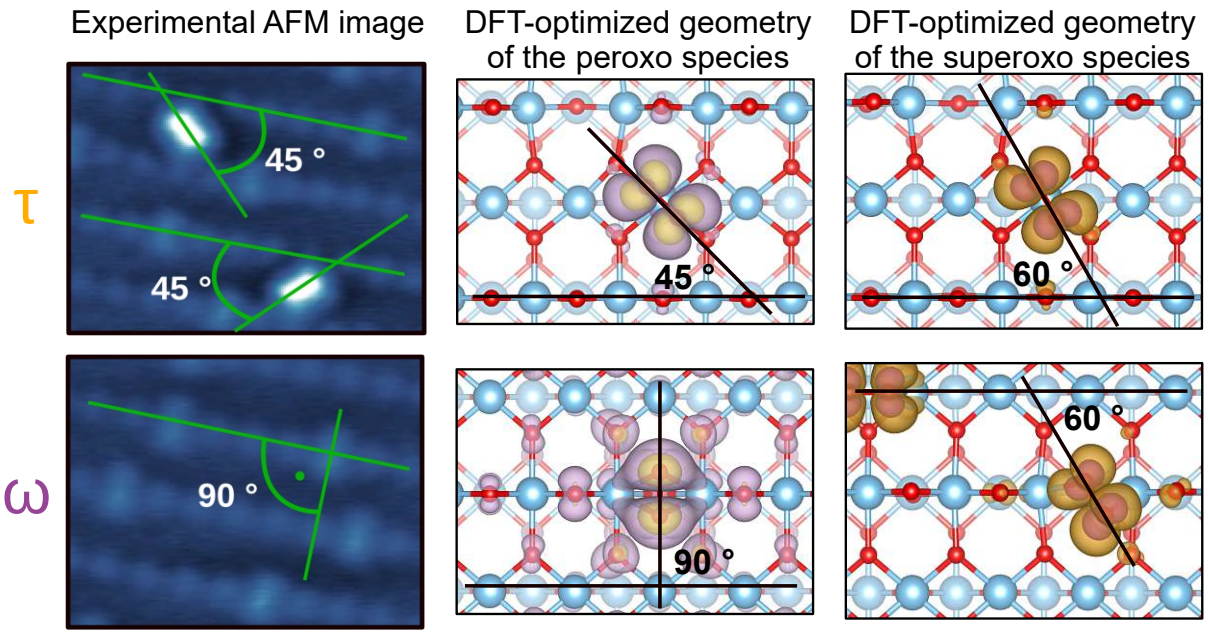

Figure 43: **Comparison between the experimentally observed O_2 adsorbed species and the stable O_2 species obtained through DFT calculations.** Experimentally observed ω and τ molecules have distinct orientation of 90° and 45° with respect to the O_{br} rows, respectively. The same orientation is obtained from DFT calculations for the peroxo ω and τ species, while their calculated superoxo counterparts have distinctly different geometries.

the slab containing one V_O. The spin-projected DOS of the co-adsorbed pairs of molecules is now characterized by two empty spin-down in-gap states, one for each adsorbed molecule, while the populated spin-up states associated with the molecules are located within the valence band. Projected partial-charge-density plots associated with the spin-down, in-gap empty states are plotted at the right side of the panels in Figures 42a and 42b. These empty states have the symmetry of the antibonding $2\pi^*$ orbital and simultaneously illustrate the spatial distribution of the filled spin-up $2\pi^*$ states at each molecule. The table in Fig. 42c quantifies the properties of the adsorbed superoxo species. The adsorption energy per molecule implies chemical bonding of the superoxo species, but in a metastable state at this level of theory, due to the weaker adsorption energies than single peroxo species adsorbed to the same slab. The bond lengths of the co-adsorbed molecules are ≈1.39 Å, which is in agreement with the expected values for superoxo species [250]. Bader charges of the superoxo species is roughly equal to one half of the Bader charges for the peroxo species. Singly charged oxygen adatoms O^-_{ad} could not be stabilized employing the methods used to calculate the other peroxo and superoxo species (Figures 41 and 42), indicating that they are unstable or at least not preferable.

Figure 42d shows a table with the stability of adsorbates as a function of electron doping to the non-reduced surface slab with the V_O populated with an ω molecule. These calculations are simulating the observed adsorption after O_2 exposure to a surface at 80 K (Fig. 39b), where all oxygen vacancies are populated by the energetically most favorable ω molecules. Then, all the polaronic electrons are transfered to the ω^{2-} molecules first and the surface has no further electrons to donate to additional O_2 molecules. Therefore, no chemisorption occurs without the addition of excess electrons (first column), described by the positive adsorption energy for all adsorbates. In order for further chemisorption to occur, additional electron doping is required. The excess electrons introduced to the slab tend to localize on the additional O_2 molecule on the Ti_{5c} row. The resulting, stable solutions are non-metallic. Addition of only one electron to a non-reduced slab will stabilize only the π molecules in the superoxo charge state, while the other species do not adsorb (second column). When two electrons are added to a slab with the oxygen vacancy populated by an ω^{2-} molecule, an additional molecule can be adsorbed to the surface (third column). The additional, chemisorbed molecule or an adatom has roughly equal adsorption energy as a single peroxo molecule adsorbed to a reduced slab. The other properties of the molecules adsorbed this way are the same as shown in Fig. 41.

The charge state of adsorbed O_2 molecules is a long-standing question in oxygen chemistry. The chemically

Die approbierte gedruckte Originalversion dieser Dissertation ist an der TU Wien Bibliothek verfügbar.
The approved original version of this doctoral thesis is available in print at TU Wien Bibliothek.
TU Bibliothek Your knowledge hub WIEN

inert oxygen-terminated tip does not provide direct information on the charge state of the adsorbed molecules, and no significant differences in the frequency shift above different molecules adsorbed at equivalent sites can be seen. Therefore, the comparison between the geometry of calculated species and the geometry of experimentally observed species is used to identify whether the adsorbed molecules are superoxo or peroxo species. Fig. 43 shows the experimental and calculated geometries of τ and ω molecules. In experiments, the τ molecules are always rotated by 45° towards the O_{br} rows, while ω molecules are always perpendicular to the O_{br} rows (first column of Fig. 43). Calculated superoxo τ and ω species show a rotation by 60° with respect to the [001] axis. On the other hand, calculated peroxo τ molecules are rotated by exactly 45° and the ω molecules are exactly perpendicular to the O_{br} rows. The angles of the calculated peroxo τ and superoxo τ are not dependent on the distance from the V_O in calculations, and consistently relax in the 45° and 60° with respect to the [001] axis, respectively. Therefore, experimentally observed τ and ω species are assigned to be in the peroxo charge states. The geometry of the π molecule does not allow for similar, direct comparisons of experiment and theory. No preference for the appearance of π and τ molecules on the surface was observed, making them equivalent during adsorption and similar in properties. Therefore, π molecules are assigned to the peroxo charge state as well. According to calculations, doubly ionized singlet O_{ad}^{2-} is the only stable species, hence the charge of oxygen adatoms is assigned accordingly. The absence of theoretically metastable superoxo species on the surface exposed to 0.5 L of O_2 at the temperature of 80 K (Fig. 39b) implies that once the peroxo species is adsorbed, it will not share charge with the next molecule that arrives to the surface. Furthermore, the calculated adsorption energies of the peroxo and superoxo species (Figures 41f and 42c) show that if the co-adsorption of two superoxo species were to occur, it is energetically favorable for one superoxo molecule to donate an electron to the other one and subsequently desorb, resulting in a surface with exclusively peroxo O_2^{2-} species.

Assuming that all the molecular species are in the peroxo charge state, the ω molecules use all excess charge provided by the surface oxygen vacancies, while the other chemisorbed species must drain electrons from subsurface dopants, *i.e.* interstitial Ti atoms [211, 251, 252] or bulk oxygen vacancies [145]. They donate electrons for further chemisorption of π and τ molecules dosed at 80 K, up to a saturation coverage of 0.5–1 per oxygen vacancy. It is noteworthy that all the molecular species are oriented parallel to the surface, making them hard to detect in infrared absorption techniques [253]. Also, their peroxo state makes them undetectable by electron paramagnetic resonance [254]. Electron energy loss spectroscopy measurements on O_2-exposed rutile $TiO_2(110)$ surfaces support the peroxo charge state assignment [185].

When comparing the thermodynamical stability of the superoxo and peroxo species, none of the superoxo species would be preferred, even if they have to compete for electrons with peroxo species. The calculations in Figures 41f and 42c show that, out of all combinations, only two superoxo τ molecules would be preferred to one peroxo τ molecule, at extremely high O_2 chemical potentials, above -0.1 eV, which corresponds to temperatures below 150 K at a pressure of 10 bar. However, even this preference is lost because it is energetically downhill to convert two superoxo τ molecules into one peroxo π molecule and one gas molecule.

2.5.3 AFM contrast and the $F_{ts}(z)$ curves

All AFM images presented in this study were measured with the same O-functionalized AFM tip termination. This tip consistently displays a characteristic contrast over the adsorbed O_2 molecules, and also provides excellent resolution of the oxygen sublattice of the substrate. In order to better understand this unique tip functionalization, force-distance $F_{ts}(z)$ curves were measured above all adsorbed species, and compared to DFT+U calculations.

Figure 44a shows the experimentally measured force-distance $F_{ts}(z)$ curves above all surface species. The positions of the minima in the $F_{ts}(z)$ curves are related to the relative heights of the different adsorbed species. The τ molecule is the highest protruding one, followed by the O_{ad} and the π molecule, while the lowest-lying ω molecule lies in-plane with the O_{br} rows (the force minimum above the O_{br} is taken as zero in the z scale in Fig. 44a). Figure 44b compares the minima of the experimental $F_{ts}(z)$ curves (left), with the vertical heights of the molecules corresponding to the relaxed slabs in Figures 41 and 42 (right). DFT calculations "overestimate" the protrusion of different adsorbed O_2 species, but calculated results are in qualitative agreement with the experimentally obtained values. The relative order of the heights of different adsorbates is preserved in the calculations when compared to the experiment, which provides additional confirmation of the correct assignment of the charge state to the adsorbates: The superoxo τ molecule is calculated to be lower-protruding than the O_{ad}, while the peroxo τ molecule is calculated to be higher-protruding than the O_{ad}, in agreement with the experimental results.

The depth of the attraction minima is related to the strength of the chemical interaction between the tip and

Die approbierte gedruckte Originalversion dieser Dissertation ist an der TU Wien Bibliothek verfügbar.
The approved original version of this doctoral thesis is available in print at TU Wien Bibliothek.
TU Bibliothek Your knowledge hub WIEN

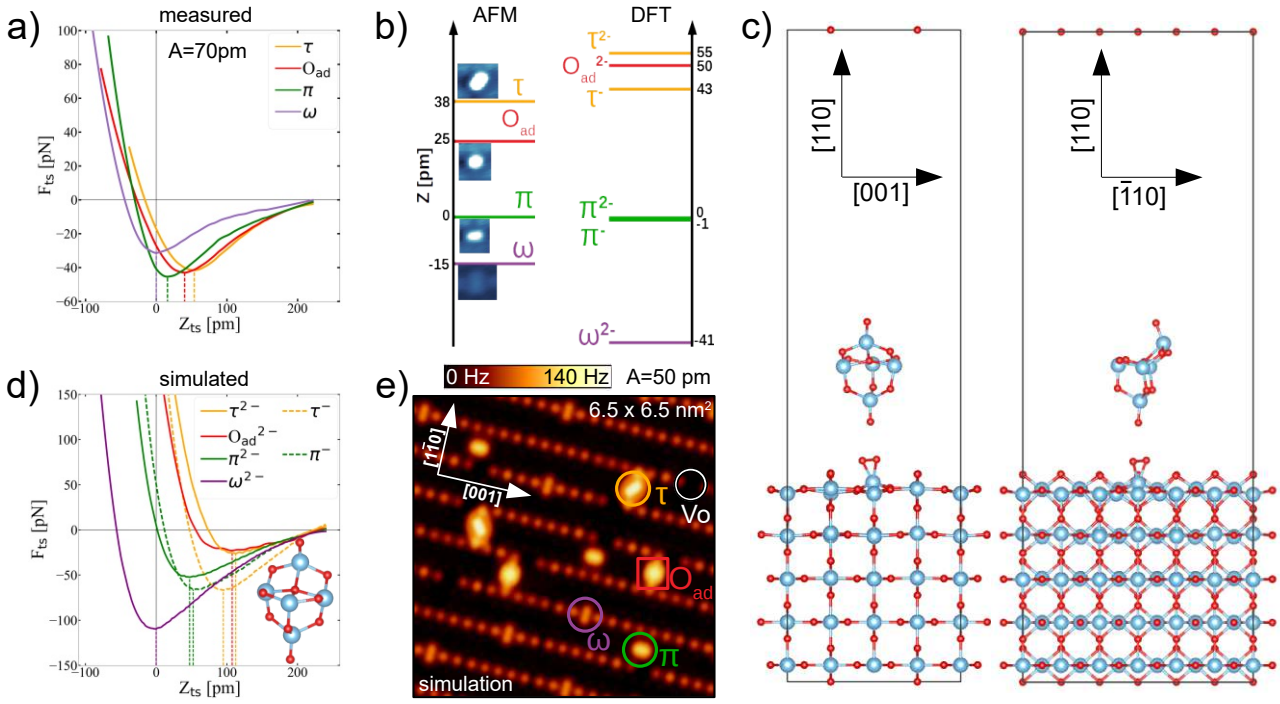

Figure 44: **Experimental and DFT-simulated $F_{ts}(z)$ curves.** a) Measured $F_{ts}(z)$ curves above different O_2 species, obtained with the O-terminated AFM tip. b) Comparison of the height of the adsorbates obtained from the experimental $F_{ts}(z)$ curves (left column) and the DFT calculations presented in Figs. 41 and 42. c) Ball-and-stick models of the DFT setup for performing simulated $F_{ts}(z)$ curves above the adsorbed species (τ molecule in this example), viewed from two perspectives. d) Simulated $F_{ts}(z)$ curves above different adsorbates in different charge states. The inset magnifies the tip shape used for calculations. e) Simulated constant-height AFM image above the surface with all adsorbates, constructed from the $F_{ts}(z)$ curves in (d).

the adsorbates. The maxima of the experimentally measured attractive forces above the species are in the order of tens of pN. This implies no chemical interaction between the tip and the adsorbates, because the chemical interaction usually results in a strength of the attractive force in order of 1 nN. The $F_{ts}(z)$ curves, and all AFM images in this research, were obtained by a chemically inert tip. This is consistent with the oxygen-terminated TiO_2 tip apex obtained by the purposeful tip functionalization. The O-terminated AFM tip proved to be an excellent tool for studying adsorption of O_2 on this surface, making the exact structure of this tip interesting for further studies as well. For this reason, $F_{ts}(z)$ curves were simulated using a $(TiO_2)_5$ cluster tip model, developed in previous works [255, 256, 257], which were later compared to the experimentally measured ones.

The setup for simulating the $F_{ts}(z)$ curves is shown in Fig. 44c. The simulated $F_{ts}(z)$ curves were calculated by placing the tip model at different distances from the surface, and performing a full DFT+U calculation at each point. The calculation slab has to be large to perform calculations of this sort, in order to minimize the interaction of the atoms at the bottom of the surface slab with the atoms at the backside of the tip model due to the periodic boundary conditions. In these calculations, a surface slab with 34 Å of vacuum above the surface was used. To emulate the experimental procedure as closely as possible, the tip model is initially placed far away from the surface, and then approached in small increments (2.5 pm in this case), such that any deformation or relaxation of the tip model is carried over into the next calculation. The DFT calculations always tend to minimize the forces on each atom involved in the calculation slab, which would result in the net zero force on the tip measured at each point during a simulation of a $F_{ts}(z)$ curve. For this reason, only the atoms that are oriented closer to the surface are fully relaxed, while the atoms positioned on the far end of the tip model are fixed throughout the approach, and they experience the forces that act between the relaxed atoms at the tip apex and the adsorbates at the surface. At each point of the tip approach, the force on the tip is measured as a sum of forces acting on each constituent atom of the simulated AFM tip, but commonly only the fixed atoms at the further end of the tip actually experience measurable forces.

Figure 44d shows the resulting simulated $F_{ts}(z)$ curves above all adsorbates in both charge states, and the

Die approbierte gedruckte Originalversion dieser Dissertation ist an der TU Wien Bibliothek verfügbar.
The approved original version of this doctoral thesis is available in print at TU Wien Bibliothek.
TU Bibliothek Your knowledge hub WIEN

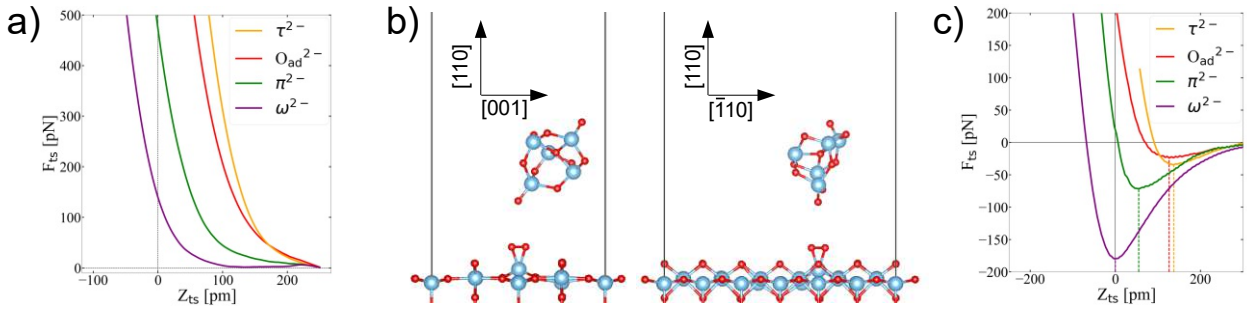

Figure 45: **DFT-simulated $F_{ts}(z)$ curves under different conditions.** a) Simulated $F_{ts}(z)$ curves above different adsorbates using the same setup for calculating the $F_{ts}(z)$ curves in Fig. 44, but with no accounting for the long-range van der Waals forces between the simulated tip and the surface. b) Ball-and-stick models of the DFT setup used for performing the simulated $F_{ts}(z)$ curves with a slanted (biased) tip above the adsorbed species (τ molecule in this example), viewed from two perspectives. c) Simulated $F_{ts}(z)$ curves above different adsorbates using the slanted tip displayed in (b).

tip model enlarged in the inset (in a 3D view). Qualitatively, the simulated $F_{ts}(z)$ curves correspond to the experimentally obtained ones (Fig. 44a) remarkably well: they exhibit a very shallow attraction basin (<150 pN) and generally resemble the shape of the experimental curves, proving that the $(TiO_2)_5$ cluster tip model is a reasonable description of the actual O-terminated AFM tip used in experiments. Additionally, the minima of the attraction basin above different adsorbates matches the relative order when compared to the experiments. This relative order is also preserved when compared to obtained values for the protrusion of each species just from the adsorption calculations (Fig. 44b). All simulated $F_{ts}(z)$ curves behave similarly, characterized by the absence of forces at large distance, shallow attraction minima at intermediate distances, and an onset of repulsive forces at small distances between the tip and the surface. At lower tip-sample distances, both, the tip and the adsorbate start to deform. When the tip is sufficiently close, the chemical attraction between the bottom Ti atom of the tip with the surface O atoms becomes relevant, but these cases are not displayed in Fig. 44d because they could already be considered as a tip crash, followed by the exchange of material between the tip and the surface.

Figure 44e shows a simulated constant-height AFM image of the surface constructed using only the simulated $F_{ts}(z)$ curves in Fig. 44d, and the geometries of the adsorbed species from Fig. 41. Two-dimensional maps of the force above the O_2-covered surface at different heights were constructed by calculating the pair-wise interaction between each of the constituent atoms of the surface and the adsorbates, with the O-terminated apex of the tip. Each pair-wise interaction is adsorbate specific, implying that the simulation recognized the type of the surface atom and applied the appropriate calculated $F_{ts}(z)$ curve to this interaction. At each point in the calculation grid, the force to the nearest surface atom is found by measuring the mutual separation of the tip and the nearest surface atom d, and assigning the value of the calculated $F_{ts}(z = d)$ curve for this surface atom at the calculated distance. The force maps within the range of heights spanned by the oscillation amplitude A, $F(z \in [h - A, h + A])$, were converted to a constant-height frequency shift image $\Delta f(h = const.)$ at the distance of 2.6 Å from the O_{br} rows, by using the small-oscillation-amplitude approximation [104]. The frequency shift simulated this way is larger by a factor of 5 when compared to the highly resolved experimental AFM images, because the DFT+U calculations overestimated the protrusion of each species (Figures 44b and 44e); the simulated tip had to approach closer to the surface in order to show repulsion above both the adsorbed and the lattice oxygen atoms. The process of creating a simulated constant-height AFM image such is the one in Figure 44e will be introduced in more detail in Chapter 4.

The very shallow attraction basin in the experimental and simulated $F_{ts}(z)$ curves, *i.e.*, absence of chemical interaction between the AFM tip and the adsorbate, indicates that the origin of the observed attraction is in the weak van der Waals interaction that was included in the calculations presented in Fig. 44d. Indeed, when the $F_{ts}(z)$ curves are simulated without the inclusion of the van der Waals corrected functionals, they exhibit absolutely no attraction basin, as seen in Fig. 45a. When the $F_{ts}(z)$ curves are simulated with a differently oriented AFM tip, as illustrated in Fig. 45b, the resulting curves are slightly different than the curves obtained with the same tip in normal orientation towards the surface, as can be seen by comparing Figs. 45c and 44d. The tip in Fig. 45b is inclined towards the surface, exposing more of its constituent atoms to the surface. The van der Waals force between the tip atoms and the surface is therefore increased, and the $F(z)$ curves in Fig. 45c

Die approbierte gedruckte Originalversion dieser Dissertation ist an der TU Wien Bibliothek verfügbar.
The approved original version of this doctoral thesis is available in print at TU Wien Bibliothek.
TU Bibliothek Your knowledge hub WIEN

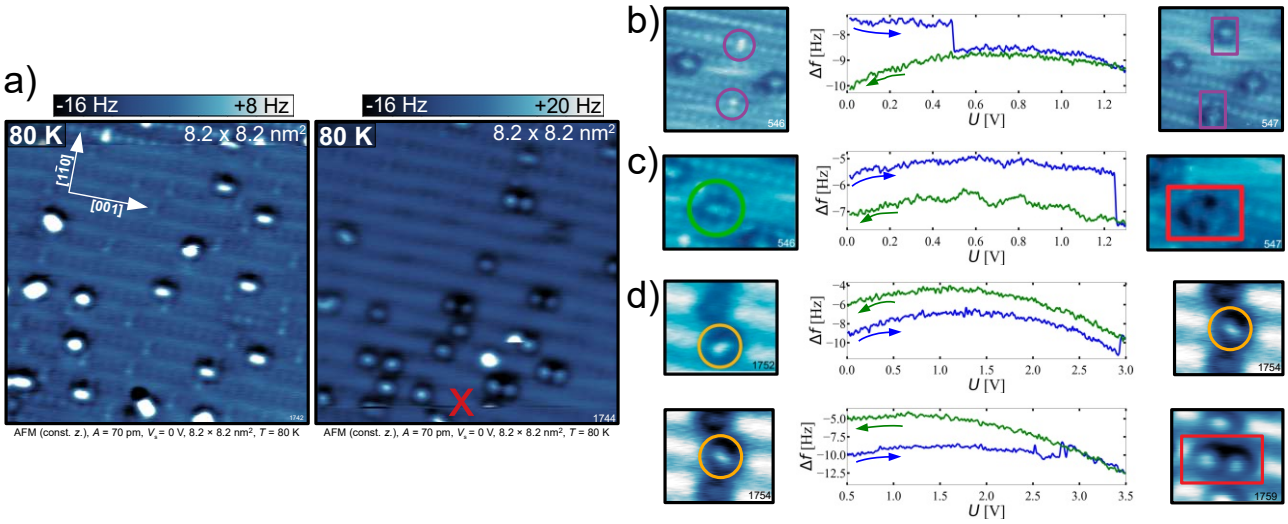

Figure 46: **Tip-induced dissociation** a) AFM image of the O_2-covered surface b) AFM image of the same area as in (a), after a +3 V bias pulse at the spot marked by the red "x". b–d) AFM images of the ω, π, and τ molecules respectively, before (left) and after (right) tip-induced dissociation. The frequency shift vs. bias voltage graphs, showing the forward and backward bias ramp, are shown in the center of the panels. The τ molecule shown in panel (d) was observed to either rotate (top) or dissociate (bottom).

consequently have deeper attraction minima. The increase in attraction is most noticeable in the $F_{\mathrm{ts}}(z)$ curve above the ω molecule, where the tip is approached closest to the surface before the onset of repulsion. It was indeed observed experimentally that some tips exhibited such stronger interaction. The rearrangement of the atoms at the tip apex is highly probable in experiments, but the oxygen at the tip apex is nevertheless responsible for the excellent lateral resolution and the absence of chemical interaction with the surface.

An important aspect of this work is the AFM imaging with an O-terminated tip. Purposely functionalized tips play a major role for non-contact AFM, and an AFM tip with the O-terminated apex results in exceptional resolution and offers many opportunities for the future. The key aspects of this tip termination are its inert character towards the surface oxygen atoms, high stability (works well for measurements performed at 80 K), and rigid character with respect to lateral bending. When applying the traditional CO-terminated tips to TiO_2 surfaces, there are difficulties caused by their stronger attractive interaction with surface atoms, and low stability during measurements performed at 80 K. Also, the lateral bending of the CO [230, 231], which is a key requirement for submolecular imaging of organic molecules [111], is not helpful on ionic surfaces; it distorts the image and creates artificial lines connecting neighboring anions.

Oxygen-terminated AFM tips have also been reported to be successful in imaging CuO thin films [109, 258]. The main obstacle is the difficulty to functionalize the tip in the desired way. This type of tip functionalization could not be obtained on clean TiO_2 surfaces; the oxygen could only be picked from a chemisorbed O_2 molecule by dissociating it by a positive sample bias voltage pulse, while the tip is close enough to "catch" one of the O atoms, while the other remains on the surface. On the other hand, the data reported on CuO thin films indicate easy functionalization. It is likely that the enthalpy of oxide formation [259] plays a role here – it is energetically expensive to extract a single atom from the TiO_2 lattice, while the energy cost on copper oxide is much lower.

2.5.4 Charge injection/removal from the O_2

Oxygen molecules on the surface are susceptible to the injection and removal of electrons, and these processes govern the O_2 reactivity and its kinetics at a crystal surface. Figure 46 shows dissociation events induced by electron injection. AFM and STM, as highly local techniques, allow manipulation of the charge of the adsorbed species in a very localized manner, *i.e.*, molecule-by-molecule. The controlled charge manipulation is easiest to perform on insulating substrates, where the charge can be inserted/removed from a single adsorbate without influencing other adsorbates at the surface. On metal substrates, where the states close to the Fermi level lie

Die approbierte gedruckte Originalversion dieser Dissertation ist an der TU Wien Bibliothek verfügbar.
The approved original version of this doctoral thesis is available in print at TU Wien Bibliothek.
TU Bibliothek Your knowledge hub WIEN

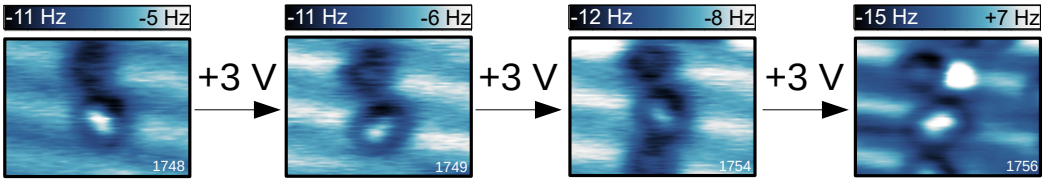

Figure 47: **Sequence of images showing tip-induced rotation of a single τ molecule.** A positive bias-ramp from 0 V to +3 V was performed above the molecule between each frame of the figure.

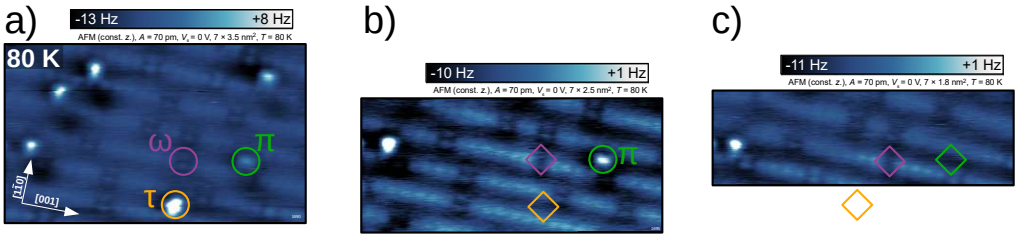

Figure 48: **Tip-induced desorption** a) AFM image of the O_2-covered surface. b) AFM image of the same region after negative bias was ramped above the ω and τ molecules causing their desorption. c) AFM image of the same region after negative bias was ramped above the π molecule causing its desorption.

in the conduction band of a solid, charge manipulation of single adsorbates is more difficult to perform, since injected or removed charge will propagate through a vast volume of the crystal. The semiconducting $TiO_2(110)$ surface partially allows the charge manipulation of single molecules, but the injected/removed charge is likely to propagate across a given surface area. The influence of a large quantity of injected charge to a $TiO_2(110)$ surface with adsorbed O_2 can be seen in Fig. 46a. The AFM image in the right panel of Fig. 46a shows the O_2-covered surface at 80 K. Applying a +3.0 V sample bias pulse over a point on this surface dissociates most of the molecules in the vicinity, as revealed by the AFM image in the left panel in Fig. 46a. These two figures additionally illustrate one of the difficulties of studying this adsorption scenario using STM alone. Besides dissociating the molecules, submolecular resolution in STM is extremely rare and can be obtained only in immediate proximity to the surface where the tip flexibility contributes to the contrast [260, 261, 262], as demonstrated in Fig. 40b.

Molecular species can be deliberately dissociated in a more controlled fashion by using smaller bias values. Figures 46b–46d show the controlled dissociation of each adsorbed O_2 species, performed by ramping the sample bias voltage in the positive direction. The probed molecules can experience a structural or electronic change due to tunneling from the tip to the unoccupied states of the adsorbate. These changes are visible in the Kelvin parabolas [116] taken above the adsorbate, due to the changed electrostatic forces acting on the tip. Namely, the electrostatic forces experienced by the tip are different between a single O_2^{2-} and a pair of doubly ionized oxygen adatoms $2 \times {O_{ad}}^{2-}$. Taking AFM images before and after the positive sample bias ramps confirms that all molecular adsorbates can dissociate. The bias voltage necessary for dissociation varies for different species: ω molecules typically dissociate at a bias of +0.3 to +0.5 V (Fig. 46b), π molecules at a bias of +1.25 V (Fig. 46c), and τ molecules above +3.0 V (Fig. 46d). The τ molecules were observed to either rotate (Fig. 46d top) or dissociate (Fig. 46d bottom) at bias voltages close to +3.0 V.

Dissociation of τ molecules by electron injection appears to be the least probable molecular dissociation channel. Unlike π and ω molecules, which dissociate at much smaller bias voltages, the τ molecules can rotate rather than dissociate when a bias larger than +3 V is applied above them. Figure 47 shows a series of AFM images showing the rotation of a single τ molecule. Between each image, a positive bias ramp was performed above the τ molecule in the same way as in Fig. 46d. Rotation can be performed until the molecule finally dissociates. This series of experiments confirms the robustness of τ molecules to electron injection, noticeable by comparing AFM images before and after electron injection in Fig. 46a. There, some τ molecules remained undissociated while the π molecules dissociated, even though they were located further away from the charge injection point.

Removal of electrons from the adsorbed O_2 leads to the breaking of covalent bonds with the underlying sub-

Die approbierte gedruckte Originalversion dieser Dissertation ist an der TU Wien Bibliothek verfügbar.
The approved original version of this doctoral thesis is available in print at TU Wien Bibliothek.
TU Bibliothek Your knowledge hub WIEN

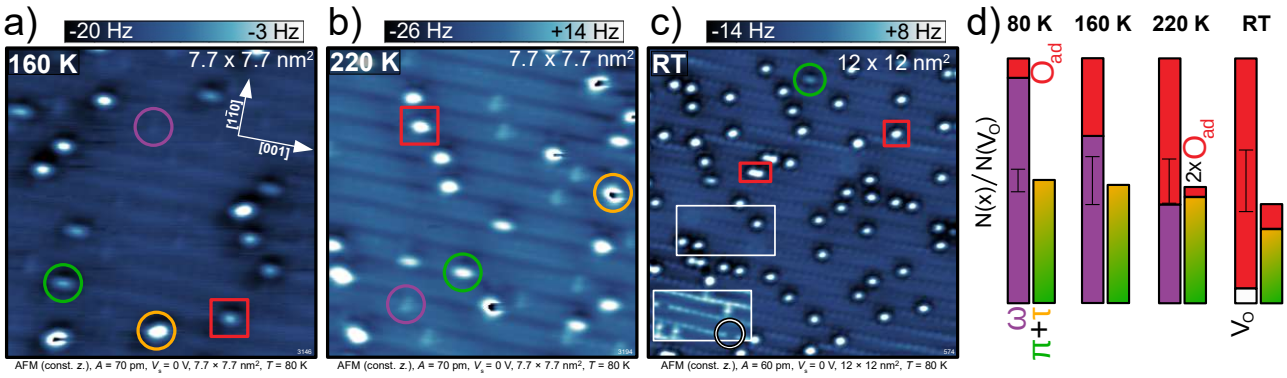

Figure 49: **Annealing of the $TiO_2(110)$ with a close-to-saturation O_2 coverage dosed at 80 K.** AFM images (taken at 80 K) after annealing to a temperature of a) 160 K, b) 220 K, and c) room temperature (RT). The adsorbed molecules and adatoms are marked with the same colors and symbols as in Fig. 39, with one red rectangle marking a pair of atomic O adatoms ($2\times O_{ad}$). The inset in (c) is an AFM image of the white rectangle imaged closer to the surface, showing an empty V_O more clearly in a different contrast. d) Number of adsorbed species $N(x)|x\in\{\omega, \pi+\tau, O_{ad}\}$ at each annealing temperature; both columns are normalized to the number of (empty and filled) oxygen vacancies $N(V_O)$ on the surface.

strate, and the molecules subsequently desorb according to the well-accepted scenario of hole-induced desorption [229, 225]. Figure 48 shows desorption events of all three species, induced by negative sample bias ramps. In this case, electrons are removed (holes are injected) directly above the adsorbed molecules, leading to their desorption. The deliberate desorption of O_2 is experimentally challenging because the desorbing molecule has a high probability of readsorbing at the tip apex, thus destroying the tip functionalization. The desorption experiments were therefore performed with the tip retracted 2 Å from the surface. The change in the electrostatic forces before and after the desorption of molecules is very small at these distances, and the Kelvin parabolas are not observably different. The bias was ramped down to a minimum of -3.0 V for desorption of ω and τ molecules (between Fig. 48a and Fig. 48b) and down to a minimum of -2.0 V for desorption of the π molecules (between Fig. 48b and Fig. 48c). Evidently, the desorption of each molecule performed in Fig. 48 was highly local, mainly because removal of charge immediately results in the removal of the adsorbate, which closes off a pathway for hole tunneling between the tip and the surface.

2.5.5 Annealing

The addition of thermal energy to the surface and the adsorbates triggers exothermic reactions that are otherwise frozen at 80 K. Previous sections showed that the charge manipulation of the adsorbates can lead to either dissociation of molecular desorption. The increase in temperature results in an increased electron mobility on the $TiO_2(110)$ surface, and is therefore expected to induce electron-mediated processes on the adsorbates. Indeed, annealing the O_2-covered surface reveals the gradual activation of various O_2 dissociation channels. Figures 49a–49c show constant-height AFM images taken after exposing the sample to O_2 at 80 K, followed by annealing to different temperatures. All images were taken after the sample was cooled to the measurement temperature of 80 K, hence they reveal the products of thermally activated processes. The amount of adsorbed O_2 was initially close to the saturation coverage.

Single O_{ad} on the surface solely result from the dissociation of the ω molecules, which heals the oxygen vacancy and leaves an isolated O_{ad}. There is no spontaneous appearance of O_{ad} after dosing O_2 at 10 K (the O_{ad} pair on Fig. 39a comes from deliberate O_2/Ti_{5c} dissociation), while the surface exposed to O_2 at 80 K (Fig. 39a) does show a small concentration of isolated O_{ad}. The well-known "vacancy-healing" dissociation channel [212, 206, 213, 187] is therefore active at temperatures below 80 K. This dissociation channel is further promoted by thermal annealing, and already at 160 K the concentration of of ω molecules has notably decreased, followed by a proportional increase of the O_{ad} coverage. This trend continues through the 220 K temperature and no ω molecules are left after room temperature (RT) annealing. Most of them dissociated with the resulting concentration of isolated O_{ad} close to the initial concentration of oxygen vacancies. Additionally, a small fraction of oxygen vacancies reappear empty, indicating a possible weak desorption channel of ω molecules to the gas

Die approbierte gedruckte Originalversion dieser Dissertation ist an der TU Wien Bibliothek verfügbar.
The approved original version of this doctoral thesis is available in print at TU Wien Bibliothek.
TU Bibliothek Your knowledge hub WIEN

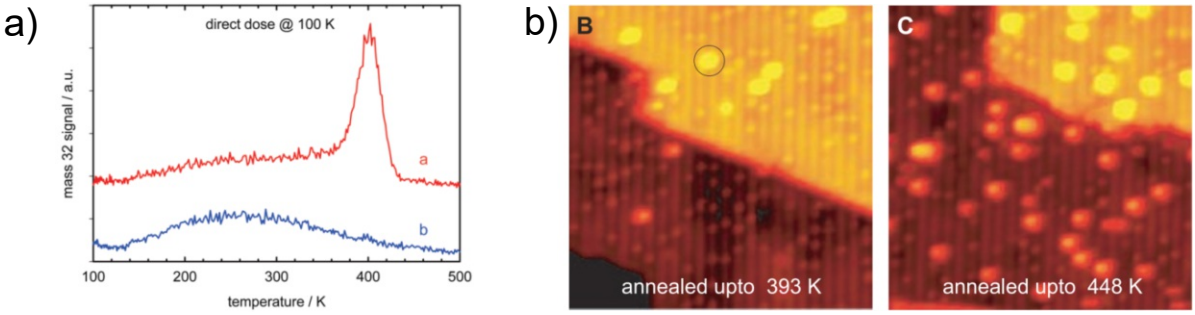

Figure 50: **Literature results on the annealing of the $TiO_2(110)$ surface with O_2 adsorbed at low temperatures.**
a) TPD spectra of a reduced $TiO_2(110)$ surface covered with O_2 at 100 K. Red curve represents the TPD spectra of the as-adsorbed O_2, ramped from 100–500 K with a 2 K/s rate. A clear desorption peak is observable at ≈400 K. The blue curve represents the TPD spectra of the O_2-covered surface after exposure to the UV light, and will be discussed in the following section.
Reprinted top panel of Figure 3 [222] with permission from [David Sporleder, Daniel P. Wilson, and Michael G. White, *The Journal of Physical Chemistry C*, 113, 13180 (2009)]. Copyright (2009) American Chemical Society.
b) STM images (taken at 80 K) of a reduced $TiO_2(110)$ surface exposed to 5 L of O_2 at 120 K, and subsequently annealed to 393 K (left panel) and 448 K (right panel). Both STM images are covered with O_{ad}, while the surface annealed to 448 K exhibits the formation of TiO_2 islands as a result of Ti_{int} segregation towards the surface at elevated temperatures.
Reprinted Figure 4(b,c) [211] from [Stefan Wendt, Phillip T. Sprunger, Estephania Lira, Georg K. H. Madsen, Zheshen Li, Jonas Ø. Hansen, Jesper Matthiesen, Asger Blekinge-Rasmussen, Erik Lægsgaard, Bjørk Hammer, Flemming Besenbacher, *Science*, 320, 1755 (2008)] with permission from AAAS.

phase (O_2(gas) ↑). Empty V_Os were never observed straight after dosing 0.5 L of O_2 at 80 K.

The dissociation of π or τ molecules through the dissociation channel along the Ti_{5c} rows [251] becomes active above 160 K. After annealing the surface to 220 K, O_{ad} pairs appear. With increasing the temperature up to RT, their concentration continues to increase at the expense of the π or τ molecules. Both π and τ molecules are still present on the surfaces after RT annealing, indicating a higher activation energy for dissociation compared to the ω molecules. The increase of the concentration of O_{ad} pairs with the increase in temperatures is not exactly followed by the decrease of the concentration of π and τ molecules (especially after room temperature annealing), implying that a portion of π and τ molecules could desorb during the annealing process.

The statistics in Fig. 49d summarize the abundance of different O_2 species on the surface. They were collected by counting the number of each species $N(\mathrm{x})|\mathrm{x}\in\{\omega, \pi+\tau, \mathrm{O_{ad}}\}$ in at least two representative 60 nm^2 images at each given temperature, and normalizing this number to the number of oxygen vacancies $N(\mathrm{V_O})$ on the respective images (error bars in the stacked bar graphs are equal to $\sqrt{N(\mathrm{V_O})}$). The histogram at each temperature is divided in two columns. The left column represents the total number of oxygen vacancies obtained as a sum of empty oxygen vacancies, ω molecules, and isolated O_{ad} atoms. The right column is the sum of the total number of π and τ molecules, and the number of O_{ad} pairs on the same Ti_{5c} row ($2\times O_{ad}$), which are the products of a dissociation channel along the Ti_{5c} rows, normalized to the concentration of oxygen vacancies as well. The observed, thermally induced reactions, together with the range at which their respective onset temperatures $T_{\min}$ fall, can be summarized as:

$$\begin{aligned}
\omega &\xrightarrow{+T} \mathrm{O_{ad}} + \mathrm{O_{br}} \quad ; \quad 10\ \mathrm{K} < T_{\min} < 80\ \mathrm{K} \\
\pi &\xrightarrow{+T} 2\times\mathrm{O_{ad}} \quad ; \quad 160\ \mathrm{K} < T_{\min} < 220\ \mathrm{K} \\
\tau &\xrightarrow{+T} 2\times\mathrm{O_{ad}} \quad ; \quad 160\ \mathrm{K} < T_{\min} < 220\ \mathrm{K} \\
\omega &\xrightarrow{+T} \mathrm{O_2(gas)} + \mathrm{V_O} \quad ; \quad 220\ \mathrm{K} < T_{\min} < 300\ \mathrm{K}
\end{aligned} \tag{2.3}$$

According to the observations summarized in eq. 2.3, the vacancy-mediated dissociation channel [212, 206, 224, 213] - the dissociation of ω molecules - becomes active at temperatures around 80 K. The dissociation channel of τ and π molecules along Ti_{5c} rows [186, 210, 208, 213] is activated above 160 K. The AFM images

Die approbierte gedruckte Originalversion dieser Dissertation ist an der TU Wien Bibliothek verfügbar.
The approved original version of this doctoral thesis is available in print at TU Wien Bibliothek.
TU Bibliothek Your knowledge hub WIEN

of the O_2-covered surface at 80 K generally show lower concentrations of isolated oxygen adatoms compared to previous STM works [187, 228, 208, 186, 229, 185, 212, 211, 206, 214, 213], mainly due to the prevention of artificial, STM-induced dissociation. The large temperature range of the dissociation events indicates that the process is limited by availability of electrons rather than thermal barriers for dissociation. According to the results in Fig. 46, the dissociation reactions require excess electrons from the substrate which become available upon annealing:

$$\begin{aligned} \omega^{2-} + 2e^- &\rightarrow O_{ad}^{2-} + O_{br}^{2-} \\ \pi^{2-} + 2e^- &\rightarrow 2 \times O_{ad}^{2-} \\ \tau^{2-} + 2e^- &\rightarrow 2 \times O_{ad}^{2-} \end{aligned} \tag{2.4}$$

Each of the thermally activated dissociation reactions drains electrons from the bulk and localizes them at the adsorbed oxygen adatoms. This increases the upwards band bending [116] near the surface and makes every further reaction more difficult. The band bending may be counteracted first by thermal excitations of electrons closest to the Fermi level that help overcome activation barriers, and at higher temperatures by slow diffusion of titanium interstitials Ti_{int} [211, 251, 252, 216] or bulk oxygen vacancies [145] towards the surface.

Some of the oxygen vacancies become empty after annealing, as can be seen in Fig. 49c. This was also apparent in previous STM studies [214] where the O_2-covered surface was exposed to room temperature as well. This result is surprising considering that the dissociation of ω molecules is active already at 80 K, but not all ω molecules are dissociated even at 220 K. This indicates that the competition for electrons at elevated temperatures between the co-adsorbed species is responsible for the desorption of ω molecules. One possibility is that the excess electrons for dissociating π or τ molecules come from an ω molecule co-adsorbed at the surface, leading to breaking the bond of the ω molecules towards the surface and its subsequent desorption. The energy balance calculated from Fig. 41f indicates that such a process could be energetically feasible, while a sole desorption of the ω molecule is unlikely.

The results presented in this section provide additional interpretation to the data obtained in literature, as illustrated in Fig. 50. A typical TPD spectrum of a reduced $TiO_2(110)$ surface exposed to O_2 at low temperatures can be seen in the red curve in Fig. 50a. It exhibits a clear desorption peak at ≈400 K, while a gradual desorption occurs at lower temperatures as well. According to the results presented in Fig. 49d, this TPD peak corresponds to the desorption of π and τ molecules, which were the only molecular species observed to remain adsorbed at the surface exposed to room temperature annealing. The only other species present on the surface after room temperature annealing are the O_{ad}, which cannot desorb spontaneously without association into an O_2 molecule. The TPD peak at ≈400 K is likely not due to the association of the remaining O_{ad}s into O_2 molecule and subsequent desorption, because the O_{ad} experience a different reaction instead, as can be seen in Fig. 50b. At elevated temperatures (>400 K in Fig. 50b), titanium interstitials can segregate towards the surface. Additionally, the increased concentration of Ti_{int}s at the surface or at near-subsurface regions is further promoted by the presence of the remaining O_{ad}s, which induce an oxidizing environment at the surface. Figure 50b therefore illustrates the binding of the remaining O_{ad}s with the out-segregated Ti_{int}s to form stoichiometric TiO_2 islands at the surface at temperatures larger than 400 K, after the desorption of π and τ molecules.

2.5.6 UV-induced reactions

TiO_2 is considered to be a good photocatalyst due to the good separation of the created electrons and holes – the recombination time is long and the free charge carriers are responsible for the observed photochemistry of many adsorbates on this surface. Figure 51 shows the effect of UV light irradiation on the surface exposed to O_2 at 80 K. The UV light was generated by a laboratory Hg lamp, which produced the highest characteristic radiation at 256 nm. This wavelength of the incoming light is sufficiently energetic to overcome the 3 eV band gap of TiO_2 and generate electrons and holes.

Fig. 51a is the starting point of the experiment, before the UV light was applied onto the O_2-covered surface. The highlighted species in Fig. 51a are a guide to the eye for following the reactions after a low dose of UV irradiation (20 W for 20 s), resulting in the surface shown in Fig. 51b. The initial surface was covered with all types of oxygen adsorbates as in Fig. 39. The reactants following the UV irradiation were monitored on the same surface area before and after UV irradiation. The oxygen adatoms are unaffected by UV irradiation irrespective of the dose, and provide reference patterns (red squares in Fig. 51) for locating the same region on the surface after the UV irradiation. Following the evolution of the highlighted molecular species from Fig. 51a to Fig. 51b reveals that very few ω molecules dissociated and left one adatom right next to the now-healed vacancy. On the

Die approbierte gedruckte Originalversion dieser Dissertation ist an der TU Wien Bibliothek verfügbar.
The approved original version of this doctoral thesis is available in print at TU Wien Bibliothek.
TU Bibliothek Your knowledge hub WIEN

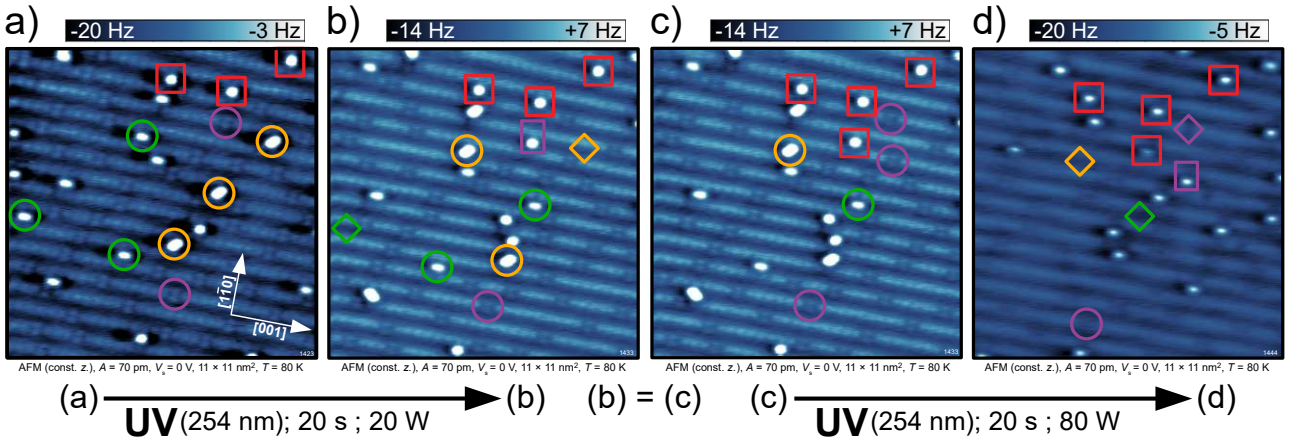

Figure 51: **UV light irradiation of the $TiO_2(110)$ with a close-to-saturation O_2 coverage dosed at 80 K.** AFM images (taken at 80 K) of the same region on the surface a) prior to UV irradiation, b,c) after shining 20 W of UV light for 20 s and d) after additional shining of 80 W of UV light for 20 s. The adsorbed molecules and adatoms are marked with the same colors and symbols as in Fig.39, with the same four O_{ad}s marked in all panels. Desorbed molecules are marked with a correspondingly colored diamond, depending on the type of the desorbed molecule. Panels (b) and (c) show the same AFM image, only differently marked to emphasize different UV-induced reactions after small and large UV doses.

other hand, dissociation of π and τ molecules was not observed. They either remained unaffected, switched the configuration between each other, or molecularly desorbed (marked by diamonds in Fig. 51b). No preference for the desorption of either π or τ molecules was observed. The observed reactions under the first UV dose of 20 W can be summarized as:

$$\begin{aligned} \omega &\xrightarrow{UV} O_{ad} + O_{br} \\ \pi &\xrightarrow{UV} O_2(gas) \\ \pi &\xrightarrow{UV} \tau \\ \tau &\xrightarrow{UV} O_2(gas) \\ \tau &\xrightarrow{UV} \pi \end{aligned} \tag{2.5}$$

An additional dose of 80 W for 20 s of UV light has a stronger impact on the adsorbed O_2, as can be seen by comparing Figures 51c and 51d. All π and τ molecules desorbed (with the exception of a single τ molecule per 121 nm^2 of the surface, not shown). The molecular desorption is therefore the end product of O_2/Ti_{5c} photochemistry. On the other hand, the ω molecules started desorbing under increased UV dose as well:

$$\omega \xrightarrow{UV} O_2(gas) \tag{2.6}$$

Most of the ω molecules still either remained adsorbed or dissociated, similar to their behavior under a small UV dose. The process of molecular desorption of ω molecules under UV illumination demonstrates a lower cross section than the desorption of π or τ molecules, and there is a strong possibility that the ω molecules continue desorbing with the extended exposure to UV light. Altogether, the end product of O_2 photochemistry is a surface with no molecular species adsorbed, but a rather clean surface with a few oxygen vacancies and adatoms.

It is well-established that the UV-induced O_2 dissociation is an electron-induced process, while holes induce O_2 desorption [221, 223, 198, 229, 224, 219, 200, 185, 201, 263, 226]; this has been explicitly demonstrated in Figures 46 and 48. Events observed upon UV irradiation follow the same underlying principle, but appear naturally and provide additional insights. Namely, the coupled electron and hole dynamics occurring under UV illumination is not reflected in the tip-induced events. Additionally, in STM-induced events the potential between the tip and the sample is controlled, but the amount of exchanged charge between the adsorbate and the surface is not well defined: the injection of single charges to the O_2 is hardly achievable on a semiconducting surface, while the removal of charge from the adsorbate is undetectable in the tunneling current.

Die approbierte gedruckte Originalversion dieser Dissertation ist an der TU Wien Bibliothek verfügbar.
The approved original version of this doctoral thesis is available in print at TU Wien Bibliothek.
TU WIEN Bibliothek Your knowledge hub

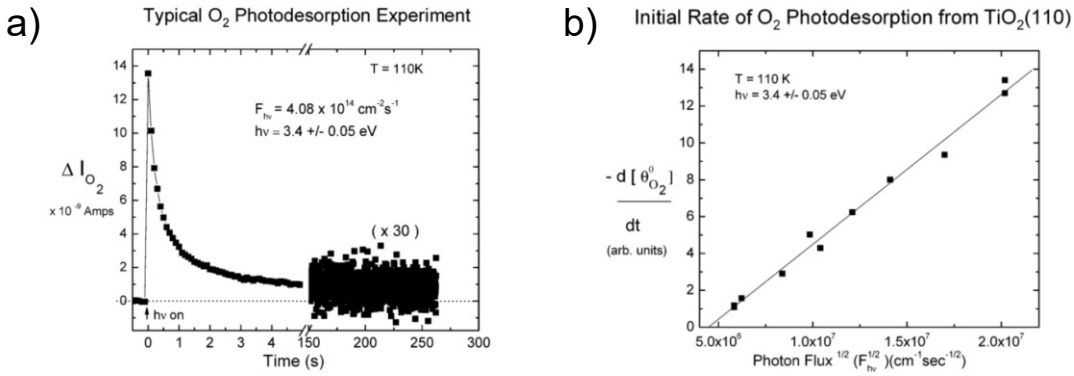

Figure 52: **Literature results of the photo-stimulated desorption (PSD) experiments on the reduced rutile TiO_2(110) surface covered with ≈0.3 ML of O_2 dosed at 110 K.**
a) A single PSD spectrum showing the initial "fast" desorption channel, where a significant amount of O_2 molecules desorb very soon after the onset of UV irradiation, and the subsequent "slow" desorption channel, where O_2 molecules continue to desorb over extended periods of time during the UV irradiation.
Reprinted Figure 2 [221] with permission from [Tracy L. Thompson and John T. Yates, Jr., *The Journal of Physical Chemistry B*, 110, 7431 (2006)]. Copyright (2006) American Chemical Society.
b) A systematic investigation of the "fast" desorption channel from various PSD experiments. Each point of the graph represents a separate experiment, where a surface was repeatedly re-prepared and covered with O_2, and the amount of desorbed O_2 was monitored depending on the flux of the UV irradiation.
Reprinted Figure 3 [221] with permission from [Tracy L. Thompson and John T. Yates, Jr., *The Journal of Physical Chemistry B*, 110, 7431 (2006)]. Copyright (2006) American Chemical Society.

The UV irradiation experiments show that the ω molecules are predominantly active for dissociation, while the π and τ species prefer desorption. This can be related to the fact that the π and τ species have an in-gap state (Fig. 41), which allows them to accept photoexcited holes. Additionally, they are negatively charges species, electrostatically attracting the holes. This is not the case for the ω species: the original oxygen vacancy is 2+ while the ω molecule is 2-. In other words, the charge of the ω molecule is the same as that of the O_{br} atom that it replaces. Together with the absence of an in-gap state, this results in a preference of ω molecules to electron-mediated events.

Results presented here directly shine light on the desorption behaviors reported in literature. Figure 52a shows a typical photo-stimulated desorption (PSD) experiment on a rutile TiO_2(110) surface exposed to O_2 at low temperatures. There, a mass spectrometer was used to measure the quantity of desorbed O_2 molecules during UV irradiation. The PSD spectrum in Fig. 52a clearly shows that a large quantity of O_2 molecules suddenly desorbed, immediately after sample illumination with the UV light. This commonly-observed process is referred to as the "fast" desorption channel [220, 221, 222]. According to the change in the adsorbed species after a small UV dose, presented in Figures 51a and 51b, it is clear that the "fast" desorption channel consists of π and τ molecules that are the first species observed to desorb. After the increased UV dose, the effect of which is presented in Figures 51c and 51d, ω molecules are continuously desorbing with a low cross-section. They constitute a "slow" desorption channel [220, 221, 222], which is commonly observed in PSD spectra, such is the one Fig. 52a, as a long tail of slowly desorbing molecules.

The direct insight into the products of UV induced O_2 reactions presented here also reveals the observed difference between the TPD spectra of the TiO_2(110) surface as-covered with O_2 molecules, and the same surface that was first irradiated with UV, reported in Fig. 50a. Since π and τ molecules are observed to constitute the TPD peak at the temperature of ≈400 K, the absence of this peak after the surface was irradiated with the UV light is not surprising: all π and τ molecules tend to desorb quickly from the surface under UV irradiation and therefore cannot thermally desorb at ≈400 K.

So far, PSD experiments were the strongest indicator of the O_2 charge state in the literature. The desorption rate of O_2 was routinely reported to directly (linearly) depend on the square root of the flux of the UV irradiation, as shown in Fig. 52b. There, each measured point is an entire experiment as the one shown in Fig. 52a: a reduced TiO_2(110) surface was re-prepared and covered with the same ≈0.3 ML of O_2 at 110 K, an altered UV dose was applied, and the number of desorbed molecules in the "fast" desorption channel was counted. This procedure

Die approbierte gedruckte Originalversion dieser Dissertation ist an der TU Wien Bibliothek verfügbar.
The approved original version of this doctoral thesis is available in print at TU Wien Bibliothek.
TU Bibliothek Your knowledge hub WIEN

directly relates the O_2 desorption rate with the increase in the UV flux. The concentration of the UV-generated holes that are available for O_2 photodesorption $[h^+]$ is a crucial quantity in the hole-mediated O_2 desorption processes (Fig. 48). In a kinematic theory, once all hole-trapping sites (such as impurities) are saturated, the concentration of holes available for reaction with the adsorbed O_2 is proportional to the square root of the incoming UV light intensity $\sqrt{F_{h\nu}}$, because a portion of the UV-generated holes are naturally recombined with the UV-generated electrons. Therefore, the graphs such is the one in Fig. 52b are commonly plotted against $\sqrt{F_{h\nu}}$. A linear dependence in Fig. 52b implies that the rate of O_2 desorption is linearly related to the number of available holes $[h^+]$, and therefore that the adsorbed O_2 molecules require only a single hole for desorption. In the same picture, the slope of Fig. 52b is determined by the number of adsorbed molecules and probability of the hole-capture by the adsorbate (both are kept constant in the experiment in Fig. 52b), and the electron-hole recombination probability in a given material. The PSD results in Fig. 52b are a strong indicator that the O_2 desorption from a reduced $TiO_2(110)$ is a one-hole process, *i.e.*, that the adsorbed O_2 are in the superoxo state O_2^-.

The results presented in this Thesis assign the adsorbed molecules to be in the peroxo charge state (Figures 41, 43, and 44), which would yield a quadratic dependence of the desorption rate with the hole concentration $[h^+]$: the desorption of peroxo molecules is an event that requires the simultaneous presence of two holes at the adsorbed molecules and therefore proceeds with the probability of $[h^+]^2$. This is in clear contrast to the strong experimental evidence that the adsorbed O_2 are in the superoxo state O_2^- [220, 221, 222, 223, 226, 225, 224] exemplified in Fig. 52b. However, insights into the atomic-level mechanisms presented here reveal that there are processes that can explain this discrepancy, and result in the number of the desorbed peroxo molecules that linearly depend on the hole-concentration.

The UV-induced desorption of ω molecules was observed to constitute the "slow" desorption channel according to Fig. 51. The reported PSD experiments in Fig. 52 do not focus on the desorption rate within the slow desorption channel, because their quantitative detection is experimentally challenging. This very low desorption rate of ω molecules is consistent with the low cross-section of ω molecules for accepting simultaneously two holes:

$$\omega^{2-} + 2h^+ \rightarrow O_2(\text{gas}) \uparrow$$

and the peroxo assignment of ω molecules is therefore not in conflict with the literature results presented in Fig. 52, that focuses on the desorption mechanisms of the "fast" desorption channel.

The O_2 molecules that constitute the "fast" UV-induced desorption channel were identified in Fig. 51 to be the π and τ molecules. It can be seen by comparing Figures 51a and 51b that these two molecules commonly switch configurations under small UV irradiation $\pi \overset{\text{UV}}{\longleftrightarrow} \tau$, which is at least as frequent as the desorption of either molecule. This atomic-level insight reveals that the π and τ molecules are susceptible to finer transitions, likely to an intermediate metastable state, which can lead to either the the desorption of molecules, or the return to the stable peroxo state. The superoxo variants of the π and τ molecules are a good candidate for this transition state, as they were shown to be metastable on the surface (Fig. 42), and never observed experimentally. Therefore, the proposed desorption model for π and τ molecules would be a two-step two-hole process, proceeding through the metastable superoxo species. In the first step of the two-step process, a peroxo molecule captures a single hole h^+ and transitions to a metastable superoxo species O_2^-/Ti_{5c}:

$$\left(\pi^{2-} \text{ or } \tau^{2-}\right) + h^+ \rightarrow O_2^-/Ti_{5c}. \tag{2.7}$$

In the second step of the two-step process, the metastable state can either desorb in several ways, or revert to the peroxo state with the addition of one electron from the surface. Thermal desorption of metastable superoxo species with a calculated adsorption energy of $E_{\text{ads}} \approx -0.7\,\text{eV}$ (additionally reduced by band bending) is unlikely at the temperature of 80 K in the experiments in Fig. 51. The desorption likely proceeds from the metastable superoxo state O_2^-/Ti_{5c}, by capturing an additional UV-generated hole and leaving the surface as a neutral gas molecule $O_2(g) \uparrow$. However, under UV irradiation, both electrons e^- and holes h^+ are generated. The availability of both charge carriers at the surface implies that the metastable state can also capture an UV-generated electron and return to the stable peroxo species. The geometry of the newly stabilized peroxo species does not have to coincide with the original peroxo configuration, which results in the observed configuration switching $\pi \overset{\text{UV}}{\longleftrightarrow} \tau$. The second step of the two-step process therefore branches in two possibilities:

$$\begin{aligned} O_2^-/Ti_{5c} + h^+ &\rightarrow O_2(g) \uparrow \\ O_2^-/Ti_{5c} + e^- &\rightarrow \pi^{2-} \text{ or } \tau^{2-}. \end{aligned} \tag{2.8}$$

Die approbierte gedruckte Originalversion dieser Dissertation ist an der TU Wien Bibliothek verfügbar.
The approved original version of this doctoral thesis is available in print at TU Wien Bibliothek.
TU Bibliothek Your knowledge hub WIEN

The data in Fig. 51 is too scarce to estimate the probability of processes in equations 2.7 and 2.8, but the two processes in eq. 2.8 appear to occur with similar probabilities.

The proposed two-step two-hole process for π and τ molecules follows the linear dependence on the number of available UV-generated holes, because the only limiting factor for the process is the first step (eq. 2.7). The other step is independent on the UV-generated charge concentration, since it can always revert to the original state. In other words, the probability of the desorption of the peroxo molecules can be expressed as:

$$P\left(\mathrm{O}_2^{2-} \rightarrow \mathrm{O(g)} \uparrow\right) = P\left(\mathrm{O}_2^{2-} \rightarrow \mathrm{O}_2^{-}\right) \cdot P\left(\mathrm{O}_2^{-} \rightarrow \mathrm{O(g)} \uparrow\right) \propto [h^+] \cdot const. \tag{2.9}$$

where $P\left(\mathrm{O}_2^{2-} \rightarrow \mathrm{O(g)} \uparrow\right)$ is the overall probability of desorption ($\propto$ the total number of desorbed molecules), $P\left(\mathrm{O}_2^{2-} \rightarrow \mathrm{O}_2^{-}\right)$ is the probability of peroxo hole capture, and $P\left(\mathrm{O}_2^{-} \rightarrow \mathrm{O(g)} \uparrow\right)$ is the probability of the superoxo hole capture. In eq. 2.9, only the $P\left(\mathrm{O}_2^{2-} \rightarrow \mathrm{O(g)} \uparrow\right)$ term depends on the concentration of available holes $[h^+]$, because the probability of superoxo hole capture is directly related to the probability of superoxo electron capture $P\left(\mathrm{O}_2^{-} \rightarrow \mathrm{O(g)} \uparrow\right) = C - P\left(\mathrm{O}_2^{-} \rightarrow \mathrm{O}_2^{-}\right) = const.$, making the overall probability of the desorption of peroxo molecules linear in the concentration of holes in a two-step two-hole process, in accordance with the results reported in literature (Fig. 52).

It is noteworthy that disproportionation, *i.e.*, converting two metastable superoxo molecules into one peroxo molecule and an additional gas molecule can be ruled out as the desorption mechanism. It is based on a one-hole process, but the reaction rate would still be proportional to $[\mathrm{h}^+]^2$ like a one-step two-hole process, which does not agree with the literature results in Fig. 52. One other possibility for the desorption would be a one-step one-hole desorption process, where a metastable superoxo desorbs due to the kinetic energy it gains in the transition from the peroxo state $\mathrm{O}_2^{-}/\mathrm{Ti}_{5c} + E_{\mathrm{kin}} \rightarrow \mathrm{O}_2(\mathrm{gas}) + \mathrm{e}^-$. This process is more likely to desorb τ molecules than π molecules, because the adsorption geometry of π^{2-} and π^- is very similar, while the adsorption geometry of τ^{2-} and τ^- significantly differ in both in the rotational angle and height (Figures 41, 43, and 44). However, no desorption preference for π and τ molecules was observed. Moreover, the configurations switching $\pi \xleftrightarrow{\mathrm{UV}} \tau$ is less likely within this model, since the energy gain in the peroxo to metastable superoxo transition is sufficient to desorb the molecules. Although this desorption model remains an open possibility, its likelihood is lower than the two-step two-hole process described below.

Figure 53 explores the dependence of the number of desorbed π and τ molecules numerically, with respect to the number of available holes per molecule, for the two-step two-hole desorption model (in Figs. 53a and 53b) and other models for comparison (Figs. 53c and 53d). The presented simulations were realized by performing a Markov chain process on 10^4 peroxo molecules, according to the defined models, where each subsequent step of the Markov process makes an increasing number of UV-generated e^- and h^+ available for reaction with the peroxo molecules. Naturally, the interaction probability of the UV-generated e^- and h^+ with the peroxo molecules is a defined constant, much smaller than 1 to avoid immediate saturation of the desorbed molecules in simulations. Each result in Fig. 53 was averaged over 10 independent simulations of the entire Markov chain for a given model. The results in Fig. 53 are directly comparable with the experiments in Fig. 52, as the observed dependencies on the number of available holes is equivalent to the dependencies on the square root of the incoming UV flux $\sqrt{F_{\mathrm{h}\nu}}$.

The proposed two-step two-hole desorption model for the desorption of π and τ molecules is investigated in Figs. 53a and 53b, as a reversible process which takes into account both equations 2.7 and 2.8. The cross-section for peroxo hole capture $\mathrm{O}_2^{2-} \xrightarrow{+h^+} \mathrm{O}_2^{-}$ is set to a fixed value of 0.01 in both models in Figs. 53a and 53b, and it defines the probability of the initiation of the entire process. However, the second-step branching ratio is different for the two models in Figs. 53a and 53b, and illustrates the proclivity of the metastable superoxo species for the electron capture (readsorption into the peroxo state $\mathrm{O}_2^{-} \xrightarrow{+e^-} \mathrm{O}_2^{2-}$) and the hole capture (desorption as a gas molecules $\mathrm{O}_2^{-} \xrightarrow{+h^+} \mathrm{O(g)} \uparrow$). The sum of the second-step readsorption and desorption probabilities must be equal to unity, because the superoxo species is only metastable and does not persist on the surface. The model in Fig. 53a assumes a high probability of readsorption to the peroxo state at the expense of the desorption probability, while the model in Fig. 53b assumes an equal probability of desorption and readsorption in the peroxo state. Both models yield a linear dependence of the number of desorbed molecules with the increase in available hole concentration, making the proposed two-step two-hole desorption model for π and τ molecules completely in accord with the literature results in Fig. 52.

The validity of the simulation process is verified by simulating the well known one-step two-hole desorption process, the result of which is shown in Fig. 53c. The one-step two-hole peroxo desorption process is well-adopted throughout literature, whenever the desorption rate scales with the square of the UV-generated

Die approbierte gedruckte Originalversion dieser Dissertation ist an der TU Wien Bibliothek verfügbar.
The approved original version of this doctoral thesis is available in print at TU Wien Bibliothek.
TU Bibliothek Your knowledge hub WIEN

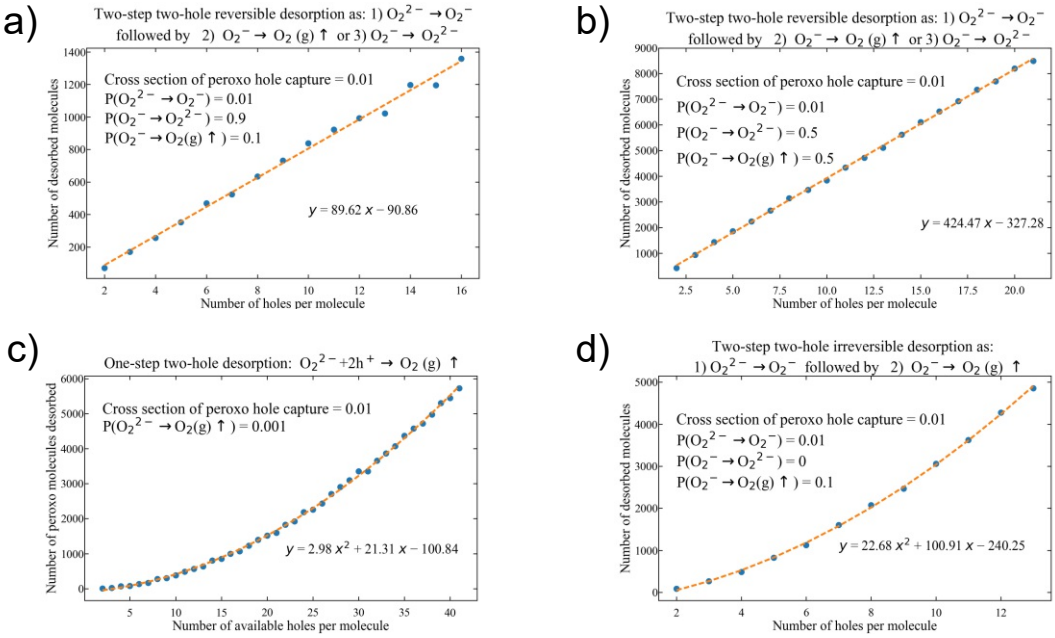

Figure 53: **Markov chain simulations of the UV-induced O_2 desorption in four different models.** a) The proposed two-hole two-step reversible process (described in the text) for the desorption of π and τ molecules in the "fast" desorption channel. The probability of superoxo electron capture (and subsequent return to peroxo) is much greater than the probability of superoxo hole capture (and subsequent desorption) in this simulation. b) The same proposed model as in (a), but the probability of electron capture (return to peroxo) and hole capture (desorption) of the superoxo O_2 is equal. c) The one-step two-hole desorption model of the peroxo molecules, requiring the presence of two simultaneous holes on the peroxo O_2 for desorption. Switching between the stable peroxo and the metastable superoxo state is not permitted. d) The same model as in (c), but it proceeds in two steps: peroxo molecule can capture a hole and transform to a long-lived superoxo species, from which it cannot return back to the peroxo state by capturing an electron. Instead, it can only desorb once the superoxo molecule accepts another hole.

hole concentration, *i.e.*, linearly with the UV flux $F_{h\nu}$. In it, there is no transition to the metastable state, and the probability of desorption can be estimated as the square of the capture probability of a single hole $P\left(O_2^{2-} \rightarrow O(g) \uparrow\right) \approx \left|\left|P\left(O_2^{2-} \rightarrow O_2^-\right)\right|\right|^2 \propto [h^+]^2$. The curve in Fig. 53c clearly exhibits a quadratic dependence on $[h^+]$, thereby validating the approach. In this research, the desorption of ω molecules is assigned to proceed through such a process. An irreversible two-step two-hole peroxo desorption model is investigated in Fig. 53d. There, the desorption proceeds through the transition superoxo state, but this state is considered stable at the surface and does not switch back to the peroxo state. This model converges to the one-step two-hole process (Fig. 53c) when the probability of superoxo hole capture is set to be equal to the peroxo hole capture probability. In the model in Fig. 53d, this probability is ten times higher than the probability of the peroxo hole capture. This model, with the long-lived superoxo species as an intermediate state, not-surprisingly also yields a quadratic dependence on the number of available holes. This type of desorption process is not observed in this research, since the superoxo O_2 species are only metastable at the surface.

The described two-step two-hole process explains the observed transitions between the π and τ molecules under small UV dose in Figs. 51a and 51b. The detailed view on some of these transformations reveals that π and τ molecules diffuse along the same Ti_{5c} row during UV irradiation, probably due to a sequence of $\pi \xrightarrow{UV} \tau$ transformations, as can be seen in Fig. 54. The photo-blind O_{ad} is used as a reference for following this diffusion, marked by the intersection of red broken lines. Figures 54a and 54b focus on the evolution of a τ molecule before and after 20 s of 20 W of UV irradiation. Even though the τ molecule has not been desorbed or transformed to a π molecule, it shifted its position two unit cells closer to the reference O_{ad}. In a two-step two-hole process, the diffusion of the τ molecule can be rationalized by first accepting a UV-generated hole to become an unstable superoxo O_2^-, and subsequently capturing an electron to return to the stable peroxo state. However, during

Die approbierte gedruckte Originalversion dieser Dissertation ist an der TU Wien Bibliothek verfügbar.
The approved original version of this doctoral thesis is available in print at TU Wien Bibliothek.
TU Bibliothek Your knowledge hub WIEN

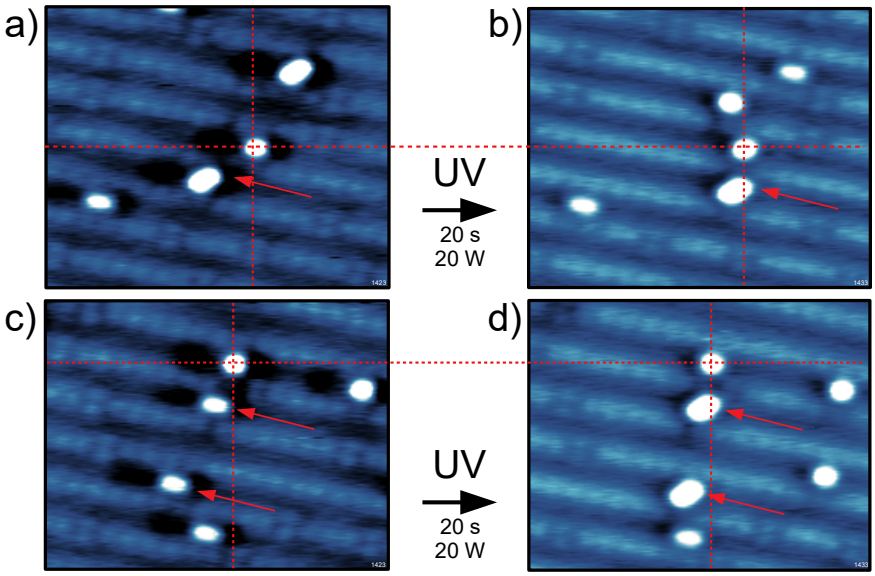

Figure 54: **UV-induced diffusion and switching of π and τ molecules.** a,c) Constant-height AFM images of the surface prior to UV irradiation. b,c) Constant-height AFM images of the surface after 20 s of 20 W UV irradiation: Panels (a) and (c) are the enlarged segments of Fig. 51a while panels (b) and (d) are enlarged segments of Fig. 51b. Molecules of interest are marked with a red arrow, while the photo-blind O_{ad} is used as a reference point.

this process, the electron captured by the intermediate superoxo species forms a new bond to a lattice Ti_{5c}, which does not have to coincide with the original bond to the substrate. This molecule has effectively moved two unit cells at temperatures of 80 K, by transforming to the unstable superoxo and readsorbing back to the stable peroxo state in a new configuration. A similar example is seen when comparing Figs. 54a and 54b, which focus on two π molecules before and after 20 s of 20 W of UV irradiation. Both π molecules have transformed to a τ molecule. However, one has diffused one unit cell further than the other one. The longer translation of one molecule can be either because this molecule had undergone more transformation processes than the other (at least one reaction more), or because the metastable superoxo O_2^- species is mobile on the surface and can diffuse several unit cells.

2.5.7 Conclusions

This research identified *all* adsorption configurations of molecular O_2 species adsorbed to a reduced rutile $TiO_2(110)$ surface at low temperature, in a controlled environment like UHV. This was made possible through the use of non-intrusive nc-AFM imaging, which reveals the true adsorption geometry without interfering with the surface. The clear imaging contrast in AFM images is due to the use of passivated O-terminated tips that were explicitly shown to exhibit small attractive force between the tip and the adsorbates of a purely van der Waals character. This type of tip termination shows promise for further studies of oxide surfaces.

Clear AFM imaging without dissociation recorded three molecular O_2 species: two adsorbed on the Ti_{5c} rows, and one adsorbed in the oxygen vacancy. The isolated oxygen adatoms O_{ad} sitting above Ti_{5c} atoms at the surface appear as a result of the molecular O_2 dissociation. The adsorption was simulated using DFT+U on a reduced slab and all the molecular adsorbates were assigned to be peroxo O_2^{2-}, while the adatoms are doubly ionized O_{ad}^{2-}. The calculations show charge transfer from the polaron-hosting Ti_{6c} sites to the adsorbed oxygen species followed by a change or complete disappearance of the in-gap state characterizing a reduced slab with oxygen vacancies.

The unintentional O_2 dissociation in previous STM studies made it difficult to judge the stability of molecular species for dissociation through two well-known dissociation channels. The non-intrusive AFM imaging revealed temperature ranges in which different O_2 species spontaneously dissociate: vacancy-assisted dissociation is active at temperatures below 80 K and dissociation of molecules on the Ti_{5c} rows is active at temperatures above 160 K. At room temperature, no molecules are left inside oxygen vacancies, but some remain on the Ti_{5c} rows, giving

Die approbierte gedruckte Originalversion dieser Dissertation ist an der TU Wien Bibliothek verfügbar.
The approved original version of this doctoral thesis is available in print at TU Wien Bibliothek.
TU Bibliothek Your knowledge hub WIEN

rise to the well-known TPD peak around 400 K. The same methodology was applied to studying the UV-induced reaction at the surface, to reveal that O_2/Ti_{5c} molecules prefer photodesorption under UV irradiation, while O_2/V_O mostly dissociate under the same conditions. The dissociation/desorption of O_2 was explicit shown to be electron-/hole-mediated process, through local injection/removal of electrons with the AFM/STM tip. Within the model of O_2 peroxo adsorption, the desorption of O_2/Ti_{5c} is either a one-step one-hole process, where the single hole can desorb a peroxo molecule, or a two-step two-hole process with an intermediate, metastable superoxo state.

Results presented in this research aimed to provide a clear insight into the long-standing questions of O_2 adsorption to this surface. With these insights, previous literature data were furnished with a new interpretation, and several inconsistencies caused by unintentional disturbance of the adsorbed molecules were settled. The knowledge of the charge state of the adsorbed molecules, their thermal stability and the preference for UV-induced reactions is of paramount importance for further studies of interaction of oxygen with rutile $TiO_2(110)$ surface and the faces of rutile TiO_2 nano-particles. Moreover, the methodology presented here is readily applicable to studies of different oxides and their interaction with adsorbates.

Die approbierte gedruckte Originalversion dieser Dissertation ist an der TU Wien Bibliothek verfügbar.
The approved original version of this doctoral thesis is available in print at TU Wien Bibliothek.
TU Bibliothek Your knowledge hub WIEN

2.6 Summary and Outlook

In this Chapter, the application of the nc-AFM technique that provides unprecedented atomic resolution, in combination with STM and DFT calculations that properly describe the polaronic ground state of the system, greatly aided resolving several long-standing questions regarding the interaction of adsorbates with a clean rutile $TiO_2(110)$. Revealing these interactions at a fundamental level in a well-controlled environment is a necessary foundation for understanding and predicting the behavior of this technologically important surface at more realistic conditions.

The rutile $TiO_2(110)$ surface reduced by intrinsic oxygen vacancies was examined in UHV and at low temperatures. The bulk properties of rutile $TiO_2(110)$ are introduced in Section 2.1, while its (110) surface properties and preparation methods are introduced in Section 2.2. Such surface hosts small electronic polarons at subsurface Ti atoms in the vicinity of each electron-donating oxygen vacancy, a result deduced jointly from experiments and theory. This polaronic ground state is introduced in Section 2.3; it is altered upon the adsorption of small gas molecules.

Weakly adsorbed (physisorbed) CO molecules are shown in Section 2.4 to cause only a slight alteration to the polaronic ground state. They promote the subsurface polarons towards the surface, by weakly coupling to them and accepting a fraction of the polaronic charge into their anti-bonding $2\pi^*$ molecular orbital. The adsorbed molecules were imaged with AFM as single protrusions. Simultaneous filled-states STM on the other hand, provided the resolution of a single electronic orbital. CO molecules that are coupled to a surface polaron are imaged as a double-lobed feature with STM, in a geometry that corresponds to the shape of the CO $2\pi^*$ anti-bonding molecular orbital. Three CO adsorption sites were revealed with AFM, and the DFT calculations predicted the CO molecules adsorbed at regular Ti sites on the surface to be the least energetic of the three, while the adsorption of CO inside an oxygen vacancy or the adsorption *via* coupling to a polaron at a Ti site are preferable with a similar adsorption energy. The adsorption of CO in the nearest-neighboring site to an oxygen vacancy was rarely observed in AFM even after increased CO coverage, and this configuration was predicted as unfavorable by DFT.

Strongly adsorbed (chemisorbed) O_2 molecules are shown in Section 2.5 to accept electron polarons and use them for creating strong chemical bonds to the substrate, thereby depleting electron polarons from the bulk and canceling the polaronic distortions. Four different oxygen adsorption configurations, imaged with AFM, are discussed in Subsection 2.5.1: two molecular species bound to the Ti rows, one molecular species within an oxygen vacancy, and isolated oxygen adatoms that are the product of O_2 dissociation at the surface. DFT calculations in Subsection 2.5.2 predict that all molecular configurations are in a peroxo charge state, while the isolated adatoms are doubly ionized. The convergence between AFM and DFT was described in Subsection 2.5.3. Experimental force-distance curves above the adsorbates were simulated using a realistic AFM tip model, and a simulated constant-height AFM image was constructed. All adsorbed O_2 molecules were shown in Subsection 2.5.4 to be susceptible to electron-mediated dissociation and hole-mediated desorption. On the other hand, differently adsorbed O_2 molecules prefer different reaction pathways when the system is provided with thermal energy during annealing: the strongest-adsorbed molecules within oxygen vacancies tend to dissociate and desorb at much lower temperatures than the molecules that reside on the Ti rows, which remain adsorbed even after the surface was heated to room temperature. Temperatures at which different dissociation channels are active were recognized by direct observation. It was shown in Subsection 2.5.6 that O_2 adsorbed at inequivalent sites behave differently when provided excess charge *via* UV irradiation: molecules within oxygen vacancies prefer dissociation and constitute the previously-described "slow" desorption channel, while molecules at the Ti rows prefer desorption and constitute the "fast" desorption channel. It was also observed that two molecular configurations on the Ti rows can mutually interchange upon UV irradiation, which led to the development of the two-step two-hole desorption model for these molecules; the validity of which was confirmed by simulated Markov chains. Such a model successfully explains the observed behavior and furnished previous literature results with a new interpretation.

Beside answering several long-standing questions regarding the interaction of the rutile $TiO_2(110)$ surface with CO and O_2 molecules, this Chapter laid-out the methodology that enables well-posed studies of oxide surfaces. Namely, AFM was shown to not disturb the adsorbates, while proper treatment of the ground state of the surface with DFT was shown to explain the observed behavior of the adsorbates. The employed methodology is widely applicable to other oxide surfaces, many of which are technologically relevant.

Die approbierte gedruckte Originalversion dieser Dissertation ist an der TU Wien Bibliothek verfügbar.
The approved original version of this doctoral thesis is available in print at TU Wien Bibliothek.
TU Bibliothek Your knowledge hub WIEN

Chapter 3

Bulk-truncated $SrTiO_3$(001) surface

3.1 Introduction $SrTiO_3$

$SrTiO_3$ crystallizes in a cubic perovskite ABO_3 structure at room temperature, and is commonly referred to as the model system for the entire perovskite oxide class of materials. The occurrence of natural $SrTiO_3$ crystals is rare, and only the synthetic $SrTiO_3$ crystals were believed to exist until the discovery of tausonite in 1982 [264]. The standard procedure for the growth of synthetic $SrTiO_3$ is flame-fusion [265], after which the desired crystal surfaces can be obtained by milling and high quality polishing. Optical photographs of $SrTiO_3$ single crystals with different doping levels are shown later, in Fig. 87.

Bulk $SrTiO_3$ is characterized by a cubic unit cell with $Pm3m$ symmetry and a lattice parameter of $a = 3.905$ Å [266], as illustrated in Fig. 55a. Within the solid, each Sr atom is centered in a surrounding O cuboctahedron, while each Ti atom is centered in the surrounding O octahedron. Along the main crystallographic axes, *i.e.*, the (100) family of directions, $SrTiO_3$ can be decomposed into SrO and TiO_2 layers, illustrated in Fig. 55b. The overall bonding in a $SrTiO_3$ solid is considered to be mixed ionic and covalent, since the SrO layers exhibit mostly ionic bonding while the TiO_2 layers are characterized by strong covalent bonding [267]; the covalent bonding is particularly strong within the TiO_6 octahedra due to hybridization of Ti $3d$ states with the O $2p$ states [268]. In bulk $SrTiO_3$, the bottom of the conduction band is built from the t_{2g} and e_g states of the Ti $3d$ orbitals, while the top of the valence band stems from the O $2p$ states. The band structure of the bulk crystal obtained with DFT calculations using the B3PW hybrid functional is reported in Fig. 55c. The bottom of the conduction band lies at the Γ point, while the top of the valence band is displaced to the R point [269]. This makes the $SrTiO_3$ a semiconductor with an indirect R–Γ band gap of 3.25 eV and a direct Γ–Γ band gap of 3.75 eV [270].

$SrTiO_3$ is suitable for a wide range of technologically relevant applications [271]. The indirect band gap of $SrTiO_3$ (Fig. 55c) makes it a promising candidate for photocatalytic reactions, due to longer lifetime of electron-hole pairs compared to materials with a direct band gap [272]; granted that it is illuminated with UV light that can excite electrons across the wide band gap. Several photocatalytic reactions were demonstrated to occur on various $SrTiO_3$ surfaces such as water splitting [273, 274, 275], water oxidation [276], antibiotic degradation [277], gas-phase NO removal [278], CO_2 reduction [279] and many others. $SrTiO_3$ can be used as a gas-sensor, most commonly for oxygen sensing, as a resistance-based gas sensor [280]. In this approach, the conductivity of $SrTiO_3$ changes depending on the partial pressure of O_2 gas at the active side of the material: it drops in the presence of a high concentration of O_2. This increase of $SrTiO_3$ resistivity is commonly attributed to the O incorporation into $SrTiO_3$ that is intrinsically doped with the electron-donating oxygen vacancies. The successful incorporation of external O into the defect-rich $SrTiO_3$ requires elevated temperatures of 850–950 °C [281], while this process can also be efficient at temperatures as low as 40 °C when $SrTiO_3$ is used in a nano-faceted form [282]. It is noteworthy that undoped $SrTiO_3$ is a natural choice for this type of gas-sensing, because the Nb-doped $SrTiO_3$ has a negligible concentration of intrinsic V_Os [283]. The ready availability of $SrTiO_3$ makes it a promising and affordable anode material for solid oxide fuel cells. Here, both the ionic and the electronic conductivity are necessary for providing a good catalyst for hydrogen fuel oxidation, that results in the generated heat and current, with water as a by-product if H_2 is used as a fuel [284]. For this purpose, $SrTiO_3$ anodes are prepared such that they are substitutionally doped with La/Y or Fe/Nb at A- and B-cation sites, respectively [285, 286]. A-site doping is performed to achieve improved conductivity, while B-site doping additionally promotes ionic conductivity [287]. $SrTiO_3$, either alone, or with added heterostructures

Die approbierte gedruckte Originalversion dieser Dissertation ist an der TU Wien Bibliothek verfügbar.
The approved original version of this doctoral thesis is available in print at TU Wien Bibliothek.
TU Bibliothek Your knowledge hub WIEN

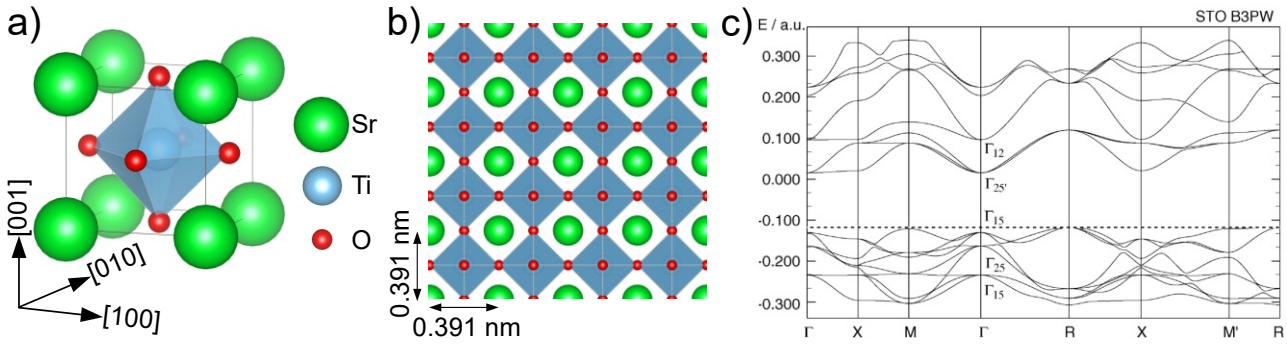

Figure 55: **Bulk $SrTiO_3$ crystallographic and electronic properties.**
a) Ball-and-stick model of a single unit cell of the cubic $SrTiO_3$ perovskite.
b) Ball-and-stick model of several bulk unit cells, viewed from the front of one of the main crystallographic planes.
c) Calculated band structure of stoichiometric $SrTiO_3$ across the first Brillouin zone.
Reprinted Figure 2(a) [269] with permission from [S. Piskunov, E. Heifets, R.I. Eglitis, and G. Borstel, *Computational Materials Science*, 29, 165 (2004)]. Copyright (2004) Elsevier.

on its surface, was also reported as a promising memristive material [288, 289], where the transport of oxygen vacancies through the bulk can provide non-linear, weighted memory pathways useful for the physical realization of neural networks [290].

In most of these applications, the bulk properties and the mesoscopic surface properties of $SrTiO_3$ are exploited, while the atomically clean $SrTiO_3$ surfaces also provide a plethora of possibilities for applications, discussed in the following Section.

3.1.1 Introduction to the $SrTiO_3$(001) surface

Studies and applications of $SrTiO_3$ are exclusively performed on synthetically grown crystals that can be custom-shaped and grown in the desired orientation; therefore the natural occurrence of differently faceted crystals cannot be used to judge the lowest-energy facets. The stability of different surfaces can be calculated however, and the energetically most favorable $SrTiO_3$ surfaces are (100), (110), and (111), with the (100) face having the smallest, and (111) the largest surface Gibbs free energy of the three [291]. The choice of different facets of $SrTiO_3$ mostly depends on the desired chemical structure of the terminating surface: In theory, the (100) surface can be terminated by either a SrO or a TiO_2 layer, the (110) surface by either $SrTiO^{4+}$ or ${O_2}^{4-}$ layer, and the (111) by either Ti^{4+} or ${SrO_3}^{4-}$ [292]. Differently faced $SrTiO_3$ surfaces are also desired in homeoepitaxy, each face has a distinct lattice constant that is useful for growing crystalline films of materials with differently sized unit cells. $SrTiO_3$ surfaces are a common substrate for the growth of other perovskites, due to the small lattice mismatch with many superconductors [293, 294, 295], topological insulators [296, 297, 298], and other perovskite oxides [299, 300, 301, 302].

$SrTiO_3$ surfaces have attracted significant attention in fundamental studies ever since the seminal discovery of a two-dimensional electron gas (2DEG) at a surface of this otherwise insulating (wide band gap semiconducting) solid [303]. Figure 56a reports the appearance of a 2DEG at a bare $SrTiO_3$(001) surface. The rationale behind the appearance of this highly-mobile electron carrier sheet at the surface of bare $SrTiO_3$ can be understood through the argumentation of a tight-binding model. The overlap of the Ti $3d$ orbitals at the bottom of the conduction band (d_{xy}, d_{yz}, and d_{xz}) makes each band highly dispersive along two directions, and weakly dispersive along the third axis — for example, d_{xy} is highly dispersive along x and y axes, while weakly dispersive along the z axis. Due to the symmetry breaking at the surface, the degeneracy of the orbitals that contain the z component is lifted, while the d_{xy} remains degenerate. At the same time, symmetry breaking at the surface yields the highest overlap of the d_{xy} orbitals at the neighboring Ti sites, and this band is therefore the only one that can host the observed 2DEG [304]. The Fermi surface of this band is therefore a circle, as can be seen in the red broken line in the simulated Fermi surface shape in Fig. 56a, and angle-resolved photoelectron emission (ARPES) measurements coincide with this shape. A $SrTiO_3$ surface is not conducting however, and the origin of intrinsic charge carriers (electrons) that constitute the 2DEG is commonly assigned to electron-donating

Die approbierte gedruckte Originalversion dieser Dissertation ist an der TU Wien Bibliothek verfügbar.
The approved original version of this doctoral thesis is available in print at TU Wien Bibliothek.
TU Bibliothek Your knowledge hub WIEN

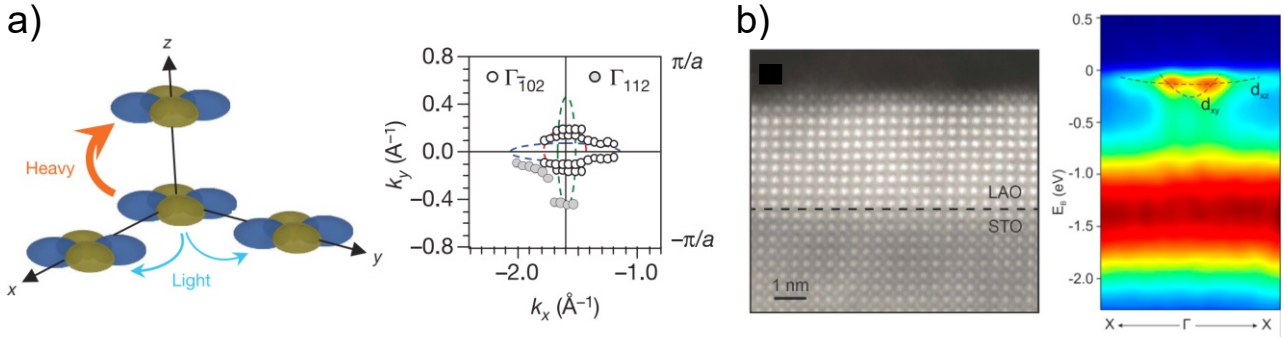

Figure 56: **Two-dimensional electron gas at the $SrTiO_3$(001) surface.**
a) The left panel shows a model of the bottom of the conduction band in $SrTiO_3$, formed by the Ti 3d states. A tight-binding model predicts d_{xy} and d_{yz} as the highly-dispersive (light) bands, and d_{xz} as the weakly-dispersive (heavy) bands, due to the different wavefunction overlap between the neighboring atoms. The right panel shows calculations (broken lines) and ARPES measurements (circles) of the Fermi surfaces at the bottom of the conduction band, consistent with the presence of a 2DEG.
Reprinted Figure 1(b) and Figure 4(c) [304] with permission from [A. F. Santander-Syro, O. Copie, T. Kondo, F. Fortuna, S. Pailhès, R. Weht, X. G. Qiu, F. Bertran, A. Nicolaou, A. Taleb-Ibrahimi, P. Le Fèvre, G. Herranz, M. Bibes, N. Reyren, Y. Apertet, P. Lecoeur, A. Barthélémy, and M. J. Rozenberg, *Nature*, 469, 189 (2011)]. Copyright (2011) Springer Nature.
b) The left panel shows a TEM image of the interface between $LaAlO_3$ grown on $SrTiO_3$(001).
Reprinted Figure 1(a) [316] with permission from [Nicholas J. Goble, Richard Akrobetu, Hicham Zaid, Sukrit Sucharitakul, Marie-Hélène Berger, Alp Sehirlioglu, and Xuan P. A. Gao, *Scientific Reports*, 7, 1 (2017)] under the Creative Commons CC BY license.
The right panel shows the ARPES measurements of the band structure at the interface between $LaAlO_3$ grown on $SrTiO_3$(001), showing both, the highly- and weakly-dispersive bands as on the bare $SrTiO_3$(001) surface.
Reprinted Figure 1(b) [307] with permission from [Alla Chikina, Frank Lechermann, Marius-Adrian Husanu, Marco Caputo, Claudia Cancellieri, Xiaoqiang Wang, Thorsten Schmitt, Milan Radović, and Vladimir N. Strocov, *ACS Nano*, 12, 7927 (2018)]. Copyright (2018) American Chemical Society.

oxygen vacancies at the surface or in the near-surface region, continuously created by the synchrotron radiation during an ARPES experiment [305]. A similar 2DEG also appears at the interface of the $SrTiO_3$(001) surface with other bulk-insulators like $LaAlO_3$ [303, 306, 307], γ–Al_2O_3 [308, 309], $NdAlO_3$ [310], and others [311]. Figure 56b reports on the most studied case of such 2DEG, appearing at the $LaAlO_3/SrTiO_3$(001) interface. The lattice mismatch between these two insulating materials is small, and the growth of $LaAlO_3$ can be readily performed; a cross-sectional TEM image of this interface is seen in the left panel of Fig. 56b. The appearance of a 2DEG at this interface is also commonly attributed to the oxygen deficiency either during ARPES measurements [307], or during growth, but it is also sometimes attributed to the necessary polarization compensation at the interface of a polar $LaAlO_3$ and non-polar $SrTiO_3$ along the [001] direction [312]. In either case, the high carrier mobility sheet buried at the interface of two insulating oxides provides a promising leap towards the realization of all-oxide electronics [313, 314, 315].

3.1.2 Standard $SrTiO_3$(001) surface preparation

The preparation of a clean and unreconstructed $SrTiO_3$(001) surface has been long discussed, since particular care must be taken to avoid surface reconstructions – perovskite surfaces in general have a tendency to reconstruct [317, 318, 319]. On a $SrTiO_3$(001) surface in particular, many different surface reconstructions were observed after typical cleaning procedures in UHV (high-temperature annealing and/or ion sputtering) that remove air-borne contaminants. Surfaces prepared by all preparation methods advocated throughout the literature have never however been explicitly shown to be (1×1)-terminated, and in the remainder of this Chapter it will be shown that the existence of such an unreconstructed surface termination through standard preparation techniques is questionable.

Die approbierte gedruckte Originalversion dieser Dissertation ist an der TU Wien Bibliothek verfügbar.
The approved original version of this doctoral thesis is available in print at TU Wien Bibliothek.
TU Bibliothek Your knowledge hub WIEN

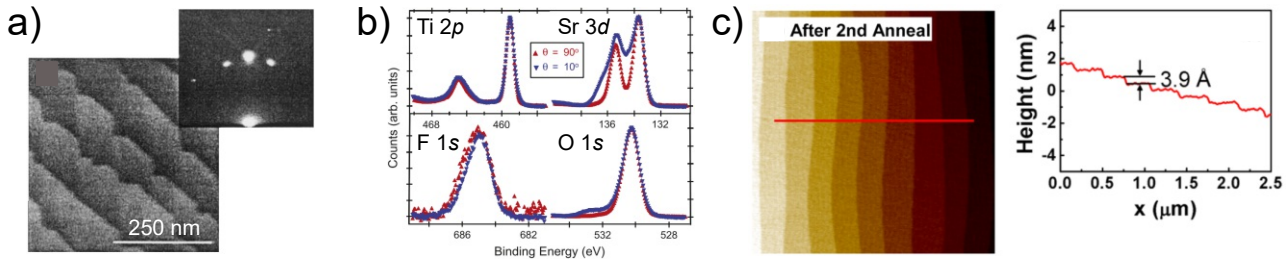

Figure 57: **Standard $SrTiO_3$(001) preparation using wet-chemical treatment.**
a) Ambient AFM image of a $SrTiO_3$(001) prepared by etching with buffered-HF and baking in atmosphere at 950 °C, showing large flat terraces. The RHEED pattern shown in the inset is consistent with a (1×1)-terminated surface.
Reprinted Figure 1(b) [320] with permission from [Gertjan Koster, Boike L. Kropman, Guus J. H. M. Rijnders, Dave H. A. Blank, and Horst Rogalla, *Materials Science and Engineering: B*, 56, 209 (1998)]. Copyright (1998) Elsevier.
b) XPS core-level spectra of Sr, Ti, and O of a $SrTiO_3$(001) surface prepared by etching with buffered-HF, with the addition of a XPS signal originating from the unintentionally implemented F atoms during this surface preparation.
Reprinted Figure 2 [321] with permission from [S. A. Chambers, T. C. Droubay, C. Capan, and G. Y. Sun, *Surface Science*, 606, 554 (2012)]. Copyright (2012) Elsevier.
c) Ambient AFM image of a $SrTiO_3$(001) prepared by etching with ultra-pure water and baking in atmosphere at 950 °C, showing large flat terraces. The line profile at the right side shows that all terrace steps are one unit cell high, confirming the presence of the TiO_2-termination only.
Reprinted Figure 1(e,f) [322] with permission from [J. G. Connell, B. J. Isaac, G. B. Ekanayake, D. R. Strachan, and S. S. A. Seo, *Applied Physics Letters*, 101, 251607 (2012)]. Copyright (2012) AIP Publishing.

The most common $SrTiO_3$(001)(1×1) surface preparation method is wet-chemical treatment, summarized in Fig. 57. Since the first report of a flat surface on a large-scale [323], etching the polished-surfaces by buffered-HF has been extensively applied up to this date. Etching with buffered-HF preferentially removes the SrO layer from the mixed-layered surfaces after polishing, and leaves the surface fully TiO_2-terminated. These surfaces are subsequently baked to high temperatures in atmosphere (950 °C for several hours), which transforms the ill-defied surface to a surface fully covered with flat, TiO_2-terminated terraces [324, 320], as can be seen in Fig. 57a. Such surface treatment is commonly applied for preparing of substrates for homeoepitaxy, and their RHEED patterns are commonly in accord with a perfectly (1×1)-terminated surface. However, this method was re-examined several times [325, 326, 327, 328, 329] and it was shown by XPS it can induce an unintentional substitution of oxygen with F [321], as shown in Fig. 57b. The substitution of O atoms with F atoms is not straightforward to measure with XPS because the F 1*s* signal in XPS is weak due to modest concentrations of substituted F in the surface and near-subsurface layers compared to the bulk, and due to the weak cross-section of F for photo-electron emission, and due to the x-ray induced desorption of F during measurements. For this reason, the F substitution has probably occurred far more than anticipated and desired. The F-doping can be avoided by etching the surface with HCl–HNO_3 [330] or non-acidic solvents like ultra-pure H_2O [321, 322, 331]. Boiling a sample in H_2O also etches away the SrO, due to its solubility in water, albeit increased temperatures are necessary for a quick surface preparation – typically less than 1 min of boiling in ultra-pure water is sufficient for creating solely TiO_2-terminated surface. Surfaces etched with H_2O can also be smoothed by baking in atmosphere to above 900 °C, as can be seen in an ambient AFM image in Fig. 57c together with the line profile along the indicated red line.

Regardless of the etching method, etched surfaces must undergo annealing to at least 600 °C after introduction into vacuum to remove air-borne and other adsorbates. Up to this temperature, perfectly flat, TiO_2-terminated surfaces usually display a (1×1) pattern in LEED or reflection high-energy electron diffraction (RHEED) [326, 332], while a series of surface reconstructions appear after annealing at higher temperatures [329, 333, 327, 334]. Some reconstructions were atomically resolved using STM including the (1×2), (2×2), c(4×2), c(4×4), and c(6×2) [326, 335, 336, 331], and several more on surfaces that were sputtered and annealed in UHV [325]. Reconstructed surface of perovskites are very stable and chemically inert, which is exactly the opposite to their desired behavior in most applications.

Die approbierte gedruckte Originalversion dieser Dissertation ist an der TU Wien Bibliothek verfügbar.
The approved original version of this doctoral thesis is available in print at TU Wien Bibliothek.
TU Bibliothek Your knowledge hub WIEN

Thermal treatment of the crystal surface in order to desorb the contaminants is a highly energetic process, which is the probable cause of the observed plethora of reconstructions. The reconstructions seem to be energetically more stable against high temperature treatment, and obtaining the unreconstructed surface should be performed through a process that would kinematically hinder the (1×1) termination. Cleaving a single crystal in UHV at room or low temperature would therefore be an obvious solution for obtaining a pristine surface, because the thermal treatment could be completely circumvented. However, the main impediment in cleaving the $SrTiO_3$ lies in its cubic bulk symmetry, which, in general, does not provide cubic perovskites with a natural cleaving plane. They commonly exhibit the conchoidal fracture, which is not atomically defined and does not posses well-oriented planes at the cleaved surface: this type of cleavage is common for amorphous materials such as glass. It is important to distinguish that some cubic crystals like NaCl cleave easily due to the weak ionic character of the bonds between atoms. The cleaving in $SrTiO_3$ is difficult due to the strong covalent bonding within TiO_6 octahedra, where each of the 6 covalent bonds is equivalent due to the cubic symmetry. This consideration generally holds true for other cubic perovskite oxides as well.

Cleaving a single crystal $SrTiO_3$ doped with Nb in UHV was attempted previously with limited success. Large, flat terraces along on the (001) surface were obtained in [337, 338], while stripped, irregular terraces were obtained in [339, 340]; none of the studies revealed an atomic resolution of the (1×1) termination. An overall understanding of the cleaved surfaces is lacking, since the literature results are not consistent with each other in terms of the cleaved surfaces' morphology, termination distribution, and electronic structure, which is why the cleaved $SrTiO_3$(001) surface remains undefined.

Die approbierte gedruckte Originalversion dieser Dissertation ist an der TU Wien Bibliothek verfügbar.
The approved original version of this doctoral thesis is available in print at TU Wien Bibliothek.
TU Bibliothek Your knowledge hub WIEN

3.2 Utilizing strain-induced ferroelectricity to cleave atomically flat surfaces

The path to obtaining a pristine $SrTiO_3(001)$ surface is not straightforward, as illustrated in the previous Section. No report of an atomically resolved, unreconstructed (1×1)-terminated $SrTiO_3(001)$ surface is found in literature, raising suspicion on whether this surface was ever achieved. As will be shown in this Section, the key to obtaining an unreconstructed $SrTiO_3(001)$ surface lies in utilizing its incipient ferroelectric nature that enables cleaving of this cubic perovskite. This Section is based on the publication "Incipient ferroelectricity: A route towards bulk-terminated $SrTiO_3(001)$" [341].

3.2.1 $SrTiO_3$ as an incipient ferroelectric

An $SrTiO_3$ solid has cubic symmetry at room temperature, and undergoes a phase transition to tetragonal symmetry with an elongated c-axis (along the [001] direction) and shortened $a = b$ axes at 105 K [342]. In this tetragonal phase, many perovskites favor a transition to ferroelectricity by shifting the central B-cation within the BO_6 octahedra along the [001] axis [343]. $SrTiO_3$ however, experiences an antiferrodistortive structural transition by slightly rotating the TiO_6 octahedra around the [001] rotation axis, where the rotation of neighboring TiO_6 octahedra is out of phase, while every other octahedra rotates in phase [344]. This antiferrodistortive phase suppresses the ferroelectricity, and tetragonal $SrTiO_3$ retains paraelectric properties as in the high-temperature cubic state. As the temperature is lowered a ferroelectric phase is expected to occur, and the dielectric susceptibility of $SrTiO_3$ starts growing as the temperature is lowered towards 35.5 K. The dielectric susceptibility does not diverge with temperature however, but instead saturates and steadily decreases down to the temperature of 0.035 K, indicating that $SrTiO_3$ is in the quantum paraelectric regime in this temperature range [345]. The quantum paraelectric state prevents the ferroelectric transition, and $SrTiO_3$ is therefore categorized as an incipient (or improper) ferroelectric. In other words, although $SrTiO_3$ is very close to being ferroelectric, it never spontaneously enters this state, and the Curie temperature for the ferroelectric transition in $SrTiO_3$ is commonly described as being slightly lower than 0 K.

The incipient ferroelectric character of $SrTiO_3$ implies that it can experience a ferroelectric phase transition under moderate amount of external stimuli. The application of uniaxial stress/strain along the [100], [010], or [110] direction was shown to induce a ferroelectric phase transition in $SrTiO_3$, as reported in Fig. 58a. The top panel in Fig. 58a illustrates the application of uniaxial stress on a monodomain $SrTiO_3$ crystal originally used for investigating the quantum paraelectric state, while the bottom panels in Fig. 58a illustrate the electric polarization during application of uniaxial strain along the [010] axis: After a critical amount of stress $\sigma_c = 10.1\,\mathrm{kg/mm^2}$ was applied at 4.2 K, $SrTiO_3$ crystals developed a hysteresis with respect to the magnitude and the orientation of the applied field, clearly indicating that they experienced a phase transition to the ferroelectric state. The setup illustrated in Fig. 58a allows only for compression of samples along a chosen direction, while "stretching" the samples is experimentally very challenging. Subjecting $SrTiO_3$ crystals to precise amounts of either tensile or compressive strain ε_s can be achieved by growing $SrTiO_3$ thin films on the underlying substrates with lattice parameters different than $SrTiO_3$: when an underlying substrate has a larger unit cell size than $SrTiO_3$ the films will be subjected to tensile strain $\varepsilon_s > 0$, while the films will be subjected to compressive in-plane strain $\varepsilon_s < 0$ when the substrate has a smaller unit cell size. The effect of different types of strain on the $SrTiO_3$ thin films is reported in Fig. 58b. A $(LaAlO_3)_{0.3}(Sr_2TaAlO_6)_{0.7}$ (abbreviated as LSAT) substrate has a slightly smaller unit cell size, while a $DyScO_3$ has a slightly larger unit cell than the $SrTiO_3$, and the $SrTiO_3$ film is therefore subjected to compressive and tensile strain when grown on these substrates, respectively. Figure 58b reports the calculated temperature vs. strain phase diagram for $SrTiO_3$ films, and clearly shows that the ferroelectric state can exist in a wide temperature range depending on the amount of applied strain.

Literature findings on the strain-induced ferroelectricity, pertinent for the cleaving procedure described below, are summarized in Fig. 58c. When the [001] axis is subjected to compression, $SrTiO_3$ develops an in-plane polarization with respect ot the (001) surface because Ti atoms displace in the direction that is a linear combination of [100] and [010] directions. On the other hand, when the [001] axis is subjected to extension, Ti atoms displace along the [001] direction and create polarization domains with out-of-plane polarization vector with respect to the (001) surface. Creating inequivalent planes parallel to the (001) plane requires out of plane polarization, by elongating the [001] unit cell size and subsequently shortening and elongating the Ti-O covalent bonds along the [001] direction. This can be achieved by tensile strain along the [001] axis, but "stretching" the single crystals is unnecessarily complicated. Instead, the same effect can be achieved by compressing the unit cell in a direction perpendicular to [001], as sketched in Fig. 58d. Throughout the research that led to this

Die approbierte gedruckte Originalversion dieser Dissertation ist an der TU Wien Bibliothek verfügbar.
The approved original version of this doctoral thesis is available in print at TU Wien Bibliothek.
TU Bibliothek Your knowledge hub WIEN

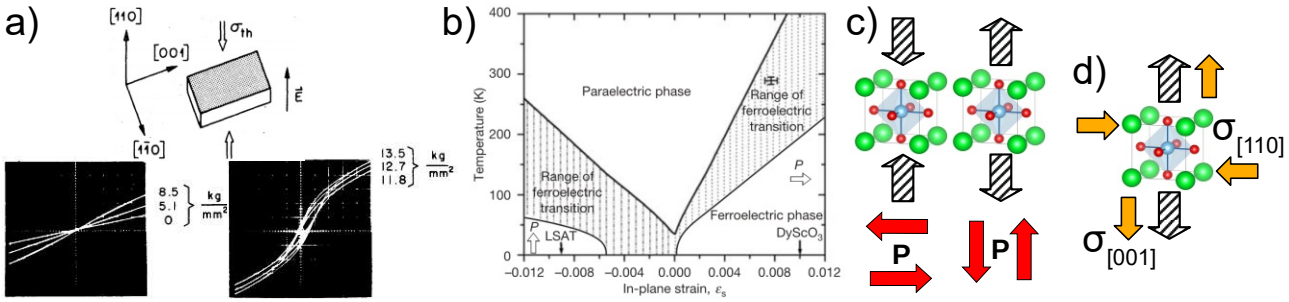

Figure 58: **Literature observations of the strain-induced ferroelectricity in $SrTiO_3$**
a) (Top panel) Sketch of a setup used for applying a uniaxial pressure along a [110] axis to a $SrTiO_3$ crystal. Reprinted bottom panel of Figure 2 [345] from [K. A. Müller and H. Burkard, *Physical Review B*, 19, 3593 (1979)] with permission of APS. Copyright (1979) American Physical Society.
(Bottom panels) Observed stress dependent polarization during application of strain to a $SrTiO_3$ crystal along the [010] axis, measured at 4.2 K. After the application of a critical value of stress of $\sigma_c = 10.1\,\mathrm{kg/mm^2}$, the polarization develops a hysteresis with respect to the varying electric field.
Reprinted Figure 1 [347] with permission from [W.J. Burke and R.J. Pressley, *Solid State Communications*, 9, 191 (1971)]. Copyright (1971) Elsevier.
b) Calculated in-plane strain vs. temperature two-dimensional phase diagram of $SrTiO_3$(001) thin films. Compressive and tensile strain along [001] is performed by growing on LSAT or $DyScO_3$ substrates, respectively, due to the lattice mismatch with $SrTiO_3$. At certain parameters, $SrTiO_3$(001) thin films are ferroelectric even at room temperature.
Reprinted Figure 1 [348] with permission from [J. H. Haeni, P. Irvin, W. Chang, R. Uecker, P. Reiche, Y. L. Li, S. Choudhury, W. Tian, M. E. Hawley, B. Craigo, A. K. Tagantsev, X. Q. Pan, S. K. Streiffer, L. Q. Chen, S. W. Kirchoefer, J. Levy, and D. G. Schlom, *Nature*, 430, 758 (2004)]. Copyright (2004) Springer Nature.
c) Illustration of the induced polarization with respect to the (001) plane obtained from literature: compressive strain induces in-plane ferroelectricity (left panel), while tensile strain induces out-of-plane ferroelectricity (right panel).
d) Illustration of the possible stress application directions (yellow arrows) to perform tensile strain in $SrTiO_3$ along the [001] direction (dashed arrows).

Thesis, strain was applied to $SrTiO_3$ single crystals along the [110] direction, which can in theory transform the unit cell from cubic to tetragonal; the tensile elongation along the [001] direction is related to the compression along the perpendicular [110] axis through the Poisson's ratio that equals 0.232 in $SrTiO_3$ [346].

3.2.2 Cleaving procedure

To induce a strain-induced ferroelectric phase transition in $SrTiO_3$ single crystals at room temperature, a device for cleaving $SrTiO_3$ was designed, as sketched in Fig. 59a. The $SrTiO_3$ crystals used were custom cut and polished, to measure 3.5 mm in width, 7 mm in height, and 1 mm in thickness, as illustrated (not to scale) in Fig. 59a, with the (110) face polished with high quality. A device for straining single crystals was constructed from stainless steel, and consists of four separate steel blocks, two of which have an M2 thread and the other two with an ⌀2 hole. Pairs of steel blocks are connected through M2 screws, such that the $SrTiO_3$ single crystal is compressed by tightening the screws. This construction applies uniaxial compressive strain to the $SrTiO_3$ single crystal along the [110] direction in the bottom and the top of the crystal (with respect to the [001] axis), but a small fraction of the volume is spared between the pairs of compressive blocks (shaded region in Fig. 59a) where the cleavage is intended to occur. Once a single crystal was compressed outside of vacuum, the entire mount was placed in UHV to cleave it in an ultra-pure environment. Samples that were compressed this way became brittle and easily cleave, in complete contrast to samples that are not strained prior to cleaving, which require a lot of force to break in half and commonly shatter due to application of such high forces. Strained $SrTiO_3$ single crystals are cleaved by applying a mild force $\mathbf{F}_{\mathrm{ext}}$ to the top of the cleaving device along the [110] axis. Cleaving produces two pieces of a single crystal with surfaces that are a mirror image to each other, and both surfaces can be used for subsequent measurements. The details of the cleaving device, the crystal geometry and the cleaving procedure will be discussed in more detail in Section 3.4.

Die approbierte gedruckte Originalversion dieser Dissertation ist an der TU Wien Bibliothek verfügbar.
The approved original version of this doctoral thesis is available in print at TU Wien Bibliothek.
TU Bibliothek WIEN Your knowledge hub

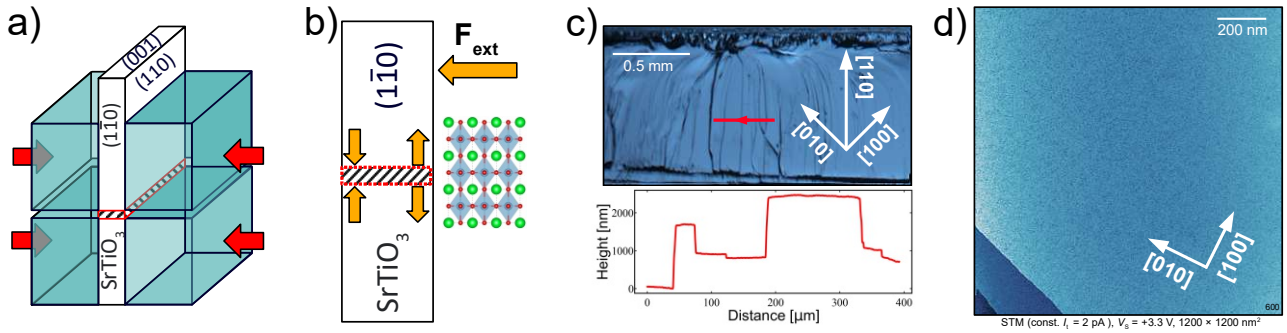

Figure 59: **Cleaving $SrTiO_3$ and creation of an atomically flat, bulk-terminated (001) surface.** a) Drawing of the sample mount. A $SrTiO_3$ sample is pressed by steel blocks to induce directed strain in the cleavage region. b) Sketch of the strain distribution during the cleavage process (orange) and the unit cell distortion (Sr - green, Ti - blue, O - red; the distortion is not to scale) c) Photograph of the as-cleaved surface. A height profile (obtained on a Bruker DektakXTL profiler) measured along the red arrow shows that all facets are flat and have the same (001) orientation. d) Large-area STM image of the as-cleaved surface, showing a μm-sized, atomically flat region and steps with a height of one unit cell.

The clear change in the cleaving behavior of strained and unstrained $SrTiO_3$ single crystals already indicates that a significant structural effect in the cleaving region of the crystal is achieved by using the cleaving device, *i.e.*, that the sample experiences a quantum phase transition to a ferroelectric tetragonal phase caused only by a change in pressure (strain). $SrTiO_3$ requires at least 1% of biaxial compressive strain to experience a ferroelectric phase transition at room temperature [348], or even higher uniaxial compressive strain. However, the designed cleaving device for $in-situ$ cleaving can achieve a maximum strain that is estimated to induce less than 0.4% of uniaxial strain on the unit cell. This is clearly below the value necessary for the ferroelectric phase transition, but it already guarantees an easy cleave. The main role in the ferroelectric phase transition is therefore played by the tensile strain present at the tip of the crack, which propagates through the crystal during the cleavage [349], as illustrated in Fig. 59b. Once the crack is initiated, due to the application of the compressive stain from the cleaving device and the additional external force necessary for cleaving, it propagates along the [110] direction, until it spans the entire crystal width and separates the two newly-obtained $SrTiO_3$ pieces. The compressive strain from the sample mount therefore serves mainly to confine the tensile strain into a well-defined region. The cleaving region is represented by a shaded region in Fig. 59b, while the yellow arrows indicate the tensile/compressive strain that occurs during the crack propagation and the subsequent cubic-to-tetragonal phase transition is illustrated on a few unit cells (out of proportion).

An optical photograph of a successful cleavage is shown in Fig. 59c. The cleaved surface is characterized by a train of terraces that optically appear flat, and are connecting the two edges of the crystal along the [110] direction and span hundreds of micrometers along the [$\bar{1}$10] direction. Terraces are separated by macroscopically visible steps oriented along the [110] direction, parallel to the external strain. Scanning microscopy techniques such are STM and AFM reveal that these optically flat terraces are also atomically flat, as can be seen in a large-area STM image in Fig. 59d. Naturally, optically flat terraces do not consist of only a single atomically flat terrace, and STM reveals that there are single- or multiple-unit-cell-sized steps separating the atomically flat terraces – in the example in Fig. 59d only the single-unit-cell-high steps are present.

Figure 60 shows the difference between the typical conchoidal fracture and the (001)-oriented cleavage of a $SrTiO_3$ single crystal. It shows an optical photograph of one of the first successful $SrTiO_3$(001) cleavages. The sample cleavage was only partially successful though, and the right side of the sample (≈80% of the surface) shows conchoidal fracture. The conchoidal region is a typical surface resulting from fracturing $SrTiO_3$ when no external strain is applied. The fractured surface is optically flat, but slightly curved – the light is reflected in different ways in different regions, resulting in darker and brighter areas in the photograph in Fig. 60. In contrast to the conchoidal fracture, the left part is atomically flat and all facets are (001)-oriented. This is apparent already in an optical microscope; the terraces appear homogeneously illuminated, because the incoming light is reflected in a well-defined direction. This region contains macroscopic steps. An STM image taken in the flat-cleavage region (marked as 1) shows an atomically flat surface, with a single-unit-cell-high step. All portions of a flat-cleaved surface have the same tilt with respect to the [001] axis. On the other hand, an example of an

Die approbierte gedruckte Originalversion dieser Dissertation ist an der TU Wien Bibliothek verfügbar.
The approved original version of this doctoral thesis is available in print at TU Wien Bibliothek.
TU Bibliothek Your knowledge hub WIEN

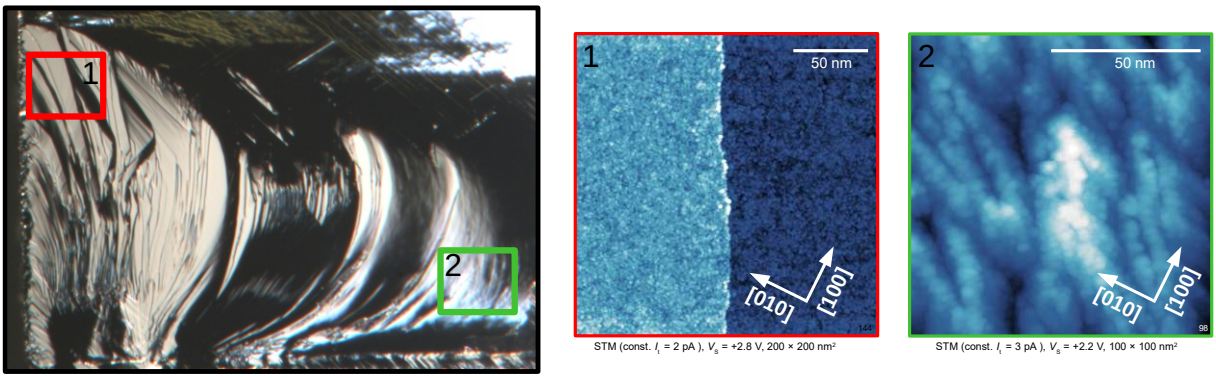

Figure 60: **Optical photograph of a cleaved $SrTiO_3$(001) surface showing both, the conchoidal and atomically flat surfaces.** The two highlighted regions 1 and 2 correspond to a flat and conchoidal fracture, respectively. The two are shown in STM; while a well-cleaved part of the surface shows well-defined flat terraces and steps between them, a part of the surface that underwent conchoidal fracturing is not atomically defined.

STM image from the conchoidal-fracture region (marked as 2) shows that the surface is not flat, and lacks a well-defined atomic structure. The typical surface roughness of the unsuccessful cleavage of this type is in the order of nanometers, and the overall surface is randomly tilted across the conchoidal-fracture region.

3.2.3 Atomically resolved terminations

Atomically flat terraces on the cleaved $SrTiO_3$(001), as the one in Fig. 59d, are suitable for studies with STM and AFM. These techniques unambiguously reveal that the surface consists of two distinct terminations, SrO and TiO_2, seen in Figures 61 and 62, respectively. The two terminations are complementary yet different in many ways.

Figure 61 focuses on the details of a SrO-terminated surface. A clear, bulk-terminated (1×1) SrO surface is seen in the constant-height AFM image in Fig. 61a. This termination is well-resolved, with individual atoms organized in a square pattern. In principle, the two periodic grids that are imaged as dark (attractive forces) and bright (repulsive forces) cannot be *a priori* be assigned to either Sr or O sublattices, because AFM imaging on ionic surfaces is highly tip dependent: Cation-terminated tips interact attractively with surface anions and repulsively with cations, while an anion-terminated tip will show an inverted contrast [350, 351]. The AFM image in Fig. 61a was obtained with a cation-terminated tip (more details below), so the bright atoms correspond to the Sr sublattice, and the dark atoms to the O sublattice, as illustrated with the superimposed ball model consisting of green and red spheres, respectively. The bulk-terminated SrO termination is not perfect however, since there are point defects present in the lattice, as is seen in the enlarged view in the inset at the right side of Fig. 61a. These point defects, marked with open circles in Fig. 61a, exhibit a negative frequency shift, which, in AFM images taken this close to the surface, implies an absence of signal. The point defects are therefore missing atoms that are located at the position where a Sr atom should reside, and can be assigned as strontium vacancies (V_{Sr}). Sr vacancies appear either isolated, or in a group of 2–4 vacancies that span either along the [100] or [010] direction; a congregation of vacancies along both main crystallographic axes at the surface was never observed on the as-cleaved surfaces. Throughout different experiments, the concentration of V_{Sr}s at the SrO termination was always $\eta(V_{Sr}) = (14\pm2)\%$.

The constant-height AFM image of the SrO termination in Fig. 61a was obtained in the region marked with a green broken-lined rectangle in the constant-height STM image in Fig. 61b. While AFM provides excellent resolution of the SrO termination, STM is incapable of capturing the atomic arrangement. The constant-height, empty-states STM image in Fig. 61b shows mostly an undefined distribution of the tunneling current, with several spots significantly brighter than the rest. These bright spots do not correlate with the atomic arrangement seen in AFM, and their concentration roughly matches the concentration of Nb dopants in the 0.5 wt%=0.69 at.% Nb-doped samples that were used. The lack of atomic resolution in STM can be attributed to an absence of localized surface states associated with the position of the atoms; *i.e.*, conduction orbitals at the SrO termination are oriented in-plane, and their out-of-plane component is so weak that it does not provide atomic corrugation. The only correlation between the STM signal and the atomic arrangement revealed with

Die approbierte gedruckte Originalversion dieser Dissertation ist an der TU Wien Bibliothek verfügbar.
The approved original version of this doctoral thesis is available in print at TU Wien Bibliothek.
TU Bibliothek Your knowledge hub WIEN

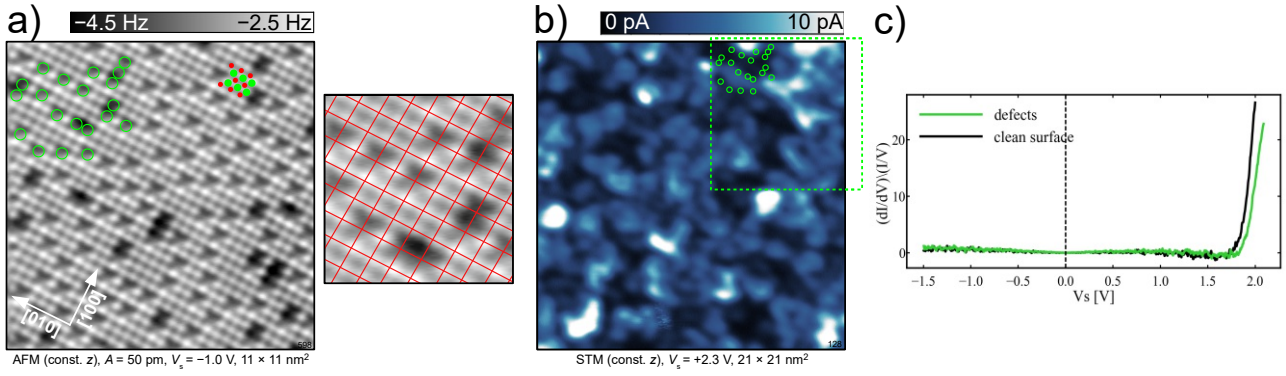

Figure 61: **SrO termination on the cleaved $SrTiO_3$(001) surface** a) Constant-height AFM image of the SrO termination. This termination is clearly resolved with AFM, and consists of a regular square lattice with 14% of point defects. Point defects are marked by open circles, while the drawn model puts emphasis on the lattice. The image was obtained with a cation-terminated AFM tip (Sr or Ti). A few unit cells are enlarged in the inset with a red (1×1) grid overlay. b) Constant-height STM image, which cannot capture the atomic resolution of the SrO termination. The green broken-lined square indicates the area where the image in (a) was obtained. Some Sr vacancies observed in (a) are marked in the image. c) STS taken above regular lattice sites and defects.

AFM is in the position of V_{Sr}s, as can be seen by comparing the marked V_{Sr}s in Figs, 61a and 61b: The position of V_{Sr}s roughly corresponds to the regions where the constant-height, empty-states STM does not detect any tunneling current.

The electronic properties of the SrO termination was investigated in more details with STS, shown in Fig. 61c. The DOS at the SrO-terminated surface implies that it can be characterized as a large band-gap semiconductor, with no states within the band gap. The DOS at the lattice sites and at the point defects differ, plotted in black and green, respectively. Point defects exhibit the upward bend bending in the DOS, and the onset of the conduction band is shifted 0.2 eV higher than in the DOS taken above the lattice sites. This is consistent with the identification of the point defects as negatively charged V_{Sr}, formally twice negative V_{Sr}^{2-}, because they act as negatively-charged acceptor impurities, which always exhibit an upward bend bending on a n-type semiconductor surface. This upward bend bending is in part responsible for the absence of tunneling current above the V_{Sr} in constant-height, empty-state STM image in Fig. 61b: the STM image was obtained with $V_S = +2.3$ V sample bias, and the STS shows that at this bias value the regular lattice sites will have more empty states to tunnel into compared to the V_{Sr}s. It is noteworthy that the only other possible intrinsic point defects, O vacancies on the SrO termination, would lead to downwards band bending, opposite to what is observed experimentally.

Figure 62 focuses on the other atomically flat termination observed with STM/AFM. The constant-height AFM image in Fig. 62a shows single atoms distributed across the surface, marked with open circles, which obscure the view to the underlying substrate. This termination is distinctly different from the observed SrO termination in AFM, and the geometry of the scanning implies that it is perfectly flat, in contrast to the areas of conchoidal fracture. Since the only other (001) termination beside SrO can be the TiO_2 termination, the surface areas like the one shown in Fig. 62 are assigned to be TiO_2-terminated regions of the cleaved surface. The distribution of adatoms on the TiO_2 termination, also magnified in the inset in the right panel of Fig. 62a, roughly correlates to the distribution of V_{Sr}s on the SrO termination. Since these point defects are intrinsic to the surface and the cleaving process, the adatoms on the TiO_2 termination are assigned to be Sr adatoms (Sr_{ad}), that are pulled out from the SrO termination during the cleaving process, and remain on the TiO_2 termination afterwards. Throughout different experiments, the concentration of Sr adatoms on the TiO_2 termination is always $\eta(Sr_{ad}) = (14\pm2)\%$, which exactly matches the concentration of V_{Sr}s on the opposite termination. The Sr adatoms are formally twice positive Sr_{ad}^{2+} and tend to be separated on the TiO_2 termination to reduce the electrostatic repulsion between them. They are mostly isolated, but a characteristic pattern along the [100] or [010] directions is sometimes observed, which matches the patterns of V_{Sr}s on the opposite termination. The AFM image in Fig. 62a was obtained with an anion-terminated tip, a single oxygen atom in this case, which detects the single Sr adatoms at the surface in an attractive mode with a negative frequency shift. Repulsion

Die approbierte gedruckte Originalversion dieser Dissertation ist an der TU Wien Bibliothek verfügbar.
The approved original version of this doctoral thesis is available in print at TU Wien Bibliothek.
TU Bibliothek Your knowledge hub WIEN

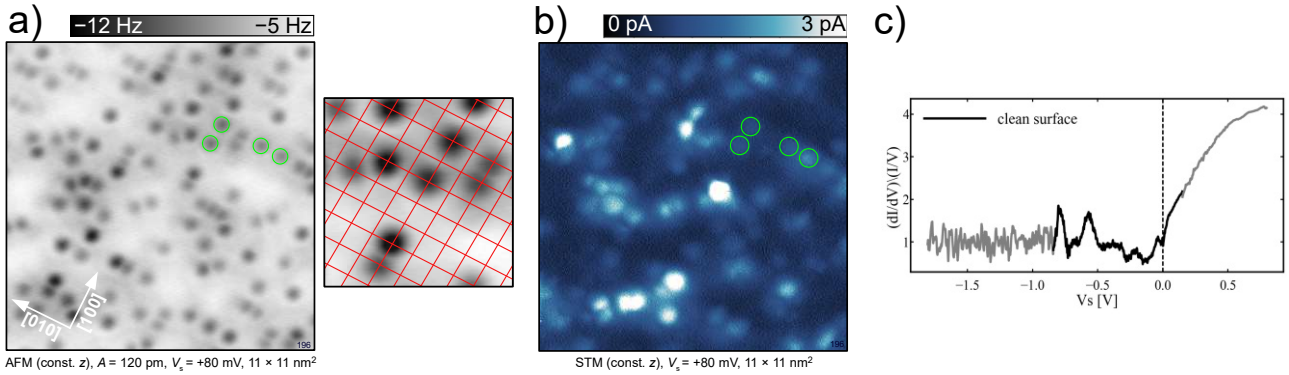

Figure 62: **TiO_2 termination on the cleaved $SrTiO_3$(001) surface** a) Constant-height AFM image of the TiO_2 termination. The underlying termination is obscured by the geometrically protruding point defects. The image was obtained with an anion-terminated AFM tip . A few unit cells are enlarged in the inset with a red (1×1) grid overlay. a) Constant-height STM image, taken simultaneously with the image in (a), revealing only the position of point defects on the TiO_2 termination. c) STS taken above a regular lattice site.

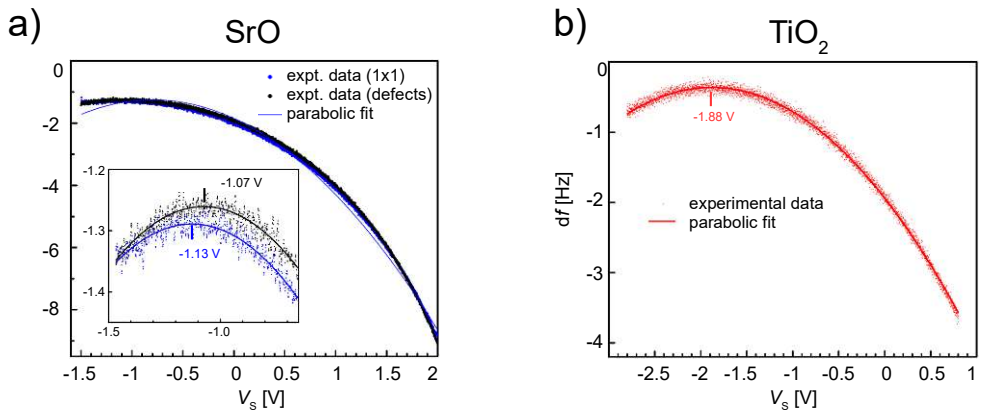

Figure 63: **Kelvin parabolas over the two terminations of as-cleaved $SrTiO_3$(001)** a) Bias sweeps above the lattice points and the defects at the as-cleaved SrO termination. b) Bias sweeps over the underlying surface at the as-cleaved TiO_2 termination.

over the Sr_{ad}s cannot be obtained with an anion-terminated tip in AFM, because they are highly reactive and the oxygen atom from the AFM tip easily transfers to the adatoms, thereby causing a tip crash. The relatively high concentration of these point defects, their scattered distribution, and their high reactivity, do not allow obtaining atomic resolution on the underlying TiO_2 termination.

An empty-states, constant-height STM image in Fig. 62b shows that the STM imaging cannot atomically resolve the underlying TiO_2-terminated surface either. This STM image was obtained simultaneously with the AFM image in Fig. 62a, and the two images are correlated only at the positions of Sr_{ad}s, marked with open circles in both images. The correlation stems from the geometric protrusion of Sr_{ad}s from the TiO_2 termination since they serve as a high-probability conduit for tunneling between the sample and the tip, while a direct tunneling to and from the underlying substrate is less probable in constant-height STM at these tip-sample distances. The brightest species in the STM image in Fig. 62b are potentially linked to extrinsic Nb-impurities, similarly as on the SrO termination.

In contrast to the bulk $SrTiO_3$, the as-cleaved TiO_2 termination is metallic, as revealed by the STS measurements in Fig. 62c. A semiconductor-to-metal transition is energetically highly unfavorable, and surfaces often try avoiding this phenomenon by undergoing a series of electronic and structural rearrangements. The origin of the metallicity on the TiO_2 termination of the as-cleaved surfaces can be in part attributed to the presence of electron-donating Sr_{ad}, but subsequent experiments in the following sections (Section 3.5) indicate that this

Die approbierte gedruckte Originalversion dieser Dissertation ist an der TU Wien Bibliothek verfügbar.
The approved original version of this doctoral thesis is available in print at TU Wien Bibliothek.
TU Bibliothek Your knowledge hub WIEN

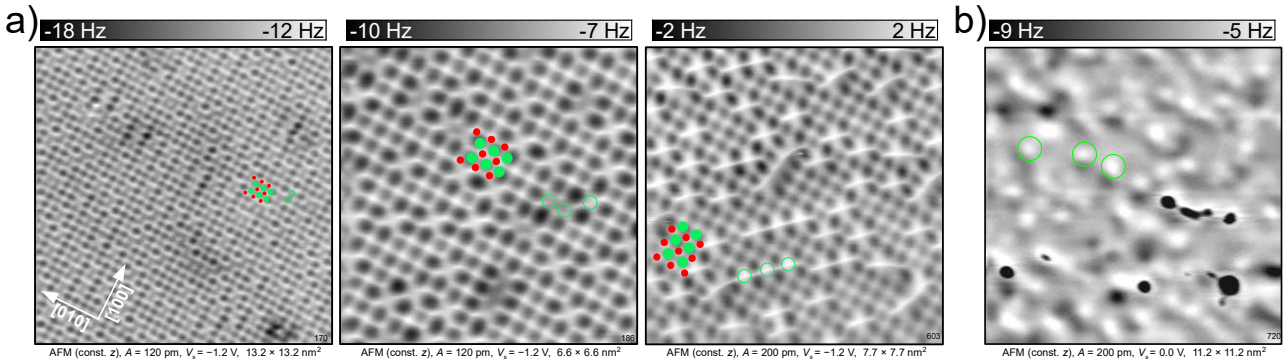

Figure 64: **AFM contrasts over the two terminations obtained with different tip terminations.** a) The SrO termination imaged with different anion-terminated tips. b) The TiO_2 termination imaged with a cation-terminated tip.

electron donation is not a significant-enough phenomena to ensure transition to metallicity. The semiconductor-to-metal transition can also in part occur to compensate the strain-induced polarity, as well as the screening mechanism for the ferroelectric polarization vector penetrating the cleaved surface. The DOS at the TiO_2 termination is non-zero throughout the investigated energy range, with several pronounced filled-state peaks at −40 meV, −0.2 eV, −0.55 eV, and −0.75 eV. The electronic states close to the Fermi level (at −40 meV) are characteristic for the appearance of the two-dimensional electron gas (2DEG), that could reside on this metallic termination. To determine whether this state corresponds to a 2DEG, its dispersion in the k-space needs to be mapped, by using angle-resolved photoelectron spectroscopy (ARPES) for example, and this investigation is currently underway. The origin of the other populated states (−0.2 eV, −0.55 eV, and −0.75 eV) could stem from the polarons residing in the subsurface layers that capture excess electrons donated by either Sr_{ad}s or Nb-dopants, which could be investigated using DFT in the future. The STS measurements were performed above both, the Sr_{ad}s and the underlying lattice, and the spectra were normalized because the STS above the lattice points was obtained with the tip approached closer to the surface, in-between the defects. The STS performed above the protruding defects and in between them showed identical DOS, *i.e.*, there is no defect-induced band bending at this termination. This is consistent with the presence of charged defects at the metallic surface, where no band bending can occur.

The charge state and the nature of the defects at both terminations was further investigated in Fig. 63. The Kelvin probe force microscopy (KPFM) measurements (introduced in Section 1.5.7) were obtained over both, the lattice points and the defects, using a Cu-terminated tip. The experimental data were fitted by a second-order polynomial fit, showing a good match on the metallic TiO_2 termination, but significant deviations on the semiconducting SrO termination where tip-induced band bending occurs. The blue spectrum in Fig. 63a was measured above a clean (1×1) region of the SrO termination, while the black spectrum was measured above a Sr vacancy. The second-order polynomial fit shows that the experimental data significantly deviate from the parabolic behavior, which can be attributed to the semiconducting character of this termination and a resulting tip-induced band bending. Here, the LCPD can be estimated by analyzing the region close to the maximum of the curve, where the electric field (and the resulting band bending) is close to zero. Processing 10 curves, in a range between −1.5 V and −0.7 V sample bias, reveals that the LCPD above the Sr vacancies is shifted towards lower values by (30±20) mV compared to the (1×1) region. The magnitude of the shift is smaller than the 0.2 V shift measured by STS (in Fig. 61c), probably due to the lower spatial resolution of the KPFM measurement. The direction of the shift is the same in both cases, supporting the assignment of this defect as the Sr vacancy. On the TiO_2 termination on the other hand, shown in Fig. 63b, LCPD is the same above and in-between the Sr_{ad}s, in accord with the metallic nature of this termination.

AFM imaging is highly tip-dependent, and Fig. 64 shows AFM images of the two terminations with the opposite contrast compared to Figs. 61a and 62a. Both terminations were most commonly imaged by functionalizing the AFM tip with an O atom during imaging, by performing weak bias pulses over the lattice oxygens on the SrO termination. Such an anion-terminated AFM imaging contrast of the SrO termination is shown in Fig. 64a; The Sr/O atoms in each panel are sketched in green/red, while the Sr vacancies are highlighted by open green circles. Common to all three AFM images is the detection of surface Sr atoms with attractive forces, and

Die approbierte gedruckte Originalversion dieser Dissertation ist an der TU Wien Bibliothek verfügbar.
The approved original version of this doctoral thesis is available in print at TU Wien Bibliothek.
TU Bibliothek Your knowledge hub WIEN

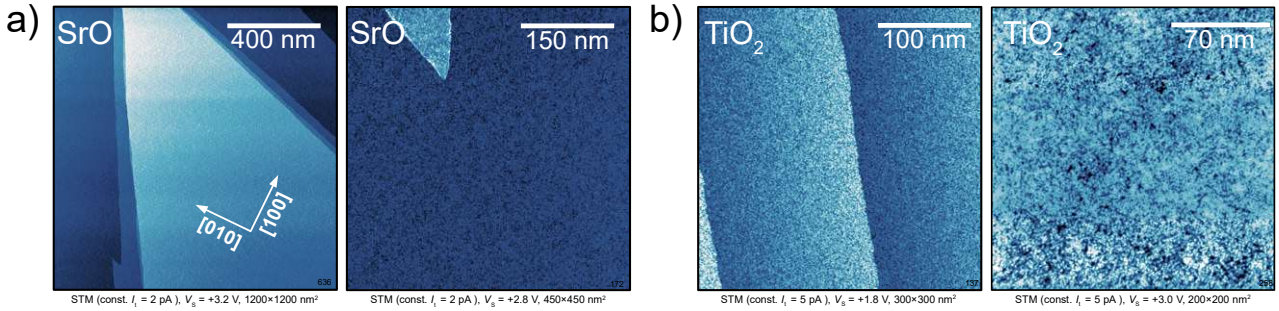

Figure 65: **Large-area empty-states STM images of the cleaved $SrTiO_3$(001) surface.** a) The SrO, and the b) TiO_2 termination.

a characteristic detection of V_{Sr}s with slightly repulsive forces. The apparent "X"-shape of the V_{Sr}s is common for imaging charged vacancies on ionic surfaces with AFM [352]. Even though all three AFM images in Fig. 64a were obtained with an O-terminated tip, they differ due to the different reorganization of the atoms at the very tip apex, and the contrast is therefore slightly different. The rightmost image in Figs. 64a was obtained with the sharpest tip of the three, as can be seen by smallest absolute values of the frequency shift. This tip was so sharp that even some tip bending occurred above the V_{Sr}s, and they were imaged with a pronounced curvature of the "X"-shaped features. While the SrO termination is well-resolved using both cation- and anion-terminated AFM tips (Figs. 61a and 64b, respectively), imaging the TiO_2 termination with an anion-terminated tip is better than with cation-terminated tip. A single Sr atom was transfered to the AFM tip before acquiring the image shown in Fig. 64b, and the Sr_{ad}s are subsequently imaged in the repulsive mode; although individual adatoms can be resolved this way, their appearance is not as clear as when they are imaged with the anion-terminated tip in an attractive regime.

3.2.4 Morphology of a cleaved surface

Figure 65 shows four large-area, empty-states STM images measured at different regions of a well-cleaved sample. The crystallographic directions are the same throughout the Figure, as marked in panel (a). All steps present in Fig. 65 are single unit cell high. In other words, each panel in Fig. 65 shows a single termination, either SrO or TiO_2. The orientation of the terrace steps varies, but they all run approximately along the [110] direction, roughly corresponding to the direction of crack propagation. The terrace size varies, ranging from 50 nm up to $> 1\,\mu$m. All STM images in Fig. 65 show similar features typical for a well-cleaved surface, which is why the STM images alone cannot be used to reveal the surface termination type. It is through atomically-resolved AFM imaging that Figs. 65a and 65b are recognized as SrO and TiO_2-terminated regions, respectively. Obtaining atomic resolution on a given region is time-consuming, and a quicker way for determining the termination type is to perform constant-height STM measurement over the unknown termination: Due to the drastically different electronic properties of the two termination, the TiO_2 termination will give rise to a tunneling current signal at much lower biases compared to the SrO termination.

The distribution of the two terminations on the cleaved surface provide valuable insight into the fracturing mechanism behind a successful cleavage. So far, it was shown that large portions of the surface are atomically flat, with sporadic appearance of terraces that are mostly single unit cell high. Figure 66 investigates the surface morphology with empty-states STM at an even larger scale than in Fig. 65, and the measured line-profiles indicated in the panels (a–c) are shown in Fig. 66d, in the respective color as indicated in the STM images. The morphology in Fig. 66a is characterized by a train of terraces, however each is a single unit cell high, and all terraces are TiO_2-terminated; the termination was identified using constant-height AFM. A morphology with step-bunches that separate large flat regions is seen in Fig. 66b. The height difference between the top and the bottom terrace is still an integer multiple of the unit cell height, indicating a single termination over the whole region – SrO in this case. A termination change was observed to occur exclusively at very high steps, on the order of 100 nm, which are oriented in the [110] direction (parallel to the applied strain). This is seen in Fig. 66c, where a multistep ≈60 nm high separates the SrO termination (left) from the TiO_2 termination (right). Imaging over such high steps on the surface with STM is challenging, so a better resolution can be seen in the high-pass filtered image in the inset, where even the single-unit-cell high steps can be resolved on the SrO termination.

Die approbierte gedruckte Originalversion dieser Dissertation ist an der TU Wien Bibliothek verfügbar.
The approved original version of this doctoral thesis is available in print at TU Wien Bibliothek.
TU Bibliothek Your knowledge hub WIEN

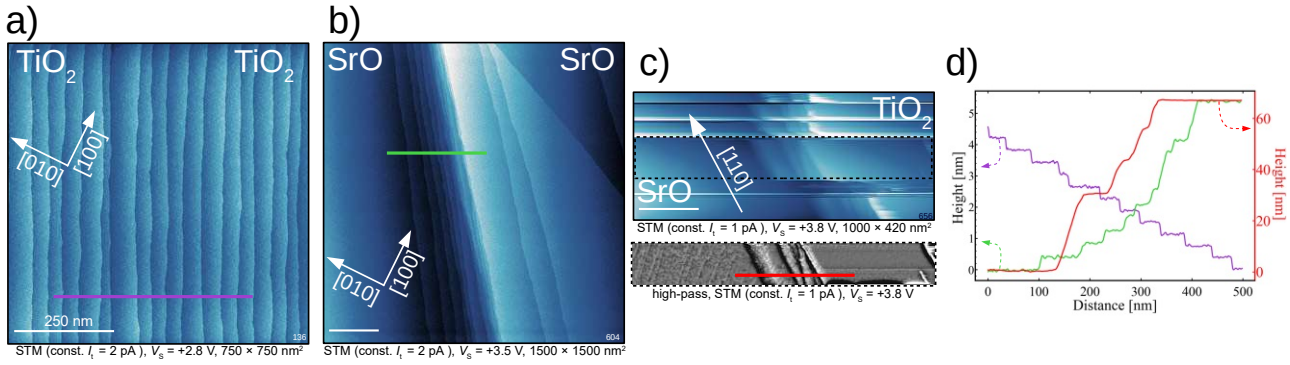

Figure 66: **Termination change on the cleaved $SrTiO_3O(001)$ surface.** Large-area empty-states STM images of a) TiO_2- and b) SrO-terminated surface regions. c) A large step along the [110] direction that separates two different terminations on either side of the step. d) Line-profiles over the panels in (a–c) that show the height of the observed terrace steps.

After thorough studies of the cleaved $SrTiO_3(001)$ surface it was also observed that the termination change can rarely occur on steps that run along the [100] and [010] directions, which will be discussed in more detail in Section 3.4.

3.2.5 Surface polarity

The appearance of charged point defects on both, the TiO_2 and the SrO termination, can be rationalized through the concept of necessary polarity compensation mechanisms on cleaved, polar surfaces.

Surface polarity is a fundamental concept that deals with the possible existence of different bulk-truncated surfaces. The concept of surface polarity is related to the presence of dipole moments within the unit cells of the bulk crystal. When a bulk unit cell can be characterized by a dipole moment along a certain axis, truncation of the bulk along the plane perpendicular to the dipole orientation will result in a polar surface. Namely, the surface layers are subjected to the symmetry breaking, as they are not coordinated in the same way as the same layers within the bulk of a crystal. Bulk crystals with a non-zero dipole moment within the unit cells readily exist in nature, but polar surfaces are never encountered in their bulk-like form, because they always host some polarity compensation mechanism.

Each crystalline solid can be decomposed into an infinite number of parallel planes perpendicular to a given direction, as in Fig. 67. The planes represent arbitrarily chosen crystal layers, and they are complimented by a surface charge $\pm\sigma$ related to the total ionic and electronic charge in the unit cell of the corresponding layer. Between two neighboring layers, a dipole moment of $\mu = \sigma R$ is developed, where R is the interlayer distance. According to Takser's classification [353], solids are considered non-polar if a repeat unit along a given direction is characterized by a zero dipole moment $\mu = 0$, and polar otherwise $\mu \neq 0$. When a solid can be decomposed in layers with no charge $\sigma = 0$, there is no dipole moment between the layers $\mu = 0$, and the bulk crystal is non-polar along a given direction. Solids that are characterized by charged layers $\sigma \neq 0$ on the other hand, have a non-zero dipole moment between the layers. These solids can either be non-polar along a given direction, if the dipole moment of the charged layers cancels out within a single repeat unit, but can also be polar if a surface consists of alternating, oppositely charged layers along the chosen direction, *i.e.*, when the repeat unit is characterized by non-zero dipole moment. Cleaving a polar or non-polar solid along a given direction [hkl], creates a polar or non-polar (hkl) surface, respectively.

The existence of polar surfaces is forbidden by simple electrostatic arguments, as illustrated in Fig. 67a. If a polar surface retains the same amount of charge $\pm\sigma$ as an equivalent layer within the bulk, the bulk crystal can be represented as $N_L/2$ capacitors connected in series (N_L is the number of layers) with $\pm|\sigma|$ charge per capacitor plate. Then, the overall electrostatic energy within the bulk crystal would diverge because it would increase with each added capacitor. This is referred to as the "polar catastrophe". Polar surfaces therefore have to alter the amount of charge on the terminating layers $\sigma' \neq \sigma$, in order to avoid the "polar catastrophe", as illustrated in Fig. 67b. When the surface charge is altered, the bulk crystal can be equivalently represented by $2 \cdot N_L/2 - 1 = N_L - 1$ inequivalent capacitors connected in series, consisting of two types of capacitors: one type

Die approbierte gedruckte Originalversion dieser Dissertation ist an der TU Wien Bibliothek verfügbar.
The approved original version of this doctoral thesis is available in print at TU Wien Bibliothek.
TU Bibliothek Your knowledge hub WIEN

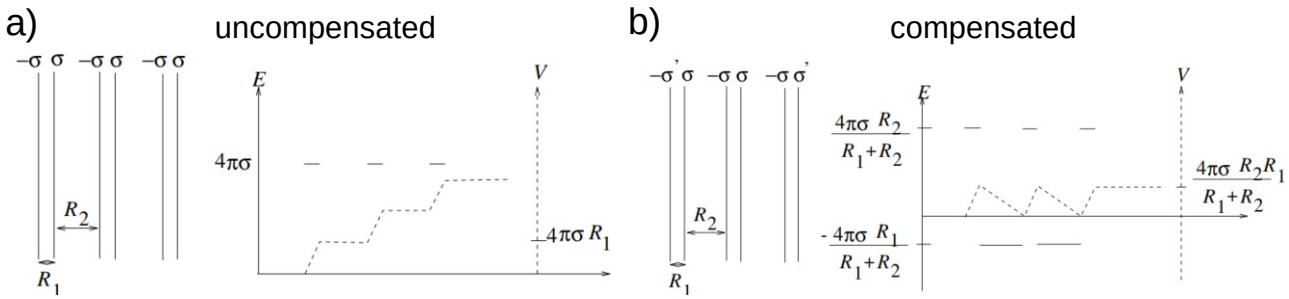

Figure 67: **Illustration of the "polar catastrophe" and the polarity-compensating mechanism.**
a) Infinite parallel plates (left panel) charged by $\pm\sigma$ surface charge represent the infinite layered structure of a solid. The total electrostatic energy and potential increment (right panel) between each pair of oppositely charged layers (thus forming a capacitor) and the "polar catastrophe" ensues.
Reprinted Figure 2(a) [354] with permission of IOP Publishing, Ltd., from [Claudine Noguera, *Journal of Physics: Condensed Matter*, 12, R367 (2000)]; permission conveyed through Copyright Clearance Center, Inc.
b) The same layered structure (left panel) as in (a), but the layers at the two opposite ends are characterized by an altered surface charge when compared to the inner layers $\sigma' \neq \sigma$, which cancels out the dipole moment within each repeat unit cell. The electrostatic energy and potential (right panel) therefore oscillate, and the "polar catastrophe" is avoided.
Reprinted Figure 2(b) [354] with permission of IOP Publishing, Ltd., from [Claudine Noguera, *Journal of Physics: Condensed Matter*, 12, R367 (2000)]; permission conveyed through Copyright Clearance Center, Inc.

with $\pm\sigma'$, and the other with $\pm|\sigma - \sigma'|$ charge per capacitor plate, where the two capacitor types are oppositely oriented. This way, the electrostatic energy would increase in one capacitor type, and decrease in the other, leading to an oscillating electrostatic energy and potential within a polar solid.

The polarity of a polar surface must be compensated by an additional charge at the surface layer(s) to ensure saturation of the electrostatic energy. This charge compensation can be either ionic or electronic, but must fulfill the criterion [354]:

$$\sum_{j=1}^{m} \sigma_j = -\frac{\sigma}{2}\left[(-1)^m - \frac{R_2 - R_1}{R_2 + R_1}\right] \tag{3.1}$$

where m is the number of surface layers that undergo charge alteration (m=1 in the illustration in Fig. 67b) and j is summation over all the altered surface layers, σ_j is the compensating charge for the j-th surface layer, σ is the surface charge of a bulk layer, and R_1 and R_2 are the distances between inequivalent bulk layers.

There is a considerable freedom for the appearance of different polarity compensation mechanism, but all alter the surface charge according to eq. 3.1. Ionic polarity compensation commonly occurs through altering the surface stoichiometry through surface reconstructions, an example of which is the $p(2\times2)$ reconstruction on the polar NiO(111) surface [355]. Polarity can also be ionically compensated by adsorption of ions onto the surface, which is very common for surfaces terminated in atmosphere, but can also occur in UHV from the residual background gas [356]. Reorganization of electronic states at the surface, without ionic rearrangement, is another efficient polarity compensating mechanism. In fact, all polar surfaces can be stabilized through electronic rearrangements alone [354], but the stoichiometry changes are sometimes energetically more favorable. The appearance of a two-dimensional electron gas was observed as an efficient compensation mechanism at the interface between the polar $LaAlO_3$ and formally non-polar $SrTiO_3$ [357, 358]. The polarity of a surface needs to compensated on both (opposite) surfaces of a polar surface slab, and indeed a two-dimensional hole gas was recently observed at the interface between $SrTiO_3$ film grown on top of a $LaAlO_3$ and $SrTiO_3$ interface [359]. The formation of ferroelectric domains with the polarization vector originating from ferroelectric distortions oriented opposite to the polarization vector originating from the intrinsic polar direction in a solid can also be considered a polarity compensation mechanism in materials that are prone to the ferroelectric distortions. This mechanism was recently proposed to partially compensate the intrinsic polarity of the bulk-terminated $KTaO_3$(001) surface [360], due to the observation of a very small concentration of intrinsic point defects insufficient for compensating the strong polarity along the [001] direction at this surface. It is noteworthy that very thin polar films, below a critical film thickness, can remain polar since the depth of the bulk is limited and the electrostatic energy and potential do not diverge [361].

Die approbierte gedruckte Originalversion dieser Dissertation ist an der TU Wien Bibliothek verfügbar.
The approved original version of this doctoral thesis is available in print at TU Wien Bibliothek.
TU Bibliothek WIEN Your knowledge hub

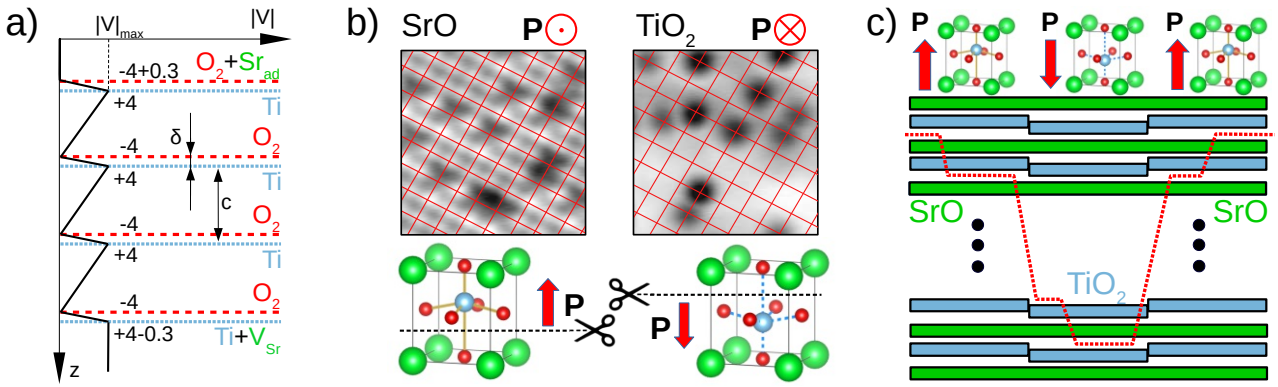

Figure 68: **Polarity compensation on the cleaved $SrTiO_3(001)$ surface.** a) Sketch illustrating the electrostatic potential in a strain-induced ferroelectric $SrTiO_3$[001] directions. Formally electroneutral TiO_2 layers split into Ti^{4+} and O_2^{4-} layers due to the strain-induced ferroelectric phase transitions, and the polarity is compensated by charged defects of the opposite charge at the two terminations. b) AFM images of the two terminations with overlayed unit-cell grids and the orientation of the polarization vector (top panel), together with the structural illustration of the symmetry breaking in the TiO_6 octahedra (bottom panel) responsible for the polarization. c) Illustration of the two terminations (domains) at the surface; large domain walls separate different terminations (domains) as seen in Fig. 66. The creation of a surface is illustrated with the broken red line.

The $SrTiO_3$ solid can be decomposed into alternating SrO and TiO_2 layers along the [001] direction, with formally $2 - 2 = 0$ and $4 - 2 \cdot 2 = 0$ charge per layer, respectively. According to Tasker's criterion [353], which takes into account only the ionic formal charges of atoms in a solid, $SrTiO_3$ surface is truly non-polar along the [001] direction. When the distribution of electrons within covalent bonds of the TiO_6 octahedra is taken into account, the bulk $SrTiO_3$ is still non-polar along the [001] direction, because $SrTiO_3$ belongs to the centro-symmetric cubic space group. However, when $SrTiO_3$ is cleaved to expose a (001) surface, symmetry-breaking at the surface leads to a weakly polar $SrTiO_3(001)$ surface that is relatively easily compensated through increase in the covalency within the TiO_4 complexes at the surface [362]. It is noteworthy that the previous concepts of polarity and the classification of polar and non-polar surfaces has been further developed and extended to include more sophisticated determination of the ionic and electronic charge distribution within the bulk, by using Berry-phase approximation [363] or exponentially localized Wanier functions [364] – these approaches classify all directions in $SrTiO_3$ (even the [111]) as completely non-polar; but it should be kept in mind that unreconstructed and pristine $SrTiO_3(111)$ and $SrTiO_3(001)$ surfaces were never observed experimentally.

Truly ferroelectric surfaces with the out-of-plane orientation of the polarization vector do not have to be polar, but usually exhibit a certain degree of screening to compensate the charge build-up from the internal electric field. When they are terminated below the Curie temperature, the created surfaces can be screened with the opposite charge to the charge that is built-up due to the internal electric field. According to the amount of charge available for screening σ_s, ferroelectric surfaces with surface charge originating from polarization σ_{pol} can be completely screened $|\sigma_s| = |\sigma_{\text{pol}}|$, partially screened $|\sigma_s| < |\sigma_{\text{pol}}|$, completely unscreened $\sigma_s = 0$, or overscreened $|\sigma_s| > |\sigma_{\text{pol}}|$ [365]. The particular type of screening, *i.e.*, the relation between σ_s and σ_{pol}, determines the size of the domains at a ferroelectric surface [366]. In $BaTiO_3$, a prototypical perovskite ferroelectric, the potential of (100) ferroelectric surface termination was shown to change with temperature, *i.e.*, with the amount of available screening charge [367]. $BaTiO_3(100)$ is considered to be either a non-polar or weakly polar surface [368], and it is commonly assumed that the electronic rearrangements at the $BaTiO_3(100)$ are sufficient to compensate the proposed weak polarity. However, an unreconstructed $BaTiO_3(100)$ surface was never directly observed. Instead, the surface is commonly reported to alter the stoichiometry through a series of reconstructions [369, 370].

Cleaving $SrTiO_3$ to successfully produce an atomically flat (001) surface likely proceeds by inducing a quantum phase transition to a ferroelectric state, through a procedure described in the previous section. In the ferroelectric state, the central symmetry is broken by central Ti atom in TiO_6 octahedra shifting either up or down along the [001] direction. This symmetry breaking is responsible for creation of inequivalent planes within the bulk, and therefore enables atomically flat cleavages. In this broken-symmetry phase, each TiO_2 layer is separated into two distinct layers, Ti and O_2, with formal ionic charge of 4+ and 4−, respectively, as

Die approbierte gedruckte Originalversion dieser Dissertation ist an der TU Wien Bibliothek verfügbar.
The approved original version of this doctoral thesis is available in print at TU Wien Bibliothek.
TU Bibliothek Your knowledge hub WIEN

illustrated in Fig. 68a. SrO layers do not experience any structural deformations in this crude approximation, and are therefore charge neutral, so they can be ignored during the decomposition of the bulk layers of $SrTiO_3$ along the [001] direction in Fig. 68a. Each unit cell that underwent the phase transition is therefore highly polar, as well as the created (001) surfaces of both the SrO and the TiO_2 termination – although SrO layers do not contribute to polarity, the TiO_2 layers underneath the SrO surface are still highly polar. This emerging polarity has to be compensated to avoid the "polar catastrophe", and the charged point defects, Sr_{ad} and V_{Sr} appear as a polarity compensation mechanism.

Figure 68a illustrates the polarity compensation of the $SrTiO_3$(001) surface created through the ferroelectric phase transition. The illustrated slab is terminated by a TiO_2 layer at the top, and a SrO layer at the bottom. AFM images of both terminations (Figs. 61 and 62) always show the canonical concentration of $14 \pm 2\%$ of charged defects on each termination. In a simple scenario, both types of point defects retain their formal charges: Sr_{ad} are formally 2+ while V_{Sr} are formally 2−. Therefore, 0.28 (≈0.3) polarity-compensating charge per unit cell can be assigned to each termination. The fact that exactly the same number defects with (formally) identical charge appear on the two terminations of the cleaved $SrTiO_3$(001) surface compliment the assigned strain-induced structural transition to a polar, ferroelectric phase. With these defects present on the two terminations, the electrostatic potential does not diverge within the bulk, as illustrated in Fig. 68a.

Equation 3.1 is commonly applied to predict how much charge is necessary for compensating the bulk-termination of formally polar surfaces. In the case of $SrTiO_3$(001), the phase transition to a polar state is novel and not yet quantified. The directly observable concentration of polarity-compensating charge on either surface can therefore be used to calculate the strength of the induced polarity within the bulk, *i.e.*, to estimate the magnitude of ionic shifting of the Ti atoms along the [001] direction. However, there are two unknown quantities in this estimation. First, the actual amount of charge within the separated Ti and O_2 layers is unknown, and is probably not well described by formal charges alone: if the Ti–O_2–Ti–O_2 layers were equidistant, the ≈0.3 compensating charge per unit cell would imply that the Ti and O_2 layers are charged by +0.6 and −0.6 charge per unit cell, respectively. The distance between neighboring layers is however certainly not equidistant, as the distance between the separated layers is expected to be very small, in the order of a few pm. By approximating the charged layers only through their formal charge, applying eq. 3.1 (with $m = 1$) allows estimating the separation between these two layers (δ, marked in Fig. 68a) to be :

$$\delta = 0.037c \tag{3.2}$$

where c is the height of the tetrahedral unit cell of $SrTiO_3$ along the [001] direction in the ferroelectric phase. With further experiments, such as the X-ray standing wave technique [371], the separation of the two layers could possibly be determined. Then, the amount of charge within the separated layers could be estimated in a similar manner to eq. 3.1, and the strength of covalency within the distorted TiO_6 octahedra (a long standing question) could be discerned.

The charge of different polarity compensating defects is also indicative of the direction of the internal electric field, and the subsequent polarization vectors, as illustrated in Fig. 68b: the polarization vector points penetrates the surface on the SrO termination, while it is oriented out of the surface on the TiO_2 termination. The bottom panel of Fig. 68b illustrates the (over-exaggerated) shifting of the central Ti atom within a unit cell. The cleavages occur by breaking the longer, weaker bonds within TiO_6 octahedra to reveal a given termination, which depends on the orientation of the local strain-induced bulk polarization. The creation of a surface during bulk cleaving is illustrated in Fig. 68c with the broken red line. During the bulk cleaving, a surface is created such that it contains small terrace steps within a single domain, but the discontinuity in the orientation of the polarization vector occurs mostly on the large steps (Fig. 66), *i.e.*, on the domain walls running along the [110] direction parallel to the applied strain. The morphology of the domains and the domain walls on the cleaved $SrTiO_3$(001) surface will be shown in Section 3.5 to strongly depend on the doping levels.

3.2.6 Conclusions

Utilizing the strain-induced ferroelectricity in an incipient ferroelectric $SrTiO_3$, atomically flat cleaved surfaces of $SrTiO_3$(001) can be obtained; the results presented in this Section were obtained by cleaving $SrTiO_3$ with 0.69 at.% of Nb-doping. The cleaved surfaces consist of two terminations, SrO and TiO_2 that span for micrometers in size and are separated by large terrace steps that can be considered as domain walls. SrO termination can be clearly resolved using AFM, while STM does not yield atomic resolution due to the delocalized nature of the electronic structure. There are point defects present on both terminations, Sr vacancies and Sr adatoms on the SrO and TiO_2 terminations, respectively. They appear to compensate the polarity of the cleaved surfaces,

Die approbierte gedruckte Originalversion dieser Dissertation ist an der TU Wien Bibliothek verfügbar.
The approved original version of this doctoral thesis is available in print at TU Wien Bibliothek.
TU Bibliothek Your knowledge hub WIEN

which is induced during cleaving. The concentration of complementary point defects is always (14±2)%, which is indicative of the distortion magnitude within the lattice in the ferroelectric state that appears during cleaving. The two surface terminations can be considered polarized in opposite directions, and they are characterized by drastically different electronic states. The SrO termination remains semiconducting like the bulk $SrTiO_3$, while TiO_2 termination experiences an insulator-to-metal transition.

Results obtained in this research lead to a well-defined procedure for obtaining atomically flat, bulk terminated $SrTiO_3(001)$, which is desirable in all experiments that deal with this technologically important and fundamentally intriguing surface. The exact characterization at the atomic level provides a clear path towards good experimental interpretations and theoretical modeling of various phenomena evidenced at this surface so far. Moreover, two terminations with two chemically and electronically distinct properties are simultaneously present at the cleaved $SrTiO_3(001)$ surface, provides a promising laboratory for future technical applications, such is the prospect of all-oxide electronics.

Die approbierte gedruckte Originalversion dieser Dissertation ist an der TU Wien Bibliothek verfügbar.
The approved original version of this doctoral thesis is available in print at TU Wien Bibliothek.
TU WIEN Bibliothek Your knowledge hub

3.3 The search for a pristine, unreconstructed $SrTiO_3(001)$ surface

$SrTiO_3(001)$ surface has attracted significant attention in the last decades (Section 3.1.1), and is used throughout the world as either the substrate for homoepitaxy or as the model system for the plethora of physical phenomena appearing at the perovskite oxide surfaces. The experience of investigating the bulk-terminated surfaces of $SrTiO_3(001)$ in the research that led to this Thesis however, indicates that acquiring these surfaces far from trivial. It will be shown in this Section that the presence of these surfaces following standard preparation techniques is not granted, and in fact becomes questionable considering that no (1×1) surface was ever atomically resolved apart from the research presented in the previous Section. This section is based on a publication titled "Quest for a pristine unreconstructed $SrTiO_3(001)$ surface: An atomically resolved study *via* noncontact atomic force microscopy" [372].

3.3.1 Thermal stability of the bulk-terminated $SrTiO_3(001)$ surface

The cleaved, bulk-terminated $SrTiO_3(001)$ surfaces are unreconstructed, but they must contain 14% of polarity compensating point defects in the form of V_{Sr} and Sr_{ad} on SrO and TiO_2 terminations, respectively. Therefore, although perfectly clean, these surfaces cannot be considered entirely perfect. A possible route to healing the Sr vacancies on SrO termination with Sr adatoms from the TiO_2 termination is annealing the system. The supply of thermal energy could be expected to help overcome the segregation of the point defects in order to restore the bulk stoichiometry on both terminations. For this reason, annealing excursions of the cleaved $SrTiO_3(001)$ to different temperatures was performed, and the resulting surfaces were observed with STM/AFM, with the addition of XPS and LEED.

Experimentally, annealing the as-cleaved surface requires that the entire cleaving device is thoroughly degassed in UHV to high temperatures prior to cleaving. This has to be done while the $SrTiO_3$ single crystal is pre-strained within the cleaving device, which limits the maximum degassing temperature. Differential thermal conductivity can lead to an increase of the strain on the $SrTiO_3$ single crystal during degassing, which can result in the self-cleaving of the crystal. Moreover, the differential expansion of the cleaving device and the M2 screws used for clamping the $SrTiO_3$ can lead to loosening of the grip on the single crystal, which results in insufficient strain after the entire cleaving device has cooled down post-degassing. For these reasons, the maximum UHV-degassing temperature of the cleaving device with the pre-strained $SrTiO_3$ mounted within has never exceeded 500 °C, thereby limiting the annealing excursions of the cleaved $SrTiO_3(001)$ surface to this temperature. The degassing usually takes several hours due to the large surface area of the entire cleaving device which is saturated with H_2O and other air-borne contaminants upon introduction to UHV. For the annealing experiments, the entire cleaving device was constructed from Mo, which can withstand much higher temperatures than the normally used stainless steel. It is noteworthy that cleaving a $SrTiO_3$ single crystal in a Mo cleaving device is not as easy and not as successful as cleaving in a stainless steel cleaving device, most probably because Mo is more resilient to plastic deformation than stainless steel - more details will be presented in Section 3.4. Annealing was performed *via* a resistive-heating wire below the sample mount.The actual annealing temperatures of the cleaved surfaces could be up to 30 °C lower than reported, due to the weak thermal contact of the surface with the heating filament where the temperature is measured; long annealing times ensure that these two temperatures are approximately the same. The experiments presented below were performed on $SrTiO_3(001)$ surfaces obtained by cleaving the $SrTiO_3$ single crystals with 0.69 at.% Nb doping.

Figures 69 and 70 focus on the thermal evolution of the SrO and the TiO_2 termination, respectively. STM images illustrate the large-scale surface morphology, while smaller-size AFM images provide details of the atomic structure. After cleaving at room temperature the surface is atomically flat, and this is the starting point of the annealing experiments (left-most panels in Figs. 69 and 70). It was previously shown (Fig. 61 and 62) that STM does not reflect the atomic arrangement that the (1×1) surface can be seen only in AFM. Large-area STM images were obtained in the empty-states mode, with sufficient sample bias that ensures safe imaging over both, the semiconducting SrO and the metallic TiO_2. AFM images were obtained with an O-terminated tip that detects Sr atoms as attractive and O atoms as repulsive interaction; the AFM contrast has been artificially inverted in Fig. 69b such that the images are clearer for scientific communities not versed in the AFM technique - bright color implies attraction while dark color implies repulsion in this case. Each annealing step in Figs. 69 and 70 was performed for 45 min on the sample that was previously degassed together with the cleaving device at the temperature of 500 °C.

A large-area STM image of the SrO termination as-cleaved at RT, left-most panel Fig. 69a, shows a corrugation as high as a full unit cell (≈0.4 nm), visible in the line profile above the image. This is a purely electronic

Die approbierte gedruckte Originalversion dieser Dissertation ist an der TU Wien Bibliothek verfügbar.
The approved original version of this doctoral thesis is available in print at TU Wien Bibliothek.
TU Bibliothek Your knowledge hub WIEN

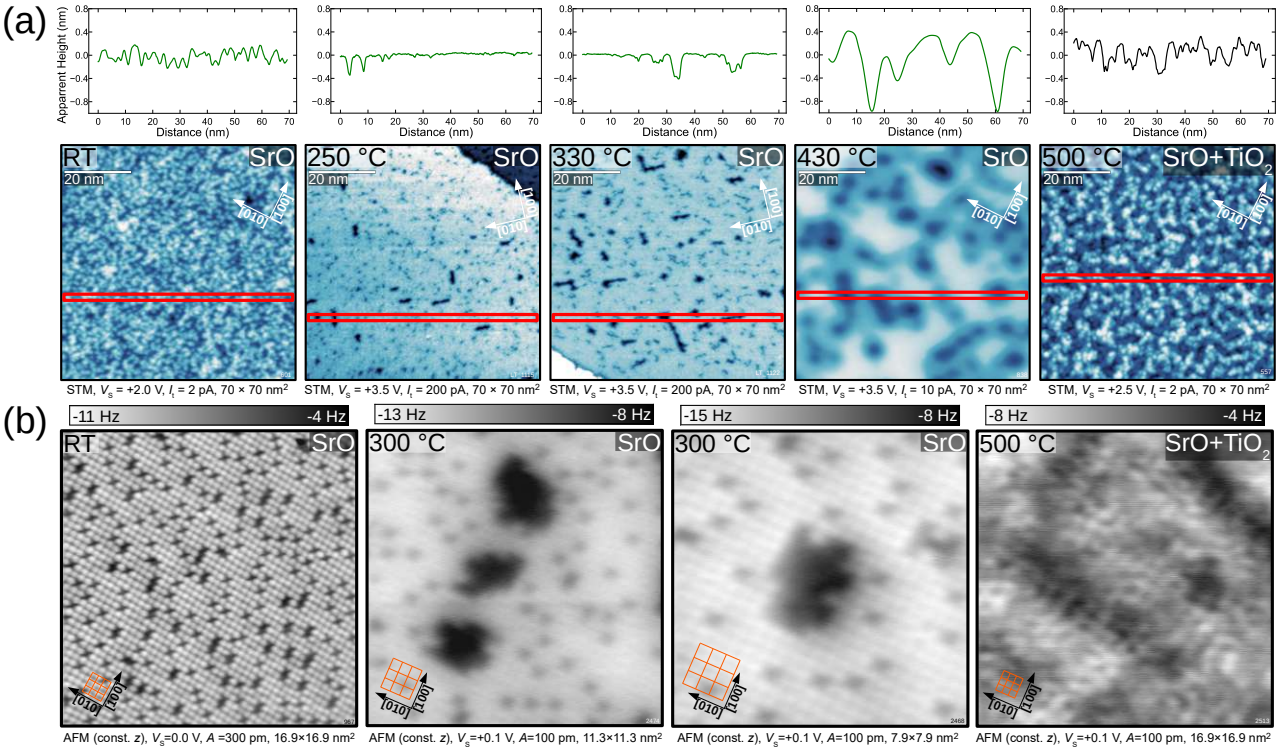

Figure 69: **SrO termination of the cleaved $SrTiO_3$(001) surface, as-cleaved and annealed at different temperatures.** Sequence of (a) empty-states STM images with line profiles extracted from the marked red rectangles; (b) atomically resolved constant-height AFM images, with the (1×1) grid shown in orange.

effect originating from the band bending induced by the charged Sr vacancies (Fig. 61c). Annealing the SrO termination at 250 °C results in the formation of pits on flat SrO terraces, visible in the STM image in Fig. 69a. The pits are preferentially oriented along the main crystallographic axes, [100] and [010]. Further annealing of the surface to 330 °C results in the increase of the lateral size of the pits, while their growth still proceeds along the [100] and [010] directions. Line profiles over the surface annealed at 250–330 °C reveal that the pits have the apparent depth of a single unit cell. Additionally, the STM corrugation seems to be much flatter in the regions of the surface without the pits, compared to the as-cleaved surface – STM shows a corrugation as small as few pm in these regions. Annealing the surface further, at 430 °C in UHV, increases the size of the pits, and they are no longer elongated along the main crystallographic axes but extend laterally in circular shapes. The coverage of the pits on the SrO termination is also increased compared to their coverage on the surface annealed at lower temperatures. The apparent STM corrugation on the surface annealed at 430 °C measures the pits as either single- or double-unit-cell-size deep — each apparently double-unit-cell-deep pit is surrounded by a halo of an apparently single-unit-cell-deep pit in STM images — while the surface regions that remained intact are featureless. This is in contrast with the as-cleaved SrO surface and the surface annealed at lower temperatures, where the intact surface always shows a certain STM corrugation (larger on the as-cleaved surface and smaller at the surface annealed at 250–330 °C in UHV). These arguments indicate that the apparent STM corrugation of the SrO termination annealed at 430 °C does not reflect the actual surface morphology, but is rather governed by the peculiar distribution of the electronic states. Annealing the surface at higher temperatures, at 500 °C shown in the right-most panel in Fig. 69a, results in the surface morphology where the pits are no longer recognizable as isolated features. This surface consists of intertwined protrusions and depressions, in equal concentration. The line profile of a SrO termination annealed at 500 °C measures the apparent height of the protrusions, and the depth of the depressions to be a single-unit-cell-deep on average, and the peculiar electronic corrugations present at the 430 °C-annealed surface are lost. In summary, STM reveals that the SrO termination evolves by developing pits that grow with temperature, until the entire surface is covered by a two-layer structure at 500 °C, consisting of an underlying substrate and single-unit-cell-high steps.

Smaller-area AFM images reveal the atomic arrangements of the SrO termination at different annealing

Die approbierte gedruckte Originalversion dieser Dissertation ist an der TU Wien Bibliothek verfügbar.
The approved original version of this doctoral thesis is available in print at TU Wien Bibliothek.
TU Bibliothek Your knowledge hub WIEN

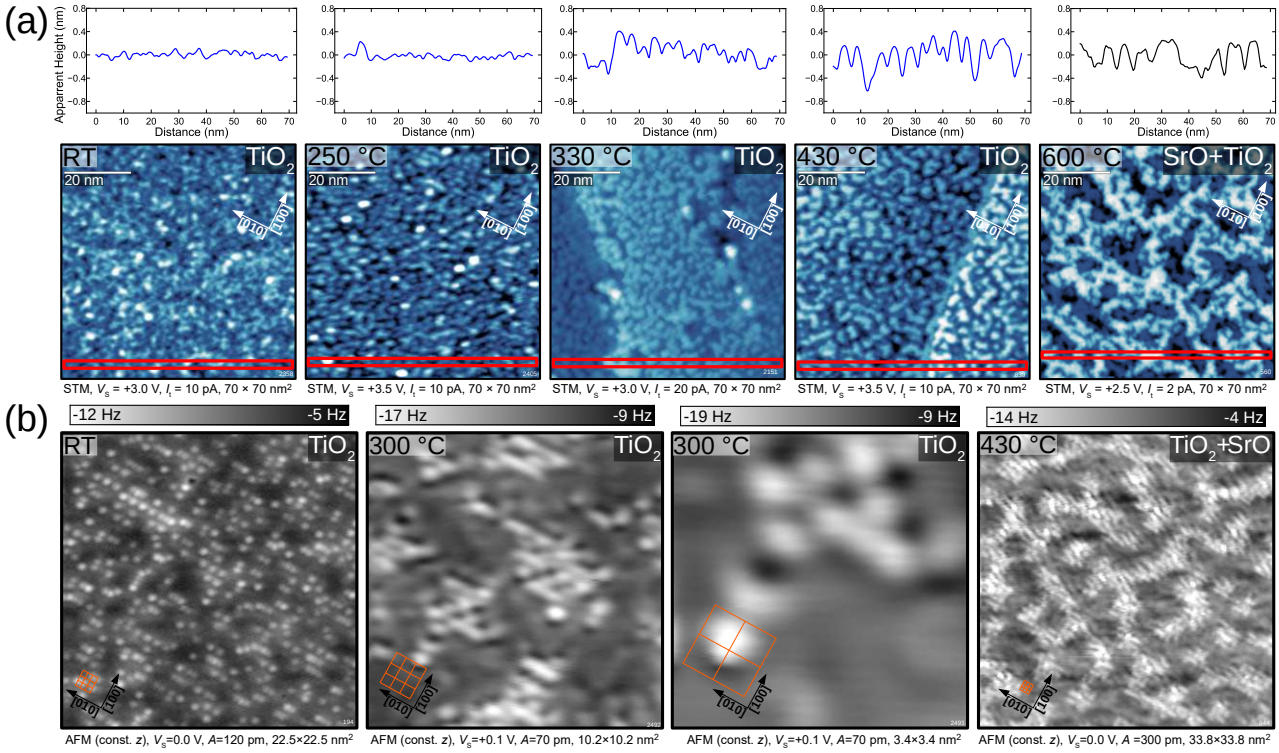

Figure 70: **TiO_2 termination of the bulk-terminated $SrTiO_3$(001) surface, as-cleaved and annealed at different temperatures.** Sequence of (a) empty-states STM images and line profiles extracted from the marked red rectangle; (b) atomically resolved constant-height AFM images, with the (1×1) grid shown in orange.

temperatures, shown in Fig. 69b. The structure of the surface containing medium-sized pits is captured at the annealing temperature of 300 °C. At this annealing temperature, V_{Sr} are already mobile. They agglomerate into larger half-unit-cell-deep pits that expose the underlying TiO_2 termination. The surroundings of the pits remain unreconstructed, with significantly fewer V_{Sr} defects compared to the as-cleaved surface. Besides missing Sr atoms, there are also no O atoms within the pits – the presence of anion/cations would be recognized by imaging with differently terminated AFM tips. The created pits are therefore stoichiometric, *i.e.*, annealing the surface results in the formation of SrO pits at the SrO termination. The absence of O atoms can be rationalized as necessary for the reduction of high electrostatic potential that would arise from the agglomerates consisting of only the negatively charged V_{Sr}^{2-}. In other words, SrO pits can be considered aggregates of Schottky-type defects [373], created by the coupling of the oppositely charged defects. The energy gain of neutralizing the charged defects fuels the diffusion of Sr vacancies and the formation of O vacancies [374], that would otherwise not be expected at temperatures as low as 300 °C. It is noteworthy that the agglomerates of V_{Sr} that span in both [100] and [010] directions have been observed only at the annealed surfaces, while these agglomerates appear exclusively along either of the main crystallographic axes at the as-cleaved surfaces; the growth of V_{Sr} agglomerates in all directions therefore seems to be conditioned by the formation of O vacancies that do not appear without supplying thermal energy.

After annealing the SrO termination at 500 °C, AFM acquired with an O-terminated tip no longer reveals any coherent structures. While STM images of the surface annealed at this temperature indicate a two-layer structure with clear steps and boundaries between the top and the bottom layer, the AFM reveals that such clear distinction does not exist, and the surface shows a smooth transition between the top-most layers and the ones beneath. The absence of clear AFM imaging on this type of surface is indeed indicative that the surface became disordered. From Fig. 69b it can be deduced that SrO termination does not remain unreconstructed once all V_{Sr} agglomerated into SrO pits. Instead, it minimizes surface energy by turning to a disordered structure between 300 °C and 500 °C through material mixing from the previously unreconstructed SrO and the underlying TiO_2, presumably aided by the fully formed SrO pits. This result demonstrates the instability

Die approbierte gedruckte Originalversion dieser Dissertation ist an der TU Wien Bibliothek verfügbar.
The approved original version of this doctoral thesis is available in print at TU Wien Bibliothek.
TU Bibliothek Your knowledge hub WIEN

of the unreconstructed SrO surface to some extent, granted the cleaved SrO termination contains point defects that might be responsible for its thermal evolution into a disordered structure.

The thermal evolution of the TiO_2 termination is seen in STM images in Fig. 70a that capture the large-area morphology, together with the line profiles displayed above each STM image. The STM corrugation of the as-cleaved surface at RT is flatter compared to that of the as-cleaved SrO termination, due to the absence of band-bending on this metallic termination. Annealing at 250 °C does not induce significant changes on the morphology nor the apparent STM corrugation over the TiO_2 termination. After annealing at 330 °C, the morphology of the TiO_2 termination starts to change. Spherical conglomerates start appearing the surface, roughly 5 nm in diameter, which are uniformly distributed across the surface. The STM corrugation indicates that the spherical protrusions are between half-unit-cell and one-unit-cell high. After the surface is annealed at 430 °C, these protrusions laterally grow and elongate in all directions. The increased size of the protrusions to roughly 8–10 nm enables smoother line profiles of the STM corrugations, which show that the apparent height of the protrusions is close to one-unit-cell. Annealing the surface at 500 °C in UHV results in a surface morphology identical to the morphology shown in the right-most panel in Fig. 69a. In other words, previously TiO_2- and SrO-terminated surface regions can no longer be distinguished after annealing the cleaved surface at the temperature of 500 °C in UHV – the entire well-cleaved surface is characterized with the same morphology of one-unit-cell-high islands on the underlying substrate. At temperatures higher than 500 °, the surface roughness does not improve and the two terminations remain indistinguishable. The top-layer islands grow and better-connected, as can be seen in the STM image of the surface annealed at 600 °C in the right-most panel of Fig. 70a. The island coverage remains the same at the surface annealed in UHV at both, 500 °C and 600 °C, while their lateral growth results in the decreased number of islands with the increase in the annealing temperature. After annealing at 500 °C the previous TiO_2 termination appears disordered and becomes indistinguishable from what was the SrO termination (rightmost panel of Figs. 69a and 69b).

The atomic structure of the observed island formation on the annealed TiO_2 termination can be seen in the series of AFM images in Fig. 70b. The left-most panel shows the TiO_2-terminated surface obtained after cleaving at RT, which is the starting point of each annealing experiment. Imaging the surface with AFM after annealing at 300 °C in UHV reveals that the spherical protrusions imaged with STM correspond to congregates of intrinsic Sr adatoms that diffused to create disconnected islands; several islands are visible in the second panel in Fig. 70b. A smaller area AFM image over one of these islands (the third panel in Fig. 70b) reveals that they do not contain solely the Sr_{ad}, imaged as white spheres, but the O atoms can also be observed as dark spheres within the island. Therefore, the islands that appear at the TiO_2 termination during annealing in UHV are SrO islands, that do not appear to be completely stoichiometric. The Sr and O atoms are organized in an incomplete $c(2\times2)$ reconstruction within the SrO islands. The intrinsic excess of Sr adatoms at the as-cleaved TiO_2 termination constitute an ideal seed for the crystal growth of the next perovskite $SrTiO_3$ layer, provided the temperature is sufficiently high for the diffusion of the adatoms and of oxygen to complete the SrO stoichiometry. The $c(2\times2)$-like areas spread with increasing temperature up to 430 °C. Islands grow more connected, while still not covering the entire surface. The maximum coverage of this SrO superstructure over the TiO_2 termination is limited by the initial 0.14 ML coverage of the Sr adatoms. When arranged in a $c(2\times2)$ superstructure, it can cover 28% of the surface area, close to the maximum coverage observed in AFM. After annealing at 500 °C the previous TiO_2 termination appears disordered and becomes indistinguishable from what was the SrO termination.

The two opposite terminations of the as-cleaved $SrTiO_3(001)$-(1×1) surface experience a complementary evolution with annealing, as demonstrated in Figs.69 and 70. The pit/island creation mechanism is induced by the presence of the intrinsic, polarity–compensating point defects, *i.e.*, Sr vacancies and Sr adatoms [341]. Migration of these charged point defects is activated at temperatures as low as 200 °C. The disappearance/appearance of O could originate from the exchange with the subsurface region, because lateral diffusion across the whole micrometers-wide domains is unlikely [375, 376]. The temperature range for migration of vacancies is slightly lower than reported in the literature for $SrTiO_3$ [377, 283], but can be rationalized by the presence of electric fields related to the charged defects, *i.e.*, the energy gain in creating Schottky-type defects compared to isolated charged defects.

The formation of SrO islands and pits on the TiO_2 and SrO terminations of the bulk-terminated $SrTiO_3(001)$, respectively, was further investigated by changing the stoichiometry of the surface. This was accomplished by either depositing Sr or annealing in 5×10^{-7} mbar O_2. Figures 71a and 71b show large-area STM (left) and atomically resolved AFM (right) images of the surface after Sr deposition at room temperature, followed by 45 min post-annealing at 150 °C in UHV. The deposited Sr atoms increase the concentration of the Sr adatoms on the TiO_2 termination, and fill up Sr vacancies on the SrO termination. The amount of evaporated Sr was

Die approbierte gedruckte Originalversion dieser Dissertation ist an der TU Wien Bibliothek verfügbar.
The approved original version of this doctoral thesis is available in print at TU Wien Bibliothek.
TU Bibliothek Your knowledge hub WIEN

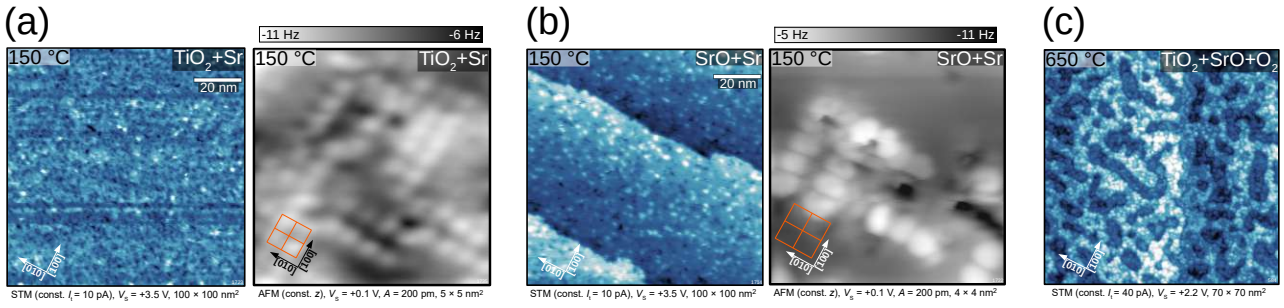

Figure 71: **The evolution of the cleaved $SrTiO_3$(001)-(1×1) surface with altered stoichiometry.** STM and AFM images of the (a) TiO_2 and (b) SrO terminations of the bulk-terminated $SrTiO_3$(001) with ≈0.25 ML of Sr atoms deposited at room temperature and subsequently annealed to 150 °C. Orange quadratic grids represent the arrangement of the $SrTiO_3$(001) unit cells on the surface. (c) STM image of the cleaved $SrTiO_3$(001) surface (previously annealed to 600 °C in UHV) annealed to 650 °C in 5×10^{-7} mbar of O_2 for 30 min.

roughly 0.25 monolayers (ML), which was larger than the intrinsic Sr adatom (Sr vacancy) concentration of 0.14 ± 0.02 ML. As a consequence, excess Sr is found as adatoms on the SrO termination as well. The post-annealing temperature of 150 °C is already sufficient for the aggregation of excess Sr adatoms into islands on both terminations. The new (1×1) SrO layer grows over the TiO_2 termination by forming one-layer-high islands, visible in the right panel of Fig. 71a. On the SrO termination, excess Sr adatoms diffuse to form a structure with partial (2×1) ordering, shown in the right panel of Fig. 71b. In this reconstruction only the Sr atoms (imaged as bright) were observed, and the absence of periodic features that would be imaged as dark may indicate the absence (or a significant shortage) of O atoms. The presence of dark features (O atoms) on the TiO_2 termination and their absence (or a significant shortage) on the SrO termination dismisses the background gas as the oxygen reservoir during annealing, and supports the argument that the oxygen is exchanged within/along the surface. This (2×1) structure is induced solely by deposition of Sr, and does not consist of Ti and O atoms organized in a (2×1) reconstruction observed on the TiO_2 terminated surfaces [378]. The STM image in Fig. 71c shows the surface morphology of the as-cleaved surface that was annealed for 30 min at 650 °C in 5×10^{-7} mbar of O_2, after gradual annealing from room temperature up to 600 °C in UHV. Compared to the final panel of the Fig. 70a (which shows the 600 °C UHV treatment), annealing at 650 °C in 5×10^{-7} mbar O_2 merely induces coarsening of the SrO islands.

The chemical composition and possible changes during annealing of the bulk-terminated $SrTiO_3$(001) surface were additionally investigated with XPS, as shown Figs. 72 and 73a. XPS measurements were obtained with either Mg $K\alpha$ or Al $K\alpha$ x-rays with a dual-anode x-ray source (SPECS XR50, Mg/Al $K\alpha$) and a SPECS Phoibos 100 hemispherical analyzer. As the Mg and Al anode films of the x-ray source are not perfect, also Ag $L\alpha$ x-rays (2983 eV) from the Ag anode block were emitted, leading to weak, additional lines in the photoelectron spectra. These lines originate from Sr 2s, Sr $2p_{1/2}$, and $2p_{3/2}$ core levels. These XPS signals can be recognized in most of the XP spectra presented here (marked with an asterisk), unless they are overlapping with a much stronger signal from a different core level. The Earth's magnetic field was compensated with a magnetic coil. The measurements were performed at room temperature in a stainless-steel UHV chamber with a base pressure below 1×10^{-10} mbar.

Overview XPS of the as-cleaved surface (marked as RT) and after annealing to different temperatures in UHV are shown in Fig. 72. The XPS could only be obtained in normal electron emission due to the sample geometry. The cleaved surface in this experiment measured $1\times3\,mm^2$, which is much smaller than the cut-and-polished crystals usually used. Additionally, the cleaved surfaces were held in the specifically designed cleaving device during measurements, which can block the incident x-rays and reduce the number of photoemitted electrons. Together with minimizing the acceptance area of the analyzer, this results in a relatively low photo-electron count. Grazing emission measurements yielded too weak signals. The cleaved surfaces are by definition perfectly clean, and the XPS confirms the absence of any contaminants. The overview spectrum of the as-cleaved surface shows only the Nb and Mo core-levels in addition to the core-levels of Sr, Ti, and O (shown in more detail in Fig. 73a). The Nb signal (superimposed on the Sr $2p_{3/2}$ excited by Ag $L\alpha$ x-rays) originates from the doping, while the Mo signal originates from the cleaving device. No additional signals appeared in the XP spectra

Die approbierte gedruckte Originalversion dieser Dissertation ist an der TU Wien Bibliothek verfügbar.
The approved original version of this doctoral thesis is available in print at TU Wien Bibliothek.
TU Bibliothek Your knowledge hub WIEN

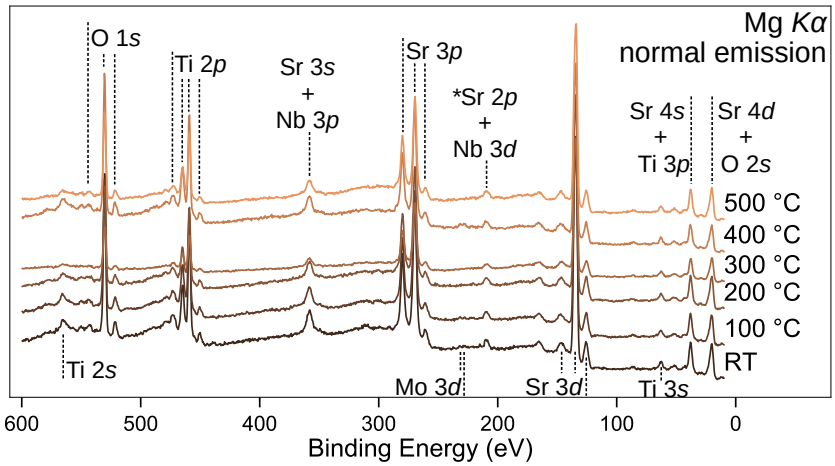

Figure 72: **$SrTiO_3$(001)-(1×1), cleaved at room temperature and annealed to increasing temperatures.** Overview XPS taken after different stages of annealing in UHV of the cleaved, bulk-terminated $SrTiO_3$(001) sample in UHV. XP spectra were obtained with Mg $K\alpha$ x-rays in normal electron emission with respect to the surface. The main peaks are marked; asterisks indicates peaks excited by stray Ag $L\alpha$ x-rays.

after different annealing temperatures. Therefore, contamination from the residual gas can be excluded, and the observed morphology changes in Figs. 69, 70 are an intrinsic property of the bulk-terminated $SrTiO_3$(001) surface.

The core-levels of the constituent atoms on the surface were investigated with detailed XPS scans shown in Fig. 73a. The detailed core-level spectra of the common C contamination in UHV (except on the cleaved surfaces) is shown together with the Sr 3p signal, and clearly the cleaved surface contains no organic contamination. More importantly, the core-level spectra of the constituents (Sr, Ti, and O) do not change shape or shift to different binding energies during annealing, which indicates that the overall surface stoichiometry is preserved. Despite the reducing character of the UHV environment, the elements retain their oxidation state, and the appearance/disappearance of O atoms on stoichiometric SrO islands/pits on TiO_2 and SrO terminations, respectively, cannot be assigned to the exchange with the background gas in UHV.

LEED measurements on the as-cleaved $SrTiO_3$(001) surface that was subsequently annealed at different temperatures in UHV are shown in Fig. 73b. The measurements were performed at room temperature in an UHV chamber with a base pressure below 1×10^{-10} mbar, with various incident electron energies in the 90–100 eV range. The as-cleaved surface exhibits a clear (1×1) LEED pattern. This periodicity does not change after various annealing steps. A distinct (1×1) LEED pattern is also reported throughout literature for polished $SrTiO_3$(001) surfaces annealed at temperatures above 600 °C, necessary for degassing after introduction into UHV. Above 850 °C, spots originating from c(4×2) [378, 379], or (1×2) [326] reconstructions start to appear.

Although the as-cleaved surface clearly undergoes structural changes upon annealing, they are not captured by LEED patterns which show a consistent (1×1) pattern. Therefore, the (1×1) LEED pattern of the annealed surface must be attributed to diffraction from the subsurface layers. The small islands that formed on the TiO_2 surface with an incomplete c(2×2) reconstruction are not detected by LEED since their lateral size is smaller than 10 nm, which is the typical transfer width of the LEED setup. On the other hand, the disordered surface layer that appears after annealing above 500 °C results in incoherent electron diffraction, and contributes to the observed (1×1) LEED pattern only as the background intensity. Although LEED patterns remain (1×1) throughout annealing, the sharpness of the LEED spots and the background intensity vary: The sharpest diffraction pattern was observed after annealing at 200 °C, while further annealing degraded the pattern. It is noteworthy that this sharpest LEED pattern coincides with the annealing temperature at which the smallest apparent STM corrugation was observed, which implies that the reduction of band-bending across the moderately annealed surface where isolated Schottky-type defects are created is responsible for the reduction of the incoherent diffraction background of the LEED pattern in this case.

In conclusion, both terminations of the cleaved, bulk-terminated $SrTiO_3$(001) surface are unstable upon thermal annealing. At lower temperatures $T < 400$ °C, the two terminations evolve in a complementary fashion, through the formation of SrO pits and SrO islands on the SrO and TiO_2 terminations, respectively. At

Die approbierte gedruckte Originalversion dieser Dissertation ist an der TU Wien Bibliothek verfügbar.
The approved original version of this doctoral thesis is available in print at TU Wien Bibliothek.
TU Bibliothek Your knowledge hub WIEN

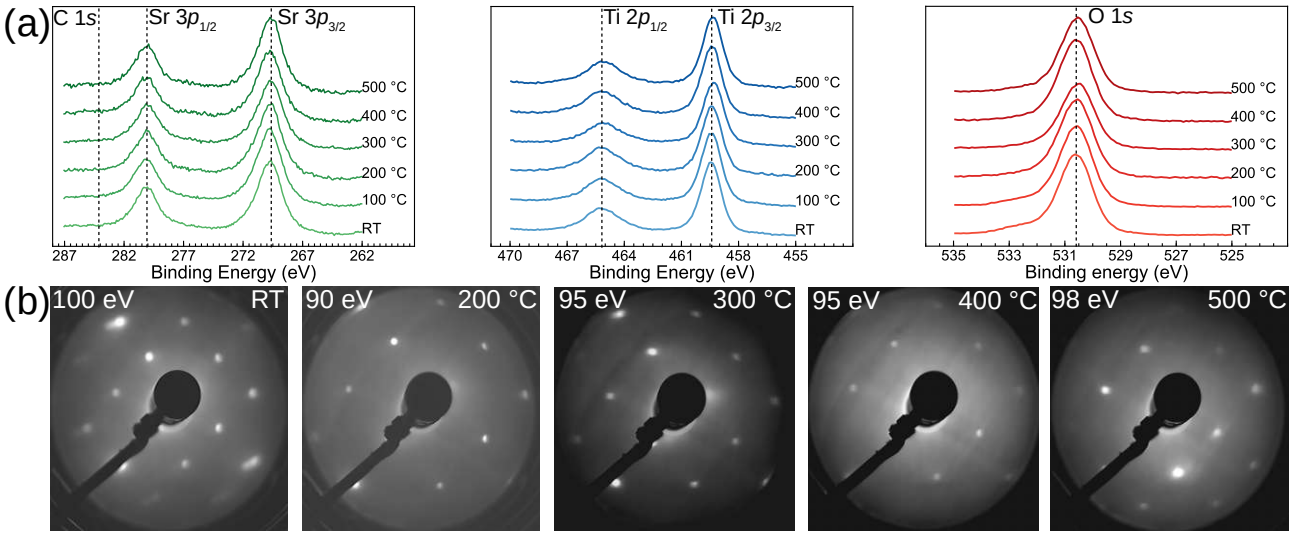

Figure 73: **$SrTiO_3$(001)-(1×1), cleaved at room temperature and annealed to increasing temperatures.** (a) XPS of the main core levels, obtained with Mg $K\alpha$ radiation. Spectra are offset vertically for clarity. (b) LEED patterns recorded at room temperature after cleavage, and after various annealing steps. No substantial change is discerned in these area-averaging measurements.

elevated temperatures $T > 500\,°C$ the entire surface becomes unstable, and the two terminations can no longer be distinguished because they are covered by a disordered surface layer. This thermal instability of the unreconstructed-terminated surface indicates that the (1×1) termination is not stable at higher temperatures. However, all surface preparation techniques encountered in literature include the annealing step to at least 600 °C in order to remove adsorbates upon introduction of a surface to UHV. Results presented here imply that the presence of a (1×1)-terminated surface is therefore not likely on surfaces prepared this way. Moreover, it was shown that the LEED pattern cannot be taken as a clear indication that the $SrTiO_3$(001) surface is unreconstructed: on the cleaved surfaces, both the as-cleaved surface with a true (1×1) periodicity and the disordered surface after annealing to 500 °C show the same (1×1) LEED patterns. Considering the absence of atomically resolved studies of the unreconstructed $SrTiO_3$(001) surfaces, and the most common way of identifying the surface structure as (1×1) is through electron diffraction techniques such is LEED, results presented here raise a question whether the unreconstructed $SrTiO_3$(001) surface was ever encountered previously.

Die approbierte gedruckte Originalversion dieser Dissertation ist an der TU Wien Bibliothek verfügbar.
The approved original version of this doctoral thesis is available in print at TU Wien Bibliothek.
TU Bibliothek Your knowledge hub WIEN

3.3.2 Atomically resolved study of etched $SrTiO_3(001)$ surfaces

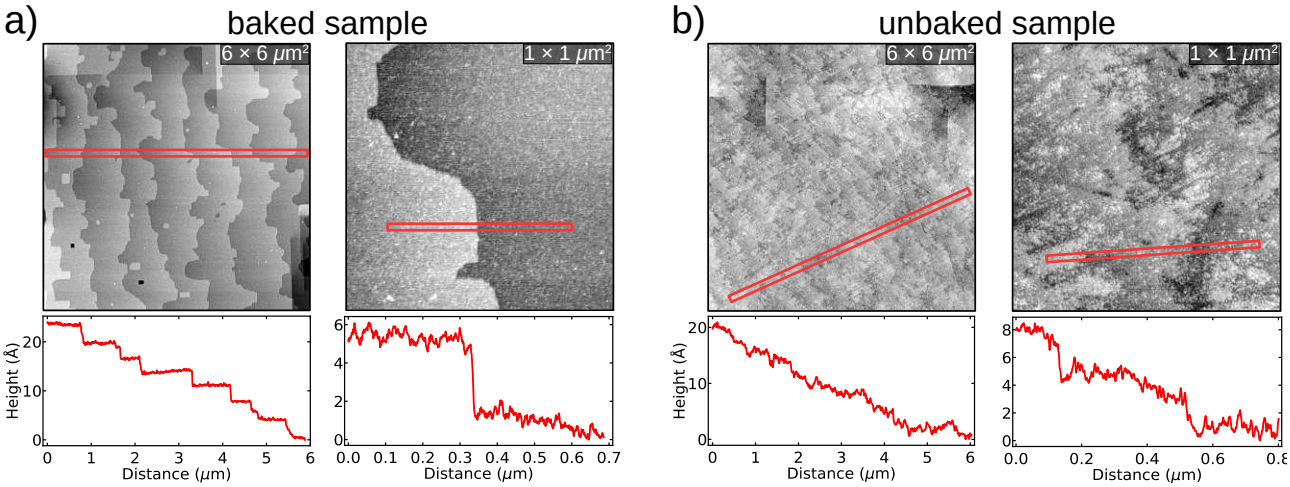

Figure 74: **Ambient AFM of two cut-and-polished $SrTiO_3(001)$ samples after *ex-situ* preparation and prior to introduction to UHV.** Linescans across (a) the baked sample and (b) the unbaked sample (right column) measure only single-unit-cell-high steps. Large- (left panel) and small-area (right panel) ambient AFM images show that the surfaces have large flat areas, which were later investigated with STM/AFM in UHV.

The previous section shows that the intrinsic point defects dominate the thermal behavior of the cleaved crystals. The search for the pristine, unreconstructed $SrTiO_3(001)$ surface was expanded to the traditionally prepared surfaces, by wet-chemical etching and subsequent degassing in UHV; the details of the commonly used preparation techniques are laid out in Section 3.1.1. These surfaces are are terminated with TiO_2 only [323, 320, 324, 380, 381], contrary to cleaved, bulk-terminated $SrTiO_3(001)$, and presumably contain no polarity-compensating point defects because ferroelectricity is not involved in the creation of etched surfaces. Even though the probability of obtaining the pristine, unreconstructed surfaces on the chemically etched TiO_2-terminated surfaces is slim, because it was shown that an unreconstructed surface turns disordered at the temperature lower than the one traditionally used for degassing the etched samples in UHV, two cut-and-polished $SrTiO_3(001)$ crystals (CrysTec GmbH, $5{\times}5{\times}1$ mm^3) with 0.5 wt.% of Nb_2O_5 doping (0.69 at.% Nb-doping) were investigated. Annealing excursions to gradually increased temperatures were performed, and the surface morphology and atomic structure was characterized with high precision using STM/AFM, while the integral techniques such are XPS and LEED were used to judge surface cleanliness and the presence of structures with long range ordering at the surface.

Both cut-and-polished $SrTiO_3(001)$ samples were prepared *ex situ*. They were initially cleaned in the same manner, with cycles of sonication in warm ($\approx 60\,^{\circ}$C) neutral detergent (3% Extran®MA02) and ultrapure deionized water (milliQ®). Each sonication cycle consisted of two sonication procedures in diluted Extran for 10 min each, followed by sonication in milliQ water for 15 min. Thorough rinsing with milliQ water was performed after each step. The glassware used in the cleaning procedure was boiled in diluted nitric acid (20% HNO_3) beforehand, and thoroughly rinsed with milliQ water. The morphology of the surface was routinely checked with ambient AFM to observe the distribution of large contaminants and verify that after each cleaning cycle the surface was cleaner. After the surfaces were free of particles, both samples were boiled in milliQ water for 15 min in order to etch away any layers of the SrO terminations on the surface. After additional cleaning cycles, the surfaces were again investigated with ambient AFM to confirm that flat terraces on the surface are separated by single- or multiple-unit-cell-high steps. All of these steps were done independently for the two samples. The two samples prepared this way combine the best practices for cut-and-polished $SrTiO_3(001)$ preparation found in the literature [321, 322, 331]. The other preparation protocol, i.e. etching in buffered HF (bHF) instead of milliQ water [323, 320, 324], was not investigated due to the reports that the samples prepared using bHF contain fluorine contamination [321].

One of the samples cleaned this way was introduced directly to UHV, referred to as the *unbaked sample* from now on, while the other sample was additionally annealed in air at 950 °C in a muffle furnace, and is referred to

Die approbierte gedruckte Originalversion dieser Dissertation ist an der TU Wien Bibliothek verfügbar.
The approved original version of this doctoral thesis is available in print at TU Wien Bibliothek.
TU Bibliothek Your knowledge hub WIEN

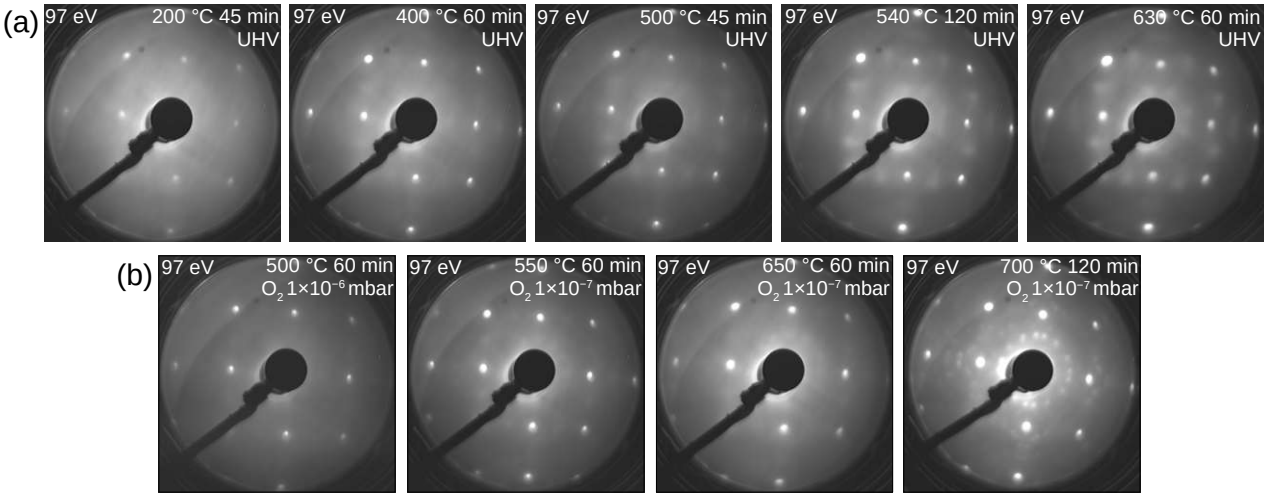

Figure 75: **LEED patterns taken after different stages of annealing of the cut-and-polished $SrTiO_3$(001) sample that was not baked prior to introduction to UHV – the *unbaked sample*.** LEED patterns of the unbaked sample annealed in (a) UHV and (b) in p_{O_2} ranging between 1×10^{-7} and 1×10^{-6} mbar. LEED patterns are organized in chronological order, i.e. the sample was first annealed in UHV from room temperature up to 630 °C, followed by progressive annealing in O_2 from 500 °C to 700 °C. LEED patterns are shown at two electron energies. The annealing temperature, the annealing environment (UHV or O_2 pressure), and the annealing time are indicated in each LEED pattern, together with the electron energy.

as the *baked sample* in the rest of the text. After annealing, the baked sample was additionally cleaned with a few cycles of sonication (Extran and milliQ) and investigated with ambient AFM prior to introduction to UHV. Each of the samples was mounted on a flag-style sample plate made from molybdenum, and held in place by Ta clips spot-welded to the plate. The time from the final cleaning cycle up to the introduction to UHV was kept below 1 h for both samples.

Ambient AFM images of both samples are shown in Fig. 74. The baked sample shows large, atomically flat terraces separated by single-unit-cell-high (≈ 4 Å) steps. The solely TiO_2-terminated surface was achieved by boiling in milliQ water, while the smoothness of the surface was achieved by baking at high temperature at ambient pressure [320, 324]. The unbaked sample has a rougher surface morphology (especially at the step edges) because the highest temperature this sample experienced is 100 °C during boiling in milliQ water. The unbaked sample also exposes only one termination (TiO_2), confirmed by the absence of half-unit-cell-high steps between the terraces, visible in the line profiles over the ambient AFM images in Fig. 74.

The unbaked sample was not exposed to high temperatures before introduction to UHV, making it a more suitable candidate for finding the unreconstructed surface. LEED patterns acquired on this sample after annealing in UHV, and later annealing in O_2, acquired at 97 eV impinging electron energy, are shown in Figs. 75a and 75b, respectively. After the lowest degassing temperature in UHV of 200 °C, the (1×1) LEED pattern is visible with a noticeable background contribution. At 400 °C, the (1×1) LEED pattern persists, with more pronounced LEED spots, and a weaker background. However, some additional, faint LEED spots are visible. Already at 500 °C, the previously faint LEED spots become much clearer, implying a superstructure on the surface. These spots may originate from a $p(2\times1)$ ordering (and the corresponding 90°-rotated domain), or $p(2\times2)$ periodicity (the latter if not all spots are visible). At 540 °C additional spots appear close to the (0,0) diffraction beam. The same holds true for the surface annealed to 630 °C, which is the highest annealing temperature this sample experienced in UHV. The extra spots in the LEED pattern could be recognized as the (1/4,1/2) spots originating from the $c(4\times2)$ reconstruction [382] – the remaining spots of the $c(4\times2)$ might be too weak in intensity and are not visible in the LEED patterns. Clearly, annealing in UHV to temperatures higher than 400 °C does not result in (1×1) LEED patterns but reconstructions are present at the surface.

The (1×1) LEED pattern reappeared only after additional annealing for 1 h in 1×10^{-6} mbar O_2, as shown in Fig. 75b. All LEED spots originating from a mixture of reconstructions vanished, and the LEED pattern exhibited only crisp (1×1) spots, although the surface is not flat and (1×1) terminated, as shown by STM/AFM in Fig. 78a. The background signal was also lower compared to previously obtained (1×1) LEED patterns during

Die approbierte gedruckte Originalversion dieser Dissertation ist an der TU Wien Bibliothek verfügbar.
The approved original version of this doctoral thesis is available in print at TU Wien Bibliothek.
TU Bibliothek Your knowledge hub WIEN

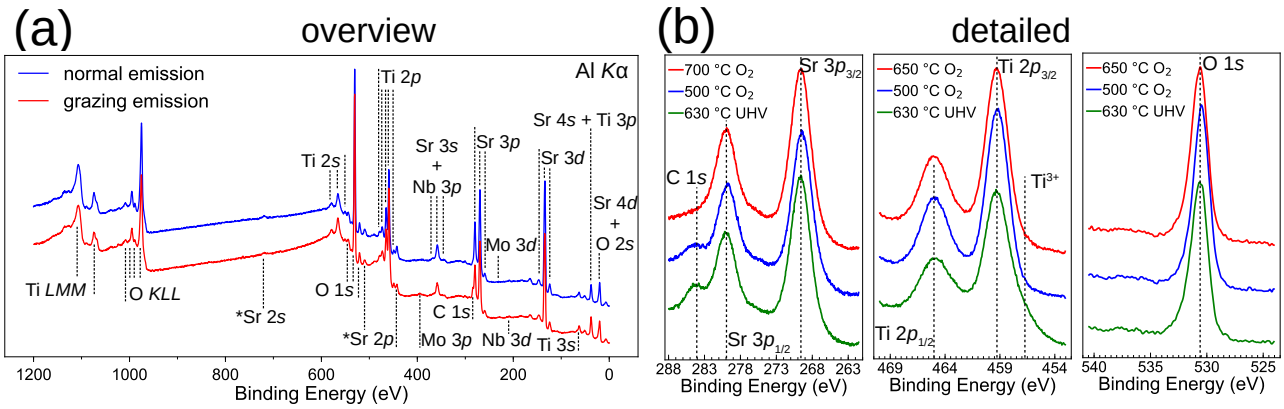

Figure 76: **XPS taken after different stages of the cut-and-polished $SrTiO_3$(001) sample that was not baked prior to introduction to UHV – the *unbaked sample*.** (a) XPS obtained with the Al $K\alpha$ x-rays in normal and grazing electron emission (65° with respect to the surface normal). Both spectra were obtained after annealing the unbaked sample at 630 °C in UHV. The main core-level and Auger peaks are identified and labeled, while the Sr core levels that are excited by stray Ag $L\alpha$ x-rays are marked with an asterisk. (b) Detailed XPS core-level spectra of the main elements at different annealing conditions, obtained with Al $K\alpha$ line in grazing emission.

annealing in UHV to 200 °C and 400 °C. Additional annealing in O_2 at higher temperatures resulted in the appearance of LEED spots associated with a mixture of reconstructions. Finally, at the annealing temperature of 700 °C in 1×10^{-7} mbar O_2, a clear $(\sqrt{13} \times \sqrt{13})R33.7°$ LEED pattern was observed. The surface was not annealed to higher temperatures because the transition from this complex reconstruction to an unreconstructed surface cannot be expected by simply increasing the annealing temperature.

The chemical composition of the surface was examined with XPS, as seen in Fig. 76. XP spectra were always obtained at room temperature, after the sample was investigated with STM/AFM and LEED, after each given annealing step. Figure 76a shows the XP spectra of the unbaked sample after annealing at 630 °C in UHV. Besides the expected core-level and Auger peaks of Sr, Ti, and O, there are also signals originating from Mo and Ta, and possibly a faint signal originating from Ca, a common contaminant in $SrTiO_3$ samples. Mo and Ta peaks originate from the sample plate and the clips used for mounting the sample. These peaks depend on the exact alignment of the sample with respect to the incident x-rays and the analyzer, and they do not influence the experiments. Their contribution is usually more pronounced in grazing emission, as the area from which the electrons are collected becomes larger. The C 1s peak comes from the organic contamination (adventitious carbon) remaining from the *ex-situ* preparation. According to the result in Fig. 76a, carbon is the only contaminant that is present only on the surface layer: the C 1s peak is undetectable in the XPS obtained in normal electron emission, while it is significant in grazing emission geometry.

Removal of carbon contamination from the surface is challenging in UHV. The easiest way is to sputter it off with high-energy Ar^+ ions, but this is known to also alter the cation composition at the $SrTiO_3$(001) surface, leading to the formation of surface reconstructions [325]. Annealing in UHV up to 630 °C was not sufficient to remove organic contaminants, as seen in Fig. 76a and in the detailed Sr XPS core-level spectra in Fig. 76b. However, the C 1s signal significantly decreased when this sample was subsequently annealed at 500 °C in 1×10^{-6} mbar O_2. Annealing in O_2 at higher temperatures further reduces the C 1s signal, until no more carbon is detected when the sample is annealed at 700 °C in 1×10^{-6} mbar O_2. At the same time, the LEED pattern of the surface annealed at these conditions (rightmost column of Fig. 75b) displays a clear reconstruction. Therefore, the annealing conditions necessary for removal of organic contaminants from the surface are sufficient to induce a surface reconstruction. Besides removal of C, the core-level spectra in Fig. 76b reveal that the increase in the annealing temperature and the addition of O from the background gas oxidizes the surface. The Ti^{3+} signal, on the lower-biding-energy side of the Ti 2 p core-level, decreases as the sample is annealed in oxygen atmosphere. This signal is associated with oxygen vacancies on the surface that donate electrons, which are known to form electron polarons on the Ti atoms in other materials, TiO_2 for example as investigated in Chapter 2. XPS core-level spectra of O does not significantly shift at different annealing conditions.

Die approbierte gedruckte Originalversion dieser Dissertation ist an der TU Wien Bibliothek verfügbar.
The approved original version of this doctoral thesis is available in print at TU Wien Bibliothek.
TU Bibliothek Your knowledge hub WIEN

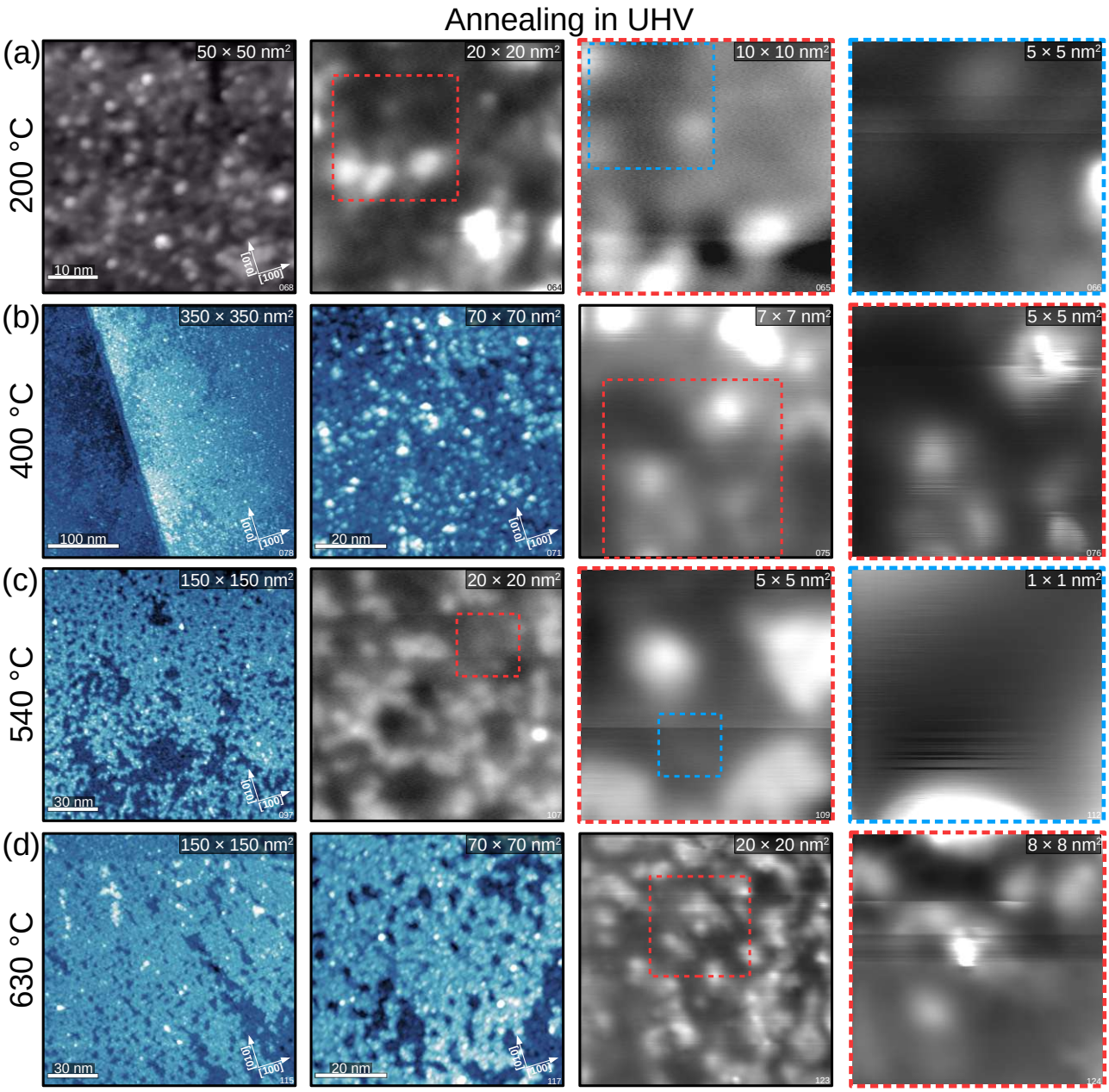

Figure 77: **STM and AFM images taken after different stages of annealing in UHV of the cut-and-polished $SrTiO_3$(001) sample that was not baked prior to introduction to UHV – the *unbaked sample.*** Empty-states STM images obtained with a bias voltage of +2 V (blue–white color scheme) and constant-height AFM images (gray scale), obtained with samples biased to +0.1 V and the oscillation amplitude in the 50–150 pm range (depending on the image), of the unbaked sample annealed in UHV at (a) 200 °C for 45 min, (b) 400 °C for 60 min, (c) 540 °C for 120 min, and (d) 630 °C for 60 min. Grey scale AFM images show strong attractive interaction as white, and weak interaction as black. Image size decreases from left to right, focusing on smaller details and evading large contamination blobs.

The unbaked sample was investigated with STM/AFM at each annealing conditions introduced in Figs. 75 and 76, and the details are shown in Figs. 77 and 78.

Figure 77 shows details of the surface of the unbaked sample annealed in UHV up to a final temperature of 630 °C. The surface annealed up to only 200 °C (Fig. 77a) was not scanned with STM, because this temperature is usually not sufficient to remove the contaminants that can interact strongly and damage the STM/AFM tip

Die approbierte gedruckte Originalversion dieser Dissertation ist an der TU Wien Bibliothek verfügbar.
The approved original version of this doctoral thesis is available in print at TU Wien Bibliothek.
TU Bibliothek Your knowledge hub WIEN

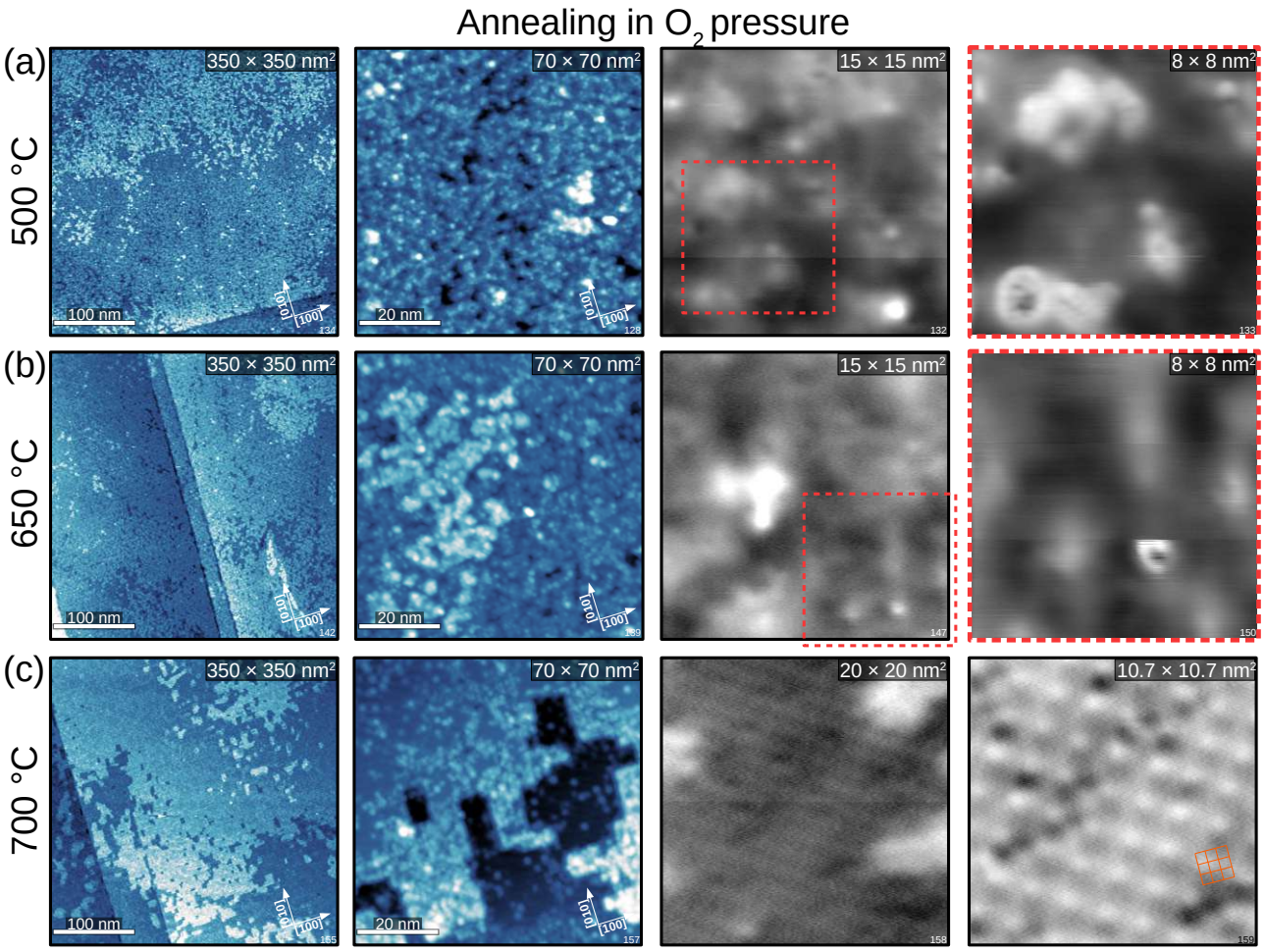

Figure 78: **STM and AFM images taken after different stages of annealing in O_2 pressure of the cut-and-polished $SrTiO_3$(001) sample that was not baked prior to introduction to UHV – the *unbaked sample.*** Empty-states STM images obtained with a bias voltage of +2 V (blue–white color scheme) and constant-height AFM images (gray scale), obtained with samples biased to +0.1 V and the oscillation amplitude in the 50–150 pm range (depending on the image), of the unbaked sample annealed at (a) 500 °C in 10^{-6} mbar O_2 for 60 min, (b) 650 °C in 10^{-6} mbar O_2 for 60 min, (c) 700 °C in 10^{-6} mbar O_2 for 120 min. Grey scale AFM images show strong attractive interaction as white, and weak interaction as black. Image size decreases from left to right, focusing on smaller details and evading large contamination blobs.

irreparably. Instead, Fig. 77a features an AFM overview image taken without applying a bias voltage, in order to avoid the transfer of contaminants between the surface and the tip due to the applied electric field, or the tunneling current. After annealing to 400–630 °C, the STM images in Figs. 77b–77d show terraces and single- or multiple-unit-cell-high steps, but the terraces appear covered with a disordered layer of bright spots. It is likely that the bright spots are due to organic contaminants, still present on the surface when annealing in UHV (according to the XPS in Fig. 76). The contamination is readily observed in constant-height AFM images shown in Figs. 77a–77d. These images lack any atomic order, and display a variety of different contaminants (bright features) with various shapes, lateral sizes and heights. Sequences of AFM images in Fig. 77 focus on smaller and smaller areas (from left to right), in order to avoid the prominent contaminants and attempt finding a clear region where atomic resolution could be obtained. This could not be achieved, and even the smallest images (rightmost panel in Fig. 77c) do not show the substrate, indicating that the contaminants are completely spread out across the surface. They cover the majority of the surface. This is in clear contrast to UHV-cleaved, TiO_2-terminated surfaces, where even in the absence of atomic resolution Sr adatoms nicely follow the substrate lattice and the terraces are large. The sample was afterwards annealed in O_2, which reduced

Die approbierte gedruckte Originalversion dieser Dissertation ist an der TU Wien Bibliothek verfügbar.
The approved original version of this doctoral thesis is available in print at TU Wien Bibliothek.
TU Bibliothek Your knowledge hub WIEN

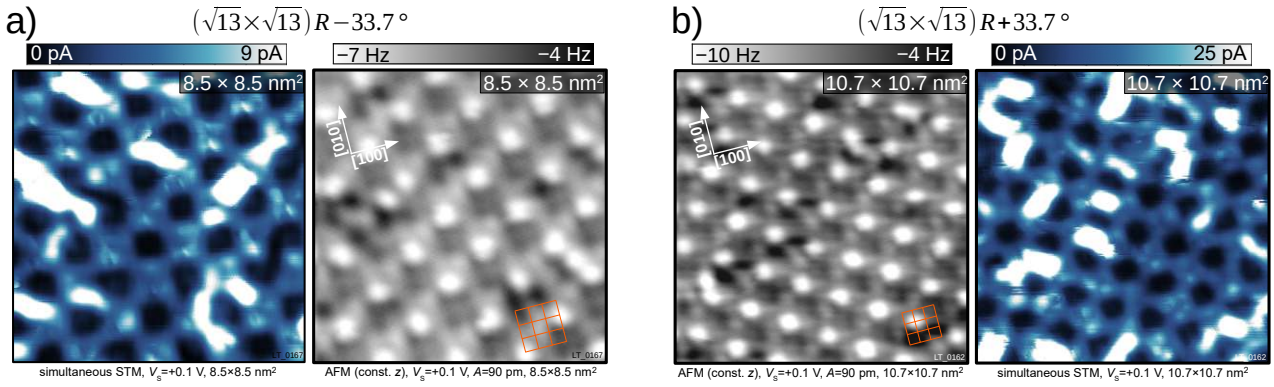

Figure 79: **Atomically resolved $(\sqrt{13}\times\sqrt{13})R\pm33.7°$ reconstruction on the *unbaked sample*.** Constant-height AFM and simultaneous empty-states STM images of the two rotationally equivalent domains, shown separately in (a) and (b), obtained on two distinct terraces separated by a single-unit-cell-high-step. This reconstruction appeared after removal of carbon from the unbaked sample after annealing treatment at 700 °C in 10^{-6} mbar O_2 for 120 min. The orange grid represents the (1×1) unit cell.

carbon contamination (Fig. 76) and restored the original (1×1) LEED pattern (Fig. 75).

Figure 78 shows STM/AFM images of the same unbaked sample that was subsequently annealed in O_2. Fig. 78a focuses on the first surface that was annealed in O_2 at 500 °C and showed reduced carbon contamination (Fig. 76) and a (1×1) pattern in LEED (Fig. 75). These STM and AFM images do not significantly differ from the images obtained after annealing in UHV. Disconnected bright patches persist in STM, and it is not clear whether their concentration has decreased when compared to Fig. 77d. Constant-height AFM still shows only contamination, and the rightmost panel of Fig. 78a even resolves a feature that might be an organic molecule, or some graphene-like structure. Further annealing in O_2 to 650 °C was shown to decrease the carbon contamination in XPS, but the STM/AFM images in 78b do not resolve a cleaner surface; no regions were located where the underlying surface could be imaged with atomic resolution. Only after annealing at 700 °C in O_2, the surface was sufficiently clean to resolve the $SrTiO_3(001)$ substrate, shown in Fig. 78c. XPS shows no detectable C 1*s* signal, while LEED shows a clear superstructure. The surface consists of large terraces separated by single-unit-cell-high steps, covered by the $(\sqrt{13}\times\sqrt{13})R\pm33.7°$ reconstruction.

The $(\sqrt{13}\times\sqrt{13})R\pm33.7°$ reconstruction is atomically resolved in Fig. 79. The two domains were scanned with the same azimuthal orientation, and they are rotated by $2\times33.7° = 67.4°$ with respect to each other. The azimuthal orientations are also in agreement with the sample orientation as specified by the crystal manufacturer and the fact that straight steps are usually oriented along ⟨100⟩ (seen in STM images in Fig. 78c). The constant height AFM shows that the protruding (bright) features are organized in a square grid larger than, and rotated with respect to the unreconstructed unit cell, marked by an orange grid. The simultaneous STM shows that the current signal directly correlates to the position of the geometrically protruding spots. However, empty-states STM also shows a significant concentration of highly conducting point defects or defects that run along the reconstruction. These points of increased conduction correlate to the positions of very faint features in AFM images, that are less protruding compared to the reconstructed lattice. Moreover, these defects can be responsible for the observation of the scattered spherical points in the STM image of the surface in Fig. 78c, yet they do not obstruct clear atomically resolved imaging using AFM (unlike the contamination present after previous annealing conditions). The concentration of these defects greatly exceeds the concentration of Nb-dopants, and their origin requires further investigation.

The $(\sqrt{13}\times\sqrt{13})R\pm33.7°$ reconstruction was previously reported in literature only after sufficient thermal treatment of the surface, which is here shown to be necessary for removing the C contamination. In remains to be investigated whether the C contamination prevents the appearance of this reconstruction at an earlier stage of the annealing, and whether it is responsible for stabilizing the (1×1) subsurface reconstruction beneath the contaminating layer.

The other cut-and-polished $SrTiO_3(001)$ sample that was prepared by *ex-situ* cleaning and boiling in milliQ water, and then baked to 950 °C in atmosphere for 2 h, was investigated with the same methods. This sample had a much smoother surface prior to introduction in UHV compared to the unbaked sample. According to ambient AFM, large and flat terraces spanned micrometers on this sample, visible in Fig. 74, with steps following

Die approbierte gedruckte Originalversion dieser Dissertation ist an der TU Wien Bibliothek verfügbar.
The approved original version of this doctoral thesis is available in print at TU Wien Bibliothek.
TU Bibliothek Your knowledge hub WIEN

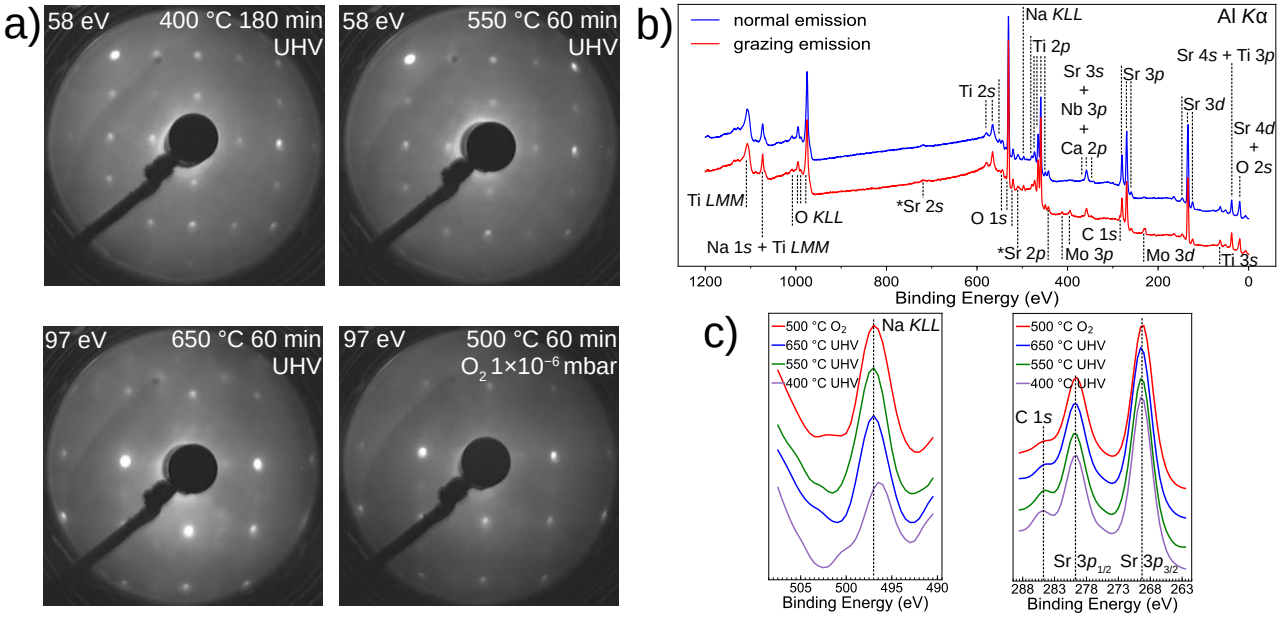

Figure 80: **LEED patterns and XP spectra taken after different stages of annealing of the cut-and-polished $SrTiO_3$(001) sample that was baked at 950 °C prior to introduction to UHV - the *baked sample.*** (a) LEED patterns of the baked sample annealed in UHV and in 1×10^{-6} mbar O_2. LEED patterns are organized in chronological order, i.e. the sample was first annealed in UHV from room temperature up to 650 °C, followed by annealing at 500 °C in 1×10^{-6} mbar O_2. The annealing temperatures, the annealing environments, and the annealing times are indicated for each LEED pattern, together with the energy of the incident electrons. (b) XPS obtained with Al $K\alpha$ x-rays in normal and grazing electron emission (65° with respect to the surface normal) Both spectra were obtained after annealing the baked sample at 650 °C in UHV. The main core-level and Auger peaks are identified and labeled, while the Sr core levels that are excited by stray Ag $L\alpha$ x-rays are marked with an asterisk. It is noticeable that the peak at 1073 eV is higher than in Fig. 76a, thus there is a contribution in addition to Ti *LMM*, which can be identified as Na 1*s*. (c) Detailed XPS focusing on Na Auger and C core-level lines, as the main contributors to the surface contamination. The detailed spectra is shown as the function of the annealing conditions, and they were obtained with Al $K\alpha$ x-rays in grazing electron emission at room temperature.

the main crystallographic axes. Baking in atmosphere is known to produce such smooth surfaces [320, 324, 323]. The high annealing temperature however, is not a promising route towards an unreconstructed $SrTiO_3$(001) surface.

Figure 80a shows LEED and XPS results obtained on the baked sample. This sample was first degassed in UHV at 400 °C to remove air-borne contaminants. The degassing was performed until the pressure in the UHV chamber dropped below 3×10^{-10} mbar, comparable to the UHV base pressure. After this degassing step, the surface immediately exhibits a $c(2\times2)$ periodicity (faint (1/2,1/2) spots are visible), combined with a $p(2\times1)$ superstructure (together with the 90°-rotated domain) or possibly a $p(2\times2)$ superstructure. Higher temperatures do not remove these reconstructions, but rather introduce more complex reconstructions: probably including contributions from a $c(4\times2)$ and a $c(6\times2)$ reconstruction after annealing at 650 °C in UHV. Subsequent annealing at 500 °C in 1×10^{-6} mbar O_2 removed this reconstruction, and the sample exhibited a LEED pattern with some faint spots that could correspond to remnants of $p(2\times1)$ or $p(2\times2)$ reconstructions. This sample was not investigated at further temperatures, because the transition from a reconstructed surface to the unreconstructed one has never been observed on $SrTiO_3$(001) surface just by thermal treatment.

Figure 80b shows XP spectra of the baked sample after annealing at 630 °C in UHV, obtained with Al $K\alpha$ x-rays in normal and grazing emission. Core-level and Auger peaks of Sr, Ti, and O are present, but the XP spectra also exhibit peaks corresponding to Na, C, Mo, Ta, and Ca. Mo and Ta peaks are caused by the sample plate and the clips, respectively, and are not related to the sample. Na and Ca are common and hardly avoidable contaminants in $SrTiO_3$, and the high-temperature annealing might favor their segregation. The

Die approbierte gedruckte Originalversion dieser Dissertation ist an der TU Wien Bibliothek verfügbar.
The approved original version of this doctoral thesis is available in print at TU Wien Bibliothek.
TU Bibliothek Your knowledge hub WIEN

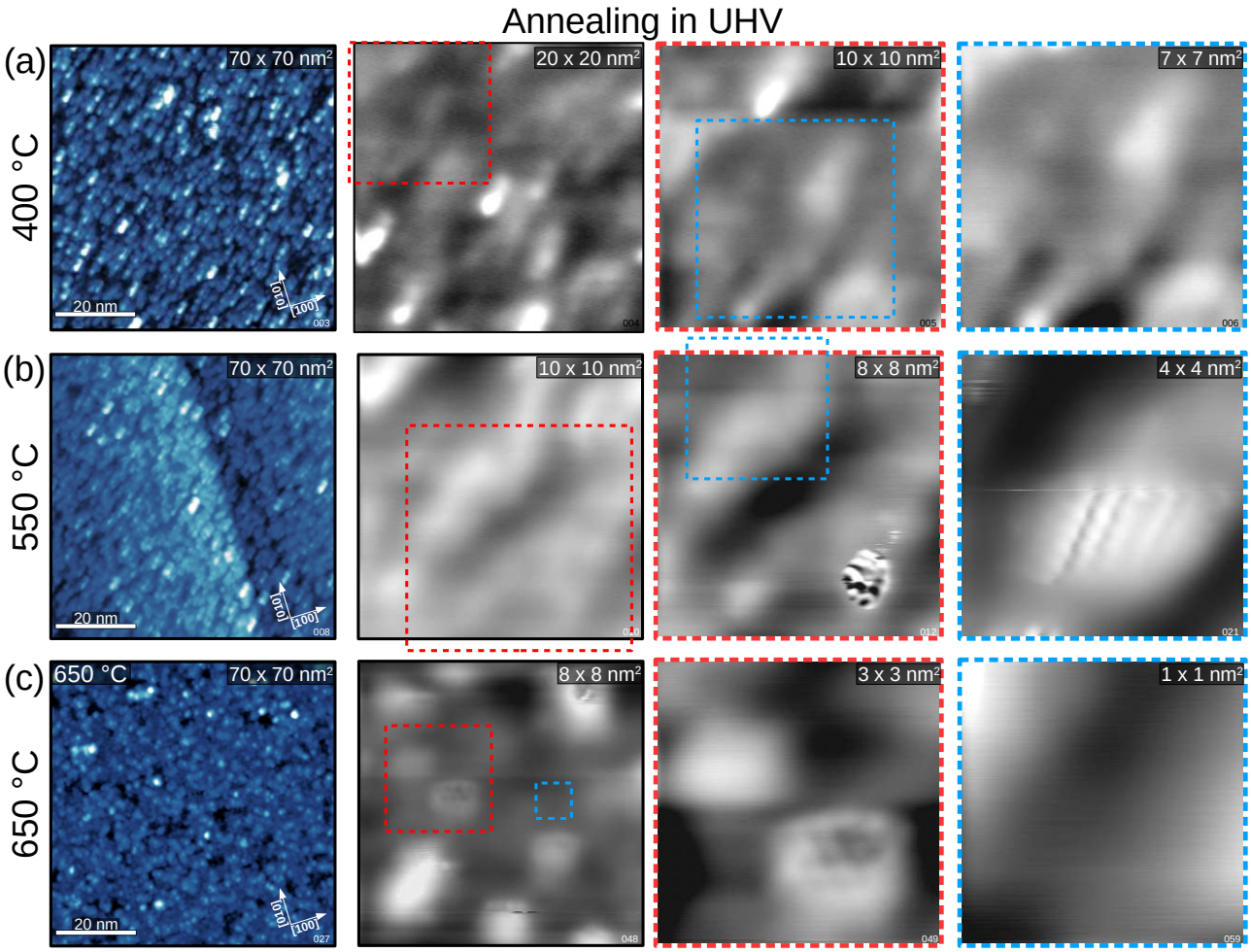

Figure 81: **STM and AFM images taken after different stages of annealing in UHV of the cut-and-polished $SrTiO_3$(001) sample that was baked to 950 °C prior to introduction to UHV - the *baked sample*.** Empty-states STM images obtained with a bias voltage of +2 V (blue-white color scheme) and constant-height AFM images (gray scale) of the baked sample annealed in UHV at (a) 400 °C for 180 min, (b) 550 °C for 60 min, and (c) 650 °C for 60 min. Grey scale AFM images show strong attractive interaction as white, and weak interaction as black. Image size decreases from left to right, focusing on smaller details and evading large contamination blobs.

temperature evolution of carbon and Na contamination is shown in more details in Fig. 80c. Both Na *KLL* and Na 1*s* signals appear slightly more intense at grazing emission, and their intensity slightly increases with increasing annealing temperatures. This indicates segregation of Na from the bulk towards the surface with the increase in temperature, which is known to influence the surface properties by favoring certain reconstructions [383]. The Ca 2*p* signal is less pronounced compared to Na *KLL* signal, and additionally overlaps with both Sr 3*s* and Nb 3*p* signals, but is most likely present on the baked sample, while its presence is questionable in the unbaked sample. Therefore, the Na and Ca contaminants might originate from oxygen-induced segregation from the bulk to the surface while baking at 950 °C in air. The presence of carbon on the surface introduced to UHV is unavoidable. Annealing at increasingly higher temperatures in UHV does not significantly reduce the C 1*s* signal, as seen in the XP spectra in Fig. 80c. This peak is only reduced after annealing at 500 °C in 1×10^{-6} mbar O_2. This behavior is very similar to the unbaked sample (Fig. 76b), implying that annealing in O_2 pressure is a necessity for removing carbonaceous contaminants.

The largest difference between the unbaked sample and the baked sample is that the latter was clearly reconstructed after the initial annealing at 400 °C in UHV. In principle, this reconstruction might be due to the impurities present after baking in air (Ca, Na). Since the reconstruction pattern changes with annealing in

Die approbierte gedruckte Originalversion dieser Dissertation ist an der TU Wien Bibliothek verfügbar.
The approved original version of this doctoral thesis is available in print at TU Wien Bibliothek.
TU Bibliothek Your knowledge hub WIEN

UHV or 10^{-6} mbar O_2, while these impurities do not disappear, the reconstruction appearing immediately after degassing in UHV (top-left panel in Fig. 80a) could be a result of baking in air, irrespective of impurities. On the other hand, these surface contaminants could induce various structures with long-range order, which could be further promoted by out-segregation of impurities towards the surface as the temperature is increased.

STM/AFM images of the baked sample annealed at different temperatures in UHV are shown in Fig. 81. The morphology resembles that of the unbaked sample, with the exception that the steps are much rarer due to the larger terrace sizes. STM images acquired after different annealing temperatures resemble each other, and predominantly show contamination scattered across the surface. The number of large spots in the STM images seems to be reduced after annealing at the highest temperature 650 °C (all the features visible in the STM images in Figs.81a and 81b are duplicated due to a double termination of the STM tip). Even though the LEED patters of this sample (Fig. 80a) show clear reconstructions after annealing in UHV, ordered structures were not observed in either STM or AFM. The constant-height AFM images were taken at progressively smaller areas in order to evade badly contaminated spots. However, none of the annealing conditions resulted in a surface that would show ordered structures in AFM images of this sample. Therefore, it can be concluded that a majority of the surface is covered by a contaminant layer.

In conclusion, the study on the baked sample, as well as the unbaked sample, demonstrates that the (1×1)-terminated surface is far from being granted following the standard preparation protocols. Moreover, it shows that a clear LEED pattern is not indicative of a clean surface, nor of an ordered termination layer on the $SrTiO_3$(001) surface.

3.3.3 Conclusions

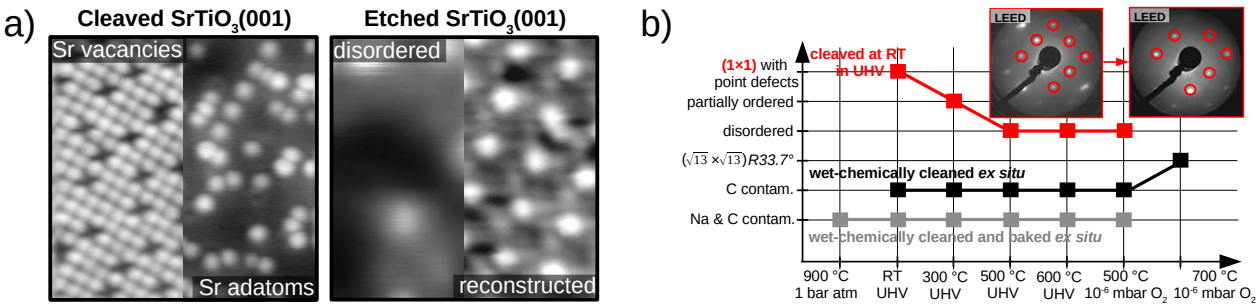

Figure 82: **A thorough search for a pristine, unreconstructed $SrTiO_3$(001) surface was not successful so far.** (a) Three observed possibilities for the differently prepared surfaces; cleaved surfaces are the closest to pristine, but necessarily contain polarity-compensating point defects (Sr_{ad} and V_{Sr}). Etched surfaces are either disordered while carbon-contaminated, or reconstructed after removal of carbon. (b) Summary of the detailed study presented in this Section.

The search for an $SrTiO_3$(001)-(1×1) surface that can be considered 'pristine' — crystalline and well-ordered, with a negligible amount of defects and contaminants — was not successful so far, as highlighted in Fig. 82a. The results of the thorough study on three distinct $SrTiO_3$(001) surfaces, prepared by either the novel cleaving procedure [341], or by traditional methods involving wet-chemical etching, are summarized in Fig. 82b. As-cleaved surfaces come the closest to the pristine (1×1) surface, but necessarily contain both, SrO- and TiO_2-terminated domains (albeit of considerable size), and charged point defects (Sr_{ad} and V_{Sr}). The temperature-induced transformation to an ill-defined, disordered top layer, indicates that the (1×1) has a high surface energy and is only metastable. The same is true for the etched TiO_2-terminated surfaces that are used to great extent as substrates in the growth of heteroepitaxial oxide films. While such surfaces can display a flat morphology with a high-quality diffraction pattern, nc-AFM shows no signs of the unreconstructed surface. The temperature required for removing carbon lies above the stability region of the bulk-terminated surface.

Results presented here directly demonstrate that the LEED diffraction patterns (and especially less-sensitive RHEED patterns [384]) are not a reliable indicator of an unreconstructed $SrTiO_3$(001) surface. The same holds true for techniques generally applied to judge surface quality (XPS, large-area STM or ambient AFM), which give results that would be consistent with a perfect (1×1) termination; but are contradicted by atomically resolved nc-AFM. Since no previous work explicitly showed an atomically resolved (1×1) surface, it is questionable whether

Die approbierte gedruckte Originalversion dieser Dissertation ist an der TU Wien Bibliothek verfügbar.
The approved original version of this doctoral thesis is available in print at TU Wien Bibliothek.
TU Bibliothek Your knowledge hub WIEN

a pristine, unreconstructed $SrTiO_3(001)$ surface was ever encountered. A plethora of intriguing phenomena observed on this surface, such is the appearance of a two-dimensional electron gas [304, 385, 305, 386, 387], can therefore be assigned to occur in the subsurface layers, and potentially be protected by a contaminated or a disordered surface layer. Moreover, theoretical considerations assign $SrTiO_3$ solids to be either "weakly polar" [354, 368] or completely non-polar [363, 364] along the [001] direction, which implies ready availability of pristine $SrTiO_3(001)$ surfaces – this is the basis for the common belief that it is easy to prepare pristine, unreconstructed $SrTiO_3(001)$ surfaces. The research presented in this Section conclusively shows that the use of bulk-terminated surfaces in theoretical modeling does not reflect reality and may thus lead to imprecise predictions; this is additionally supported by a well-known proclivity of these surfaces for reconstructions [331, 388, 389, 336, 325]. Interestingly, these results indicate that the presence of excess material (possibly in the form of extrinsic contamination) at the top of the surface could be responsible for stabilizing the (1×1)-termination, as is the case of interfaces of $SrTiO_3(001)$ with epitaxially grown films [390, 391, 392, 393, 394].

Die approbierte gedruckte Originalversion dieser Dissertation ist an der TU Wien Bibliothek verfügbar.
The approved original version of this doctoral thesis is available in print at TU Wien Bibliothek.
TU Bibliothek Your knowledge hub WIEN

3.4 Empirical insights into the novel perovskite cleaving procedure

Cleaving is a preferred preparation method for many surfaces, because cleaving *in situ*, *i.e.*, in UHV, creates perfectly clean surfaces that do not require further treatments [395, 396, 397, 398, 399]. Materials that posses preferential cleavage planes readily cleave when subjected to external forces in a proper geometry. In the case of $SrTiO_3$ however, surfaces commonly fracture and rarely cleave unless preferable cleavage plains are first created. This Chapter discusses a novel cleaving device that helps to overcome this limitation. The properties of cleaved $SrTiO_3(001)$ surfaces at the atomic scale reveal certain insights into the processes behind cleaving. However, the exact mechanism of cleaving using the cleaving device developed and applied in the previous two Sections remains secluded, since there were no experimental methods that would allow studying the cleaving process in real time in the research that led to this Thesis. A systematic investigation of the cleaved surfaces at both, macroscopic and microscopic scales, provides valuable insights, however. It also reveals good practices and common pitfalls in constructing and applying the cleaving device. This Section is based on the forthcoming publication "Universal cubic perovskite oxide cleaving device – applied insights from $SrTiO_3$" [400].

3.4.1 Cleaving device

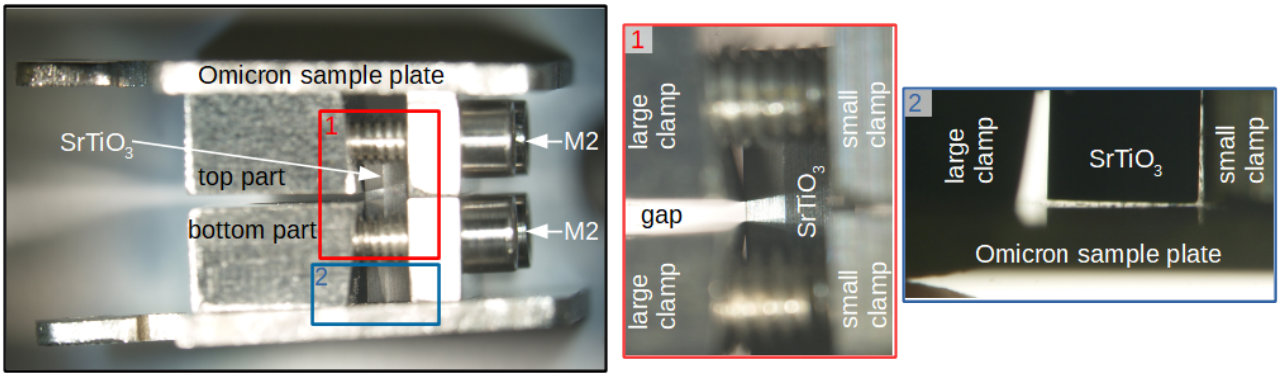

Figure 83: **Detailed photographs of the device used for cleaving the $SrTiO_3(001)$ surface.** The leftmost panel shows the photograph of the cleaving device in a "sandwich" configuration, with a $SrTiO_3$ single crystal mounted and squeezed between the clamps on the bottom and the top half. A small fraction of crystal volume is spared from squeezing in a gap between the top and the bottom clamp, where the cleaving is intended to occur – the photograph in the middle panel shows a magnified view of this region. Squeezing the crystal during mounting results in tilting and elevation of the crystal, visible as the gap between the bottom part of the crystal and the sample plate it stood on prior to squeezing – the photograph in the rightmost panel magnifies the view on this region. The entire device together with the squeezed $SrTiO_3$ crystal is inserted in UHV where it is cleaved to produce two mirrored surfaces, both available for immediate measurements in UHV.

Cleaving $SrTiO_3$ proved is a reliable and reproducible pathway for obtaining the (001) surface, as shown in Section 3.2. Moreover, Section 3.3 demonstrates that the cleaving procedure creates $SrTiO_3(001)$ surfaces that are the closest to being pristine, and questions whether such surfaces are even encountered in literature. For these reasons, this Section lays out the practical details of the cleaving procedure, and shares the experience gained by systematically cleaving $SrTiO_3(001)$ surfaces that were used in various experiments presented in this Thesis. All data shown in this Section were obtained on a 0.5 wt.% (0.69 at.%) Nb-doped single crystals, but the results and the findings are to a great extent applicable to different Nb-doping levels, as well as to other perovskite oxides.

Figure 83 shows a detailed photograph of the cleaving device. Through an iterative process, it was found that the optimized cleaving device consists of two identical clamping sets that squeeze a single crystal at the top and the bottom, such that they create a "sandwich" structure visible in the largest photograph in Fig. 83. Both, the bottom and the top set of clamps, consist of a large and a small clamp that are connected by two M2 screws; the small clamp has ⌀2 holes while the large clamp has M2 threads at the corresponding positions. All clamps in a cleaving device must be well polished, in order to have the asserted pressure to a single crystal squeezed between them distributed as equally as possible. The optimum polishing for the large clamp was found to be at

Die approbierte gedruckte Originalversion dieser Dissertation ist an der TU Wien Bibliothek verfügbar.
The approved original version of this doctoral thesis is available in print at TU Wien Bibliothek.
TU Bibliothek Your knowledge hub WIEN

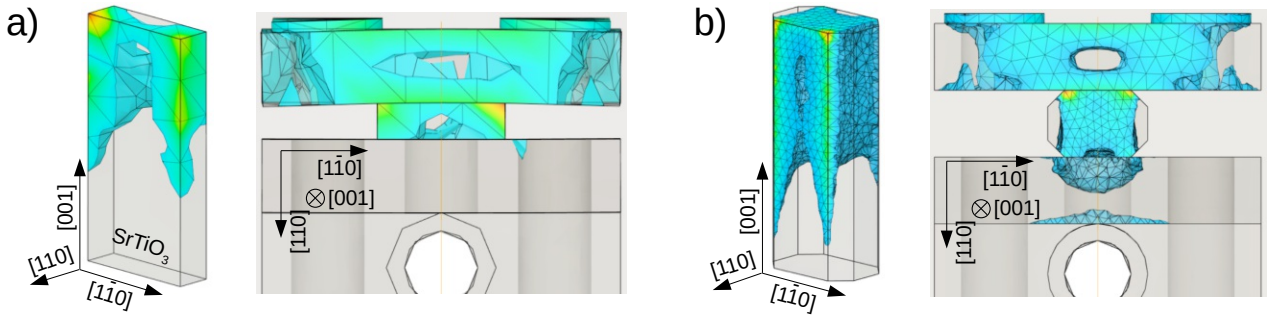

Figure 84: **Simulated strain distribution across the clamped $SrTiO_3$ single crystal prior to cleaving.** The distribution of strain in pre-strained single crystals was investigated by simulating the clamping with steel blocks, and applying a force along the [110] direction to the top part of the cleaving device, *i.e.*, modeling experimental cleaving conditions. Two subfigures show the calculated strain distribution on two sample geometries: a) a regular rectangular single crystal and b) the same single crystal (but twice as thick) after four edges parallel to the [001] direction were additionally polished off. Results are visible in the frontal view of the crystal alone, and in the top view together with the clamps; for clarity, in each view only the strain that exceeds the 30% of the overall strain on the crystal is displayed. The calculations were performed and the results visualized using the Fusion 360 software by Autodesk [401].

a 5° angle at the face that will be touching a single crystal, such that the contact between a single crystal and the large clamp occurs in a very small area at the very edge of the large clamp. This is depicted in the zoomed-in photograph marked with "1" in Fig. 83 – both the top and the bottom large clamps were polished with ≈ 5° angle such that the contact occurs only at the very small region, at the border of the volume where the cleavage is intended to occur. The quality of alignment is easily checked by placing the cleaving device, with a single crystal mounted inside, in front of a light source and verifying that the contact between the large clamp and a single crystal is as small as possible, as the one depicted in the photograph marked with "1" in Fig. 83. Large clamps are fixed to an Omicron sample plate via an M2 screw as well. The small clamps on the other hand are free to move, and are fixed only by screwing in the M2 screws and applying pressure to a single crystal. For this reason, small clamps should not be polished with the same inclination as the large clamps, and instead should be as flat as possible. When the crystal is clamped between the large and the small clamp, it will be lifted from the sample plate it previously stood on, as seen in the zoom-in photograph marked with "2" in Fig. 83. This happens because the application of force to a single crystal will incline it towards the small clamp by an angle that cannot exceed the ≈ 5° polishing angle of the large clamp. In turn, the small clamp will also incline (by a smaller angle) away from a single crystal, and this will enable the smallest contact between the sample and the small clamp as well – the inclination of the small clamp can be seen in the zoomed-in photograph marked with "2" in Fig. 83 as a space between the bottom of the small clamp and the single crystal. The bottom and the top set of clamps are held together only *via* the squeezed single crystal between them: after a single crystal has been sufficiently squeezed by the bottom set of clamps, a small spacer needs to be inserted on top of the bottom part so that the top part can be mounted such that there is a small crystal volume that is not directly subjected to the uniaxial stress. This separation can be easily achieved by placing two pieces of light paper at each side of the clamped single crystal, and resting the top set of clamps on top of them. After tightening the top set of clamps, they will not be parallel to the bottom set of clamps any more, but instead incline due to the inclination of the already squeezed single crystal at the bottom side.

The clamping procedure requires experience and caution. Proper alignment of the bottom set of clamps is crucial for a good cleavage. Initially, a single crystal is situated on the sample plate close to the already fixed large bottom clamp, resting on the bottom (001) face. It is then squeezed by turning the M2 screws which drive the small clamp towards the single crystal. It is imperative that the gradual squeezing occurs in a way as equal as possible through the two screws: if one side of the small bottom clamp is prematurely squeezing the crystal while the other side is still not in contact, the clamping will be inefficient and the desired cleavage will not be achieved. Once the small bottom clamp is securely in contact with a single crystal in as parallel manner as possible, M2 screws need to be tightened with appropriate torque. The exact value of torque necessary to ensure high-quality cleavage was not evaluated, but it is important that the maximum torque is not applied on the screws. Namely, if one of the screws is tightened to a maximum, a disbalance between the sides of the single

Die approbierte gedruckte Originalversion dieser Dissertation ist an der TU Wien Bibliothek verfügbar.
The approved original version of this doctoral thesis is available in print at TU Wien Bibliothek.
TU Bibliothek WIEN Your knowledge hub

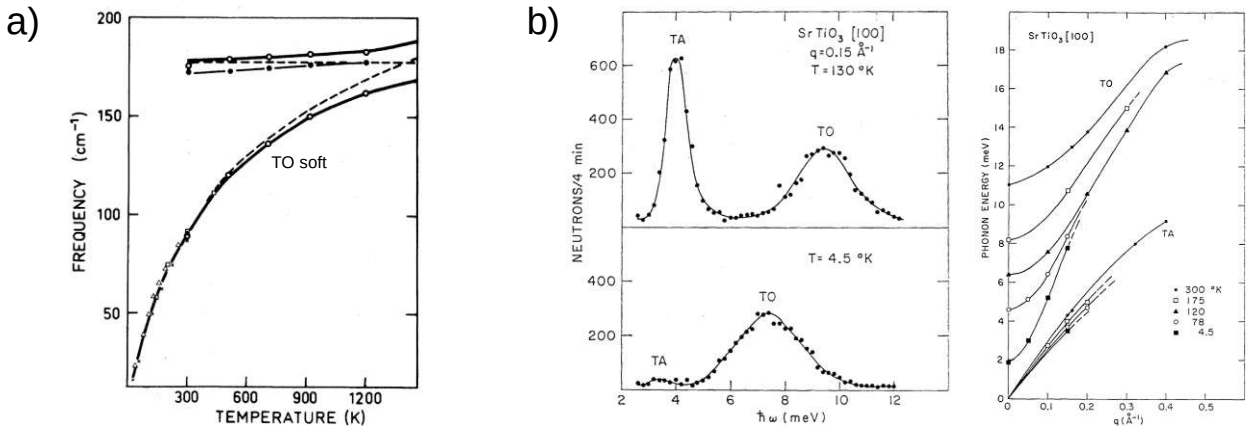

Figure 85: **Soft transverse optical phonon at $SrTiO_3$(001) surfaces.**
a) Infrared reflection spectra of the transverse optical phonon (TO) as a function of temperature. The frequency of the TO converges to zero as the Curie temperature is approached form the top.
Reprinted bottom panel of Figure 4 [402] from [J. L. Servoin, Y. Luspin, and F. Gervais, *Physical Review B*, 22, 5501 (1980)] with permission of Author(s) and APS. Copyright (2018) American Physical Society.
b) Neutron scattering spectra on the transverse acoustic phonon (TA) and the transverse optical phonon (TO) at room and low temperatures. While TA vanishes at low temperatures, TO is persistent at all temperatures.
Reprinted Figure 1 and Figure 2 [403] with permission from [Yasusada Yamada and Gen Shirane *Journal of the Physical Society of Japan*, 26, 396 (1969)]. Copyright (1969) The Physical Society of Japan.

crystal will occur and this can induce spontaneous fracturing. Even if the two M2 screws can be maximally tightened "simultaneously", such large stress will crush the single crystal at the contact point with the clamps and a new single crystal will have to be used. When the clamping with the bottom set of clamps is completed, tightening the top set of clamps is more challenging because this is the final step of preparation after which the sample is ready for cleaving. In other words, the possibility of spontaneous cleavage is high when mounting the top set of clamps, which is why they should be tightened using less torque than the bottom set. A complete cleaving device with the mounted sample is then transfered to UHV with caution, to avoid accidental cleaving during transport, insertion into the loadlock transfer arm, or insertion into a sample storage.

Any material of choice for constructing the clamps can be used, and clamps made out of stainless steel, molybdenum, and aluminum(99.6% pure) were tested in the research that led to this Thesis. Experience shows that stainless steel clamps are by far the best. A successful cleavage will leave an imprint on the steel clamps in the contact area with the sample – this is not observed with other materials. This imprint appears because the stainless steel clamps locally plastically deform due to the application of stress during screw tightening, with the addition of strain from the application of force necessary for cleaving. This imprint can also serve as an indicator of how strong the sample was clamped, what the contact area with the sample was, and whether the clamping was properly parallel with respect to the face of the sample that was oriented towards the small clamp. After each cleaving, all clamps have to be re-polished at those faces that were in contact with the sample in order to remove the local plastic deformation visible as an imprint. This step usually requires very little polishing as the imprint into the stainless steel is not significant, *i.e.*, gentle sandpaper is preferred for this step. After polishing, the entire device requires cleaning prior to the next mounting, and stainless steel construction offers the possibility of boiling in 20% diluted HNO_3 for efficient cleaning. The only downside of the stainless steel cleaving device is that is cannot withstand high temperatures necessary for investigating the annealed bulk-terminated $SrTiO_3$(001) surface, in which case molybdenum is the material of choice.

The sample is finally cleaved in UHV by pushing the ear of the Omicron sample plate that is a part of the top half of the "sandwitch" shown in Fig. 83, using the UHV wobblestick. One of the Omicron sample plates was preferably held inside the manipulator of the UHV chamber, or the sample storage in UHV, which is sturdier. After cleaving, the bottom set of clamps with one half of the cleaved crystal remains in this position, while the top set of clamps and the remaining half of the cleaved crystal is held in the wobble stick by the ear on the Omicron sample plate. Therefore, a succesfull cleavage creates two well-defined $SrTiO_3$(001) surfaces, one held by the bottom set of clamps and the other held by the top set of clamps. Since both are mounted

Die approbierte gedruckte Originalversion dieser Dissertation ist an der TU Wien Bibliothek verfügbar.
The approved original version of this doctoral thesis is available in print at TU Wien Bibliothek.
TU Bibliothek Your knowledge hub WIEN

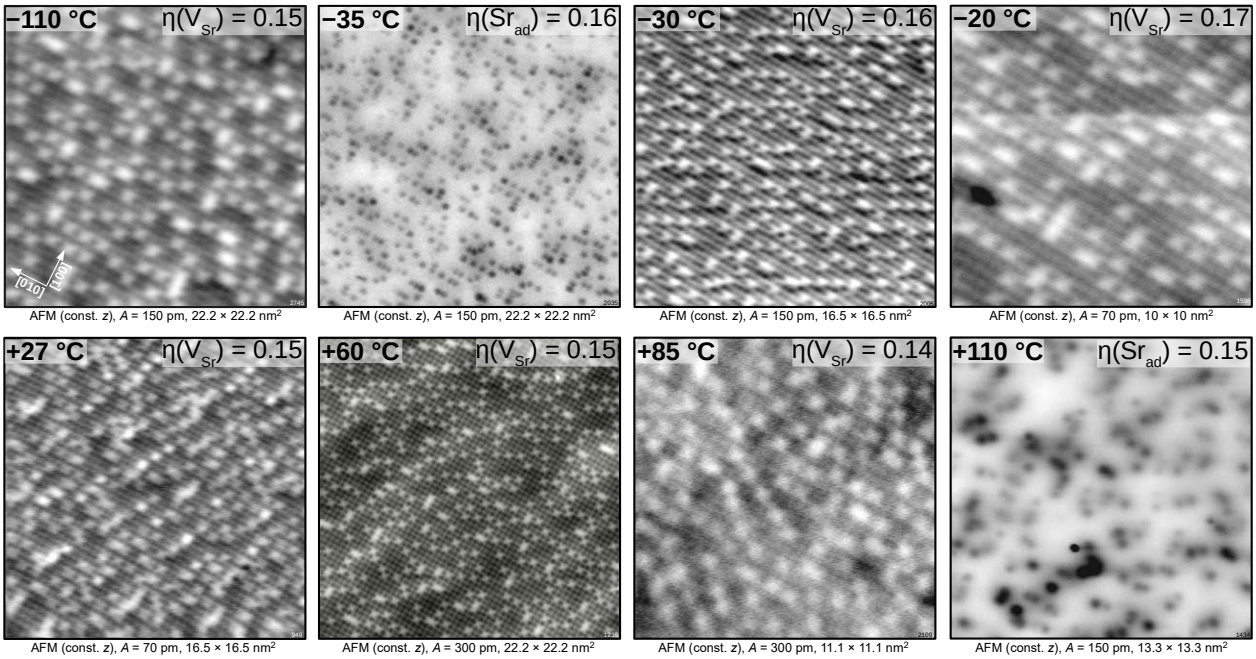

Figure 86: **Concentration of polarity-compensating point defects at the cleaved $SrTiO_3$(001) surface as a function of temperature.** Series of constant-height AFM images obtained on surfaces that were cleaved at different temperatures, indicated in each image; the surface orientation is the same in each image, as indicated in the first panel. Before cleaving, the entire cleaving device with mounted $SrTiO_3$ single crystal was equilibrated at a given temperature in UHV – each AFM image represents a separate cleavage. The concentration of point defects, either V_{Sr} on the SrO, or Sr_{ad} on the TiO_2 termination, was counted and averaged between several images obtained on the same cleaved surface; the results are indicated in each image in units of ML, and are reported with ±0.02 ML accuracy. There is no clear variation of the concentration of point defects at cleavages performed at different sample temperatures.

on standardized Omicron sample plates, either or both can be used for subsequent measurements in UHV. Both the bottom and the top set of clamps are keeping the two halves of a cleaved single crystal firm enough that AFM/STM measurements can be performed at low temperatures, without the interference of mechanical vibrations. When a single crystal sample is properly pre-strained outside of UHV, very little force is necessary to cleave it with a wobblestick in UHV. The rule of thumb is that the easier the sample cleaves, the better the cleavage, *i.e.*, the ferroelectric phase transition is successfully carried out across the vast majority of the crystal volume where the cleavage is intended to occur. However, the application of force required for cleaving can also be higher than simply touching the top part of the device, in which case a successful cleavage could also be achieved, albeit with lower probability. When a single crystal requires a lot of force to cleave, it is better to halt the cleaving, and instead take the cleaving device outside of UHV for adjustment of the clamps and the application of higher strain to the single crystal.

The small size of the cleaving device limits the size of the single crystal used for cleaving. The entire cleaving device is situated on a $18\times15\,mm^2$ Omicron sample plate that is suited for a typical UHV system, namely for the wobble sticks, transfer arms, manipulators, sample storages and the low-temperature AFM/STM head. A cleaving device with M2 screws,depicted in Fig. 83, is close to the upper size limit for such UHV systems; a cleaving device with M3 screws for example is already too large to fit into the UHV components. Same considerations apply to the size of the $SrTiO_3$ single crystals designed for cleaving, where their height is limit but their width could be as large as 5 mm and still fit into this cleaving device. However, cleaving 5mm thick single crystals with this setup is challenging because only a limited amount of strain can be achieved using the clamping sets and the M2 screws. If the cleaving device was not limited in size to fit on an Omicron sample plate, larger clamps and larger diameter screws which can withstand higher torque could be used – this would potentially enable cleaving arbitrarily thick samples. Experience shows that application of such larger clamps outside of UHV does enable easier cleaving.

Die approbierte gedruckte Originalversion dieser Dissertation ist an der TU Wien Bibliothek verfügbar.
The approved original version of this doctoral thesis is available in print at TU Wien Bibliothek.
TU Bibliothek Your knowledge hub WIEN

Due to the limited amount of strain that can be applied with a cleaving device depicted in Fig. 83, 1 mm thick samples are preferred for cleaving. Such samples successfully cleave, and the majority of the surface is atomically well-defined and flat as the one depicted in an optical photograph in Fig. 87, below. In area-averaging experimental methods, having a large surface area is preferred due to the finite irradiation spot size of the incident x-rays in XPS , low energy electrons in LEED, or synchrotron radiation in ARPES for example. Cleaving $SrTiO_3$ crystals thicker than 1 mm, which is comparable to the spot size, is necessary for such measurements, but the limited amount of applicable strain poses a challenge.

Figure 84 shows results of the static-strain simulations applied to a $SrTiO_3$ crystal in the cleaving device made from stainless steel. Clamping with M2 screws tensioned with 2 kN/m is efficient for 1 mm thick crystals, depicted in Fig. 84a, since the strain is distributed across the crystal volume along the (001) direction. For samples that are 2 mm thick, the application of the same amount of strain was calculated to result in the highest strain distribution on the [001] edges of a single crystal that are closest to the M2 threads. In other words, most of the strain is applied at the corners of a rectangular (001) surface, which is additionally magnified by convex deformation (with respect to the single crystal) of the small clamp after clamping. This results in an undesirable strain distribution and these samples cannot be properly cleaved. The strain distribution during clamping can be designed to efficiently span the crystal volume of 2 mm thick crystals by removing (polishing off) [001] edges that would otherwise experience the highest strain, as shown in a static-strain simulation in Fig. 84b. After such procedure, the strain distribution in the 2 mm and 1 mm thick crystals is alike. This enables succesfull cleavages 2 mm thick crystals as well, albeit the proportion of well cleaved surface compared to fractured surface is commonly lower compared to thinner crystals. Nevertheless, the overall surface area that is well-cleaved on 2 mm thick samples cleaved this way is much larger than a typical well-cleaved area obtained on 1 mm thick samples, and therefore enables reliable measurements with the area-averaging techniques. Cleaving even thicker $SrTiO_3$ single crystals is desirable, but requires different cleaving device constructions that do not fit into the low-temperature STM/AFM measurement heads of the UHV chambers used in the research that led to this Thesis.

3.4.2 Quantum phase transition during cleaving

Landau's theory of phase transitions [404], which is applicable for second order phase transitions to ferroelectricity or ferromagnetism in solids with more than one atom in the base of a unit cell, assigns these phase transitions to the freezing of soft optical phonons as the temperature is reduced towards the Curie temperature. When a soft optical phonon (TO) is frozen, its frequency converges to zero, while its period diverges to infinity. This creates "infinitely" large domains with same direction of electric or magnetic polarization vector that are switched at the domain walls. In cubic perovskite oxides, this TO shifts the central B cation and the O atoms within the BO_2 layers in opposite directions within each polarization domain. Some perovskites relax through the freezing of longitudinal, and other through freezing of the transverse optical phonons.

The only possibility of cleaving a $SrTiO_3$(001) surface such that it exposes an atomically flat surface comes through creating inequivalent, preferable cleavage planes by performing a strain-induced ferroelectric transition. This quantum phase transition occurs during the cleaving: once a crack in single crystal has been initiated, it propagates in the direction of the applied force (along the (110) direction in this case) and subjects the volume of the crystal where the cleavage is intended to occur to tensile strain. This in turn transforms the crystal unit cells into a tetragonal phase and induces symmetry breaking of the TiO_2 layers, with Ti and O atoms shifting in opposite directions along the [001] axis. The direction in which Ti atoms shift, either positive or negative along the [001] axis, and the opposite shift direction of O atoms is arbitrary, therefore the cleaved surface contains both possible surface terminations, SrO and TiO_2, which are characterized by the opposite direction of the polarization vector, as illustrated in Fig. 68. In other words, in this ferroelectric state, the positions of the Ti and O atoms within the TiO_2 layers are modulated by a transverse optical phonon with zero frequency.

The optical phonon spectrum at a surface of a solid can be probed by infrared reflection spectrometry or inelastic neutron scattering. Figure 85 shows the results of such measurements and focuses on the soft transverse optical phonon (TO) in $SrTiO_3$. The temperature dependence of the soft phonon mode in Fig. 85a indicates that this phonon mode is hardening as the temperature is reduced from high temperatures towards the temperature of 105 K, when the $SrTiO_3$ experiences a cubic to tetragonal transition. Complementary to this data, the spectral width and the dispersion of phonons, shown in Fig. 85b, indicate that the transverse acoustic phonon vanishes as the temperature is reduced, while the transverse optical phonon persists at both the cubic (300 K) and the tetragonal phase (4 K) of $SrTiO_3$. Even though $SrTiO_3$ spontaneously never becomes ferroelectric due to its quantum paraelectric (incipient ferroelectric) nature at low temperatures, the results in Fig. 85 clearly

Die approbierte gedruckte Originalversion dieser Dissertation ist an der TU Wien Bibliothek verfügbar.
The approved original version of this doctoral thesis is available in print at TU Wien Bibliothek.
TU Bibliothek Your knowledge hub WIEN

indicate that transverse optical phonons could be utilized for achieving ferroelectricity.

Cleaving of a $SrTiO_3$ single crystal is a destructive and ultra-fast process, so the behavior of the soft phonon mode cannot be systematically and gradually monitored during cleaving. However, temperature dependent cleaving provides some insights into this mechanism. For this reason, $SrTiO_3$ crystals were systematically cleaved at different temperatures, and afterwards used for various experiments. According to the results in Fig. 85, the strain-induced transition to ferroelectricity should be easier to achieve at low temperatures, close to the cubic to tetragonal phase transition, and more difficult to achieve at room temperature (at which the $SrTiO_3$ crystals were originally cleaved) or elevated temperatures. Figure 86 shows atomically resolved $SrTiO_3(001)$ surfaces obtained after cleaving the crystals at different temperatures. The relevant quantity for evaluating the TiO_2 layer splitting due to the ferroelectric phase transition that occurs during cleaving is the concentration of polarity-compensating defects, V_{Sr}s and Sr_{ad}s on the SrO and the TiO_2 termination, respectively.

The concentration of polarity-compensating point defects on cleaved $SrTiO_3(001)$ surfaces is independent of temperature, as can be seen by counting their concentration in Fig. 86. The reported point defect concentration was averaged over several constant-height AFM images of a cleavage at a given temperature that were obtained on both terminations. Fig. 86 indicates that cleaved $SrTiO_3(001)$ surfaces will always be the same at the atomic scale regardless of the cleaving temperature. This provides an important insight into the cleaving procedure: succesfull cleaving will always occur once the soft transverse optical phonon becomes frozen. Additionally, this provides direct evidence that the concentration of polarity-compensating defects on a cleaved $SrTiO_3(001)$ surface cannot be manipulated by applying different amounts of strain with the cleaving device. After a sufficient amount of strain was applied by a cleaving device, a $SrTiO_3$ crystal will always cleave in the same manner, dictated by the crack propagation, which hardens the soft transverse optical phonon responsible for ferroelectricity. It remains imperative however, that the clamping is performed thoroughly and with sufficient force, such that the crack is well-initiated and well-contained in a controlled fraction of crystal volume while it propagates. The possibility that the domain size on a cleaved $SrTiO_3(001)$ surface depends on the cleaving temperature was not investigated in the research that led to this Thesis, but the existing data indicates that such relation does not exist: after cleaving at different temperatures, the domain sizes always exceeded 1 μm, while the upper size limit could not be investigated using AFM/STM. Experience shows however, that cleaving at lower temperatures usually requires less force for pushing the top part of the cleaving device. A possibility remains that the $SrTiO_3$ single crystals become more brittle and more susceptible to the ferroelectric phase transition during cleaving as the cleaving temperature approaches the temperature of cubic to tetragonal phase transition. Samples were never cleaved below the temperature of the tetragonal phase transition due to experimental limitations.

3.4.3 Optical photographs

A successful cleavage of a $SrTiO_3(001)$ surface can be recognized under an optical microscope, as demonstrated in Fig. 87. It is common that a cleaved surface contains both, the conchoidal fracture and the well-cleaved surface. No two cleavages are ever the same, although almost all ($> 90\%$ of cleaved crystals) contain at least some portion of a well-cleaved surface. Figure 87 is divided in three rows: a completely well-cleaved surface is shown in Fig. 87a, partially cleaved and partially fractured surfaces are shown in Fig. 87b, and completely fractured surfaces characterized by a conchoidal fracture throughout the entire surface are shown in Fig. 87c.

The best cleavages are either macroscopically flat, as the one in Fig. 59c, or contain many well-cleaved regions that are mutually separated by large steps, as the one visible in the first panel of Fig. 87a. The second two panels in Fig. 87a focus on individual well-cleaved areas on the same surface shown in the first panel. Each region contains visible terrace steps, which are possibly domain walls where the surface termination switches between SrO and TiO_2. These steps are most commonly oriented parallel to the [110] direction of strain, but can be oriented perpendicular to this direction or rotated by 45°, *i.e.*, along the $[1\bar{1}0]$ and [100] directions, respectively. Such well-defined steps are a fingerprint of a good cleavage. The particular cleavage shown in Fig. 87a was cleaved at the sample temperature of -110°C, which is a recommended temperature for cleaving the $SrTiO_3$ – at lower temperatures the soft transverse optical phonon is easier to freeze (Fig. 85), and cleaving noticeably proceeds with greater ease. It remains uncertain why the cleavage in Fig. 87a is so different from the cleavage in Fig. 59c while both are exceptional, but one reason may be that the cleavage in Fig. 87a was performed on a 2 mm thick crystal where the strain distribution following clamping is not as well-distributed as on the 1 mm thick crystal that was cleaved to obtain the cleavage in Fig. 59c.

Several partially-successful cleavages are shown in Fig. 87b, all of which were obtained by cleaving 2 mm thick crystals at room temperature or in a range of ±20°C. From an AFM/STM perspective, these cleavages

Die approbierte gedruckte Originalversion dieser Dissertation ist an der TU Wien Bibliothek verfügbar.
The approved original version of this doctoral thesis is available in print at TU Wien Bibliothek.
TU Bibliothek Your knowledge hub WIEN

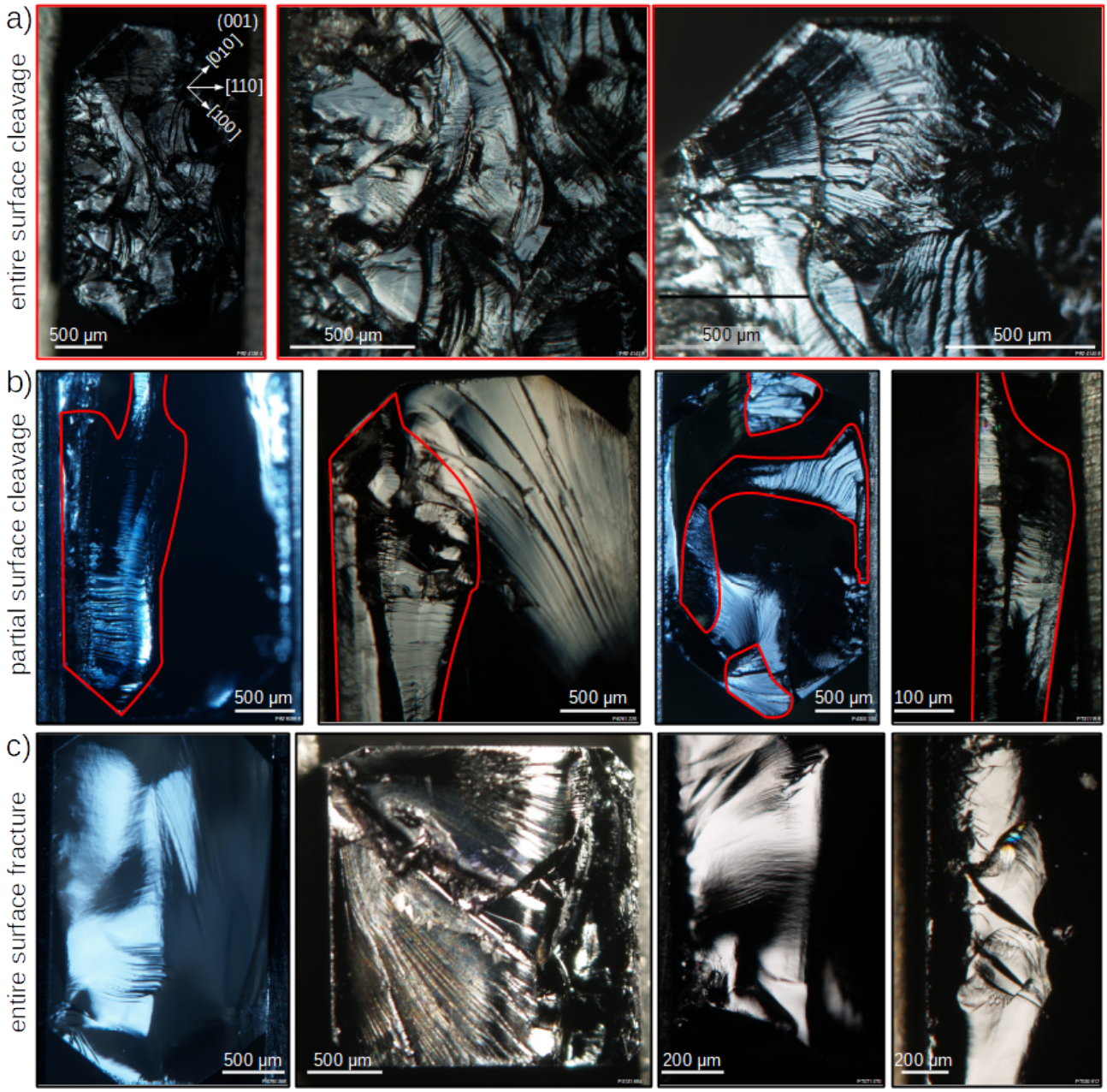

Figure 87: **Optical photographs of several different $SrTiO_3$(001) cleavages.** a) Photographs of a surface that cleaved in entirety. The first panel shows the entire surface, while the remaining panels focus on smaller areas of the same cleavage. This cleavage was achieved at the sample temperature of −110 °C. b) Photographs of several commonly-obtained $SrTiO_3$(001) cleavages, where a significant portion of the surface is cleaved (outlined by red lines), while the remaining portion is fractured. Cleaved surface areas are outlined by red lines. c) Photographs of several completely fractured cleavages. There are no regions with proper atomic arrangement at these surfaces, instead they exhibit conchoidal fracture in entirety. All photographs follow the same orientation as indicated in the top-left panel.

can also be considered exceptional because macroscopically large regions are atomically flat and well defined. The red outline at each panel in Fig. 87b marks the cleaved surface areas, while the remaining portions of the surface are covered by conchoidal fracture that is ill-defined and randomly oriented (Fig. 60). Common to all these well-cleaved areas is the presence of optically visible steps, presumably domain walls that are parallel to each other within each separate area. A train of terraces separated by optically visible straight, or partially

Die approbierte gedruckte Originalversion dieser Dissertation ist an der TU Wien Bibliothek verfügbar.
The approved original version of this doctoral thesis is available in print at TU Wien Bibliothek.
TU Bibliothek Your knowledge hub WIEN

straight steps is a fingerprint of the well-cleaved areas. Well-cleaved areas commonly span for hundreds of micrometers, or several millimeters. Most of these areas have steps running parallel to [110], but even if they are not, the well-cleaved areas will always have the steps mutually parallel. Some well-cleaved areas like the one in the bottom of the third panel in Fig. 87b have a different distribution of steps, but these areas are uncommon and can be recognized as well-cleaved areas by the behavior of the reflected light under a microscope: all well cleaved surface areas should reflect the optical light under the same angle, *i.e.*, all ⟨001⟩ oriented planes will reflect light simultaneously unless some are blocked by the geometry of the cleaved surface or the cleaving device. Although it is common to observe only the well-cleaved areas under the same illumination angle with respect to the surface normal, this does not imply that all surfaces which reflect optical light simultaneously are well-cleaved, a good example of which are the second and the third panel of Fig. 87b. There, both the ⟨001⟩ oriented, well-cleaved surface areas and the randomly oriented conchoidal surface areas can be observed simultaneously. However, in these cases, the conchoidal fracture can be recognized as those surface areas that reflect the optical light under almost all angles due to their random inclination to and from the lenses of the microscope. Another very important fingerprint of the conchoidal fractures is that they have no clear terrace trains, but rather either large steps that are not parallel to any of the main crystallographic axes at the surface (right part of the second panel of Fig. 87b), or more commonly, no steps at all (center part of the third panel in Fig. 87b).

Photographs of completely badly cleaved, fractured surfaces can be seen in Fig. 87c. Although such cleavages are rare, they sometimes occur either due to the badly aligned clamps during straining a $SrTiO_3$ crystal outside of UHV, or insufficient straining force. They can be easily recognized under an optical microscope as completely lacking any terrace trains, and additionally they randomly scatter the light under an optical microscope. While the first and the third panel in Fig. 87c show the completely featureless fractured surface areas, the second and the fourth panel show fractured surfaces with some large steps, but they run in random directions unrelated to the main crystallographic axes. Beside human errors that occur while pre-straining the $SrTiO_3$ crystals in the cleaving device, it is unclear why some single crystal completely fracture. On the cleaved surface shown in the second panel in Fig. 87c, there are indications that the crack was initiated only in a single point of the single crystal, instead of being simultaneously initiated across the entire surface edge normal to the direction of the applied strain: this can be recognized as a series of dislocations originating from a single point situated in the top right corner of the surface in Fig. 87c. However, even when this does happen, some $SrTiO_3$ single crystals manage to produce well-cleaved surface areas, like the one in the second panel of Fig. 87b that contains both, a series of dislocations originating from a single point, and well-defined terrace trains in a neighboring surface area.

3.4.4 SEM measurements

Scanning electron microscopy is commonly applied to study material surfaces at a larger scale than AFM or STM. At the heart of the technique lies the interaction of high energy incident electrons (E_k >5 keV) with the surface and the near-surface region of the sample [405, 406]. Irradiated electrons are commonly elastically scattered from the sample surface, and the detection of these backscattered electrons reveals the morphology and the geometry of a sample surface. A high portion of incident electrons inelastically scatter at a surface and within a subsurface region, gradually loosing energy and ejecting electrons from a sample. Electrons ejected this way are referred to as the secondary electrons, and their detection provides insights into the electronic structure of a surface. Namely, low energy secondary electrons (E_k <50 eV) are either emitted from the conduction band or the near-Fermi valence band of a material, and are therefore sensitive to the band structure of a sample. Detecting secondary electrons current at the electron collector provides insights into the local work function of a sample [407]. Namely, a higher secondary electron current will be detected from a surface region with a smaller work function compared to a region with higher work function, because a higher proportion of secondary electrons manage to escape from the surface to the vacuum and the detector when the work function of the surface is lower. On a cleaved $SrTiO_3$(001) surface, the two terminations have different electronic properties and different work functions, even though their structure and chemical composition differ only in the first surface layer. Therefore, the detection of secondary electrons in SEM can lead to recognition of two distinct surface terminations, as is seen in Fig. 88.

Secondary electron SEM measurements were performed on a well-cleaved $SrTiO_3$(001) surface region that is shown in Fig. 88a; this surface was partially cleaved and partially fractured , similar to those in Fig. 87b. SEM measurements were subsequently performed, shown in the left columns of Figs. 88b–88d. SEM images in the right columns of Figs. 88b–88d were performed on the opposite side of the cleaved surface shown in

Die approbierte gedruckte Originalversion dieser Dissertation ist an der TU Wien Bibliothek verfügbar.
The approved original version of this doctoral thesis is available in print at TU Wien Bibliothek.
TU Bibliothek Your knowledge hub WIEN

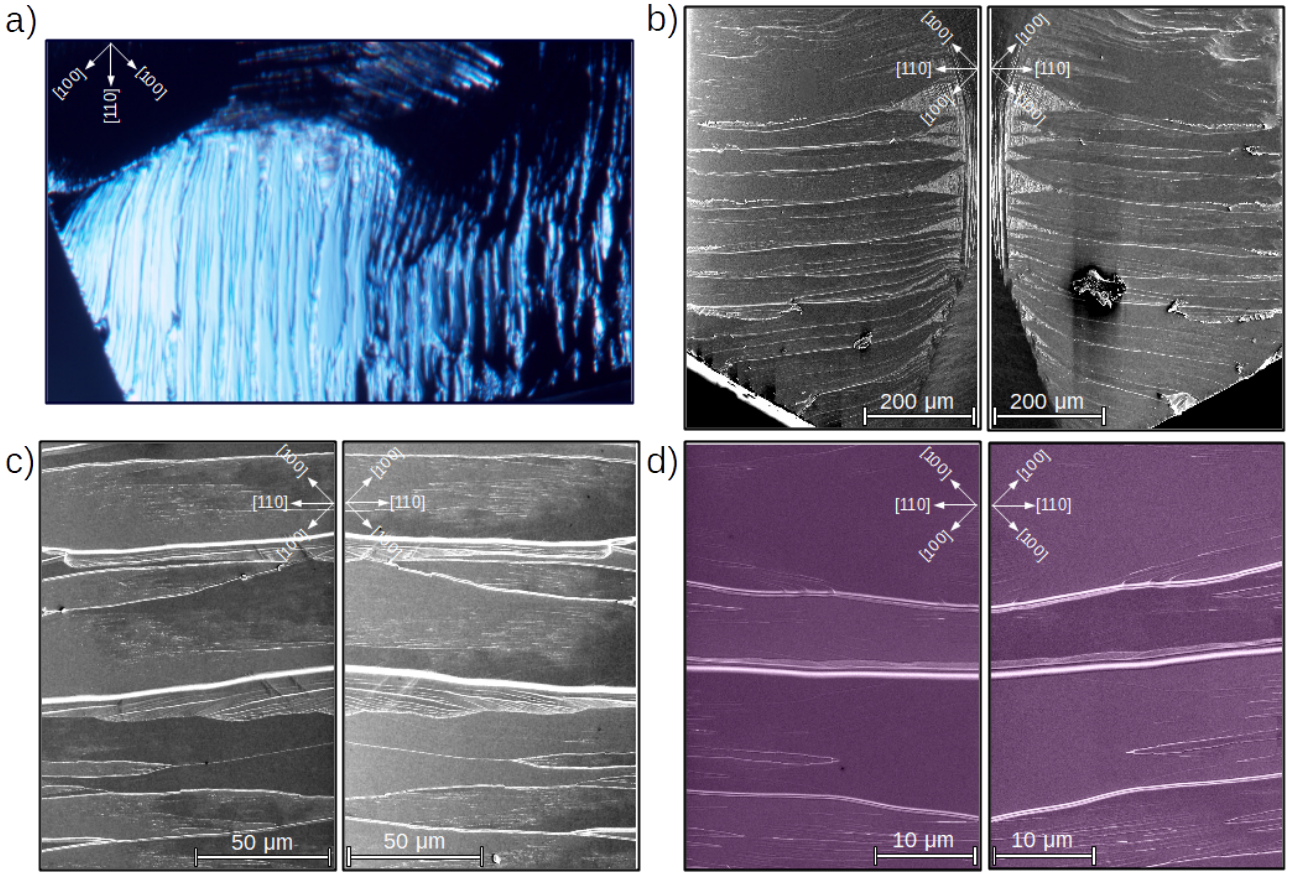

Figure 88: **SEM measurements on a cleaved $SrTiO_3(001)$ surface showing alternating domains of the two surface terminations.** a) Optical photograph of a well-cleaved $SrTiO_3(001)$ surface region, on which the following SEM measurements were performed. b)–d) Secondary electron SEM contrast at different regions of a surface photographed in (a). Each region was imaged independently on both sides of the sample cleavage, *i.e.*, on cleaved single crystal surfaces held by the bottom and the top set of clamps. The surface morphology is therefore mirrored, but the SEM contrast is opposite at the two opposite sides of a cleaved $SrTiO_3(001)$ single crystal. The contrast therefore corresponds to two distinct terminations at the cleaved surface. Subfigure (d) is represented with a colorscheme that visually emphasizes the contrast difference between different terraces. All measurements were performed in 10^{-3} mbar vacuum, while the cleaved surface was exposed to ambient for several days prior to measurements. SEM measurements performed at the USTEM facility of TU Wien [408].

Fig. 88a, *i.e.*, on its counterpart that is held in place by the opposite set of steel clamps. Therefore, the two columns in Figs. 88b–88d show mirrored surface morphology. The SEM signal intensity is not mirrored on the two surfaces however, but instead inverted. Since the distribution of the two surface terminations on two opposite sides of a cleavage must be inverted, as illustrated in Fig. 68, the SEM signal intensity corresponds to the distribution SrO and TiO_2 terminations, due to the distinct work function difference between the two. Since these SEM measurements are not quantitative, it is difficult to assign which greyscale color corresponds to which termination, especially because these measurements were performed on surfaces that were exposed to ambient for at least one month. However, this implies that the two terminations still have distinct work functions after being brought from UHV to ambient. Moreover, it is possible that different surface chemistry occurs at different terminations, namely that the two terminations preferentially adsorb different types of gas molecules in ambient pressure, which are then responsible for different work functions. This opens a possibility of utilizing the ferroelectric character of the surface after cleaving, even at conditions that are far from ideal such are the UHV pressures low temperatures. SEM measurements immediately after cleaving in UHV were not performed without breaking vacuum and exposing the surface to ambient, so the magnitude of the effect of surface chemistry on the SEM contrast cannot be evaluated at this point.

Die approbierte gedruckte Originalversion dieser Dissertation ist an der TU Wien Bibliothek verfügbar.
The approved original version of this doctoral thesis is available in print at TU Wien Bibliothek.
TU Bibliothek Your knowledge hub WIEN

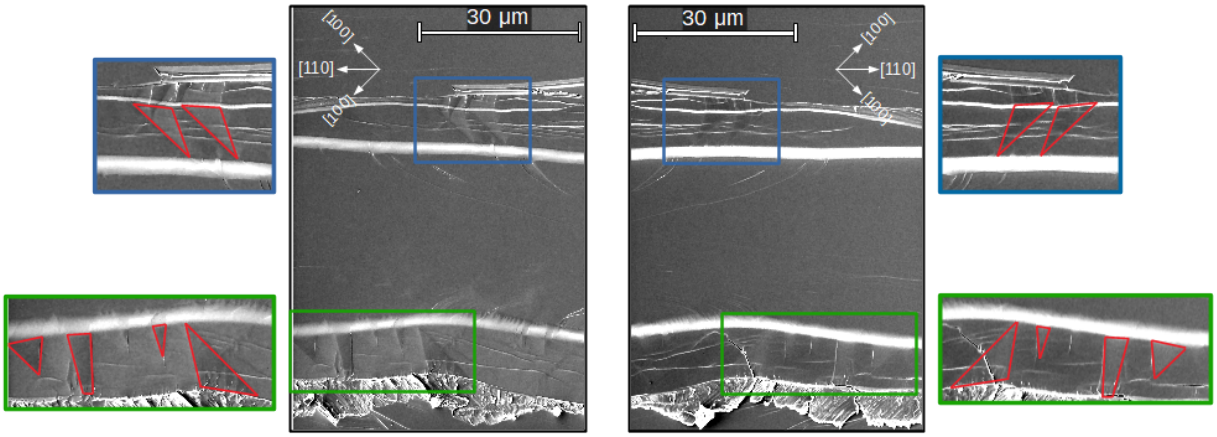

Figure 89: **SEM measurements on a cleaved $SrTiO_3(001)$ surface showing triangular domains.** Secondary electron SEM contrast on two sides of the same $SrTiO_3(001)$ cleavage (left and right side of the Figure), showing small triangular domains of the opposite termination embedded in a large, regularly shaped, singly terminated domains. Insets enlarge those regions marked in the larger images, and focus on the shape of the smaller domains. The contrast is opposite on both the large, regularly shaped domains and the small triangular domains on the two complementary sides of the same cleavage. SEM measurements performed at the USTEM Institute [408].

The distribution of the two surface terminations visible in SEM reveals more insights into the typical domain size and the distribution of domain walls than the previous STM/AFM measurements in Fig. 59, which could only guarantee that each surface domain can be larger than $2\,\mu m^2$. Figure 88 shows that on a surface characterized by a train of terraces, large steps running along the [110] direction, which are even optically visible, commonly serve as domain walls where the surface termination switches between SrO and TiO_2. In some surface regions however, terminations switch within one terrace without a large, optically-visible step. In the terrace train morphology, each termination commonly spans tens of micrometers in the direction perpendicular to the domain walls. On the other hand, each termination can span far greater distances in the direction parallel to the domain walls, up to several hundreds of micrometers. A typical domain size can therefore be estimated as $0.1\,mm^2$. An equal proportion of the two terminations on a cleaved surface is not guaranteed; even in Fig. 88 it is noticeable that one termination is preferentially present on the surface. In fact, it is not excluded that some cleavages have very large domains of single termination only, without the presence of the other termination on the same side of the cleaved surface — these cleavages are usually not characterized by a terrace train surface morphology but instead resemble the one in topmost part of the third panel in Fig. 87b.

While most domains are rectangular, peculiar domain shapes can occur on cleaved surfaces, as those shown in Fig. 89. The SEM contrast in Fig. 89 shows small triangular domains embedded in large rectangular domains of the opposite termination. These triangular domains usually have one edge parallel to the typical direction of the domain walls – the [110] direction, while other edges have arbitrary directions. The SEM images in Fig. 89 were also obtained on both sides of the same cleavage, and therefore show opposite contrasts. For example, if an SrO triangle is embedded in a TiO_2 rectangle on one side of the cleavage, the other side shows a TiO_2 triangle embedded in a SrO rectangle. Beside focusing on the infrequently observed shape of the domains, these SEM images also serve as a confirmation that the SEM contrast in Figs. 88 and 89 is not a consequence of surface geometry only, but truly reflects the distribution of two distinct terminations.

3.4.5 Relation to other works on cleaved $SrTiO_3(001)$ surfaces

It was mentioned briefly in Section 3.1.1 that there were previous successes at cleaving the $SrTiO_3(001)$, but unfortunately lacked characterization at the atomic scale, which thwarted revealing the true mechanisms behind the cleaving, and surface properties in their entirety. In this Section, a brief overview of these works is given, and the results obtained in the research that led to this Thesis are related to them.

The first successful cleaving of a $SrTiO_3$ single crystal to obtain a (001) surface was achieved by Chien *et al.* [337] and Guisinger *et al.* [339] in the Argonne National Laboratory in Argonne, Illinois, in the United States of

Die approbierte gedruckte Originalversion dieser Dissertation ist an der TU Wien Bibliothek verfügbar.
The approved original version of this doctoral thesis is available in print at TU Wien Bibliothek.
TU Bibliothek Your knowledge hub WIEN

America in 2009. It was achieved on a 0.2 wt.% Nb-doped $SrTiO_3$ single crystal, at a temperature around 50 K, below the cubic-to-tetragonal phase transition temperature of 105 K. For cleaving, $SrTiO_3$ single crystals were prepared outside UHV by removing most of the crystal material at the place where the cleavage was intended to occur. Namely, 0.5 mm thick samples were used, and 75% of the volume was removed to make the single crystal much thinner and easier to cleave. In other words, $SrTiO_3$ single crystals were effectively 125 μm thick at the place where the cleavage was intended to occur. The remaining 0.5 mm thick part of the crystals was held in place at the bottom by a set of clamps, and the cleaving was performed by pushing the thin part of the sample until it broke of. The resulting surfaces were studied with STM, and large, flat domains that laterally span up to 500 nm in one direction were observed in [337], while striped surface morphology with terrace width in the order of 10 nm was observed in [339], even though the same nominal Nb-doping levels were used in both studies. The cleaving technique and the obtained results were subsequently summarized in [338]. Another succesfull cleavage was performed by Sitaputra *et al.* at Carnegie Mellon University in Pittsburgh, Pennsylvania, in the United States of America in 2015 [340]. There, samples with much less Nb-doping than the previous group was used, namely 0.05 wt%, and the similar cutting preparation was performed to make the width of single crystals much smaller and thus easier to cleave. Cleaving occurred at room temperature, and produced a portion of the surface with atomically flat morphology. It was performed in a controlled manner, by driving the top part of a single crystal onto the chamber wall using the UHV manipulator with a well defined velocity. Cleaved surfaces were studied with STM, and a regular pattern of ≈10 nm wide terraces with alternating domains was observed.

Although neither of the previous studies used a clamping mechanism in order to promote the cubic-to-tetragonal phase transition, the results presented in this Section, combined with other results that led to this Thesis, imply that in these previous studies a strain-induced transition to ferroelectricity is likely to have had occurred during the act of cleaving, *i.e.*, during the crack propagation. The samples used were very thin, and this was likely responsible for the fact that the samples could cleave at all under application of reasonable amounts of force. Once the crack is initialized, it is likely that the small sample volume at the place where the cleavage was intended to occur could have ensured a well-defined region in which the crack could propagate, and in turn induce a ferroelectric phase transition. By engineering a specifically designed cleaving device, that controls the crack propagation, 2 mm thick samples were regularly cleaved in the research presented in this Thesis.

Previous succesfull attempts at cleaving $SrTiO_3(001)$ were achieved at either temperatures below the cubic-to-tetragonal phase transition [337, 339, 338], or at room temperature [340]. Although cleaving single crystals at lower temperatures was shown to be easier and more reproducible (Fig. 87), the systematic cleaving at various temperatures (Fig. 86) proved that the resulting surface is always the same, because the resulting surface morphology is a result of the strain-induced ferroelectric phase transition during the crack propagation.

Previously cleaved surfaces were unfortunately studied with STM only, which, in this particular system, can only hint towards the electronic structure of the surface and its morphology. Atomic resolution cannot be achieved on cleaved surfaces with STM (as shown in Figs 61 and 62) because the bottom of the conduction band is delocalized and the the tunneling current signal does not correspond to the atomic arrangement at the surface. Although information on the atomic structure is missing in these previous studies, results presented in this Thesis indicate that those surfaces were also likely to contain polarity-compensating defects, most probably in the exact same concentration of 0.14±0.02 ML that was systematically observed throughout the research presented in this Thesis.

Varying domain sizes observed by these two research groups greatly differed. While 0.2 wt.% Nb-doped samples produced domain sizes in the order of 500 nm along the direction perpendicular to the domain walls [337, 338], the 0.05 wt.% Nb-doped samples produced small domain sizes in the order of 10 nm in the same direction [340]. According to the results presented in Section 3.5, the size of the domains greatly depends on the Nb doping levels, and this discrepancy is therefore understandable. Interestingly, cleavages studied in [339] were performed on the same 0.2 wt.% Nb-doped samples as in [337, 338], but produced much smaller domains with an alternating stripe pattern. It is possible that single crystals employed in these two research groups differed in Nb doping levels although they were nominally the same, or that single crystals were inhomogeneously grown such that the concentration of Nb dopants is drastically different at different portions of crystal volume. Fortunately, single crystals employed in the research presented in this Thesis mostly did not suffer from these disadvantages, and the obtained domain size dependence on the doping level indicates that at least the relative order of doping levels in different crystals follows the relative order of their nominal doping levels, as is seen in Section 3.5.

Finally, it is imperative to notice that succesfull cleavages are far from granted. According to Fig. 87, well-cleaved regions with the surface area of 1 mm^2 can be readily expected, but they have to be identified on an entire 2×3.5 mm^2 cleaved surface that commonly consists of well-cleaved regions and conchoidally fractured

Die approbierte gedruckte Originalversion dieser Dissertation ist an der TU Wien Bibliothek verfügbar.
The approved original version of this doctoral thesis is available in print at TU Wien Bibliothek.
TU Bibliothek Your knowledge hub WIEN

surface regions. The same holds true for the previous cleaving attempts on ≈10 times thinner samples, where the cleaved surfaces also consist of both the well-cleaved and fractured conchoidal regions [338]. In most current research that is performed on "cleaved" $SrTiO_3(001)$, there is a common lack of optical photographs that report the morphology of the cleaved surface, although it would be easy to distinguish between well-cleaved and fractured regions as in Fig. 87. Moreover, the cleaving procedure presented in this Thesis enables taking the counterpart of a cleavage outside UHV (Fig. 83) prior to performing further experiments, which can be used for easy identification of well-cleaved bulk-terminated $SrTiO_3(001)$ surface regions, and subsequently focusing the experiments towards these areas only.

3.4.6 Application of the cleaving device to another perovskite oxide

The idea of creating inequivalent planes of cleavage in an otherwise non-cleavable iono-covalent solids that are characterized by cubic symmetry, is in principle applicable to other perovskite oxides. Utilizing the cleaving device presented in this Thesis (Fig. 83) that applies external strain and controls the propagation of tensile strain during the crystal fracture, should be readily possible for all perovskite oxides that are incipient ferroelectrics, or to those that can experience strain-induced structural phase transitions. To investigate this applicability further, the cleaving device was applied to cleave a $KTaO_3$ single crystal and obtain its (001) surface.

$KTaO_3$ belongs in the ABO_3 class of cubic perovskite oxides, with the same crystal structure as $SrTiO_3$. The main difference between the two is that $KTaO_3$ is, unlike $SrTiO_3$, nominally polar along the [001] directions because it consists of alternating KO and TaO_2 layers with -1 and $+1$ nominal charge per unit cell, respectively. Interestingly, $KTaO_3$ cleaves very successfully by initializing a crack using a sharp tungsten carbide blade (unlike $SrTiO_3$), as demonstrated by Setvín *et al.* [360]. Although these crystals also lack preferable planes of cleavage, once the crack is initialized using a blade it propagates uncontrollably, but creates a perfectly flat atomically defined surface that spans almost the entirety of the cleavage. Cleaved $KTaO_3(001)$ surface was shown to consist of two terminations, with $\approx 8\times8\,\mathrm{nm}^2$ large KO islands on top of the TaO_2 substrate, and, upon heating, exhibits a series of polarity-compensating mechanisms to reduce the surface energy of an otherwise polar surface [360]. The as-cleaved TaO_2 termination is metallic, while KO is semiconducting with occasional oxygen vacancies appearing in an otherwise perfectly regular (1×1) lattice. Additionally, the bulk crystal few layers beneath the surface was calculated to be in an antiferrodistortive state [360]. Similarly to $SrTiO_3$, $KTaO_3$ with the same amount of arbitrary extrinsic dopants always cleaves in the same way and exposes the same characteristic surface morphology and atomic structure, the details of which are thoroughly laid out in [360].

Figure 90 shows the results obtained of a $KTaO_3(001)$ surface cleaved by a cleaving device (used for cleaving $SrTiO_3$ as in Fig. 83) instead of cleaving with a blade as in [360]. The optical photograph shows a surface morphology different from the one obtained by cleaving with a blade. The surface is macroscopically rough with several regions having distinctly different morphologies, which is in clear contrast with a uniformly flat surface obtained by cleaving $KTaO_3(001)$ using a blade. In the optical photograph in Fig. 90, the point of crack initialization was identified and marked by a white cross symbol, and the overall surface morphology is somewhat related to the crack propagation in the crystal volume designated for cleaving (the unstrained portion of the volume between the top and the bottom set of clamps in the cleaving device). Three optically distinct regions were investigated with STM/AFM, and they are indicated in the optical photograph. In the first region (marked as "1") the optical surface morphology resembles the one commonly obtained after cleaving the $KTaO_3(001)$ with a blade. On a nanometer scale, this portion of the surface also greatly resembles a typical $KTaO_3(001)$ atomic structure, but with the slight difference that the KO island sizes are noticeably larger than usual. On the other hand, the two untypical surface morphologies (marked by "2" and "3" in the optical photograph) show drastically different properties. In the surface region marked by "2", STM reveals that the KO islands do not follow the standard shape characteristic for spinodal decomposition as in region "1", but instead form regular rectangular domains with step edges oriented along the main crystallographic axes. Atomic arrangement of the KO rectangular domains is still characterized by a perfect (1×1) lattice interrupted by occasional O vacancies. Domains vary in size, but have a characteristic width of $\approx 30\,\mathrm{nm}$. The surface region marked by "3" is the most untypical of all: it is insulating with a considerably larger band gap, and does not consist of alternating terminations, as can be seen in constant-frequency-shift AFM image in Fig. 90. Instead, the average domain size can be considered larger than at least $250 \times 250\,\mathrm{nm}^2$. The large band gap in this surface region also enabled implanting charge into such a surface, or switching the local ferroelectric polarization. A scan with a high positive sample bias of $+3.5\,\mathrm{V}$ was performed in a square $50 \times 50\,\mathrm{nm}^2$ pattern in region "3", and the subsequent constant-frequency-shift AFM image shows that the region where the high bias scan was performed appears as a square-like depression. This is because this square has a different LCPD when compared to the

Die approbierte gedruckte Originalversion dieser Dissertation ist an der TU Wien Bibliothek verfügbar.
The approved original version of this doctoral thesis is available in print at TU Wien Bibliothek.
TU Bibliothek Your knowledge hub WIEN

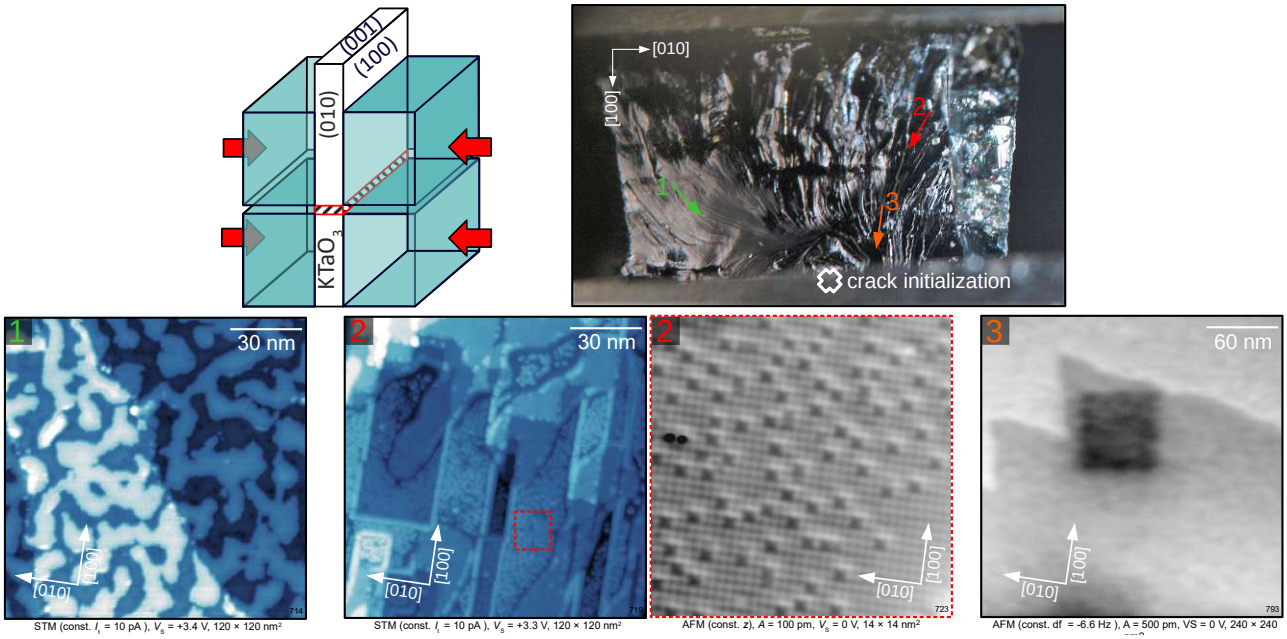

Figure 90: **Application of the cleaving device for cleaving a polar cubic perovskite $KTaO_3$(001) surface.** A single crystal $KTaO_3$ was cleaved by application of strain, in a same manner as commonly applied to $SrTiO_3$ throughout this Thesis. The optical photograph shows the cleaved surface, which displays different surface morphologies across the cleavage. Three sites with distinct optical appearance, indicated by arrows and corresponding numbers, were examined with STM/AFM, shown in the bottom row of the Figure. The 50×50 square feature in the AFM image in the region marked as "3" is a consequence of high-bias experiments, discussed in the text.

rest of the surface, or to the same region prior to the high-bias scan.

In conclusion, applying the cleaving device to $KTaO_3$ created a (001) surface that is drastically different than the one obtained by applying a blade. Distribution of the strain prior and during the cleaving was therefore manipulated using the cleaving device. It is possible that the well-defined volume in which the crack could propagate during cleaving, defined by the cleaving device geometry, could have led to an increased amount of tensile strain in different portions of the sample, and therefore created several distinct surfaces: it is noticeable that the most peculiar surfaces occurred in the close vicinity to the place where the crack was initialized, and further away from this point the cleaved surface resembles a typical surface morphology, albeit with larger domain sizes. This experiment therefore shows that the cleaving device can be readily applied to those cubic perovskites that otherwise readily cleave ($KTaO_3$), as well as those that are hardly ever cleavable ($SrTiO_3$). This opens up a wide range of opportunities since perovskite oxides are a rich class of materials with many intriguing properties and possible applications. It is expected however, that a plethora of various polarity compensating mechanisms appear when cleaving this class of materials, for both, the nominally polar [360] and nominally non-polar [341] solids.

3.4.7 Conclusions

The cleaving device can be readily applied to reproducibly create atomically flat $SrTiO_3$(001) surfaces. The geometry of the cleaving device, its optimized shape, and the procedure of straining the single crystals prior to cleaving, are all important aspects behind a successful cleavage. Some experience is necessary before achieving well-cleaved surfaces, but the steps laid-out in this Section should provide a good pathway to success. The small cleaving device, fitted for Omicron UHV machines used in the research that led to this Thesis, can cleave crystals that are up to 2 mm thick. Cleaving thicker crystals would require using a larger cleaving device, which can apply higher compressive strains by using larger screws. Well-cleaved regions of a surface can be recognized using an optical microscope, since most of them reflect light simultaneously under a given angle, in clear contrast to conchoidally fractured surface regions. A terrace train, which run runs perpendicularly to the direction of

Die approbierte gedruckte Originalversion dieser Dissertation ist an der TU Wien Bibliothek verfügbar.
The approved original version of this doctoral thesis is available in print at TU Wien Bibliothek.
TU Bibliothek Your knowledge hub WIEN

the applied strain, is the most typical morphology of well-cleaved surfaces

The cleaving process was inferred to proceed through freezing of the soft transverse optical phonon in $SrTiO_3$ that is responsible for a transition to ferroelectricity and splitting the TiO_2 layers along the [001] direction. Properties of the cleaved surfaces do not depend on the crystal temperature during cleavage, at least not in a range between $-170\,°C$ and $+100\,°C$. Namely, cleaved surfaces always have the same electronic properties, and are always covered with the same 0.14 ± 0.02 ML of polarity-compensating defects, regardless of temperature. A possible reason could be that the cleavage always occurs once the tensile strain that propagates together with the crack freezes the soft transverse optical phonon. SEM measurements discriminate between two surface terminations even after exposure to ambient conditions, and reveal that the terminations span for tens of micrometers between the domain walls.

Samples that were systematically cleaved in this Section were all doped with 0.69 at.% of Nb, but the cleaving procedure and the underlying mechanism is well-applicable to $SrTiO_3$ crystals with different Nb-doping levels, as will be shown in Section 3.5. The cleaving device is also universal in the sense that it is applicable to other cubic perovskites, as was shown on the example of $KTaO_3$, while its versatile design enables transferability between different UHV systems.

Die approbierte gedruckte Originalversion dieser Dissertation ist an der TU Wien Bibliothek verfügbar.
The approved original version of this doctoral thesis is available in print at TU Wien Bibliothek.
TU Bibliothek Your knowledge hub WIEN

3.5 Influence of variable Nb doping levels on the properties of cleaved $SrTiO_3(001)$

All $SrTiO_3(001)$ surface properties discussed in this Thesis, with the exception of this Section, were obtained on surfaces nominally doped with 0.67 at.% of Nb. Here, the influence of the Nb-doping on the properties of cleaved Nb:$SrTiO_3(001)$ surfaces is investigated, and Nb doping levels are always explicitly mentioned. This Section is based on the forthcoming publication "Screening-dependent macroscopic properties of cleaved $SrTiO_3(001)$ surfaces" [409].

Niobium acts as substitutional dopant, *i.e.*, some Nb atoms replace some Ti atoms (B cations) in a $SrTiO_3$ lattice, and act as n-type electron donors since Nb has a formal charge of 5+ compared to Ti with 4+. Niobium is commonly used as a dopant in $SrTiO_3$ because its extrinsic n-type doping lifts the $SrTiO_3$ Fermi level closer to the onset of the conduction band. This makes otherwise insulating (wide-band-gap semiconducting) $SrTiO_3$ surfaces susceptible to studies using STM. The technique of choice for studying cleaved $SrTiO_3(001)$ surfaces was shown to be nc-AFM, because, unlike STM, it provides atomically resolved images. Therefore, it is not imperative that the cleaved $SrTiO_3(001)$ surfaces are conducting, because AFM is readily applicable to insulators. This allows for investigating the influence of the Nb dopant concentration on the properties of cleaved $SrTiO_3$ with variable Nb doping levels, or $SrTiO_3$ crystals with nominally no doping at all.

For this purpose, a series of differently Nb-doped $SrTiO_3$ single crystals were grown, in the same custom shape as the single crystals throughout this Thesis. Namely, five different Nb doping levels were investigated: $SrTiO_3$ crystals supplemented with either 0.5 wt.% (the one used throughout this Thesis), 0.2 wt.%, 0.1 wt.%, 0.02 wt.%, or 0 wt.% of Nb_2O_5 powder during growth. In other words, single crystals with 0.69 at.% (the one used throughout this Thesis), 0.28 at.%, 0.14 at.%, 0.03 wt%, or no Nb doping (0 at.%) were cleaved. The exact doping levels were unfortunately not verified by independent techniques, so the doping levels are taken as the nominal values provided by the manufacturer. It is noteworthy that the relative order of the Nb doping levels in different $SrTiO_3$ single crystals could be recognized by their macroscopic appearance: while $SrTiO_3$ single crystals with the most Nb doping used are black and opaque, they become progressively transparent as the Nb content is reduced, and finally become white and transparent when no nominal doping is used. Substitutional Nb dopants were never observed on the cleaved 0.5 wt.% Nb-doped $SrTiO_3(001)$ surfaces throughout this Thesis, implying that their influence on the cleaving procedure and the properties of cleaved surfaces could have been insignificant. However, the amount of Nb doping is shown here to drastically the morphology and the electronic properties of the cleaved surfaces.

The effect of Nb doping levels on the cleaved Nb:$SrTiO_3(001)$ surfaces is shown in Fig. 91. Four doping levels are shown, and the highest doping level is omitted since it is already thoroughly studied throughout this Thesis. A series of STM images in Fig. 91 show that the domain and terrace sizes drastically depend on the Nb concentration. At the highest doping level (0.28 at.%) presented in Fig. 91, the surface morphology differs from region to region, as can be seen by comparing the large-area image obtained at one region (top panel), and the small-area image (bottom panel) obtained at a different region on the cleaved 0.28 at.%–Nb:$SrTiO_3(001)$ surface. On a large-area image, a clear asymmetry is noticeable between the distribution of the two terminations: SrO termination appeared in large domains, ≈300 nm wide between the domain walls, while the TiO_2 termination is significantly smaller. Naturally, on the other side of the cleavage, the distribution is exactly the opposite with the predominant presence of the TiO_2 termination at the expense of the SrO termination. On the contrary, small-area STM image shows a striped morphology, with equally present SrO and TiO_2 terminations, each being ≈80 nm wide between the domain walls. Terminations switch at the domain walls that are drastically different compared to the typically studied cleaved 0.69 at.%–Nb:$SrTiO_3(001)$ surfaces: for smaller doping levels, the domain walls are not large, optically visible steps, but instead either half- or one-and-a-half-unit-cell-size-high.

The morphology of cleaved Nb:$SrTiO_3(001)$ surfaces with Nb doping levels smaller than 0.28 at.% are exclusively striped, with the same morphology covering all well-cleaved regions on a cleaved surface. Their surface morphology is characterized by alternating, equally sized SrO and TiO_2 terraces that mutually switch at the half-a-unit-cell-large terrace steps, as can be seen in the last three columns of Fig. 91. Domain walls are typically oriented parallel to the application of external strain, namely the [110] direction, with some deviation that could be possibly explained by a slight miscut of different samples, or a slight misalignment of the single crystals squeezed in the cleaving device. The average domain width $\langle w_d \rangle$ decreases with the nominal Nb doping levels, from 35 nm to 13 nm for 0.14 at.%– and 0.03 at.%–Nb:$SrTiO_3(001)$ samples, and finally to 9.5 nm for the nominally undoped, cleaved $SrTiO_3(001)$ samples. Average domain widths were calculated from the line profiles performed on large-area STM images in Fig. 91, to reduce the effects that originate from the convolution of the tip shape and the surface shape.

Die approbierte gedruckte Originalversion dieser Dissertation ist an der TU Wien Bibliothek verfügbar.
The approved original version of this doctoral thesis is available in print at TU Wien Bibliothek.
TU Bibliothek Your knowledge hub WIEN

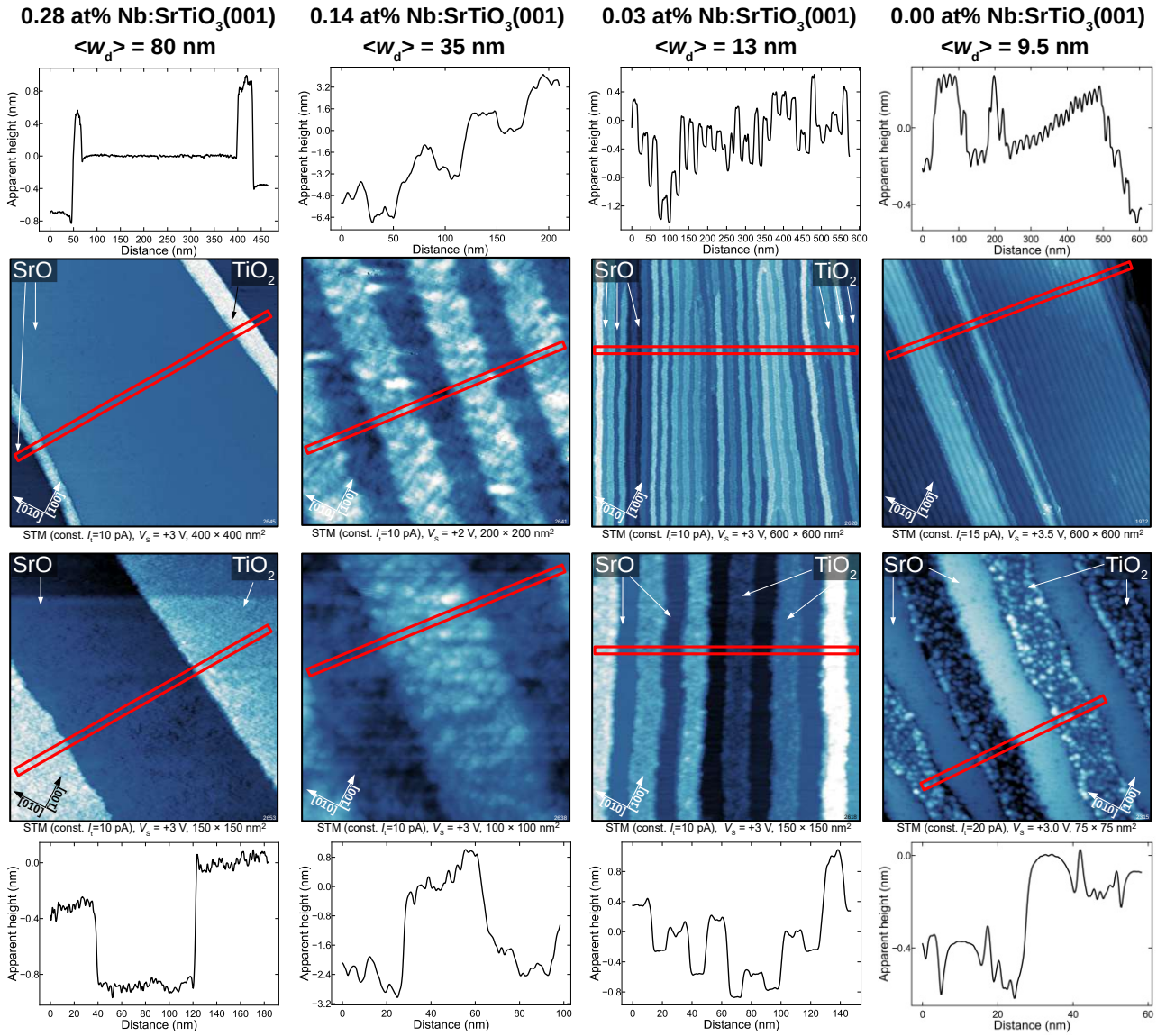

Figure 91: **Morphology of cleaved Nb:$SrTiO_3$(001) surfaces with different nominal Nb doping levels.** Large- and small-area STM images (second and third row, respectively) of Nb:$SrTiO_3$(001) surfaces obtained by cleaving Nb:$SrTiO_3$ single crystals with different nominal levels of Nb-doping. Namely, presented cleavages were obtained on Nb:$SrTiO_3$ single crystals that were supplemented with 0.2 wt.%, 0.1 wt.%, 0.02 wt.%, and 0 wt.% of Nb_2O_5 powder during growth. Each column represents a single Nb doping level, reported in atomic percent, with doping levels decreasing from left to right. A single line profile along each STM image is presented, above and below the large- and small-area STM images, respectively. The average domain width $\langle w_\mathrm{d} \rangle$ is reported for each doping level. Domain identification is reported in those images where it was subsequently achieved by atomically resolved AFM. Cleaving of differently doped crystals was performed at variable temperatures between $-50\,\mathrm{C}^\circ$ and $80\,\mathrm{C}^\circ$, and STM measurements were performed at either LN_2 or LHe temperatures.

A comparison of cleaved differently-doped Nb:$SrTiO_3$(001) surfaces reveals that below a certain Nb-doping threshold, the surface morphology becomes striped, with alternating SrO and TiO_2 terraces. The data in Fig. 91 indicates that this critical Nb-doping level is between 0.28 at.% and 0.14 at.%. Above this critical doping level, the domains sizes are very large, and the two terminations are commonly unequally distributed on one side of the cleavage. Therefore, the average domain width and the surface morphology can be predicted and considered granted only for cleaved Nb:$SrTiO_3$(001) surfaces below the critical Nb-doping level, while those Nb:$SrTiO_3$ single crystals with Nb doping levels above the critical value must be examined in detail to discern their

Die approbierte gedruckte Originalversion dieser Dissertation ist an der TU Wien Bibliothek verfügbar.
The approved original version of this doctoral thesis is available in print at TU Wien Bibliothek.
TU Bibliothek Your knowledge hub WIEN

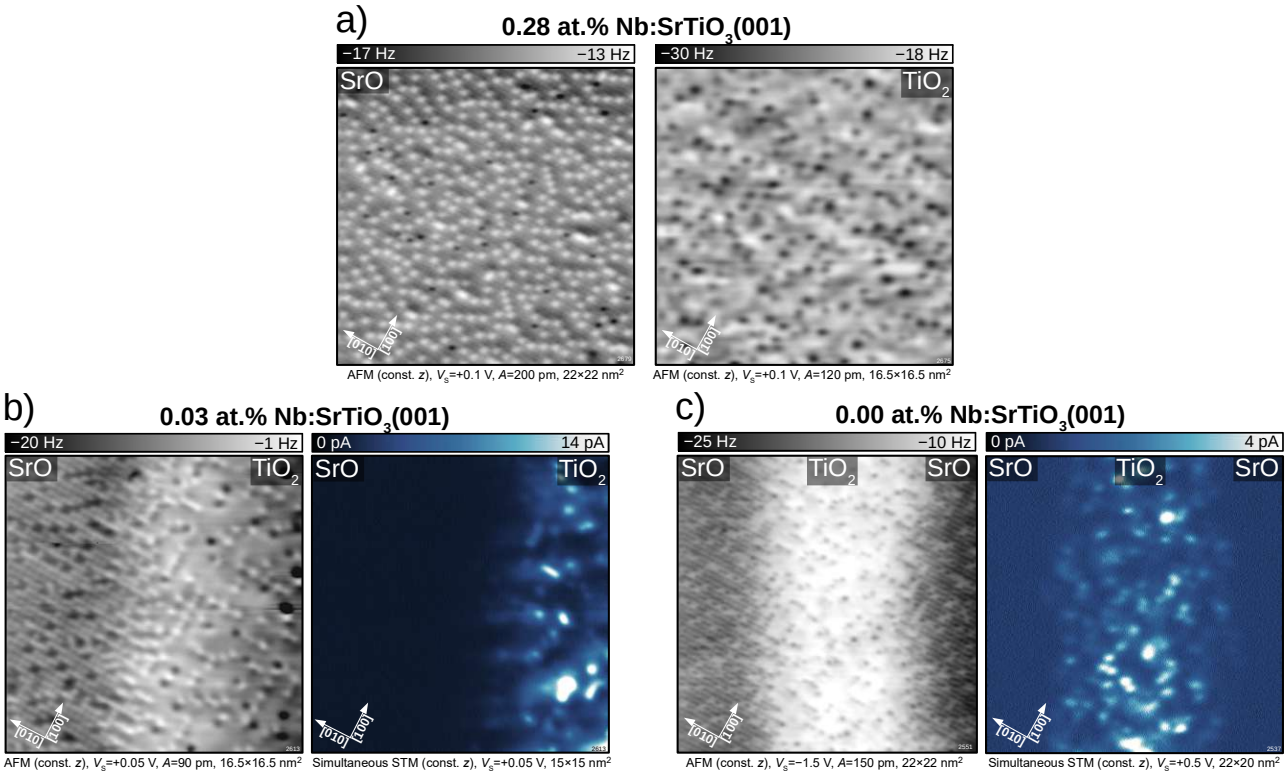

Figure 92: **Atomically resolved AFM imaging of cleaved Nb:SrTiO$_3$(001) surfaces with different nominal Nb doping levels.** a) AFM images of two surface terminations on a cleaved Nb:SrTiO$_3$(001) surface doped with 0.28 at.% of Nb, obtained separately on two distinct domains. b) A single AFM image (left) showing the transition from one termination to the other, and a simultaneous empty-states STM image (right) showing the conduction band distribution at the sample bias of $V_S = +50\,\mathrm{mV}$. The AFM image was obtained with an uncommon cation-terminated tip, so the $\mathrm{Sr_{ad}}$s appear repulsive and $\mathrm{V_{Sr}}$s appear attractive. c) A single AFM image (left) showing two transitions between the domains, with a TiO_2 termination between two SrO-terminated domains, and a simultaneous empty-states STM image (right) showing the distribution of empty states at a sample bias of $V_S = +500\,\mathrm{mV}$.

individual surface morphologies and identify the distribution of the two termination. Interestingly, regardless of the Nb-doping levels in cleaved Nb:SrTiO$_3$ single crystals, STM measurements are to be always possible, as demonstrated in Fig. 91.

Figure 92 shows atomically resolved AFM images of three differently doped Nb:SrTiO$_3$(001) surfaces. The atomic structure of cleaved Nb:SrTiO$_3$(001) surfaces can be discerned only using AFM, because empty-states STM shows a delocalized bottom of the conduction band just like for the SrTiO$_3$(001) surfaces with highest Nb doping content studied throughout this Chapter (Fig. 61). On the highest-doped Nb:SrTiO$_3$(001) surface in Fig. 92, atomic resolution was obtained on the two terminations independently, because the average domain width is $\langle w_\mathrm{d}\rangle \approx 80\,\mathrm{nm}$ (first column in Fig. 91). Both terminations are characterized by the presence of polarity-compensating defects, namely $\mathrm{V_{Sr}}$ on the SrO, and $\mathrm{Sr_{ad}}$ on the TiO_2 termination. The concentration of these point defects at the cleaved 0.28 at.%–Nb:SrTiO$_3$(001) surface in Fig. 92a ammounts to 0.14±0.02 ML on average, exactly the same as at the cleaved Nb:SrTiO$_3$(001) surfaces studied throughout this Thesis. The distribution of these point defects is also consistent with the results presented so far, with occasional clustering of $\mathrm{V_{Sr}}$s along one of the two main crystallographic axes at the SrO, and the characteristic dispersal of $\mathrm{Sr_{ad}}$s at the TiO_2 termination.

The small domain width on the cleaved Nb:SrTiO$_3$(001) surfaces, obtained on single crystals below the critical Nb-doping level, allows imaging both terminations simultaneously in constant-height AFM, as shown in Figs. 92b and 92c. Naturally, this is possible only if the SrO termination covers a terrace that is situated half-a-unit-cell-higher than the neighboring TiO_2-terminated terrace, because the SrO (1×1) lattice and the

Die approbierte gedruckte Originalversion dieser Dissertation ist an der TU Wien Bibliothek verfügbar.
The approved original version of this doctoral thesis is available in print at TU Wien Bibliothek.
TU Bibliothek Your knowledge hub WIEN

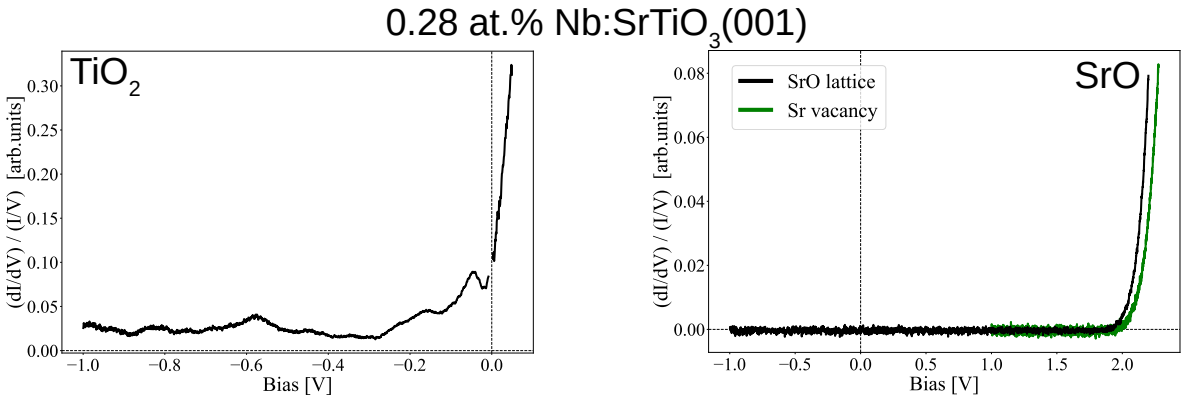

Figure 93: **Electronic structure of the two terminations on a cleaved Nb:$SrTiO_3$(001) surface with nominally 0.28 at.% of Nb doping.** STS measurements reveal the DOS of the TiO_2 and SrO terminations. Metallic TiO_2 termination shows the same DOS above a lattice point and above a Sr_{ad}, while on the SrO termination, STS measurements above a regular lattice point and above a V_{Sr} are reported.

Sr_{ad}s at the lower-lying TiO_2 termination are approximately at the same height under this condition. It is necessary to find a region on a cleaved surface where this condition is met, because the relative order of the two terminations along [001] direction changes across a cleaved surface: sometimes SrO lies higher than the TiO_2, and sometimes the opposite is true. This is the case in Fig. 92b with the higher-lying SrO termination at the left side of the AFM image, and in Fig. 92c with the higher-lying SrO terminations on the left and the right terrace, and the lower-lying TiO_2 termination in between. Simultaneous STM/AFM images in Figs. 92b and 92c show that the application of a small positive sample bias results in electron tunneling into the empty states of the TiO_2 termination, where the current signal corresponds to the position of the Sr adatoms, while the SrO termination requires higher sample bias values for the tunneling current to appear (not shown).

Counting the polarity-compensating defects for cleaved Nb:$SrTiO_3$(001) with small, or no nominal Nb content in Figs. 92b and 92c is not trivial, because the transition between the domains is smooth – there is no clear border between the two terminations. Namely, for both 0.03 at.%–Nb:$SrTiO_3$(001) and nominally undoped $SrTiO_3$(001), the concentration of V_{Sr}s and Sr_{ad}s in the center of the SrO- and TiO_2-terminated domains, respectively, is roughly 0.1±0.02 ML. However, there is an additional concentration of point defects at the step edges where the transition from SrO to TiO_2 termination occurs smoothly. Considering that on all other Nb:$SrTiO_3$(001) surfaces, where the domains were significantly larger and the concentration of point defects was possible to calculate on the two termination separately, the concentration of polarity-compensating defects always amounted to the canonical 0.14±0.02 ML, it is safe to assume that it also amounts to this value on the striped surface morphology of low- or undoped $SrTiO_3$(001) surfaces, when the points defects that appear in the vicinity of the "smooth" terrace steps are accounted for.

The electronic structure of the two terminations was studied with STS on a cleaved 0.28 at.%–Nb:$SrTiO_3$(001) surface in Fig. 93. The DOS at the surface is to great extent similar to the DOS as the $SrTiO_3$(001) surface with the highest Nb-doping levels used, reported in Figs. 61 and 62. The TiO_2 termination is metallic, with the Fermi level crossing the conduction band, while the SrO termination is semiconducting. The conduction band onset on the SrO termination is ≈1.8 eV away from the Fermi level, and the Sr vacancies exhibit upward band bending, consistent with the behavior of negatively charged defects on a n-type semiconductor surface. The band gap of the SrO termination is featureless, and the DOS is equal to zero in this energy range. The bulk band gap is filled with in-gap states on the TiO_2 termination, and the DOS never drops to zero. The appearance of a STS peak at -40 meV, characteristic for a 2DEG, is still present at this doping level as in Fig. 62. Other peaks also correspond to the same peaks observed on the Nb:$SrTiO_3$(001) surfaces throughout this Thesis, namely at −0.18, −0.6, −0.85, and −1 eV, but the origin of these peaks remains to be identified. Altogether, the electronic structure of 0.28 at.%–Nb:$SrTiO_3$(001) is almost exactly the same as 0.69 at.%–Nb:$SrTiO_3$(001), which is unsurprising considering both of these doping levels are above the critical Nb-doping level discerned from Fig. 91.

Figure. 94 shows the electronic structure of a nominally undoped, cleaved $SrTiO_3$(001) surface. It was evident that STM measurements are readily possible on these surfaces already in Fig. 91, which is surprising

Die approbierte gedruckte Originalversion dieser Dissertation ist an der TU Wien Bibliothek verfügbar.
The approved original version of this doctoral thesis is available in print at TU Wien Bibliothek.
TU Bibliothek Your knowledge hub WIEN

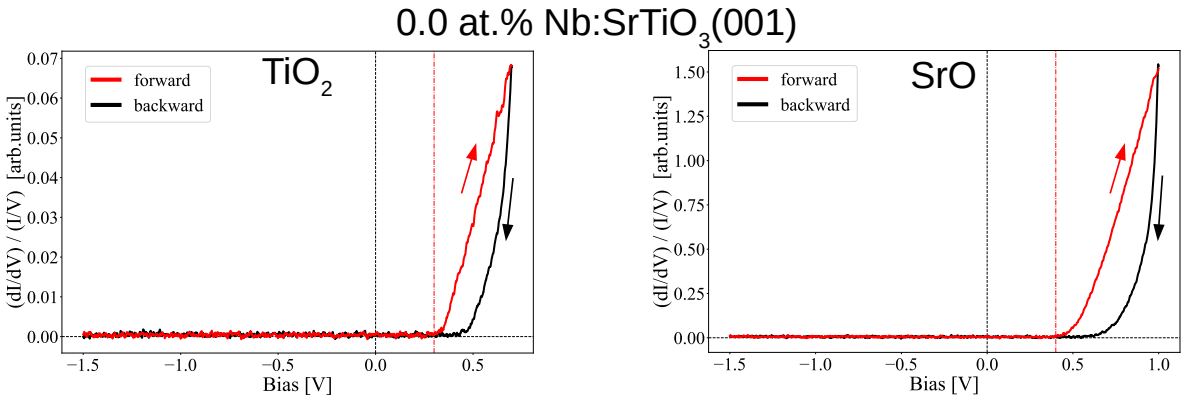

Figure 94: **Electronic structure of the two terminations on a cleaved $SrTiO_3(001)$ surface nominally without Nb doping.** STS measurements reveal the DOS of the TiO_2 and SrO terminations. Both terminations are semiconducting, with a clear hysteresis in the backward and forward bias scan: when the sample bias is ramped from low to high values, the conduction band offset is closer to the Fermi level compared to the subsequent bias ramp from high to low values.

because the undoped bulk crystals lack n-type doping. After all, these undoped single crystals were white and transparent. The DOS in Fig. 94 suggests that on the SrO termination, the conduction band onset lies closest to the Fermi level when compared to any other cleaved Nb:$SrTiO_3(001)$ surface. This would otherwise imply a stronger n-type doping on these undoped single crystals compared to the other, doped $SrTiO_3$ crystals. However, this effect is possibly explained by the lower band bending on the cleaved undoped $SrTiO_3(001)$ surfaces compared to the doped ones instead, due to small domain sizes where the band bending is not fully developed and is not as pronounced as on the larger domains. Additionally, the proximity of the TiO_2 termination to the SrO termination could be responsible for the reduction of upward band bending. The electronic structure of the TiO_2 termination is drastically different on the undoped cleaved $SrTiO_3(001)$ surfaces compared to cleaved Nb:$SrTiO_3(001)$ surfaces. It is no longer metallic, and the DOS instead resembles the one of a n-type semiconductor. Therefore, both terminations on a cleaved undoped $SrTiO_3(001)$ surface are semiconducting, with the conduction band onset closer to the Fermi level on the TiO_2 termination compared to the SrO termination. For this reason, the constant-height empty-states STM image in Fig. 92c shows tunneling current only on the TiO_2 termination. The DOS at the undoped TiO_2 termination does not exhibit the in-gap features observed at any other Nb-doping level. Instead, the DOS is equal to zero across the bulk band gap, just as on the SrO termination. This implies that these previously-identified peaks in the DOS of TiO_2-terminated surface regions are directly related to the subsurface Nb defects. Moreover, the absence of metallicity on the TiO_2 termination of the cleaved undoped $SrTiO_3(001)$, and its presence at cleaved Nb:$SrTiO_3(001)$ surfaces with Nb concentrations in the range from 0.03 at.% to 0.69 at.%, implies that the Nb dopants are responsible for the semiconductor-to-metal transition on the cleaved Nb:$SrTiO_3(001)$ surfaces. This is additionally confirmed by the fact that cleaved undoped $SrTiO_3(001)$ surfaces are characterized with the same concentration of polarity-compensating defects as the cleaved Nb:$SrTiO_3(001)$ surfaces, which implies that the electron donation from the charged defects is insufficient for turning the semiconducting TiO_2 termination metallic.

The DOS at the undoped cleaved $SrTiO_3(001)$ surfaces reveals another peculiarity that appears on both surface terminations. Figure 94 reports the forward and backward bias sweeps for both terminations, displayed in red and black, respectively. The conduction band onset is closer to the Fermi level in the forward scan, while the sample bias is ramped from low to high values, and it shifts further away from the Fermi level once the sample bias is subsequently ramped from high to low values. This hysteresis in the STS was consistent throughout measurements, *i.e.*, bias sweeps do not irreversibly alter the electronic structure of the two terminations, and each subsequent STS measurement performed at the same spot on the surface displays exactly the same behavior. Such behavior could indicate a short-lived charging processes with electron doping into the both surface terminations: a forward bias sweep could potentially dope a surface with electrons once they start tunneling into the bottom of the conduction band, which in turn induces an upward band bending that shifts the conduction band minimum offset from the Fermi level, visible in the backward bias scan. This charging is apparently short-lived, since a bias sweep performed 1 s after the previous one would still show the same

Die approbierte gedruckte Originalversion dieser Dissertation ist an der TU Wien Bibliothek verfügbar.
The approved original version of this doctoral thesis is available in print at TU Wien Bibliothek.
TU Bibliothek Your knowledge hub WIEN

behavior, *i.e.*, accumulated charges from the previous bias sweep are potentially dispersed or diminished in the 1 s period until the subsequent bias sweep is performed. Such behavior was not yet observed for any cleaved Nb-doped $SrTiO_3$(001) surfaces, and it could be further examined by experimenting with temperature: if injected electrons are temporarily trapped in the form of polarons that thermally hop through lattice vibrations within a 1 s period, increased sample temperatures would dissipate them more rapidly and the hysteresis might not be present. It remains to be investigated whether the valence band maximum of the undoped cleaved $SrTiO_3$(001) surface hosts the same hysteresis phenomenon, although experiments in Section 3.7 (below) indicate that these experiments could induce some irreversible changes to a surface. It also remains to be investigated up to how high sample bias values the hysteresis reported in Fig. 94 pertains, and whether the application of high positive sample bias values will induce some trapped charges with longer lifetimes.

The variable Nb content in $SrTiO_3$ single crystals was shown to drastically alter the properties of the cleaved $SrTiO_3$(001) surfaces. Mainly, the domain size and the electronic properties of the cleaved surfaces can be manipulated by using differently-doped Nb:$SrTiO_3$ single crystals, but the atomic structure of the cleaved surfaces remains the same, regardless of the dopant concentration. This indicates that the same ferroelectric phase transition is responsible for well-cleaved $SrTiO_3$(001) surfaces with any Nb-doping level that occurs by freezing the soft optical phonon (Fig. 85), but that the period of the soft optical phonon reduces from infinity for highly doped crystals, to ≈10 nm for nominally undoped $SrTiO_3$ single crystals. The exact origin of the Nb-induced changes to the cleaved $SrTiO_3$(001) surfaces remains to be identified. The experimental setup of creating cleaved $SrTiO_3$(001) surfaces in UHV does not allow for sources of extrinsic charges, so the intrinsic dopants are the only source of excess charge. One possibility is that the addition of free electrons by the Nb dopants account for more efficient screening of the ferroelectric domains, and therefore their increased lateral size. Namely, efficient screening of the ferroelectric domains allows for spontaneous creation of even monodomain ferroelectric surfaces as energetically favorable structures, without the presence of domain walls or domains with opposite polarity that would be necessary to reduce the surface energy [410]. In other words, when the depolarization field is reduced by bound charges, *i.e.*, enough charge carriers are available for screening, a ferroelectric surface does not have to converge to a striped domain structure with high depolarizing energy [411, 366]. Applied to the case of Nb:$SrTiO_3$(001), this implies that the high Nb-content is capable of providing sufficient screening charges to create giant single-domain structures, while the absence of Nb results in striped surface structures with improperly screened domains. Another possibility for explaining drastic morphological differences between differently doped Nb:$SrTiO_3$(001) cleaved surfaces is the coupling of excess electrons to optical phonons, a phenomenon that readily occurs in halide perovskites [412, 413] and perovskite oxides [414, 415]. This holds true for Nb-doped $SrTiO_3$(001) as well, where excess electrons are known to couple with phonons [416] to create large electron polarons [417, 418] that could additionally enhance screening capabilities [419].

In conclusion, different surface morphologies on cleaved Nb:$SrTiO_3$(001) can be readily achieved by cleaving differently doped Nb:$SrTiO_3$ single crystals. When the Nb content is above a critical value that lies between 0.14 at.% and 0.28 at.%, cleaved surfaces can have giant, singly-terminated domains, that span between 50 nm and 100 μm in the direction normal to the domain walls. When the Nb-content is smaller than the critical value, surfaces always develop a striped morphology with alternating terraces of two opposite terminations. The width of a typical domain decreases as the Nb-content is reduced, and converges to a 9.5 nm value for nominally undoped crystals. The SrO termination is always semiconducting, and the TiO_2 termination always metallic, regardless of the amount of Nb doping. Only at the nominally undoped surface both terminations are semiconducting. All cleaved surfaces have the same concentration of polarity-compensating defects. STM measurements are possible on both the Nb-doped and nominally undoped $SrTiO_3$(001) surfaces. The role of Nb in the cleaving process is to provide screening charges for the two ferroelectric domains.

Die approbierte gedruckte Originalversion dieser Dissertation ist an der TU Wien Bibliothek verfügbar.
The approved original version of this doctoral thesis is available in print at TU Wien Bibliothek.
TU Bibliothek Your knowledge hub WIEN

3.6 UV irradiation of the two terminations

The properties of a novel surface, like the cleaved $SrTiO_3(001)$, can be probed by irradiating them with UV light at low temperatures. Experiments in this Section were performed on cleaved Nb:$SrTiO_3(001)$ surfaces with 0.69 at.% concentration of Nb-dopants. It is shown below that the UV irradiation causes spontaneous charging of the SrO termination with holes, and that the lifetime of this hole-charged state is exceptionally long, while it can be locally returned to the ground state by electron injection. This Section is based on the forthcoming publication "Charge separation on a nominally centro-symmetric $SrTiO_3(001)$." [420].

Irradiation of a material with UV light creates electron-hole pairs when the energy of the UV light is larger than the band gap of the irradiated material. In $SrTiO_3$, UV light with the central wavelength of λ=365 nm can overcome the 3.25 eV band gap Experimentally, a diode mount with two focusing lenses was constructed, such that the light emitted by the diode is reasonably focused on the surface of a cleaved $SrTiO_3(001)$ surface placed in an AFM/STM measurement head, and kept at cryogenic temperatures. Unlike the research that was performed on the rutile $TiO_2(110)$ surface covered with O_2 molecules (Section 2.5), where the products of UV photochemistry were observed, irradiating a cleaved $SrTiO_3(001)$ surface is a good tool for investigating the internal electric (polarization) fields that are a consequence of the ferroelectricity-assisted cleaving. Cubic $SrTiO_3$ is centro-symmetric, and by definition should not separate electron-hole pairs created by the UV light. In other words, photo-voltage or photo-current cannot not appear on under UV illumination on ideally bulk-truncated $SrTiO_3(001)$ surfaces. However, cleaved $SrTiO_3(001)$ surfaces are characterized by a broken cubic symmetry, through splitting of the TiO_2 layers along the [001] direction during the quantum phase transition to ferroelectricity, and could provide an adequate environment for charge separation.

Cleaved $SrTiO_3(001)$ surface, placed inside the measurement head in UHV, equilibrated at the base temperature of either liquid nitrogen or liquid helium, were irradiated with UV light through a circular opening in the cryostat shields. During the irradiation, thermal drift occurs because the thermally insulated sample stage within the measurement head is radiatively heated by the high-intensity light coming from the UV diode. This induces a thermal drift of both the sample and the tip, which prevents having the tip-sample distance small enough to ensure atomic resolution during UV irradiation. The temperature increase of the sample was in the order of 1 K for samples cooled to LHe temperature, and 0.2 K for samples at LN_2 temperature, as measured by a thermocouple located at the back-side of the sample. The temperature increase on the sensor, and the thermal expansion of the tip, were not quantified due to the absence of a thermocouple connected to a qPlus sensor. The effective thermal drift between the sample and the tip during UV irradiation is in the order of 50 nm until the temperature of both parts of the junction equilibrate with the incoming irradiation, after roughly 15 min. Due to these large changes in tip-sample distances, the tip-sample separation was kept roughly constant using the constant-frequency-shift AFM mode, with a weak set-point that ensures that the tip-sample distance is in the order of several nanometers. Since the qPlus sensor is also heated during UV irradiation, the resonance frequency of the sensor is altered, with a typical shift of the nominal resonance frequency in the order of 500 mHz. The amount of temperature-(UV-) induced shift of the resonance frequency of the qPlus sensor can be calibrated while the tip is 200 nm from the sample surface, and can therefore be compensated during measurements. After accounting for both, the thermal drift and the resonance frequency change, atomically resolved AFM imaging in constant-height is possible, albeit challenging, during UV irradiation. The intensity of the UV light is limited by the power of the UV diode, nominally rated for 1 W, but the solid angle between the diode and the sample, combined with the focusing of the light, amounts to roughly 0.1 W of UV light irradiating the sample. Before performing UV experiments on a cleaved $SrTiO_3(001)$ sample, the outer and inner cryostats were irradiated with UV light for 30 min, to ensure that the molecular species physisorbed on the cryostat walls photo-desorb prior to the insertion of a freshly-cleaved sample.

The effect of UV light on a cleaved surface was quantified by performing Kelvin parabolas (Section 1.5.7) and observing their shifts during UV irradiation. Kelvin parabolas are sensitive to long-range electrostatic forces acting between a sample and a tip; *i.e.*, they are used to measure the vacuum level mismatch between of the two, which corresponds to the bias value at which a Kelvin parabola has a maximum. A shift of the top of the Kelvin parabola indicates that the vacuum level of a tip or a sample has altered. The tips used in these experiments were coated by Cu during prior preparation on a Cu(110) single crystal surface, and additionally functionalized by an O atom. UV light does not induce changes to the electronic states of the metallic AFM tip, and the shifts in the maximum of Kelvin parabolas originate solely from the change in the electronic structure of the irradiated surface. STM/AFM measurements acquired during or after UV irradiation were performed by subjecting the AFM tip to negative tip-sample bias $V_T < 0$ while the sample was kept grounded, to repel any stray or photo-emitted electrons from the AFM tip. For this reason, STM/AFM images presented in this

Die approbierte gedruckte Originalversion dieser Dissertation ist an der TU Wien Bibliothek verfügbar.
The approved original version of this doctoral thesis is available in print at TU Wien Bibliothek.
TU Bibliothek Your knowledge hub WIEN

Section were obtained with an opposite bias polarity compared to other images in this Thesis – in STM images obtained with a negative tip bias (V_T=−3 V for example), electrons tunneled from the Fermi level of the tip into the empty states of a sample.

Figure 95 shows the effect of UV light on a cleaved $SrTiO_3$(001) surface at LN_2 temperature. Kelvin parabolas in Fig. 95a were obtained over each termination separately before, during, and after UV irradiation. LCPD values (the bias voltage that corresponds to the top of the Kelvin parabola) over the two terminations are very close to each other before the UV irradiation: 0.91 V over the SrO termination and 0.88 V over the TiO_2 termination. This difference is smaller than expected, since the largest observed LCPD difference between these the two terminations is in the order of 0.2 V. Such small difference could be due to the particular AFM tip used, or the tip-induced band bending at the relatively close distance from the surface where these Kelvin parabolas were performed. In either case, the effect of the UV light was clearly observed on both terminations. The SrO termination experiences a drastic change in electronic structure during UV irradiation. Its LCPD value shifts to 1.81 V, almost double the value of the LCPD prior to irradiation. After the UV light is turned off, the LCPD value shifts slightly towards the original value. by ≈100 meV. The lifetime of this excited surface at the LCPD value of 1.72 V is very long; it lasts for days. The most efficient way of returning the SrO termination to the original electronic structure is injection of electrons using empty-states STM, after which the LCPD value moves significantly towards its original value, and stays at 1.03 V for a very long time; it was not investigated whether it will completely return to the original value after sufficient time has passed. UV irradiation causes no changes to the electronic structure of the TiO_2 termination – Kelvin parabolas shown in the right panel of Fig. 95a are the same prior, during and after UV irradiation. This is not surprising since the TiO_2 termination is metallic (STS seen in Fig. 62), and therefore cannot accumulate either positive or negative charge. All excess free charge carriers are dispersed on the TiO_2 termination, since the Fermi level is located within the conduction band.

The effect of UV irradiation can also be observed in real space using STM/AFM, shown in Fig. 95b for the LN_2 sample temperature. Only the SrO termination is shown because the TiO_2 termination is unaffected by the UV light. The leftmost panel (first panel) in Fig. 95b is an empty-states STM image before UV irradiation, characterized by the 0.91 V LCPD value, while the second panel shows a constant-frequency-shift AFM image of the surface after irradiation with UV light. The morphology of the surface does not change during UV irradiation (same terraces and terrace steps), but the surface is characterized by an altered LCPD value of 1.72 V. Following this image, constant-height empty-states STM was performed with V_T=−1.7 V in the 20×20 nm^2 square marked with red outline and labeled as "1", *i.e.*, electrons were tunneled into this surface area; the tunneling current during this scan was as large as 2.5 nA. The effect of this experiment can be seen in a constant-frequency-shift AFM image in the third panel of Fig. 95b. While the majority of the surface remained in an altered electronic configuration induced by the UV light and characterized with the 1.81 V LCPD value, the square area where the electrons were injected was characterized by a LCPD value close to the original one. In other words, the entire surface remained charged by the UV light, while the noticeable square region was returned close to the original electronic configuration, prior to UV irradiation. The square surface region where the electrons were injected is clearly visible in this constant-frequency-shift AFM image. This feature does not correspond to any geometric changes at this particular area. Instead, different electrostatic forces that originate from different vacuum level alignment (LCPD) between the tip and these surface regions of the sample are responsible for the clear contrast in the constant-frequency-shift AFM images. Finally, the entire 200×200 nm^2 surface area marked by a blue square and labeled as "2" was scanned with constant-current empty-states STM image using V_T=−3.3 V and a tunneling current set-point of I_t=15 pA. The LCPD value over this entire region returned close to the original value, *i.e.*, the entire surface region was discharged by electron injection. This is also evident in the constant-frequency-shift AFM in the rightmost panel of Fig. 95b that does not show the previously-observed square labeled as "1", because the entire surface area marked as "2" shares the same discharged electronic configuration.

Experiments shown in Fig. 95b indicate that UV light depletes the SrO termination of electrons, *i.e.*, dopes it with with holes: UV-induced charging can be counteracted electron injection into the surface, after which the LCPD is restored close to the original value. Hole doping during UV irradiation brings the conduction band minimum and the vacuum level of the SrO termination closer to the Fermi level, *i.e.*, it either reduces the upward band bending or increases the downward band bending. This in turn yields a higher potential difference between the vacuum level of the tip and the SrO termination, and the recorded LCPD values over a hole-doped SrO termination are larger compared to the LCPD values in its ground state.

The same UV-induced charging events occur at the SrO termination cooled to LHe temperatures as well, while the TiO_2 termination remains unaffected by the UV light, as quantified with Kelvin parabolas in Fig. 96a. The series of experiments at the two cryogenic temperatures in Figs. 95 and 96 were performed on the same

Die approbierte gedruckte Originalversion dieser Dissertation ist an der TU Wien Bibliothek verfügbar.
The approved original version of this doctoral thesis is available in print at TU Wien Bibliothek.
TU Bibliothek Your knowledge hub WIEN

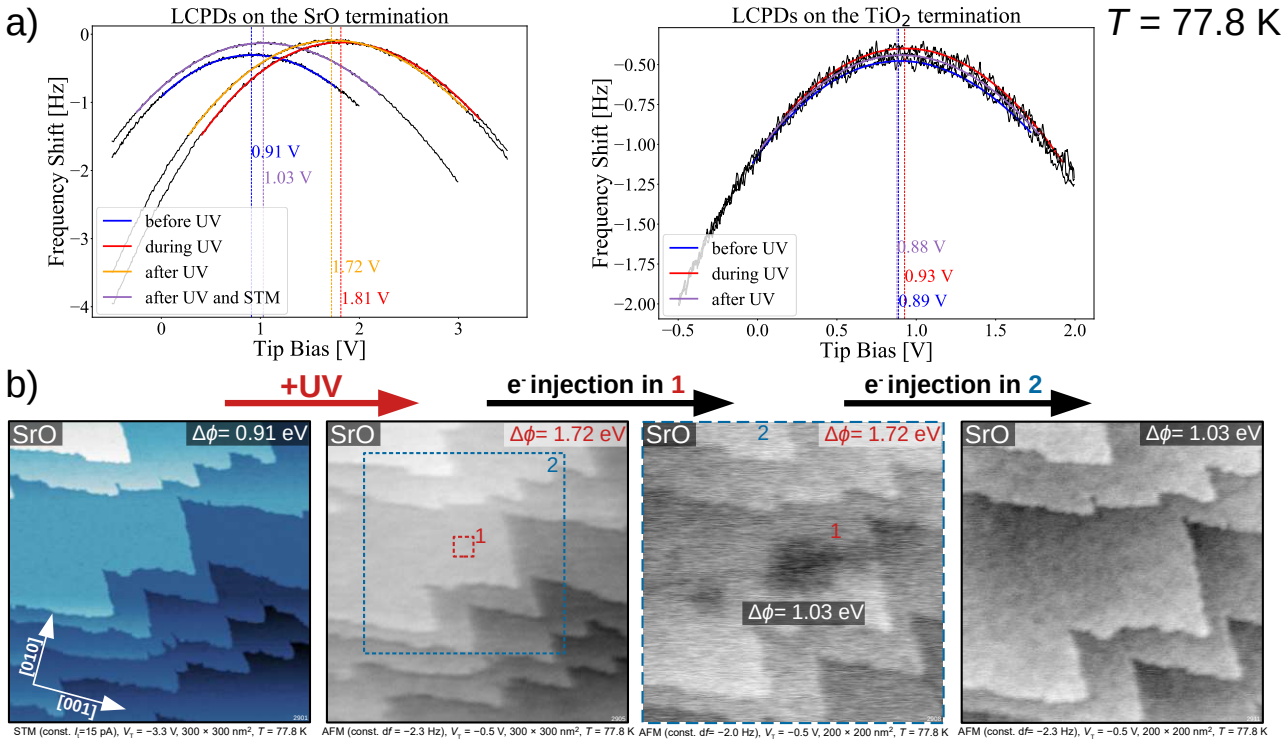

Figure 95: **The effect of UV irradiation on a clean, cleaved $SrTiO_3$(001) surface at LN_2 temperature.** a) Kelvin parabolas obtained on the SrO- (left panel) and TiO_2-terminated (right panel) before, during, and after irradiation with UV light. The SrO termination is additionally characterized by a Kelvin parabola obtained after performing empty-states STM (injecting electrons) on the surface that was irradiated with UV. b) Series of subsequent large-area empty-states STM (blue-while color scheme) and large-area constant-frequency-shift AFM (greyscale) images visualizing the effect of UV irradiation and electron injection *via* STM. The arrows and the corresponding text indicate the actions that were performed between the respective images. The LCPD values of each imaged surface, marked as $\Delta\Phi$ values, are indicative of the electronic structure of the SrO termination – white values correspond to the ground or discharged state, while the red values correspond to the charged surface.

cleaved $SrTiO_3$(001) surface, with the same AFM tip termination over the span of several days: the sample was first studied at LN_2, and subsequently cooled together with the entire measurement head to LHe temperature without removing the sample. For this reason, LCPD values obtained at two different temperatures in Figs. 95 and 96 are comparable in absolute values, provided that the AFM tip apex did not spontaneously rearrange or change its chemical composition due to cooling. At the starting point of the experiments in Fig. 96a, SrO and TiO_2 terminations are characterized by significantly different LCPD values ($\approx$1.4 V) compared to the LN_2 temperature ($\approx$0.9 V). Neither the work function of the sample nor of the AFM tip should significantly vary with temperature [421] in their respective ground states. However, the surface studied in Fig. 96 was obtained by cooling down the previously UV-irradiated $SrTiO_3$ surface (in Fig. 95), that remains in the charged state for a very long time. There is a possibility that cooling a charged surface (and sub-surface bulk regions) induces some additional structural or electronic changes that are detected as an altered LCPD value, but this remains to be investigated.

When the SrO termination at LHe temperature was irradiated with UV light, its LCPD value shifted to very similar values as those observed at LN_2 temperature, as can be seen in Fig. 96a. During UV irradiation the LCPD shifts to 1.88 V and after the irradiation it drops and relaxes at $\approx$1.8 V. This hole-doped SrO termination remains in the charged state for long periods of time, and is efficiently discharged only by empty-states STM after which the LCPD drops to 1.55 V. Discharging by electron injection is again highly confined, which is clearly observed in Fig. 96b. The same $150\times150\,nm^2$ surface region was imaged with STM and constant-frequency-shift AFM before (leftmost panel in Fig. 96b) and after the UV irradiation (second panel in Fig. 96b), respectively:

Die approbierte gedruckte Originalversion dieser Dissertation ist an der TU Wien Bibliothek verfügbar.
The approved original version of this doctoral thesis is available in print at TU Wien Bibliothek.
TU WIEN Bibliothek Your knowledge hub

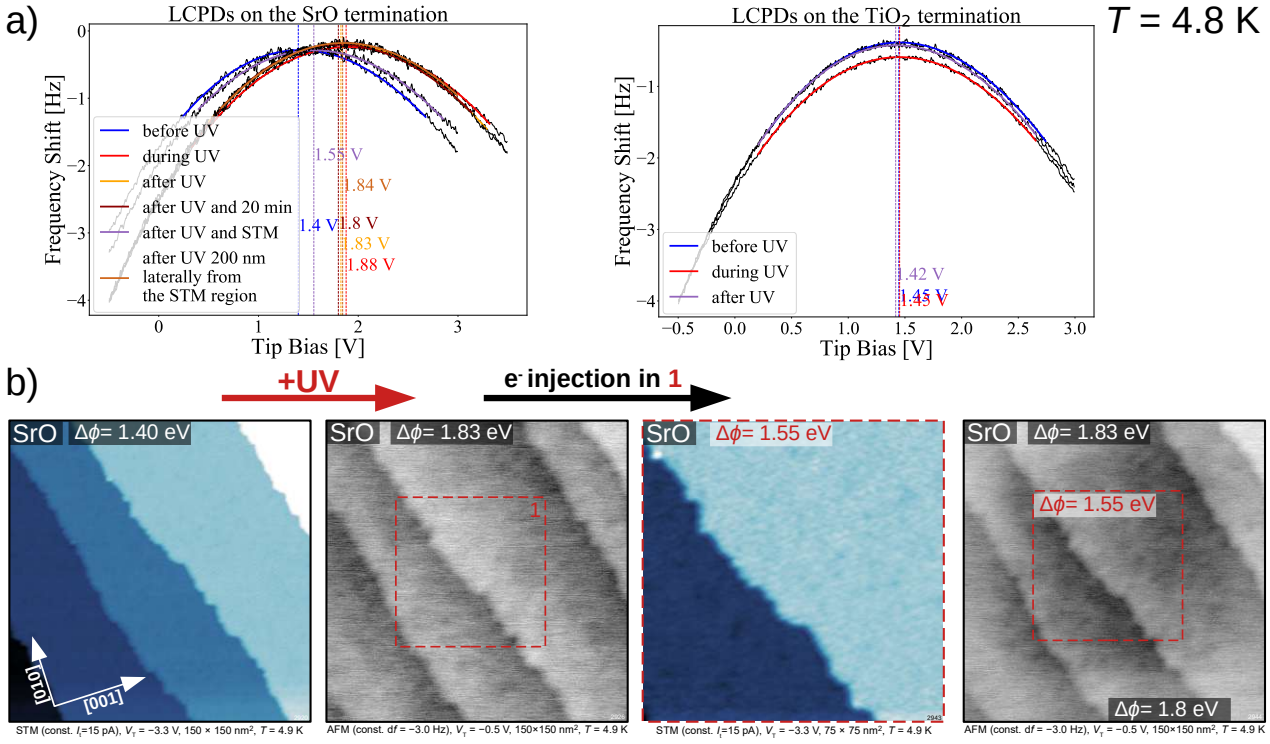

Figure 96: **The effect of UV irradiation on a clean, cleaved $SrTiO_3$(001) surface at LHe temperature.** a) Kelvin parabolas obtained on the SrO- (left panel) and TiO_2-terminated (right panel) before, during, and after irradiation with UV light. The SrO termination is additionally characterized by a Kelvin parabola obtained after performing empty-states STM (injecting electrons) on the surface that was irradiated with UV. b) Series of subsequent large-area empty-states STM (blue-while color scheme) and large-area constant-frequency-shift AFM (greyscale) images visualizing the effect of UV irradiation and electron injection *via* STM. The arrows and the corresponding text indicate the actions that were performed between the respective images; between the rightmost two panels no action was performed. The LCPD values of each imaged surface, marked as $\Delta\Phi$ values, are indicative of the electronic structure of the SrO termination – white values correspond to the ground or discharged state, while the red values correspond to the charged surface.

both show the same surface morphology, but the constant-frequency-shift AFM image was obtained on a charged surface, indicated by the LCPD value of 1.83 V. A part of the charged surface was subsequently discharged by injecting electrons in a $75\times75\,\mathrm{nm}^2$ surface patch *via* empty-states STM using $V_\mathrm{T}=-3.3\,\mathrm{V}$ and the tunneling current set-point of $I_\mathrm{t}=15\,\mathrm{pA}$, shown in the third panel in Fig. 96b. The effect of this discharging is seen in the constant-frequency-shift AFM image in the rightmost panel of Fig. 96b, as an appearance of a square with a clearly distinct contrast compared to the rest of the surface. Just as in Fig. 95b, this contrast does not correspond to any geometric rearrangements on the surface, and instead originates from the difference in LCPD values of the entire surface that remains charged (LCPD=1.83 V), and the discharged square region (LCPD=1.55 V) where the hole-doping was canceled out by injecting electrons *via* STM. The confinement of injected electrons in an otherwise hole-doped SrO surface following the UV irradiation is highly local at both, LHe temperature (fourth panel of Fig. 96b) and the LN_2 temperature (third panel in Fig. 95b). At either temperature, the square region with discharged electronic structure is well-defined with clear edges that easily span over the terrace steps, but the electron confinement is stronger at LHe temperatures — this is consistent with the higher kinetic barrier for hopping of the trapped charges between neighboring lattice sites at lower temperatures.

Figure 97 reports on the exceptionally long lifetime of trapped positive charge carriers (holes) on the SrO termination following the UV light irradiation. The measurements shown in Fig. 97a correspond to the experiments performed in Fig. 95 at LN_2 temperature, while the measurements at LHe in Fig. 97b were performed independently on a different cleavage and using a different UV light source (Hg lamp, strongest UV line at $\lambda = 254\,\mathrm{nm}$). Sets of LCPD values over each termination that were taken at approximately the same time,

Die approbierte gedruckte Originalversion dieser Dissertation ist an der TU Wien Bibliothek verfügbar.
The approved original version of this doctoral thesis is available in print at TU Wien Bibliothek.
TU Bibliothek Your knowledge hub WIEN

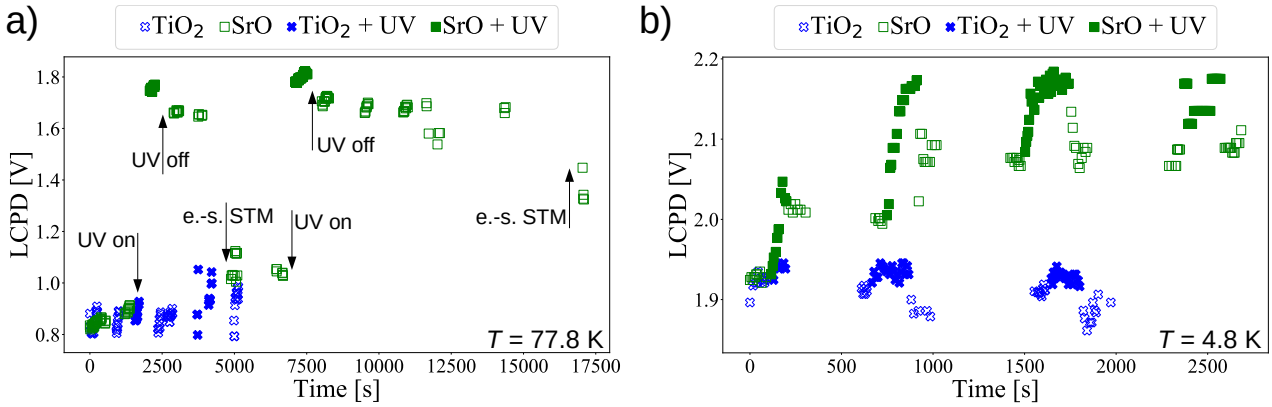

Figure 97: **Time evolution of the LCPD values over both terminations on a cleaved $SrTiO_3$(001) surface during UV irradiation experiments.** The lifetime of the accumulated holes on the SrO termination is long at both a) LN_2 and b) LHe sample temperature; the TiO_2 termination is unaffected at either temperature. The legend above the graphs distinguishes between LCPD values measured while the UV irradiation is turned either on or off, while the downwards arrows indicate when empty-states STM (electron injection) was performed; the arrows and the text correspond to events occurring only on the SrO termination, because the TiO_2 is not altered by either the UV light or the electron injection *via* STM.

with a 1 s difference. Slight differences (noticeable as "columns" of values) are due to the height dependence of the LCPDs with respect to the surface. When LCPD values are compared before/during/after UV irradiation (in Figs. 95 and 96), values that were obtained at the same distance from the surface are reported, which are therefore directly comparable. At LN_2 temperature, the SrO termination remains charged following the UV irradiation for at least 2 h, as can be seen by comparing the LCPD values from the 7500 s to the 15000 s mark in Fig. 97a. Such long lifetime indicates a high potential barrier for hopping and dissipation of the trapped charges into the bulk even at LN_2 temperature.

The speed and the effectiveness of charging of the SrO termination by UV light was investigated in a separate experiment (unrelated to Fig. 96) shown in Fig. 97b, at LHe temperature and using a Hg UV light source. The charging behavior is the same as observed after an extended UV exposure, namely the LCPD increases during UV light and relaxes to a slightly lower value after the light is turned off, but the short time intervals of the UV irradiation reveal the step-wise charging process on the surface. In the first run of the UV irradiation, that lasted ≈30 s, the SrO termination was only partially charged and the LCPD changed from 1.93 V to 2.02 V with an intermediate maximum value of 2.05 V during the UV irradiation. After 500 s from the first UV exposure, the SrO termination that remained partially charged (LCPD=2.02 V) was additionally charged with a second dose of UV irradiation that lasted ≈50 s, after which the LCPD changed from 2.02 V to 2.09 V, with an intermediate maximum value of 2.16 V during the UV irradiation. Each subsequent UV irradiation run behaves the same as the second one, implying that the surface was already fully charged with the second UV dose. Therefore, the UV-induced charging is not instantaneous and requires at least 1 min of UV exposure to reach the fully charged state with this light source, but it is reasonable to assume that the process would be much faster and more efficient with higher-intensity UV sources.

Figures 98a and 98b focus on discharging the hole-doped SrO termination by highly-local STS measurements at LN_2 and LHe, respectively. The AFM/STM tip was placed above a single point at the surface where bias sweeps were performed from the Fermi level of the sample towards its conduction band. Reported bias values and the DOS in Fig. 98 were inverted in post-processing such that they represent the standard way of reporting the STS spectra when the bias is applied to the sample, even though in these experiments the sample was grounded and the increasingly negative bias was applied to the tip. In Fig. 98a, three random points on the sample that were separated by ≈30 nm, were discharged using STS. Discharging is evident as an appearance of empty states at much lower bias values during the first bias sweep towards the conduction band, while the same states are missing when the sweep is performed in the backward direction, from high bias values towards the Fermi level. In other words, the bottom of the conduction band of the charged SrO termination is closer to the Fermi level on the charged surface compared to the normal surface. These newly appearing empty states are populated by the tunneling electrons, and they are missing in the subsequent bias sweep in the opposite direction, that

Die approbierte gedruckte Originalversion dieser Dissertation ist an der TU Wien Bibliothek verfügbar.
The approved original version of this doctoral thesis is available in print at TU Wien Bibliothek.
TU Bibliothek Your knowledge hub WIEN

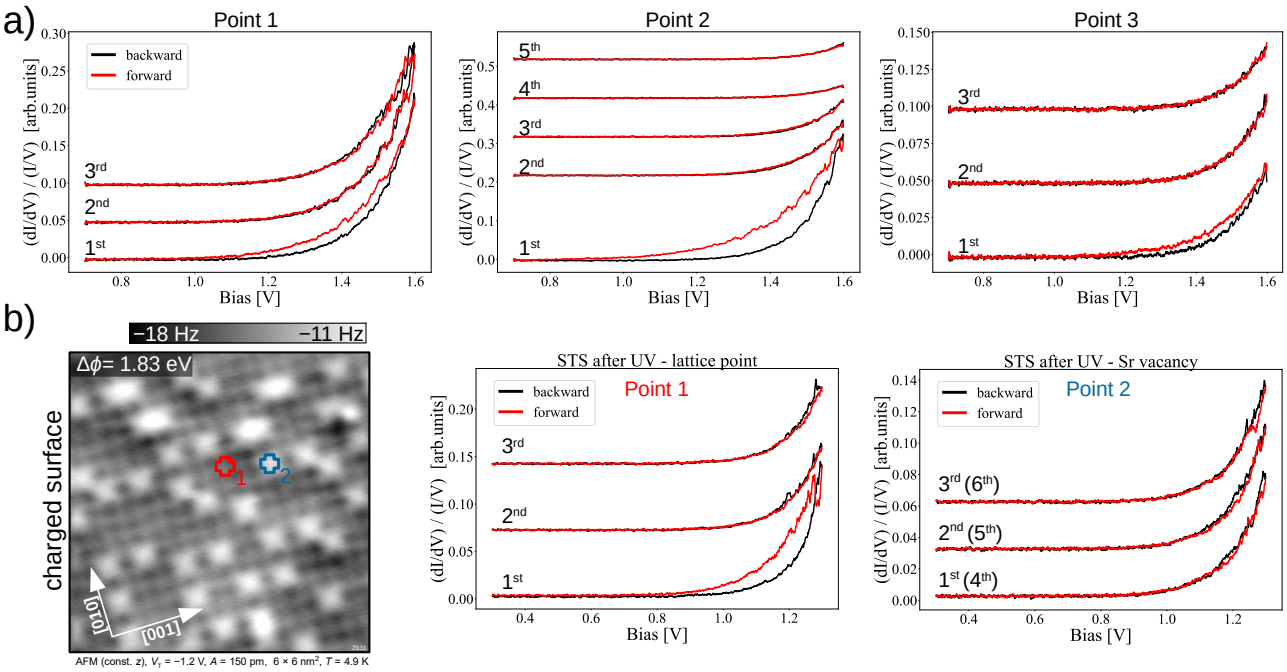

Figure 98: **Discharging the hole-doped SrO *via* STS on the UV-irradiated, cleaved $SrTiO_3$(001) surface.** a) STS performed in three different points at the surface (three panels) from the Fermi level of the sample towards its conduction band, at the LN_2 sample temperature. The three spatial points were selected at random, and they are ≈30 nm distant from each other. At each point, the surface is discharged by injecting electrons during the bias sweep, which is seen as the onset of the conduction band at much lower bias in the forward scan (from the Fermi level upwards) compared to the backward scan (from the conduction band towards the Fermi level). Only the first bias sweep in each point shows the discharging process, while each subsequent sweep shows the STS spectra identical to a normal surface (Fig. 61). b) STS performed on an atomically resolved AFM image obtained on the charged SrO termination (shown in the left panel), at the LHe sample temperature. STS spectra obtained above a lattice point, marked by red "1" in the AFM image, are shown in the central panel, and display discharging in the first bias sweep, and no discharging in the subsequent ones. STS spectra obtained on a nearby V_{Sr}, marked by blue "2" in the AFM image, show no discharging at all, most probably because the surface region in the vicinity was previously discharged during a bias sweep over the nearby lattice point (red "1"). In both (a) and (b), the reported bias values (x-axis) were post-processed such that they correspond to a typical STS spectra when the sample is biased and the tip is grounded, even though in these experiments the tip was biased and progressively higher negative tip bias values were applied to obtained the STS spectra; in the same manner the tunneling current was inverted in post-processing, *i.e.*, in reality the current was negative due to electrons flowing from the tip to the sample.

shows the same conduction band offset from the Fermi level as the normal surface (Fig. 61). At each of the three points two additional bias sweeps were performed, both of which showed that the onset of the conduction band has been permanently moved to the position it was prior to the UV irradiation. This discharging by the first bias sweep is highly local, and the STS spectra performed at three distinct spots (≈ 30 nm apart) on the surface all show the same behavior; the difference in the absolute values of the available DOS at each point are a bit different due to the different tip-sample distances used, which result in different magnitudes of the tunneling current.

An atomically resolved image of the charged SrO termination following the UV irradiation at LHe is seen in Fig. 98b. There are no discernible differences in the atomic arrangement of the charged surface compared to all other images of the SrO termination in this Thesis, with the exception of different electrostatic forces and different LCPD values of the charged surface. Discharging with STS was performed on this surface region, first above a random lattice point (marked as "1" in the AFM image), and afterwards above the nearby V_{Sr}. The very first STS performed above a random lattice point (middle panel in Fig. 98b) shows the hysteresis in the STS during the bias sweep from and towards the Fermi level. The conduction band of the charged surface is therefore

Die approbierte gedruckte Originalversion dieser Dissertation ist an der TU Wien Bibliothek verfügbar.
The approved original version of this doctoral thesis is available in print at TU Wien Bibliothek.
TU Bibliothek Your knowledge hub WIEN

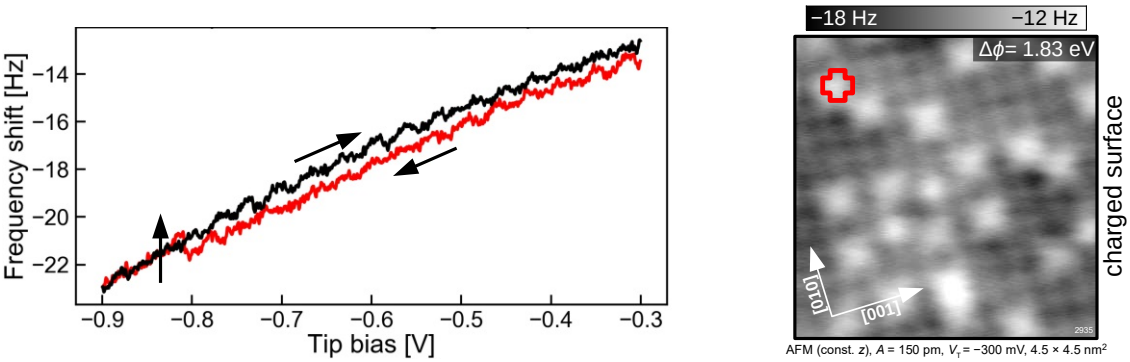

Figure 99: **Annihilation of a small number of positive charged** *via* **STS on the UV-irradiated, cleaved $SrTiO_3$(001) surface at LHe sample temperature.** A piece of the Kelvin parabola shown in the left panel displays a hysteresis in the forward and backward direction, which implies that the surface beneath has slightly changed the charge state during the bias sweep. In this image, the x-axis displays the actual bias values that were applied to the tip. The discharging event occurs at $V_T \approx -0.8\,V$, a value that corresponds to the onset of the conduction band on the charged surface shown in Fig. 98. There was no detectable current flow between the tip and the sample in this experiment. The constant-height AFM image in the right panel shows atomic resolution on the UV-charged SrO termination, and the position where the bias sweep was performed.

moved closer to the Fermi at LHe temperature as well, but this effect can be efficiently counteracted by electron injection during the first bias sweep. Each subsequent bias sweep at the same spot on the surface does not show any new electronic states because the surface was already discharged by the first STS measurement. When the same procedure is performed on the nearby site (rightmost panel in Fig. 98b) that was chosen such that it corresponds to a V_{Sr}, discharging does not occur even in the first bias sweep because the nearby surface was already discharged by the first STS run in the middle panel in Fig. 98b. Therefore, the highly local discharging by in Fig. 98b is not limited to a single atomic site, but rather spans a few unit cells — this is not surprising as the number of injected electrons in the first STS run above a nearby lattice point was in the order of $10^9\,e^-/s$.

Although not perfectly localized at a single surface site, the observable discharging by electron injection is very confined and does not laterally span the surface. Experiments suggest that tunneling $\approx 10^9$ electrons into a point on a hole-doped SrO termination discharges a surface area measuring $\approx 2.5 \times 2.5\,nm^2$. A discharging event is not a resonant process, so it proceeds with a probability much lower than 1. Nevertheless, even if a small fraction of the 10^9 injected electrons are efficient in annihilating accumulated holes, the magnitude of discharging currents indicate that the discharging proceeds along the [001] direction throughout the bulk, and that the trapped positive charges are potentially contained within the bulk regions beyond the subsurface layers following the UV irradiation.

In order to discharge a limited, small number of accumulated holes on the UV-irradiated SrO termination, a significantly smaller number of e^- than in Figs. 95–98 needs to be injected. The STM setup in the chamber used allows detecting currents as low as 1 fA, *i.e.*, a flow of $10^4 e^-/s$. This implies that discharging less than 10^4 holes on the charged surface requires the application of a bias field at further distances from the sample, such that the current flow is undetectable. This was carefully performed over a single site on the surface in the experiment shown in Fig. 99. The atomically resolved constant-height AFM image in the right panel of Fig. 99 shows the atomic arrangement on a charged surface, and a point where a single bias sweep was performed, marked by a red cross. During the increase of the tip bias in the negative direction (red curve), from the Fermi level of the sample to its conduction band, there is a discharging event at $V_T \approx -0.8\,V$, after which the frequency shift curve switches to a new Kelvin parabola. When the bias is swept in the opposite direction (black curve) there are no discharging events and the entire surface is characterized by a new Kelvin parabola as a consequence of highly local discharging. The conduction band onset of a charged SrO termination is $\approx 0.8\,eV$ above the Fermi level, and the experiment in Fig. 99 confirms that even a small number of injected electrons are able to partially discharge the surface, but only after the bias reaches this conduction band minimum. The AFM image in the right panel of Fig. 99 was obtained prior to the bias sweep in the left panel of Fig. 99, with a tip bias value of $V_T = -0.3\,V$, but the surface was not discharged during this scan because the applied bias was insufficient to ensure electron tunneling into the conduction band minimum of a charged surface.

Die approbierte gedruckte Originalversion dieser Dissertation ist an der TU Wien Bibliothek verfügbar.
The approved original version of this doctoral thesis is available in print at TU Wien Bibliothek.
TU Bibliothek Your knowledge hub WIEN

Figure 99 demonstrates a discharge of a small number ($<10^4$) of positive charges trapped on the hole-doped SrO termination. The experiment reports on a precise control over individual positive charge carriers at the surface. The trapped charges are highly localized and can be discharged in a well-defined surface area, which are general properties of charges trapped in the form of small polarons. Considering these trapped positive charges as individual hole polarons at O $2p$ orbitals, the experiment in Fig. 99 might have shown the first experimental evidence of individual hole polarons previously only predicted by theory in $SrTiO_3$ [422, 423, 424] and other perovskites [425, 426, 427, 428].

In conclusion, the research presented in this Section demonstrates that the cleaved $SrTiO_3(001)$ surface can separate excess charge. Namely, the SrO termination accumulates positive charge after the UV-irradiation, that can be controllably removed by electron injection *via* empty-states STM, while the metallic TiO_2 termination is unaffected. The accumulation of positive charge influences the conduction band minimum of the SrO termination and affects the intrinsic band bending. The lifetime of the trapped positive charges is exceptionally long following the UV exposure, in the order of a single or multiple days at both the LHe and LN_2 sample temperature. Charging and discharging of the surface occurs preferentially in the direction perpendicular to the surface (inside the bulk below), rather than spanning laterally along the surface. Controllable discharging of the surface can be highly local. The mechanism behind trapping of the positive charge remains to be investigated, but could indicate the presence of long sought-for hole polarons.

Die approbierte gedruckte Originalversion dieser Dissertation ist an der TU Wien Bibliothek verfügbar.
The approved original version of this doctoral thesis is available in print at TU Wien Bibliothek.
TU Bibliothek Your knowledge hub WIEN

3.7 Controlled charge removal from the SrO termination

Understanding the influence of injecting or removing charge, and the application of electric fields on the $SrTiO_3$(001) surface, is of fundamental interest since this material is a promising candidate for all-oxide electronics. In Section 3.6, it was revealed that the introduction of free electron-hole pairs by irradiating a cleaved $SrTiO_3$ surface with UV light charges the SrO termination with positive charges, while the TiO_2 termination remains metallic and naturally does not accumulate any charge. In this Section, one type of charge carriers (either electrons or holes) was controllably injected into the bulk-terminated $SrTiO_3$(001) surface, to reveal whether this surface has a preference for either, and whether any charge accumulation can occur under reasonable conditions. The metallic TiO_2 termination was found to be unaffected by charge removal/injection. The semiconducting SrO termination allows certain manipulations, but the effect of charge removal/injection is not the same as in the case of UV-induced hole doping, since additional ionic effects likely occur.

Tunneling electrons from the AFM/STM tip into the empty-states in the conduction band of the SrO termination on a cleaved $SrTiO_3$ surface has been found throughout this Thesis to not affect its electronic states and structure, except in the case on cleaved surfaces without Nb doping (Fig. 94). Most STM images were performed first to reveal the surface morphology, and subsequent atomically resolved AFM images were obtained in the empty-state STM mode, where sample was sufficiently positively biased such that the electrons can be continuously injected from the filled states of the metallic tips to the empty states of the SrO termination. In this sense, the SrO termination behaves as most other n-type doped semiconductors: it conducts electrons that are injected into its empty conduction band, and the accumulation of electrons at the surface does not occur. On the other hand, previous UV experiments (Section 3.6) indicated that the SrO termination is susceptible to simultaneously accumulating negative charges at the entire SrO-terminated surface area spontaneously. To controllably and locally investigate this proclivity to hole-accumulation, electrons were tunneled away from the top of the valence band of the SrO termination towards the metallic tip, as demonstrated in Figs. 100 and 101.

Figure 100 shows a sequence of AFM/STM images that illustrate the pathway of the performed experiments. The experiment starts with scanning the surface with constant-current empty-states STM to ascertain its large-area morphology, which is subsequently imaged with small-area constant-height-AFM. There are no peculiar electronic states in the STM image, and the AFM image does not show any protruding defects. At a single point on the SrO termination (marked by a red cross in the second panel of Fig. 100), at least 10^{10} electrons were tunneled away from the top of the SrO valence band towards the empty-states of the tip. The same region was subsequently scanned with constant-height AFM (third panel in Fig. 100) at approximately the same tip-sample distance as the AFM image prior to electron removal (second panel), to reveal that $\approx 8 \times 5\,\mathrm{nm}^2$ surface patch surrounding the point of electron removal appears darker than the remaining surface. Approaching this dark region (marked by a red broken rectangle in the third panel) enables obtaining a clear atomically resolved AFM image (fourth panel in Fig. 100) — this surface patch appears like any (1×1) SrO surface patch at the atomic scale, with the exception of a dark pattern superimposed on an atomically resolved signal. This particular contrast is not likely to originate from geometric alternations of the surface, that would imply upwards buckling in this region that would cause higher tip-sample attractive forces. Instead, it is likely to originate from the altered electronic states in this particular region compared to the rest of the surface, and therefore from increased tip-sample electrostatic forces due to a different LCPD mismatch between the tip and the sample in this region. This is confirmed in the simultaneous constant-height empty-states STM image (fifth panel in Fig. 100) that was obtained with drastically lower bias value (V_S=+0.4 V) than usually necessary for tunneling into the conduction band of SrO. A strong tunneling current signal only in the vicinity of the point from which electrons were tunneled out of the surface in this constant-height STM image, implying that the SrO conduction band in this surface region is located closer to the Fermi level. This shift in the conduction band minimum is accompanied by the same shift in the vacuum level at this point at the surface, making the LCPD locally different, and accounting for the dark contrast in the constant-height AFM images. Finally, the same surface region was imaged on a larger surface area with empty-states constant-tunneling-current STM at two different sample bias values (sixth and seventh panel in Fig. 100). Both images show a large protruding defect at the point where electrons were removed from the surface, albeit they appear differently sized depending on the applied sample bias during STM imaging. At larger bias value, the defect appears as a $\approx 9 \times 9$ central bright spot surrounded by $\approx 30 \times 30$ faint halo, while at lower bias value the central point appears smaller and the faint hallo is imaged as a large bright island. Due to the atomically resolved AFM imaging in this region (third and fourth panel in Fig. 100) that shows nothing peculiar, it is clear that this large feature in STM images is just a local electronic defect. It appears as a protrusion in STM because the conduction band is closer to the Fermi level at this point on the surface compared to the entire SrO-termination; the constant-current STM feedback moves away from

Die approbierte gedruckte Originalversion dieser Dissertation ist an der TU Wien Bibliothek verfügbar.
The approved original version of this doctoral thesis is available in print at TU Wien Bibliothek.
TU Bibliothek Your knowledge hub WIEN

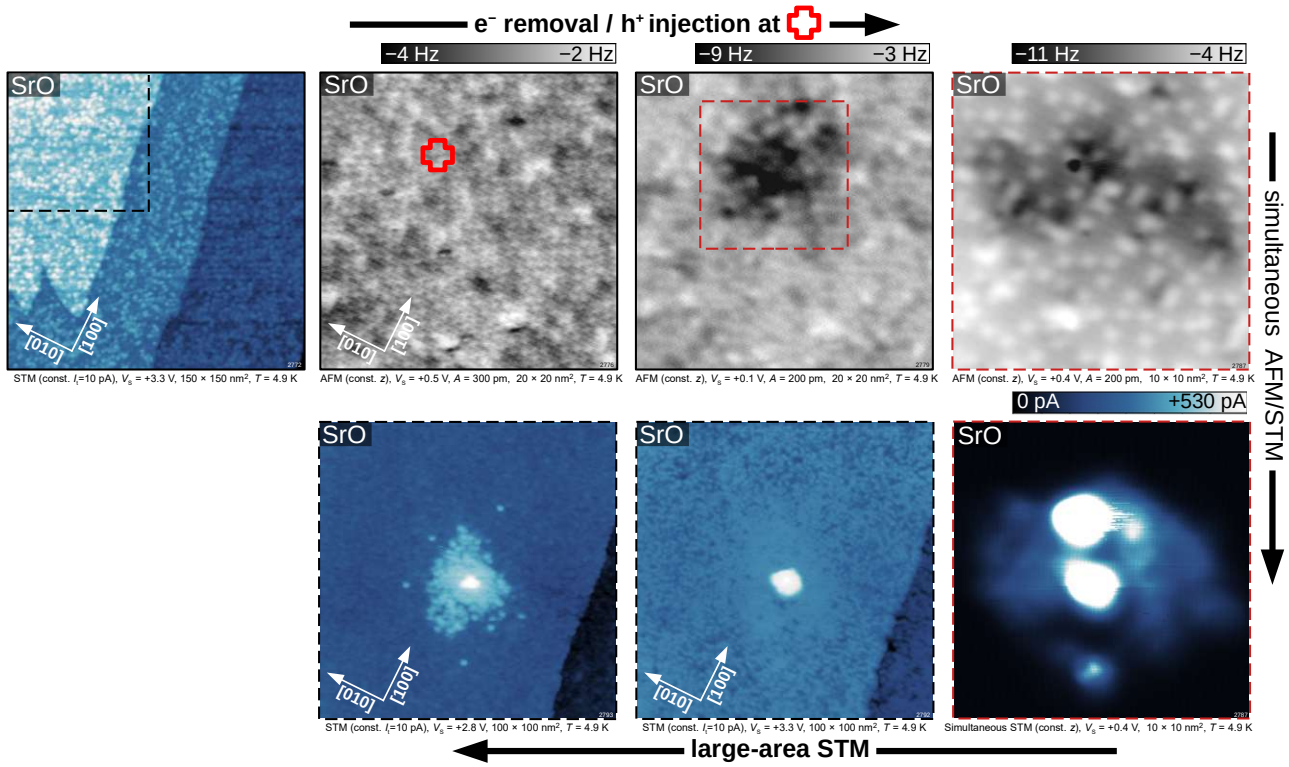

Figure 100: **Tunneling electrons from the top of the valence band on the SrO termination of the bulk-terminated $SrTiO_3$(001).** The experiment progresses left-to-right in the top row, and right-to-left in the bottom row, *i.e.*, the top left image is the starting point and the bottom left image is the final image of the experiment. Overview STM image (first panel) and a constant-height AFM image (second panel) show the surface prior to electron extraction by biasing the sample with $V_S = -5\,\mathrm{V}$ for the duration of 1 min, while the tunneling current exceeded 2 nA throughout this time interval. This region was subsequently scanned with constant-height AFM image (third panel), simultaneous atomically resolved AFM and STM (fourth and fifth panel), and large-area empty-states STM images at two different sample bias values (sixth and seventh panel). More details are given in the text.

this surface area because tunneling to empty-states at a fixed sample bias value is more efficient there compared to the surroundings.

According to the result in Fig. 100, removing electrons from a single point on the SrO termination creates a large electronic defect with the conduction band shifted closer to the Fermi level. The effect is most significant immediately at the point of electron extraction, but also spans laterally 15 nm away from the central point with a slightly lower intensity. Careful inspection of the atomically resolved AFM image (fourth panel in Fig. 100) reveals a presence of three or four dark spots that appeared in the affected region, which most probably dropped from the tip during high-current-density tunneling at the point marked by a red cross in the second panel in Fig. 100. It is unlikely however, that these few impurities can be responsible for an effect of such magnitude.

Since electrons were removed from the surface during experiments shown in Fig. 100, the observed effect is likely due to positive ionization of the subsurface atoms. This ionization can occur in the form of small hole-polarons for example, *i.e.*, through creation of subsurface sites with fewer electrons in their valence orbitals. Due to small thermal hopping probability at LHe temperatures, these bound positive charges could remain in the vicinity of the point where electron were removed, and their isotropic spread in a circular manner (sixth and seventh panel in Fig. 100) supports this interpretation. The proclivity of a SrO termination to positive charge trapping was already observed in the UV experiments in Section 3.6. However, a large-area defect with accumulated positive charge in Fig. 100 could not be subsequently removed by injecting electrons back to this region like in the UV-induced charging experiments. This implies that an additional effect potentially occurs with the positively charged ions upon electron extraction, which can be responsible for their rearrangement beneath the surface. This migration and rearrangement of positively charged subsurface ions could be additionally

Die approbierte gedruckte Originalversion dieser Dissertation ist an der TU Wien Bibliothek verfügbar.
The approved original version of this doctoral thesis is available in print at TU Wien Bibliothek.
TU Bibliothek Your knowledge hub WIEN

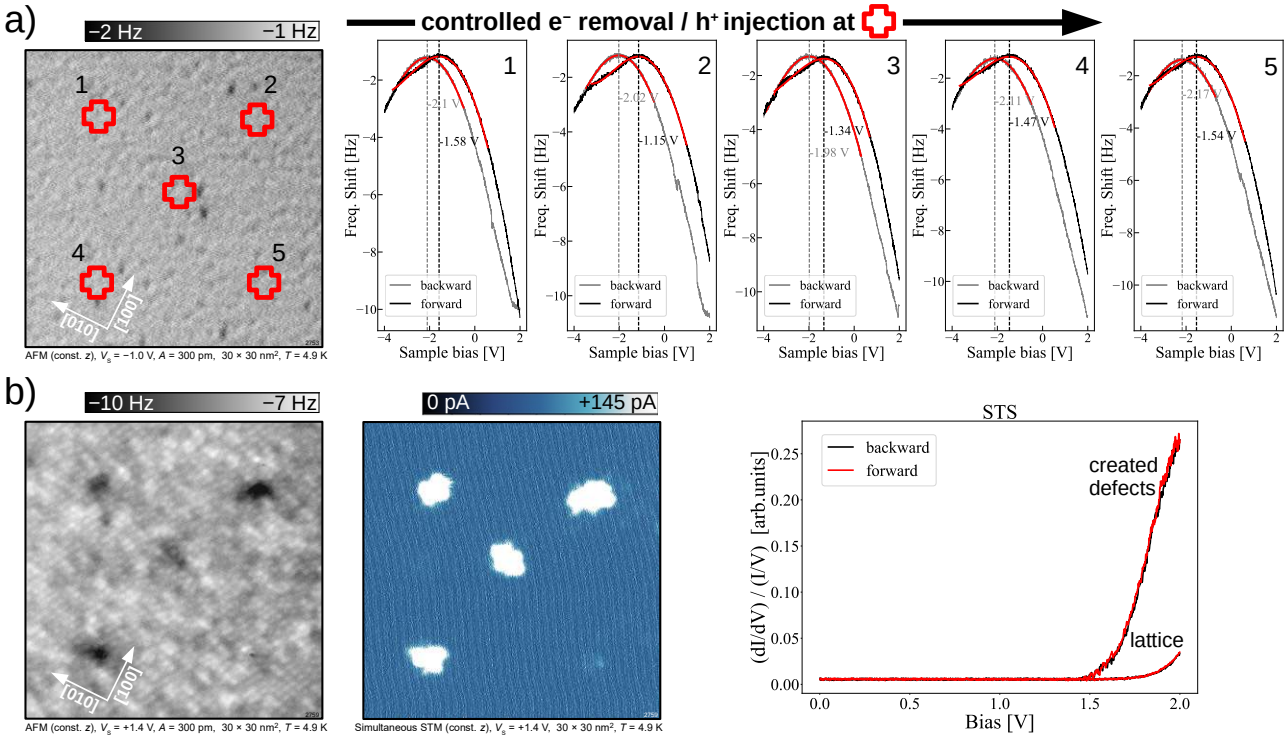

Figure 101: **Negative sample bias sweeps on the SrO termination of the bulk-terminated $SrTiO_3$(001).** a) Constant-height AFM image that shows the surface on which negative sample bias sweeps were performed at five different points, marked by red crosses. Each point is labeled with a number, and the corresponding bias sweeps that are shown in the right are labeled with the respective number. Bias sweeps were performed starting from positive sample bias and down to the negative sample bias, and immediately back to the positive sample bias values; these curves are marked in black and gray, respectively. Maxima of the Kelvin parabolas are explicitly indicated in the corresponding color of the forward/backward sweeps, and red lines indicate the range of values used for fitting a fourth-order polynomial used for determining the top of each parabola. b) Constant-height AFM and simultaneous empty-states STM image after the bias sweeps. The experiment was performed at LHe so the lateral sample drift is negligible and these images correspond to the same surface area as in (a). The panel on the right side compares DOS (measured with STS) above the created defects and the unaffected lattice.

supported by the presence of the positively charged AFM tip that develops a strong electrostatic field towards the sample at negative sample bias values necessary for electron removal from the surface. The shape of the created defect would then be related to the macroscopic shape of the AFM tip apex, which would appear to be almost perfectly circular in the experiments performed in Fig. 100. Such tip shape is certainly possible, especially for freshly prepared tips, but this hypothesis will be further tested in the future by performing the same set of experiments as in Fig. 100 with an arbitrarily shaped tip that can be obtained after deliberately crashing the AFM tip. Another alternative is that the polarization vector is altered in the surface region that corresponds to the created defect, either by removal of charge or the subsequent ion migration. It is noteworthy that ion migration or their rearrangement is not visible in the atomically resolved AFM image in the fourth panel of Fig. 100.

A SrO termination was depleted of electrons in a more controlled way in the experiment shown in Figure 101. The constant-height AFM image in Fig. 101a was taken at large tip-sample distances, and shows the starting point of the experiment; there are only small discernible point defects, and no large protruding defects in this $30 \times 30\,\mathrm{nm}^2$ surface region. At five different points, marked by red crosses, bias sweeps were performed starting from positive sample bias of $V_S = +2\,\mathrm{V}$ towards negative sample bias of $V_S = -4\,\mathrm{V}$ and immediately back, for a total duration of $\approx$20 s. Each bias sweep was performed across the entire band-gap of the semiconducting SrO termination, including the bottom of the conduction band and the top of the valence band. Therefore, tunneling current was detectable only at the two extreme points of each bias sweep: at the positive end $\approx$100 pA

Die approbierte gedruckte Originalversion dieser Dissertation ist an der TU Wien Bibliothek verfügbar.
The approved original version of this doctoral thesis is available in print at TU Wien Bibliothek.
TU Bibliothek Your knowledge hub WIEN

of electrons were tunneled into the surface, while at the negative end ≈2 pA were tunneled out of the surface towards the grounded tip.

Each of the five bias sweeps in Fig. 101a exhibit similar behavior. Initially, each of the five points on the SrO termination is characterized by a LCPD value of ≈ -1.5 V, except point "2" with a LCPD of ≈ -1.2 V. During the sweep towards negative sample bias values, each bias sweep showed a transition from the original Kelvin parabola towards a new Kelvin parabola occurring at $V_S = -3.5$ V. Sweeping the bias backward, from negative to positive sample bias values, did not induce any switches between Kelvin parabolas, and the tip-sample system remained characterized by an altered Kelvin parabola with a new LCPD value of ≈ -2 V. The sample bias at which the switching between Kelvin parabolas occurs, at roughly -3.5 V, coincides with the top of the valence band on the SrO termination: at this bias value the current is undetectable, but as the sample bias is further reduced, a small tunneling current of ≈2 pA becomes measurable.

The effect of the five bias sweeps on the surface is seen in the constant-height AFM image and simultaneous empty-states STM image in Fig. 101b. The two images focus on the same surface area as the one prior to the bias sweeps, and they show that a clear change is observed on four out of five spots where bias sweeps were performed: it remains unclear why the fifth point did not experience the same changes, especially because the bias sweep over this point behaved the same as the remaining four. The AFM image shows the appearance of stronger attractive forces at these points. The appearance of dark, localized contrast in the AFM image is due to the different LCPD value at the points: the AFM image was obtained with $V_S = +1.4$ V, and therefore points with a LCPD value shifted to higher negative values exhibit stronger electrostatic attraction towards the tip. The empty-states STM image, taken with the sample bias insufficient to reach the bottom of the conduction band of a typical SrO-terminated surface, shows significant current signal at the points where bias sweeps were performed (four out of five), implying that the conduction band minimum was shifted closer to the Fermi level after the switch in the Kelvin parabolas during the bias sweeps. This shift was quantified in the STS measurements shown at the right side of Fig. 101b, by comparing the local DOS above the points where bias sweeps were performed and the local DOS above typical lattice points. While a regular lattice point shows the same DOS as commonly observed, with the conduction band onset around ≈ 1.8 eV above the Fermi level, the conduction band onset is shifted by ≈ 0.4 eV closer to the Fermi level at the points where bias sweeps were performed. The inability to reverse the effect of electron depletion in these experiments is also evident in the STS measurements, as there is no hysteresis in the backward and forward scan.

In conclusion, both experiments in Figs. 100 and 101 show that the electronic structure of the SrO termination can be irreversibly changed by depleting the surface from electrons *via* tunneling them to the tip. The magnitude of the effect is proportional to the number of removed electrons, rather than the strength of the applied bias necessary for electron removal. Kelvin parabolas in Fig. 101b show that after a critical negative sample bias value necessary for electron tunneling is reached, the system switches to a new Kelvin parabola and stays in this states throughout the further decrease of the sample bias. Therefore, the magnitude of the observed effect (both the lateral size and the shift of the conduction band towards the Fermi level) is much larger in Fig. 100, where at least three orders of magnitude more electrons were removed from the surface compared to quick experiments in Fig. 101 where the tunneling electron flow lasted for a short period of time only. The inability to annihilate accumulated positive charges by injecting electrons back to the surface suggests that the migration of positively charged ions occurs in the subsurface region, although these effects are not noticeable in the atomically resolved AFM images.

Die approbierte gedruckte Originalversion dieser Dissertation ist an der TU Wien Bibliothek verfügbar.
The approved original version of this doctoral thesis is available in print at TU Wien Bibliothek.
TU Bibliothek Your knowledge hub WIEN

3.8 Peculiar dissipation

This Section records and reports peculiar dissipation signals detected during AFM measurements on some cleaved $SrTiO_3(001)$ surfaces that indicate energy exchange between a tip and a surface. Although similar phenomena were encountered on different systems in literature [429, 430], a consistent interpretation applicable throughout various systems including the results presented below, is still out of reach. The data presented in this Section are insufficient to provide such a general interpretation, and the work on understanding this phenomena is still ongoing.

3.8.1 CO adsorption on the cleaved SrO termination

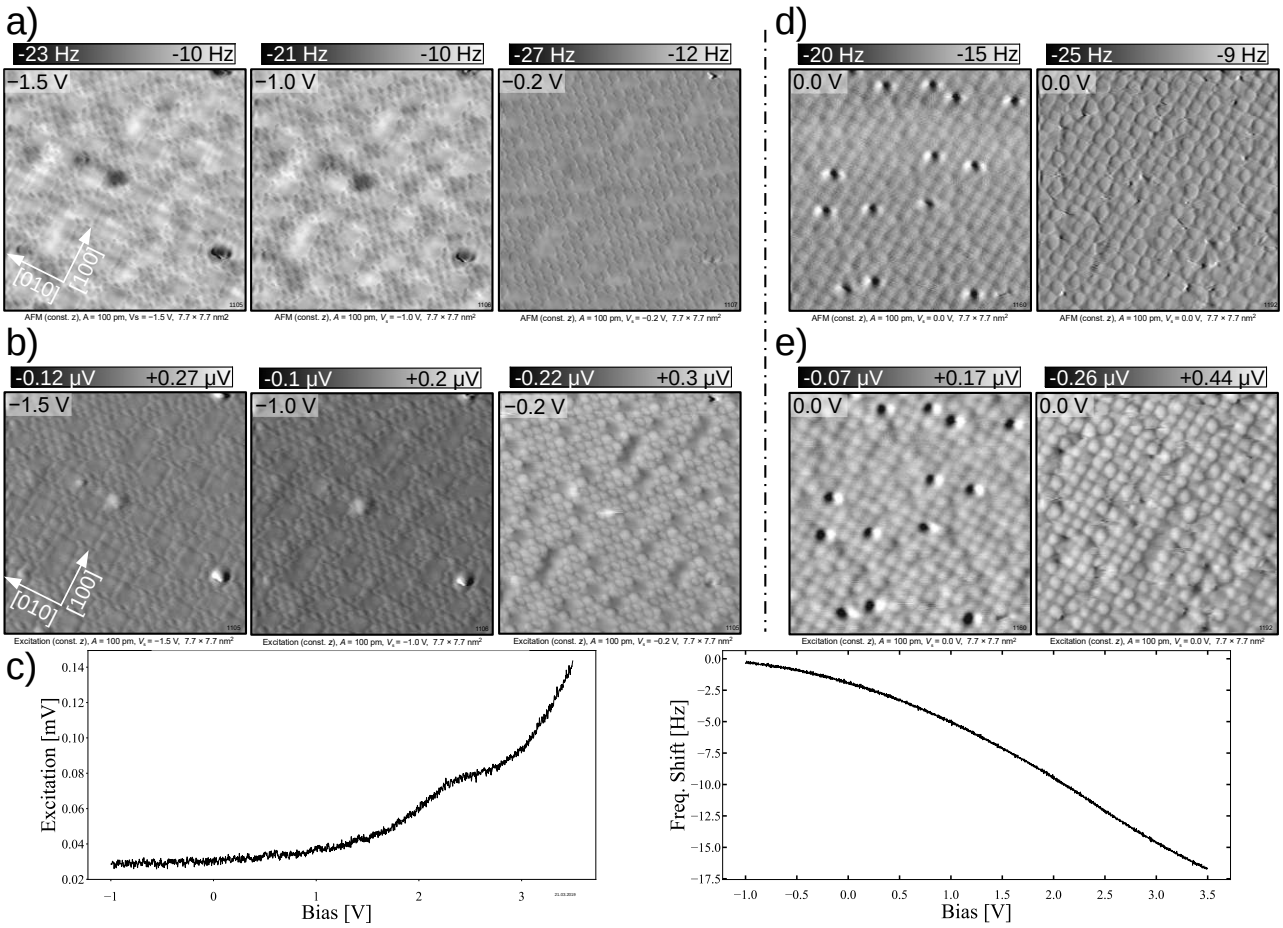

Figure 102: **SrO termination of the cleaved $SrTiO_3(001)$ exposed to 2 L of CO at T< 30 K** a,b) Constant-height AFM images and the simultaneous excitation images, respectively, of a SrO termination with full-coverage of CO, taken at different bias values. c) Recorded excitation curve (left panel) and the simultaneous Kelvin parabola (right panel) during a bias sweep, taken over the surface shown in (a–b) d,e) Constant-height AFM images and their corresponding simultaneous excitation images, respectively, of a SrO termination originally covered by CO and additionally annealed to 130 K for 10 min, taken with a slightly different AFM tip termination.

The adsorption of CO is a promising approach to studying the electronic and quantum mechanic properties of a surface, as demonstrated in Section 2.4. This holds especially true for novel surfaces, such is the cleaved $SrTiO_3(001)$, where CO molecules stand out as one of the first candidates for the adsorption studies. However, as this Section demonstrates, this adsorption phenomenon is significantly more complex than one would expect.

The adsorption of CO to a cleaved $SrTiO_3(001)$ surface was studied at low temperatures because it would be unsurprising for CO to be only physisorbed at the surface. Dosing was performed to a sample that was

Die approbierte gedruckte Originalversion dieser Dissertation ist an der TU Wien Bibliothek verfügbar.
The approved original version of this doctoral thesis is available in print at TU Wien Bibliothek.
TU Bibliothek Your knowledge hub WIEN

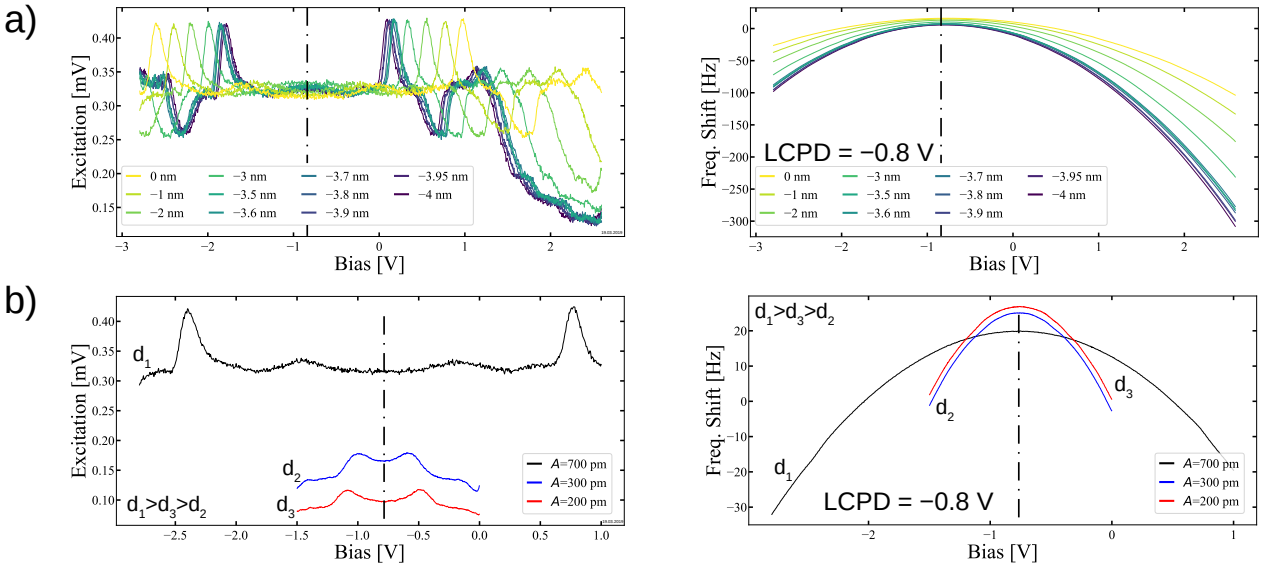

Figure 103: **Excitation curves over the CO-covered SrO termination annealed to room temperature for 1 h.** a) Distance-dependent shape of the excitation curves with respect to the applied bias (left panel), and simultaneously collected Kelvin parabolas (right panel). The legend shows relative tip-sample distances indicated with respect to the largest tip-sample distance. b) Amplitude-dependent shape of the excitation curves with respect to the applied bias (left panel), and simultaneously collected Kelvin parabolas (right panel). The legend indicates the constant oscillation amplitudes used. The curves are not obtained at the same tip-sample separation.

thermalized at 4.8 K, but held in a pre-cooled wobblestick at the temperature of 78 K. The pincers of a wobblestick were cooled by keeping it in contact with the outer cryostat of the LT measurement head for 10 min. CO dosing was performed for a duration in under one minute, during which time the cleaved $SrTiO_3(001)$ sample could not have reached the 78 K, especially due to the bad thermal contact of the sample with the cleaving device (contact area of $3500\times100\,\mu m^2$, Fig. 83). Therefore, it is reasonable to estimate that CO was dosed to a sample at T< 30 K temperature. Molecules were not dosed directly inside the low-temperature measurement head where the sample is stored at 4.8 K, because the majority of the evacuated molecules from the leak valve would stick to the cold walls rather than reach the sample, and the measurement head would also be saturated with CO molecules. The CO adsorption is studied in detail only for the SrO termination, because on the TiO_2 termination (not shown) the CO binds to Sr adatoms, and the imaging carries little information.

Figure 102 focuses on the SrO termination exposed to 2 L of CO at T< 30 K. Constant-height AFM images in Fig. 102a were obtained with a CO-terminated tip, that was spontaneously functionalized by scanning the CO-covered surface using STM. Constant-height AFM images are not well-resolved, and only faint circular features can be recognized that most likely correspond to single CO molecules. On the other hand, images of the collected excitation signal in Fig. 102b show superior resolution compared to the simultaneously recorded AFM images. This type of signal is peculiar since the excitation is supposed to be constant at the energy value that is necessary for keeping the oscillation amplitude constant, or at least varying in a very small range (Fig. 13b). Any deviation from a constant value in excitation implies an energy exchange between an AFM tip and a surface, because a cantilever is additionally damped or excited by the potential arising form a surface. The excitation signal images in Fig. 102b can be interpreted as showing real atomic resolution at the surface. According to the image obtained with the sample bias of −0.2 V, each spot corresponds to a single CO molecule. This image indicates that CO molecules do not adsorb within strontium vacancies: there are point and line defects in the excitation signal whose shape and size correspond to the distribution of strontium vacancies on the as-cleaved SrO termination. Another curiosity is the appearance of negative excitation signals over the unpopulated strontium vacancies. Imaging with the excitation signal requires additional interpretation compared to AFM images, but a crude interpretation would assign the damping (positive excitation) signal over the adsorbed CO molecules, and the exciting (negative) signal above the strontium vacancies.

Images in Figs. 102a and 102b imply that the excitation is dependent on the applied bias. This can be inves-

Die approbierte gedruckte Originalversion dieser Dissertation ist an der TU Wien Bibliothek verfügbar.
The approved original version of this doctoral thesis is available in print at TU Wien Bibliothek.
TU Bibliothek Your knowledge hub WIEN

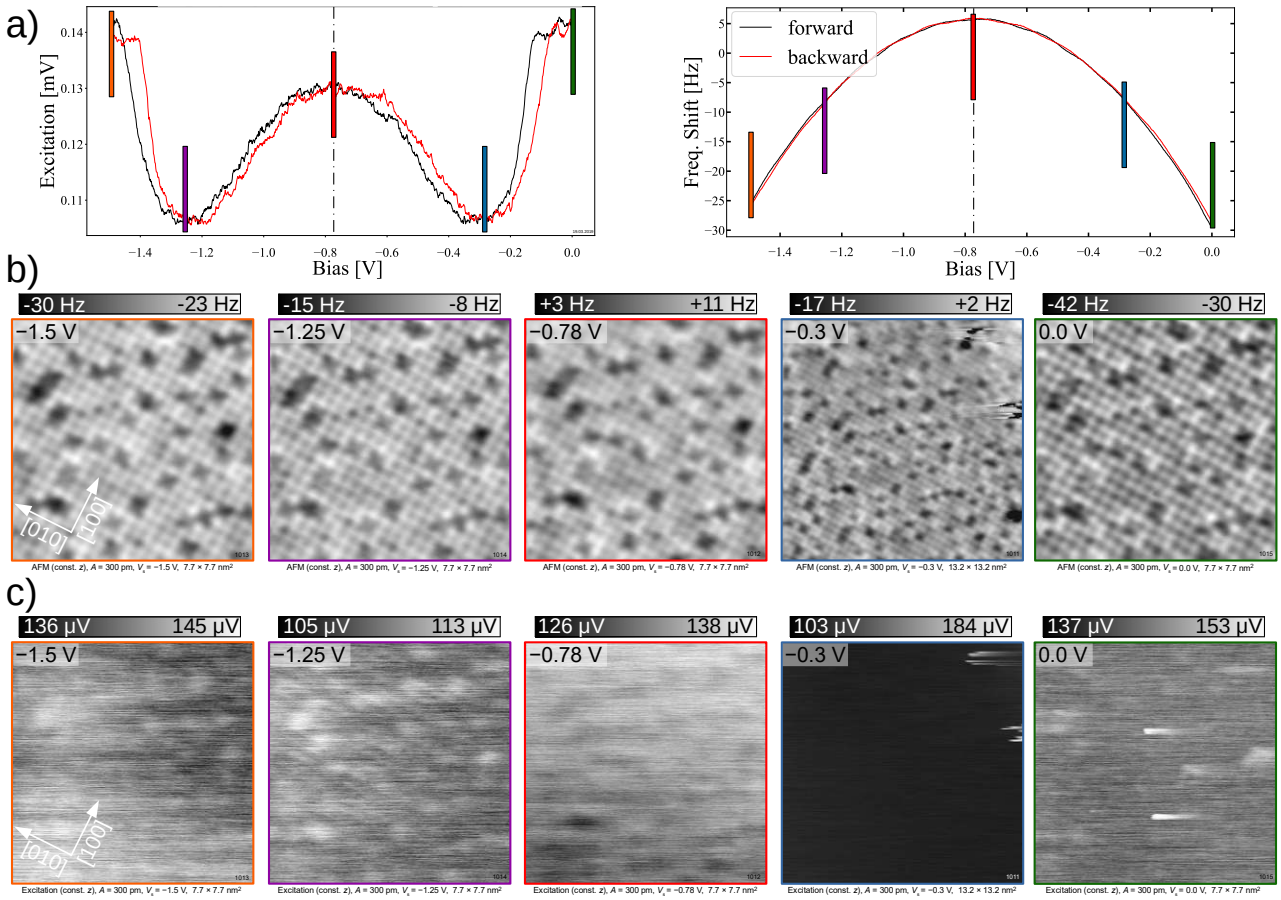

Figure 104: **Atomic resolution over the CO-covered SrO termination annealed to room temperature for 1 h.** a) A single excitation curve obtained very close to the surface (left panel), at distances small enough for clear atomic resolution, and simultaneously collected Kelvin parabola (right panel). Bias values are marked where the atomically resolved images were obtained b-c) Constant-height AFM images and their corresponding simultaneous excitation images, respectively, taken at different bias values marked in (a).

tigated by performing bias sweeps over the surface, and simultaneously collecting the excitation and frequency signals, as shown in the left and right panel of Fig. 102c respectively. The resulting excitation curve is bias dependent, which is a deviant behavior compared to usual AFM imaging; the Kelvin parabola on the other hand, shows a smooth, locally quadratic dependence, with a certain deviation for bias values corresponding to the peak in the excitation curve at ≈+2.5 V. This rare excitation dependence on the applied bias was reproducibly observed on the cleaved $SrTiO_3(001)$ surfaces only after the adsorption of CO molecules.

Figures 102d and 102e show the same CO-covered surface after annealing to 130 K for 10 min. This temperature was not sufficient to desorb all CO molecules since the same badly resolved features are seen in AFM images, and the excitation images provide the atomic resolution instead. The comparison of the excitation images before and after annealing to 130 K reveals that some CO molecules did desorb from the surface. In the image of the annealed surface, bright features in the excitation channel appear to be organized along rows, interrupted by strontium vacancies that again exhibit negative excitation. On the other hand, the excitation image of the surface after CO dosing imply a more complex arrangement of CO atoms, which seem to be adsorbed at both the Sr and the O atoms. Therefore, annealing to 130 K desorbed the CO molecules from the surface O atoms but not from the Sr atoms, and the two adsorption configurations seem to have significantly different adsorption energies.

The peculiar behavior of the excitation curves with respect to the applied sample bias is studied in more details over the CO-covered SrO termination that was annealed to room temperature for 1 h, shown in Fig. 103, where each excitation curve shows several peaks. In Fig. 103a, the distance dependence of the excitation curves

Die approbierte gedruckte Originalversion dieser Dissertation ist an der TU Wien Bibliothek verfügbar.
The approved original version of this doctoral thesis is available in print at TU Wien Bibliothek.
TU Bibliothek Your knowledge hub WIEN

is investigated. All excitation curves have common peaks, regardless of the distance to the surface, but the position of the peaks (bias values at which they appear) changes with varying distances. They are symmetric with respect to the position of the LCPD, inferred from the simultaneous Kelvin parabolas. They are initially well separated at large distance from the surface, but come closer as the tip-sample distance is reduced. The size and the shape of most of the peaks remains unchanged however. The overall shape of the excitation curves only varies in the vicinity of the LCPD as the tip-sample distance is varied: At large distances, excitation curves have a local minimum at the LCPD, while at small distances excitation curves exhibit a local maximum at the LCPD instead. Kelvin parabolas in Fig. 103a show no peculiar behavior, and demonstrate the distance-dependent strength of the electrostatic interaction (equation 1.30): Parabolas obtained close to the surface have the focal point much closer to the parabola maximum than the ones obtained further from the surface. The oscillation-amplitude-dependence of the excitation curves is shown in Fig. 103b. Smaller oscillation amplitudes require less energy to oscillate, and the excitation curves obtained with different oscillation amplitudes are therefore centered at different strengths of the necessary excitations. All curves have the same set of peaks, and can be considered equivalent but were unfortunately not obtained at the same tip-sample separation. As previously observed, the excitation curves obtained closer to the surface (blue and red) have a more pronounced set of peaks closest to the LCPD compared to the curve taken at larger tip-sample distance (black).

Figure. 104 focuses on the atomic resolution over the CO-covered SrO termination annealed to room temperature for 1 h. In Fig. 104a a single excitation curve is shown, which was taken very close to the surface. At this distance, atomically resolved imaging is possible; the tip-sample separation in Fig. 104a is much smaller during the bias sweeps in Figs.103a and 103b. This excitation curve exhibits a local maximum at the LCPD, which, when combined with the results in Figs.103a and 103b obtained over the same surface, reveals that the excitation value at the LCPD exhibits an oscillatory behavior: At large distances, the excitation has a local maximum at the LCPD, when the distance is reduced the excitation has a local minimum at the LCPD, while when the distance is reduced even further the excitation again develops a local maximum at the LCPD.

Atomically resolved AFM images in Fig. 104b reveal that the CO-covered SrO termination desorbed all CO molecules once exposed to room temperature. The imaging is again straightforward, with clear resolution on the Sr and O sublattices, as well as the strontium vacancies. The sequence of AFM images were taken at different bias values which correspond to local minima and maxima in the excitation curve in Fig. 104a. No apparent correlation between the chosen bias value and the peculiar behavior of excitation at that value is observed in the AFM images. The contrast in the AFM images does slightly differ, but this can probably be assigned to different field-dependent strengths of the electrostatic tip-sample interaction visible in the different absolute values of the frequency shift at different bias values. Simultaneously collected excitation images in Fig. 104c show no significant correlation with AFM images at the room-temperature annealed SrO termination, which implies that the CO molecules are responsible for the peculiar contrast in the excitation images on a CO-covered surface in Fig. 102. Even though no significant contrast can be observed in the excitation images once the CO molecules are desorbed, the excitation curve in Fig. 104a still clearly shows the peculiar behavior. The CO molecules therefore seem to have influenced the bare surface in some fashion, such that this effect is persistent even after their desorption. Alternatively, the CO terminated tip could be responsible for the peculiar signal in the excitation curves, and the absence of CO molecules on the surface enable atomically-resolved imaging in frequency shift channel; it is noteworthy that CO-terminated AFM tip are not usually reported to exhibit such behavior.

3.8.2 Crashed tip on a contaminated surface

The peculiar excitation behavior was reproducibly obtained on the $SrTiO_3(001)$ surface, in two separate experiments with different tuning forks and tips, only when the SrO termination was exposed to CO at low temperature. However, similar behavior was observed only once more on a cleaved $SrTiO_3(001)$ surface that was not exposed to CO, when the surface was exposed to the background pressure of 1×10^{-11} mbar for 10 h. Additionally, the AFM/STM tip was badly crashed on the cleaved $SrTiO_3(001)$ surface such that no well-resolved imaging was possible.

Figure 105 shows the excitation curves obtained in this experiment with a crashed tip over the contaminated cleaved $SrTiO_3(001)$ surface. In Fig. 105a, two curves obtained at the same distance from the surface with two different biasing possibilities, when the biasing voltage is applied to the sample and to the tip, are shown. Both curves show recognizable excitation peaks, symmetric to the position of the LCPD. The shape of the peaks is not symmetric however, an effect that can probably be assigned to the irregular tip shape. Simultaneously collected oscillation amplitude signal shows that the amplitude is hardly kept constant throughout this bias sweep, and

Die approbierte gedruckte Originalversion dieser Dissertation ist an der TU Wien Bibliothek verfügbar.
The approved original version of this doctoral thesis is available in print at TU Wien Bibliothek.
TU Bibliothek Your knowledge hub WIEN

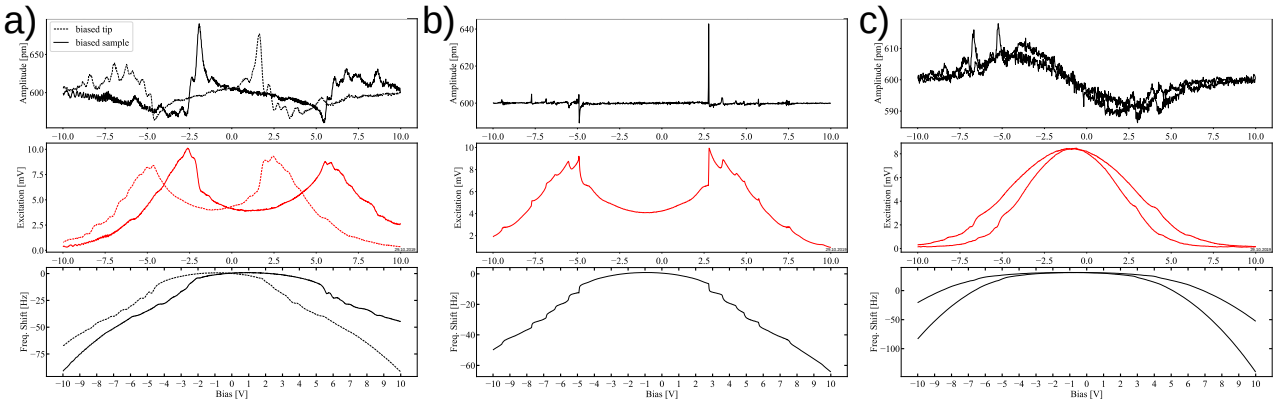

Figure 105: **Excitation curves over contaminated, cleaved $SrTiO_3$(001), obtained with a very crashed tip.** a) Two bias sweeps in the same ±10 V range obtained at approximately the same tip-sample distance but with opposite electric field orientation, *i.e.*, one was obtained with a biased tip and the other with a biased sample, as indicated in the legend. b) The bias sweep as in (a), and at the approximately same tip-sample distance, but it was obtained with much higher integration and settling time, *i.e.*, the bias was swept much slower than the sweeps in (a). c) The bias sweep at the approximately same tip-sample distance as in (a,b), but it was taken after the tip was retracted 15 nm away from the surface where the resonance of the cantilever was re-calibrated. The curve was obtained when the tip was subsequently moved 15 nm towards the surface, making it comparable to the curves in (a,b).

that the excitation peaks strongly influence the PLL responsible for ensuring constant amplitude of oscillations (Fig. 13). Simultaneously recorded Kelvin parabolas show peculiar behavior however, contrary to the case of a CO-covered surface: they are not smooth throughout the bias sweep range but instead exhibit several jumps that appear to be indicative of switching between different Kelvin parabolas. Distance-dependent behavior of these excitation curves and Kelvin parabolas is the same as seen on a CO-covered surface: the symmetric excitation peaks approach the LCPD as the tip-sample distance is reduced. The effect on the excitation can be observed even when the AFM tip is ≈80 nm from the surface, as can be seen in a video that focuses on the distance-dependent behavior of the excitation peaks, available online [431].

Figure 105b shows the same bias sweeps as in Fig. 105a, but taken much slower such that the PLL controller responsible for keeping the oscillation amplitude constant can react sufficiently fast to the changes in the excitation. By comparing the "slow" and "fast" bias sweeps, it is evident that the "slow" bias sweep in Fig. 105b produced a much smoother excitation curve and Kelvin parabola, and that the PLL does indeed manage to keep the amplitude constant. The largest deviations in oscillation amplitude appear at the points of sharp excitation peaks, but the constant 600 pm amplitude soon recovers afterwards. The excitation peaks and the Kelvin parabola also develop a better-defined shape during a "slow" bias sweep. Switching between different Kelvin parabolas is much better resolved in the "slow" scan, and the switching occurs at those bias values that correspond to the excitation peaks, or *vice versa*. Once extrapolated, different Kelvin parabolas within one bias sweep seem to have the common position of the maximum (the LCPD).

To try and remedy this peculiar dissipation behavior, the resonance frequency and the resonance curve of the AFM sensor were recalibrated. This was performed by moving the tip 15 nm away from the surface and performing the sweep of the driving frequency, as in Fig. 13a. The measured resonance curve was excellent, with the same quality as in the absence of a sample (not shown). After the recalibration, the AFM tip was brought back towards the surface by 15 nm, where the excitation curves together with the Kelvin parabolas were measured again, as can be seen in Fig. 105c. Both the excitation curves and the Kelvin parabolas seem drastically different than before the resonance curve of the cantilever was adjusted. Many excitation peaks were replaces by a single large peak centered at the LCPD, while the many-featured Kelvin parabola was replaced by a single parabola, with an unusually large focal distance. The LCPD remained apparently unchanged however.

Die approbierte gedruckte Originalversion dieser Dissertation ist an der TU Wien Bibliothek verfügbar.
The approved original version of this doctoral thesis is available in print at TU Wien Bibliothek.
TU Bibliothek Your knowledge hub WIEN

3.9 Summary and Outlook

In this Chapter, a method was developed for cleaving a prototypical cubic perovskite $SrTiO_3(001)$ sample. Cleaved surfaces were thoroughly characterized, and a series of experiments were performed to determine their potential utilization in the fields of catalysis and oxide electronics at the nano- and micro-scale. In Section 3.1 general properties of the $SrTiO_3$ bulk and its (001) surface are introduced.

The cubic symmetry and the iono-covalent bonding in the bulk $SrTiO_3$ are major setbacks for obtaining atomically flat (001) surfaces *via* cleaving. Section 3.2 introduces a novel method of utilizing strain-induced ferroelectricity to create inequivalent planes along the [001] direction of the pre-strained samples. Cleaving proceeds through breaking the weaker of the two inequivalent bonds along the [001] direction, and exposes an atomically flat (001) surface with both, SrO and TiO_2 terminations. The SrO termination is semiconducting while the TiO_2 termination is metallic, and they are covered by the same concentration of point defects in the form of Sr vacancies and Sr adatoms, respectively. Charged point defects appear to compensate the polarization vector along the [001] direction that appears during cleaving on this otherwise nominally non-polar surface. These results provide an exciting pathway to performing quantum phase transitions in $SrTiO_3$ by hand.

The two bulk-terminated surface terminations on a cleaved $SrTiO_3(001)$ surface are unstable after annealing in UHV, as investigated in Section. 3.3. At moderate annealing temperatures in UHV, SrO and TiO_2 terminations first develop stoichiometric SrO pits and islands, respectively. Upon annealing at 500 °C in UHV, both terminations converge to the same disordered surface structure. The rich variety of surface structures upon annealing is not recognized by LEED that shows a persistent (1×1) diffraction pattern. The standard $SrTiO_3(001)$ preparation method by wet-chemistry was examined, and it was revealed that such surfaces are routinely contaminated with carbon – once carbon is removed by annealing in UHV at 700 °C in 10^{-6} mbar O_2, the surface immediately rearranges to a $(\sqrt{13} \times \sqrt{13})R{\pm}33.7^\circ$ surface reconstruction. This indicates that a pristine and unreconstructed $SrTiO_3(001)$ surface is far from warranted, and that the cleaved surfaces likely come closest. These results send a strong message of precaution to a large community that deals with $SrTiO_3(001)$ surfaces, and indicate that the stability region of bulk-terminated surfaces lies below typically applied temperatures during sample preparation.

Details of the cleaving procedure are further laid out in Section 3.4. Proper cleaving proceeds through freezing of the transverse optical phonon responsible for the phase transition to ferroelectricity. Pre-straining single crystals must be done with caution and precision to ensure large surface regions of well-cleaved $SrTiO_3(001)$. Well-cleaved areas can be recognized from the ill-defined fractured surface regions under an optical microscope. The cleaving device is easily transferable between differently designed laboratories, and cleaving thick crystals is possible by optimizing the geometry of the samples and the cleaving device. The two surface terminations, characterized by different electronic structure and work functions, can be recognized in SEM even after exposure to ambient. Each domain spans ≈10 μm between the domain walls, and reach much further in a direction parallel to the domain walls. The cleaving device was applied to a different perovskite oxide, and it was demonstrated that the cleaved $KTaO_3(001)$ surface morphology and properties can be altered using this cleaving procedure. These results indicate the universality of the cleaving device primarily used for $SrTiO_3$, and open a wide research area on cleaved perovskite surfaces that are expected to exhibit a series of intriguing surface and bulk phenomena.

Extrinsic doping of $SrTiO_3$ single crystals with various content of niobium results in different morphologies of cleaved Nb:$SrTiO_3(001)$ surfaces, as shown in Section 3.5. The standard 0.69 at.% doped Nb:$SrTiO_3$ samples used throughout this Chapter lie above the critical Nb-doping level which is larger than 0.14 at.% and smaller than 0.28 at%. Surfaces above this doping level develop large singly-terminated domains that switch at large domain walls, while surface below the critical doping level developed striped morphologies. The domain width decreases with decreasing Nb content, and the smallest domain width of 9.5 nm was observed for the nominally undoped samples. Niobium acts primarily as an electron donor in $SrTiO_3$ and provides sufficient screening charge to enable development of large domains on highly doped samples, while the low-doped samples must create small domains to lower the surface energy in the absence of efficient screening. All Nb-doped surfaces have a similar electronic structure, while the nominally undoped surfaces have both terminations semiconducting that exhibit short-lived charging upon electron injection. These results demonstrate how the availability of external charge necessary for screening directly influences the two domains, and provide a pathway to manipulating the properties of cleaved $SrTiO_3(001)$ surfaces.

Cleaved $SrTiO_3$ have a broken cubic symmetry and were therefore shown separate free charge carriers introduced by UV irradiation in Section 3.6. The metallic TiO_2 termination is unaffected by the UV light, while the entire semiconducting SrO termination is simultaneously hole-doped with only a small UV dose.

Die approbierte gedruckte Originalversion dieser Dissertation ist an der TU Wien Bibliothek verfügbar.
The approved original version of this doctoral thesis is available in print at TU Wien Bibliothek.
TU Bibliothek Your knowledge hub WIEN

Accumulated charges on the SrO termination are presumably localized in the form of small hole polarons. Their lifetime is exceptionally long at both LN_2 and LHe temperatures, and the surface remains charged for days. Charged SrO termination can be returned to its ground state by injecting electrons into the conduction band *via* empty-states STM. Such discharging is highly localized, as injected electrons do not annihilate holes laterally across the surface but rather within the near surface and bulk regions. These results demonstrate that a cubic $SrTiO_3$ perovskite can be turned into an efficient charge separator simply by cleaving. Moreover, they provide the basis for applications of cleaved $SrTiO_3(001)$ surfaces as ferroelectricity-assisted catalysts, and photo-sensitive electronic components.

Section 3.7 shows that the deliberate removal of charge from cleaved $SrTiO_3(001)$ surfaces *via* filled-states STM results in similar effects as observed with UV irradiation, but likely accompanied by other ionic effects. Namely, SrO termination that is locally depleted of electrons develops large electronic defects that do not correspond to any surface rearrangement. To perform filled-states STM the AFM/STM tip at lower potential than the surface must be in its close proximity, and the electric field originating from the tip could be responsible for subsurface ion migration upon electron depletion. The created defects cannot be erased by subsequent electron injection.

Experimental peculiarities during AFM measurements of CO-covered cleaved $SrTiO_3(001)$ surfaces are reported in Section 3.8. The dissipation channel indicates energy exchange between the AFM/STM tip and the CO-covered surface, that depends on the applied tip-sample bias. This effect was never observed on a freshly cleaved surface, and occurs only after CO dosing at low temperature; the effect of different adsorbates remains to be studied. Although not yet interpreted, the data is presented in detail. It resembles the published data on several different systems, yet there is no direct physical link connecting the cleaved $SrTiO_3(001)$ to these systems.

Die approbierte gedruckte Originalversion dieser Dissertation ist an der TU Wien Bibliothek verfügbar.
The approved original version of this doctoral thesis is available in print at TU Wien Bibliothek.
TU Bibliothek Your knowledge hub WIEN

Chapter 4

AFM contrast simulations

Many recent surface physics and chemistry studies examine the same phenomena jointly through a combination of experimental and theoretical techniques. It was shown so far that studying crystal surfaces at the atomic level is experimentally feasible using AFM and STM, while the same phenomena are readily theoretically modeled at the quantum mechanical level using DFT. The entirety of Chapter 2 shows that comparison of experimental and theoretical results on the adsorption of small gas molecules on the reduced rutile $TiO_2(110)$ surface provides more insights than any of the two techniques separately, and of course, that this approach provides a method for verification of independently obtained results from experiment and from theory. The comparison of experimental and theoretical results proceeds in many different aspects, through the convergence of the crystal structure and/or the extrinsic adsorbates, the electronic properties of the surface and the adsorbates, transport properties of solids, their stability under different temperatures, pressures or strains *etc.*. These properties can usually be compared between a plethora of experimental techniques, and a vast range of theoretical tools and approximations. This Chapter focuses on only one aspect of this comparison: comparing atomically resolved AFM images in real space with the simulated AFM contrast over the same crystal structure that was previously theoretically modeled.

The procedure of comparing experimentally obtained STM images (in constant height mostly) with the STM images that would be obtained over the theoretically modeled crystal structures, was developed by Tersoff and Hamann soon after the experimental realization of the fist STM machine. The Tersoff-Hamann approach [68, 69] successfully illustrates how the DOS are spatially distributed across the surface in two dimensions, and how far the wavefunctions of the sample protrude out of the surface in the third dimension, at a given arbitrary energy with respect to the calculated Fermi level of the sample. Although this approach is highly versatile and still widely employed today [432, 433], there is a series of setbacks when realistic experimental conditions are to be emulated by theory. The biggest setback lies in the well-known drawback of DFT in correctly quantitatively estimating the band gap of semiconductors, and the position of the Fermi level. The other setbacks lie in the underestimation of the calculated protrusion of wavefunctions from the sample surface into vacuum, the not-so-realistic requirements for the perfect metallicity of the STM tip, the spatial orientation of wavefunctions at the tip apex *etc.*. These setbacks can be overlooked to a certain degree, and still allow an excellent qualitative comparison of the experimental and simulated STM images. In the case of simulating AFM contrast however, many of the aforementioned setbacks cannot be ignored, especially because the particular AFM tip termination and the non-monotonic dependence of tip-sample forces from the tip-sample separation play a crucial role in the AFM contrast formation.

There are several approaches to simulating AFM contrast, each with varying levels of approximations. In the most course level of approximations, the AFM tip can be considered a single point charge that is moving in the electrostatic field of the sample that can be obtained from calculations [104, 434, 435]. A more precise approximation is the Probe Particle model [230, 436] that accounts for the mechanics of a flexible CO-terminated AFM tip during scanning. This approximation yields excellent results for simulating AFM images of organic molecules adsorbed at metal or insulating surfaces, where experimentally, CO-terminated AFM tips are almost always used due to their flexibility that adds valuable contrast to the AFM images. For studying oxide surfaces however, CO-terminated tips are not usually employed, because their flexibility adds artifacts to the contrast obtained over oxygen-saturated surfaces with strong covalent bonding. For this reason, a promising approach to studying oxides is employing carefully-prepared oxygen-terminated tips [437, 109, 202] that provide excellent repulsive contrast over the surface oxygens, as demonstrated in Section 2.5. Simulating such AFM

Die approbierte gedruckte Originalversion dieser Dissertation ist an der TU Wien Bibliothek verfügbar.
The approved original version of this doctoral thesis is available in print at TU Wien Bibliothek.
TU Bibliothek Your knowledge hub WIEN

images requires more precise approximations, like the one used for simulating an AFM image in Fig. 44, which will be further introduced in the Section below. This Chapter will investigate each of the three mentioned approximations in simulating AFM contrast, and show that each can reasonably be applied to certain systems. The choice of preferred level of AFM simulation complexity remains to be chosen according to the system at hand, and according to the available computational resources, since increasingly accurate simulations require increasingly more processing hours.

4.1 Transforming simulated force-distance curves to AFM images – DAC simulator

This Section is based on the forthcoming publication titled "Efficient chemically sensitive AFM contrast simulations" [438].

Simulated force-distance curves obtained through DFT completely describe the interaction of a modeled AFM tip and a single point on the surface. They include contributions from electrostatic forces, van der Waals forces, and chemical forces that can be either attractive or repulsive depending on the tip-sample distance and the chemical properties or affinities of both the modeled tip and surface atoms. Moreover, a simulated force-distance curve above a single point on a calculated surface structure accounts for the long-range interactions with the surrounding surface atoms, just like in experiments where an AFM tip detects the same long-range contributions. For these reasons, simulated force-distance curves are the most precise method to simulating experimental AFM contrast.

The highest-quality simulation of constant-height AFM images, with as little approximations as possible, would consist of performing a simulated force-distance curve above each point in an equidistant grid above a calculated surface structure using DFT, and transforming each curve into a single value of the frequency shift at a desired tip-sample distance. To create simulated AFM images that resemble experimental ones as close as possible, it would be desirable to simulate force-distance curves with a calculated AFM tip model that reflects real experimental AFM tips used for obtaining images. This poses a significant challenge because the structure of the experimental AFM tips is unknown, and can be inferred only through the obtained AFM contrast. Additionally, the process of simulating a single force-distance curves is computationally expensive and requires significant time, in the order of several processor weeks for a single curve. This means that evaluating frequency shifts in a grid of 100×100 points would require several decades. For these reasons, many approximations are necessary to make the process of simulating the contrast in a single AFM image computationally feasible.

To obtain a simulated AFM image that realistically reflects the experimental conditions, but still remains computationally feasible, a procedure is introduced here that constructs a simulated AFM contrast using explicitly simulated force-distance curves, but employs as little of them as possible for a given system. Since the simulated contrast is derived from DFT calculations of force-distance curves, the procedure goes by the name DFT-derived AFM contrast (DAC) simulator hereafter, the principle of which is laid-out in Fig. 106.

In the first step of the DAC simulator, force-distance curves are explicitly simulated above a DFT-optimized surface structure, using a suitable AFM tip model. Namely, for each simulated force-distance curve, a modeled AFM tip is placed at progressively lower tip-sample distances and the entire system is relaxed with DFT [439, 96, 440, 256, 441, 442, 231, 443]. The atoms at the "bottom" of the modeled AFM tip that are oriented towards the surface are left free to relax *via* minimization of the forces on each atom, together with the surface atoms on the calculated surface slab. At the same time, atoms at the "top" of the modeled AFM tip are forced to be frozen, such that they reflect the internal distribution of forces on the atoms within the modeled AFM tips. After the DFT-optimization of the sample and tip system is relaxed at each tip-sample distance, force vectors acting on the backside of the modeled AFM tip are added, and the z-projection of the resultant force is considered as the force acting between the calculated surface slab and the AFM tip. Plotting these calculated forces against the corresponding tip-sample distance, creates a simulated force-distance curve above the selected point of the surface slab. It is necessary, however, to ensure that the vacuum volume is sufficiently large, such that the backside of the tip does not interact with the periodically repeated bottom of the surface slab, and to avoid the interaction of the modeled AFM tip with periodic repetitions of itself along the lateral directions. This first step in the DAC simulator is the only one that requires performing DFT calculations, and the subsequent steps of the simulation procedure proceed only through geometrical considerations.

To minimize the number of simulated force-distance curves, and achieve computational feasibility, force-distance curves are simulated only over carefully selected points on a surface slab. The choice of these representative points is therefore an important aspect of the first step in the DAC simulator. The points of interest

Die approbierte gedruckte Originalversion dieser Dissertation ist an der TU Wien Bibliothek verfügbar.
The approved original version of this doctoral thesis is available in print at TU Wien Bibliothek.
TU Bibliothek Your knowledge hub WIEN

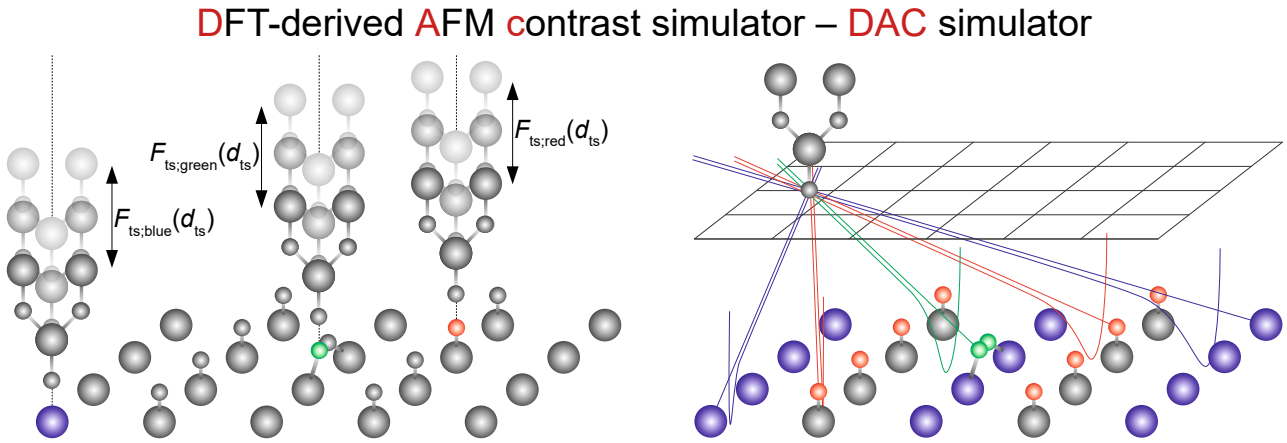

Figure 106: **Principle of operation of the DAC simulator.** Chemical sensitivity of the DAC simulator lies in explicitly simulating force-distance curves above representative sites on a surface, and considering all equivalent sites as chemically identical, *i.e.*, as characterized by a same force-distance curve. A simulated constant-height AFM image is then created by calculating the force contribution of all atoms in each point of a grid above a surface. Namely, the distance to each atom is calculated at each point of the grid, and the corresponding force-distance curve is applied for each group of atoms (blue, red, and green in the illustration).

are manually selected such that they represent the whole class of chemically equivalent points on the surface, *i.e.*, simulated-force distance curves are performed over surface atoms that will represent the whole class of chemically equivalent sites. In the example in the left panel in Fig. 106, force-distance curves are simulated over three surface atoms only: the blue, the orange, and the green atom. The second step of the DAC simulator is grouping chemically equivalent atoms as in the right panel in Fig.106 in the groups of blue, orange, and green atoms. In this particular example, blue and orange atoms correspond to the periodically repeating surface atoms, and all equivalent surface sites can be assigned to be either blue or orange. Green atoms correspond to an isolated structure (an adsorbed molecule for example) that is not periodically repeated, and for this reason the group of green atoms is the smallest, counting only two members. By assigning surface atoms to chemically equivalent groups, a simulated force-distance curve above a single member of a group can be considered as being performed above each member of the group. It is imperative of course, to correctly group atoms such that the second step of the DAC simulator is performed rationally – experimental AFM images greatly aid this procedure because they indicate whether equivalent surface sites are also chemically equivalent.

In the third step of the DAC simulator, an equidistant grid of points is constructed parallel to the surface at a fixed distance, on which the frequency shift will be evaluated. At each point of such a grid, the relative position to *each* atom in the surface slab is calculated in the form of a vector. A corresponding simulated force-distance curve is then applied between a point in the grid and *each* atom in the surface slab: an orange force-distance curve is applied to *each* orange atom, and the same is performed for blue and green atoms in the example in Fig. 106. Force acting at the simulated AFM tip is then obtained by taking the value of the force from the simulated force-distance curve at the distance that was calculated for *each* atom of *each* group of atoms. In other words, each point in the equidistant grid where the frequency shift is evaluated (marked by three spatial coordinates $i, j,$ and k) is assigned with as many values for the force as there are surface atoms, which are then summed to provide a single scalar value for the force F_{ijk}. This single value reflects the force acting on the simulated AFM tip originating from *all* surface atoms in a single point above the surface:

$$F_{ijk} = \sum_{\{red\}} F_{\text{ts;red}}(d = |\overrightarrow{r_{ijk}} - \overrightarrow{r_{red}}|) + \sum_{\{blue\}} F_{\text{ts;blue}}(d = |\overrightarrow{r_{ijk}} - \overrightarrow{r_{blue}}|) + \sum_{\{green\}} F_{\text{ts;green}}(d = |\overrightarrow{r_{ijk}} - \overrightarrow{r_{green}}|). \tag{4.1}$$

where $\overrightarrow{r_{ijk}}$ is the position of a single point on the three dimensional grid above a surface at which the F_{ijk} force is evaluated, and $F_{\text{ts;blue}}, F_{\text{ts;red}}, F_{\text{ts;green}}$ are the calculated force-distance curves above a single representative member of the blue, red, and green group of atoms, respectively, according to Fig. 106. The position of each atom in their respective groups is given as $\overrightarrow{r_{red}}, \overrightarrow{r_{blue}}, \overrightarrow{r_{green}}$, and the summation over $\{blue, red, green\}$ accounts for all atoms on a surface. In reality, the highest contribution to the overall force originates from the nearest

Die approbierte gedruckte Originalversion dieser Dissertation ist an der TU Wien Bibliothek verfügbar.
The approved original version of this doctoral thesis is available in print at TU Wien Bibliothek.
TU Bibliothek Your knowledge hub WIEN

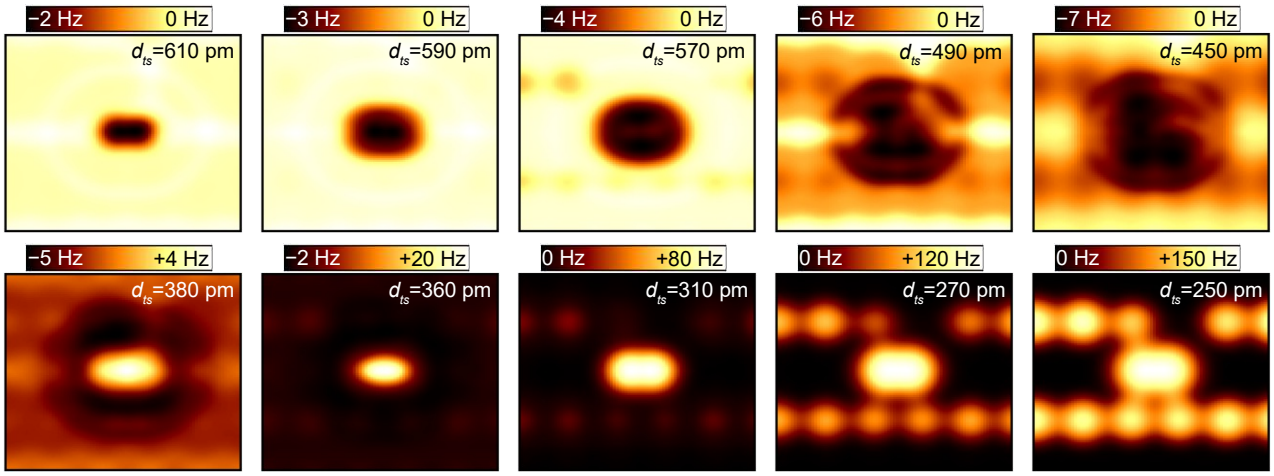

Figure 107: **Series of simulated constant-height AFM images at different heights obtained with the DAC simulator.** Simulated constant-height AFM images were obtained on the rutile $TiO_2(110)$ surface with one V_O and one adsorbed π molecule, in a configuration calculated in Fig. 41e, using the AFM tip model shown in Fig. 44. Force-distance curves from Fig. 44e were provided to the DAC simulator. Tip-sample distances d_{ts} are expressed as the separation between the simulated AFM tip apex and the O_{br} rows – they are indicated in each panel and decrease from the top left to the bottom right panel. Images were created with an oscillation amplitude of $A = 50\,\text{pm}$.

surface atom to the selected point in a grid, while the rest of the surface atoms contribute only slightly (less than 5%). When the procedure is performed in all points of an equidistant grid, the two-dimensional map of the force on the simulated AFM tip at a given height above the surface is obtained.

Finally, in the fourth step of the DAC simulator an actual constant-height AFM image is simulated. This is performed by repeating the third step of the DAC simulator at several (many) different separations of the simulated AFM tip and the surface. Such procedure creates a three-dimensional force matrix above the surface, and the frequency shift at a fixed height from the surface can be calculated for arbitrary values of AFM tip oscillation amplitudes. The transformation between the array of values for the force along the AFM tip oscillation trajectory in the direction perpendicular to a surface, to a single value of the frequency shift at the tip-sample separation defined as the center point of the oscillation, can then be achieved by using Giessibl's small-oscillation-amplitude approximation [104].

The precision of the simulated AFM contrast with the described procedure in largest part depends on the quality of the explicitly simulated force-distance curves with DFT: the better the correlation between experimental and simulated force-distance curves, the better the simulated constant-height AFM image using the DAC simulator. From the aspect of computational cost, this is the bottleneck for creating good simulated AFM images, and further efforts to reduce the computational cost of simulated force-distance curves are being developed at the moment.

Figure 107 illustrates the quality of the simulated constant-height AFM image using the DAC simulator on the reduced rutile $TiO_2(110)$ (6×2) unit cell surface with one V_O, and one adsorbed π molecule – a configuration experimentally observed and simulated using DFT in Fig. 41e. The only input to the DAC simulator necessary for obtaining the images shown in Fig. 107 are: the calculated geometry of the surface and adsorbate system (Fig. 41e), and the explicitly calculated force-distance curves above the bridging oxygen atom O_{br}, the five-fold coordinated Ti_{5c} atom, and the peroxo π molecule from Fig. 44e. This procedure was already used to simulate a constant-height AFM image over all different O_2 species on the surface, shown in Fig. 44f, but only at a single tip-sample distance ($d_{ts} = const.$) that images the adsorbed molecules and the bridging oxygen atoms in clear repulsion and a positive frequency shift with respect to the long-range background forces.

In Fig. 107, the height-dependent simulated AFM contrast is investigated in more detail. At large tip-sample distance ($d_{ts} = 610\,\text{pm}$), simulated constant height image exhibits only a feature that corresponds to the most protruding species on the surface, the π molecule, that is imaged in the attractive regime with a negative frequency shift. This attraction of the O atom at the tip apex and O atoms within a π molecules is very weak and originates solely from the van der Waals forces between the tip and the sample (Figs. 44f and 45). When the

Die approbierte gedruckte Originalversion dieser Dissertation ist an der TU Wien Bibliothek verfügbar.
The approved original version of this doctoral thesis is available in print at TU Wien Bibliothek.
TU Bibliothek Your knowledge hub WIEN

tip is located 20 pm closer to the surface, weak attractive forces can be detected at further lateral distances from the π molecule, and it is imaged as larger. At $d_{\mathrm{ts}} = 570\,\mathrm{pm}$, $\mathrm{O_{br}}$ rows become detectable in the weak attractive regime, and the π molecule is still detected in attraction, but its feature grows laterally even larger. As d_{ts} is progressively decreased, at $d_{\mathrm{ts}} = 490\,\mathrm{pm}$ and $d_{\mathrm{ts}} = 450\,\mathrm{pm}$, all protruding oxygen atoms are still imaged in attraction, with the π molecule dominating the contrast as a large feature with a strong negative frequency shift. This large size of the π molecule at these distances is a consequence of accounting for this molecule with its corresponding force-distance curve at *each* point in the simulated AFM image, leading to its over-exaggerated size in the simulations at these intermediate tip-sample distances.

When the tip-sample distance is further decreased to $d_{\mathrm{ts}} = 380\,\mathrm{pm}$, shown in the bottom row of Fig. 107, the protruding π molecule starts being simulated in the repulsive regime, with a positive frequency shift. The rest of the surface atoms, and the vicinity of the π molecule, are still characterized by a weak attraction and a negative frequency shift. At $d_{\mathrm{ts}} = 310\,\mathrm{pm}$, all oxygens on the surface are imaged in the repulsive regime with a positive frequency shift, just like in the experimental conditions. The geometry of the surface $\mathrm{O_{br}}$ rows is well reflected in the simulated AFM image at $d_{\mathrm{ts}} = 310\,\mathrm{pm}$ and $d_{\mathrm{ts}} = 270\,\mathrm{pm}$, regardless of the fact that all $\mathrm{O_{br}}$ atoms were considered chemically equivalent and treated with the same simulated force-distance curve. Namely, the lattice relaxation surrounding the oxygen vacancy is clearly visible in this simulated AFM image, as well as in the experimental images in Fig. 39. Further decrease of the tip-sample distance causes the surface oxygens to be imaged as increasingly larger repulsive features with a strong positive frequency shift. At the closest approach to the surface $d_{\mathrm{ts}} = 250\,\mathrm{pm}$, some artifact lines connecting the π molecule to the $\mathrm{O_{br}}$ rows develop due to the specifics of the image formation algorithms, but experimental AFM images over this particular system are never obtained at such small tip-sample distances.

In conclusion, the DAC simulator is an efficient tool for simulating realistic and experimentally relevant constant-height AFM images. In essence, the DAC simulator is a procedure for superposition of forces obtained through as little explicitly simulated force-distance curves as possible. Since the calculated force-distance curves are obtained through DFT, the tip-sample interaction is chemically sensitive. Even in the case of very small attraction basin between the AFM tip and the surface species, as is the one studied in Fig. 107, simulated AFM images capture the AFM contrast inversion: surface species are imaged as attractive at large distances and become repulsive as the tip-sample distance is reduced. Moreover, the reported tip-sample distances in Fig. 107 correspond well to the tip-sample distances usually used for measuring experimental AFM images, and the reported values for the simulated frequency shifts are reasonable and in the same order of magnitude as the experimentally obtained ones. This provides possibilities for discerning the experimental tip-sample distances, which are always unknown, by comparing the frequency shift values and details of the contrast with the simulated AFM images at arbitrary distances.

Die approbierte gedruckte Originalversion dieser Dissertation ist an der TU Wien Bibliothek verfügbar.
The approved original version of this doctoral thesis is available in print at TU Wien Bibliothek.
TU Bibliothek WIEN Your knowledge hub

4.2 Case study on NaI(001)

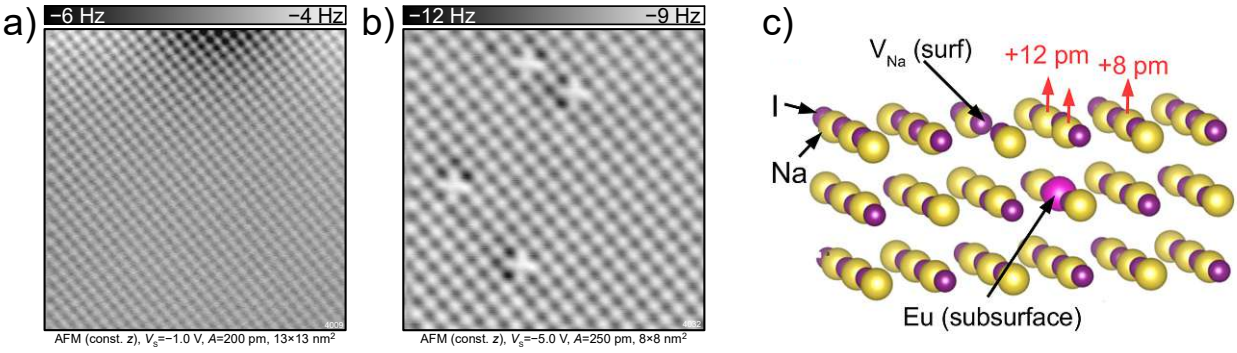

Figure 108: **NaI(001) surface with Na vacancies and substitutional subsurface Eu atoms.** a,b) Constant-height AFM images obtained with an anion-terminated AFM tip showing the (1×1) surface of a cleaved NaI(001) surface. Several isolated Na vacancies are seen in (b) as a missing single Na atom, surrounded by slightly protruding Na ions pushed from beneath by a substitutional subsurface Eu atom. Experimental AFM images obtained by Manuel Ulreich and Martin Setvín. c) DFT-optimized lowest-energy structure of the NaI(001) surface with a single substitutional Eu^{2+} atom in the subsurface region, located in the close vicinity of the Na vacancy. Na atoms surrounding the vacancy are calculated to slightly relax outwards with respect to the surface, explaining their observed contrast in AFM images. These results are published as a part of the publication "Defect chemistry of Eu dopants in NaI scintillators studied by atomically resolved force microscopy" [352].

An important aspect of AFM contrast simulations is chemical sensitivity, *i.e.*, correctly simulating both attractive and repulsive interactions between a simulated AFM tip and a simulated surface structure. A mixture of both types of tip-sample interactions, attractive and repulsive, is commonly distance-dependent as shown in the example in Fig. 107 obtained with the DAC simulator, but can also be encountered on surfaces that contain both, surface anions and cations, as in the example of experimental AFM images of the SrO termination on the bulk-terminated $SrTiO_3$(001) surface in Figs. 61, 64. A much simpler example of ionic solids are binary rock salt structures. Their bulk-terminated (001) surfaces are of purely ionic character with oppositely charged surface ions [353, 445, 446, 447]. This is the case for the cleaved NaI(001) surface [448, 449], and this Section compares two commonly-used AFM simulation procedures with the output of the DAC simulator on such an ionic surface.

Figure 108 shows the experimentally obtained constant-height AFM images on the bulk-terminated NaI(001) surface, and the calculated surface structure of a slab substitutionally doped with a single Eu dopant [352]. An atomically resolved AFM image of the defect-free surface is seen in Fig. 108a. The image was taken with an anion-terminated AFM tip. Such negatively charged tip detects formally positive Na^+ ions as electrostatically attractive and formally negative I^- ions as electrostatically repulsive. The perfect (1×1) NaI(001) lattice is therefore imaged as a perfectly arranged grid of dark (attractive) and bright (repulsive) spots. The tip-sample separation was relatively large in Fig. 108a (according to low values of the frequency shift), and an additional thermal drift towards the surface is noticeable from the bottom to the top of the image. The drift implies that the image is not performed in constant-height, and it clearly illustrates the distance-dependent AFM contrast. As expected, there is no contrast inversion on this ionic surface, as Na atoms are attractive and I atoms repulsive towards the negatively-charged AFM tip at all tip-sample distances. A truly constant-height AFM image with even better atomic resolution can be seen in Fig. 108b. At this surface region, there are Na vacancies recognized as isolated missing Na atoms. Three Na atoms, two nearest neighbors and one next-nearest neighbor to the Na vacancy, are imaged in slightly stronger attraction (darker) than a regular Na lattice site. The DFT-optimized lowest-energy structure of a NaI(001) surface doped with Eu, shown in Fig. 108c, indicates that the substitutional Eu dopant lies in the next-nearest-neighboring-subsurface site to the Na vacancy, and that the Na atoms above this Eu site are slightly relaxed outwards from the surface. The slight calculated protrusion of these atoms from the surface is sufficient to explain their stronger contrast in experimental AFM images, considering that the Fig. 108b image was obtained at a relatively small tip-sample distance.

Die approbierte gedruckte Originalversion dieser Dissertation ist an der TU Wien Bibliothek verfügbar.
The approved original version of this doctoral thesis is available in print at TU Wien Bibliothek.
TU Bibliothek Your knowledge hub WIEN

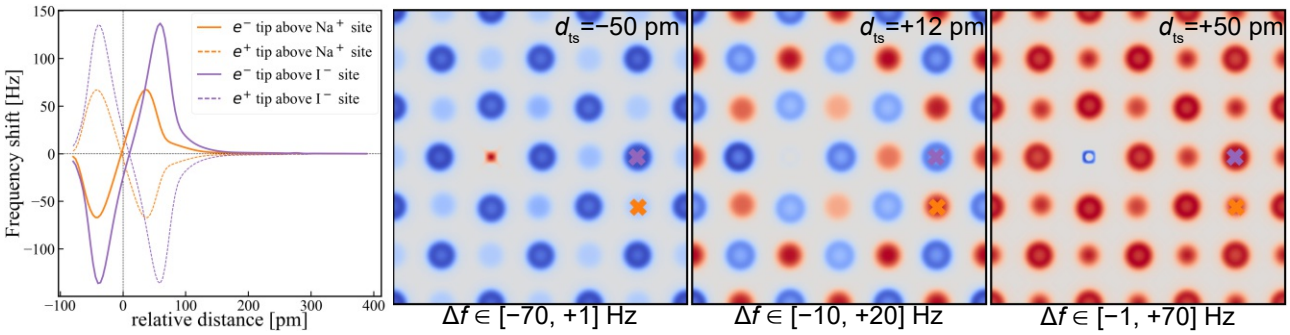

Figure 109: **AFM contrast simulation over the NaI(001) surface with a single Na vacancy, using a unit probe charge in an electric field of the sample derived from DFT.** The electrostatic model was applied to a DFT-optimized NaI(001) surface with one Na vacancy and one Eu substitutional dopant, as calculated in Fig. 108c, by oscillating a probe charge in the calculated potential above the surface. Frequency-shift vs. distance curves illustrate the interaction between a point charge (either positive or negative) and two distinct ions on the surface. Simulated constant-height AFM images with a negatively charged tip at three different tip-sample distances d_{ts} illustrate the distance-dependent simulated contrast; the tip-sample distance d_{ts} is defined as the distance between the center point of the oscillation and the most-protruding atom at the surface. The first simulated AFM image at $d_{\mathrm{ts}} = -50\,\mathrm{pm}$ is unphysical because it is obtained within the surface, below surface ions. Only the simulated AFM image displayed in the middle panel shows opposite contrast over the two oppositely charged ions, which can be achieved only in the immediate vicinity to the surface, at d_{ts} =12 pm. Purple and orange crosses indicate where the frequency-shift vs. distance curves were obtained over I and Na surface ions, respectively. Color scheme indicates attractive interaction as blue and repulsive interaction as red.

4.2.1 Electrostatic model

AFM contrast on an purely ionic surface should originate solely from electrostatic interaction between the tip and the sample, therefore the contrast over the NaI(001) surface should be readily simulated using the simplest AFM simulation procedure with the most crude approximations, *i.e.*, considering an AFM tip a single probe charge that oscillates in the electrostatic field of the sample. The DFT-optimized structure using VASP provides the electrostatic field of the sample as one of the outputs; naturally, a surface with sufficient vacuum volume must be modeled such that the obtained electrostatic field at further distances from the surface can be considered reliable. Figure 109 shows the result of such AFM simulations. The tip-sample interaction is quantified by simulated force-distance (frequency shift vs distance in this example) curves using a single negatively or positively charged electron as an AFM tip, shown in full and broken lines, respectively. The electrostatic interaction is of the same sign above both types of oppositely charged surface ions at $d_{\mathrm{ts}} > 20\,\mathrm{pm}$, regardless of the tip charge. This implies that the calculated electrostatic field above the sample does not chemically distinguish the two oppositely charged ions. This is further illustrated in the simulated AFM images in the first and the third panel that were obtained at symmetric distances from the surface atoms along the z-direction; negative tip-sample separation is unphysical but is displayed to illustrate the sign inversion of the electrostatic field at the two sides of a surface atom. Both AFM images show only one type of interaction, *i.e.*, all surface ions are either repulsive ($d_{\mathrm{ts}} = 50\,\mathrm{pm}$) or attractive ($d_{\mathrm{ts}} = -50\,\mathrm{pm}$) towards a negatively charged tip. Only in the immediate vicinity of the surface ($d_{\mathrm{ts}} = 12\,\mathrm{pm}$) the two ions can be chemically identified and imaged in opposite contrast. Naturally, an AFM tip with an opposite point charge would invert the contrast, just like the force-distance curve of two oppositely charged tips are simply inverted. The immediate vicinity to the surface where the two surface ions can be chemically distinguished is unphysical, and cannot be considered as originating from a rapidly decaying electrostatic field in the calculations – it most likely originates from the difference in the ionic radii of the two ions, an effect that might play a role in the vicinity of $d_{\mathrm{ts}} = 0$. This argument is further supported by the shape of the frequency-shift vs. distance curve in Fig. 109, since the curves resemble the Lennard-Jones curves at further distances from the surface. At these tip-sample distances ($d_{\mathrm{ts}} > 100\,\mathrm{pm}$) the AFM contrast should be well-simulated.

Die approbierte gedruckte Originalversion dieser Dissertation ist an der TU Wien Bibliothek verfügbar.
The approved original version of this doctoral thesis is available in print at TU Wien Bibliothek.
TU Bibliothek Your knowledge hub WIEN

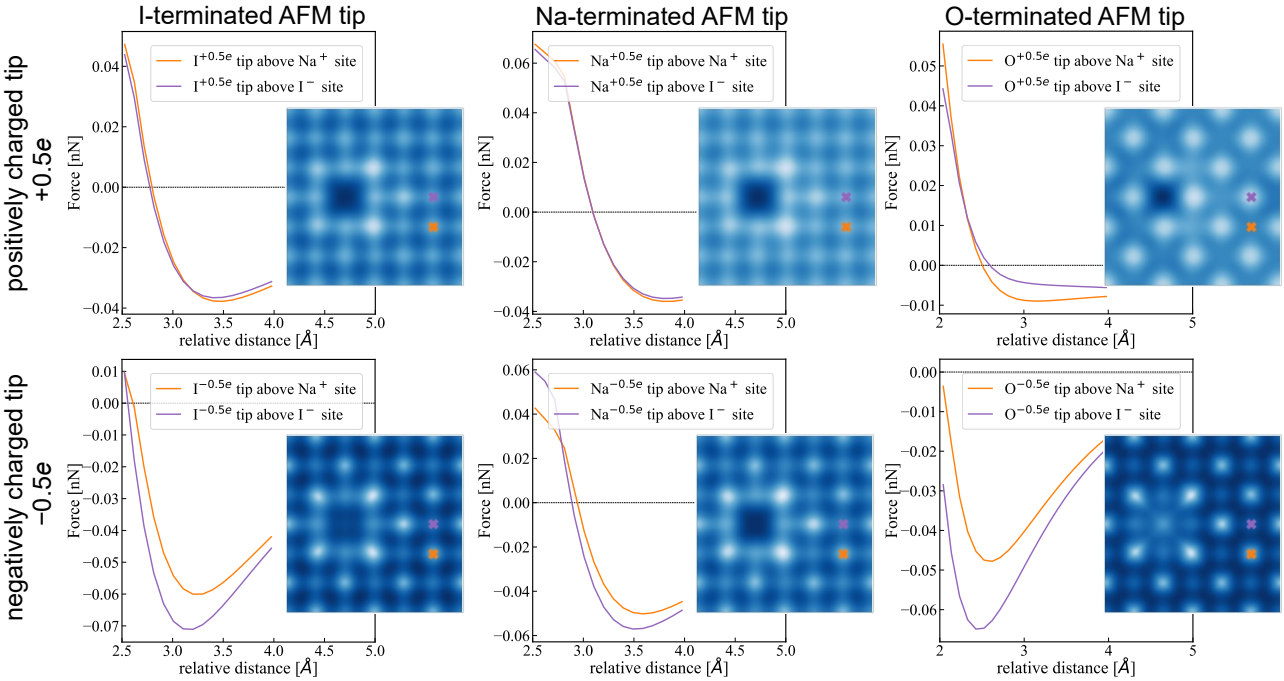

Figure 110: **AFM contrast simulation over the NaI(001) surface with a single Na vacancy, using the Probe Particle Model.** The Probe Particle model [230, 436] was applied to a DFT-optimized NaI(001) surface with one Na vacancy and one Eu substitutional dopant, as calculated in Fig. 108c; The model was additionally provided with the electric field of the sample derived from DFT. Simulated force-distance curves were calculated above Na/I sites on the surface, marked by orange/purple crosses, using three different tip terminations (I, Na, and O) and both tip charge polarities for each chemically different tip. The force-distance curve for each combination of tips and their polarities is supplemented by a single simulated constant-height AFM image ($d_{\mathrm{ts}} \approx 350\,\mathrm{pm}$) obtained from the Probe Particle model with $A = 50\,\mathrm{pm}$. The tip-sample distance d_{ts} is defined as the distance between the center point of the oscillation and the most-protruding atom at the surface. Each simulated AFM image showed attraction towards all surface ions, and the color scheme is correspondingly only blue-white (repulsion would be represented with red, as in Fig. 109).

4.2.2 Probe Particle model

AFM simulation technique with a better approximation compared to technique that uses only the electrostatic considerations is the Probe Particle model developed by Hapala *et al.* [230, 436], available for download at [450]. In this model, a selected probe particle is used as an AFM tip apex – almost any element in the periodic table can be selected, but the O atom as the apex of the CO molecule is commonly used. This model accounts to some degree for the chemical reactivity of the selected atom at an apex of an AFM tip, by constructing a Lennard-Jones type potential between a selected atom at the tip and the atoms at the surface using the available general parameters. The model can additionally be supplemented by a Hartree potential above the surface obtained from DFT-calculations, to add electrostatic contributions to the AFM contrast based on the selected charge quantity and polarity on the tip apex, as described for the previous model demonstrated in Fig. 109.

The results obtained from the Probe Particle model on the same NaI(001) surface as in Fig. 109 are shown in Fig. 110. The AFM contrast was simulated with three chemically different atoms at the AFM tip apex, and each tip was tested with both negative and positive charge at the tip. From the electrostatic considerations, it would be expected that all tips with positive/negative charge show repulsion/attraction towards Na/I atoms at the surface, but the purely electrostatic AFM simulations in Fig. 109 indicate that this is not easily achievable. On the same note, it would be expected that the Probe Particle model simulates chemical repulsion and attraction over the same and opposite ions on the surface as the one on the simulated AFM tip, respectively. Namely, a Na-terminated tip is expected to image surface Na and I ions in repulsion and attraction, respectively, while the opposite simulated AFM contrast is expected for I-terminated tips. The O-terminated tip is included in the

Die approbierte gedruckte Originalversion dieser Dissertation ist an der TU Wien Bibliothek verfügbar.
The approved original version of this doctoral thesis is available in print at TU Wien Bibliothek.
TU Bibliothek Your knowledge hub WIEN

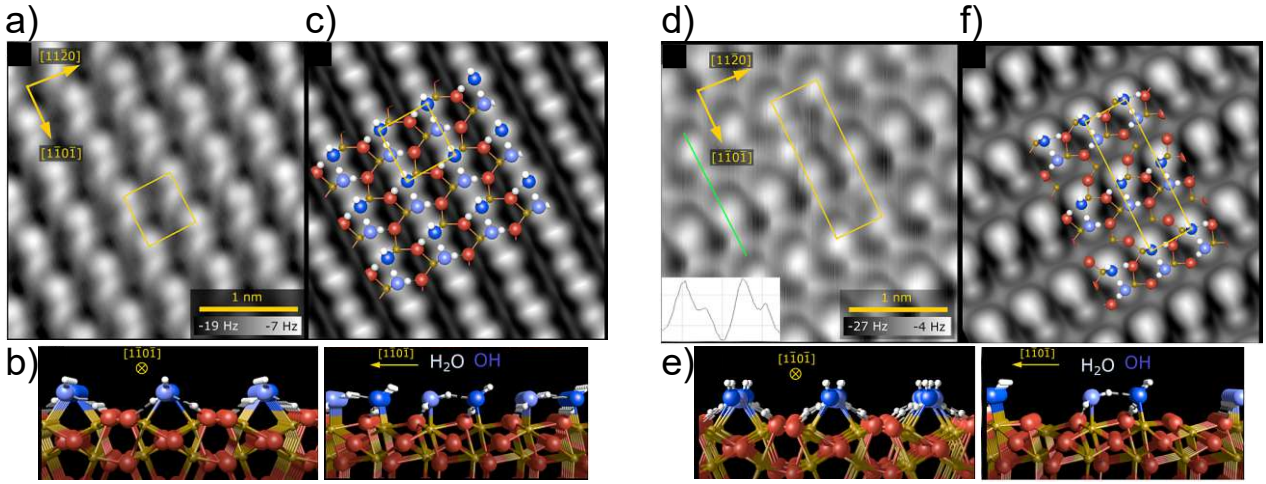

Figure 111: **Water-covered hematite α-Fe_2O_3(1$\bar{1}$02)-(1×1) surface.** a,b,c) Constant-height AFM image, DFT-optimized configuration, and Probe Particle model simulation of the AFM contrast on the clean hematite (1$\bar{1}$02) surface exposed to 6 L of gaseous H_2O in UHV, at the sample temperature of 240 K. d,e,f) Constant-height AFM image, DFT-optimized configuration, and Probe Particle model simulation of the AFM contrast on the clean hematite (1$\bar{1}$02) surface exposed to 10 L of H_2O in UHV, at the sample temperature of 300 K. AFM images were obtained with CO-terminated tips at sample temperature of 5 K by Zděnek Jakub and Martin Setvín, DFT calculations were performed within a PBE+U framework using WIEN2k by Magdalena Bichler and Peter Blaha, and Probe Particle model simulations of the AFM contrast were performed using a negatively-charged flexible CO-terminated AFM tip model with the addition of an electrostatic Hartree potential above the calculated surface structure, which is overlayed on the simulated AFM image. This Figure is a part of the publication titled "Partially dissociated water dimers at the water–hematite interface" [444].

considerations in Fig. 110 to illustrate an interaction of a chemically independent atom with the purely ionic NaI system, which should be highly dependent on the chosen tip polarity. Contrary to these considerations, Fig. 110 indicates that chemical identification of surface ions cannot be achieved this way. All combinations of tip apexes and tip polarities result in similar force-distance curves. Tip polarity seems to be the strongest contributing factor to the force-distance curves in the Probe Particle model. All positively charged tips show similar force-distance curves, that are attractive at large distances and become repulsive as tip-sample distance is lowered below ≈300 pm. Positively charged Na- and I-terminated tips do not distinguish between surface Na and I atoms, while the positively charged O-terminated tip is the most promising and shows the largest difference between force-distance curves above these surface ions. All negatively charged AFM tips also produce force-distance curves that show attractive interaction to both surface ions, regardless of the tip termination. However, negatively charged Na- and I-terminated tips do show some distinction between surface ions, but in a non-consistent way: both exhibit stronger attraction towards surface I ions than surface Na ions, although the opposite behavior is expected for the two tip terminations. The negatively charged O-terminated tip proves as the best choice for distinguishing surface ions, as the force-distance curve above a surface Na atom shows significantly less attraction than the one above a surface I atom. Simulated constant-height AFM images, shown in the inset of the corresponding force-distance curves in Fig. 110, are plotted in a blue-white-red color scheme, where blue represents attraction and red repulsion. All simulated AFM images record surface atoms in attraction, in line with the calculated force-distance curves. Altogether, the Probe Particle model AFM simulator, just like the electrostatic AFM simulator, does not chemically distinguish between oppositely charged ions on a NaI(001) surface. It is noteworthy that the publicly available version of the Probe Particle model at [450] was used to perform these simulations – this Author is unaware of any available improvements, although some seem to be implemented already [451, 452].

The Probe Particle model serves as an excellent tool for simulating AFM images and comparing them to the experimentally obtained ones, when chemical sensitivity towards surface atoms is not required. Moreover, in systems where the tip flexibility plays a role in forming experimental AFM contrast, the Probe Particle model is the tool of choice because it accounts for the lateral movement of a rigid circular atom at the tip-apex by relaxing the position of this atom at each point of an equidistant grid on which the AFM contrast is being

Die approbierte gedruckte Originalversion dieser Dissertation ist an der TU Wien Bibliothek verfügbar.
The approved original version of this doctoral thesis is available in print at TU Wien Bibliothek.
TU Bibliothek Your knowledge hub WIEN

simulated. This feature is particularly useful for simulating AFM images of large complex molecules, often organic, obtained with CO-terminated tips that provide excellent resolution [453, 454, 455], in large part due to their flexibility above long chemical bonds in the molecules. Figure 111 illustrates the applicability of the Probe Particle model to a water-covered hematite α-Fe_2O_3 $(1\bar{1}02)$ surface. In Figs. 111a–c the adsorption of H_2O in a (1×1) pattern (H_2O dosed at 240 K) is studied, while Figs. 111d–f focus on the adsorption of H_2O in a (1×3) periodicity (H_2 dosed at 300 K) with respect to the underlying unreconstructed surface. In both cases, some water molecules dissociate to create terminal OH groups, while others remain in their molecular form. These structures are additionally stabilized by hydrogen bonds between the adsorbed water molecules and hydroxyl groups. In other words, the entire surface is covered by partially dissociated water dimers in both cases [444]. The constant-height AFM images in Fig. 111 were obtained with a CO-terminated tip. Therefore, the Probe Particle model using a negatively-charged, flexible AFM tip, supplemented with the electrostatic potential above the surface obtained through DFT, was applied to the two DFT-optimized structures, and side-by-side comparison with experimental AFM images in Fig. 111 illustrates their qualitative agreement. On the surface exposed to water at a lower temperature, that forms an adsorbate structure with a (1×1) periodicity, simulated AFM images correctly reflect experimental imaging of the H-terminated OH groups and O atoms in undissociated H_2O molecules as an alternating sequence of large and small circular features running along the $[1\bar{1}0\bar{1}]$ direction. On the surface exposed to water at a higher temperature, a sequence of OH groups along the $[1\bar{1}0\bar{1}]$ direction displays the (1×3) periodicity, with the two subsequent OH groups differently tilted. This is also reflected in the simulated AFM images where the large circular features, corresponding to the OH groups, and the small circular features, corresponding to undissociated H_2O molecules, are organized in a zig-zag pattern.

4.2.3 DAC simulator

Figure 112 shows DFT-derived force-distance curves and the corresponding AFM contrast obtained using the DAC simulator on a perfect NaI(001) lattice, without defects. The experimentally-applied, anion-terminated tip for studying the NaI(001) surface in Fig. 108 was mimicked by considering the AFM tip as a single CO molecule, with the negatively charged O atom oriented towards the surface. In reality, an AFM tip termination is far more complex, but discerning the true model of an AFM tip through DFT simulations is an extensive task that requires significant computational effort.

Explicitly simulating force-distance curves with DFT over the two surface ions, seen in Fig. 112a, shows that the approximation of an AFM tip as a single CO molecule yields qualitatively reasonable results. There is no tip-sample interaction at far distance from the surface in both simulated force-distance curves, but as the d_{ts} is reduced, force-distance curve above a surface Na ion exhibits attractive interaction, while the one above a surface I ion is purely repulsive. This trend continues through tip-sample distances relevant for obtaining experimental AFM images. Such behavior is exactly as expected for a negatively charged AFM tip, but it was shown in the two previous models (Figs. 109 and 110) that such behavior is not warranted. At even closer tip-sample distances (d_{ts} <270 pm), Na ions become repulsive towards the CO tip, due to the Pauli repulsion of the ions at the surface and at the tip. In both simulated force-distance curves DFT functionals that treat long-range van der Waals forces were included, yet no attraction is detectable above surface I ions. The attraction/repulsion above Na/I ions is therefore of purely electrostatic origin. The absence of even a small attraction basin above surface I ions in the simulated force-distance curves is possibly due to the small size of the modeled AFM tip, unlike the case in Fig. 44e where the force-distance curves were simulated with a relatively large AFM tip model, which was shown to experience various magnitudes of the attractive van der Waals tip-sample forces depending on its orientation with respect to the surface normal. Explicitly simulated force-distance curves in Fig. 112a can be considered a realistic descriptor of experimental conditions, as they show consistent behavior at tip-sample distance used for obtaining high-quality constant-height AFM images that typically exceed 350 pm.

Chemical distinction of the two surface ions is possible already at large distances from the surface, immediately after the tip-sample interaction becomes detectable, as is seen in Fig. 112b that focuses on this region of the calculated force-distance curves. In experimental AFM conditions, it is desirable to keep an AFM tip as far away as possible from a surface to avoid high tip-sample forces, but still achieve atomically resolved imaging – in the case of the tip-sample interaction shown in Fig. 112b, this would correspond to tip-sample distance of roughly 400 pm, using a small oscillation amplitude. The black rectangle in Fig. 112b marks the values of the tip-sample force in the ±25 pm range around $d_{\mathrm{ts}} = 425$ pm, which are encompassed by an AFM tip fixed at this tip-sample distance and oscillating with an oscillation amplitude of $A = 50$ pm. A simulated AFM image under these conditions was constructed using the DAC simulator and can be seen in Fig. 112c. This simulated constant-height AFM image was constructed by using only the simulated force-distance curves in the black rect-

Die approbierte gedruckte Originalversion dieser Dissertation ist an der TU Wien Bibliothek verfügbar.
The approved original version of this doctoral thesis is available in print at TU Wien Bibliothek.
TU Bibliothek Your knowledge hub WIEN

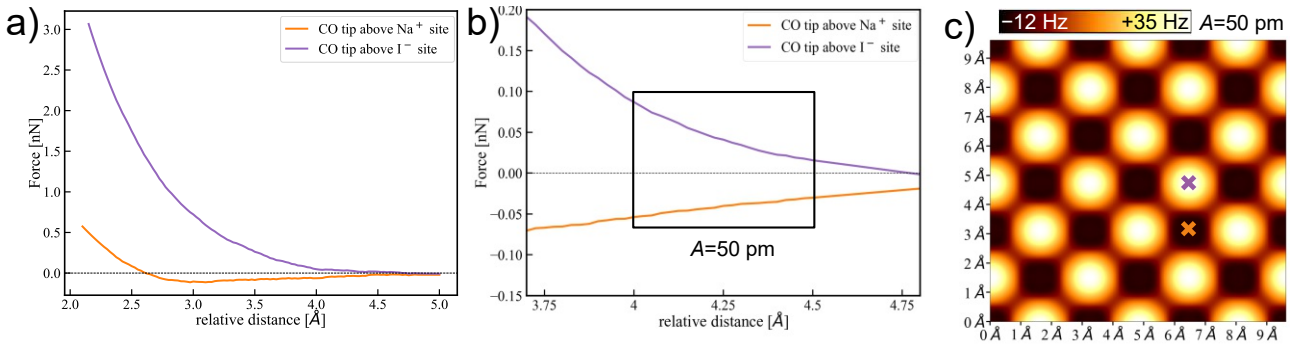

Figure 112: **AFM contrast simulation over the NaI(001) surface using the DAC simulator.** a,b) Explicitly simulated force-distance curves using DFT, necessary as an input for the DAC simulator, performed using a CO terminated tip over a single Na and a single I surface ion on a DFT-optimized structure of a NaI(001) surface, without Na vacancies. A full range of tip-sample distances is shown in (a), while (b) focuses on tip-sample distances relevant for constant-height AFM simulations. Curves were smoothed with a Savitzky-Golay. c) Simulated constant-height AFM image using force-distance curves from (b), with an oscillation amplitude of A =50 pm; the range of forces encompassed by this oscillation amplitude is marked with a rectangle in (b), while purple and orange crosses indicate where the simulated force-distance curves were obtained over I and Na surface ions, respectively. Simulated AFM image displays attraction and repulsion towards differently charged ions, in accord with experimental AFM images.

angle range in Fig. 112b, and the DFT-optimized surface structure of (1×1) NaI(001) surface. Simulating this flat geometry (with a little bit of rumpling, seen in the surface region unrelated to a Na vacancy in Fig. 108) can be considered a good additional test for the DAC simulator, since previous examples in Sections 2.5 and 4.1 were performed on a surface with several protruding species. As can be seen from Fig. 112c, all Na atoms are imaged the same, and the same holds true for all I atoms – the flat surface geometry is therefore properly captured. The biggest advantage of the DAC simulator stems from correctly simulating the opposite contrast over the two oppositely charged ions at the surface. The CO-terminated tip simulates contrast over Na atoms as attractive with a negative frequency shift (black features in Fig. 112c), and I atoms as repulsive with a positive frequency shift (bright features in Fig. 112c). The stronger frequency shift is simulated above the surface I ions, according to the force-distance curves in Fig. 112b that exhibit stronger electrostatic repulsion towards I ions compared to the electrostatic attraction towards Na ions. The I ions are simulated as slightly larger features than Na ions, and a similar effect, albeit less pronounced, is visible in the experimentally measured AFM images in Fig. 108a and Fig. 108b. The slight discrepancy between the size of the ions in experimental and simulated AFM images can likely be attributed to the difference in the ionic radii of the atom terminating the experimental AFM tip and the O atom from the CO molecule used in calculations. Comparison of the simulated (Fig. 112c) and experimentally measured (Fig. 108a and Fig. 108b) AFM images also reveals that the artifact faint bright lines that connect the neighboring I atoms in simulations are also present in experiments, and their origin can therefore be attributed to purely electrostatic effects because the DAC simulator does not recognize the lateral flexibility of a CO tip.

It remains to be investigated how a single Na vacancy in an otherwise perfect (1×1) lattice would be simulated using the DAC simulator. A single O vacancy on a rutile TiO_2(110) surface was already successfully simulated using this method in Figs. 44f and 107, and showed an excellent match with experimental AFM images, *i.e.*, even the lattice distortion surrounding the V_O was well-replicated. However, this was a point defect on a covalent surface. Charged defects on a purely ionic surface typically have a recognizable shape and contrast – both the Na vacancy on the NaI(001) surface in Fig. 108b and the Sr vacancy on the SrO-terminated $SrTiO_3$(001) surface in Fig. 64 for example, are imaged very similarly. Experience shows that simulating an AFM contrast over these charged defects on an ionic surface is challenging, and neither the electrostatic model (Fig. 109) nor the Probe Particle model (Fig. 110) showed much success in simulating the contrast above a Na vacancy.

To simulate the contrast above a Na vacancy using the DAC simulator, the two force-distance curves in Fig. 108b would most probably not be sufficient, and an additional force-distance curve should be calculated directly above a Na vacancy in a DFT-optimized structure. This would complete the first step of the DAC simulator. Then, surface ions would be divided and grouped in three groups, according to the procedure in

Die approbierte gedruckte Originalversion dieser Dissertation ist an der TU Wien Bibliothek verfügbar.
The approved original version of this doctoral thesis is available in print at TU Wien Bibliothek.
TU Bibliothek Your knowledge hub WIEN

Fig. 106. In this example, Na ions would constitute the blue group, I ions the red group, and a single Na vacancy would be considered as an excess atom replacing a single Na atom, and constitute a sole member of the green group. Then, three force-distance curves would be applied to the three groups, and the simulated AFM image would be formed. Since a force-distance curve would be explicitly simulated above a Na vacancy to capture the tip-sample interaction at this point, it is expected that the simulated AFM images would reasonably reflect the experimental observations.

4.2.4 Conclusions

All procedures presented here simulate experimentally obtained AFM images over the NaI(001) surface to some extent. It was shown that the electrostatic model and the Probe Particle model do not chemically distinguish between Na^+ and I^- ions at this ionic surface. Instead, they correctly simulate the surface geometry, but all surface ions are imaged with the same type of tip-sample interaction: either all are attractive or all are repulsive, depending mainly on the charge of a simulated AFM tip termination. Under certain conditions, there is a distinction between the two ions, but the distinction lies only in the strength of the interaction and not in its nature. This distinction can be used to simulate AFM images after suitable processing, but cannot provide chemical identification of surface ions.

The simulated force-distance curves using a negatively-charged CO tip as a model for an AFM tip proved as the most promising approach to simulating the opposite tip-sample interaction above the two oppositely charged surface ions. They exhibit attraction towards Na^+ ions, and repulsion towards I^- surface ions. These simulated force-distance curves can be efficiently transformed to simulated constant-height AFM images using the DAC simulator, that are obtained at far distances from the surface and properly simulate experimental AFM imaging conditions. Moreover, it was demonstrated that the DAC simulator creates well-resolved and realistic simulated AFM images with only a very limited number of simulated force-distance curves, which significantly reduces the computational effort but still provides chemical sensitivity.

Die approbierte gedruckte Originalversion dieser Dissertation ist an der TU Wien Bibliothek verfügbar.
The approved original version of this doctoral thesis is available in print at TU Wien Bibliothek.
TU Bibliothek Your knowledge hub WIEN

4.3 Summary and Outlook

The concept of comparison between experimentally and theoretically obtained results at the atomic level, obtained by AFM and DFT respectively, was explored in this Chapter. Several approaches to simulating AFM contrast are introduced and explored, namely the electrostatic model, the Probe Particle model, and the DFT-derived AFM contrast (DAC) simulator. To illustrate and quantify the contrast simulation procedure in each, all three were applied to a NaI(001) surface. The three approaches vary in their level of approximation, and DAC simulator employs the finest of the three. It is therefore most reliable in simulating the forces between an AFM tip and surface atoms, and provides chemical distinction between different atoms at a surface. However, it is also computationally the most expensive method, despite significant efforts in minimizing the number of necessary DFT calculations for obtaining a DFT-derived AFM contrast simulation. All three simulation methods provide good results up to a certain degree, and the choice of preferred method depends on the available computational resources and the desired level of precision. The DAC simulator is currently employed in studies on several different systems where the chemical identification of surface atoms is desirable. Further improvements to the DAC procedure developed and applied in the research that led to this Thesis still remain to be implemented, with a wide range of extensions to the method remaining open.

Die approbierte gedruckte Originalversion dieser Dissertation ist an der TU Wien Bibliothek verfügbar.
The approved original version of this doctoral thesis is available in print at TU Wien Bibliothek.
TU Bibliothek Your knowledge hub WIEN

Chapter 5

Summary and Outlook

This Thesis systematically applied AFM/STM to image complex oxide surfaces with a resolution of a single atom. Surfaces were computationally modeled at the quantum mechanical level within the framework of DFT. The experimental and theoretical results were used to unravel surface structures and electronic properties. Direct comparison between experimentally obtained and DFT-derived AFM simulations was shown to give useful insights.

It was shown on an example of a model binary oxide surface, reduced rutile $TiO_2(110)$, that the proper characterization of its interactions with small gas molecules requires a precise knowledge of its ground state. Taking electron polarons at a reduced surface into account during DFT calculations greatly aids in explaining the experimental observations. Physisorbed CO molecules were shown to slightly alter the polaronic state, while chemisorbed O_2 molecules use the excess electrons to form strong bonds to the substrate, thereby depleting the surface of polarons. Therefore, two extreme cases of gas adsorbates interacting with a polaronic surface were pursued. It remains interesting to investigate whether adsorption of some gases could completely preserve the polaronic ground state: chemisorbed molecules that deplete other electron sources, or physisorbed molecules (excluding noble gases) that bound so weekly that the polarons remain unaffected. Experimentally, it was shown that the use of the non-destructive AFM technique is advantageous for studying the adsorption of small gas molecules to a reduced rutile $TiO_2(110)$, because the adsorbates are not disturbed *via* injected electrons necessary for STM. When applicable, simultaneous STM imaging provided complementary insights into the electronic structure of surfaces, with a resolution of a single molecular orbital of the adsorbed CO molecules. In the case of O_2, STM imaging of the molecular orbitals was not achievable because addition/removal of electrons from the adsorbates activates electron- and hole-mediated processes, and the non-destructive imaging was the key to observing all adsorption configurations. Such insights, combined with a series of experiments after which the reaction products were observed, answered several discrepancies and long-standing questions in literature.

Beside revealing fundamental, quantum mechanical processes that occur during adsorption of small gas molecules in UHV at low temperatures, the two presented studies provide solid grounds for technical applications. It was demonstrated that the electronic structure of the rutile $TiO_2(110)$ surface is sensitive to the presence of gases – it changes in the case of both CO and O_2. This demonstrates the applicability of rutile $TiO_2(110)$ surfaces as gas sensing materials, albeit more efficiently as an O_2 sensor. The precise characterization of UV- and temperature-induced O_2 reaction products offers possibility for designing chemical reactions on the surface. The dissociation of some O_2 species at a surface, due to UV irradiation or invested thermal energy, provides isolated oxygen atoms, which can potentially mediate oxidation of other co-adsorbed gases. Finally, the methodology applied to these two adsorption cases is expandable readily applicable to studying other oxide surfaces and their interaction with gases.

A novel method was developed for creating bulk-terminated surfaces of a model perovskite oxide surface, $SrTiO_3(001)$, that overcomes the limitations of the bulk cubic symmetry by creating inequivalent planes of cleavage *via* a strain-induced quantum phase transition to ferroelectricity. AFM was shown to be the technique of choice for studying the two terminations of an as-cleaved surface, the TiO_2 and SrO terminations, since STM does not provide atomic resolution. The surfaces were thoroughly characterized at the atomic level to reveal that they are covered by polarity-compensating point defects, and that they exhibit drastically different electronic properties. The concentration of adatoms/vacancies is always the same on cleaved surfaces, regardless of cleaving temperatures or the concentration of extrinsic Nb-dopants. This makes the cleaving procedure a reproducible pathway to obtaining a surface which is *a priori* characterized by a dispersed distribution of

Die approbierte gedruckte Originalversion dieser Dissertation ist an der TU Wien Bibliothek verfügbar.
The approved original version of this doctoral thesis is available in print at TU Wien Bibliothek.
TU Bibliothek Your knowledge hub WIEN

charged point defects that are likely highly-reactive, and could mediate a series of chemical reactions.

Both terminations of the as-cleaved surface were shown to be unstable upon annealing, and become disordered even below 500 °C. The $SrTiO_3(001)$ surfaces prepared by wet-chemical treatment were shown to be contaminated, and the temperature necessary for removing carbon-based contaminants in UHV conditions lie beyond the stability range of the unreconstructed surface. In other words, (1×1) $SrTiO_3(001)$ surfaces were achieved only *via* cleaving. These results are somewhat at odds with the conventional approach to $SrTiO_3(001)$ surfaces. They imply that the assumption of a (1×1) terminated surface is far from warranted, and that a simple picture of a bulk-terminated surface structures on $SrTiO_3(001)$, and possibly on the surfaces of other cubic perovskite oxides, needs to be re-evaluated. Structurally well-characterized surfaces are essential for their reliable modeling from first principles, and for understanding the fundamental processes that occur at them. The results obtained during the research that led to this Thesis provide a pathway to achieving this requirement at surfaces of this complex oxide.

Cleaved surfaces were additionally systematically investigated through macroscopic techniques, and both the cleaving process and the pre-straining procedure were investigated and explained in detail. It was shown that the application of in-plane strain prior to cleaving can also be used on another perovskite oxide. This opens up a possibility of universality, and it remains to be investigated in which portion can other perovskite oxide cleave using this procedure; it is expected however, that they exhibit a plethora of polarity-compensating mechanisms that could be responsible for additional unexpected surface properties, as in the case of $SrTiO_3$. Cleaved $SrTiO_3(001)$ with 0.69 at.% of Nb-doping were used for a case study for almost all experiments, where the two domains span several micrometers between the domain walls; cleaved surfaces with a lower Nb-content develop smaller domains. This implies that a difference of one electron per 100 unit cells can greatly influence the mesoscopic properties of cleaved surfaces, providing a pathway to well-controlled manipulation of the desired surface morphology. Moreover, the two terminations, the size of which was shown to be susceptible to engineering, have drastically different electronic properties. The broken symmetry responsible for succesfull cleavages was shown to induce several phenomena otherwise not expected for a $SrTiO_3(001)$ surface. Cleaved surfaces were shown to separate free charge carriers upon UV irradiation, but only on the semiconducting SrO. The two completely inequivalent surface terminations can therefore provide a good foundation for performing heterogeneous catalysis or photocatalysis through different processes occurring at different surface terminations. The long lifetime of the charged SrO termination upon UV irradiation, and its well controlled charge state manipulation *via* injecting or removing electrons, provide promising grounds for its utilization in electronics: the entire SrO termination can be simultaneously charged by UV, while engineered charge injection returns it locally to its ground state. These processes add a wide range of possible applications on this already technologically relevant surface. This entire research demonstrated that a surface with intriguing properties, otherwise not characteristic for $SrTiO_3(001)$ surfaces, can be created by simply breaking a $SrTiO_3$ crystal in half.

The explicitly simulated force-distance curves *via* DFT were shown to be a most reliable descriptor of the experimentally observed AFM contrast. In order to simulate constant-height AFM images with a DFT-derived contrast, a procedure was developed based on the superposition of calculated forces with as few DFT-calculated force-distance curves as possible. This procedure was applied to simulating realistic AFM images, and chemical sensitivity was demonstrated. It was shown that such procedure can be used to cross check and validate theoretically proposed structural models by comparison of the experimental and simulated AFM images. This approach is therefore promising for simulating experimentally relevant AFM images, and it was demonstrated to be to well-applicable to various systems.

Die approbierte gedruckte Originalversion dieser Dissertation ist an der TU Wien Bibliothek verfügbar.
The approved original version of this doctoral thesis is available in print at TU Wien Bibliothek.
TU Bibliothek Your knowledge hub WIEN

Bibliography

[1] P. Hohenberg and W. Kohn. Inhomogeneous electron gas. *Physical Review*, 136:B864, 1964.

[2] W. Kohn and L. J. Sham. Self-consistent equations including exchange and correlation effects. *Physical Review*, 140:A1133, 1965.

[3] Walter Kohn. Nobel lecture: Electronic structure of matter—wave functions and density functionals. *Reviews of Modern Physics*, 71:1253, 1999.

[4] M. Planck. *The theory of heat radiation*. Courier Corporation, 1913.

[5] P. Ágoston, K. Albe, R. M. Nieminen, and M. J. Puska. Intrinsic n-type behavior in transparent conducting oxides: A comparative hybrid-functional study of In_2O_3, SnO_2, and ZnO. *Physical Review Letters*, 103:245501, 2009. DOI: 10.1103/PhysRevLett.103.245501.

[6] C. Franchini, R. Podloucky, J. Paier, M. Marsman, and G. Kresse. Ground-state properties of multivalent manganese oxides: Density functional and hybrid density functional calculations. *Physical Review B*, 75:195128, 2007. DOI: 10.1103/PhysRevB.75.195128.

[7] L. Y. Lim, S. Lany, Y. J. Chang, E. Rotenberg, A. Zunger, and M. F. Toney. Angle-resolved photoemission and quasiparticle calculation of ZnO: The need for d band shift in oxide semiconductors. *Physical Review B*, 86:235113, 2012. DOI: 10.1103/PhysRevB.86.235113.

[8] D. R. Hartree. The wave mechanics of an atom with a non-Coulomb central field. part II. Some results and discussion. In *Mathematical Proceedings of the Cambridge Philosophical Society*, volume 24, page 111. Cambridge University Press, 1928.

[9] V. Fock. Näherungsmethode zur Lösung des quantenmechanischen Mehrkörperproblems. *Zeitschrift für Physik*, 61:126, 1930.

[10] Chr. Møller and M. S. Plesset. Note on an approximation treatment for many-electron systems. *Physical Review*, 46:618, 1934.

[11] P. A. M. Dirac. Note on exchange phenomena in the Thomas atom. In *Mathematical Proceedings of the Cambridge Philosophical Society*, volume 26, page 376. Cambridge University Press, 1930.

[12] G. Seifert, D. Porezag, and Th. Frauenheim. Calculations of molecules, clusters, and solids with a simplified LCAO-DFT-LDA scheme. *International Journal of Quantum Chemistry*, 58:185, 1996.

[13] K. Burke. Perspective on density functional theory. *The Journal of Chemical Physics*, 136:150901, 2012.

[14] J. P. Perdew and Y. Wang. Accurate and simple analytic representation of the electron-gas correlation energy. *Physical Review B*, 45:13244, 1992.

[15] J. P. Perdew, K. Burke, and M. Ernzerhof. Generalized gradient approximation made simple. *Physical Review Letters*, 77:3865, 1996.

[16] O. F. Sankey and D. J. Niklewski. *Ab initio* multicenter tight-binding model for molecular-dynamics simulations and other applications in covalent systems. *Physical Review B*, 40:3979, 1989.

[17] V. I. Anisimov, J. Zaanen, and O. K. Andersen. Band theory and Mott insulators: Hubbard U instead of Stoner I. *Physical Review B*, 44:943, 1991.

Die approbierte gedruckte Originalversion dieser Dissertation ist an der TU Wien Bibliothek verfügbar.
The approved original version of this doctoral thesis is available in print at TU Wien Bibliothek.
TU Bibliothek Your knowledge hub WIEN

[18] L. Hedin. New method for calculating the one-particle Green's function with application to the electron-gas problem. *Physical Review*, 139:A796, 1965.

[19] L. Dagum and R. Menon. OpenMP: an industry standard API for shared-memory programming. *IEEE Computational Science and Engineering*, 5:46, 1998.

[20] W. Gropp, E. Lusk, N. Doss, and A. Skjellum. A high-performance, portable implementation of the MPI message passing interface standard. *Parallel Computing*, 22:789, 1996.

[21] VSC-3 homepage. URL: https://vsc.ac.at//systems/vsc-3/.

[22] G. Kresse and J. Furthmüller. Efficient iterative schemes for *ab-initio* total-energy calculations using a plane-wave basis set. *Physical Review B*, 54:11169, 1996.

[23] G. Kresse and J. Furthmüller. Efficiency of *ab-initio* total energy calculations for metals and semiconductors using a plane-wave basis set. *Computational Materials Science*, 6:15, 1996.

[24] VASP wiki. URL: https://www.vasp.at/wiki/index.php/The_VASP_Manual.

[25] P. Blaha, K. Schwarz, G. K. H. Madsen, D. Kvasnicka, J. Luitz, R. Laskowski, F. Tran, and L. D. Marks. WIEN2k, an augmented plane wave+local orbitals program for calculating crystal properties. *(Karlheinz Schwarz, Techn. Universität Wien, Austria)*, 2018. ISBN: 3-9501031-1-2.

[26] K. Schwarz and P. Blaha. Solid state calculations using WIEN2k. *Computational Materials Science*, 28:259, 2003.

[27] P. Blaha, K. Schwarz, F. Tran, R. Laskowski, G. K. H. Madsen, and L. D. Marks. WIEN2k: An APW+lo program for calculating the properties of solids. *The Journal of Chemical Physics*, 152:074101, 2020.

[28] G. Kresse and D. Joubert. From ultrasoft pseudopotentials to the projector augmented-wave method. *Physical Review B*, 59:1758, 1999.

[29] F. Bloch. Über die Quantenmechanik der Elektronen in Kristallgittern. *Zeitschrift für Physik*, 52:555, 1929.

[30] R. Bliem, E. McDermott, P. Ferstl, M. Setvin, O. Gamba, J. Pavelec, M. A. Schneider, M. Schmid, U. Diebold, P. Blaha, L. Hammer, and G. S. Parkinson. Subsurface cation vacancy stabilization of the magnetite (001) surface. *Science*, 346:1215, 2014. DOI: 10.1126/science.1260556.

[31] M. Smeu, H. Guo, W. Ji, and R. A. Wolkow. Electronic properties of Si(111) – 7×7 and related reconstructions: Density functional theory calculations. *Physical Review B*, 85:195315, 2012. DOI: 10.1103/PhysRevB.85.195315.

[32] C. Davisson and L. H. Germer. Diffraction of electrons by a crystal of nickel. *Physical Review*, 30:705, 1927.

[33] C. Davisson and L. H. Germer. The scattering of electrons by a single crystal of nickel. *Nature*, 119:558, 1927.

[34] L. De Broglie. *Recherches sur la théorie des quanta*. PhD thesis, Migration-université en cours d'affectation, 1924.

[35] W. H. Bragg and W. L. Bragg. The reflection of X-rays by crystals. *Proceedings of the Royal Society of London. Series A, Containing Papers of a Mathematical and Physical Character*, 88:428, 1913.

[36] A. Einstein. Zur Elektrodynamik Bewegter Körper. *Annalen der Physik*, 4, 1905.

[37] M. P. Seah and W. A. Dench. Quantitative electron spectroscopy of surfaces: A standard data base for electron inelastic mean free paths in solids. *Surface and Interface Analysis*, 1:2, 1979.

[38] J. Henk. Theory of low-energy electron diffraction and photoelectron spectroscopy from ultra-thin films. In *Handbook of Thin Films*, page 479. Elsevier, 2002.

Die approbierte gedruckte Originalversion dieser Dissertation ist an der TU Wien Bibliothek verfügbar.
The approved original version of this doctoral thesis is available in print at TU Wien Bibliothek.
TU Bibliothek Your knowledge hub WIEN

[39] R. N. Bracewell. *The Fourier transform and its applications*, volume 31999. McGraw-Hill New York, 1986.

[40] P. P. Ewald. Die Berechnung optischer und elektrostatischer Gitterpotentiale. *Annalen der Physik*, 369:253, 1921.

[41] Dr. Peter Kury. WinSPA documentation. URL: http://www.winspa.de/.

[42] M. M. M. Jansen, B. E. Nieuwenhuys, D. C. Ferré, and J. W. Niemantsverdriet. Influence of nitrogen atoms on the adsorption of CO on a Rh(100) single crystal surface. *The Journal of Physical Chemistry C*, 113:12277, 2009. DOI: 10.1021/jp8111028.

[43] D. J. Chadi, R. S. Bauer, R. H. Williams, G. V. Hansson, R. Z. Bachrach, J. C. Mikkelsen Jr, F. Houzay, G. M. Guichar, R. Pinchaux, and Y. Petroff. Atomic and electronic structure of the 7×7 reconstructed Si(111) surface. *Physical Review Letters*, 44:799, 1980.

[44] B. Qi, S. Ólafsson, M. Göthelid, H. P. Gislason, and B. Agnarsson. Photoemission and low energy electron microscopy study on the formation and nitridation of indium droplets on Si(111) 7×7 surfaces. *Thin Solid Films*, 531:61, 2013. DOI: 10.1016/j.tsf.2012.12.022.

[45] P. Steiner, F. J. Reiter, H. Höchst, S. Hüfner, and J. C. Fuggle. Lineshape of the KL2L3(^{1}D2) Auger line in magnesium and sodium metal. *Physics Letters A*, 66:229, 1978.

[46] J. E. Castle, L. B. Hazell, and R. D. Whitehead. X-ray photoelectron spectroscopy using Si $K\alpha$ radiation. *Journal of Electron Spectroscopy and Related Phenomena*, 9:247, 1976.

[47] C. J. Powell. Recommended Auger parameters for 42 elemental solids. *Journal of Electron Spectroscopy and Related Phenomena*, 185:1, 2012.

[48] J. A. Taylor and J. W. Rabalais. Reaction of N_2^+ beams with aluminum surfaces. *The Journal of Chemical Physics*, 75:1735, 1981.

[49] M. Siegbahn. *Spektroskopie der Röntgenstrahlen*. Springer, Berlin, Heidelberg, 1931. ISBN: 978-3-642-50783-0.

[50] R. Jenkins, R. Manne, R. Robin, and C. Senemaud. IUPAC–nomenclature system for X-ray spectroscopy. *X-Ray Spectrometry*, 20:149, 1991.

[51] Scienta Omicron homepage. URL: https://scientaomicron.com/en.

[52] D. R. Baer and S. Thevuthasan. Characterization of thin films and coatings. In *Handbook of Deposition Technologies for Films and Coatings*, page 749. Elsevier, 2010. DOI: 10.1016/B978-0-8155-2031-3.00016-8.

[53] A. G. Shard. X-ray photoelectron spectroscopy. In *Characterization of Nanoparticles*, page 349. Elsevier, 2020. DOI: 10.1016/B978-0-12-814182-3.00019-5.

[54] T. L. Alford, L. C. Feldman, and J. W. Mayer. X-ray photoelectron spectroscopy. In *Fundamentals of Nanoscale Film Analysis*, page 149. Springer US, 2007. DOI: 10.1007/978-0-387-29261-8_10.

[55] R. Bliem, J. E. S. van der Hoeven, J. Hulva, J. Pavelec, O. Gamba, P. E. de Jongh, M. Schmid, P. Blaha, U. Diebold, and G. S. Parkinson. Dual role of CO in the stability of subnano Pt clusters at the Fe_3O_4(001) surface. *Proceedings of the National Academy of Sciences*, 113:8921, 2016. DOI: 10.1073/pnas.1605649113.

[56] NIST xps database. URL: https://srdata.nist.gov/xps/main_search_menu.aspxl.

[57] N. Gurker, M. F. Ebel, and H. Ebel. Imaging XPS–A new technique, I–principles. *Surface and interface analysis*, 5:13, 1983.

[58] S. Kundu, W. Xia, W. Busser, M. Becker, D. A. Schmidt, M. Havenith, and M. Mühler. The formation of nitrogen-containing functional groups on carbon nanotube surfaces: a quantitative XPS and TPD study. *Physical Chemistry Chemical Physics*, 12:4351, 2010.

[59] S. A. Chambers. Epitaxial film crystallography by high-energy Auger and X-ray photoelectron diffraction. *Advances in Physics*, 40:357, 1991.

Die approbierte gedruckte Originalversion dieser Dissertation ist an der TU Wien Bibliothek verfügbar.
The approved original version of this doctoral thesis is available in print at TU Wien Bibliothek.
TU Bibliothek Your knowledge hub WIEN

[60] G. Binnig, H. Rohrer, C. Gerber, and E. Weibel. Surface studies by scanning tunneling microscopy. *Physical Review Letters*, 49:57, 1982.

[61] G. Binnig, H. Rohrer, C. Gerber, and E. Weibel. 7×7 reconstruction on Si(111) resolved in real space. *Physical Review Letters*, 50:120, 1983.

[62] G. Binnig and H. Rohrer. Scanning tunneling microscopy—from birth to adolescence. *Reviews of Modern Physics*, 59:615, 1987. DOI: 10.1103/RevModPhys.59.615.

[63] S. C. Miller Jr and R. H. Good Jr. A WKB-type approximation to the Schrödinger equation. *Physical Review*, 91:174, 1953.

[64] M. A. Johnson and M. H. Moradi. *PID control*. Springer, 2005.

[65] A. Luican-Mayer and E. Y. Andrei. Probing Dirac fermions in graphene by scanning tunneling microscopy and spectroscopy. In *Physics of Graphene*, page 29. Springer, 2014. DOI: 10.1007/978-3-319-02633-6_2.

[66] S. C. Ganguli. Real space investigation of order-disorder transition of vortex lattice in Co-intercalated 2H–$NbSe_2$. *arXiv preprint arXiv:1609.03487*, 2016. URL: https://arxiv.org/abs/1609.03487.

[67] M. S. J. Marshall and M. R. Castell. Scanning tunnelling microscopy of epitaxial nanostructures. *Chemical Society Reviews*, 43:2226, 2014. DOI: 10.1039/C3CS60458F.

[68] J. Tersoff and D. R. Hamann. Theory and application for the scanning tunneling microscope. *Physical Review Letters*, 50:1998, 1983.

[69] J. Tersoff and D. R. Hamann. Theory of the scanning tunneling microscope. *Physical Review B*, 31:805, 1985.

[70] J. Bardeen. Tunnelling from a many-particle point of view. *Physical Review Letters*, 6:57, 1961.

[71] J. C. Chen. Origin of atomic resolution on metal surfaces in scanning tunneling microscopy. *Physical Review Letters*, 65:448, 1990.

[72] R. Wolkow and P. Avouris. Atom-resolved surface chemistry using scanning tunneling microscopy. *Physical Review Letters*, 60:1049, 1988. DOI: 10.1103/PhysRevLett.60.1049.

[73] L. Jones, S. Wang, X. Hu, S. ur Rahman, and M. R. Castell. Maximising the resolving power of the scanning tunneling microscope. *Advanced Structural and Chemical Imaging*, 4:1, 2018. DOI: 10.1186/s40679-018-0056-7.

[74] G. Binnig, C. F. Quate, and C. Gerber. Atomic force microscope. *Physical Review letters*, 56:930, 1986.

[75] D. Rugar and P. Hansma. Atomic force microscopy. *Physics Today*, 43:23, 1990.

[76] Q. Zhong, D. Inniss, K. Kjoller, and V. B. Elings. Fractured polymer/silica fiber surface studied by tapping mode atomic force microscopy. *Surface Science*, 290:L688, 1993.

[77] P. K. Hansma, J. P. Cleveland, M. Radmacher, D. A. Walters, P. E. Hillner, M. Bezanilla, M. Fritz, D. Vie, H. G. Hansma, C. B. Prater, J. Massie, L. Fukunaga, J. Gurley, and V. Elings. Tapping mode atomic force microscopy in liquids. *Applied Physics Letters*, 64:1738, 1994.

[78] F. J. Giessibl. Advances in atomic force microscopy. *Reviews of Modern Physics*, 75:949, 2003.

[79] B. Voigtländer. *Scanning probe microscopy: Atomic force microscopy and scanning tunneling microscopy*. Springer, 2015.

[80] F. J. Giessibl. The qPlus sensor, a powerful core for the atomic force microscope. *Review of Scientific Instruments*, 90:011101, 2019. DOI: 10.1063/1.5052264.

[81] F. Huber and F. J. Giessibl. Low noise current preamplifier for qPlus sensor deflection signal detection in atomic force microscopy at room and low temperatures. *Review of Scientific Instruments*, 88:073702, 2017.

Die approbierte gedruckte Originalversion dieser Dissertation ist an der TU Wien Bibliothek verfügbar.
The approved original version of this doctoral thesis is available in print at TU Wien Bibliothek.
TU Bibliothek Your knowledge hub WIEN

[82] F. J. Giessibl. Sensor for noncontact profiling of a surface, 2013. US Patent 8,393,009.

[83] M. Setvín, J. Javorskỳ, D. Turčinková, I. Matolínová, P. Sobotík, P. Kocán, and I. Ošt'ádal. Ultrasharp tungsten tips—characterization and nondestructive cleaning. *Ultramicroscopy*, 113:152, 2012. DOI: 10.1016/j.ultramic.2011.10.005.

[84] F. J. Giessibl. High-speed force sensor for force microscopy and profilometry utilizing a quartz tuning fork. *Applied Physics Letters*, 73:3956, 1998.

[85] F. J. Giessibl, S. Hembacher, M. Herz, C. Schiller, and J. Mannhart. Stability considerations and implementation of cantilevers allowing dynamic force microscopy with optimal resolution: the qPlus sensor. *Nanotechnology*, 15:S79, 2004.

[86] J. K. Schoelz, P. Xu, S. D. Barber, D. Qi, M. L. Ackerman, G. Basnet, C. T. Cook, and P. M. Thibado. High-percentage success method for preparing and pre-evaluating tungsten tips for atomic-resolution scanning tunneling microscopy. *Journal of Vacuum Science & Technology B, Nanotechnology and Microelectronics: Materials, Processing, Measurement, and Phenomena*, 30:033201, 2012.

[87] N. Pavliček and L. Gross. Generation, manipulation and characterization of molecules by atomic force microscopy. *Nature Reviews Chemistry*, 1:1, 2017. DOI: 10.1038/s41570-016-0005.

[88] L. Almonte and J. Colchero. True non-contact atomic force microscopy imaging of heterogeneous biological samples in liquids: Topography and material contrast. *Nanoscale*, 9:2903, 2017. DOI: 10.1039/C6NR07967A.

[89] Y. Sugimoto, Y. Nakajima, D. Sawada, K. Morita, M. Abe, and S. Morita. Simultaneous AFM and STM measurements on the Si(111)-(7× 7) surface. *Physical Review B*, 81:245322, 2010. DOI: 10.1103/PhysRevB.81.245322.

[90] M. P. Boneschanscher, J. van der Lit, Z. Sun, I. Swart, P. Liljeroth, and D. Vanmaekelbergh. Quantitative atomic resolution force imaging on epitaxial graphene with reactive and nonreactive AFM probes. *ACS Nano*, 6:10216, 2012. DOI: 10.1021/nn3040155.

[91] S. Sadewasser and T. Glatzel. *Kelvin probe force microscopy*, volume 48. Springer, 2012.

[92] A. Sadeghi, A. Baratoff, S. A. Ghasemi, S. Goedecker, T. Glatzel, S. Kawai, and E. Meyer. Multiscale approach for simulations of Kelvin probe force microscopy with atomic resolution. *Physical Review B*, 86:075407, 2012.

[93] H. C. Hamaker. The London–van der Waals attraction between spherical particles. *Physica*, 4:1058, 1937.

[94] M. Guggisberg, M. Bammerlin, C. Loppacher, O. Pfeiffer, A. Abdurixit, V. Barwich, R. Bennewitz, A. Baratoff, E. Meyer, and H.-J. Güntherodt. Separation of interactions by noncontact force microscopy. *Physical Review B*, 61:11151, 2000.

[95] C. Argento and R. H. French. Parametric tip model and force–distance relation for Hamaker constant determination from atomic force microscopy. *Journal of Applied Physics*, 80:6081, 1996.

[96] R. Pérez, M. C. Payne, I. Štich, and K. Terakura. Role of covalent tip-surface interactions in noncontact atomic force microscopy on reactive surfaces. *Physical Review Letters*, 78:678, 1997.

[97] P. Rahe, R. Bechstein, J. Schütte, F. Ostendorf, and A. Kühnle. Repulsive interaction and contrast inversion in noncontact atomic force microscopy imaging of adsorbates. *Physical Review B*, 77:195410, 2008.

[98] J. E. Lennard-Jones. Cohesion. *Proceedings of the Physical Society*, 43:461, 1931.

[99] T.-C. Lim. The relationship between Lennard–Jones (12–6) and Morse potential functions. *Zeitschrift für Naturforschung A*, 58:615, 2003.

[100] Y. Sugimoto, P. Pou, M. Abe, P. Jelinek, R. Pérez, S. Morita, and O. Custance. Chemical identification of individual surface atoms by atomic force microscopy. *Nature*, 446:64, 2007.

Die approbierte gedruckte Originalversion dieser Dissertation ist an der TU Wien Bibliothek verfügbar.
The approved original version of this doctoral thesis is available in print at TU Wien Bibliothek.
TU Bibliothek Your knowledge hub WIEN

[101] S. Kawai, A. S. Foster, T. Björkman, S. Nowakowska, J. Björk, F. F. Canova, L. H. Gade, T. A. Jung, and E. Meyer. Van der Waals interactions and the limits of isolated atom models at interfaces. *Nature Communications*, 7:11559, 2016.

[102] M. A. Lantz, R. Hoffmann, A. S. Foster, A. Baratoff, H. J. Hug, H. R. Hidber, and H.-J. Güntherodt. Site-specific force-distance characteristics on NaCl(001): Measurements versus atomistic simulations. *Physical Review B*, 74:245426, 2006. DOI: 10.1103/PhysRevB.74.245426.

[103] S. Fujii and M. Fujihira. Atomic contrast on a point defect on CaF_2(111) imaged by non-contact atomic force microscopy. *Nanotechnology*, (8):084011, 2007. DOI: 10.1088/0957-4484/18/8/084011.

[104] F. J. Giessibl. Forces and frequency shifts in atomic-resolution dynamic-force microscopy. *Physical Review B*, 56:16010, 1997.

[105] J. E. Sader and S. P. Jarvis. Accurate formulas for interaction force and energy in frequency modulation force spectroscopy. *Applied Physics Letters*, 84:1801, 2004.

[106] J. E. Sader, B. D. Hughes, F. Huber, and F. J. Giessibl. Interatomic force laws that evade dynamic measurement. *Nature Nanotechnology*, 13:1088, 2018.

[107] F. Huber and F. J. Giessibl. Experimental use of the inflection point test for force deconvolution in frequency-modulation atomic force microscopy to turn an ill-posed situation into a well-posed one by proper choice of amplitude. *Journal of Applied Physics*, 127:184301, 2020.

[108] H. Mönig. Copper-oxide tip functionalization for submolecular atomic force microscopy. *Chemical Communications*, 54:9874, 2018. DOI: 10.1039/C8CC05332D.

[109] H. Mönig, S. Amirjalayer, A. Timmer, Z. Hu, L. Liu, O. D. Arado, M. Cnudde, C. A. Strassert, W. Ji, M. Rohlfing, and H. Fuchs. Quantitative assessment of intermolecular interactions by atomic force microscopy imaging using copper oxide tips. *Nature Nanotechnology*, 13:371, 2018. DOI: 10.1038/s41565-018-0104-4.

[110] A. Gustafsson, N. Okabayashi, A. Peronio, F. J. Giessibl, and M. Paulsson. Analysis of STM images with pure and CO-functionalized tips: A first-principles and experimental study. *Physical Review B*, 96:085415, 2017. DOI: 10.1103/PhysRevB.96.085415.

[111] L. Gross, F. Mohn, N. Moll, P. Liljeroth, and G. Meyer. The chemical structure of a molecule resolved by atomic force microscopy. *Science*, 325:1110, 2009. DOI: 10.1126/science.1176210.

[112] B. Schuler, S. Fatayer, F. Mohn, N. Moll, N. Pavliček, G. Meyer, D. Peña, and L. Gross. Reversible Bergman cyclization by atomic manipulation. *Nature Chemistry*, 8:220, 2016. DOI: 10.1038/nchem.2438.

[113] J. Welker and F. J. Giessibl. Revealing the angular symmetry of chemical bonds by atomic force microscopy. *Science*, 336:444, 2012.

[114] T. Hofmann, F. Pielmeier, and F. J. Giessibl. Chemical and crystallographic characterization of the tip apex in scanning probe microscopy. *Physical Review Letters*, 112:066101, 2014.

[115] R. Pawlak, T. Glatzel, V. Pichot, L. Schmidlin, S. Kawai, S. Fremy, D. Spitzer, and E. Meyer. Local detection of nitrogen-vacancy centers in a nanodiamond monolayer. *Nano Letters*, 13:5803, 2013. DOI: 10.1021/nl402243s.

[116] M. Setvin, J. Hulva, G. S. Parkinson, M. Schmid, and U. Diebold. Electron transfer between anatase TiO_2 and an O_2 molecule directly observed by atomic force microscopy. *Proceedings of the National Academy of Sciences*, 114:E2556, 2017.

[117] J. H. Braun, A. Baidins, and R. E. Marganski. TiO_2 pigment technology: a review. *Progress in Organic Coatings*, 20:105, 1992.

[118] L. K. Blevins, R. B. Crawford, A. Bach, M. D. Rizzo, J. Zhou, J. E. Henriquez, D. M. Isha Oliver Khan, S. Sermet, L. L. Arnold, K. L. Pennington, N. P. Souza, S. M. Cohen, and N. E. Kaminski. Evaluation of immunologic and intestinal effects in rats administered an E171-containing diet, a food grade titanium dioxide (TiO_2). *Food and Chemical Toxicology*, 133:110793, 2019.

Die approbierte gedruckte Originalversion dieser Dissertation ist an der TU Wien Bibliothek verfügbar.
The approved original version of this doctoral thesis is available in print at TU Wien Bibliothek.
TU Bibliothek WIEN Your knowledge hub

[119] A. Magrez, L. Horváth, R. Smajda, V. Salicio, N. Pasquier, L. Forro, and B. Schwaller. Cellular toxicity of TiO_2-based nanofilaments. *ACS Nano*, 3:2274, 2009.

[120] M. S. Robinson, B. W. Hapke, J. B. Garvin, D. Skillman, J. F. Bell, M. P. Ulmer, and C. M. Pieters. High resolution mapping of TiO_2 abundances on the Moon using the Hubble Space Telescope. *Geophysical Research Letters*, 34, 2007.

[121] Y. Luo, A. Benali, L. Shulenburger, J. T. Krogel, O. Heinonen, and P. R. C. Kent. Phase stability of TiO_2 polymorphs from diffusion Quantum Monte Carlo. *New Journal of Physics*, 18:113049, 2016.

[122] K. Thamaphat, P. Limsuwan, and B. Ngotawornchai. Phase characterization of TiO_2 powder by XRD and TEM. *Kasetsart Journal (Natural Science)*, 42:357, 2008.

[123] G. Liu, H. G. Yang, J. Pan, Y. Q. Yang, G. Q. Lu, and H.-M. Cheng. Titanium dioxide crystals with tailored facets. *Chemical Reviews*, 114:9559, 2014.

[124] Rob Lavinsky. Photograph from irocks.com and wikipedia. URL: https://www.irocks.com/.

[125] G. C. Vásquez, S. Zh. Karazhanov, D. Maestre, A. Cremades, J. Piqueras, and S. E. Foss. Oxygen vacancy related distortions in rutile TiO_2 nanoparticles: A combined experimental and theoretical study. *Physical Review B*, 94:235209, 2016. DOI: 10.1103/PhysRevB.94.235209.

[126] F. Jiang, L. Yang, D. Zhou, G. He, J. Zhou, F. Wang, and Z.-G. Chen. First-principles atomistic Wulff constructions for an equilibrium rutile TiO_2 shape modeling. *Applied Surface Science*, 436:989, 2018. DOI: 10.1016/j.apsusc.2017.12.050.

[127] S. C. Abrahams and J. L. Bernstein. Rutile: normal probability plot analysis and accurate measurement of crystal structure. *The Journal of Chemical Physics*, 55:3206, 1971.

[128] D. Reyes-Coronado, G. Rodríguez-Gattorno, M. E. Espinosa-Pesqueira, C. Cab, R. D. de Coss, and G. Oskam. Phase-pure TiO_2 nanoparticles: anatase, brookite and rutile. *Nanotechnology*, 19:145605, 2008.

[129] A. S. Barnard. One-to-one comparison of sunscreen efficacy, aesthetics and potential nanotoxicity. *Nature Nanotechnology*, 5:271, 2010.

[130] C. Franchini, M. Reticcioli, M. Setvín, and U. Diebold. Polarons in materials. *Nature Reviews Materials*, 6:560, 2021.

[131] A. Janotti, C. Franchini, J. B. Varley, G. Kresse, and C. G. Van de Walle. Dual behavior of excess electrons in rutile TiO_2. *Physica Status Solidi (RRL)–Rapid Research Letters*, 7:199, 2013.

[132] E. Finazzi, C. di Valentin, and G. Pacchioni. Nature of Ti interstitials in reduced bulk anatase and rutile TiO_2. *The Journal of Physical Chemistry C*, 113:3382, 2009.

[133] S. J. Song, J. Y. Seok, J. H. Yoon, K. M. Kim, G. H. Kim, M. H. Lee, and C. S. Hwang. Real-time identification of the evolution of conducting nano-filaments in TiO_2 thin film ReRAM. *Scientific Reports*, 3:1, 2013.

[134] E. Gale. TiO_2–based memristors and reRAM: materials, mechanisms and models (a review). *Semiconductor Science and Technology*, 29:104004, 2014.

[135] D. Wang, D. Choi, Z. Yang, V. V. Viswanathan, Z. Nie, C. Wang, Y. Song, J.-G. Zhang, and J. Liu. Synthesis and Li-ion insertion properties of highly crystalline mesoporous rutile TiO_2. *Chemistry of Materials*, 20:3435, 2008.

[136] J.-W. Lee, T.-Y. Lee, P. J. Yoo, M. Grätzel, S. Mhaisalkar, and N.-G. Park. Rutile TiO_2–based perovskite solar cells. *Journal of Materials Chemistry A*, 2:9251, 2014.

[137] H. Choi, S. R. Al-Abed, D. D. Dionysiou, E. Stathatos, and P. Lianos. TiO_2–based advanced oxidation nanotechnologies for water purification and reuse. *Sustainability Science and Engineering*, 2:229, 2010.

Die approbierte gedruckte Originalversion dieser Dissertation ist an der TU Wien Bibliothek verfügbar.
The approved original version of this doctoral thesis is available in print at TU Wien Bibliothek.
TU Bibliothek Your knowledge hub WIEN

[138] P. M. Kowalski, B. Meyer, and D. Marx. Composition, structure, and stability of the rutile $TiO_2(110)$ surface: Oxygen depletion, hydroxylation, hydrogen migration, and water adsorption. *Physical Review B*, 79:115410, 2009.

[139] U. Diebold. The surface science of titanium dioxide. *Surface Science Reports*, 48:53, 2003.

[140] R. Schaub, P. Thostrup, N. Lopez, E. Lægsgaard, I. Stensgaard, J. K. Nørskov, and F. Besenbacher. Oxygen vacancies as active sites for water dissociation on rutile $TiO_2(110)$. *Physical Review Letters*, 87:266104, 2001.

[141] T. Morikawa, R. Asahi, T. Ohwaki, K. Aoki, and Y. Taga. Band-gap narrowing of titanium dioxide by nitrogen doping. *Japanese Journal of Applied Physics*, 40:L561, 2001.

[142] A. Mills, R. H. Davies, and D. Worsley. Water purification by semiconductor photocatalysis. *Chemical Society Reviews*, 22:417, 1993.

[143] Y. Yu, X. Yang, Y. Zhao, X. Zhang, L. An, M. Huang, G. Chen, and R. Zhang. Engineering the band gap states of the rutile $TiO_2(110)$ surface by modulating the active heteroatom. *Angewandte Chemie International Edition*, 57:8550, 2018.

[144] H. Onishi and Y. Iwasawa. Reconstruction of $TiO_2(110)$ surface: STM study with atomic-scale resolution. *Surface Science*, 313:L783, 1994.

[145] M. Li, W. Hebenstreit, U. Diebold, A. M. Tyryshkin, M. K. Bowman, G. G. Dunham, and M. A. Henderson. The influence of the bulk reduction state on the surface structure and morphology of rutile $TiO_2(110)$ single crystals. *The Journal of Physical Chemistry B*, 104:4944, 2000.

[146] T. Bak, J. Nowotny, and M. K. Nowotny. Defect disorder of titanium dioxide. *The Journal of Physical Chemistry B*, 110:21560, 2006.

[147] P. G. Moses, A. Janotti, C. Franchini, G. Kresse, and C. G. Van de Walle. Donor defects and small polarons on the $TiO_2(110)$ surface. *Journal of Applied Physics*, 119:181503, 2016. DOI: https://doi.org/10.1063/1.4948239.

[148] M. Reticcioli, M. Setvín, M. Schmid, U. Diebold, and C. Franchini. Formation and dynamics of small polarons on the rutile $TiO_2(110)$ surface. *Physical Review B*, 98:045306, 2018. DOI: 10.1103/PhysRevB.98.045306.

[149] U. Diebold, J. F. Anderson, K.-O. Ng, and D. Vanderbilt. Evidence for the tunneling site on transition-metal oxides: $TiO_2(110)$. *Physical Review Letters*, 77:1322, 1996.

[150] U. Diebold, J. Lehman, T. Mahmoud, M. Kuhn, G. Leonardelli, W. Hebenstreit, M. Schmid, and P. Varga. Intrinsic defects on a $TiO_2(110)(1\times1)$ surface and their reaction with oxygen: a scanning tunneling microscopy study. *Surface Science*, 411:137, 1998.

[151] I. G. Austin and N. Fr. Mott. Polarons in crystalline and non-crystalline materials. *Advances in Physics*, 18:41, 1969. DOI: 10.1080/00018736900101267.

[152] Y. Natanzon, A. Azulay, and Y. Amouyal. Evaluation of polaron transport in solids from first-principles. *Israel Journal of Chemistry*, 60:768, 2020. DOI: 10.1002/ijch.201900101.

[153] W.-J. Yin, B. Wen, C. Zhou, A. Selloni, and L.-M. Liu. Excess electrons in reduced rutile and anatase TiO_2. *Surface Science Reports*, 73:58, 2018.

[154] U. Diebold and T. E. Madey. TiO_2 by XPS. *Surface Science Spectra*, 4:227, 1996.

[155] G. Lu, A. Linsebigler, and J. T. Yates Jr. Ti^{3+} defect sites on $TiO_2(110)$: production and chemical detection of active sites. *The Journal of Physical Chemistry*, 98:11733, 1994.

[156] X. Mao, X. Lang, Z. Wang, Q. Hao, B. Wen, Z. Ren, D. Dai, C. Zhou, L.-M. Liu, and X. Yang. Band-gap states of $TiO_2(110)$: major contribution from surface defects. *The Journal of Physical Chemistry Letters*, 4:3839, 2013.

Die approbierte gedruckte Originalversion dieser Dissertation ist an der TU Wien Bibliothek verfügbar.
The approved original version of this doctoral thesis is available in print at TU Wien Bibliothek.
TU Bibliothek Your knowledge hub WIEN

[157] M. Reticcioli, M. Setvín, X. Hao, P. Flauger, G. Kresse, M. Schmid, U. Diebold, and C. Franchini. Polaron-driven surface reconstructions. *Physical Review X*, 7:031053, 2017. DOI: 10.1103/PhysRevX.7.031053.

[158] Small polarons in transition metal oxides. In *Handbook of Materials Modeling*.

[159] L. D. Landau. Electron motion in crystal lattices. *Physikalische Zeitschrift der Sowjetunion*, 3:664, 1933.

[160] Th. Holstein. Studies of polaron motion: Part I. The molecular-crystal model. *Annals of Physics*, 8:325, 1959.

[161] H. Fröhlich, H. Pelzer, and S. Zienau. XX. Properties of slow electrons in polar materials. *The London, Edinburgh, and Dublin Philosophical Magazine and Journal of Science*, 41:221, 1950.

[162] P. Krüger, S. Bourgeois, B. Domenichini, H. Magnan, D. Chandesris, P. Le Fevre, A. M. Flank, J. Jupille, L. Floreano, A. Cossaro, A. Verdini, and A. Morgante. Defect states at the TiO_2 surface probed by resonant photoelectron diffraction. *Physical Review Letters*, 100:055501, 2008.

[163] R. Ramakumar and A. N. Das. Polaron cross-overs and d-wave superconductivity in Hubbard-Holstein model. *The European Physical Journal B-Condensed Matter and Complex Systems*, 41:197, 2004.

[164] P. M. Kowalski, M. F. Camellone, N. N. Nair, B. Meyer, and D. Marx. Charge localization dynamics induced by oxygen vacancies on the TiO_2(110) surface. *Physical Review Letters*, 105:146405, 2010.

[165] A. Yildiz, F. Iacomi, and D. Mardare. Polaron transport in TiO_2 thin films. *Journal of Applied Physics*, 108:083701, 2010.

[166] S. Yang, A. T. Brant, N. C. Giles, and L. E. Halliburton. Intrinsic small polarons in rutile TiO_2. *Physical Review B*, 87:125201, 2013.

[167] S. X. Zhang, D. C. Kundaliya, W. Yu, S. Dhar, S. Y. Young, L. G. Salamanca-Riba, S. B. Ogale, R. D. Vispute, and T. Venkatesan. Niobium doped TiO_2: Intrinsic transparent metallic anatase versus highly resistive rutile phase. *Journal of Applied Physics*, 102:013701, 2007.

[168] V. N. Bogomolov and D. N. Mirlin. Optical absorption by polarons in rutile (TiO_2) single crystals. *Physica Status Solidi (B)*, 27:443, 1968.

[169] Y. Yoon, Y. Du, J. C. Garcia, Z. Zhu, Z.-T. Wang, N. G. Petrik, G. A. Kimmel, Z. Dohnálek, M. A. Henderson, R. Rousseau, N. A. Deskins, and I. Lyubinetsky. Anticorrelation between surface and subsurface point defects and the impact on the redox chemistry of TiO_2(110). *ChemPhysChem*, 16:313, 2015.

[170] S. L. Dudarev, G. A. Botton, S. Y. Savrasov, C. J. Humphreys, and A. P. Sutton. Electron-energy-loss spectra and the structural stability of nickel oxide: An LSDA+U study. *Physical Review B*, 57:1505, 1998.

[171] M. Setvín, C. Franchini, X. Hao, M. Schmid, A. Janotti, M. Kaltak, C. G. Van de Walle, G. Kresse, and U. Diebold. Direct view at excess electrons in TiO_2 rutile and anatase. *Physical Review Letters*, 113:086402, 2014.

[172] A. M. Stoneham. Small polarons and polaron transitions. *Journal of the Chemical Society, Faraday Transactions 2: Molecular and Chemical Physics*, 85:505, 1989.

[173] A. L. Shluger and A. M. Stoneham. Small polarons in real crystals: concepts and problems. *Journal of Physics: Condensed Matter*, 5:3049, 1993.

[174] P. Deák, B. Aradi, and T. Frauenheim. Polaronic effects in TiO_2 calculated by the HSE06 hybrid functional: Dopant passivation by carrier self-trapping. *Physical Review B*, 83:155207, 2011.

[175] P. Deák, B. Aradi, and T. Frauenheim. Quantitative theory of the oxygen vacancy and carrier self-trapping in bulk TiO_2. *Physical Review B*, 86:195206, 2012.

[176] Y. Zhao, Z. Wang, X. Cui, T. Huang, B. Wang, Y. Luo, J. Yang, and J. Hou. What are the adsorption sites for CO on the reduced TiO_2(110)-1×1 surface? *Journal of the American Chemical Society*, 131:7958, 2009. DOI: 10.1021/ja902259k.

Die approbierte gedruckte Originalversion dieser Dissertation ist an der TU Wien Bibliothek verfügbar.
The approved original version of this doctoral thesis is available in print at TU Wien Bibliothek.
TU Bibliothek Your knowledge hub WIEN

[177] N. G. Petrik and G. A. Kimmel. Adsorption geometry of CO versus coverage on $TiO_2(110)$ from *s*- and *p*-polarized infrared spectroscopy. *The Journal of Physical Chemistry Letters*, 3:3425, 2012. DOI: 10.1021/jz301413v.

[178] M. Xu, H. Noei, K. Fink, M. Muhler, Y. Wang, and C. Wöll. The surface science approach for understanding reactions on oxide powders: the importance of IR spectroscopy. *Angewandte Chemie International Edition*, 51:4731, 2012. DOI: 10.1002/anie.201200585.

[179] S. Lee, C. Fan, T. Wu, and S. L. Anderson. CO oxidation on Au_n/TiO_2 catalysts produced by size-selected cluster deposition. *Journal of the American Chemical Society*, 126:5682, 2004.

[180] S. Chrétien and H. Metiu. Density functional study of the CO oxidation on a doped rutile $TiO_2(110)$: Effect of ionic Au in catalysis. *Catalysis Letters*, 107:143, 2006.

[181] M. Reticcioli, I. Sokolović, M. Schmid, U. Diebold, M. Setvín, and C. Franchini. Interplay between adsorbates and polarons: CO on rutile $TiO_2(110)$. *Physical Review Letters*, 122:016805, 2019.

[182] P. S. Bagus, C. J. Nelin, and C. W. Bauschlicher Jr. Bonding of CO to metal surfaces: a new interpretation. *Physical Review B*, 28:5423, 1983.

[183] A. C. Papageorgiou, N. S. Beglitis, C. L. Pang, G. Teobaldi, G. Cabailh, Q. Chen, A. J. Fisher, W. A. Hofer, and G. Thornton. Electron traps and their effect on the surface chemistry of $TiO_2(110)$. *Proceedings of the National Academy of Sciences*, 107:2391, 2010.

[184] B. Wen, W.-J. Yin, A. Selloni, and L.-M. Liu. Defects, adsorbates, and photoactivity of rutile $TiO_2(110)$: Insight by first-principles calculations. *The Journal of Physical Chemistry Letters*, 9:5281, 2018.

[185] M. A. Henderson, M. Shen, Z.-T. Wang, and I. Lyubinetsky. Characterization of the active surface species responsible for UV-induced desorption of O_2 from the rutile $TiO_2(110)$ surface. *The Journal of Physical Chemistry C*, 117:5774, 2013. DOI: 10.1021/jp312161y.

[186] Z.-T. Wang, Y. Du, Z. Dohnálek, and I. Lyubinetsky. Direct observation of site-specific molecular chemisorption of O_2 on $TiO_2(110)$. *The Journal of Physical Chemistry Letters*, 1:3524, 2010. DOI: 10.1021/jz101535f.

[187] P. Scheiber, A. Riss, M. Schmid, P. Varga, and U. Diebold. Observation and destruction of an elusive adsorbate with STM: $O_2/TiO_2(110)$. *Physical Review Letters*, 105:216101, 2010. DOI: 10.1103/PhysRevLett.105.216101.

[188] Y. Adachi, H. F. Wen, Q. Zhang, M. Miyazaki, Y. Sugawara, H. Sang, J. Brndiar, L. Kantorovich, I. Štich, and Y. J. Li. Tip-induced control of charge and molecular bonding of oxygen atoms on the rutile $TiO_2(110)$ surface with atomic force microscopy. *ACS Nano*, 13:6917, 2019. DOI: 10.1021/acsnano.9b01792.

[189] A. Gurlo and R. Riedel. In situ and operando spectroscopy for assessing mechanisms of gas sensing. *Angewandte Chemie International Edition*, 46:3826, 2007.

[190] Z. Guo, B. Liu, Q. Zhang, W. Deng, Y. Wang, and Y. Yang. Recent advances in heterogeneous selective oxidation catalysis for sustainable chemistry. *Chemical Society Review*, 43:3480, 2014.

[191] J. H. Montoya, L. C. Seitz, P. Chakthranont, A. Vojvodic, T. F. Jaramillo, and J. K. Nørskov. Materials for solar fuels and chemicals. *Nature Materials*, 16:70, 2017.

[192] M. Setvín, U. Aschauer, J. Hulva, T. Simschitz, B. Daniel, M. Schmid, A. Selloni, and U. Diebold. Following the reduction of oxygen on TiO_2 anatase (101) step by step. *Journal of the American Chemical Society*, 138:9565, 2016.

[193] K. Szot, M. Rogala, W. Speier, Z. Klusek, A. Besmehn, and R. Waser. TiO_2 - a prototypical memristive material. *Nanotechnology*, 22:254001, 2011.

[194] T. L. Thompson and J. T. Yates Jr. Surface science studies of the photoactivation of TiO_2 new photochemical processes. *Chemical Reviews*, 106:4428, 2006.

Die approbierte gedruckte Originalversion dieser Dissertation ist an der TU Wien Bibliothek verfügbar.
The approved original version of this doctoral thesis is available in print at TU Wien Bibliothek.
TU Bibliothek WIEN Your knowledge hub

[195] A. Fujishima, X. Zhang, and D. A. Tryk. TiO_2 photocatalysis and related surface phenomena. *Surface Science Reports*, 63:515, 2008.

[196] C. L. Pang, R. Lindsay, and G. Thornton. Chemical reactions on rutile TiO_2(110). *Chemical Society Reviews*, 37:2328, 2008.

[197] L.-M. Liu, P. Crawford, and P. Hu. The interaction between adsorbed OH and O_2 on TiO_2 surfaces. *Progress in Surface Science*, 84:155, 2009.

[198] J. T. Yates Jr. Photochemistry on TiO_2: Mechanisms behind the surface chemistry. *Surface Science*, 603:1605, 2009.

[199] Z. Dohnálek, I. Lyubinetsky, and R. Rousseau. Thermally-driven processes on rutile TiO_2(110)-(1×1): A direct view at the atomic scale. *Progress in Surface Science*, 85:161, 2010.

[200] M. A. Henderson and I. Lyubinetsky. Molecular-level insights into photocatalysis from scanning probe microscopy studies on TiO_2(110). *Chemical Reviews*, 113:4428, 2013.

[201] Q. Guo, C. Zhou, Z. Ma, Z. Ren, H. Fan, and X. Yang. Elementary photocatalytic chemistry on TiO_2 surfaces. *Chemical Society Reviews*, 45:3701, 2016.

[202] I. Sokolović, M. Reticcioli, M. Čalkovskỳ, M. Wagner, M. Schmid, C. Franchini, U. Diebold, and M. Setvín. Resolving the adsorption of molecular O_2 on the rutile TiO_2(110) surface by noncontact atomic force microscopy. *Proceedings of the National Academy of Sciences*, 11:14827, 2020.

[203] R. Schaub, E. Wahlström, A. Rønnau, E. Lægsgaard, I. Stensgaard, and F. Besenbacher. Oxygen-mediated diffusion of oxygen vacancies on the TiO_2(110) surface. *Science*, 299:377, 2003.

[204] X. Cui, B. Wang, Z. Wang, T. Huang, Y. Zhao, J. Yang, and J. G. Hou. Formation and diffusion of oxygen-vacancy pairs on TiO_2(110)-(1×1). *The Journal of Chemical Physics*, 129:044703, 2008.

[205] M. Setvín, U. Aschauer, P. Scheiber, Y.-F. Li, W. Hou, M. Schmid, A. Selloni, and U. Diebold. Reaction of O_2 with subsurface oxygen vacancies on TiO_2 anatase (101). *Science*, 341:988, 2013.

[206] Y. Du, Z. Dohnálek, and I. Lyubinetsky. Transient mobility of oxygen adatoms upon O_2 dissociation on reduced TiO_2(110). *The Journal of Physical Chemistry C*, 112:2649, 2008.

[207] N. G. Petrik, Z. Zhang, Y. Du, Z. Dohnálek, I. Lyubinetsky, and G. A. Kimmel. Chemical reactivity of reduced TiO_2(110): the dominant role of surface defects in oxygen chemisorption. *The Journal of Physical Chemistry C*, 113:12407, 2009.

[208] Y. Du, N. A Deskins, Z. Zhang, Z. Dohnálek, M. Dupuis, and I. Lyubinetsky. Formation of O adatom pairs and charge transfer upon O_2 dissociation on reduced TiO_2(110). *Physical Chemistry Chemical Physics*, 12:6337, 2010.

[209] E. Arima, H. F. Wen, Y. Naitoh, Y. J. Li, and Y. Sugawara. KPFM/AFM imaging on TiO_2(110) surface in O_2 gas. *Nanotechnology*, 29:105504, 2018.

[210] Q. Zhang, Y. J. Li, H. F. Wen, Y. Adachi, M. Miyazaki, Y. Sugawara, R. Xu, Z. H. Cheng, J. Brndiar, L. Kantorovich, and I. Štich. Measurement and manipulation of the charge state of an adsorbed oxygen adatom on the rutile TiO_2(110)-1×1 surface by nc-AFM and KPFM. *Journal of the American Chemical Society*, 140:15668, 2018.

[211] S. Wendt, P. T. Sprunger, E. Lira, G. K. H. Madsen, Z. Li, J. Ø. Hansen, J. Matthiesen, A. Blekinge-Rasmussen, E. Lægsgaard, B. Hammer, and F. Besenbacher. The role of interstitial sites in the Ti3*d* defect state in the band gap of titania. *Science*, 320:1755, 2008. DOI: 10.1126/science.1159846.

[212] S. Wendt, R. Schaub, J. Matthiesen, E. K. Vestergaard, E. Wahlström, M. D. Rasmussen, P. Thostrup, L. M. Molina, E. Lægsgaard, I. Stensgaard, B. Hammer, and F. Besenbacher. Oxygen vacancies on TiO_2(110) and their interaction with H_2O and O_2: A combined high-resolution STM and DFT study. *Surface Science*, 598:226, 2005.

Die approbierte gedruckte Originalversion dieser Dissertation ist an der TU Wien Bibliothek verfügbar.
The approved original version of this doctoral thesis is available in print at TU Wien Bibliothek.
TU Bibliothek Your knowledge hub WIEN

[213] E. Lira, J. Ø. Hansen, P. Huo, R. Bechstein, P. Galliker, E. Lægsgaard, B. Hammer, S. Wendt, and F. Besenbacher. Dissociative and molecular oxygen chemisorption channels on reduced rutile $TiO_2(110)$: An STM and TPD study. *Surface Science*, 604:1945, 2010.

[214] E. Lira, P. Huo, J. Ø. Hansen, F. Rieboldt, R. Bechstein, Y. Wei, R. Streber, S. Porsgaard, Z. Li, E. Lægsgaard, S. Wendt, and F. Besenbacher. Effects of the crystal reduction state on the interaction of oxygen with rutile $TiO_2(110)$. *Catalysis Today*, 182:25, 2012.

[215] T. L. Thompson, O. Diwald, and J. T. Yates Jr. Molecular oxygen-mediated vacancy diffusion on $TiO_2(110)$-new studies of the proposed mechanism. *Chemical Physics Letters*, 393:28, 2004.

[216] E. Lira, S. Wendt, P. Huo, J. Ø. Hansen, R. Streber, S. Porsgaard, Y. Wei, R. Bechstein, E. Lægsgaard, and F. Besenbacher. The importance of bulk Ti^{3+} defects in the oxygen chemistry on titania surfaces. *Journal of the American Chemical Society*, 133:6529, 2011.

[217] M. A. Henderson, W. S. Epling, C. L. Perkins, C. H. F. Peden, and U. Diebold. Interaction of molecular oxygen with the vacuum-annealed $TiO_2(110)$ surface: molecular and dissociative channels. *The Journal of Physical Chemistry B*, 103:5328, 1999.

[218] T. Berger, M. Sterrer, O. Diwald, and E. Knözinger. Charge trapping and photoadsorption of O_2 on dehydroxylated TiO_2 nanocrystals-an electron paramagnetic resonance study. *ChemPhysChem*, 6:2104, 2005.

[219] J. Lee, Z. Zhang, and J. T. Yates Jr. Electron-stimulated positive-ion desorption caused by charge transfer from adsorbate to substrate: oxygen adsorbed on $TiO_2(110)$. *Physical Review B*, 79:081408, 2009.

[220] T. L. Thompson and J. T. Yates Jr. Monitoring hole trapping in photoexcited $TiO_2(110)$ using a surface photoreaction. *Journal of Physical Chemistry B*, 109:18230, 2005.

[221] T. L. Thompson and J. T. Yates Jr. Control of a surface photochemical process by fractal electron transport across the surface: O_2 photodesorption from $TiO_2(110)$. *The Journal of Physical Chemistry B*, 110:7431, 2006. DOI: 10.1021/jp0562126.

[222] D. Sporleder, D. P. Wilson, and M. G. White. Final state distributions of O_2 photodesorbed from $TiO_2(110)$. *The Journal of Physical Chemistry C*, 113:13180, 2009. DOI: 10.1021/jp901065j.

[223] Z. Zhang and J. T. Yates Jr. Direct observation of surface-mediated electron-hole pair recombination in $TiO_2(110)$. *The Journal of Physical Chemistry C*, 114:3098, 2010.

[224] N. G. Petrik and G. A. Kimmel. Photoinduced dissociation of O_2 on rutile $TiO_2(110)$. *The Journal of Physical Chemistry Letters*, 1:1758, 2010.

[225] N. G. Petrik and G. A. Kimmel. Electron-and hole-mediated reactions in UV-irradiated O_2 adsorbed on reduced rutile $TiO_2(110)$. *The Journal of Physical Chemistry C*, 115:152, 2011.

[226] N. G. Petrik and G. A. Kimmel. Oxygen photochemistry on $TiO_2(110)$: recyclable, photoactive oxygen produced by annealing adsorbed O_2. *The Journal of Physical Chemistry Letters*, 2:2790, 2011.

[227] N. G. Petrik and G. A. Kimmel. Probing the photochemistry of chemisorbed oxygen on $TiO_2(110)$ with Kr and other co-adsorbates. *Physical Chemistry Chemical Physics*, 16:2338, 2014.

[228] S. Tan, Y. Ji, Y. Zhao, A. Zhao, B. Wang, J. Yang, and J. G. Hou. Molecular oxygen adsorption behaviors on the rutile $TiO_2(110)$-1×1 surface: an in situ study with low-temperature scanning tunneling microscopy. *Journal of the American Chemical Society*, 133:2002, 2011.

[229] Z.-T. Wang, N. A. Deskins, and I. Lyubinetsky. Direct imaging of site-specific photocatalytical reactions of O_2 on $TiO_2(110)$. *The Journal of Physical Chemistry Letters*, 3:102, 2011.

[230] P. Hapala, G. Kichin, Ch. Wagner, F. S. Tautz, R. Temirov, and P. Jelinek. Mechanism of high-resolution STM/AFM imaging with functionalized tips. *Physical Review B*, 90:085421, 2014.

[231] M. Ellner, N. Pavliček, P. Pou, B. Schuler, N. Moll, G. Meyer, L. Gross, and R. Peréz. The electric field of CO tips and its relevance for atomic force microscopy. *Nano Letters*, 16:1974, 2016.

Die approbierte gedruckte Originalversion dieser Dissertation ist an der TU Wien Bibliothek verfügbar.
The approved original version of this doctoral thesis is available in print at TU Wien Bibliothek.
TU Bibliothek WIEN Your knowledge hub

[232] D. Pillay, Y. Wang, and G. S. Hwang. Prediction of tetraoxygen formation on rutile $TiO_2(110)$. *Journal of the American Chemical Society*, 128:14000, 2006.

[233] G. A. Kimmel and N. G. Petrik. Tetraoxygen on reduced $TiO_2(110)$: Oxygen adsorption and reactions with bridging oxygen vacancies. *Physical Review Letters*, 100:196102, 2008.

[234] X. Wu, A. Selloni, M. Lazzeri, and S. K. Nayak. Oxygen vacancy mediated adsorption and reactions of molecular oxygen on the $TiO_2(110)$ surface. *Physical Review B*, 68:241402, 2003.

[235] M. D. Rasmussen, L. M. Molina, and B. Hammer. Adsorption, diffusion, and dissociation of molecular oxygen at defected $TiO_2(110)$: A density functional theory study. *The Journal of Chemical Physics*, 120:988, 2004.

[236] S. Chrétien and H. Metiu. O_2 evolution on a clean partially reduced rutile $TiO_2(110)$ surface and on the same surface precovered with Au_1 and Au_2 : the importance of spin conservation. *The Journal of Chemical Physics*, 129:074705, 2008.

[237] Y. Ji, B. Wang, and Y. Luo. First principles study of O_2 adsorption on reduced rutile $TiO_2(110)$ surface under UV illumination and its role on CO oxidation. *The Journal of Physical Chemistry C*, 117:956, 2013.

[238] H. Xu and S. Y. Tong. Interaction of O_2 with reduced rutile $TiO_2(110)$ surface. *Surface Science*, 610:33, 2013.

[239] H. Tian, B. Xu, J. Fan, and H. Xu. Intrinsic role of excess electrons in surface reactions on rutile $TiO_2(110)$: Using water and oxygen as probes. *The Journal of Physical Chemistry C*, 122:8270, 2018.

[240] A. Tilocca and A. Selloni. O_2 and vacancy diffusion on rutile (110): pathways and electronic properties. *ChemPhysChem*, 6:1911, 2005.

[241] L. M. Molina, M. D. Rasmussen, and B. Hammer. Adsorption of O_2 and oxidation of CO at Au nanoparticles supported by $TiO_2(110)$. *The Journal of Chemical Physics*, 120:7673, 2004.

[242] S. Chrétien and H. Metiu. Enhanced adsorption energy of Au_1 and O_2 on the stoichiometric $TiO_2(110)$ surface by coadsorption with other molecules. *The Journal of Chemical Physics*, 128:044714, 2008.

[243] N. A. Deskins, R. Rousseau, and M. Dupuis. Defining the role of excess electrons in the surface chemistry of TiO_2. *The Journal of Physical Chemistry C*, 114:5891, 2010.

[244] V. E. Henrich and P. A. Cox. *The surface science of metal oxides*. Cambridge university press, 1996.

[245] Z. Dohnálek, J. Kim, O. Bondarchuk, J. M. White, and B. D. Kay. Physisorption of N_2, O_2, and CO on fully oxidized $TiO_2(110)$. *The Journal of Physical Chemistry B*, 110:6229, 2006.

[246] R. F. W. Bader. Atoms in molecules. *Accounts of Chemical Research*, 18:9, 1985.

[247] T. Akbay, A. Staykov, J. Druce, H. Téllez, T. Ishihara, and J. A. Kilner. The interaction of molecular oxygen on LaO terminated surfaces of $LaNiO_4$. *Journal of Materials Chemistry A*, 4:13113, 2016.

[248] G. Preda and G. Pacchioni. Formation of oxygen active species in Ag-modified CeO_2 catalyst for soot oxidation: A DFT study. *Catalysis Today*, 177:31, 2011.

[249] Z. Chen, J. Li, and X. C. Zeng. Unraveling oxygen evolution in Li-rich oxides: A unified modeling of the intermediate peroxo/superoxo-like dimers. *Journal of the American Chemical Society*, 141:10751, 2019.

[250] C. J. Kramer, W. B. Tolman, K. H. Theopold, and A. L. Rheingold. Variable character of O-O and M-O bonding in side-on (η^2) 1:1 metal complexes of O_2. *Proceeding of the National Academy of Sciences*, 100:3635, 2003.

[251] Z. Zhang, J. Lee, J. T. Yates Jr., R. Bechstein, E. Lira, J. Ø. Hansen, S. Wendt, and F. Besenbacher. Unraveling the diffusion of bulk Ti interstitials in rutile $TiO_2(110)$ by monitoring their reaction with O adatoms. *The Journal of Physical Chemistry C*, 114:3059, 2010.

[252] M. Bowker and R. A. Bennett. The role of Ti^{3+} interstitials in $TiO_2(110)$ reduction and oxidation. *Journal of Physics: Condensed Matter*, 21:474224, 2009.

Die approbierte gedruckte Originalversion dieser Dissertation ist an der TU Wien Bibliothek verfügbar.
The approved original version of this doctoral thesis is available in print at TU Wien Bibliothek.
TU Bibliothek Your knowledge hub WIEN

[253] C. Yang and C. Wöll. IR spectroscopy applied to metal oxide surfaces: adsorbate vibrations and beyond. *Advances in Physics: X*, 2:373, 2017.

[254] A. Abragam and B. Bleaney. *Electron paramagnetic resonance of transition ions*. OUP Oxford, 2012.

[255] M. J. Lundqvist, M. Nilsing, P. Persson, and S. Lunell. DFT study of bare and dye-sensitized TiO_2 clusters and nanocrystals. *International Journal of Quantum Chemistry*, 106:3214, 2006.

[256] A. Yurtsever, D. Fernández-Torre, C. González, P. Jelínek, P. Pou, Y. Sugimoto, M. Abe, R. Pérez, and S. Morita. Understanding image contrast formation in $TiO_2$with force spectroscopy. *Physical Review B*, 85:125416, 2012.

[257] O. Stetsovych, M. Todorović, T. K. Shimizu, C. Moreno, J. W. Ryan, C. P. León, K. Sagisaka, E. Palomares, V. Matolín, D. Fujita, et al. Atomic species identification at the (101) anatase surface by simultaneous scanning tunnelling and atomic force microscopy. *Nature Communications*, 6:7265, 2015.

[258] A. Liebig and F. J. Giessibl. In-situ characterization of O-terminated Cu tips for high-resolution atomic force microscopy. *Applied Physics Letters*, 114:143103, 2019.

[259] C. T. Campbell. Ultrathin metal films and particles on oxide surfaces: structural, electronic and chemisorptive properties. *Surface Science Reports*, 27:1, 1997.

[260] O. Krejčí, P. Hapala, M. Ondráček, and P. Jelínek. Principles and simulations of high-resolution STM imaging with a flexible tip apex. *Physical Review B*, 95:045407, 2017.

[261] B. de la Torre, M. Švec, G. Foti, O. Krejčí, P. Hapala, A. Garcia-Lekue, T. Frederiksen, R. Zbořil, A. Arnau, H. Vázquez, et al. Submolecular resolution by variation of the inelastic electron tunneling spectroscopy amplitude and its relation to the AFM/STM signal. *Physical Review Letters*, 119:166001, 2017.

[262] C. Barth, A. S. Foster, C. R. Henry, and A. L. Shluger. Recent trends in surface characterization and chemistry with high-resolution scanning force methods. *Advanced Materials*, 23:477, 2011.

[263] M. A. Henderson. A surface science perspective on TiO_2 photocatalysis. *Surface Science Reports*, 66:185, 2011.

[264] Y. I. Vorob'yev, A. A. Konev, Y. V. Malyshonok, G. F. Afonina, and A. N. Sapozhnikov. Tausonite, $SrTiO_3$, a new mineral of the perovskite group. *International Geology Review*, 26:462, 1984.

[265] J. G. Bednorz and H. J. Scheel. Flame-fusion growth of $SrTiO_3$. *Journal of Crystal Growth*, 41:5, 1977.

[266] F. W. Lytle. X-ray diffractometry of low-temperature phase transformations in strontium titanate. *Journal of Applied Physics*, 35:2212, 1964.

[267] Y. A. Abramov, V. G. Tsirelson, V. E. Zavodnik, S. A. Ivanov, and I. D. Brown. The chemical bond and atomic displacements in $SrTiO_3$ from X-ray diffraction analysis. *Acta Crystallographica Section B: Structural Science*, 51:942, 1995.

[268] R. D. Leapman, L. A. Grunes, and P. L. Fejes. Study of the L_{23} edges in the $3d$ transition metals and their oxides by electron-energy-loss spectroscopy with comparisons to theory. *Physical Review B*, 26:614, 1982.

[269] S. Piskunov, E. Heifets, R. I. Eglitis, and G. Borstel. Bulk properties and electronic structure of $SrTiO_3$, $BaTiO_3$, $PbTiO_3$ perovskites: an ab initio HF/DFT study. *Computational Materials Science*, 29:165, 2004. DOI: 10.1016/j.commatsci.2003.08.036.

[270] K. van Benthem, C. Elsässer, and R. H. French. Bulk electronic structure of $SrTiO_3$: Experiment and theory. *Journal of Applied Physics*, 90:6156, 2001.

[271] B. L. Phoon, C. W. Lai, J. C. Juan, P.-L. Show, and W.-H. Chen. A review of synthesis and morphology of $SrTiO_3$ for energy and other applications. *International Journal of Energy Research*, 43:5151, 2019.

Die approbierte gedruckte Originalversion dieser Dissertation ist an der TU Wien Bibliothek verfügbar.
The approved original version of this doctoral thesis is available in print at TU Wien Bibliothek.
TU Bibliothek Your knowledge hub WIEN

[272] J. Zhang, P. Zhou, J. Liu, and J. Yu. New understanding of the difference of photocatalytic activity among anatase, rutile and brookite TiO_2. *Physical Chemistry Chemical Physics*, 16:20382, 2014.

[273] K. Domen, A. Kudo, and T. Onishi. Mechanism of photocatalytic decomposition of water into H_2 and O_2 over NiO–$SrTiO_3$. *Journal of Catalysis*, 102:92, 1986.

[274] N. B. Brookes, G. Thornton, and F. M. Quinn. $SrTiO_3$(100) step sites as catalytic centers for H_2O dissociation. *Solid State Communications*, 64:383, 1987.

[275] Y. Liu, L. Xie, Y. Li, R. Yang, J. Qu, Y. Li, and X. Li. Synthesis and high photocatalytic hydrogen production of $SrTiO_3$ nanoparticles from water splitting under UV irradiation. *Journal of Power Sources*, 183:701, 2008.

[276] X. Guan and L. Guo. Cocatalytic effect of $SrTiO_3$ on Ag_3PO_4 toward enhanced photocatalytic water oxidation. *ACS Catalysis*, 4:3020, 2014.

[277] A. Kumar, A. Rana, G. Sharma, M. Naushad, A. Al-Muhtaseb, C. Guo, A. Iglesias-Juez, and F. J. Stadler. High-performance photocatalytic hydrogen production and degradation of levofloxacin by wide spectrum-responsive Ag/Fe_3O_4 bridged $SrTiO_3$/g-C_3N_4 plasmonic nanojunctions: joint effect of Ag and Fe_3O_4. *ACS Applied Materials & Interfaces*, 10:40474, 2018.

[278] Q. Zhang, Y. Huang, L. Xu, J. Cao, W. Ho, and S. C. Lee. Visible-light-active plasmonic Ag–$SrTiO_3$ nanocomposites for the degradation of NO in air with high selectivity. *ACS Applied Materials & Interfaces*, 8:4165, 2016.

[279] S. Shoji, G. Yin, M. Nishikawa, D. Atarashi, E. Sakai, and M. Miyauchi. Photocatalytic reduction of CO_2 by Cu_xO nanocluster loaded $SrTiO_3$ nanorod thin film. *Chemical Physics Letters*, page 309, 2016.

[280] B. Szafraniak, Ł. Fuśnik, J. Xu, F. Gao, A. Brudnik, and A. Rydosz. Semiconducting metal oxides: $SrTiO_3$, $BaTiO_3$ and $BaSrTiO_3$ in gas-sensing applications: A review. *Coatings*, 11:185, 2021.

[281] R. Meyer and R. Waser. Resistive donor-doped $SrTiO_3$ sensors: I, basic model for a fast sensor response. *Sensors and Actuators B: Chemical*, 101:335, 2004.

[282] Y. Hu, O. K. Tan, J. S. Pan, and X. Yao. A new form of nanosized $SrTiO_3$ material for near-human-body temperature oxygen sensing applications. *The Journal of Physical Chemistry B*, 108:11214, 2004.

[283] M. Riva, M. Kubicek, X. Hao, G. Franceschi, S. Gerhold, M. Schmid, H. Hutter, J. Fleig, C. Franchini, B. Yildiz, et al. Influence of surface atomic structure demonstrated on oxygen incorporation mechanism at a model perovskite oxide. *Nature Communications*, 9:1, 2018.

[284] R. M. Ormerod. Solid oxide fuel cells. *Chemical Society Reviews*, 32:17, 2003.

[285] C. D Savaniu and J. T. S. Irvine. La-doped $SrTiO_3$ as anode material for IT-SOFC. *Solid State Ionics*, 192:491, 2011.

[286] A. Viernstein, M. Kubicek, M. Morgenbesser, G. Walch, G. C. Brunauer, and J. Fleig. High-temperature photochromism of Fe-doped $SrTiO_3$ caused by UV-induced bulk stoichiometry changes. *Advanced Functional Materials*, 29:1900196, 2019.

[287] R. Li, C. Zhang, J. Liu, J. Zhou, and L. Xu. A review on the electrical properties of doped $SrTiO_3$ as anode materials for solid oxide fuel cells. *Materials Research Express*, 6:102006, 2019.

[288] Z. Hu, Q. Li, M. Li, Q. Wang, Y. Zhu, X. Liu, X. Zhao, Y. Liu, and S. Dong. Ferroelectric memristor based on Pt/$BiFeO_3$/Nb-doped $SrTiO_3$ heterostructure. *Applied Physics Letters*, 102:102901, 2013.

[289] G. Dou, Y. Yu, M. Guo, Y.-M. Zhang, Z. Sun, and Y.-X. Li. Memristive behavior based on Ba-doped $SrTiO_3$ films. *Chinese Physics Letters*, 34:038502, 2017.

[290] A. Thomas. Memristor-based neural networks. *Journal of Physics D: Applied Physics*, 46:093001, 2013.

[291] S. Woo, H. Jeong, S. A. Lee, H. Seo, M. Lacotte, A. David, H. Y. Kim, W. Prellier, Y. Kim, and W. S. Choi. Surface properties of atomically flat poly-crystalline $SrTiO_3$. *Scientific Reports*, 5:1, 2015.

Die approbierte gedruckte Originalversion dieser Dissertation ist an der TU Wien Bibliothek verfügbar.
The approved original version of this doctoral thesis is available in print at TU Wien Bibliothek.
TU Bibliothek Your knowledge hub WIEN

[292] G. M. Vanacore, L. F. Zagonel, and N. Barrett. Surface enhanced covalency and Madelung potentials in Nb doped $SrTiO_3$ (100),(110) and (111) single crystals. *Surface Science*, 604:1674, 2010.

[293] B. Roas, L. Schultz, and G. Endres. Epitaxial growth of $YBa_2Cu_3O_{7-x}$ thin films by a laser evaporation process. *Applied Physics Letters*, 53:1557, 1988.

[294] K. Ueda and M. Naito. As-grown superconducting MgB_2 thin films prepared by molecular beam epitaxy. *Applied Physics Letters*, 79:2046–2048, 2001.

[295] W. Si, Q. Jie, L. Wu, J. Zhou, G. Gu, P. D. Johnson, and Q. Li. Superconductivity in epitaxial thin films of $Fe_{1.08}Te{:}O_x$. *Physical Review B*, 81:092506, 2010.

[296] H. Guo, C.-H. Yan, J.-W. Liu, Z.-Y. Wang, R. Wu, Z.-D. Zhang, L.-L. Wang, K. He, X.-C. Ma, S.-H. Ji, et al. Topological crystalline insulator $Pb_xSn_{1-x}Te$ thin films on $SrTiO_3$(001) with tunable fermi levels. *APL Materials*, 2:056106, 2014.

[297] Z. Wen-Hao, S. Yi, Z. Jin-Song, L. Fang-Sen, G. Ming-Hua, Z. Yan-Fei, Z. Hui-Min, P. Jun-Ping, X. Ying, W. Hui-Chao, et al. Direct observation of high-temperature superconductivity in one-unit-cell FeSe films. *Chinese Physics Letters*, 31:017401, 2014.

[298] X. Chen, X.-C. Ma, K. He, J.-F. Jia, and Q.-K. Xue. Molecular beam epitaxial growth of topological insulators. *Advanced Materials*, 23:1162, 2011.

[299] Y. Chen, N. Pryds, J. E. Kleibeuker, G. Koster, J. Sun, E. Stamate, B. Shen, G. Rijnders, and S. Linderoth. Metallic and insulating interfaces of amorphous $SrTiO_3$-based oxide heterostructures. *Nano Letters*, 11:3774, 2011.

[300] A. Vailionis, H. Boschker, W. Siemons, E. P. Houwman, D. H. A. Blank, G. Rijnders, and G. Koster. Misfit strain accommodation in epitaxial ABO_3 perovskites: Lattice rotations and lattice modulations. *Physical Review B*, 83:064101, 2011.

[301] D. J. Keeble, S. Wicklein, R. Dittmann, L. Ravelli, R. A. Mackie, and W. Egger. Identification of A-and B-site cation vacancy defects in perovskite oxide thin films. *Physical Review Letters*, 105:226102, 2010.

[302] D. Pesquera, G. Herranz, A. Barla, E. Pellegrin, F. Bondino, E. Magnano, F. Sánchez, and J. Fontcuberta. Surface symmetry-breaking and strain effects on orbital occupancy in transition metal perovskite epitaxial films. *Nature Communications*, 3:1, 2012.

[303] A. Ohtomo and H. Y. Hwang. A high-mobility electron gas at the $LaAlO_3/SrTiO_3$ heterointerface. *Nature*, 427:423, 2004.

[304] A. F. Santander-Syro, O. Copie, T. Kondo, F. Fortuna, S. Pailhes, R. Weht, X. G. Qiu, F. Bertran, A. Nicolaou, A. Taleb-Ibrahimi, et al. Two-dimensional electron gas with universal subbands at the surface of $SrTiO_3$. *Nature*, 469:189, 2011. DOI: 10.1038/nature09720.

[305] S. M. Walker, F. Y. Bruno, Z. Wang, A. de La Torre, S. Riccó, A. Tamai, T. K. Kim, M. Hoesch, M. Shi, M. S. Bahramy, et al. Carrier-density control of the $SrTiO_3$(001) surface 2D electron gas studied by ARPES. *Advanced Materials*, 27:3894, 2015.

[306] Z. S. Popović, S. Satpathy, and R. M. Martin. Origin of the two-dimensional electron gas carrier density at the $LaAlO_3$ on $SrTiO_3$ interface. *Physical Review Letters*, 101:256801, 2008.

[307] A. Chikina, F. Lechermann, M.-A. Husanu, M. Caputo, C. Cancellieri, X. Wang, T. Schmitt, M. Radović, and V. N. Strocov. Orbital ordering of the mobile and localized electrons at oxygen-deficient $LaAlO_3/SrTiO_3$ interfaces. *ACS Nano*, 12:7927, 2018. DOI: 10.1021/acsnano.8b02335.

[308] Y. Z. Chen, N. Bovet, F. Trier, D. V. Christensen, F. M. Qu, N. H. Andersen, T. Kasama, W. Zhang, R. Giraud, J. Dufouleur, et al. A high-mobility two-dimensional electron gas at the spinel/perovskite interface of γ-$Al_2O_3/SrTiO_3$. *Nature Communications*, 4:1, 2013.

[309] W. Niu, Y. Zhang, Y. Gan, D. V. Christensen, M. V. Soosten, E. J. Garcia-Suarez, A. Riisager, X. Wang, Y. Xu, R. Zhang, et al. Giant tunability of the two-dimensional electron gas at the interface of γ-$Al_2O_3/SrTiO_3$. *Nano Letters*, 17:6878, 2017.

Die approbierte gedruckte Originalversion dieser Dissertation ist an der TU Wien Bibliothek verfügbar.
The approved original version of this doctoral thesis is available in print at TU Wien Bibliothek.
TU Bibliothek WIEN Your knowledge hub

[310] X. Xiang, L. Qiao, H. Y. Xiao, F. Gao, X. T. Zu, S. Li, and W. L. Zhou. Effects of surface defects on two-dimensional electron gas at $NdAlO_3/SrTiO_3$ interface. *Scientific Reports*, 4:1, 2014.

[311] S. W. Lee, Y. Liu, J. Heo, and R. G. Gordon. Creation and control of two-dimensional electron gas using Al-based amorphous oxides/$SrTiO_3$ heterostructures grown by atomic layer deposition. *Nano Letters*, 12:4775, 2012.

[312] Z. Huang, K. Han, S. Zeng, M. Motapothula, A. Y. Borisevich, S. Ghosh, W. Lü, C. Li, W. Zhou, Z. Liu, et al. The effect of polar fluctuation and lattice mismatch on carrier mobility at oxide interfaces. *Nano Letters*, 16:2307, 2016.

[313] D. G. Schlom and J. Mannhart. Oxide electronics: Interface takes charge over Si. *Nature Materials*, 10:168, 2011.

[314] S. D. Ha and S. Ramanathan. Adaptive oxide electronics: A review. *Journal of Applied Physics*, 110:14, 2011.

[315] H. H. Sønsteby, E. Skaar, Ø. S. Fjellvåg, J. E. Bratvold, H. Fjellvåg, and O. Nilsen. A foundation for complex oxide electronics-low temperature perovskite epitaxy. *Nature Communications*, 11:1, 2020.

[316] N. J. Goble, R. Akrobetu, H. Zaid, S. Sucharitakul, M.-H. Berger, A. Sehirlioglu, and X. P. A. Gao. Anisotropic electrical resistance in mesoscopic $LaAlO_3/SrTiO_3$ devices with individual domain walls. *Scientific Reports*, 7:1, 2017. DOI: 10.1038/srep44361.

[317] E. Fabbri, M. Nachtegaal, T. Binninger, X. Cheng, B.-J. Kim, J. Durst, F. Bozza, T. Graule, R. Schäublin, L. Wiles, et al. Dynamic surface self-reconstruction is the key of highly active perovskite nano-electrocatalysts for water splitting. *Nature Materials*, 16:925, 2017.

[318] F. Polo-Garzon, V. Fung, X. Liu, Z. D. Hood, E. E. Bickel, L. Bai, H. Tian, G. S. Foo, M. Chi, D.-E. Jiang, et al. Understanding the impact of surface reconstruction of perovskite catalysts on CH_4 activation and combustion. *ACS Catalysis*, 8:10306, 2018.

[319] G. Franceschi, M. Schmid, U. Diebold, and M. Riva. Atomically resolved surface phases of $La_{0.8}Sr_{0.2}MnO_3(110)$ thin films. *Journal of Materials Chemistry A*, 8:22947, 2020.

[320] G. Koster, B. L. Kropman, G. J. H. M. Rijnders, D. H. A. Blank, and H. Rogalla. Influence of the surface treatment on the homoepitaxial growth of $SrTiO_3$. *Materials Science and Engineering: B*, 56:209, 1998. DOI: 10.1016/S0921-5107(98)00238-4.

[321] S. A. Chambers, T. C. Droubay, C. Capan, and G. Y. Sun. Unintentional F doping of $SrTiO_3$ (001) etched in HF acid-structure and electronic properties. *Surface Science*, 606:554, 2012. DOI: 10.1016/j.susc.2011.11.029.

[322] J. G. Connell, B. J. Isaac, G. B. Ekanayake, D. R. Strachan, and S. S. A. Seo. Preparation of atomically flat $SrTiO_3$ surfaces using a deionized-water leaching and thermal annealing procedure. *Applied Physics Letters*, 101:251607, 2012. DOI: 10.1063/1.4773052.

[323] M. Kawasaki, K. Takahashi, T. Maeda, R. Tsuchiya, M. Shinohara, O. Ishiyama, T. Yonezawa, M. Yoshimoto, and H. Koinuma. Atomic control of the $SrTiO_3$ crystal surface. *Science*, 266:1540, 1994.

[324] G. Koster, B. L. Kropman, G. J. H. M. Rijnders, D. H. A. Blank, and H. Rogalla. Quasi-ideal strontium titanate crystal surfaces through formation of strontium hydroxide. *Applied Physics Letters*, 73:2920, 1998.

[325] D. S. Deak, F. Silly, D. T. Newell, and M. R. Castell. Ordering of TiO_2-based nanostructures on $SrTiO_3(001)$ surfaces. *The Journal of Physical Chemistry B*, 110:9246, 2006.

[326] M. R. Castell. Scanning tunneling microscopy of reconstructions on the $SrTiO_3(001)$ surface. *Surface Science*, 505:1, 2002.

[327] F. Silly, D. T. Newell, and M. R Castell. $SrTiO_3(001)$ reconstructions: the (2×2) to $c(4\times4)$ transition. *Surface Science*, 600:219, 2006.

Die approbierte gedruckte Originalversion dieser Dissertation ist an der TU Wien Bibliothek verfügbar.
The approved original version of this doctoral thesis is available in print at TU Wien Bibliothek.
TU Bibliothek Your knowledge hub WIEN

[328] J. D. Baniecki, M. Ishii, K. Kurihara, K. Yamanaka, T. Yano, K. Shinozaki, T. Imada, K. Nozaki, and N. Kin. Photoemission and quantum chemical study of $SrTiO_3$(001) surfaces and their interaction with CO_2. *Physical Review B*, 78:195415, 2008.

[329] R. Herger, P. R. Willmott, O. Bunk, C. M. Schlepütz, B. D. Patterson, and B. Delley. Surface of strontium titanate. *Physical Review Letters*, 98:076102, 2007.

[330] M. Kareev, S. Prosandeev, J. Liu, C. Gan, A. Kareev, J. W. Freeland, M. Xiao, and J. Chakhalian. Atomic control and characterization of surface defect states of TiO_2 terminated $SrTiO_3$ single crystals. *Applied Physics Letters*, 93:061909, 2008.

[331] S. Gerhold, Z. Wang, M. Schmid, and U. Diebold. Stoichiometry-driven switching between surface reconstructions on $SrTiO_3$ (001). *Surface Science*, 621:L1, 2014.

[332] R. Di Capua, M. Radović, G. M. De Luca, I. Maggio-Aprile, F. M. Granozio, N. C. Plumb, Z. Ristic, U. S. Di Uccio, R. Vaglio, and M. Salluzzo. Observation of a two-dimensional electron gas at the surface of annealed $SrTiO_3$ single crystals by scanning tunneling spectroscopy. *Physical Review B*, 86:155425, 2012.

[333] R. Herger, P. R. Willmott, O. Bunk, C. M. Schlepütz, B. D. Patterson, B. Delley, V. L. Shneerson, P. F. Lyman, and D. K. Saldin. Surface structure of $SrTiO_3$(001). *Physical Review B*, 76:195435, 2007.

[334] O. E. Dagdeviren, G. H. Simon, K. Zou, F. J. Walker, C. Ahn, E. I. Altman, and U. D. Schwarz. Surface phase, morphology, and charge distribution transitions on vacuum and ambient annealed $SrTiO_3$(100). *Physical Review B*, 93:195303, 2016.

[335] N. Erdman, O. Warschkow, M. Asta, K. R. Poeppelmeier, D. E. Ellis, and L. Marks. Surface structures of $SrTiO_3$(001): A TiO_2-rich reconstruction with a $c(4\times2)$ unit cell. *Journal of the American Chemical Society*, 125:10050, 2003.

[336] C. H. Lanier, A. van de Walle, N. Erdman, E. Landree, O. Warschkow, A. Kazimirov, K. R. Poeppelmeier, J. Zegenhagen, M. Asta, and L. D. Marks. Atomic-scale structure of the $SrTiO_3$(001)-$c(6\times2)$ reconstruction: Experiments and first-principles calculations. *Physical Review B*, 76(4):045421, 2007.

[337] T.-Y. Chien, T. S. Santos, M. Bode, N. P. Guisinger, and J. W. Freeland. Controllable local modification of fractured Nb-doped $SrTiO_3$ surfaces. *Applied Physics Letters*, 95:163107, 2009.

[338] T.-Y. Chien, N. P. Guisinger, and J. W. Freeland. Survey of fractured $SrTiO_3$ surfaces: from the micrometer to nanometer scale. *Journal of Vacuum Science & Technology B, Nanotechnology and Microelectronics: Materials, Processing, Measurement, and Phenomena*, 28:C5A11, 2010.

[339] N. P. Guisinger, T. S. Santos, J. R. Guest, T.-Y. Chien, A. Bhattacharya, J. W. Freeland, and M. Bode. Nanometer-scale striped surface terminations on fractured $SrTiO_3$ surfaces. *ACS Nano*, 3:4132, 2009.

[340] W. Sitaputra, M. Skowronski, and R. M. Feenstra. Topographic and electronic structure of cleaved $SrTiO_3$ (001) surfaces. *Journal of Vacuum Science & Technology A: Vacuum, Surfaces, and Films*, 33:031402, 2015.

[341] I. Sokolović, M. Schmid, U. Diebold, and M. Setvín. Incipient ferroelectricity: A route towards bulk-terminated $SrTiO_3$. *Physical Review Materials*, 3:034407, 2019.

[342] T. Sakudo and H. Unoki. Dielectric properties of $SrTiO_3$ at low temperatures. *Physical Review Letters*, 26:851, 1971.

[343] K. A. Müller, W. Berlinger, and F. Waldner. Characteristic structural phase transition in perovskite-type compounds. *Physical Review Letters*, 21:814, 1968.

[344] U. Aschauer and N. A. Spaldin. Competition and cooperation between antiferrodistortive and ferroelectric instabilities in the model perovskite $SrTiO_3$. *Journal of Physics: Condensed Matter*, 26:122203, 2014.

[345] K. A. Müller and H. Burkard. $SrTiO_3$: An intrinsic quantum paraelectric below 4 K. *Physical Review B*, 19:3593, 1979. DOI: 10.1103/PhysRevB.19.3593.

Die approbierte gedruckte Originalversion dieser Dissertation ist an der TU Wien Bibliothek verfügbar.
The approved original version of this doctoral thesis is available in print at TU Wien Bibliothek.
TU Bibliothek Your knowledge hub WIEN

[346] H. M. Christen, E. D. Specht, S. S. Silliman, and K. S. Harshavardhan. Ferroelectric and antiferroelectric coupling in superlattices of paraelectric perovskites at room temperature. *Physical Review B*, 68:020101, 2003.

[347] W. J. Burke and R. J. Pressley. Stress induced ferroelectricity in $SrTiO_3$. *Solid State Communications*, 9:191, 1971. DOI: 10.1016/0038-1098(71)90115-3.

[348] J. H. Haeni, P. Irvin, W. Chang, R. Uecker, P. Reiche, Y. L. Li, S. Choudhury, W. Tian, M. E. Hawley, B. Craigo, A. K. Tagantsev, X. Q. Pan, S. K. Streiffer, L. Q. Chen, S. W. Kirchoefer, J. Levy, and D. G. Schlom. Room-temperature ferroelectricity in strained $SrTio_3$. *Nature*, 430:758, 2004. DOI: 10.1038/nature02773.

[349] A. A. Griffith. The phenomena of rupture and flow in solids. *Philosophical Transactions of the Royal Society A*, 221:163, 1921.

[350] R. Bechstein, C. Gonzalez, J. Schutte, P. Jelinek, R. Perez, and A. Kuhnle. 'All-inclusive' imaging of the rutile $TiO_2(110)$ surface using nc-AFM. *Nanotechnology*, 20:505703, 2009.

[351] A. S. Foster, C. Barth, and C. R. Henry. Chemical identification of ions in doped NaCl by scanning force microscopy. *Physical Review Letters*, 102:256103, 2009.

[352] M. Ulreich, L. A. Boatner, I. Sokolović, M. Reticcioli, B. Stoeger, F. Poelzleitner, C. Franchini, M. Schmid, U. Diebold, and M. Setvín. Defect chemistry of Eu dopants in NaI scintillators studied by atomically resolved force microscopy. *Physical Review Materials*, 3:075004, 2019.

[353] P. W. Tasker. The stability of ionic crystal surfaces. *Journal of Physics C: Solid State Physics*, 12:4977, 1979.

[354] C. Noguera. Polar oxide surfaces. *Journal of Physics: Condensed Matter*, 12:R367, 2000. DOI: 10.1088/0953-8984/12/31/201.

[355] C. A. Ventrice Jr, Th. Bertrams, H. Hannemann, A. Brodde, and H. Neddermeyer. Stable reconstruction of the polar (111) surface of NiO on Au(111). *Physical Review B*, 49:5773, 1994.

[356] B. Kronberg and P. Stenius. The effect of surface polarity on the adsorption of nonionic surfactants. I. Thermodynamic considerations. *Journal of Colloid and Interface Science*, 102:410, 1984.

[357] S. Thiel, G. Hammerl, A. Schmehl, C. W. Schneider, and J. Mannhart. Tunable quasi-two-dimensional electron gases in oxide heterostructures. *Science*, 313:1942, 2006.

[358] P. R. Willmott, S. A. Pauli, R. Herger, C. M. Schlepütz, D. Martoccia, B. D. Patterson, B. Delley, R. Clarke, D. Kumah, C. Cionca, et al. Structural basis for the conducting interface between $LaAlO_3$ and $SrTiO_3$. *Physical Review Letters*, 99:155502, 2007.

[359] H. Lee, N. Campbell, J. Lee, T. J. Asel, T. R. Paudel, H. Zhou, J. W. Lee, B. Noesges, J. Seo, B. Park, et al. Direct observation of a two-dimensional hole gas at oxide interfaces. *Nature materials*, 17:231, 2018.

[360] M. Setvín, M. Reticcioli, F. Poelzleitner, J. Hulva, M. Schmid, L. A. Boatner, C. Franchini, and U. Diebold. Polarity compensation mechanisms on the perovskite surface $KTaO_3(001)$. *Science*, 359:572, 2018.

[361] J. Goniakowski, C. Noguera, and L. Giordano. Prediction of uncompensated polarity in ultrathin films. *Physical Review Letters*, 98:205701, 2007.

[362] J. Goniakowski and C. Noguera. The concept of weak polarity: an application to the $SrTiO_3(001)$ surface. *Surface science*, 365:L657, 1996.

[363] M. Stengel and D. Vanderbilt. Berry-phase theory of polar discontinuities at oxide-oxide interfaces. *Physical Review B*, 80:241103, 2009.

[364] M. Stengel. Electrostatic stability of insulating surfaces: Theory and applications. *Physical Review B*, 84:205432, 2011.

Die approbierte gedruckte Originalversion dieser Dissertation ist an der TU Wien Bibliothek verfügbar.
The approved original version of this doctoral thesis is available in print at TU Wien Bibliothek.
TU Bibliothek Your knowledge hub WIEN

[365] S. V. Kalinin and D. A. Bonnell. Local potential and polarization screening on ferroelectric surfaces. *Physical Review B*, 63:125411, 2001.

[366] S. V. Kalinin, Y. Kim, D. D. Fong, and A. N. Morozovska. Surface-screening mechanisms in ferroelectric thin films and their effect on polarization dynamics and domain structures. *Reports on Progress in Physics*, 81:036502, 2018.

[367] S. V. Kalinin, C. Y. Johnson, and D. A. Bonnell. Domain polarity and temperature induced potential inversion on the $BaTiO_3$(100) surface. *Journal of Applied Physics*, 91:3816, 2002.

[368] J. Goniakowski, F. Finocchi, and C. Noguera. Polarity of oxide surfaces and nanostructures. *Reports on Progress in Physics*, 71:016501, 2007.

[369] A. M. Kolpak, D. Li, R. Shao, A. M. Rappe, and D. A. Bonnell. Evolution of the structure and thermodynamic stability of the $BaTiO_3$(001) surface. *Physical Review Letters*, 101:036102, 2008.

[370] J. M. P. Martirez, E. H. Morales, W. A. Saidi, D. A. Bonnell, and A. M. Rappe. Atomic and electronic structure of the $BaTiO_3(001)(5\times5)R26.6°$ surface reconstruction. *Physical Review Letters*, 109:256802, 2012.

[371] J. Zegenhagen. Surface structure determination with X-ray standing waves. *Surface Science Reports*, 18:202, 1993.

[372] I. Sokolović, G. Franceschi, Z. Wang, J. Xu, J. Pavelec, M. Riva, M. Schmid, U. Diebold, and M. Setvín. Quest for a pristine unreconstructed $SrTiO_3$(001) surface: An atomically resolved study via noncontact atomic force microscopy. *Physical Review B*, 103:L241406, 2021.

[373] A. Walsh, D. O. Scanlon, S. Chen, X. G. Gong, and S.-H. Wei. Self-regulation mechanism for charged point defects in hybrid halide perovskites. *Angewandte Chemie*, 127:1811, 2015.

[374] A. Walsh, C. R. A. Catlow, A. G. H. Smith, A. A. Sokol, and S. M. Woodley. Strontium migration assisted by oxygen vacancies in $SrTiO_3$ from classical and quantum mechanical simulations. *Physical Review B*, 83:220301, 2011.

[375] M. Riva, G. Franceschi, Q. Lu, B. Schmid, M.and Yildiz, and U. Diebold. Pushing the detection of cation nonstoichiometry to the limit. *Physical Review Materials*, 3:043802, 2019.

[376] M. Riva, G. Franceschi, M. Schmid, and U. Diebold. Epitaxial growth of complex oxide films: Role of surface reconstructions. *Physical Review Research*, 1:033059, 2019.

[377] R. A. De Souza. Oxygen diffusion in $SrTiO_3$ and related perovskite oxides. *Advanced Functional Materials*, 25:6326, 2015.

[378] N. Erdman, K. R. Poeppelmeier, M. Asta, O. Warschkow, D. E. Ellis, and L. D. Marks. The structure and chemistry of the TiO_2-rich surface of $SrTiO_3$(001). *Nature*, 419:55, 2002.

[379] N. Erdman and L. D. Marks. $SrTiO_3$(001) surface structures under oxidizing conditions. *Surface Science*, 526:107, 2003.

[380] T. Nishimura, A. Ikeda, H. Namba, T. Morishita, and Y. Kido. Structure change of TiO_2-terminated $SrTiO_3$(001) surfaces by annealing in O_2 atmosphere and ultrahigh vacuum. *Surface science*, 421:273, 1999.

[381] F. Gellé, R. Chirita, D. Mertz, M. V. Rastei, A. Dinia, and S. Colis. Guideline to atomically flat TiO_2-terminated $SrTiO_3$(001) surfaces. *Surface Science*, 677:39, 2018.

[382] QD Jiang and J Zegenhagen. $c(6\times2)$ and $c(4\times2)$ reconstruction of $SrTiO_3$(001). *Surface Science*, 425:343, 1999.

[383] J. E. T. Andersen and P. J. Möller. Impurity-induced 900 °c (2×2) surface reconstruction of $SrTiO_3$(100). *Applied Physics Letters*, 56:1847, 1990.

Die approbierte gedruckte Originalversion dieser Dissertation ist an der TU Wien Bibliothek verfügbar.
The approved original version of this doctoral thesis is available in print at TU Wien Bibliothek.
TU Bibliothek Your knowledge hub WIEN

[384] W. Braun, M. Jäger, G. Laskin, P. Ngabonziza, W. Voesch, P. Wittlich, and J. Mannhart. *In situ* thermal preparation of oxide surfaces. *APL Materials*, 8:071112, 2020.

[385] W. Meevasana, P. D. C. King, R. H. He, S. K. Mo, M. Hashimoto, A. Tamai, P. Songsiriritthigul, F. Baumberger, and Z. X. Shen. Creation and control of a two-dimensional electron liquid at the bare $SrTiO_3$ surface. *Nature Materials*, 10:114, 2011.

[386] P. D. C. King, S. M. Walker, A. Tamai, A. de La Torre, T. Eknapakul, P. Buaphet, S.-K. Mo, W. Meevasana, M. S. Bahramy, and F. Baumberger. Quasiparticle dynamics and spin–orbital texture of the $SrTiO_3$ two-dimensional electron gas. *Nature Communications*, 5:1, 2014.

[387] Z. Wang, S. M. Walker, A. Tamai, Y. Wang, Z. Ristic, F. Y. Bruno, A. de La Torre, S. Riccò, N. C. Plumb, M. Shi, et al. Tailoring the nature and strength of electron–phonon interactions in the $SrTiO_3(001)$ 2D electron liquid. *Nature Materials*, 15:835, 2016.

[388] D. M. Kienzle, A. E. Becerra-Toledo, and L. D. Marks. Vacant-site octahedral tilings on $SrTiO_3(001)$, the $(\sqrt{13} \times \sqrt{13})R33.7°$ surface, and related structures. *Physical Review Letters*, 106:176102, 2011.

[389] T. Ohsawa, R. Shimizu, K. Iwaya, S. Shiraki, and T. Hitosugi. Negligible Sr segregation on $SrTiO_3(001)$-$(\sqrt{13} \times \sqrt{13})R33.7°$ reconstructed surfaces. *Applied Physics Letters*, 108:161603, 2016.

[390] CW Bark, DA Felker, Yong Wang, Y Zhang, HW Jang, CM Folkman, JW Park, SH Baek, H Zhou, DD Fong, et al. Tailoring a two-dimensional electron gas at the $LaAlO_3/SrTiO_3(001)$ interface by epitaxial strain. *Proceedings of the National Academy of Sciences*, 108:4720, 2011.

[391] Maria A Torija, Manish Sharma, Jaume Gazquez, Maria Varela, Chunyong He, Josh Schmitt, Julie A Borchers, Mark Laver, Sami El-Khatib, and Chris Leighton. Chemically driven nanoscopic magnetic phase separation at the $SrTiO_3(001)/La_{1-x}Sr_xCoO_3$ interface. *Advanced Matererials*, 23:2711, 2011.

[392] Fangsen Li, Qinghua Zhang, Chenjia Tang, Chong Liu, Jinan Shi, CaiNa Nie, Guanyu Zhou, Zheng Li, Wenhao Zhang, Can-Li Song, et al. Atomically resolved $FeSe/SrTiO_3(001)$interface structure by scanning transmission electron microscopy. *2D Materials*, 3:024002, 2016.

[393] Weiwei Zhao, Mingda Li, Cui-Zu Chang, Jue Jiang, Lijun Wu, Chaoxing Liu, Jagadeesh S Moodera, Yimei Zhu, and Moses HW Chan. Direct imaging of electron transfer and its influence on superconducting pairing at $FeSe/SrTiO_3$ interface. *Science Advances*, 4:eaao2682, 2018.

[394] S. Cook, K. Letchworth-Weaver, I.-C. Tung, T. K. Andersen, H. Hong, L. D. Marks, and D. D. Fong. How heteroepitaxy occurs on strontium titanate. *Science Advances*, 5:eaav0764, 2019.

[395] N. Barišić, Y. Li, Y.-C. Zhao, X.and Cho, G. Chabot-Couture, G. Yu, and M. Greven. Demonstrating the model nature of the high-temperature superconductor $HgBa_2CuO_{4+\delta}$. *Physical Review B*, 78:054518, 2008.

[396] N. Barišić, M. K. Chan, Y. Li, G. Yu, X. Zhao, M. Dressel, A. Smontara, and M. Greven. Universal sheet resistance and revised phase diagram of the cuprate high-temperature superconductors. *Proceedings of the National Academy of Sciences*, 110:12235, 2013.

[397] D. Halwidl, B. Stöger, W. Mayr-Schmölzer, J. Pavelec, D. Fobes, J. Peng, G. S. Mao, Z.and Parkinson, M. Schmid, F. Mittendorfer, J. Redinger, and U. Diebold. Adsorption of water at the SrO surface of ruthenates. *Nature Materials*, 15:450, 2016.

[398] D. Halwidl, W. Mayr-Schmölzer, D. Fobes, J. Peng, Z. Mao, M. Schmid, F. Mittendorfer, J. Redinger, and U. Diebold. Ordered hydroxyls on $Ca_3Ru_2O_7(001)$. *Nature Communications*, 8:1, 2017.

[399] O. Dulub and U. Diebold. Preparation of a pristine TiO_2 anatase (101) surface by cleaving. *Journal of Physics: Condensed Matter*, 22:084014, 2010.

[400] I. Sokolović *et al.* Universal cubic perovskite oxide cleaving device – applied insights from $SrTiO_3$. *in preparation.*

[401] Fusion 360 by autodesk. https://www.autodesk.com.

Die approbierte gedruckte Originalversion dieser Dissertation ist an der TU Wien Bibliothek verfügbar.
The approved original version of this doctoral thesis is available in print at TU Wien Bibliothek.
TU Bibliothek Your knowledge hub WIEN

[402] J. L. Servoin, Y. Luspin, and F. Gervais. Infrared dispersion in $SrTiO_3$ at high temperature. *Physical Review B*, 22:5501, 1980. DOI: 10.1103/PhysRevB.22.5501.

[403] Y. Yamada and G. Shirane. Neutron scattering and nature of the soft optical phonon in $SrTiO_3$. *Journal of the Physical Society of Japan*, 26:396, 1969. DOI: 10.1143/JPSJ.26.396.

[404] L. D. Landau. On the theory of phase transitions. I. *Journal of Experimental and Theoretical Physics (JETP)*, 11:19, 1937.

[405] L. Reimer. *Scanning electron microscopy: physics of image formation and microanalysis*. IOP Publishing, 2000.

[406] J. Goldstein. *Practical scanning electron microscopy: electron and ion microprobe analysis*. Springer Science & Business Media, 2012.

[407] J. Cazaux. Material contrast in SEM: Fermi energy and work function effects. *Ultramicroscopy*, 110:242, 2010.

[408] University Service Centre for Transmission Electron Microscopy (USTEM), TU Wien, Austria. https://www.ustem.tuwien.ac.at/EN/.

[409] I. Sokolović *et al.* Screening-dependent macroscopic properties of cleaved $SrTiO_3(001)$ surfaces. *in preparation*.

[410] G. Catalan, J. Seidel, R. Ramesh, and J. F. Scott. Domain wall nanoelectronics. *Reviews of Modern Physics*, 84:119, 2012.

[411] R. Takahashi, Ø. Dahl, E. Eberg, J. K. Grepstad, and T. Tybell. Ferroelectric stripe domains in $PbTiO_3$ thin films: Depolarization field and domain randomness. *Journal of Applied Physics*, 104:064109, 2008.

[412] A. D. Wright, C. Verdi, R. L. Milot, G. E. Eperon, M. A. Pérez-Osorio, H. J. Snaith, F. Giustino, M. B. Johnston, and L. M. Herz. Electron–phonon coupling in hybrid lead halide perovskites. *Nature Communications*, 7:1, 2016.

[413] K. Miyata and X.-Y. Zhu. Ferroelectric large polarons. *Nature Materials*, 17:379, 2018.

[414] M. Braden, W. Reichardt, Y. Sidis, Z. Mao, and Y. Maeno. Lattice dynamics and electron-phonon coupling in Sr_2RuO_4: Inelastic neutron scattering and shell-model calculations. *Physical Review B*, 76:014505, 2007.

[415] S. Driza, N .and Blanco-Canosa, M. Bakr, S. Soltan, M. Khalid, L. Mustafa, K. Kawashima, G. Christiani, H. U. Habermeier, G. Khaliullin, et al. Long-range transfer of electron–phonon coupling in oxide superlattices. *Nature Materials*, 11:675, 2012.

[416] Jin-Jian Zhou, Olle Hellman, and Marco Bernardi. Electron-phonon scattering in the presence of soft modes and electron mobility in $SrTiO_3$ perovskite from first principles. *Physical Review Letters*, 121:226603, 2018.

[417] J. L. M. van Mechelen, D. van der Marel, C. Grimaldi, A. B. Kuzmenko, N. P. Armitage, N. Reyren, H. Hagemann, and I. I. Mazin. Electron-phonon interaction and charge carrier mass enhancement in $SrTiO_3$. *Physical Review Letters*, 100:226403, 2008.

[418] M. Takizawa, K. Maekawa, H. Wadati, T. Yoshida, A. Fujimori, H. Kumigashira, and M. Oshima. Angle-resolved photoemission study of Nb-doped $SrTiO_3$. *Physical Review B*, 79:113103, 2009.

[419] T. Jarlborg. Tuning of the electronic screening and electron-phonon coupling in doped $SrTiO_3$ and WO_3. *Physical Review B*, 61:9887, 2000.

[420] I. Sokolović *et al.* Charge separation on a nominally centro-symmetric $SrTiO_3(001)$. *in preparation*.

[421] E. H. Blevis and C. R. Crowell. Temperature dependence of the work function of single-crystal faces of copper. *Physical Review*, 133:A580, 1964.

[422] H. Chen and N. Umezawa. Hole localization, migration, and the formation of peroxide anion in perovskite $SrTiO_3$. *Physical Review B*, 90:035202, 2014.

Die approbierte gedruckte Originalversion dieser Dissertation ist an der TU Wien Bibliothek verfügbar.
The approved original version of this doctoral thesis is available in print at TU Wien Bibliothek.
TU Bibliothek WIEN Your knowledge hub

[423] P. Erhart, A. Klein, D. Åberg, and B. Sadigh. Efficacy of the DFT+U formalism for modeling hole polarons in perovskite oxides. *Physical Review B*, 90:035204, 2014.

[424] T. Shimada, Y. Ichiki, G. Fujimoto, T. Xu, J. Wang, H. Hirakata, et al. Ferrotoroidic polarons in antiferrodistortive $SrTiO_3$. *Physical Review B*, 101:214101, 2020.

[425] S. P. Ong, Y. Mo, and G. Ceder. Low hole polaron migration barrier in lithium peroxide. *Physical Review B*, 85:081105, 2012.

[426] T. Liu, M. Cui, and M. Dupuis. Hole polaron transport in bismuth vanadate $BiVO_4$ from hybrid density functional theory. *The Journal of Physical Chemistry C*, 124:23038, 2020.

[427] B. Himmetoglu, A. Janotti, L. Bjaalie, and C. G. van de Walle. Interband and polaronic excitations in $YTiO_3$ from first principles. *Physical Review B*, 90:161102, 2014.

[428] L. Bjaalie, A. Janotti, K. Krishnaswamy, and C. G. van de Walle. Point defects, impurities, and small hole polarons in $GdTiO_3$. *Physical Review B*, 93:115316, 2016.

[429] M. Kisiel, O. O. Brovko, D. Yildiz, R. Pawlak, U. Gysin, E. Tosatti, and E. Meyer. Mechanical dissipation from charge and spin transitions in oxygen-deficient $SrTiO_3$ surfaces. *Nature Communications*, 9:1, 2018.

[430] D. Yildiz, M. Kisiel, U. Gysin, O. Gürlü, and E. Meyer. Mechanical dissipation via image potential states on a topological insulator surface. *Nature Materials*, 18:1201, 2019.

[431] I. Sokolović. Distance-dependence of the excitation curves video. https://drive.google.com/file/d/1ozkytgXwtahuY4y-7iscfPbHe_2gGtJL/view?usp=sharing.

[432] G. Teobaldi, W. A. Hofer, O. Bikondoa, C. L. Pang, G. Cabailh, and G. Thornton. Modelling STM images of $TiO_2(110)$ from first-principles: Defects, water adsorption and dissociation products. *Chemical Physics Letters*, 437:73, 2007.

[433] P. Rivero, C. M. Horvath, Z. Zhu, J. Guan, D. Tománek, and S. Barraza-Lopez. Simulated scanning tunneling microscopy images of few-layer phosphorus capped by graphene and hexagonal boron nitride monolayers. *Physical Review B*, 91:115413, 2015.

[434] T-L Chan, CZ Wang, KM Ho, and James R Chelikowsky. Efficient first-principles simulation of noncontact atomic force microscopy for structural analysis. *Physical Review Letters*, 102:176101, 2009.

[435] M. Kim and J. R. Chelikowsky. Simulated non-contact atomic force microscopy for GaAs surfaces based on real-space pseudopotentials. *Applied Surface Science*, 303:163, 2014.

[436] P. Hapala, R. Temirov, F. Stefan Tautz, and P. Jelínek. Origin of high-resolution IETS-STM images of organic molecules with functionalized tips. *Physical Review Letters*, 113:226101, 2014.

[437] H. Mönig, D. R. Hermoso, O. Díaz Arado, M. Todorović, A. Timmer, S. Schüer, G. Langewisch, R. Pérez, and H. Fuchs. Submolecular imaging by noncontact atomic force microscopy with an oxygen atom rigidly connected to a metallic probe. *ACS Nano*, 10:1201, 2016.

[438] I. Sokolović *et al.* Efficient chemically sensitive AFM contrast simulations. *in preparation.*

[439] A. L. Shluger, A. L. Rohl, D. H. Gay, and R. T. Williams. Atomistic theory of the interaction between AFM tips and ionic surfaces. *Journal of Physics: Condensed Matter*, 6:1825, 1994.

[440] A. S. Foster, A. Y. Gal, J. M. Airaksinen, O. H. Pakarinen, Y. J. Lee, J. D. Gale, A. L. Shluger, and R. M. Nieminen. Towards chemical identification in atomic-resolution noncontact AFM imaging with silicon tips. *Physical Review B*, 68:195420, 2003.

[441] M. Ondráček, C. González, and P. Jelínek. Reversal of atomic contrast in scanning probe microscopy on (111) metal surfaces. *Journal of Physics: Condensed Matter*, 24:084003, 2012.

[442] H. Mönig, M. Todorović, M. Z. Baykara, T. C. Schwendemann, L. Rodrigo, E. I. Altman, R. Pérez, and U. D. Schwarz. Understanding scanning tunneling microscopy contrast mechanisms on metal oxides: a case study. *ACS Nano*, 7:10233, 2013.

Die approbierte gedruckte Originalversion dieser Dissertation ist an der TU Wien Bibliothek verfügbar.
The approved original version of this doctoral thesis is available in print at TU Wien Bibliothek.
TU Bibliothek Your knowledge hub WIEN

[443] T. Chutora, B. de la Torre, P. Mutombo, J. Hellerstedt, J. Kopeček, P. Jelínek, and M. Švec. Nitrous oxide as an effective AFM tip functionalization: a comparative study. *Beilstein Journal of Nanotechnology*, 10:315, 2019.

[444] Z. Jakub, F. Kraushofer, M. Bichler, J. Balajka, J. Hulva, J. Pavelec, I. Sokolović, M. Müllner, M. Setvín, M. Schmid, U. Diebold, P. Blaha, and G. Parkinson. Partially dissociated water dimers at the water–hematite interface. *ACS Energy Letters*, 4:390, 2019.

[445] T. S. Chen, F. W. de Wette, and G. P. Alldredge. Studies of vibrational surface modes in ionic crystals. I. detailed shell-model studies for the unrelaxed (001) face of seven crystals having the rocksalt structure. *Physical Review B*, 15:1167, 1977.

[446] S. Sawada and K. Nakamura. Theory of surface rumpling in rock-salt structured ionic crystals. *Journal of Physics C: Solid State Physics*, 12:1183, 1979.

[447] Q. Dai, J. Hu, and M. Salmeron. Adsorption of water on NaCl(100) surfaces: Role of atomic steps. *The Journal of Physical Chemistry B*, 101:1994, 1997.

[448] H. Tissot, J.-J. Gallet, F. Bournel, G. Olivieri, M. G. Silly, F. Sirotti, A. Boucly, and F. Rochet. The electronic structure of saturated NaCl and NaI solutions in contact with a gold substrate. *Topics in Catalysis*, 59:605, 2016.

[449] W. P. Brug, G. Chern, J. Duan, S. A. Safron, J. G. Skofronick, and G. Benedek. Surface phonon modes of the NaI(001) crystal surface by inelastic He atom scattering. *Journal of Vacuum Science & Technology A: Vacuum, Surfaces, and Films*, 8:2632, 1990.

[450] P. Hapala. Probe particle model availabe at github. https://github.com/ProkopHapala/ProbeParticleModel.

[451] J. Peng, D. Cao, Z. He, J. Guo, P. Hapala, R. Ma, B. Cheng, J. Chen, W. J. Xie, X.-Z. Li, P. Jelínek, L.-M. Xu, Y. Q. Gao, E.-G. Wang, and Y. Jiang. The effect of hydration number on the interfacial transport of sodium ions. *Nature*, 557:701, 2018.

[452] A. Liebig, P. Hapala, A. J. Weymouth, and F. J. Giessibl. Quantifying the evolution of atomic interaction of a complex surface with a functionalized atomic force microscopy tip. *Scientific Reports*, 10:1, 2020.

[453] N. Pavliček, B. Schuler, S. Collazos, N. Moll, D. Pérez, E. Guitián, G. Meyer, D. Peña, and L. Gross. On-surface generation and imaging of arynes by atomic force microscopy. *Nature Chemistry*, 7:623, 2015.

[454] A. Riss, A. P. Paz, S. Wickenburg, H.-Z. Tsai, D. G. de Oteyza, A. J. Bradley, M. M. Ugeda, P. Gorman, H. S. Jung, M. F. Crommie, et al. Imaging single-molecule reaction intermediates stabilized by surface dissipation and entropy. *Nature Chemistry*, 8:678, 2016.

[455] A. Shiotari and Y. Sugimoto. Ultrahigh-resolution imaging of water networks by atomic force microscopy. *Nature Communications*, 8:1, 2017.

Die approbierte gedruckte Originalversion dieser Dissertation ist an der TU Wien Bibliothek verfügbar.
The approved original version of this doctoral thesis is available in print at TU Wien Bibliothek.
TU Bibliothek Your knowledge hub WIEN

Curriculum vitae

PERSONAL INFORMATION

Igor Sokolović

Linke Wienzeile 126/21, 1060 Vienna, Republic of Austria

+43 677 6208 5162 igrsklvc@gmail.com

Skype igrsklvc@hotmail.com

Gender Male | Date of birth October 1st, 1989

Nationality Republic of Serbia

EDUCATION

2017-2021

Doctor scientiae technicorum

TU Wien, Vienna University of Technology, Vienna, Republic of Austria

Thesis title: "Compex oxide surfaces studied with noncontact AFM/STM and DFT"

Education in the field of Surface Science in both experiment and theory. Extensive research was conducted on either the bare surfaces of complex oxides or their interaction with adsorbing gas molecules, under mentorship of Prof. Martin Setvín, Prof. Michael Schmid, Prof. Cesare Franchini and Prof. Ulrike Diebold, and resulted in several publications (list below). Scientific contribution consisted of approaching the same fundamentally and technologically relevant surfaces through performing experiments and quantum mechanical modeling. Fully enrolled in the Doctoral School "Solids4Fun" with wide insight into various cutting-edge research groups at the TU Wien.

2013-2016

Master in Physics

Faculty of Sciences, University of Novi Sad, Republic of Serbia

Thesis title: "Dissipative Dynamics of Commensurate Frenkel-Kontorova Model under external forces"

Master's studies completed at the department of Theoretical Condensed Matter Physics.

Detailed theoretical studies of the Solid State Physics, including the phase transitions, non-linear physics, and numerical methods. Thesis focused on the non-linear behavior of coupled classic oscillators through numerical simulations.

2008-2013

Bachelor with Honours in Physics

Faculty of Sciences, University of Novi Sad, Republic of Serbia

Bachelor with Honours studies completed at the department of Astronomy and Astrophysics.

Detailed introduction to all branches of classical and modern Physics with the emphasis on Astrophysics and Astronomy. Personal focus on the subjects of Theoretical Physics.

PERTINENT WORK EXPERIENCE

April 2017 – September 2021

Research Assistant

Professor Diebold's Surface Physics group, Institute of Applied Physics, TU Wien

Conducted independent and supervised research in the area of Surface Physics by designing and performing experiments, as well as designing and performing theoretical calculations and AFM contrast simulations. Most experimental research was performed with low-temperature noncontact atomic force microscopy combined with scanning tunneling microscopy (LT-AFM/STM). The quantum-mechanical theoretical research was performed in the framework of density functional theory (DFT) using Vienna ab initio Simulation Package (VASP) on the Vienna Scientific Cluster (VSC-3).

August 9, 2021

© European Union, 2002-2021 | http://europass.cedefop.europa.eu

Die approbierte gedruckte Originalversion dieser Dissertation ist an der TU Wien Bibliothek verfügbar.
The approved original version of this doctoral thesis is available in print at TU Wien Bibliothek.
TU WIEN Bibliothek Your knowledge hub

October 2010 – April 2017

Science Communicator and Lecturer

Popularization of science. Designed and demonstrated experiments which appeal to elementary school and high school students.

Held lectures in popular science, mainly in the field of Astronomy and Astrophysics, sometimes combined with organized observations of the Sun or the night sky, within Astronomical Society of Novi Sad.

October 2010 – April 2017

Tutor

Tutored and supported university and high school students in the fields of Physics, Mathematics and Statistics, either individually, in small groups, or online.

April 2014 – April 2017

Statistics and Programming Freelancer

Freelancer.com

Various projects in Statistical Analysis, Optimization, Prediction, Inference, Visualization etc.

PERSONAL SKILLS

Mother tongue: Serbian

Other languages

	UNDERSTANDING		SPEAKING		WRITING
	Listening	Reading	Spoken interaction	Spoken production	
English	C2	C2	C2	C2	C2
German	B1/B2	B1/B2	B1/B2	B1/B2	B1/B2

Levels: A1/A2: Basic user - B1/B2: Independent user - C1/C2: Proficient user
Common European Framework of Reference (CEF) level

English language standardized test scores':

TOEFL: 112/120 iBT
GRE: top 15% from the beginning of test administration
CAE: grade A

German language courses up to B2 level.

Driving licence: Category B

© European Union, 2002-2021 | http://europass.cedefop.europa.eu

Die approbierte gedruckte Originalversion dieser Dissertation ist an der TU Wien Bibliothek verfügbar.
The approved original version of this doctoral thesis is available in print at TU Wien Bibliothek.
TU Bibliothek Your knowledge hub WIEN

PUBLICATION LIST

Title: Incipient feroelectricity: a route towards bulk-terminated $SrTiO_3$
Authors: Igor Sokolović, Michael Schmid, Ulrike Diebold, Martin Setvín
Journal: Physical Review Materials 3 (2019): 034407.
DOI: https://doi.org/10.1103/PhysRevMaterials.3.034407
Short summary: Successfully cleaving the widely-studied technologically and fundamentally important $SrTiO_3$(001) surface which was considered impossible to cleave for the past several decades.
Contribution: Designed the cleaving procedure, performed the AFM/STM experiments, and wrote the paper.

Title: Interplay between polarons and adsorbates: CO on rutile TiO_2(110)
Authors: Michele Reticcioli, Igor Sokolović, Michael Schmid, Ulrike Diebold, Martin Setvín, Cesare Franchini
Journal: Physical Review Letters 122 (2019): 016805.
DOI: https://doi.org/10.1103/PhysRevLett.122.016805
Short summary: Observing several types of CO coupling to the polarons in the substrate surface.
Contribution: Designed the experiments, performed the AFM/STM experiments.

Title: Partially Dissociated Water Dimers at the Water-Hematite Interface
Authors: Zdenek Jakub, Florian Kraushofer, Magdalena Bichler, Jan Balajka, Jan Hulva, Jiri Pavelec, Igor Sokolović, Matthias Müllner, Martin Setvín, Michael Schmid, Ulrike Diebold, Peter Blaha, Gareth S. Parkinson
Journal: ACS Energy Letters 4 (2019): 390-396.
DOI: https://doi.org/10.1021/acsenergylett.8b02324
Short summary: Observation of strongly bound water agglomerates on the surface which need to be taken into account while considering oxygen evolution reaction.
Contribution: Performed the simulations of the obtained AFM contrast.

Title: Defect chemistry of Eu dopants in NaI scintillators studied by atomically resolved force microscopy
Authors: Manuel Ulreich, Lynn A. Boatner, Igor Sokolović, Michele Reticcioli, Berthold Stöger, Flora Pölzleitner, Cesare Franchini, Michael Schmid, Ulrike Diebold, Martin Setvín
Journal: Physical Review Materials 3 (2019): 075004.
DOI: https://doi.org/10.1103/PhysRevMaterials.3.075004
Short summary: Observation of various Eu-based precipitates in a home-grown Eu-doped scintillator.
Contribution: Performed DFT calculations to optimize one of the observed structures.

Title: Devil's staircase and the absence of chaos in the dc-and ac-driven overdamped Frenkel-Kontorova model
Authors: Igor Sokolović, Petar Mali, J Odavić, Slobodan Radošević, S Yu Medvedeva, Andre E Botha, Yu M Shukrinov, Jasmina Tekić
Journal: Physical Review E 96 (2017): 022210.
DOI: https://doi.org/10.1103/PhysRevE.96.022210
Short summary: Observation of the fractal (infinitely resonant) response function of a non-chaotic, classical, driven oscillator system.
Contribution: Designed the research, performed extensive data exploration and analysis, wrote the paper.

Title: Resolving the adsorption of molecular O_2 on the rutile TiO_2(110) surface by non-contact atomic force microscopy
Authors: Igor Sokolović, Michele Reticcioli, Martin Čalkovský, Margareta Wagner, Michael Schmid, Cesare Franchini, Ulrike Diebold, Martin Setvín
Journal: Proceedings of the National Academy of Sciences of the United States of America

© European Union, 2002-2021 | http://europass.cedefop.europa.eu

Die approbierte gedruckte Originalversion dieser Dissertation ist an der TU Wien Bibliothek verfügbar.
The approved original version of this doctoral thesis is available in print at TU Wien Bibliothek.
TU WIEN Bibliothek Your knowledge hub

DOI: https://doi.org/10.1073/pnas.1922452117
Short summary: Revisiting several long-standing questions regarding this technologically and fundamentally relevant research topic, and resolving them using state-of-the-art AFM measurements and polaronic DFT calculations.
Contribution: Designed the research, performed the experiments, performed the DFT simulations, performed the AFM simulations, wrote the paper.

Title: Quest for a pristine unreconstructed $SrTiO_3$(001) surface: An atomically resolved study *via* noncontact atomic force microscopy
Authors: Igor Sokolović, Giada Franceschi, Zhichang Wang, Jian Xu, Jiři Pavelec, Michele Riva, Michael Schmid, Ulrike Diebold, Martin Setvín
Journal: Physical Review B 103 (2021): L241406.
DOI: https://doi.org/10.1103/PhysRevB.103.L241406
Short summary: Cleaved $SrTiO_3$(001) surfaces were explicitly shown to be the closest to a pristine, bulk-terminated surface.
Contribution: Designed the research, performed the experiments, wrote the paper.

Title: Charge separation on a nominally centro-symmetric $SrTiO_3$(001)
Authors: Igor Sokolović *et al.*
Journal: *In preparation*
Short summary: Broken inversion symmetry in the near-surface region of the bulk-terminated $SrTiO_3$(001) surface leads to charge separation under UV light.
Contribution: Designed the research, performed the experiments, writing the paper.

Title: Screening-dependent macroscopic properties of cleaved $SrTiO_3$(001) surfaces
Authors: Igor Sokolović *et al.*
Journal: *In preparation*
Short summary: The morphology and the electronic properties of the cleaved $SrTiO_3$(001) surface depend on the concentration of extrinsic Nb-dopants in bulk $SrTiO_3$ single crystals through the availability of the screening charges.
Contribution: Designed the research, performed the experiments, writing the paper.

Title: Universal perovskite cleaving device – applied insights from $SrTiO_3$
Authors: Igor Sokolović *et al.*
Journal: *In preparation*
Short summary: Systematic research on the cleaved $SrTiO_3$(001) surfaces leads to insights in the cleaving procedure, extendable to other perovskites.
Contribution: Designed the research, performed the experiments, writing the paper.

Title: Efficient chemically sensitive AFM contrast simulations
Authors: Igor Sokolović *et al.*
Journal: *In preparation*
Short summary: An introduction of a procedure that realistically simulates AFM contrast by applying as little DFT-derived force-distance curves as possible, but still pertaining the chemical sensitivity.
Contribution: Developed the procedure, writing the paper.

Die approbierte gedruckte Originalversion dieser Dissertation ist an der TU Wien Bibliothek verfügbar.
The approved original version of this doctoral thesis is available in print at TU Wien Bibliothek.
TU WIEN Bibliothek Your knowledge hub

SCIENTIFIC TALKS

Contributed talks:

1 *Resolving the adsorption of molecular O_2 on the rutile TiO_2(110) surface by non-contact atomic force microscopy (nc-AFM)*, April 2021, ACS spring meeting, Online

2 *Adsorption of O_2 on the rutile TiO_2(110) surface revisited by nc-AFM*, March 2020, DPG spring Dresden

3 *Atomic insight into the Adsorption of molecular O_2 on rutile TiO_2(110) (1×1) surface*, July 2019, NC-AFM Conference Regensburg

4 *Atomically-resolved AFM study of the bulk-terminated $SrTiO_3$(001) (1×1) surface*, March 2019, DPG spring Regensburg

5 *Cleaved $SrTiO_3$(001) (1×1) surface studied by non-contact atomic force microscopy*, August 2018, ECOSS Aarhus

6 Four student seminars within the Doctoral School "Solids4Fun"

7 Contributed posters at: DPG 2018 Berlin, NC-AFM Conference 2018 Porvoo, Polarons in the 21st century 2019 Vienna

Die approbierte gedruckte Originalversion dieser Dissertation ist an der TU Wien Bibliothek verfügbar.
The approved original version of this doctoral thesis is available in print at TU Wien Bibliothek.
TU WIEN Bibliothek Your knowledge hub